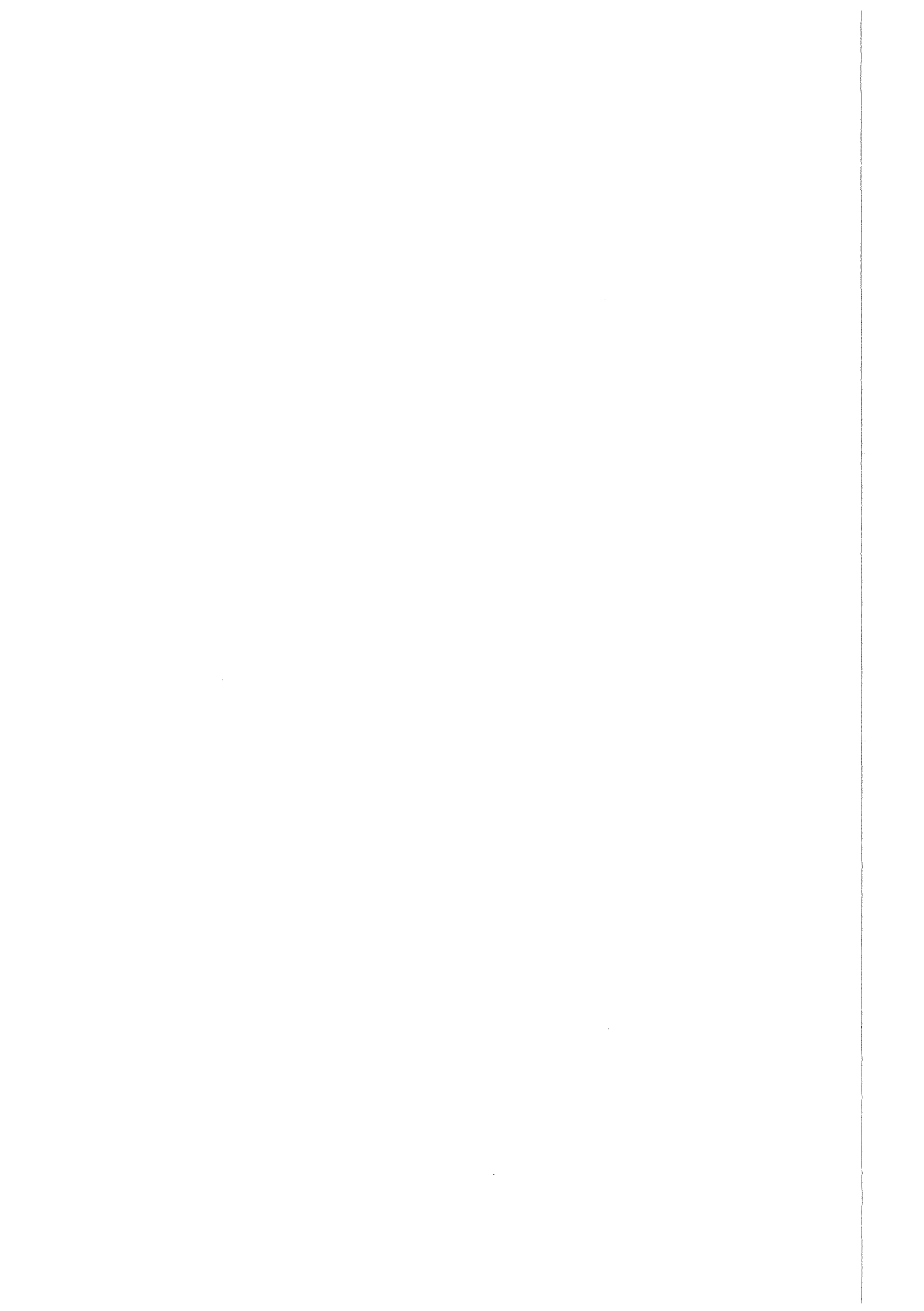


**Forschungszentrum Karlsruhe**  
in der Helmholtz-Gemeinschaft  
**Wissenschaftliche Berichte**  
**FZKA 6696**

**Multidimensional Simulation  
of Hydrogen Distribution and  
Turbulent Combustion in  
Severe Accidents**

**Compiled by U. Bielert**  
**Programm Nukleare Sicherheitsforschung**

**August 2002**



**Forschungszentrum Karlsruhe  
in der Helmholtz-Gemeinschaft**

**Wissenschaftliche Berichte  
FZKA 6696**

**Multidimensional Simulation  
of Hydrogen Distribution  
and Turbulent Combustion  
in Severe Accidents**

**EU-Projekt No. FI4S-CT-95-0001**

**Compiled by U. Bielert**

Programm Nukleare Sicherheitsforschung

**Forschungszentrum Karlsruhe GmbH, Karlsruhe  
2002**

Als Manuskript gedruckt  
Für diesen Bericht behalten wir uns alle Rechte vor  
**Forschungszentrum Karlsruhe GmbH**  
Postfach 3640, 76021 Karlsruhe  
Mitglied der Hermann von Helmholtz-Gemeinschaft  
Deutscher Forschungszentren (HGF)  
ISSN 0947-8620

# Multidimensional Simulation of Hydrogen Distribution and Turbulent Combustion in Severe Accidents

Contract No FI4S-CT-95-001 – Final Report

U. Bielert, A. Kotchourko, A. Veser, W. Breitung,  
P. Royl, W. Scholtysssek <sup>1)</sup>  
H. Wilkening, T. Huld <sup>2)</sup>  
B. Edlinger, C. Poruba, A. Eder, F. Mayinger <sup>3)</sup>  
M. Movahed <sup>4)</sup>  
F. Dabbene <sup>5)</sup>  
E. Studer <sup>6)</sup>

Common report of:

<sup>1)</sup> Forschungszentrum Karlsruhe GmbH, DE

<sup>2)</sup> Joint Research Centre Ispra, IT

<sup>3)</sup> Technical University Munich, DE

<sup>4)</sup> Framatome ANP GmbH, DE

<sup>5)</sup> Commissariat à l'Energie Atomique, FR

<sup>6)</sup> Institut de Radioprotection et de Sûreté Nucléaire, FR

Acknowledgement:

The work performed within this project was supported by EC in the 4<sup>th</sup> Framework Programme.

# **Multidimensionale Simulation von Verteilung und Turbulenter Verbrennung von Wasserstoff in Schweren Störfällen**

## **ZUSAMMENFASSUNG**

Für den Entwurf und die Bewertung eines Wasserstoffkontrollsystems in einem Kernkraftwerk wird eine detaillierte und räumlich hochauflösende Simulation der wichtigsten Phänomene, d.h. des Wasserstoffquellterms, der Gasverteilung, der Zündung und Verbrennung, unter Berücksichtigung lokaler Gasbedingungen benötigt. Das vorliegende Projekt im 4. EU Rahmenprogramm behandelt die Entwicklung und Verifikation von physikalischen und numerischen Modellen, die in multidimensionalen CFD-Codes zur Lösung der allgemeinen Gleichungen der reaktiven Fluid-Dynamik verwendet werden. Das Ziel des gemeinsamen Forschungsprojekts war die Entwicklung von CFD-Modellen für Gasverteilung, für turbulente Wasserstoffverbrennung und für Techniken der Wasserstoffkontrolle, die für die Risikoverminderung in existierenden und künftigen Kernkraftwerken angewendet werden können. Das Arbeitsprogramm umfasste, erstens, einen experimentellen Teil zur Bereitstellung einer geeigneten Datenbasis, zweitens, Modellierungs- und Validierungsaktivitäten und, drittens, eine Demonstrationsrechnung auf Reaktorskala.

Tests in zwei kleinen Versuchsanlagen am Lehrstuhl A für Thermodynamik, Technische Universität München (TUM), lieferten experimentelle Verbrennungsdaten über einen breiten Bereich von Flammenregimes, einschließlich der Wechselwirkung mit Hindernissen. Eine Versuchsanlage auf mittlerer Skala beim Forschungszentrum Karlsruhe (FZK) lieferte Daten im Bereich von schnellen turbulenten Deflagrationen bis zu Detonationen. In inerten Versuchen wurden außerdem die Bedingungen beim Durchgang einer Schockwelle durch Hindernisse untersucht. Zusätzlich wurden großskalige Tests in der RUT Anlage des Kurchatov Instituts (KI) für Modellverifikationen verwendet. Es wurde beobachtet, dass die Verbrennung in trockenen Gasmischungen mit einer Wasserstoffkonzentration von mehr als 10,5 Vol-% vollständig abläuft. Dabei hängen die Ergebnisse nur schwach von dem Abstand der Hindernisse ab. Weiterhin kann man drei Phasen im Verbrennungsablauf unterscheiden: eine anfänglich langsame Beschleunigungsphase wird von einer schnellen Phase abgelöst, schließlich breitet sich die Flamme mit konstanter Geschwindigkeit im Hindernisrohr aus.

In diesem Projekt wurden die Rechencodes COM3D und GASFLOW von FZK, REACFLOW vom Joint Research Centre Ispra (JRC), TONUS vom Commissariat a l'Energie Atomique (CEA) und in CFX4.2 implementierte Modelle von TUM eingesetzt. Die Codes wurden in einem Zweistufenprozess validiert. Zuerst wurden mit jedem Code Standardprobleme sowie verschiedene experimentelle Daten nachgerechnet. Dann wurde ein gemeinsamer Satz von Experimenten analysiert. Diese Benchmarkrechnungen ermöglichen einen direkten Vergleich der numerischen Modelle und ihrer Implementierung. Außerdem wurden Anwendungsrechnungen durchgeführt, nämlich a) eine Simulation mit TONUS von Wasserstoffverteilung und Verbrennung in Vierraumgeometrie, b) Simulationen mit GASFLOW des Battelle Helium Injektionstests Hyjet Jx7 und der Rekombinatorversuche GX6 und GX7, c) Simulationen mit GASFLOW der Wasserstoff-Dampf-Verteilung und Wasserstoffkontrolle bei einem großen Leckstörfall und d) Simulation der turbulenten Verbrennung auf voller Reaktorskala mit COM3D.

Mit neuen Daten von vier verschiedenen Versuchsanlagen wurde die experimentelle Datenbasis in diesem Projekt wesentlich komplettiert. Neben der Verwendung zur Validierung von Rechencodes ermöglichen die Ergebnisse wertvolle Einblicke in die physikalischen Phänomene bei turbulenten Verbrennungsprozessen. Die Anwendungsbereiche der in diesem Projekt verwendeten Verbrennungscodes sind

komplementär. Keines der Programme deckt den vollen Bereich von der Zündung über die Beschleunigungsphase bis hin zur voll entwickelten Detonation ab. Beschränkungen bei den verfügbaren Verbrennungsmodelle und die Notwendigkeit weiterer Validierung erlauben noch keine quantitative Vorhersagen von Containmentlasten unter allen möglichen Randbedingungen. Die Modelle sind aber geeignet, komplexe Wechselwirkungen von Turbulenz und Reaktionschemie auf realistischer Skala in 3-D Geometrien zu untersuchen.

Für praktische Anwendungen auf dem Gebiet der Reaktorsicherheit sind weitere numerische Verbesserungen sowie die Anwendung schneller Rechner notwendig, was die regelmäßige Anwendung der Codes durch Sicherheitsbehörden, Industrie und Forschungseinrichtungen erleichtern und standardisieren könnte. Die verbesserte Vorhersagemöglichkeit lokaler Wasserstoff-Dampf-Verteilungen und von Verbrennungsphänomenen kann dann den Entwurf, die Optimierung und die zuverlässige Bewertung von Wasserstoffkontrollsystmenen wirkungsvoll unterstützen.

# Multidimensional Simulation of Hydrogen Distribution and Turbulent Combustion in Severe Accidents

## ABSTRACT

The design and assessment of hydrogen mitigating systems in a nuclear power plant needs the detailed simulation with high spatial resolution of the major physical processes including hydrogen source terms, distribution, ignition, and combustion, taking into account local gas conditions. The present project in the 4<sup>th</sup> EU Framework Programme deals with the development and verification of physical and numerical models that can be used in multidimensional CFD codes, which solve the general equations of reactive fluid dynamics. The objective of the joint research programme was to develop CFD-models for hydrogen distribution, turbulent combustion, and hydrogen mitigation techniques, which can be applied to risk reduction in current and future nuclear power plants. The work programme consisted, firstly, of an experimental part with tests suitable to provide a data base, secondly, of modeling and validation work, and thirdly, of application of the validated numerical tools to full-scale demonstration cases.

In two small scale facilities at the Lehrstuhl A für Thermodynamik, Technical University of Munich (TUM), experiments provided data over a wide range of flame regimes, including the interaction of the flame front with obstacle configurations. A medium scale test facility at the Forschungszentrum Karlsruhe (FZK) provided data on turbulent combustion in the range of medium fast turbulent deflagrations up to detonation velocity. In inert tests, the conditions after a propagating shock wave through an obstacle path were also investigated. In addition, results of large-scale tests performed in the RUT facility at the Kurchatov Institute (KI) have been used for model verification. It was concluded, that incomplete combustion is not possible for dry mixtures with more than 10.5 vol-% hydrogen and that results depend weakly on obstacle spacing. Further, three phases in the combustion process can be distinguished: a slow acceleration phase is followed by a fast one, later the flame propagates with constant velocity in the tubes with repeated obstacles.

The numerical tools involved in this project are COM3D and GASFLOW at FZK, REACFLOW at Joint Research Centre Ispra (JRC), TONUS at Commissariat a l'Energie Atomique (CEA) and models implemented in CFX4.2 at TUM. The codes were verified in a two-step approach. Firstly, each code was tested against standard test cases and against different experiments. Secondly, the codes were used to calculate a common set of experiments. These benchmark calculations allowed a direct comparison of the different numerical models and implementations. Model applications were a) TONUS simulation of H<sub>2</sub>-steam distribution and combustion in four-compartment geometry, b) GASFLOW simulation of the Battelle Helium injection test Hyjet Jx7 and of Battelle recombiner tests GX6 and GX7, c) GASFLOW simulation of H<sub>2</sub>-steam distribution with mitigation during a large break LOCA and d) full reactor scale turbulent combustion simulation with COM3D

With data from four different facilities, the experimental database, which has been developed within the present project, is unique in its size and completeness. In addition to provide data for the validation of numerical codes, the experiments also provide useful insight into the physical phenomena involved in turbulent combustion processes. The range of applicability of combustion codes used within this project were found to be complementary to each other. While no single code covers the whole area of interesting combustion regimes, a combination of the different codes can describe the whole combustion process from ignition over the flame acceleration regime to fully developed detonations. Limitations of the present combustion models and need for further validation do not allow fully quantitative predictions of the detailed containment loads under all conditions. However, they allow studies of the

complex turbulence/chemistry interaction processes taking place in realistic large-scale 3-D geometry configurations.

For practical safety applications, further numerical improvement and the use of fast computers are desirable. This will allow more frequent and standardized application of the codes by safety bodies, industry and research organisations. The capability of predicting local H<sub>2</sub>-steam concentrations and combustion phenomena will support design, optimisation and reliable assessment of hydrogen mitigation systems.

# Contents

<b>1</b>	<b>Introduction</b>	<b>1</b>
<b>2</b>	<b>Experiments</b>	<b>9</b>
2.1	Theoretical background of experiments at TUM . . . . .	10
2.1.1	Basics of turbulent flows . . . . .	11
2.1.2	Interaction of the flame and the turbulent flow . . . . .	17
2.2	Experimental set-up at TUM . . . . .	23
2.2.1	Measurement techniques . . . . .	23
2.2.2	Experimental set-up of the Glastube . . . . .	28
2.2.3	Experimental set-up of the PHD-tube . . . . .	30
2.3	Experiments at TUM . . . . .	35
2.3.1	Investigation of run-up effects . . . . .	37
2.3.2	Investigation of the turbulent field in front of the flame . .	43
2.3.3	Experiments without obstacles . . . . .	56
2.3.4	Experiments with multi obstacle configurations in the PHD-tube . . . . .	59
2.4	Experimental data from TUM . . . . .	65
2.4.1	Data on run-up effects after ignition . . . . .	65
2.4.2	Data of the LDV-measurements in a single obstacle configuration . . . . .	82
2.4.3	Data of experiments without obstacle in the PHD-tube . .	91
2.5	Inert test in the FZK tubes . . . . .	98
2.5.1	Theory . . . . .	98
2.5.2	Experiments . . . . .	98
2.6	FZK 12m-Tube . . . . .	104
2.6.1	Theory of premixed turbulent combustion . . . . .	104
2.6.2	Experimental details . . . . .	108
2.6.3	Quenching experiments . . . . .	114
2.6.4	Flame acceleration experiments . . . . .	123
2.7	Bibliography of Chapter 2 . . . . .	137

<b>3 Model development and implementation</b>	<b>143</b>
3.1 Equations . . . . .	143
3.1.1 Hydrodynamic . . . . .	143
3.1.2 Turbulence . . . . .	147
3.1.3 Closure and properties . . . . .	152
3.1.4 Chemistry . . . . .	153
3.1.5 The 'presumed PDF' method . . . . .	162
3.1.6 Recombiner models . . . . .	169
3.2 Model implementation and numerical scheme . . . . .	170
3.2.1 Grid definition . . . . .	170
3.2.2 Numerical methods . . . . .	171
3.3 Bibliography of Chapter 3 . . . . .	174
<b>4 Code and Model verification</b>	<b>177</b>
4.1 GASFLOW Code and Model Validation . . . . .	178
4.2 Tonus (Distribution and combustion code from CEA) . . . . .	180
4.2.1 Low Mach number flow solver verification . . . . .	180
4.2.2 Compressible flow solver verification . . . . .	183
4.2.3 Combustion model verification . . . . .	212
4.3 COM3D (combustion code from FZK) . . . . .	219
4.3.1 Test of thermodynamic model . . . . .	219
4.3.2 Flow over forward facing step . . . . .	221
4.3.3 Flow in RRCKI CHANNEL . . . . .	223
4.3.4 Calculations of FZK-tube experiments . . . . .	225
4.3.5 Large scale test in RUT facility . . . . .	228
4.4 REACFLOW (combustion code from JRC) . . . . .	233
4.4.1 Shock tube problem . . . . .	233
4.4.2 Supersonic flow over a forward-facing step . . . . .	234
4.4.3 Shock wave diffraction over a backward facing step . . . . .	234
4.4.4 Code verification for combustion modeling . . . . .	235
4.4.5 Large scale detonation modeling . . . . .	235
4.5 Combustion code from TUM . . . . .	243
4.5.1 Geometry . . . . .	243
4.5.2 Boundary conditions and initialization . . . . .	243
4.5.3 Numerical control . . . . .	245
4.5.4 Combustion simulation . . . . .	246
4.6 Benchmark calculations . . . . .	256
4.6.1 Helium shock tube test as benchmark for the numerical solver	256
4.6.2 Small scale tests in PHD-tube . . . . .	263
4.6.3 Medium scale test in FZK-tube . . . . .	275
4.6.4 Summary of benchmark calculations . . . . .	310
4.7 Bibliography of Chapter 4 . . . . .	313

<b>5 Model application</b>	<b>317</b>
5.1 Model applications from CEA . . . . .	317
5.1.1 Numerical simulation of hydrogen/steam injection . . . . .	317
5.1.2 Numerical simulations of hydrogen deflagrations . . . . .	323
5.2 GASFLOW Analysis . . . . .	327
5.2.1 Introduction . . . . .	327
5.2.2 Distribution: Blind pre-test analysis of the Battelle Hyjet He-Injection Test JX 7 . . . . .	328
5.2.3 Mitigation by catalytic recombiners . . . . .	332
5.2.4 Distribution and Mitigation: 3D analysis of steam/hydrogen distribution in nuclear reactor containments	342
5.2.5 Application of GASFLOW to a Future Evolutionary Containment . . . . .	350
5.2.6 Conclusions . . . . .	356
5.3 Reactor scale turbulent combustion simulation . . . . .	363
5.4 Bibliography of Chapter 5 . . . . .	370
<b>6 Conclusions and recommendations</b>	<b>373</b>
6.1 Experimental investigations . . . . .	373
6.2 Code development . . . . .	374
6.3 Model application . . . . .	378
6.4 Recommendations . . . . .	379
6.5 Concluding remarks . . . . .	381
<b>Annex A - Micro-recombiner model</b>	<b>383</b>



# Chapter 1

## Introduction

Following the nuclear accidents in TMI and Chernobyl, probabilistic risk studies have been performed for various nuclear power plants (NPP) concerning the consequences, in the case of a severe accident, for the environment and for the population in the vicinity. Early containment failure due to hydrogen combustion was identified as a major contributor to potential widespread land contamination. During the recent years a general consensus has been reached among the European safety authorities, vendors, utilities and research organizations, that early containment failure must be excluded on a deterministic basis and that significant accident consequences must be limited to the plant site. This requirement is included, for instance, in the new German Atomic Law for future plants. It is also a principal safety goal in the development of the safety concept of the European Pressurized Water Reactor (EPR) which is presently under design in a common French-German co-operation effort.

In order to enable design and implementation of efficient mitigation systems against the hydrogen risk, a strong need exists for reliable simulation of the major physical processes involved, namely hydrogen distribution in the containment, ignition of the hydrogen/air/steam mixture, the subsequent deflagration process, and flame acceleration due to turbulence effects including the possibilities of deflagration-to-detonation transitions (DDT).

This project aimed at the development of multidimensional, efficient, verified and commonly agreed physical and numerical models for the description of the governing processes in hydrogen distribution and combustion during severe accidents. The main emphasis of the work was on the prediction of accident consequences important for containment integrity, like pressure and temperature loads. The model development addressed also potential hydrogen mitigation techniques, like recombiners and igniters.

The results provide new advanced modeling techniques which can be used for containment simulation work with multidimensional field codes by the industry, safety authorities and research organizations in Europe. Further, an improved understanding of hydrogen combustion loads and of the means for generation

of new load data were obtained. The new physical and numerical models allow improved simulation of the effects of mitigation systems on the accident progression. It is now possible to better optimize mitigation systems on a mechanistic basis, for instance concerning the positioning and distribution of spark igniters in a containment. In this way it is possible to improve the operational safety of existing plants and to optimize mitigation designs for future ones.

The project used CFD tools currently available to the project partners (GAS-FLOW, COM3D, REACFLOW, TONUS, CFX) which allow multidimensional description of the governing phenomena. The overall objective was to further develop and verify physical models and numerical algorithms for the prediction of spatial distribution and of various modes of hydrogen combustion in severe accidents.

With respect to hydrogen distribution, the work concentrated on providing sufficiently accurate results for the spatial hydrogen and steam concentration with specific emphasis on mitigation measures including catalytic recombiners. Further, model development and verification was done in the area of turbulent mixing and transport, wall heat transfer, steam condensation, film re-evaporation, and sump modeling.

In the area of hydrogen combustion, slow deflagrations and fully developed detonations could be predicted with sufficient accuracy, using methods developed under the previous EC programme. Therefore, the project gave emphasis to the complicated intermediate regime of turbulent combustion with flame acceleration due to flow generated turbulence. The work aimed at generating improved physical models and multi-dimensional numerical techniques for turbulence generation and decay, for the chemistry of H<sub>2</sub>-air-steam flames, and for turbulent combustion of premixed gases. The effect of mitigation measures like recombiners and spark igniters was addressed.

The project included the following steps:

- experiments on turbulent combustion,
- improvement of existing models for distribution and combustion,
- development and implementation of new models that were lacking in the codes,
- verification of code predictions against experimental data, and
- demonstration of the applicability of the codes by integral plant analysis.

The project consisted of 4 Work Packages.

### **Workpackage 1: Experiments on turbulent combustion**

Two partners of the consortium, FZK and TUM, conducted harmonized test series in new and existing test facilities. This included visits and short term

delegations when appropriate. The experimental results provide a common pool of data which was used by all partners for evaluation of the various physical models and numerical solution strategies.

Two types of experimental combustion programmes were conducted. The TU Munich used small scale facilities to investigate the detailed structure of turbulent H<sub>2</sub>-air flames with Laser Doppler Velocimetry and Laser Induced Fluorescence diagnostics. In addition, the possible modes for DDT in H<sub>2</sub>-air flames were studied. These programmes focus on understanding of the microscopic processes which determine the evolution of turbulent flames in complex geometries. The very advanced instrumentation of these tests provided important microscopic insights for the model development.

The experiments performed by FZK and by Russian subcontractors investigated turbulent combustion and transition to detonation on larger scales using different facilities: a tube with windows for optical observation of the flame propagation (3.6 m long, 10 x 10 cm wide), the INR tube facility (12 m long, 0.35 m diameter), and the large scale RUT facility (70 m long). The latter is operated by the Russian Kurchatov Institute for the investigation of turbulent combustion and explosion processes. The instrumentation of these facilities provided macroscopic results of the combustion process like pressure loads, flame position, and burning velocities. The INR experiments had some overlapping in scale with the experiments performed at the TU Munich for confirmation. The experimental data from the RUT facility were used to validate codes on full reactor containment dimensions.

## Workpackage 2: Model development

### Computational tools

Development and evaluation of the physical and chemical models were performed within the framework of the computational tools presently existing at the participating organizations.

At CEA/IPSN the system code TONUS is under development which integrates existing versions of TRIO and PLEXUS on the basis of a new common data structure. The numerical method in the TONUS code is based on a finite volume scheme and allows the use of unstructured grids. The code was used as a test environment for the evaluation of various numerical modules describing the governing processes related to hydrogen distribution and combustion.

At FZK, the GASFLOW code was used. GASFLOW uses finite volume numerical methods based on cartesian and cylindrical grids. The code served as a test bed for the implementation and validation of specific H<sub>2</sub>-distribution models, especially for recombiner operation. For turbulent combustion the COM3D code was applied. This code uses a structured grid and an efficient explicit solver. It combines a verified k- $\epsilon$  model with an extended eddy-break-up model.

At the JRC Ispra, the REACFLOW code is under development. It is based on

advanced numerical techniques providing a high resolution of flow discontinuities, if so needed. The code uses unstructured grids and allows a grid adaptation depending on local flow information.

The different computational tools involved in the project allowed the evaluation of various numerical techniques with respect to accuracy, resolution of local phenomena, code stability, robustness, and code efficiency (running times). The sensitivity of the results with regard to the degree of spatial resolution (grid effects) was also investigated.

### Development of physical models

The work concentrated on those processes where models were lacking or which were inappropriate for the analysis of severe accidents.

In the area of hydrogen distribution further model improvement covered the following topics:

- turbulent mixing and transport processes with emphasis on turbulence generation and decay in large, complex geometries
- wall heat transfer and related two-phase processes like steam condensation and film re-evaporation,
- igniters and catalytic recombiners.

A key problem of any combustion code is the description of the turbulent combustion process which requires validated models for two processes:

- chemistry of H<sub>2</sub>-air-steam flames,
- turbulent combustion of premixed gases for a range of flow regimes.

A broad diversity of the model approaches is absolutely necessary in order to identify the most promising approach for the prediction of combustion loads. The work concentrated on semi-empirical, fast-running models which have been bench-marked on a sufficiently wide spectrum of prototypical experiments with realistic mixture compositions (H<sub>2</sub>/air/steam), initial temperatures (300 - 450 K), and initial pressures (1 - 3 bar).

Duplications in model development was avoided as far as possible and practical. The models are of modular structure which allowed easy transfer among the partners and, further, to potential external users.

### Workpackage 3: Model verification

The models for describing distribution and turbulent combustion processes were validated on a number of commonly agreed experiments in order to compare the different numerical tools with respect to accuracy, efficiency and stability. The selected experiments included distribution without mitigation and distribution

with various mitigation measures. Turbulent combustion experiments on different scales were analyzed.

Some of the initially selected tests were analyzed in 2-d approximations to obtain fast results, however the final goal was model verification by analysis of three-dimensional experiments.

#### **Workpackage 4: Model application**

The project used the new validated models for the analysis of distribution and combustion processes in existing and future plants, including a German PWR (Biblis A) and EPR, with the goal to optimize hydrogen mitigation techniques. The potential mitigation measures investigated were catalytic recombiners and spark igniters.

The partners of this project represented together the main activities currently underway in Europe in the field of modeling hydrogen distribution and combustion for reactor safety. Table 1.1 gives an overview of the partners activities in the Work Packages.

The contract for this project started on February 1, 1996. At the kick-off meeting and in two technical meetings at Karlsruhe and at Munich, the project gained significant momentum, and agreement on a more detailed working schedule was obtained. During the early phase of the project, priority was given to the experimental side which was essential in order to provide the data needed for model development and validation. A common test matrix for FZK and TUM experiments was agreed. Significant work was also performed on the modeling and validation fields. In addition, plant specific analysis was started.

Major achievements during the first 12 months period were the installation and upgrading of experimental facilities at TUM, FZK and Kurchatov Institute (RUT facility). Shakedown tests were performed and first experimental series were started. Two RUT experiments, the number agreed in the contract, were completed. Combustion parameters in simple geometries were measured on laboratory scale at TUM. Highly sophisticated techniques as described in section 2.2 provided experimental data on various parameters which are important for modeling and validation.

Modeling efforts were underway for important phenomena including heat transfer, turbulent combustion for a wide parameter range, and numerical simulation of mitigating systems. A turbulent combustion model (Eddy Break-up method) was implemented into the combined lumped-parameter and multidimensional code TONUS. The REACFLOW-code was extended by an axisymmetric solver, including axisymmetric version of the  $k-\epsilon$  equations, and the Eddy-dissipation model for turbulent combustion was implemented. A new version of the GASFLOW code was prepared by merging the FZK version with a version from LANL. Validation was continued by analysis of Battelle recombiner and

Table 1.1: Partners activities in the project's Work Packages

	Activity	FZK	CEA	Ispra	TUM	Siemens
<b>WP0 Project Management</b>						
WP0.1	Scientific coordination	X				
WP0.2	Administrative coordination	X				
<b>WP1 Experiments on turb. comb. and DDT</b>						
WP1.1	3 m tube, FZK	X				
WP1.2	12 m tube, FZK	X				
WP1.3	70 m RUT facility	X				
WP1.4	6 m PHD tube, TUM				X	
WP1.5	6 m Glas tube, TUM				X	
<b>WP2 Model development</b>						
WP2.1	Distribution models					
WP2.2	Turbulence	X	X	X		
WP2.3	Heat transfer	X	X			
WP2.4	Recombiners	X				X
WP2.5	Ignitors	X				X
WP2.6	Combustion models					
WP2.7	Turbulence	X	X	X	X	
WP2.8	Reaction Kinetics	X	X	X	X	
<b>WP3 Model verification</b>						
WP3.1	Distribution models					
WP3.2	Without mitigation	X		X		
WP3.3	With recombiners	X				X
WP3.4	With ignitors	X				
WP3.5	With recomb. and ignitors	X				X
WP3.6	Combustion models					
WP3.7	Turbulence	X	X	X	X	
WP3.8	Turbulent combustion	X	X	X	X	
<b>WP4 Model application for H2 mitigation</b>						
WP4.1	Existing plants	X				
WP4.2	Future plants	X				X

igniter tests. The 3-D version of the COM code was applied to vortex problems and analysis of RUT experiments in order to evaluate the empirical constant  $C_f$  in the EBU combustion model.

During the second 12 months period, experiments at TUM and FZK were continued. According to the agreed test matrix, complementary tests were run on different scales and with different resolution of flame front progression.

At TUM, dismantling and reinstallation of the experimental facilities which were necessary because of movement of the institute to a new site, were used for improvement of instrumentation. Highly sophisticated techniques including high-speed Schlieren photography and Laser-Doppler-Velocimetry (LDV) allowed to resolve the microstructure of flame evolution in complex configurations. Tests to investigate run-up of flames and turbulent flame acceleration with single and multiple obstacle configurations were carried out for a range of H<sub>2</sub>-concentrations.

Several test series in the 12 m tube at FZK addressed various combustion phenomena. Inert tests and tests in lean hydrogen mixtures were run to investigate turbulence generation and dissipation in obstructed geometry with the aim to enable decoupled model development in two steps, first turbulence alone, then turbulence with combustion. Flame quenching was studied in configurations with obstacle arrangements of different blocking ratio and spacing. Concentration boundaries between regions of complete and incomplete combustion were clearly identified.

Test on flame acceleration were performed on different scales. These tests provided the data base to derive conservative criteria for flame acceleration limits and scaling laws for turbulent flame propagation.

On the modeling side, significant effort was put in the improvement of codes. This includes implementation and assessment of solver techniques and application of grid adaption methods in 2d and 3d.

Different reaction kinetics models were implemented in the partners CFD codes. An Arrhenius type reaction rate is used for slow and laminar flames. Eddy-Break-Up (EBU) and Eddy-Dissipation (ED) concepts are used to describe turbulent flames. The different approaches chosen by the partners to derive the governing coefficients were subject of a special workshop held in summer 1997. Modeling activities addressed further topics including sump heating and behavior of safety components. Work was started at Siemens for the development of a micro-model for recombiner behavior. The basic equations were formulated and the boundary conditions were evaluated. Such a model is important to optimize recombiner design and efficiency and to reliably predict recombiner behavior in accident situations.

Code validation continued in various fields on the basis of Battelle tests and on experiments performed by the partners. A turbulence benchmark was specified on the basis of a FZK shock- tube test which simulated turbulent flow ahead of a fast flame. This test was calculated with the FZK codes COM3D, GASFLOW and V3D.

Model application to NPP's were performed for H2-distribution in EPR and to assess mitigation effectiveness in Biblis A and in EPR.

During the last 12 months period, experimental work was successfully completed at TUM by performing combustion experiments in the PHD-tube which cover the full range of combustion modes with flame speeds from several m/s up to detonative cases. Thus the range of applicability of models can now be clearly identified on small scale. In addition to global parameters, turbulence intensities were also obtained using the LDV measurement technique. Also, heat flux measurements were performed with semi-conductors having short response times.

On the analytical side, the effort concentrated on the validation of models and codes, determination of ranges of applicability, numerical improvements and benchmark applications. A significant improvement of combustion modeling was achieved by introducing the Said-Borghi extension into the EBU combustion model. Using this extension, one constant value for  $C_f$ , a free parameter in the model, can be found which allows analytical description of a wide range of combustion modes.

The COM3D code (FZK) has reached a state which gives confidence in prediction of combustion events on a wide range of parameters. An application calculation was performed for a large containment with a weakly stratified atmosphere. It was observed that local turbulence generation significantly influences the progress of flames and the built up of local loads.

The TONUS development activities concentrated on Low Mach Number flow solver validation with non reactive and reactive mixtures on one hand, and compressible flow solver validation with detonation on the other hand. Good results can be achieved with the Low Mach Number flow solver for cases with Mach number  $< 0,3$ .

At TUM, a combustion model based on PDF-formulation was implemented into the CFX-code. A formulation for the momentary reaction rate  $w(c)$  was derived using reaction kinetics programmes.

Detailed studies on different scales were performed at ISPRA to investigate the eddy-dissipation model in the CFD-code REACFLOW. Further, a 3D version of REACFLOW was developed and the applicability of numerical techniques in 2D and 3D were compared.

# Chapter 2

## Experiments

To provide a data basis for the development of combustion models for numerical simulations experiments have been carried out on differently scaled test facilities within this project. In two small scale facilities ("Glastube" and "PhD-Tube") at the Lehrstuhl A für Thermodynamik experiments provided data over a wide range of flame regimes from the laminar reaction phase after ignition, the interaction of the flame front with a single obstacle and the acceleration of the flame by different multiple obstacle configurations up to detonation. The two tubes allow flame diagnostics by means of optical measurement methods. They are equipped with a Laser Doppler Velocimetry set-up for the investigation of the influence of turbulence to the flame propagation and a Schlieren set-up for the detection of the flame shape. The conventional measurement equipment consisting of pressure transducers and photodiodes for the detection of the flameposition is comparable to the instrumentation of medium and large scaled test facilities.

A medium scaled test facility ("12-m Tube") at the Forschungszentrum Karlsruhe provides data on turbulent combustion experiments in the range of semi fast turbulent deflagrations up to detonations and in inert tests the conditions after a propagating shock wave through an obstacle path. The facility is very well equipped with conventional measurement techniques. Large scale tests were carried out in the RUT test facility at the Kurchatov Institute.

The experimental results cover a wide range of flame regimes as well as a wide range in scale. They allow the validation of combustion models, which were developped in this project as well as the detection of the limits of their scope.

## 2.1 Theoretical background of the experiments in the PHD-tube and Glastube at the TU München

It is commonly agreed that both, the origin and acceleration of a fast deflagrating flame is based on different regimes of combustion, which depend on each other (see Fig. 2.19). The first regime of the combustion is a laminar flame around a small ignition kernel. Disturbances lead early, after a short spreading distance, to the formation of flame pockets and in the further course to a turbulent flame. Further introduction of turbulence, e.g. by obstacles in front of the flame, allow the acceleration of the flame by mechanisms discussed in this chapter. Propagation velocities of turbulent deflagrations of 1 m/s up to 1000 m/s can be measured in the experiments carried out in this project.

Typical for fast turbulent deflagrating flames are strong pressure waves, which are released by the flame and form a shock-system in front of the flame. The preceding shock-system modifies the initial conditions for the following flame and lead to a further acceleration of the flame. The shock system is not coupled strongly with the flame and a distance between shocks and flame can be measured (see chapter 2.3.3). Fast turbulent flames are often unstable. If the turbulence entry e.g. due to obstacles vanishes, the shock-system decouples from the flame and the propagation velocity can decrease.

In literature several mechanisms are known, which can trigger a detonation from an initial fast deflagration [Bre88], [Kuo86], [Cha95]:

First, the flame acceleration due to turbulence, generated by obstacles, can end in a quasi-detonation within an obstacle path. The quasi-detonation changes to a regular Chapman-Jouguet detonation after leaving the obstacle path [Bre88]. A second mechanism is the formation of an explosion kernel (or so called "explosion in an explosion") with a center located in the vicinity of the boundary layer due to instabilities [Kuo86].

Third, the formation of a detonation in front of and far away of the combustion zone by the focusing of the leading shock wave by means of obstacles has been shown by Chan [Cha95].

The experimental programme of the Lehrstuhl A für Thermodynamik covered all of the above described flame regimes to generate a wide basis of data for the validation of combustion models in numerical simulations. To cover the laminar flame regime in the early beginning of the flame propagation experiments have been performed in the "Glastube" test facility. To investigate the flame acceleration due to turbulence introduced by an obstacle detailed investigations have been carried out in the PHD-tube. The regime of fast turbulent flames has been investigated with multi-obstacle configurations in the PHD-tube.

This chapter describes the principles of turbulent flows occurring in the relevant combustion regimes and defines the relevant terms to understand the interaction of turbulence and flame and is necessary for the understanding of the experimental outcome. Because of its complexity the problem is split into the view of the non reacting case (Section 2.1.1) and the reacting case, which will be described in Section 2.1.2.

### 2.1.1 Basics of turbulent flows

Characteristical for turbulent flows is the irregularity in time and space. Although each fluid element follows the main flow it follows a random course. The turbulent flow consists of eddies of different sizes, which change consecutively. Considered globally, large eddies disintegrate continuously into smaller ones. The kinetic energy of the eddies is transported through a cascade of different sized eddies until it dissipates to heat.

The turbulent flow is commonly represented with statistical methods. The actual local velocity of each flow component is separated into a moving average value and its fluctuation.

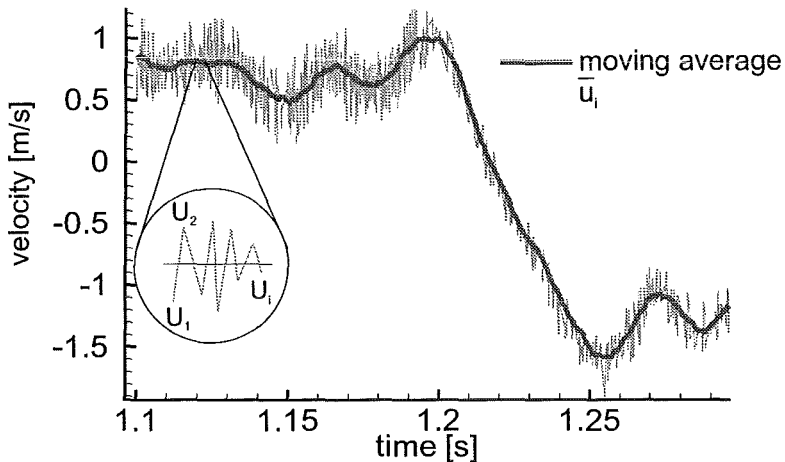


Figure 2.1: Typical turbulent flow trace and its separation into moving average and fluctuation, measured in the PhD-tube in front of a propagating flame.

To quantify the turbulent fluctuation the *turbulence intensity* of the fluctuations is defined by.

$$\overline{u'^2}, \overline{v'^2}, \overline{w'^2}. \quad (2.1)$$

For the unity of all three components of the turbulence intensity in one measurement point the flow is called *isotropic*. For the unity of all three components in

time the flow is called *homogenous*. The widely used numerical turbulence models assume at least isotropic conditions. The following relations assume mostly isotropic and homogenous conditions, which are given in the case of the slow turbulent flows, which are investigated in this experimental programme. In the case of isotropic turbulence the *turbulence number*  $Tu$  is defined by.

$$Tu = \frac{\sqrt{\overline{u'^2}}}{\bar{u}} \quad (2.2)$$

or in general

$$Tu = \frac{\sqrt{\frac{1}{3}(\overline{u'^2} + \overline{v'^2} + \overline{w'^2})}}{\bar{u}}. \quad (2.3)$$

The turbulence number is related to the average velocity of the main flow direction. The turbulence number is a degree for the force of the eddies in the flow [Kuo86]. According to Reynolds [Rey74] the turbulence number can be estimated i.e. behind fine meshed grids  $Tu \sim 1\%$ , near the walls  $Tu \sim 10\%$  and in free turbulent jets  $Tu > 10\%$ .

An important parameter which is widely used in numerical simulations is the *turbulent kinetic energy*

$$k = \frac{1}{2}(\overline{u'^2} + \overline{v'^2} + \overline{w'^2}) \quad (2.4)$$

The knowledge of the fluctuation quantity only is not sufficient for the characterization of the turbulent flow. The dimensions of the eddies have an important influence on the flame propagation. For this reason length scales play an important role for the explanation of the turbulence-flame interaction as shown in chapter 2.1.2. The evaluation of the measured LDV-data is also based on the knowledge of the length scales.

The following list gives an overview over the length scales and their meaning:

- The *macro length scale* describes the largest eddies. The size of these eddies is limited by the confining geometry of the flow. The number of macro scaled eddies is small and, compared to the total kinetic energy contained in the turbulent flow, their energy content is relatively small.
- The *integral length scale* or *Eulerian length scale* describes the size of the characteristic eddies in the flow. The characteristic eddies dominate the turbulent flow. They contain the largest part of the kinetic energy of the turbulence.
- A length scale used for the numerical approach to turbulence is the *micro length scale* or *Taylor microscale*. The micro length scale is used for the estimation of the stress tensor [TeLa87]. The micro length scale is always smaller than the integral length scale.

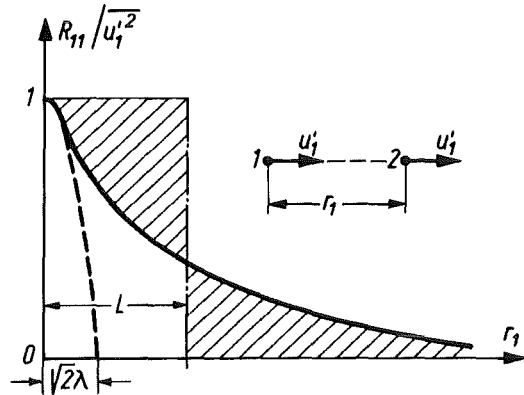


Figure 2.2: Course of the spatial autocorrelation function  $R$  according to Rotta [Rot72]

- The smallest eddies in a flow are of the size of the *Kolmogorov micro scale*. While dissipating the energy of the Kolmogorov microscale eddies is transferred to the thermal energy of the flow.

Each length scale corresponds to an affiliated time scale.

#### 2.1.1.1 Integral length scale

In order to determine the integral length scale, the correlation of the flow fluctuations is determined at two different places in the flow field (spatial correlation). The correlation coefficient is defined as

$$\mathcal{R}_{ij}(\vec{x}, \vec{r}) = \frac{\bar{u}_i'(\vec{x}) \bar{u}_j'(\vec{x} + \vec{r})}{\sqrt{\bar{u}_i'^2(\vec{x})} \sqrt{\bar{u}_j'^2(\vec{x} + \vec{r})}} \quad (2.5)$$

The vector  $\vec{x}$  points at the first measurement point, where the velocity is recorded and  $|\vec{r}|$  is the distance between the first and the second measurement point. In figure 2.2 a typical course of the spacial correlation function over the distance between the measurement points is shown. The integration of the expression in (2.5) leads to the integral length scale

$$L = \int_0^\infty \mathcal{R}(r) dr \quad (2.6)$$

The integral length scale is the characteristical length scale for the turbulent eddies in the flow [Tay35]. In general, the integral length scale can be split into a *longitudinal* and a *transversal* one. The value for the longitudinal integral length

scale  $L_l$  is determined usually by the evaluation of the correlation coefficient  $R_{ij}$  from data of two measurement points which are shifted to each other in main flow direction. If the shift between the measurement points is chosen perpendicular to the main flow and the equation (2.5) is applied to the data, the transversal integral length scale  $L_t$  can be determined. In isotropic flows the relation between longitudinal and transversal integral length scale can be estimated as  $L_l = 1/2L_t$  according to Rotta [Rot72].

$$L_l = \int_0^\infty \mathcal{R}_l(r) dr \quad \text{and} \quad L_t = \int_0^\infty \mathcal{R}_t(r) dr \quad (2.7)$$

Another way to determine the characteristic size of the eddies of the flow is the corresponding time scale to these eddies, the *integral time scale*. The integral time scale can be determined in contrast to the integral length scale with only one measurement device. In analogy to (2.5) the integral time correlation coefficient is defined as

$$\mathcal{R}_E(\tau) = \frac{\overline{u'(t)u'(t+\tau)}}{\sqrt{\overline{u'^2(t)}}\sqrt{\overline{u'^2(t+\tau)}}} \quad (2.8)$$

and the corresponding integral time scale

$$\mathcal{T}_E = \int_0^\infty \mathcal{R}_E d\tau \quad (2.9)$$

For isotropic flows it is possible to transform integral length scale and integral time scale to each other. According to Frost [FrMo77], the Taylor Hypothesis states that, if  $\bar{u} \gg \sqrt{\overline{u'^2}}$ , the fluctuations at a fixed point of a homogeneous turbulent flow with a constant mean velocity  $\bar{u}$  in x-direction behaves as a turbulent field passing that point with a constant velocity  $\bar{u}$ . In this case the fluctuations over the time are nearly identical to the momentary velocity distribution along the mean velocity-axis at this point ("frozen turbulence").

Taylor's Hypothesis implies:

$$\overline{\left(\frac{\partial u'}{\partial x}\right)^2} = \frac{1}{\bar{u}^2} \overline{\left(\frac{\partial u'}{\partial t}\right)^2} \quad (2.10)$$

Due to  $x = \bar{u}t$ , the integral length scale can now be calculated by

$$L_l = \bar{u}\mathcal{T}_E \quad (2.11)$$

With the knowledge of the integral length and time scales other important scales can be derived, as is shown later.

### 2.1.1.2 The Taylor microscale

The Taylor micro scale is determined according to Hinze [Hin59] by:

$$\frac{1}{\lambda_l^2} = -\frac{1}{2} \left[ \frac{\partial^2 \mathcal{R}_l}{\partial r^2} \right]_{r=0} \quad \text{and} \quad \frac{1}{\lambda_t^2} = -\frac{1}{2} \left[ \frac{\partial^2 \mathcal{R}_t}{\partial r^2} \right]_{r=0} \quad (2.12)$$

As shown before, the length scale is split into a transversal and a longitudinal component. The Taylor micro scale  $\lambda$  is a size for the local variation of  $u'$  [Hin59]. Under the assumption that these variations are caused by small eddies in the flow field, the Taylor microscale contains information on these microscale eddies. It is neither a scale for a particular class of eddies nor is it a scale for dissipation, but it is valuable for the determination of the stress tensor

$$s_{xy} \sim \frac{\overline{u'^2}}{\lambda} \quad (2.13)$$

The corresponding time scale is determined in analog to (2.11):

$$\lambda_l = \bar{u}\tau \quad (2.14)$$

### 2.1.1.3 The Kolmogorov microscale

The smallest eddies in a turbulent flow are of the Kolmogorov microscale size. They are responsible for dissipation processes in the flow. They also influence the combustion process strongly, which is shown later. Kolmogorov showed, that the smallest length scales (dissipation length scales) are dependent from the dissipation rate  $\epsilon$  and the kinematic viscosity  $\nu$ . Abdel-Gayed [AbBr81] and Tennekes [TeLa87] showed, that these eddies have the form of long and randomly distributed tubes with a diameter of the Kolmogorov microscale  $l_s$  and the spacing of Taylor microscale  $\lambda$  (see figure 2.3). The Kolmogorov microscale and the appropriate rotation velocity of the eddy is defined as

$$l_s = \left( \frac{\nu^3}{\epsilon} \right)^{\frac{1}{4}} \quad \text{and} \quad u_s = (\epsilon\nu)^{\frac{1}{4}} \quad (2.15)$$

With the knowledge of the Kolmogorov microscale and the velocity of the Kolmogorov micro-eddies an according time scale can be derived:

$$\tau_s = \frac{l_s}{u_s} = \sqrt{\frac{\nu}{\epsilon}} \quad (2.16)$$

### 2.1.1.4 The dissipation rate

An expression for the dissipation rate  $\epsilon$  can be derived from Hinze [Hin59]. Hinze states the kinetic energy of large eddies to be proportional to  $u'^2$  and the energy

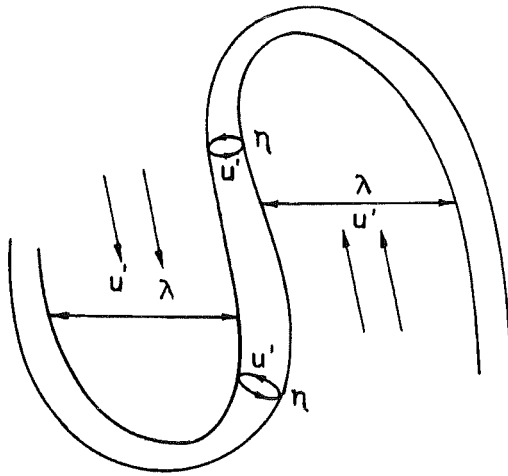


Figure 2.3: Tenneke's model of dissipative eddies according to [Cho79]. The smallest eddies consist of tubes of the diameter of the Kolmogorov length scale  $l_s$  with a spacing of the Taylor microscale  $\lambda$ .

transfer from large to small eddies due to viscosity to be proportional to  $u'/L$ . The energy transferred to smaller eddies is in the order of  $u'^2 u'/L$  and is dissipated under steady conditions by the Kolmogorov microscale eddies with the dissipation rate  $\epsilon$ .

$$\epsilon \sim \frac{u'^3}{L} \quad (2.17)$$

In the case of isotropic turbulence the decrease in time of the turbulent kinetic energy is equal to the dissipation rate

$$\epsilon = -\frac{d\left(\frac{1}{2}\bar{k^2}\right)}{dt} = -\frac{3}{2} \frac{d\bar{u'^2}}{dt} = 15\nu \overline{\left(\frac{\partial u}{\partial x}\right)^2} \quad (2.18)$$

Together with the definition of the Taylor microscale equation (2.18) leads to:

$$\epsilon = 15\nu \frac{\overline{u'^2}}{\lambda_T^2} \quad (2.19)$$

#### 2.1.1.5 Relations between the length scales

The knowledge of the integral length scale is essential for the characterization of the flow. Under the assumptions made before (isotropic and homogenous) all the other scales can be derived from the integral length scale. A relation between the integral length scale and the Taylor microscale can be derived from equation

(2.17) and (2.19)

$$\frac{\lambda_T^2}{L} = \frac{15}{A} \frac{\nu}{u'_{rms}} \quad (2.20)$$

A relation between the integral length scale and the Kolmogorov microscale can be derived from combining equations (2.17) and (2.16)

$$\frac{l_s^4}{L} = \frac{1}{A} \frac{\nu^3}{u'^3_{rms}} \quad (2.21)$$

The factor A is between 0 and 1. Abdel-Gayed et al. [ABL89] determined the value  $40.4 = 15/A$  for isotropic turbulence from experimental data.

### 2.1.2 Interaction of the flame and the turbulent flow

In the past there were many approaches to describe the turbulent flame velocity analytically [Bea94]. The common procedure starts with a laminar flame and superimposes the influence of turbulence. These laminar flame parameters are:

- the laminar flame thickness  $\delta_l$ , containing the pre-heating zone and the reaction zone
- the laminar burning velocity  $s_l$  and
- the chemical reaction time  $\tau_c$

The relation between the three parameters is given by

$$\delta_l = s_l \tau_c \quad (2.22)$$

with the definition of the laminar flame thickness:

$$\delta_l = \frac{a}{s_l} \quad (2.23)$$

with the temperature conductivity  $a = \lambda/\rho c_p$ . Often the Prandtl-number  $Pr = \nu/a \approx 1$  is simplified for hydrogen-air mixtures in literature. This leads to the laminar flame thickness:

$$\delta_l = \frac{\nu}{s_l} \quad (2.24)$$

The interaction of a flat flame front with eddies of different sizes can be seen in figure 2.4. Large eddies only stretch the flame front. They increase the flame surface and contribute in this way to a certain flame acceleration compared to the laminar flame, but they don't increase the mass transport into the flame area. Large eddies lead to a curvature of the flame which can be seen for example in Schlieren images of the propagating flame. The average flame thickness of a hydrogen-air flame is in the order of several micrometer. Compared to the typical



Figure 2.4: Influence of eddies of different sizes to the flame front [Kuo86].

sizes of eddies in the turbulent flow, the flame thickness corresponds to the size of the Kolmogorov micro eddies. These eddies influence the mass transport into the flame front and increase the flame velocity much stronger than larger eddies. If the strength of the Kolmogorov micro scale eddies increase, an intense mixing of the hot gases, produced by the flame and gas in front of the flame can be observed. In these cases a decrease of the reaction rate can be found in experiments. Flame quenching is observed at very high turbulence intensities, which occur e.g. in burning free jets [Jor99].

To classify the turbulent flames it is useful to define dimensionless parameters, which describe the different flame regimes [Bor64]. One important parameter of the turbulent flame propagation is the *Damköhler number*  $Da$ , which is the quotient of the order of the integral time scale and the chemical time scale.

$$Da = \frac{\tau_L}{\tau_c} = \frac{s_l L}{u'_{rms} \delta_l} \quad (2.25)$$

The Damköhler number describes the influence of large eddies on the combustion process. It relates the time in which a large eddy rotates and the chemical reaction time. The reciprocal to the Damköhler number is the *Kovasznay number*, which is also used in literature. For  $Da < 1$  the large eddies disintegrate into smaller ones before they can be burned completely and Damköhler numbers larger than one mean, that the reaction time is faster than the turbulence time scale of large eddies, so the volume of the eddies are burned before they can dissolve into smaller ones.

Another important parameter is the *Karlovitz number* which describes the influence of Kolmogorov scale eddies to the flame structure.

$$Ka = \frac{\tau_c}{\tau_s} = \frac{\delta_l}{s_l} \sqrt{\frac{\epsilon}{\nu}} \quad (2.26)$$

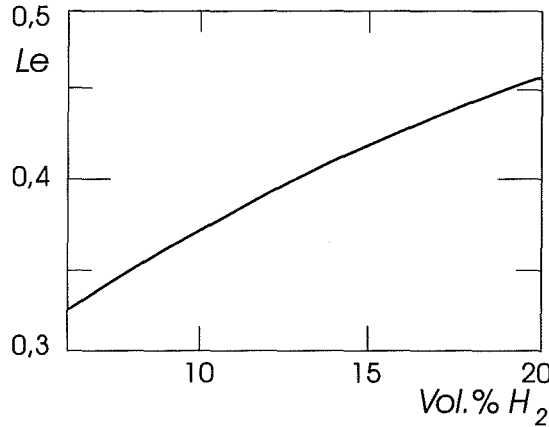


Figure 2.5: Course of the Lewis number of a hydrogen-air mixture dependent on the hydrogen concentration

For Karlovitz numbers larger than one the chemical timescale is larger than the time the Kolmogorov microscale eddies need to rotate around their center. In this case material is transported out of the reaction zone before it could burn out completely and cold gas is transported into the reaction zone. The flame thickness increases compared with the laminar case and the flame itself is quenched locally. For Karlovitz numbers smaller than unity the size of the Kolmogorov eddies is larger than the flame thickness. The reaction zone is not widened by the Kolmogorov microscale eddies.

With the definition of the turbulent Reynolds number, the Damköhler number and the Karlovitz number as well as the estimation  $\nu = s_l \delta_l$  and  $\epsilon = u'_{rms}^3 / L$  the following relations can be posed:

$$\frac{u'_{rms}}{s_l} = Re_L \left( \frac{L}{\delta_l} \right)^{-1} \quad (2.27)$$

$$\frac{u'_{rms}}{s_l} = Da^{-1} \left( \frac{L}{\delta_l} \right) \quad (2.28)$$

$$\frac{u'_{rms}}{s_l} = Ka^{\frac{2}{3}} \left( \frac{L}{\delta_l} \right)^{\frac{1}{3}} \quad (2.29)$$

$$Re_L = Da^2 Ka^2 \quad (2.30)$$

With these relations characteristical lines for  $Re_L = 1$ ,  $Da = 1$ ,  $Ka = 1$  and  $u'_{rms} / s_l = 1$  can be drawn into the phase diagram according to Borghi and Peters and different flame types can be classified. The following flame types can be distinguished:

- wrinkled flames in the area 1

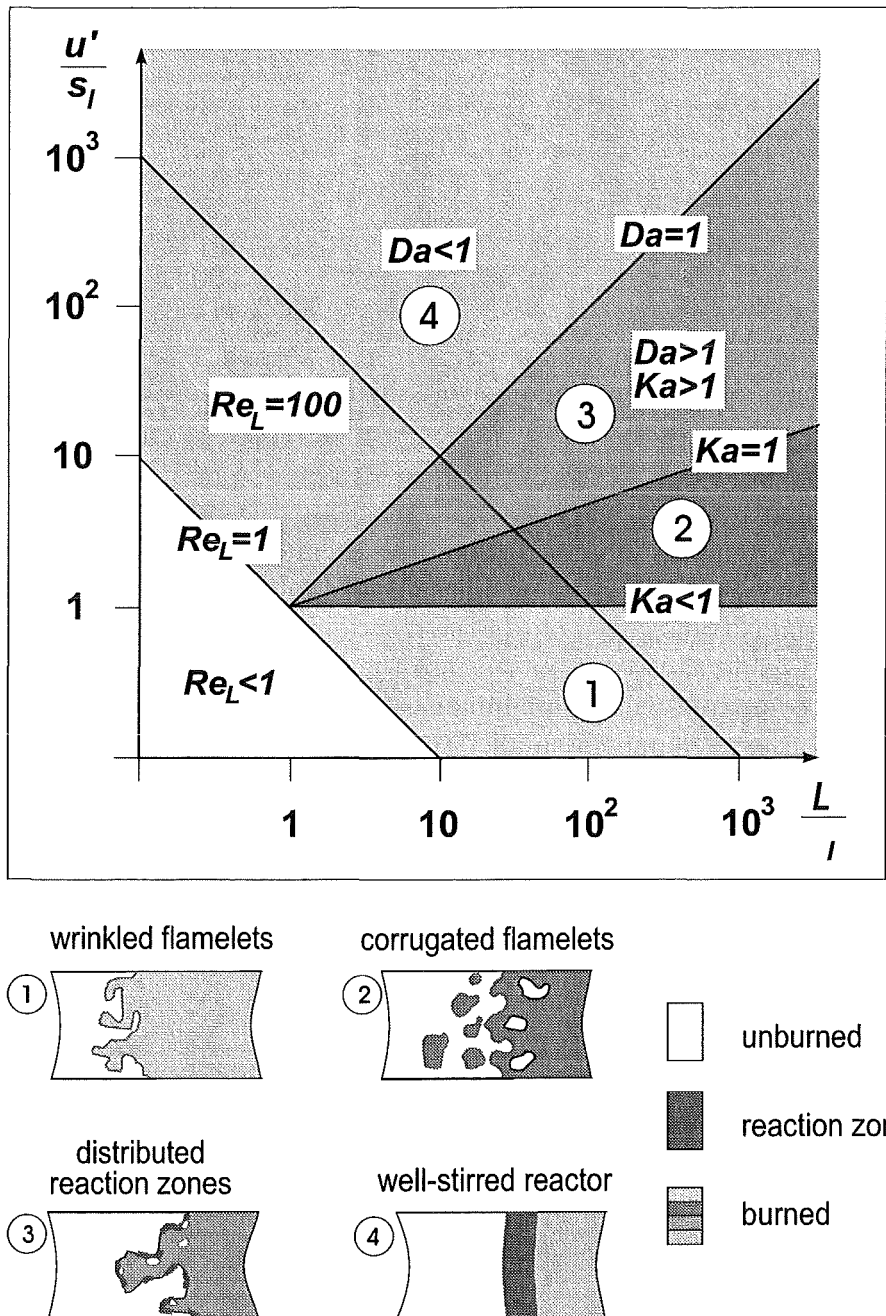


Figure 2.6: Classification of flame regimes for turbulent premixed flames according to Borghi [Bor64] and Peters [Pet86]

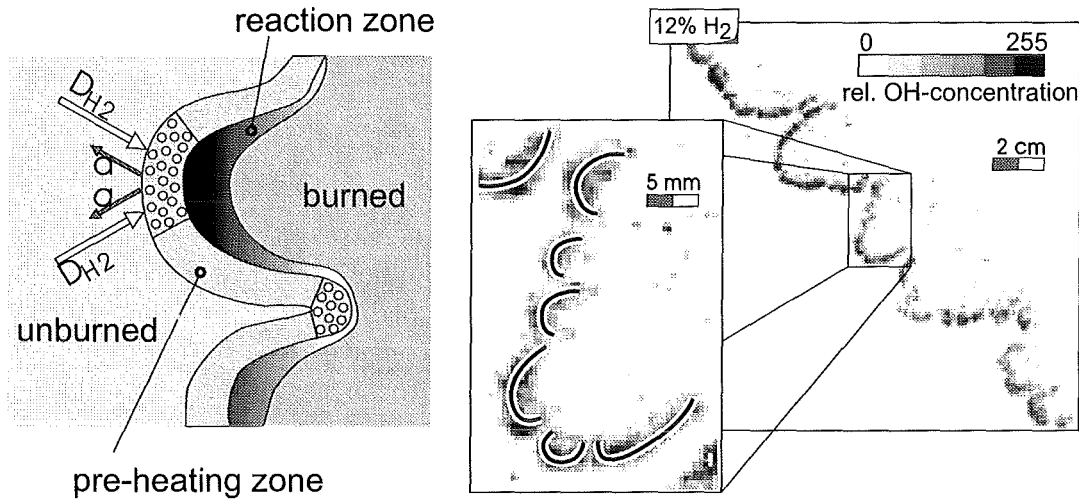


Figure 2.7: Increase of the reaction rate at convex curvatures at the flame due to the dominance of the large diffusion coefficient of hydrogen over the heat conduction to the fuel-air mixture [Ard98].

- folded flames with the formation of pockets in the *corrugated flames* area, area 2
- thick turbulent flames with possible quenching areas and *distributed reaction zones*, area 3
- thick uniform reaction zone in the *well-stirred reactor*, area 4

The laminar flame ( $Re_L < 1$ ) occurs only in some special experiments with very low hydrogen concentrations shortly after ignition (see chapter 2.3.1). The main part of the experiments covers the ranges 0 (laminar flames) to 3 (distributed reaction zones) see chapter 2.3.3.

The areas one and two distinguish themself by turbulence ( $Re_L > 1$ ), existence of a defined flame front ( $Da > 1$ ) and the non-existence of turbulent quenching ( $Ka < 1$ ). In this area the smallest eddies of the Kolmogorov type do not influence the flame front and the flame ideally consists of a laminar thin flame, which is stretched by the characteristic eddies of the flow. For  $u'_{rms}/s_l > 1$  it is possible, that pockets of unburned gas are surrounded by burned gases. The flame consists of many closed burning surfaces.

In the range of  $Ka > 1$  turbulent quenching zones occur. The limit  $Ka = 1$  is in literature often called Klimov-Williams criteria.

In hydrogen combustion the formation of flame curvature and flame pockets is forced by the properties of the hydrogen itself. Depending on the fuel and the concentration of the fuel the fuel-air mixture is influenced by its peculiar constant

of heat transport and diffusion of the limiting reaction partner. This property of the mixture is characterized by its *Lewis number*:

$$Le = \frac{a}{D} = \frac{\lambda}{\rho c_p D} \quad (2.31)$$

For a Lewis number smaller than unity  $Le < 1$  an increase of the reaction rate can be observed at convex curvatures of the flame. The heat loss to the surrounding is smaller than the heat gain of additional heat of burning hydrogen diffusing from the surrounding to the reaction zone. At concave curvatures there is an depletion of hydrogen noticeable because the hydrogen has diffused to adjacent regions and is burnt there. So the flame slows down at concave curvatures and accelerates at convex curvatures (see figure 2.7).

## 2.2 Experimental set-up and measurement techniques at the TU München

This chapter describes the Set-up of the Glastube and the PHD-tube facility. Both are small scale experimental facilities, which allow in addition to their conventional instrumentation, the application optical measurement techniques due to optical accessible sections of the tubes.

### 2.2.1 Measurement techniques

#### 2.2.1.1 Pressure transducers

Depending on the combustion regime two types of pressure transducers were applied to the combustion tubes:

**2.2.1.1.1 Burster resistive pressure transducers** For slow combustion modes resistive pressure transducers have been chosen, because of their capability for the detection of steady state pressures. The 3 applied Burster 8206R20 precision pressure transducers allow the accurate determination of the pressure in the range between 0 to 20 bar. The applied preamplifier has implemented a low-pass filter with a cut-off frequency of 100 Hz. The pressure transducers have been calibrated before the begin of the measurement.

**2.2.1.1.2 Kistler piezo pressure transducers** For the detection of fast transient pressure gradients occurring at fast turbulent deflagrations and detonations 7 piezo pressure transducers, type Kistler 601A, have been applied to the tubes. The signals were processed by an Kistler 5011 charge amplifier. The whole system show a cut-off frequency of 300 kHz and a range between 0 and 200 bar overpressure. The accuracy within the full range is given by the manufacturer with 3%.

In the experiments a strong influence of temperature gradients to the pressure transducers have been observed. To overcome this problem a 0.5 mm silicon membrane has been fixed in front of the sensor for thermal insulation. A direct comparison of two transient pressure signals, with and without silicone membrane, results in the same pressure trace until the flame reaches the transducer.

#### 2.2.1.2 UV-photodiodes

For the detection of the flame position UV-sensitive photodiodes have been applied. Depending on the flame temperature the flame is invisible blue or yellow. This results from the emission spectra of the involved species  $OH$ ,  $O_2$  and  $H_2O$ . The blue emission results from oxygen in the hot flame, the yellow emission results

from steam appearing only at high temperatures, which occurs e.g. in detonations. At lower temperatures the emission of the flame is caused mainly in the infrared area because of the rotational spectra of the steam and in the UV due to OH-radicals, which are an intermediate product of the combustion. [Bre88] The

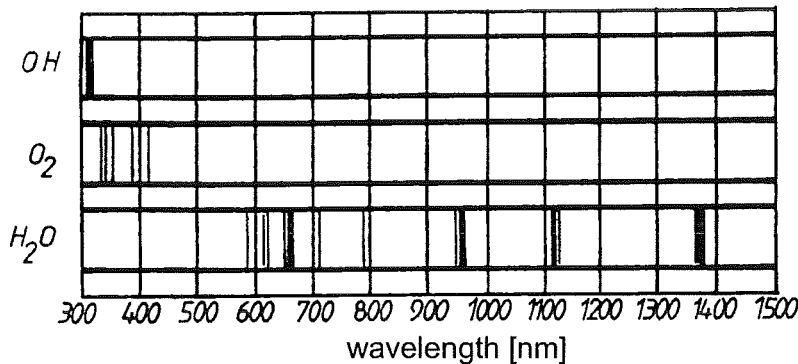


Figure 2.8: Emission spectra of the involved species in hydrogen-air flame [Bre88]

stronger emission in the infrared is easy to detect. However, the disadvantage of detecting this part of the emission spectra is the light emission by hot steam even after the flame has passed the sensor. The flame can not be distinguished from hot burned gases.

The detection of the UV part of the emission is much more difficult because of its small intensity. The advantage of detecting the ultraviolet part of the emission spectra is its close connection to the reaction front. The UV light is emitted only by OH, the intermediate radical of the reaction and follows the reaction front without time delay.

The sensor is a Hamamatsu photodiode S1336-BQ with a sensitiveness in the

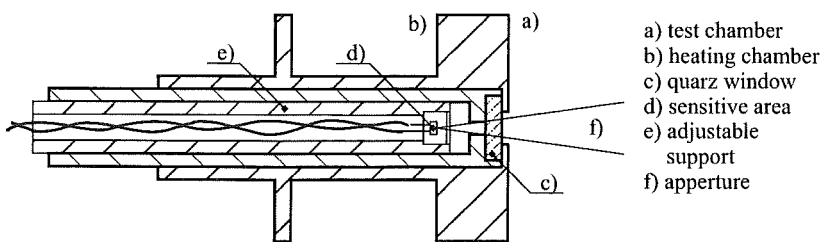


Figure 2.9: Photodiode support with adjustable aperture

spectral range between 190 nm and 1100 nm. The sensor is movable mounted in a steel tube. Its aperture amounts between 1° and 20°. The down-line amplifier was developed at the chair within this project. It allows an adjustable gain between  $10^5$  and  $3 \cdot 10^9$  with a rise time of less than 1 microsecond.

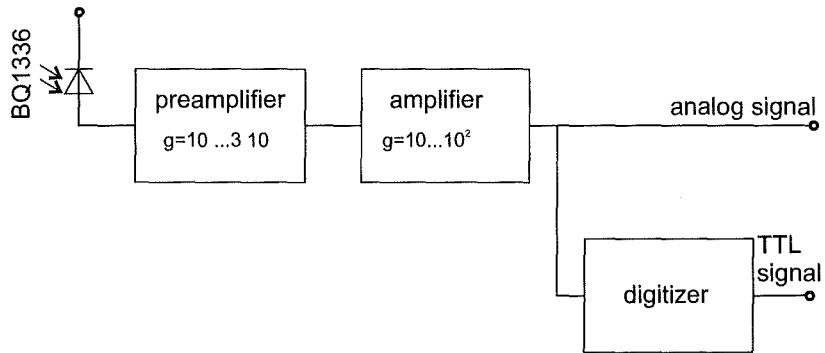


Figure 2.10: Block diagramme of the developed amplifier for the UV-emission signal

### 2.2.1.3 Laser Doppler Anemometry

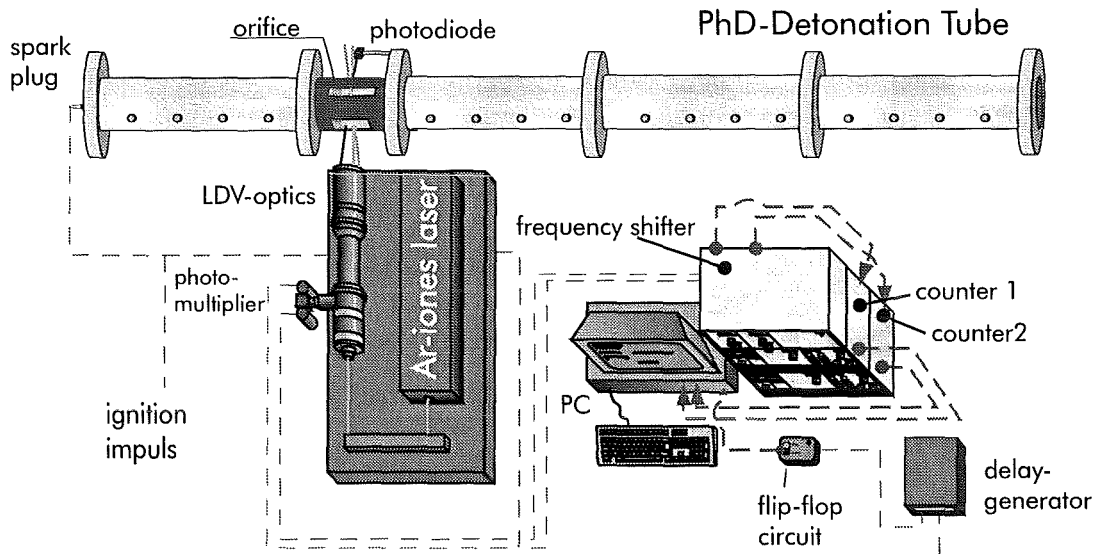


Figure 2.11: Two component Laser Doppler Velocimetry set-up at the PhD-tube.

The measurement system consists of a DANTEC Laser Doppler Velocimeter capable of detecting the flow velocity both in axial and vertical direction. A detailed description of the LDV measurement principle can be found in [DMW87] and [Ruc90] and is not explained here explicitly. A detailed description of the facility can be found in chapter 2.3.3.

The LDV-system has been used in the backscattering mode in order to facilitate traversing between the measurement positions. The optics is mounted on a linear positioning table, which is capable of moving in x,y and z-direction. The

Laser-system consists of a two color Ar-Iones laser with a maximum power of 5W, necessary to achieve a high signal to noise ratio at the low intensities in backscattering mode. The sending optics is arranged in a 3-beam configuration with the two colors of the laser (green 488nm, blue 514.5nm) and the combination of both. The size of the measurement volume is fixed by the focal length of the collecting lens (310mm) and the distance between the beams. It is determined to a diameter of  $90\mu\text{m}$  and a length of  $1.4\text{mm}$ .

For the detection of positive and negative values of the flow a  $40\text{MHz}$  Bragg-cell was mounted to shift the laser wavelength of the two pure colored beams. The scattered light is detected by two photo-multipliers. The Doppler signal is pre-conditioned by a frequency-shifter to adjust the detection range to the expected values for the flow velocities. The frequency detection of the preconditioned signal is done by a counter with a internal clock frequency of  $500\text{Mhz}$ . In order to certify the signal quality the signals are processed only if the internal quality control circuit certifies an accuracy of 1.5% or better. Additional low and high-pass filters improve the signal to noise ratio and sort out doubtful Doppler signals. The data acquisition is done by a personal computer system with two DOSTEC-LDA acquisition interfaces, which allow a maximum acquisition rate of  $100\text{kHz}$  per velocity component. The acquisition system is used with a fixed sampling rate. If no particle passes the measurement volume between two samples the last sampled value is read again. The multiple recorded values are removed in the data evaluation. Because the maximum storable data points, and therefore the recording time with high sampling rates, are limited to 49000 values per channel, the data acquisition starts delayed, related to the ignition to allow a high resolution in time shortly before the flame arrives. The flame arrival time at the measurement volume is detected by a laser light barrier, which uses one of the three laser beams, which form the LDV measurement volume. The flame arrival time has to be detected because the density gradients in the flame bend the laser beams and, therefore, move the measurement volume and no reliable data can be acquired after this event. A second method to detect the flame arrival is the analysis of the data rate of the Doppler signals (see figure 2.28). At the moment the flame passes the measurement volume the data rate decreases significantly and the correct time can be detected.

To measure the flow by Laser Doppler Velocimetry the gas has to be seeded with small tracer particles, which are capable of reflecting the laser light. The requirements to the tracer particles are among others:

- the size of the particles has to be small enough to guarantee a sufficient particle tracking capability
- the particles have to be inert and must not influence the combustion
- to prevent lumping the particles have to be moisture repellent

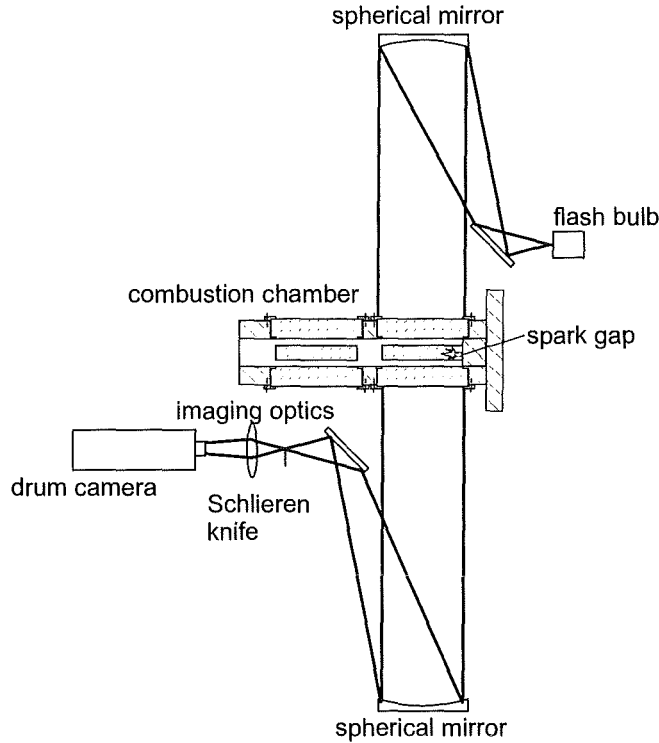


Figure 2.12: Schlieren set-up at the Glastube facility according to Toepler [Toe64] and Schardin [Sch34].

The applied tracer particles are a mixture of titaniumdioxid and Aerosil (small spherical silicadioxid, manufacturer: Degussa) with a volumetric mixture ratio of 1:9. The primary particle size of the rutil type titaniumdioxid particles is  $0.3\mu\text{m}$  according to the manufacturer. Own measurements come to a average particle size of  $1\mu\text{m}$  [DAM97]. A method for the calculation of the particle tracking capability can be found in [Bea94]. In the considered velocity range the particle size is small enough to provide a sufficient tracking to the flow. The applied Aerosil particles with a primary particle size of  $20\text{nm}$  are strongly water repellent and transfer this property to the whole mixture and prevent the agglomeration of particles due to humidity. The seeding is dissolved in air and is transported into the evacuated PHD-tube (the whole filling process is described in chapter 2.3.3). The therefore used amount of air (app.  $50\text{mbar}$ ) is taken into account for the determination of the final hydrogen concentration.

#### 2.2.1.4 Schlieren technique

The optical measurement set-up consists of a Schlieren set-up according to Toepler (see figure 2.12). In this measurement set-up the density gradient between the hot, burned gases and the initial mixture is visualized. Light coming from a

flashbulb is parallelized by the first concave mirror (focal length  $f = 1500\text{mm}$ ). The parallel beam passes the measurement volume and is focused by the second concave mirror. The Schlieren knife is located in the focus of the second concave mirror. If light is bent in the measurement volume due to density gradients perpendicular to the alignment of the Schlieren knife, it is faded out. In the used set-up light bended in the direction of the positive x-axis of the tube appears darker than the background intensity. Deflections perpendicular to the tube axis are not imaged.

To resolve the flame propagation a light exposure system with a high repetition rate is necessary. A flash bulb with a maximum repetition rate of  $10\text{kHz}$  has been used. The maximum number of pulses in one series at this rate is limited to 100, because of the thermal load to the flash bulb. The length of the light pulses is  $1\mu\text{s}$ . By the short duration of the light pulses the flame appears frozen at the moment of the exposure. A drum camera has been used as recording device. At the beginning of the exposure series the shutter of the camera has been opened and each light pulse exposed a part of the photographic material. After finishing the shutter has been closed.

A view of the optical set-up is shown in figure 2.12.

### 2.2.2 Experimental set-up of the Glastube

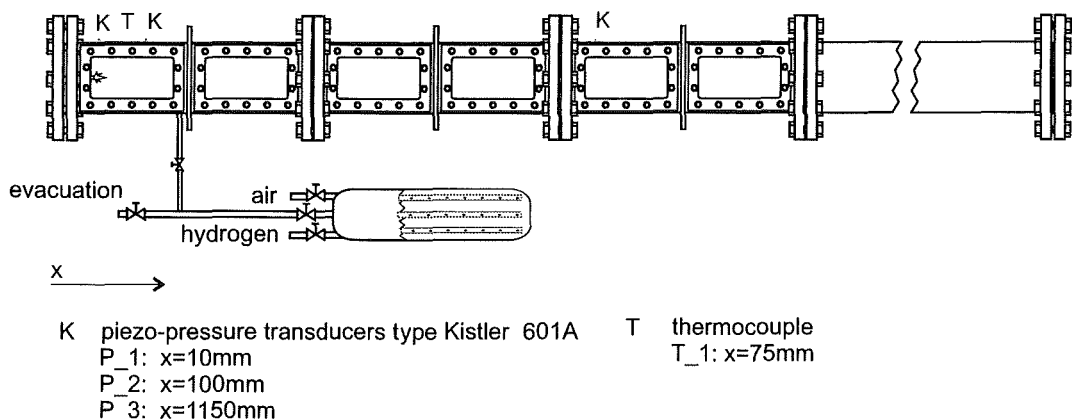


Figure 2.13: View of the Glastube facility including mixture preparation and conventional measurement equipment.

The Glastube consists of 9 exchangeable segments. Five of them can be equipped with windows for optical access. Four segments, mounted at the end of the tube serve as run out volume for the flame. The windows allow full optical access to the cross section of the tube. Due to the special construction of the tube and the windows the windows are mounted without gap to the measurement

volume (see figure 2.14). The combustion chamber has a rectangular cross section with a height of  $100\text{mm}$  and the width of  $60\text{mm}$ . The whole length of the combustion chamber is  $5070\text{mm}$ . The spark gap is located in the center of the end wall of the tube. The flashover of the spark igniter takes place  $10\text{mm}$  from the end wall.

The preparation of the mixture takes place in a separate mixture vessel. The mixture ratio is prepared by the partial pressure method. Before each experiment the tube and the mixture vessel are flushed with air to remove possible rest gases from a preceding experiment. Afterwards the facility is evacuated and the gases are filled into the mixing vessel with the pre-calculated partial pressures. The gases are fed into the mixing vessel by a tube with small holes to intensely mix them. After several minutes for homogenization, the mixture is transferred to the combustion chamber. The mixture preparation has been controlled by the evaluation of several samples, taken along the combustion chamber with a hydrogen concentration measurement device. The measured concentrations differed from the nominal value within the inaccuracy of the measurement device and is lower than  $0.16\text{vol.\%}$ . The tube material is steel and the walls are untreated and can be regarded as fluid dynamically coarse.

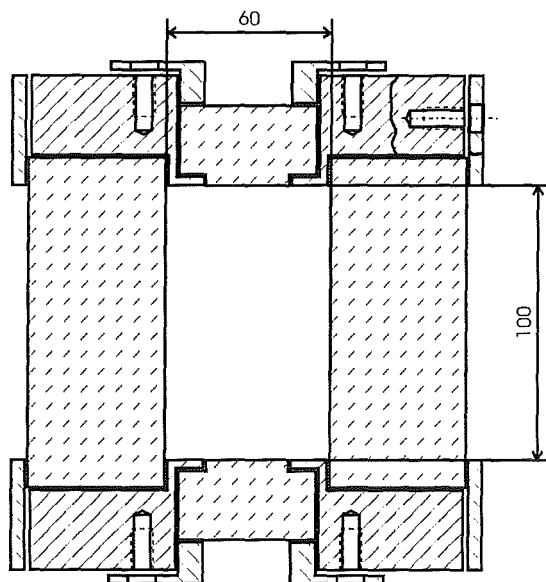


Figure 2.14: Cross section through the combustion chamber of the Glastube facility. Length of combustion chamber:  $5070\text{mm}$ , cross section of combustion chamber:  $100 \times 60\text{mm}$ , size of the windows:  $100 \times 200\text{mm}$ . The windows are mounted plane with the walls.

### 2.2.2.1 Instrumentation

The conventional instrumentation consists of one thermocouple, which is mounted in the visible area of the first window. The measurement position is located at  $x = 75mm$  from the end wall at the upper side of the tube. The pressure is measured at 3 locations with piezo pressure transducers Kistler 601A at the locations  $x = 10mm$ ,  $x = 100mm$ ,  $x = 1150mm$ . Because of the low flame speeds compared to the speed of sound in this measurement campaign no significant difference in the signal of the pressure transducers has been detected.

### 2.2.3 Experimental set-up of the PHD-tube

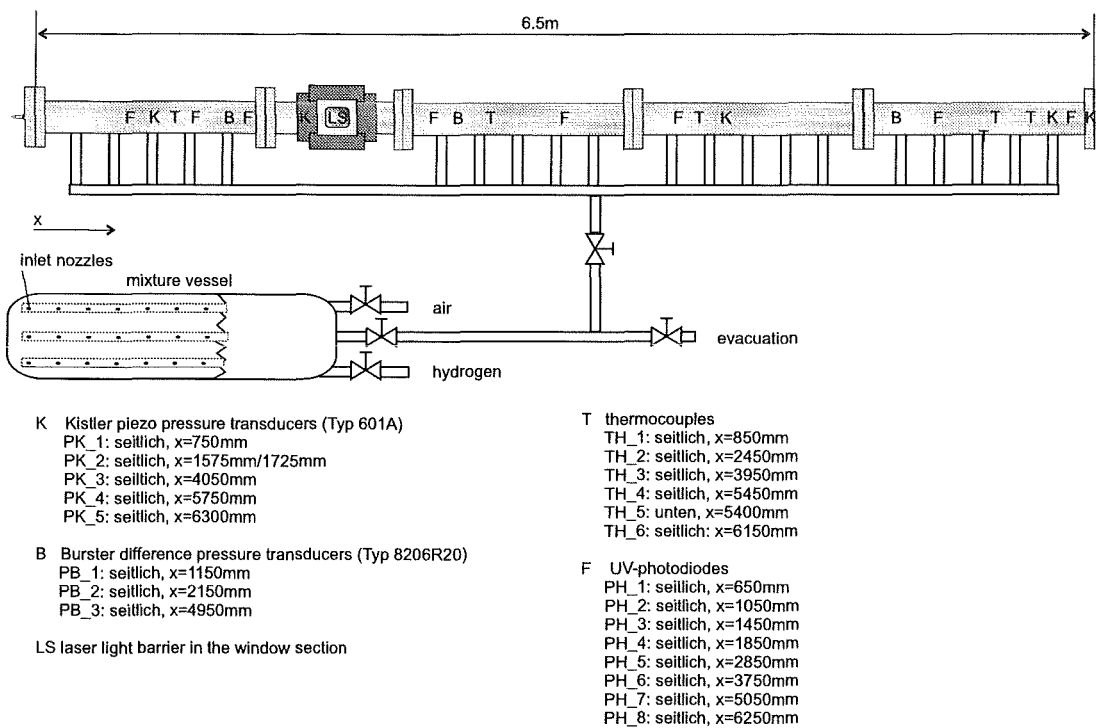


Figure 2.15: View of the PHD-tube test facility.

The combustion chamber consists of four movable segments with a length of  $1.5m$  each and a inner diameter of  $66mm$ . An optically accessible segment with a length of  $300mm$  can be mounted at different locations between the segments. So the length over all amounts  $6300mm$ . Later the optical section has been substituted by a  $500mm$  length section to increase the window size. The adequate length of the tube is given in the data files. The tube consists of high grade steel with a wall thickness of  $11mm$ . The wall at the inner side of the tube is un-worked. The inner wall can be regarded as fluid-dynamical coarse. The segments

have measurement junctions at the top and the bottom and both sides for the connection of measurement transducers such as photodiodes or pressure sensors. The optically accessible section differs from the ideal round shape of the tube. The side windows cause a back step (see figure 2.16). The windows on the top and on the bottom have been filled to reduce the turbulence entry due to the back step, because they were not used for the applied optical measurement techniques. The visible area of the windows was  $50 \times 60\text{mm}$ . Therefore at the top and bottom an area of  $8\text{mm}$  can not be observed. The tube is closed at both ends. The ignition takes place at one end flange by a sparkplug with one single spark.

To improve the reproducibility of the experiments special emphasis has been

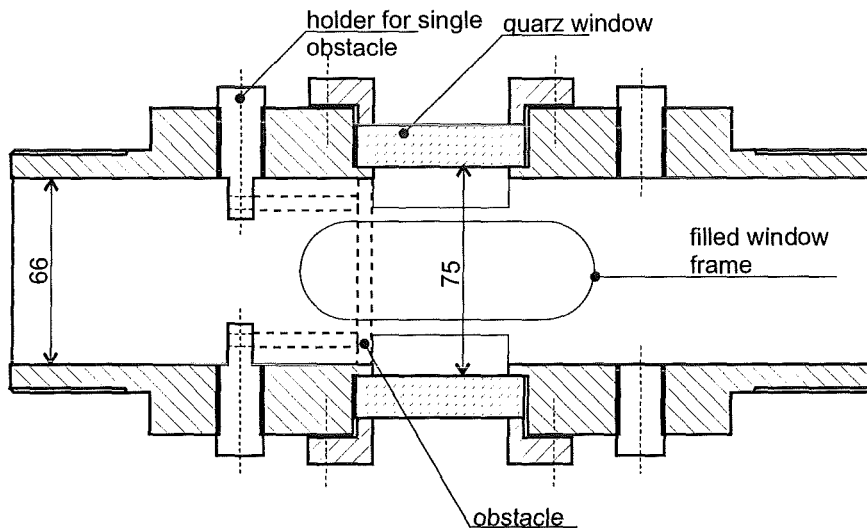


Figure 2.16: Cross section of the optically accessible segment.

spend to the filling procedure of the tube. Especially in lean hydrogen mixtures small differences in the hydrogen concentration as well as inhomogeneities in the mixture cause large effects to the flame propagation. A mixture preparation installation has been developed to keep the mixture composition within exact limits.

The mixture composition is prepared by the principle of partial pressures in an external mixture vessel. Before each experiment the vessel and the facility are flushed with air to dilute possible rest gases from the previous filling. After the evacuation of the whole facility the external mixing vessel is filled with the pre-calculated amounts of hydrogen and air by means of nozzles along tubes inside the mixing vessel. The nozzles lead to an intensive mixing of the components. After filling each component the exact partial pressure is measured by an high quality pressure transducer. The homogenized mixture is lead over to the combustion chamber. It enters through 20 nozzles, which are distributed along the

tube. After the filling procedure a delay of 5 minutes is performed to tranquilize the mixture. The concentration has been controlled in the range between 0 vol.% $H_2$  and 4 vol.% $H_2$  at several positions along the tube. The scheduled value of the concentration has been reached at all points within the error range of the measurement device of 0.16 vol.% $H_2$  absolute. The obstacles consist of round shaped orifices according to figure 2.17. They are connected to each other and fixed within the tube by 3 threaded rods. the thickness of the obstacles amounts 5mm.

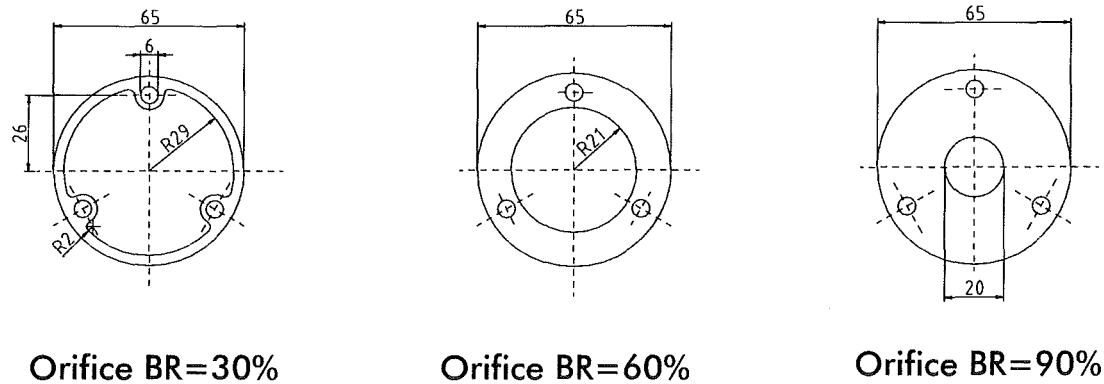


Figure 2.17: Different obstacles implemented in the PHD-tube with blockage ratios of 30%, 60% and 90%. The obstacles are fixed in the tube with 3 threaded rods.

### 2.2.3.1 Instrumentation of the PHD-Tube

The conventional instrumentation consists of 16 UV-sensitive photodiodes and 6 piezo-pressure transducers along the tube. The exact locations can be taken from tables 2.2 and 2.1. The sensors are described earlier.

To visualize the flame shape and the shock system in front of the flame at high propagation velocities a Schlieren set-up analogous to the set-up described in chapter 2.3.1 have been implemented. Different from the earlier described set-up a Kodak high speed video camera has been used as recording device. The camera allows recording frame rates up to 40.500 pictures/s with reduced resolution. To provide a good quality of the images the maximum applied frame rate has been adapted to the actual needs. For very fast propagating flames even the highest frame rate is to slow to record a series of pictures, while the flame passes the window. In this cases the recording of a image series has been abandoned and a single image has been taken with a high resolution PCO CCD camera. Because the repetition rate exceeds the allowable values of the flashbulb when using the Kodak video system the light source is changed to an argon-iones laser in connection with an acousto optic modulator to switch the continuous light

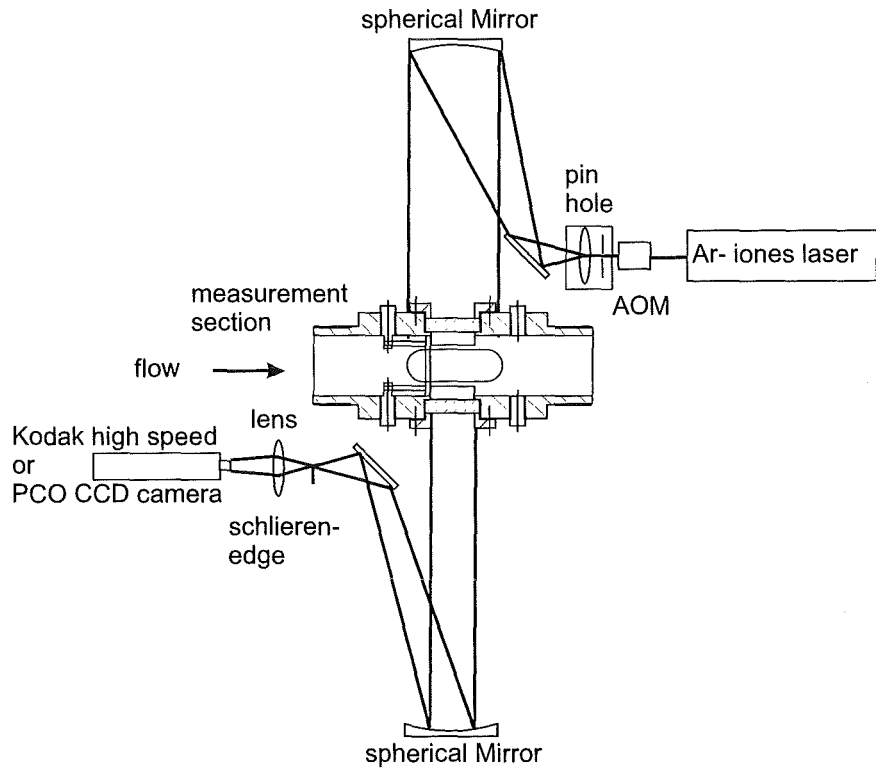


Figure 2.18: Modified Schlieren set-up for higher repetition rates.

beam of the laser. The exposure time of this arrangement amounts  $500\text{ns}$  and the repetition rate is not limited. Figure 2.18 gives a view of the changed set-up.

photodiode	position mm
F1	250
F2	650
F3	1050
F4	1450
F5	1750
F6	2150
F7	2550
F8	2950
F9	3550
F10	3950
F11	4350
F12	4750
F13	5250
F14	5650
F15	6050
F16	6450

Table 2.1: Locations of the photodiodes

pressure transducer	position mm
P1	1150
P2	2250
P3	3050
P4	4250
P5	5550
P6	6500

Table 2.2: Locations of the pressure transducers

## 2.3 Experiments on turbulence and turbulent combustion in the Glastube and the PHD-tube

The common idea of the origin and acceleration of a fast deflagrating flame is based on different regimes of combustion, which depend on each other. The first stage of the combustion is a laminar flame around a small ignition kernel. Disturbances lead early after a short spreading distance to the formation of flame pockets and in the further course to a turbulent flame. Further introduction of turbulence, e.g. by obstacles in front of the flame, allow the acceleration of the flame by mechanisms discussed in chapter 2.1. Propagation velocities of several hundred up to 1000m/s can be measured in the experiments carried out in this project.

Typical for fast turbulent deflagrating flames are strong pressure waves, which

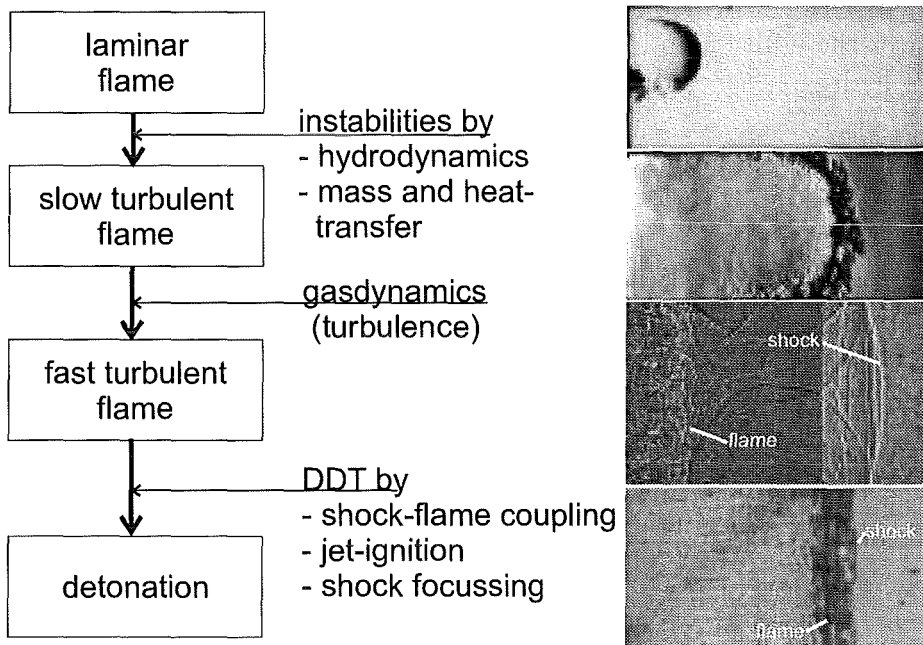


Figure 2.19: Description of the different stages in the live of a flame. Pictures are taken from PHD-Tube and Glastube experiments

are released by the flame and form a shock-system in front of the flame.

The preceding shock-system modifies the initial conditions for the following flame by heating up the unburned gases and improves the conditions for the following flame. The shock system is not coupled strongly with the flame and a distance between shocks and flame can be measured (see chapter 2.3.3). Fast turbulent flames are often not stable. If the turbulence entry due to obstacles

vanish, the shock-system decouples from the flame, the propagation velocity can decrease.

In literature several mechanisms are known, which can trigger a detonation from an initial fast deflagration [Bre88], [Kuo86] and [Cha95]: The flame acceleration due to obstacles can end in a quasi detonation within the obstacle path. The quasi-detonation changes to a regular Chapman-Jouguet detonation after leaving the obstacle path [Bre88]. A second mechanism is the formation of an explosion kernel (or so called "explosion in an explosion") with a center located in the vicinity of the boundary layer due to instabilities [Kuo86]. The formation of a detonation in front of and far away of the combustion zone by the focusing of the leading shock wave by means of obstacles has been shown by [Cha95].

The experimental programme of the Lehrstuhl A für Thermodynamik covered all of the above described flame regimes to generate a wide basis of data for the validation of numerical simulations with different combustion models. To cover the type of problems in the early beginning of the live of a flame experiments have been performed in the "Glastube". They cover the range of the laminar flame after the ignition and the change to turbulent flame propagation in a wide range of hydrogen concentrations between 9Vol.% and 16Vol.%. The Glastube is constructed for a non obstructed view to the entire cross section for optical measurement methods. High speed Schlieren cinematographs show clearly the course of the flame within the first 500mm after ignition. Several effects can be studied by the evaluation of the Schlieren-photographs, such as the transition from laminar to turbulent flame surfaces, the influence of buoyancy and experimental effects to the flame like the "tulip-flame" phenomenon.

A wide variety of experiments have been performed in the PHD-tube and many relevant combustion regimes have been observed. Different experimental configurations by changing the obstacle path as well as the initial conditions led to a large range in the observed flame velocities.

Measurements without obstacles lead to the lowest deflagration velocities, which are possible for the applied boundary conditions and serve as comparison for the turbulent flame acceleration by obstacles. Hydrogen concentrations between 9.9% and 16% were considered.

A single obstacle Configuration has been investigated in detail with LDV and Schlieren-technique to study the influence of turbulence to the flame propagation.

Multiple obstacle configurations multiplied the effect of the single obstacle and led to much higher velocities up to detonation. The data serves mainly to validate the global behavior of the combustion models. Extensive conventional measurement technique delivers pressure traces at seven measurement points along the tube, where the build up and spreading of the shock system in front of the flame is monitored. Sixteen photodiodes mounted along the tube deliver exact position traces of the flame. Additional Schlieren images have been taken to visualize the flame and the shock system after the obstacle path.

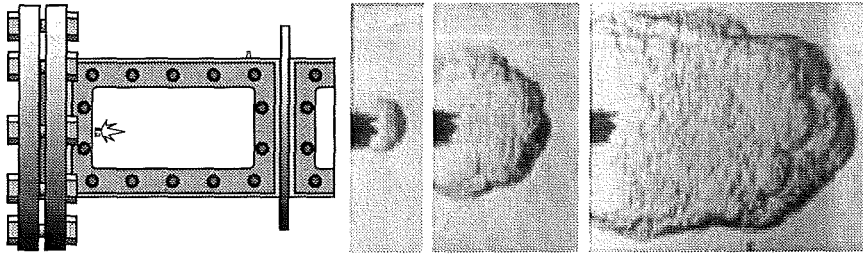


Figure 2.20: Laminar phase of a flame after ignition and transition into a slow turbulent flame in the Glastube. Initial hydrogen concentration: 13.2 vol. %.

### 2.3.1 Investigation of run-up effects

The laminar first stage of the flame and its transition into a slow turbulent flame have been visualized in this part of the experimental programme. The experimental outcome is suited to validate ignition models in numerical codes as well as the regime of slow turbulent flames. The main emphasis of this investigation has been spent to the 2-dimensional determination of the flame position and flame shape by means of high speed Schlieren cinematography. The combination of the high resolution in space and in time allows a deeper insight into the phenomena occurring in the transition from the laminar to turbulent flame regime.

The investigated range covered 9 vol. % to 16 vol. % hydrogen in air at ambient conditions (initial pressure 1 bar, initial temperature 20 °C). The measured flame velocities range from 0 m/s to 25 m/s

#### 2.3.1.1 Laminar propagation after ignition

The flame propagation after ignition in a still fuel-air mixture is laminar. Early, depending on the fuel concentration, perturbations of the originally smooth flame surface can be detected (figure 2.20). The laminar phase of the flame can be described by a diffusion based burning model e.g. according to Frank-Kamenetskii and Zelodvich [Kra96]. The flame is described by a thin reaction zone and a comparably large pre-heating zone in front of the flame. The complete process is dominated by mass diffusion and thermal conduction (see figure 2.21).

#### 2.3.1.2 Instability mechanisms

Different instability mechanisms lead to cracks in the spherical flame surface and ends up in a cellular structure of the flame. Darrieus and Landau [Dar41] described a gas dynamic instability mechanism leading to the amplification of convex structures in the flame. Following the streamlines of the flow through a

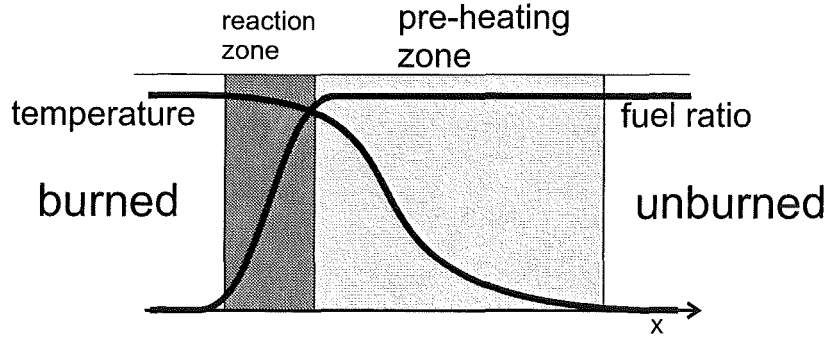


Figure 2.21: Laminar combustion model according to Zeldovich and Frank-Kamenetskii. Courses of the temperature and the fuel content of the mixture.

flame one can find, that in the burned gas the flow after the flame is perpendicular to its surface (figure 2.22). The incoming flow, however, has a tangential to the flame directed velocity component, leading to the formation of vorticity and amplifying the convexity of the flame surface. The Landau instability mechanism is independent from the mixtures composition.

Another mixture dependent instability mechanism is based on the heat and mass transfer in front of the flame. Mixture compositions with low Lewis numbers, such as lean hydrogen mixtures tend to increase the convexity of the flame surface. Initially existing convex structures lead to an increasing heat transfer to the unburned gas and causes heat losses to the flame. But because of the high diffusivity of hydrogen additional hydrogen is transported to the convex shaped flame. This mass transport overbalances the heat losses and leads to an amplification of the convex structure (see also chapter 2.1.2). Both mechanisms lead shortly after ignition to a cellular structure of the flame, therefore increasing the velocity fluctuations in front of the flame and lead to additional turbulence. The turbulence generating characteristic leads to a feed back mechanism, which accelerates the flame further.

In figure 2.47 with a hydrogen concentration of 9.2 vol.-% the flame surface appears smooth on the Schlieren image and the flame forms out in the further propagation only large scale convex structures (figures 2.47 and 2.50). With increasing hydrogen concentrations the laminar start-up phase of the flame gets shorter and the structure of the flame balls gets finer (figures 2.50, 2.55, 2.65 and 2.72).

### 2.3.1.3 Buoyancy

In mixtures with low hydrogen concentrations buoyancy effects outweigh the flame propagation in tube direction at the beginning. Like shown in figure 2.47 the flame forms, after ignition, a spherical shape, which is driven upwards by the

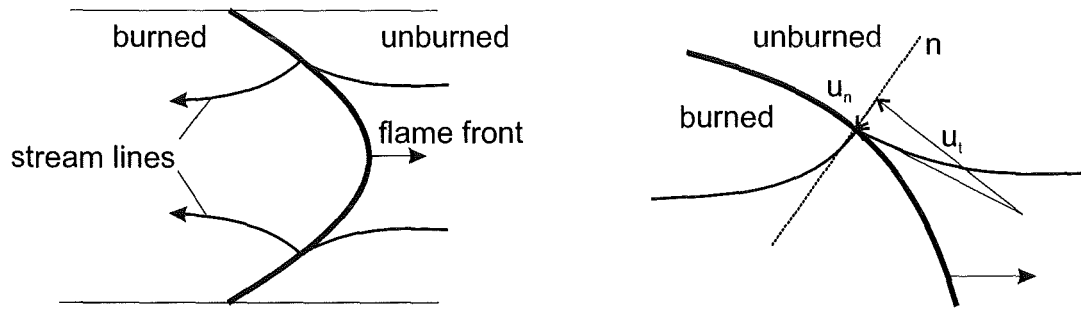


Figure 2.22: Amplification of convex structures of a flame according to Darrieux and Landau [Dar41]. A tangential component of the approaching flow to the flame leads to vorticity and the amplification of convex structures. On the left: global view of the streamlines of the flow through a flame. On the right: the tangential component of the incoming flow leads to a resulting vorticity.

buoyancy and leads to a flame, which propagates at the top wall of the tube. The influence of buoyancy decreases with rising hydrogen concentrations. With a concentration of 13 vol.-% hydrogen the flame is symmetric to the tube and the influence of buoyancy is vanished.

#### 2.3.1.4 Acoustic oscillations

In the further progress strong oscillations in the flame propagation can be observed. This oscillations in confined burning volumes and lead to a so called "tulip flame". The initial convex shaped flame increases its curvature and degenerates to a straight line. In this status the flame comes to a standstill related to the laboratory system. Subsequently a concave tulip-shaped indentation is formed by the flame, which can have a negative velocity back into the burned gases. After forming the tulip-shape the flame accelerates again and adopt the original convex curvature. In the Schlieren photographs the dynamics of this process can be studied (figure 2.23). According to Gonzalez et al. [Gon92] the geometrical requirements for the formation of a tulip flame is an exceeding ratio of length to diameter of 2. In both applied explosion tubes this ratio is largely exceeded (PHD-tube 95.5, Glastube 57.5). In both tubes the formation of a tulip flame has been observed under certain experimental conditions. The appearance of a tulip flame depends according to Guenoche [Gue64] on many parameters, such as initial pressure, diameter to length ratio, fuel concentration and geometric boundary conditions (e.g. open or closed tube).

The phenomenon is early known in literature and first examinations were performed on the problem (e.g. Ellis [Ell28]). Because of the complexity of the whole process many explanations have been given, but all of them cover only

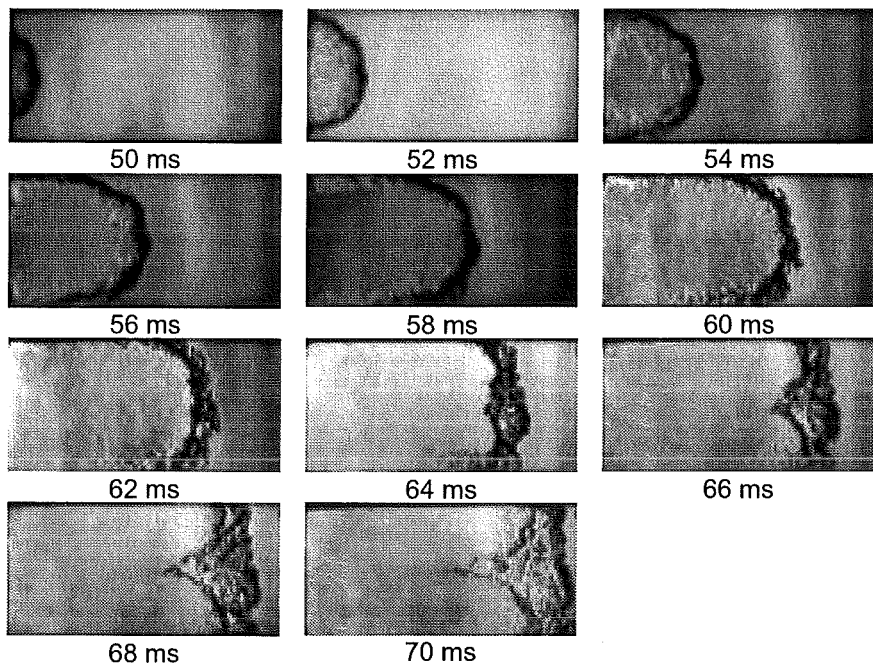


Figure 2.23: Schlieren film of the formation of a tulip flame in the Glastube. Experiment G39, 14.8 vol% hydrogen,  $p_0 = 1046 \text{ mbar}$ ,  $T_0 = 23.2^\circ \text{C}$ .

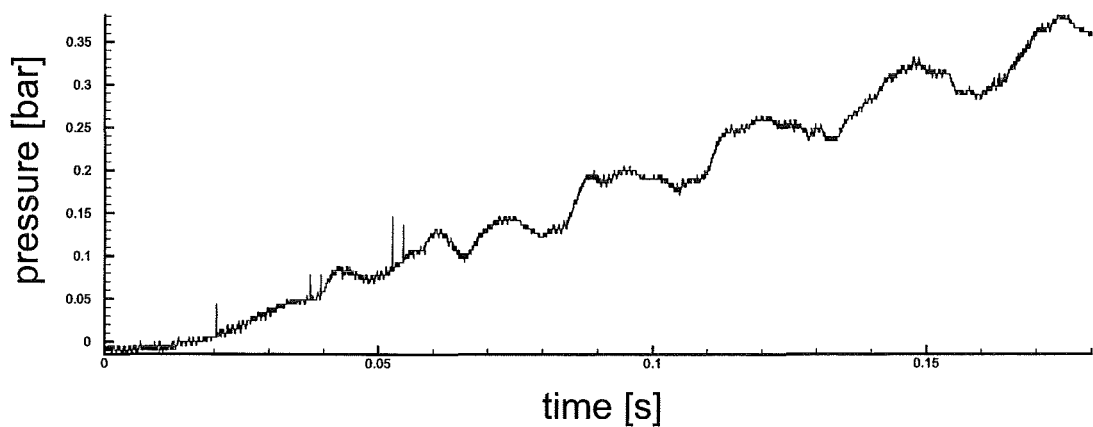


Figure 2.24: Pressure record of experiment G39. Harmonic oscillations can be observed in the pressure record, caused by the tulip flame

partially the development and the propagation of a tulip flame. Possible causes are quenching and viscosity [Ell28, Lew61], formation of vortices in the burned gas [Opp83, Dun85], interaction of pressure waves and flame [Gue64, Mar64], or fluctuating mass and heat transfer due to the changing flame surface [Sta86]. Gonzalez shows in his detailed theoretical consideration of the phenomenon, that the formation of the tulip flame has different explanations depending on the pre-conditions.

The initial conditions in both explosion tubes are comparable to those of Starke and Roth [Sta86] in their experimental investigations and those of Gonzalez in his numerical work. In this case a tulip flame can develop only after the flame attaches to the walls. This observation corresponds to the results of this investigation, where the tulip flame is formed only after reaching the second window and attaching to the walls.

The whole process is shown in figure 2.25. In the early stage of the combustion process in the upper left image the flame does not touch the walls and can freely propagate to all directions. The unburned gases are pushed before the flame in the whole cross section. As shown in figure 2.25 a complex flow field is formed in front of the flame. Because of the density decrease and the volume increase by the heat production of the flame a flow field vectored always perpendicular to the flame surface is generated behind the flame. The burned gases produced by the side part of the flame additionally boost the horizontal propagation of the flame, because a vertical component is prevented by the walls.

After 400 time steps in the calculation the flame attaches to the walls. The flow field establishes two symmetrical eddies. The flow component in the center of the tube superimposes with the flow components of the eddies and produce a backward directed flow in the center of the tube. The middle part of the flame decelerates, but the main flow is still directed into the original propagation direction. At this time the horizontal velocity component near the wall excel the velocity in the center.

This condition is enforced in the further progression (lower left). The flame is nearly plane and the flow velocity in front of the flame is very low, whereas behind the flame a further increase of the backward directed flow component can be observed. In the outer regions there is a large horizontal velocity component into the direction of flame propagation. The flame itself decelerates strongly because of the reduced flame surface.

After 2000 time steps the tulip shape flame is formed completely. The flame surface increases again and therefore the heat production increases, too. Along the whole flame front a flow field perpendicular to the flame surface can be observed in the burned part. The flame is moving again to the left and the concavity in the middle of the flame is reduced. Later the original convex shaped flame is restored and the primary propagation conditions are reached again.

In long tubes the tulip flame phenomena occurs only in the middle part of the tube. After a run-up distance harmonic oscillations are formed, which decrease

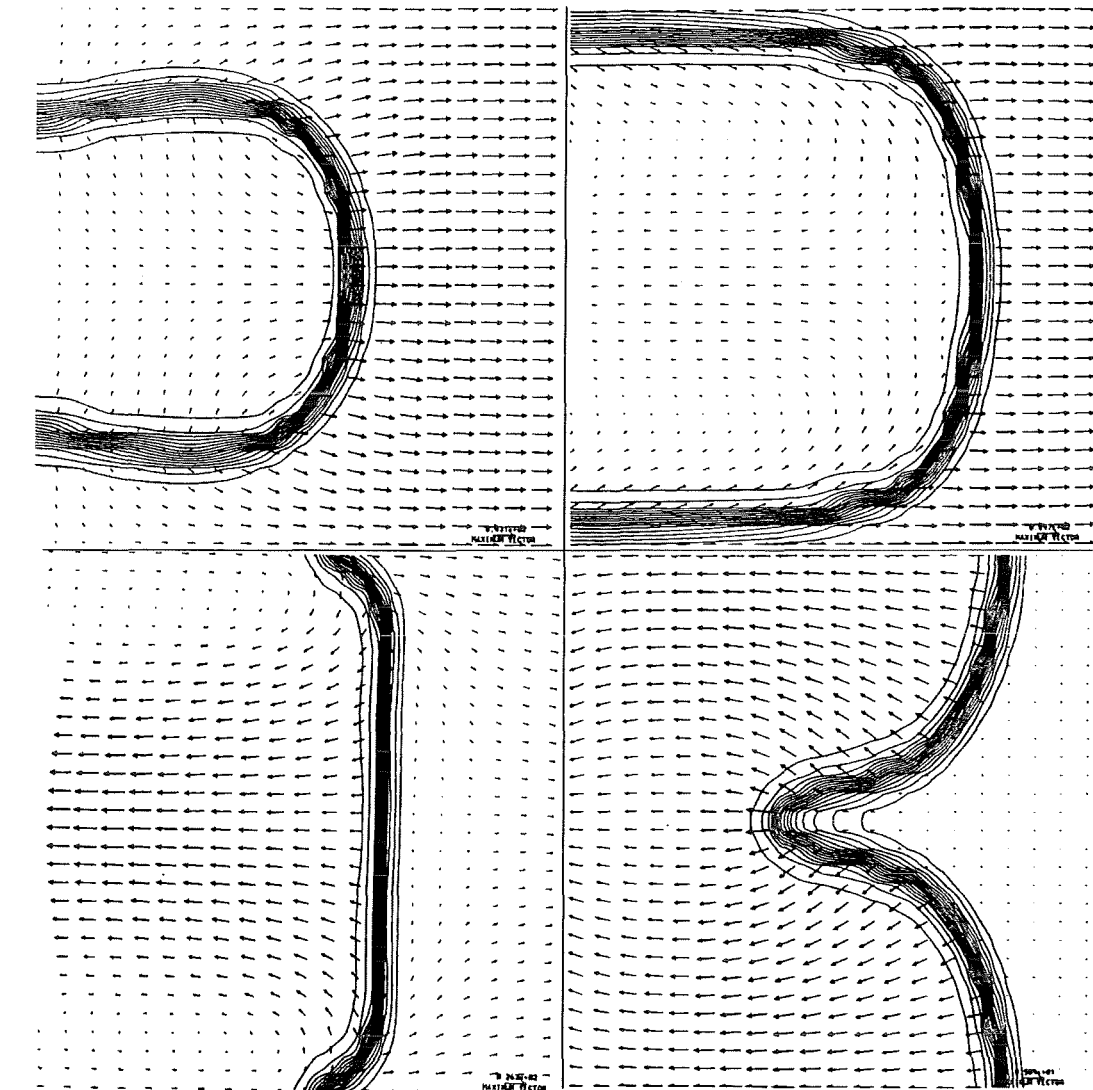


Figure 2.25: Iso-concentration lines and velocity field near the flame, while forming an tulip flame according to Gonzalez [Gon92]. Upper left  $t = 200\Delta t$ , upper right  $t = 400\Delta t$ , lower left  $t = 600\Delta t$ , lower right  $t = 2000\Delta t$

when the flame reaches the end of the tube (see [Gon92]). The occurring amplitudes of the pressure oscillations rise with the length to diameter ratio of the tube.

Analogous to the oscillations in velocity pressure oscillations can be detected. Gonzales states, that the occurring pressure oscillations are only superimposed to the flow propagation, but they do not interfere with the flow field. They are only a result of the tulip flame phenomenon. Starke and Roth disapprove this thesis and show a close connection of the occurring pressure oscillations and the flow field velocity, under the assumptions:

- the flow velocity is constant over the cross section of the tube,
- pressure and density of the unburned gas are only dependent on the time,
- the compression of the gas is isentropic

Starke and Roth deduce a direct relation between pressure and velocity oscillations as a function of time and place:

$$v_u(x, t) = \frac{1}{\kappa p} \frac{\delta p}{\delta t} (l - x) \quad (2.32)$$

With the flow velocity  $v_u$  in the unburned mixture, the length  $l$  of the tube and the distance  $x$  from ignition. In agreement to Gonzalez, Starke and Roth explain the basic mechanism for the initiation of the tulip flame by the strong decrease of the flame surface, when the flame attaches to the walls.

The tulip flame phenomenon occurs periodically in long explosion tubes under certain preconditions. The attuning frequency is the first harmonic of the tube. The frequencies determined from the Schlieren-records (66Hz) in the Glastube coincide well with this predicted value.

### 2.3.2 Investigation of the turbulent field in front of the flame

At the Lehrstuhl A für Thermodynamik extensive studies have been carried out to measure the turbulence data in front of hydrogen-air flames [Bea94], [Jor99]. To understand the influence of turbulence on the propagating flame, experiments with a single obstacle configuration, introducing turbulence to the flow, have been carried out in the PHD-tube within the scope of this project. For the measurements a two-dimensional Laser Doppler Anemometer has been applied to the flow. The measurement system allows a non-intrusive determination of the flow velocity and the turbulent fluctuations.

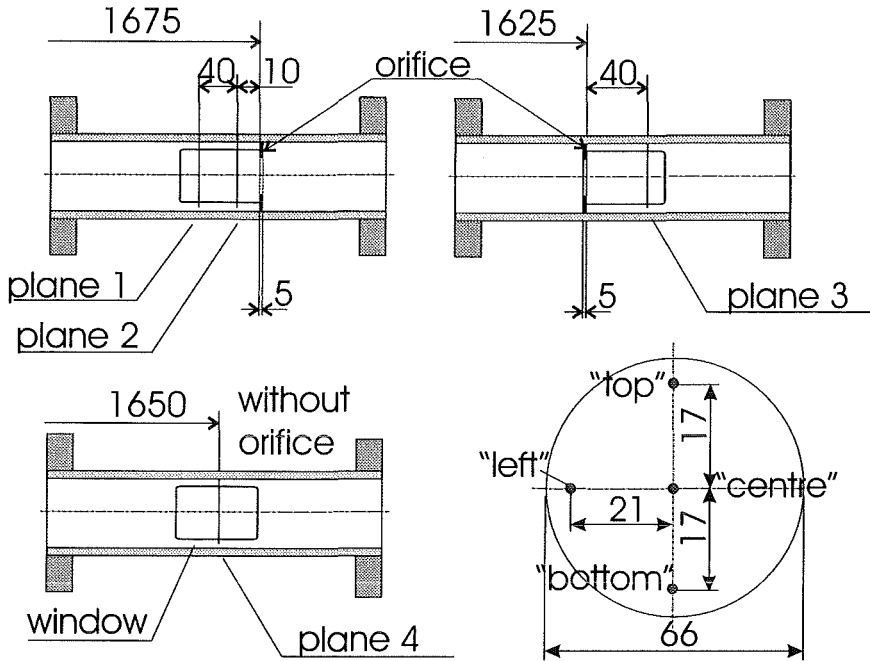


Figure 2.26: Location of the measurement planes in the PHD-tube. Upper row: distance of the obstacle to the spark plug and distance between the measurement planes and the obstacle. Lower row: location of the measurement plane in the undisturbed flow without obstacle. On the right: Position of the measurement points within the measurement planes.

### 2.3.2.1 Investigated configurations

Two different configurations are measured with the LDV-system. The first configuration covers the undisturbed flow in the tube without obstacles. The measurement plane is located 1650mm behind the ignition point. A detailed draw of the measurement configuration is shown in figure 2.26, a view of the complete facility is given in figure 2.15. For the second configuration the obstacle is placed into the window section. Three representative measurement planes, two in front of and one behind the obstacle are measured.

Past measurements [BeMa94], calculations in TASCflow as well as actual Schlieren images (figure 2.27) of the measured configuration find that the turbulence is not uniformly distributed behind the obstacle. In the middle of the tube, at the tube axis the turbulence intensity is low compared to this regions in which a shear layer between calm gases near the wall and moving gases through the orifice are formed out. To determine both turbulence intensities, at the tube axis and within the shear layers as well as the influence of buoyancy, the LDV measurements are performed at four different points ("up", "down", "left" and

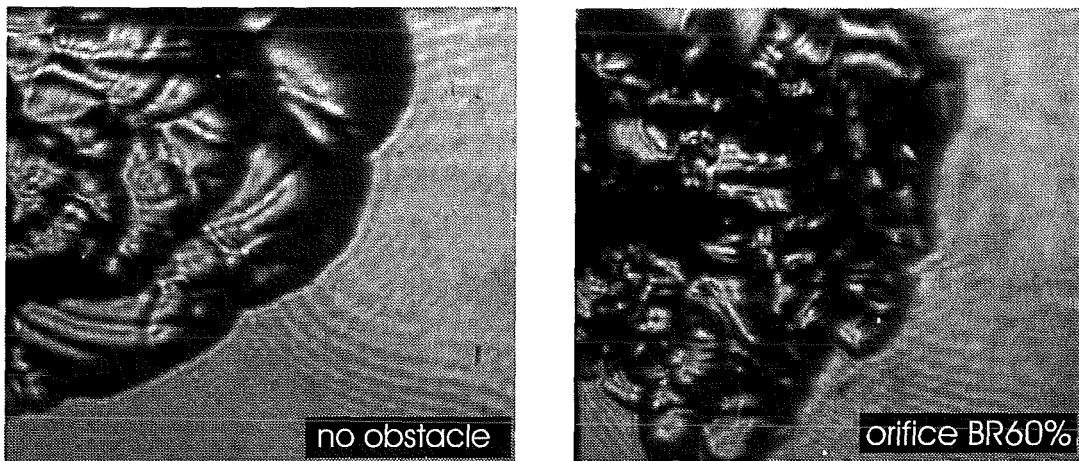


Figure 2.27: Schlieren images of a flame passing the window section of the PHD-tube at 10Vol.% hydrogen in air. On the left: undisturbed flow without obstacle. On the right: Flame passes an orifice shaped obstacle with a blockage ratio  $BR = 60\%$ .

”middle”) in each measurement plane.

The selection of the distance between the obstacle and the measurement planes have been chosen by evaluating the Schlieren images and the preceding calculations. Because of the limited size of the windows ( $50 \times 60\text{mm}$ ) it is necessary to place the obstacle at the right side of the window for the measurement of plane 1 and plane 2 and at the front of the window for the measurement of plane 3 to achieve the requested distances between obstacle and measurement planes. The location of the measurement planes is shown in table 2.26. For experiments

plane	distance from the orifice	absolute position of the orifice	absolute position of the plane
plane 1	-50 mm	1675 mm	1625 mm
plane 2	-10 mm	1675 mm	1665 mm
plane 3	+50 mm	1625 mm	1675 mm
plane 4	without obstacle		1650 mm

Table 2.3: Location of the measurement planes in the PHD-tube

with low hydrogen concentrations such as 10Vol.% or 11.5Vol.% hydrogen in air a large scattering between the different experiments has been observed. To overcome the problem of scattering and to determine the significant results out of the experimental data for each measurement point at least 20 experiments

were performed. Therefore, a statistical approved statement about the turbulent fluctuation quantities was possible. Because of the large number of necessary experiments only the configuration with 10Vol.% hydrogen has been investigated at all 4 measurement points and all planes. For 11.5Vol.% hydrogen concentration the position "middle" has been measured in all 4 planes. All experiments have been carried out with approximately 1bar initial pressure and at ambient temperature (20°C).

### 2.3.2.2 Evaluation procedure of the measured data

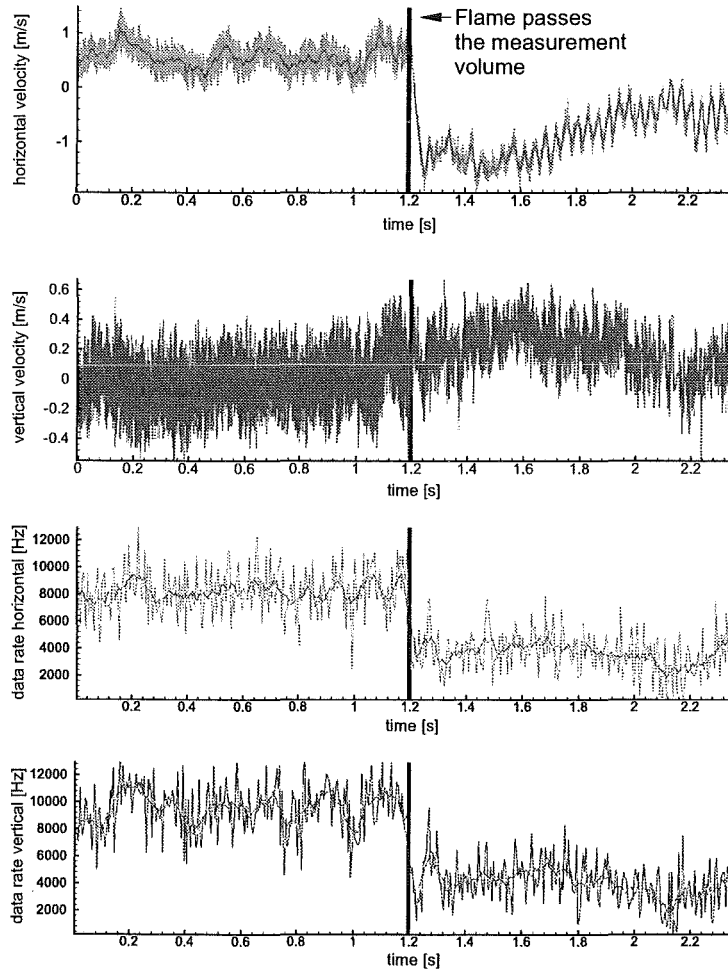


Figure 2.28: Experimental result of a Laser Doppler Velocimetry measurement in the PHD-tube of a 10Vol.% hydrogen in air flame passing an orifice with a blockage ratio  $BR = 60\%$ . Position of the measurement volume: 50mm behind the obstacle on the axis of the tube.

A typical course for the vertical and horizontal velocity component as well as their data rates are shown in figure 2.28. The data rate of the two measured velocities decreased significantly when the flame passed the measurement volume. The resulting low data rate behind the flame can be explained due to the deformation of the measurement volume by density gradients in the burned gases and the formation of condensed water on the windows. In front of the flame the data rate was limited by the number of available seeding particles, which precipitate mainly because of electrostatic attraction at the walls and the windows. The recording of the data was started with a delay of  $1.5\text{s}$  to the ignition. The measurement volume was located on measurement plane 1 and at the position "middle". The tube was filled in this example with a mixture of  $10\text{Vol.\%}$  hydrogen in air at ambient temperature and pressure. The average horizontal velocity is in the range between  $0.5\text{m/s}$  and  $1.5\text{m/s}$  before the flame front reaches the measurement volume. The moment, in which the flame passes the measurement volume, is characterized by a strong velocity drop, even to negative values. Behind the flame a back flow of gases has been observed in the order of the propagation velocity. This result can be explained by the small pressure differences along the tube axis. Because of the small flame velocity compared to the speed of sound there exist only minor pressure differences along the whole length of the tube. Because the pressure differences as a driving force are very small, they allow the expansion of the hot gases in both directions, the direction of the propagating flame and backwards. If the flow velocities in front of the flame are small, even negative values for the axial velocity can occur. Figure 2.29 shows the course of the streamlines of the expansion flow as well as the streamlines in the burned gases. These results are also shown numerically by Makhviladze [MMM87].

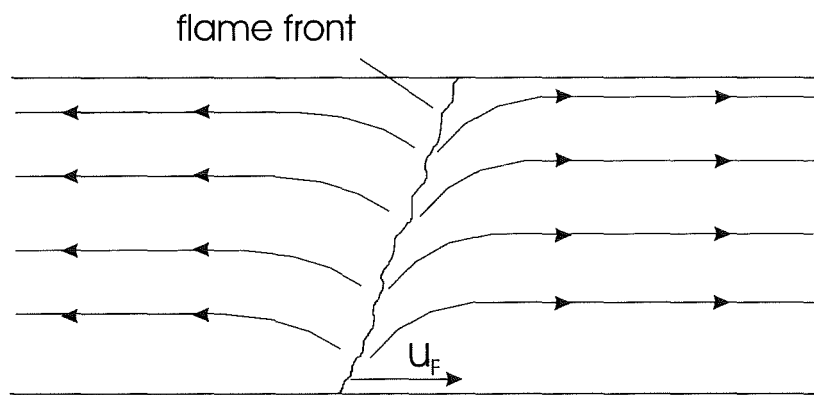


Figure 2.29: Numerically calculated streamlines of the unburned and burned gases near the flame front for a slow hydrogen flame according to Makhviladze [MMM87]. The flame is inclined due to buoyancy-effects.

In front of the flame the vertical velocity shows a tendency to the negative direction. This can be explained by buoyancy effects, which cause the flame to burn in the upper area earlier than in the lower part of the tube. The so inclined flame can be observed by the Schlieren records, too.

The experimental results differ only to a small extend between the measurement points, so it is sufficient to display only a selection of the complete data set. The evaluation of the data is done to determine the turbulent kinetic energy, which is used in the standard  $k - \epsilon$  turbulence model of CFD codes and the average velocity shortly ahead of the flame. The velocities evaluated are those from the gases of the volume element, which is burned in the next time step and, therefore, connected directly to the local reaction rate.

The first step in process the raw laser Doppler data is to eliminate spurious data. To do this the velocity data, which extends a predefined range is rejected. For the further refinement of the evaluation the moving average of the data is determined in a second step and the variance of the velocity values is calculated. Data which extends the band of 3 times the variance around the moving average is eliminated, too. If the amount of eliminated values exceed 3% of the total number of measured points, the experiment is disregarded for the statistical determination for the turbulence parameters. In a third step multiple data points, which occur if the acquisition rate extends the rate of particles passing the measurement volumes, are eliminated. The processed data is used for the further evaluation.

In order to determine the correct value of the kinetic energy the time window for the evaluation is of great importance. In the literature often a fixed amount of measurement values is used for the determination of the turbulence parameters, which is large enough to cover all appearing time scales. In an instationary flow the size of the measurement window is restricted to a short time. On the other hand the measurement window has to be large enough to cover the necessary time scales, too, which influence the flame. These time scales are influenced by the confining geometry, the absolute values of the flow velocities and the absolute values of the fluctuations. The suitable time scale to characterize the flow is the integral time scale  $\tau_E$ . It is shown in chapter 2.1.1, that this time scale covers the characteristical eddies of the flow. It is calculated directly from the measured data with equations 2.8 and 2.9. For these cases, where the autocorrelation coefficient can not be determined out of the experimental data, because of shortage of data points, the integral time scale can be estimated with the equation 2.11 and the conservative approach for the turbulent length scale with 10% of the tube diameter. The average flow velocity in front of the flame can be easily determined from the measured data. For the evaluation of the turbulent kinetic energy in front of the flame a time window of five times the integral time scale is chosen. This window covers nearly all of the appearing eddies, contains enough values for the calculation of  $k$  and is short enough to consider only the flow directly in front of the flame. The following example clarifies the procedure for the determination

of  $\tau_E$ :

For a experiment with 10Vol.% hydrogen in air the autocorrelation function  $R_E$  is determined according to equation 2.8. The result is shown in figure 2.30. The

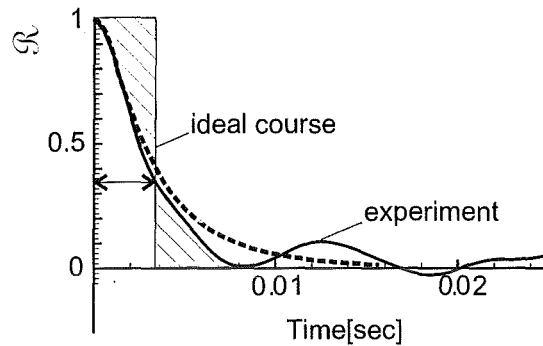


Figure 2.30: Calculated autocorrelation function for an experiment with 10Vol.% hydrogen in air.

course of the autocorrelation function results to a value of approximately 4ms for the integral time scale. This result corresponds well with the estimated integral time scale according to equation 2.11. Figure 2.31 shows the course of the corresponding Doppler record and the evaluation window of five times the integral time scale. The turbulence intensity is calculated for each data record within the evaluation window according to the following procedure: At first the moving average for the evaluation window is determined. The number of measurement points  $n_M$ , which are considered for calculating the average velocity around the central point is dependent on the evaluated data.

$$\bar{u}_i = \frac{1}{n} \sum_{i=-n_M/2}^{i=n_M/2} U_i \quad (2.33)$$

The turbulence intensity  $u'_{rms}$  is calculated from the deviation to the so determined average flow velocity  $\bar{U}_i - \bar{u}_i$  for each component:

$$u'_{rms} = \sqrt{\frac{1}{n} \sum_{i=1}^n (U_i - \bar{u}_i)^2} \quad (2.34)$$

$n$  is the number of measurement points after applying all filter processes described earlier. Figure 2.31 illustrates the determination of the turbulence intensity. In the figures 2.32 and 2.33 the influence of the single orifice to the turbulence intensity can be observed. Dependent on the measurement plane and the measurement position within the plane an increase of the turbulence intensity is visible right before and after the orifice. The increase of the axial (horizontal)

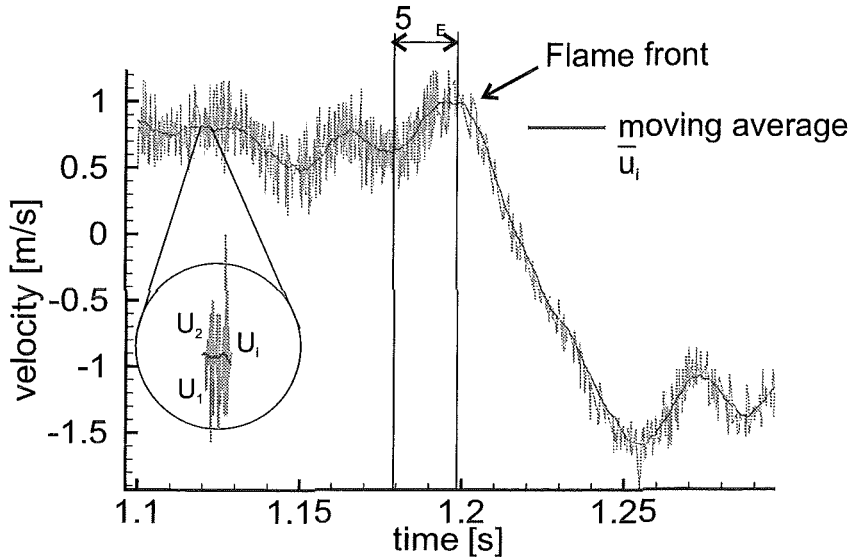


Figure 2.31: Laser Doppler record of the axial velocity of the expansion flow in front of and after the flame passing an orifice with a blockage ratio of 60% at 10 Vol.-% hydrogen. The flame front is determined with a laser light barrier, the indicated evaluation window is calculated by applying the autocorrelation function to the data.

component is stronger compared to the vertical component. This can be explained by the velocity increase of the axial component due to the reduced cross section caused by the orifice. It is also visible that the increase for the turbulence intensity is higher for the measurement position "up" compared to the "middle" position at the tube axis. This results from buoyancy effects to the flame.

The similar behavior is recognizable for higher hydrogen concentrations. In figure 2.34 the turbulence intensity for both, the axial and the vertical component is shown. The initial level for turbulence intensity of the vertical component looks similar to the experiments with lower hydrogen concentration, but the initial level of the turbulence intensity for the axial component is higher. The relative increase of both components of the turbulence intensity is comparable to the case with lower hydrogen concentration. The results are summarized in table 2.5. The absolute value for the turbulence intensity in plane 1 corresponds to the value for the tube without obstacle (see table 2.4). This allows the calculation of the relative increase of the turbulence intensity due to the obstacle between the interesting plane and plane 1.

10 Vol.%	plane 1		plane 2		plane 3		without orifice	
	$u'_{rms}$ [m/s]	$v'_{rms}$ [m/s]	$u'_{rms}$ [m/s]	$v'_{rms}$ [m/s]	$u'_{rms}$ [m/s]	$v'_{rms}$ [m/s]	$u'_{rms}$ [m/s]	$v'_{rms}$ [m/s]
middle	0.09	0.10	0.12	0.10	0.13	0.12	0.11	0.11
up	0.08	0.10	0.11	0.11	0.19	0.16	0.09	0.13
down	0.10	0.09	0.10	0.10	0.13	0.13	0.09	0.12
left	0.10	0.11	0.12	0.12	0.16	0.14	0.09	0.12
11.5 Vol.%								
middle	0.14	0.09	0.15	0.1	0.18	0.15	0.14	0.10

Table 2.4: Turbulence intensities of the expansion flow in front of the flame for 10 Vol.% and 11.5 Vol.% hydrogen in air

10 Vol.%	plane 1-2		plane 1-3	
	$u'_{rms}$ [%]	$v'_{rms}$ [%]	$u'_{rms}$ [%]	$v'_{rms}$ [%]
middle	21	7	37	25
up	26	17	128	61
down	3	5	35	44
left	20	9	60	31
11.5 Vol.%				
middle	7	11	29	66

Table 2.5: Relative increase of the turbulence intensity due to the orifice between plane 1 and 2 and between plane 1 and 3

The last step in evaluating the data is the calculation of the turbulent kinetic energy  $k$ . To determine the turbulent kinetic energy an assumption has to be made for the third component of the flow, because only two components are measured by the LDV-system. Because of symmetry it is allowed to estimate the missing component  $w$  equal to the measured vertical component  $v$ . The turbulent kinetic energy is calculated with the turbulence intensity data according to the following equation:

$$k = \frac{1}{2}(u'^2_{rms} + v'^2_{rms} + w'^2_{rms}) \approx \frac{1}{2}(u'^2_{rms} + 2v'^2_{rms}) \quad (2.35)$$

The determined course of the turbulent kinetic energy is shown in the figures

2.35 and 2.36. According to the expectations the courses are comparable with the courses of the turbulence intensities.

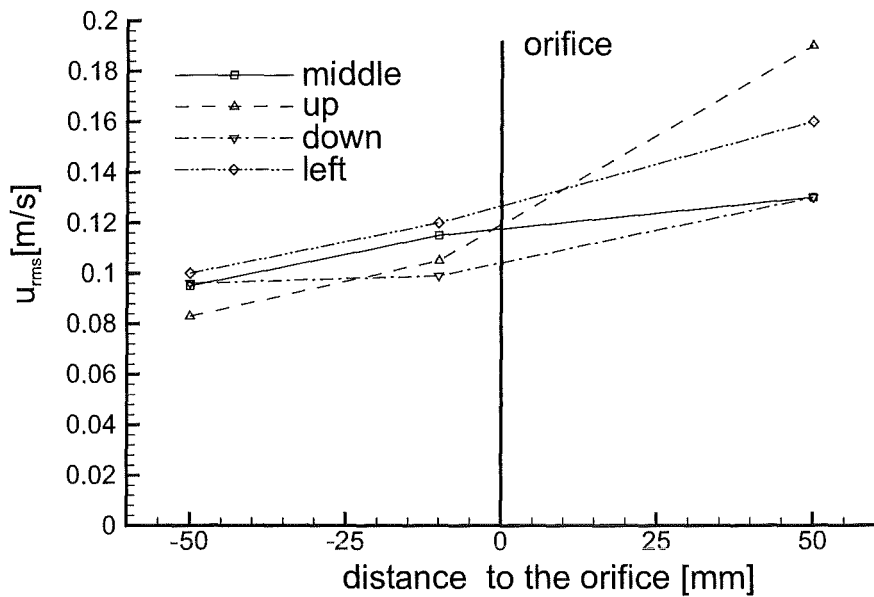


Figure 2.32: Determined turbulence intensity for the axial component around a single orifice with a blockage ratio of 60% in the PHD-tube. Initial conditions: 10Vol.% hydrogen in air, 1.0bar and 20°C

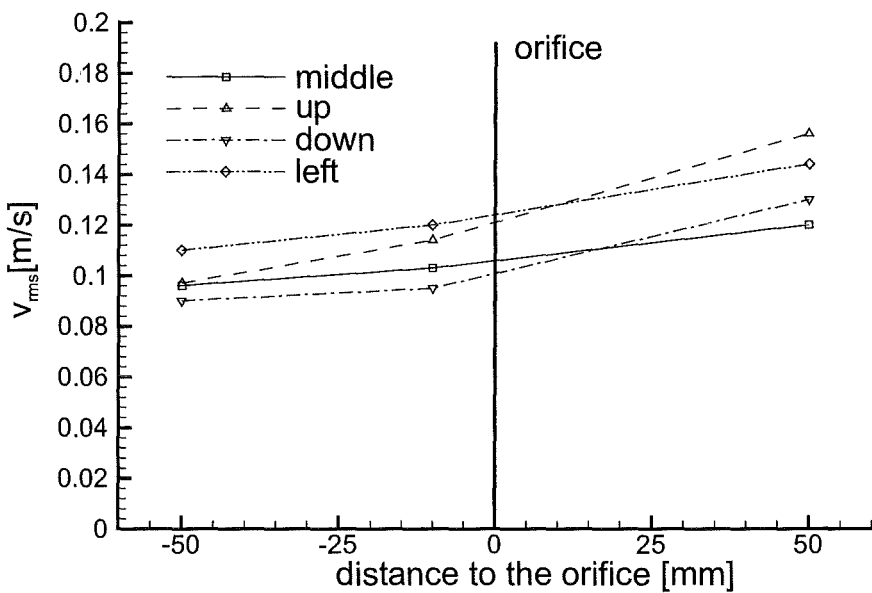


Figure 2.33: Determined turbulence intensity for the vertical component around a single orifice with a blockage ratio of 60% in the PHD-tube. Initial conditions: 10Vol.% hydrogen in air, 1.0bar and 20°C

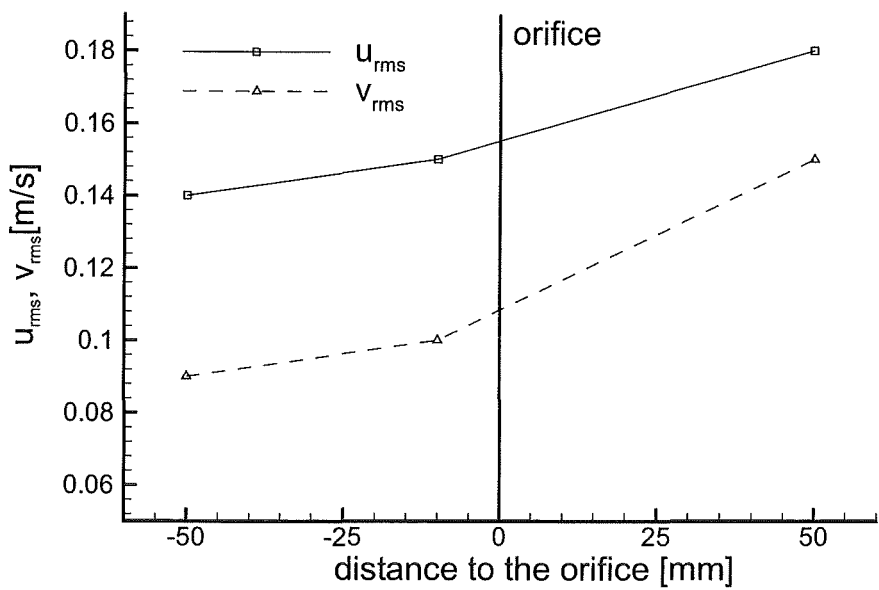


Figure 2.34: Determined turbulence intensity for the axial and the vertical component around a single orifice with a blockage ratio of 60% in the PHD-tube. Initial conditions: 11.5Vol.% hydrogen in air, 1.0bar and 20°C

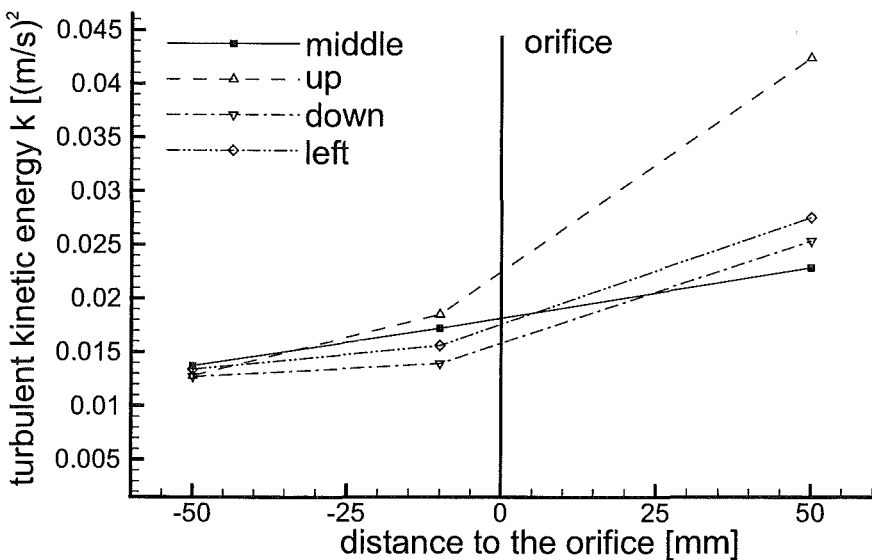


Figure 2.35: Determined turbulent kinetic energy for the different measurement positions in the PHD-tube. Initial conditions: 10Vol.% hydrogen in air, 1.0bar and 20°C

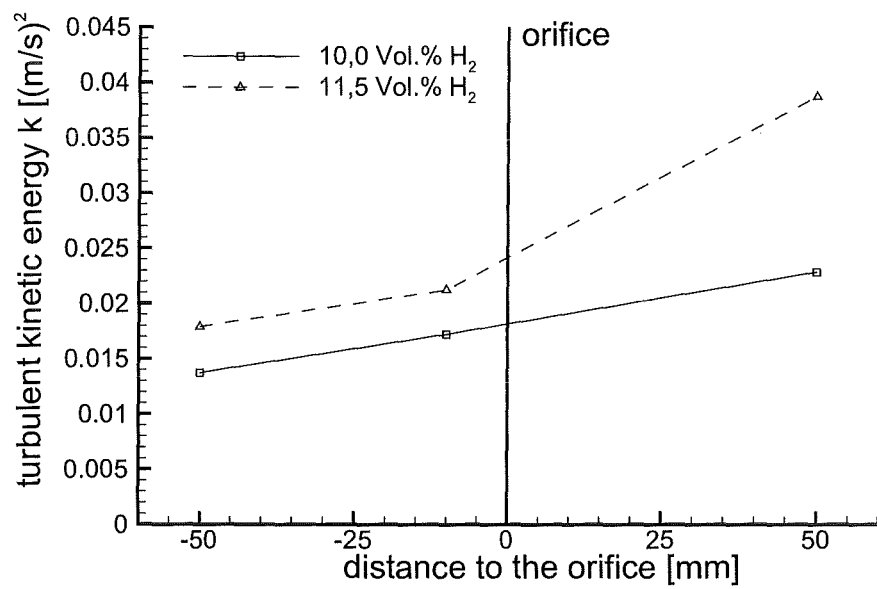


Figure 2.36: Determined turbulent kinetic energy for the measurement position "middle" in the PHD-tube. Initial conditions: 10 Vol.% and 11.5 Vol.% hydrogen in air, 1.0 bar and 20°C

### 2.3.3 Experiments without obstacles

To allow the quantification of combustion enhancement due to turbulence in single and multiple obstacle configurations, experiments have been carried out without obstacles in the PhD-tube. The experimental conditions covered a range between 10% and 16% of hydrogen in air at 1.0 bar initial pressure and ambient temperature. LDV-data of corresponding experiments in the range between 10% and 11.5% hydrogen in air are reported earlier in chapter 2.3.2. A selection of the performed experiments is shown in the annex.

Experiment phdo479 (figure 2.90) shows the typical course of the flame position and the pressure in the case of a flame with 10% hydrogen. After the ignition phase and the build up of an overpressure of approximately 0.13 bar due to the combustion in the tube, the flame approaches with a constant flame speed of 0.54 m/s until it reaches the end of the tube 11 s after ignition. Superimposed are oscillations, which are discussed earlier (see chapter 2.3.1). These oscillations can not be resolved in the photodiode records because of their spacial resolution. However, they can be seen in the high speed Schlieren records in figures 2.37 and 2.38. The flame has a coarse scale convex structure and is comparable to the flame structure under similar conditions, measured in the Glastube (see e.g. experiment G20). From the contour plot 2.38 the oscillation frequency can be determined and amounts to 28.5 Hz. This value corresponds well with the value received from the measured data from the laser Doppler measurements.

With increasing Hydrogen concentrations the flame speed and the maximum overpressure increases (see figures 2.91 to 2.94). Commonly a bend in the flame position trace can be observed when the flame has to burn against the built up pressure in the last part of the tube and the flow in front of the flame can not evade. Therefore the flame speed decreases in all cases towards the end of the tube. The maximum flame speed in the experiments has been determined to be 40.8 m/s in experiment phdo492 (figure 2.95), measured in the middle part of the tube at a hydrogen concentration of 15.99%. The Schlieren images from experiment 15o01, which is comparable to the experiment phdo492, belonging to a hydrogen concentration of 15.7% (see figures 2.39 and 2.40) show a finer structured flame in the second part of the sequence, which is responsible for the increased reaction rate and therefore the higher flame speed. The flame itself propagates with a clear shown fluctuation in the flame speed according to the tulip-flame phenomenon, which is discussed in chapter 2.3.1.4. The fluctuations can be identified clearly in the pressure trace (figure 2.95).

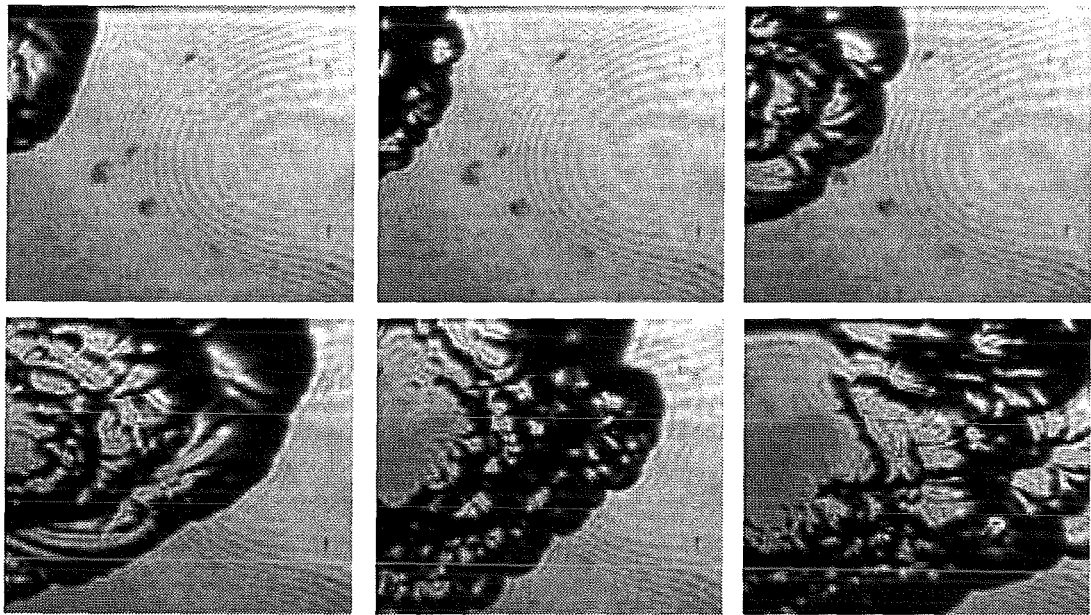


Figure 2.37: Schlieren images of a flame in the phd-tube without obstacle at 10.2% hydrogen in air. The images are taken from a high-speed schlieren film. Time between the images: 13.3 ms.

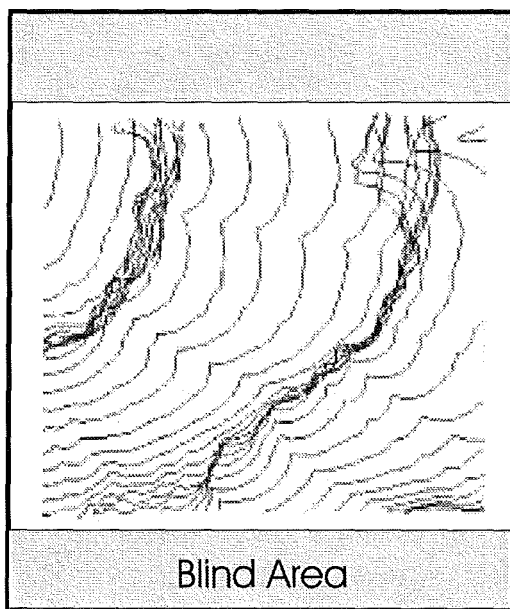


Figure 2.38: Contour Plots of the Schlieren images, showing the propagation of the flame in time. The gray areas indicate the non visible areas in the tube. Interval between the plots: 2.7 ms.

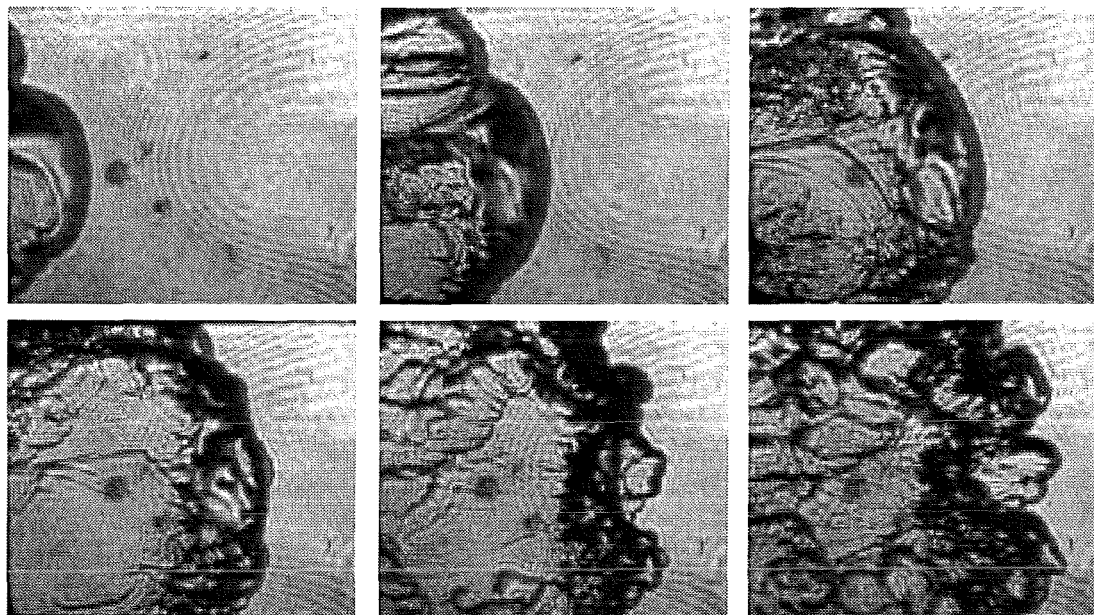


Figure 2.39: Schlieren images of a flame in the phd-tube without obstacle at 15.7% hydrogen in air. The images are taken from a high-speed schlieren film. Time between the images: 1.1 ms.

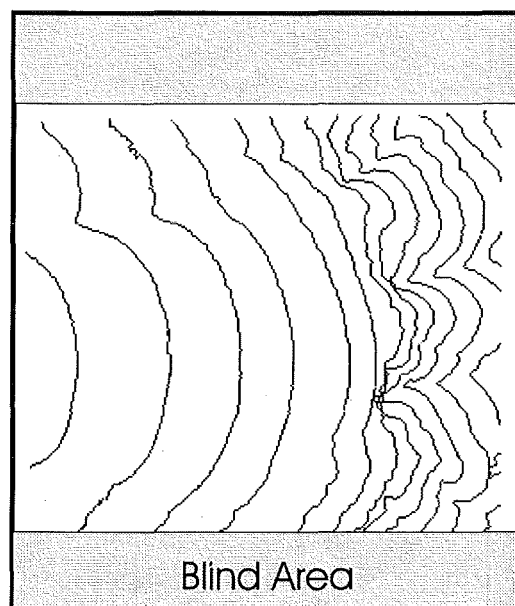


Figure 2.40: Contour Plots of the Schlieren images, showing the propagation of the flame in time. The gray areas indicate the non visible areas in the tube. Interval between the plots: 0.66 ms.

### 2.3.4 Experiments with multi obstacle configurations in the PHD-tube

To investigate the flame acceleration with multiple obstacles over 740 experiments have been carried out within this project. The test series phd-i, which is shown here exemplarily has been selected by the project partners for benchmark calculations.

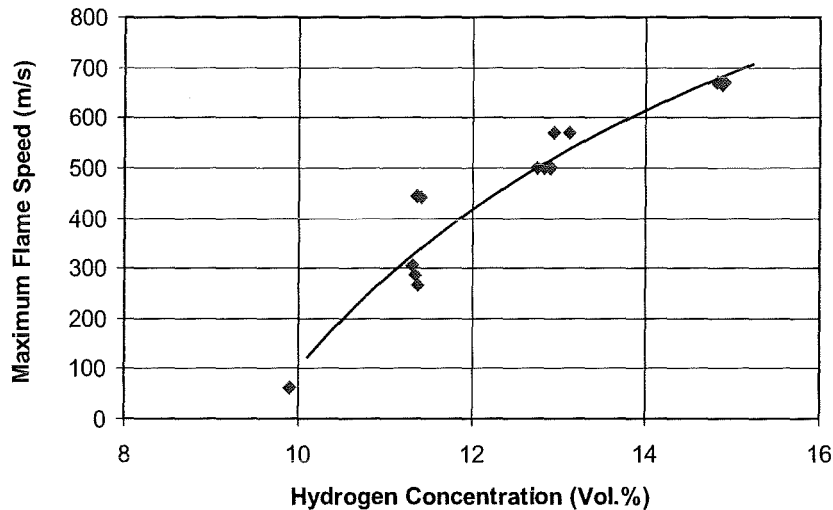


Figure 2.41: Measured maximum velocity of the flame after leaving the obstacle path.

The series phd-i has been configured with 16 obstacles with a blockage ratio of 60% and an obstacle spacing of 185mm, leading to an obstacle path length of 2960mm behind the ignition point. The observed maximum velocities for this configuration have been measured between 80m/s and 675m/s in a hydrogen range between 9.9% and 15.0%. An overview can be found in figure 2.41. The observed velocities exceed the measured velocities without obstacle by a factor of 80 in the case of low hydrogen concentrations and by a factor of 15 in the case of the maximum concentration of 15% hydrogen.

Schlieren images of the flame after leaving the obstacle path show clearly the leading shock wave in front of the flame (see figure 2.44). With increasing hydrogen concentration the distance between the shock system and the flame decreases, until the flame attaches to the shock wave at about 18.5% and leads to a detonation in the further course at such high hydrogen concentrations. As well as the distance between the shock system and the flame decreases, the maximum pressure of the shock system increases, which can be seen in figure 2.44.

Figure 2.42 shows an example of the pressure record of an experiment with 11.32% hydrogen. After leaving the obstacle path a leading shock system is formed. Its velocity can be detected by the evaluation of several pressure transducers and is indicated in the figure with dashed lines. At the end the shock system reflects and interferes with the flame. The according flame position, measured with the photodiodes is shown in figure 2.43, where the reflected shock wave is visible, too.

Figures 2.45 and 2.46 show the experimental results for 12.94% and 14.89% hydrogen.

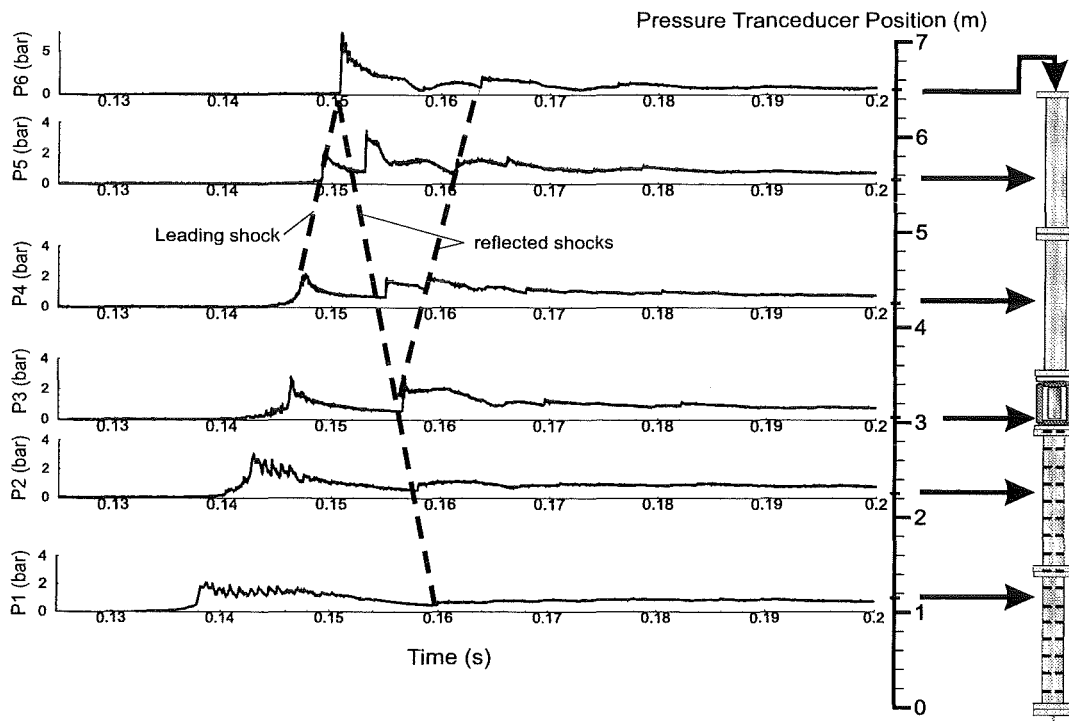


Figure 2.42: Pressure record of experiment phdi13. Dashed lines indicate the traces of the pressure waves in front of the flame. Initial conditions: 11.32% hydrogen, 0.999bar, 20.38°C.

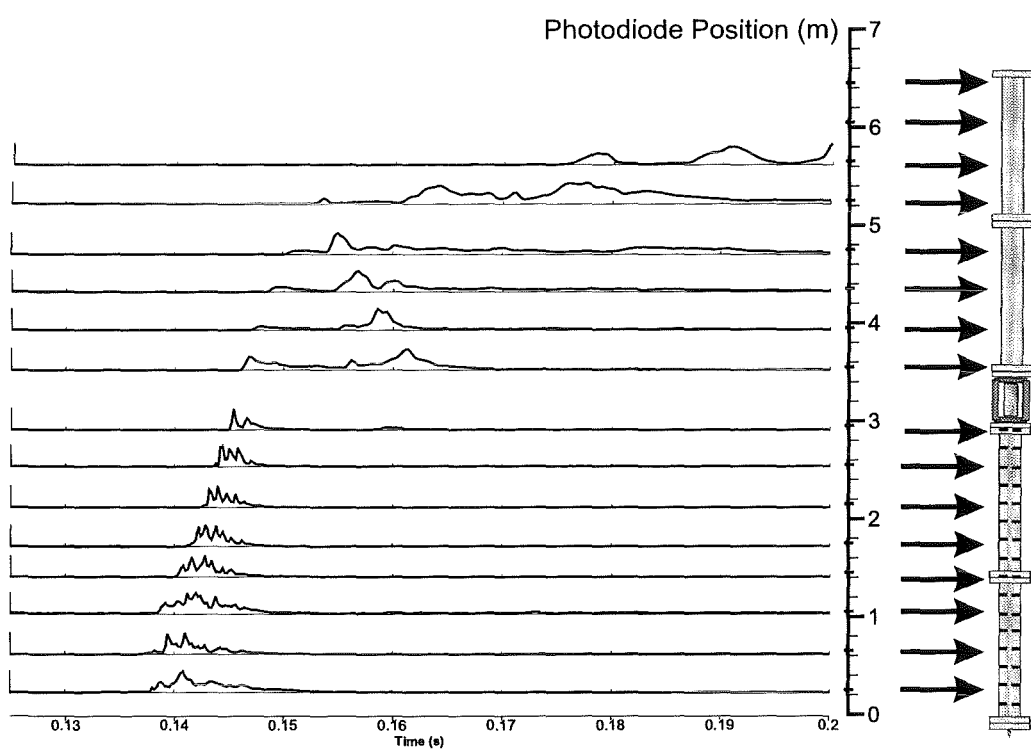


Figure 2.43: Photodiode record of experiment phdi13. Initial conditions: 11.32% hydrogen, 0.999bar, 20.38°C.

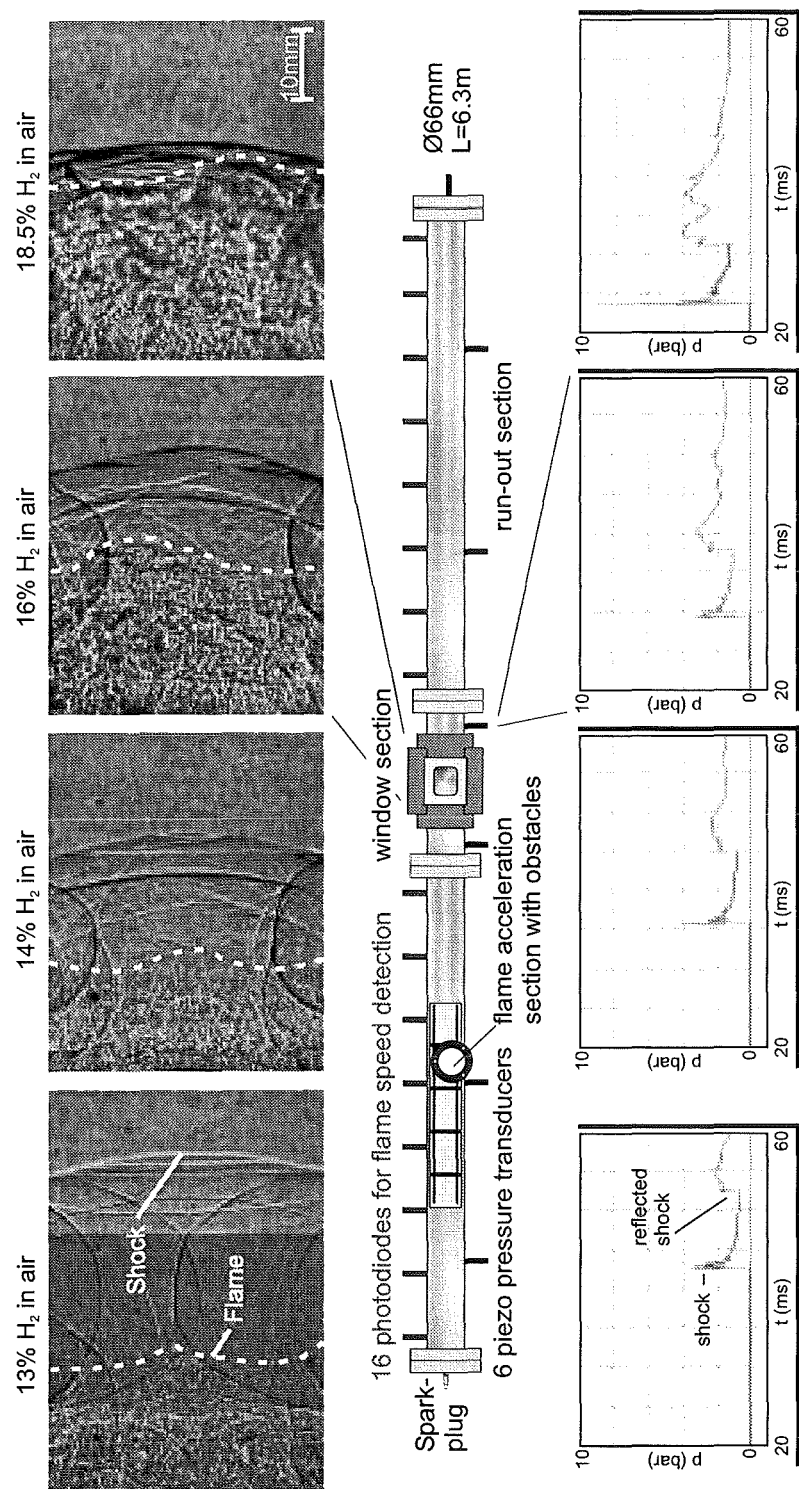


Figure 2.44: Shock system and flame after the obstacle path in the test series phd-i for various hydrogen concentrations.

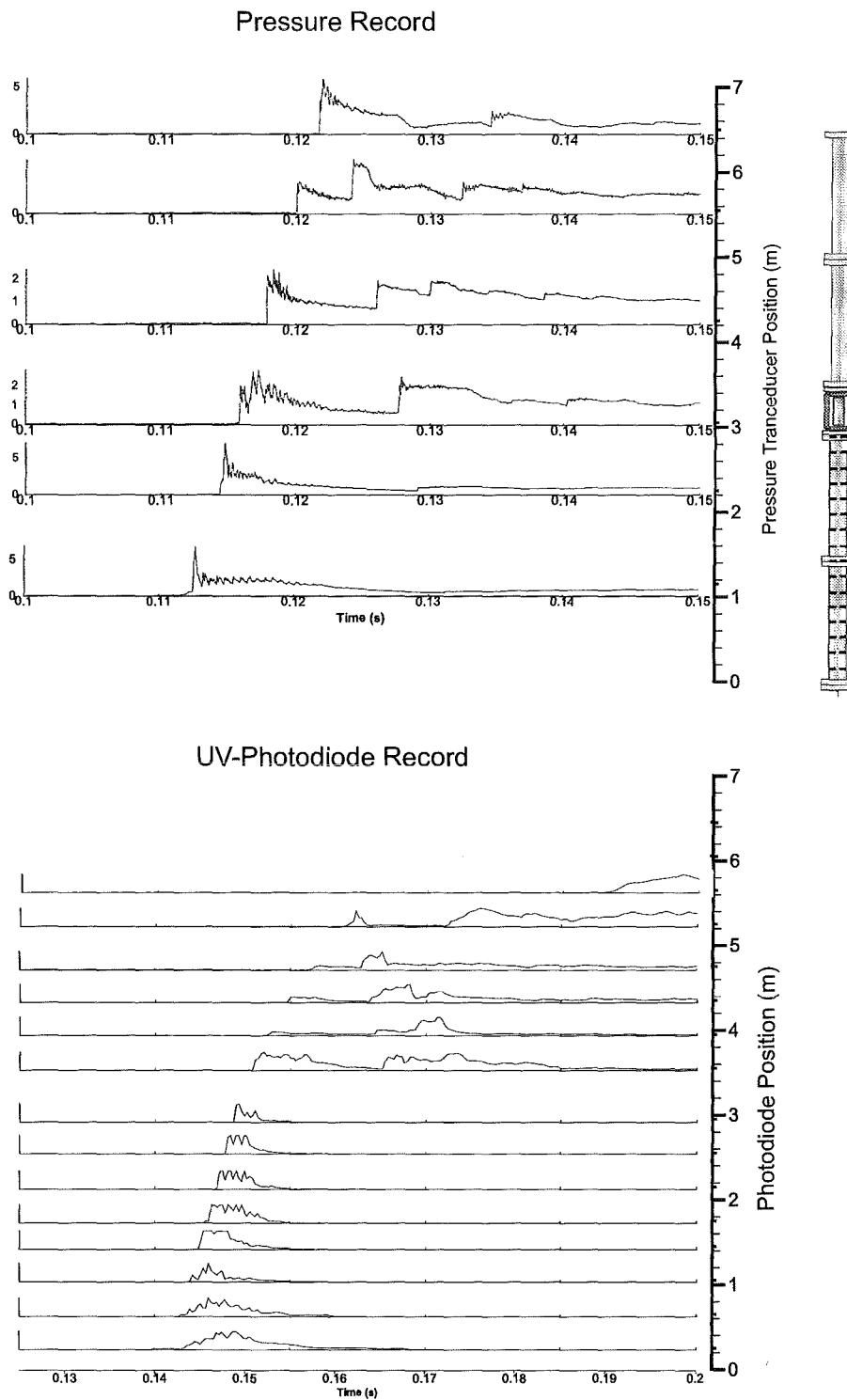


Figure 2.45: Pressure record of experiment phdi16. Initial conditions: 12.94% hydrogen, 1.002bar, 20.28°C.

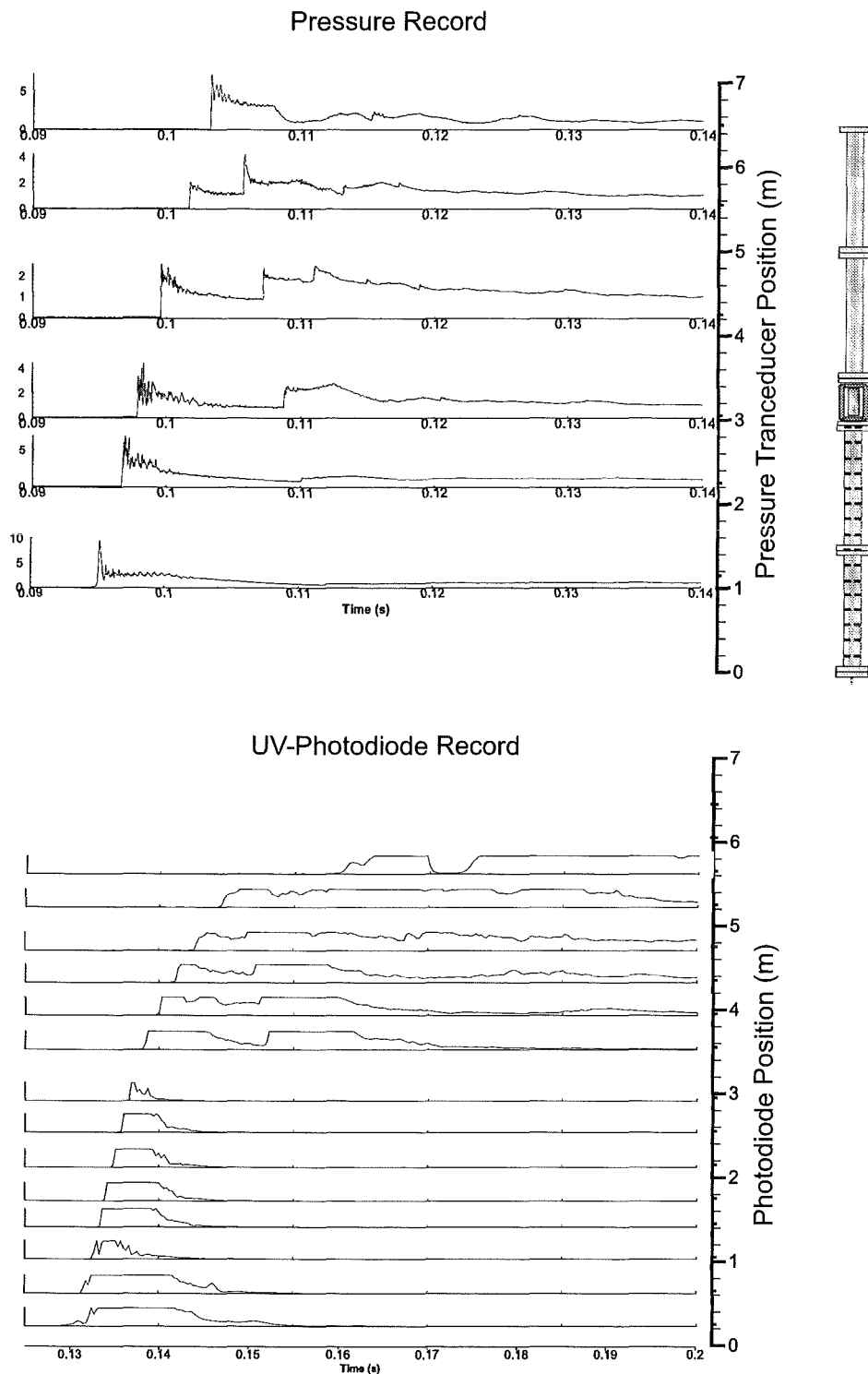


Figure 2.46: Photodiode record of experiment phdi15. Initial conditions: 14.89% hydrogen, 1.004bar, 20.99°C.

## 2.4 Experimental data on turbulence and turbulent combustion in the PHD-tube and the Glastube

### 2.4.1 Data on run-up effects after ignition

Over 60 measurements in total have been performed in this measurement campaign. For each examined hydrogen concentration two representative experiments have been selected and are presented here. For each concentration two Schlieren cinematographs show the propagation of the flame and its shape in the first and the second window. Corresponding time-position records and the calculated velocity-position records are shown. For each concentration a representative pressure trace has been selected. The pressure sensor was located 1150mm after the ignition point.

experiment	hydrogen concentration [ Vol%]	initial pressure [mbar]	initial temperature [°C]
G14	9.2	1026	23.2
G20	9.9	1028	20.0
G22	11.1	1023	21.0
G26	13.2	1028	21.4
G28	15.2	1028	24.4
G39	14.8	1046	19.5
G46	16.9	1039	27.0
G47	15.0	1035	27.5
G48	13.0	1040	27.9
G50	10.0	1048	28.1
G51	11.1	1030	27.3
G61	9.1	1040	25.2

Table 2.6: Initial conditions of the described experiments below.

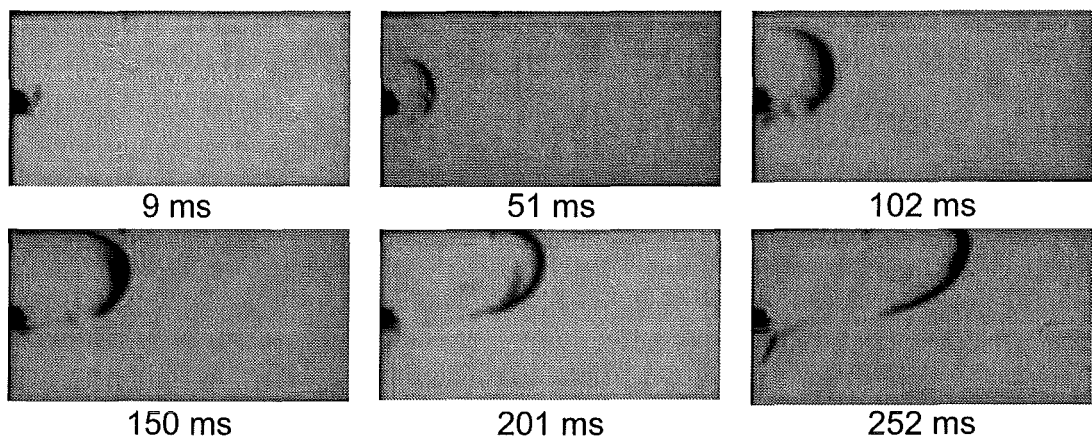


Figure 2.47: Schlieren cinematograph of experiment G14. Hydrogen concentration  $9.2\text{Vol.\%}$ ,  $p_0 = 1026\text{mbar}$ ,  $T_0 = 23.2^\circ\text{C}$

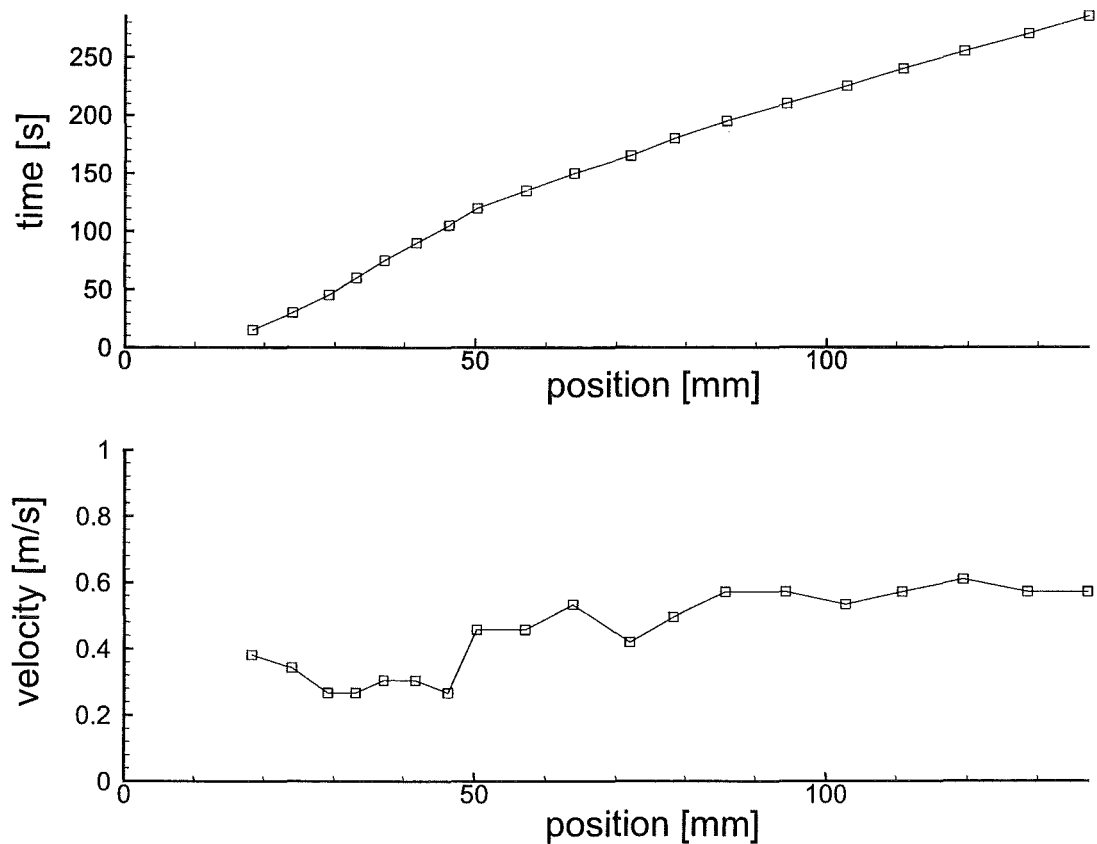


Figure 2.48: Position and velocity of the flame, experiment G14. Hydrogen concentration  $9.2\text{Vol.\%}$ ,  $p_0 = 1026\text{mbar}$ ,  $T_0 = 23.2^\circ\text{C}$

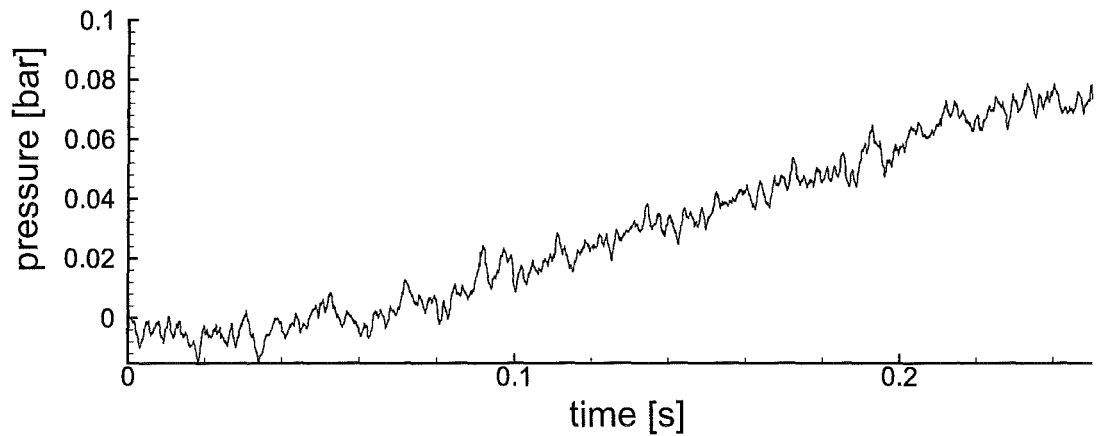


Figure 2.49: Pressure, experiment G14. Hydrogen concentration 9.2 Vol.%,  $p_0 = 1026\text{mbar}$ ,  $T_0 = 23.2^\circ\text{C}$

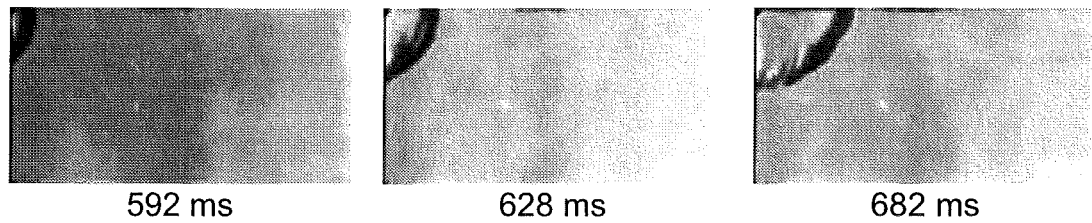


Figure 2.50: Schlieren cinematograph of experiment G61. Hydrogen concentration 9.1Vol.%,  $p_0 = 1040\text{mbar}$ ,  $T_0 = 25.2^\circ\text{C}$

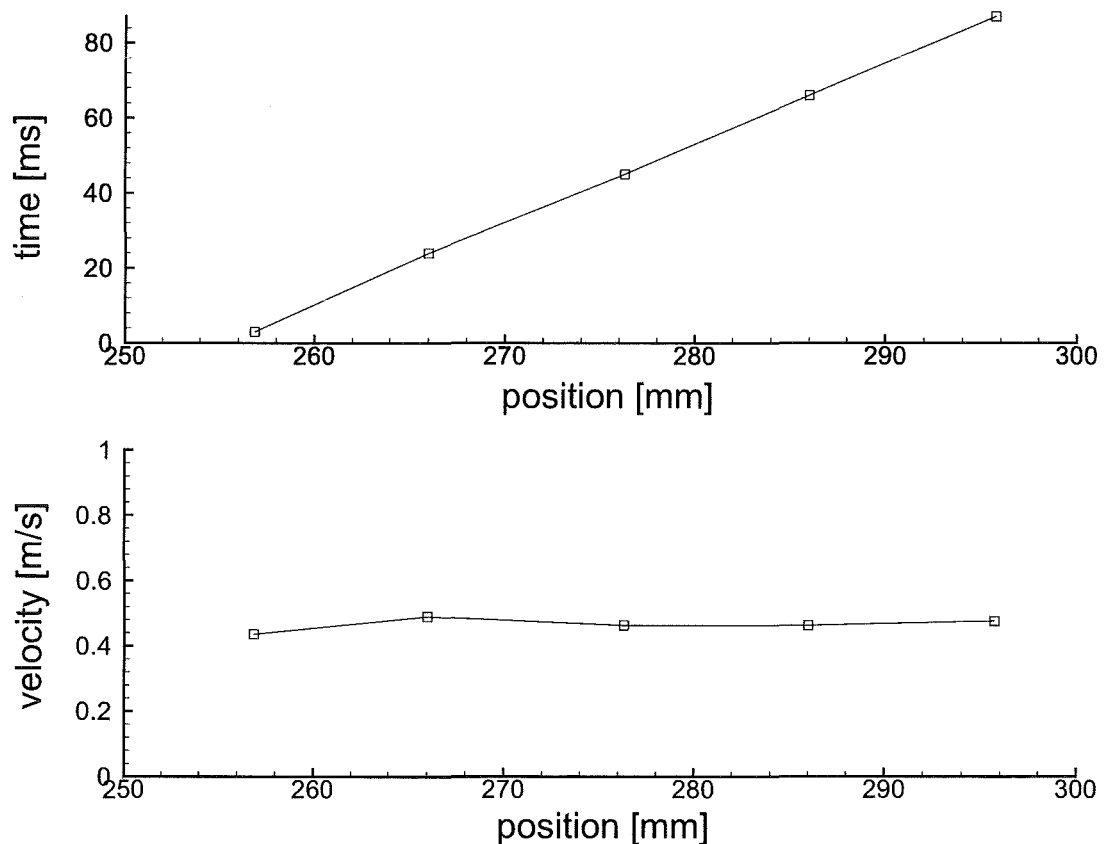


Figure 2.51: Position and velocity of the flame, experiment G61. Hydrogen concentration 9.1Vol.%,  $p_0 = 1040\text{mbar}$ ,  $T_0 = 25.2^\circ\text{C}$ , time  $t = t - 590\text{ms}$

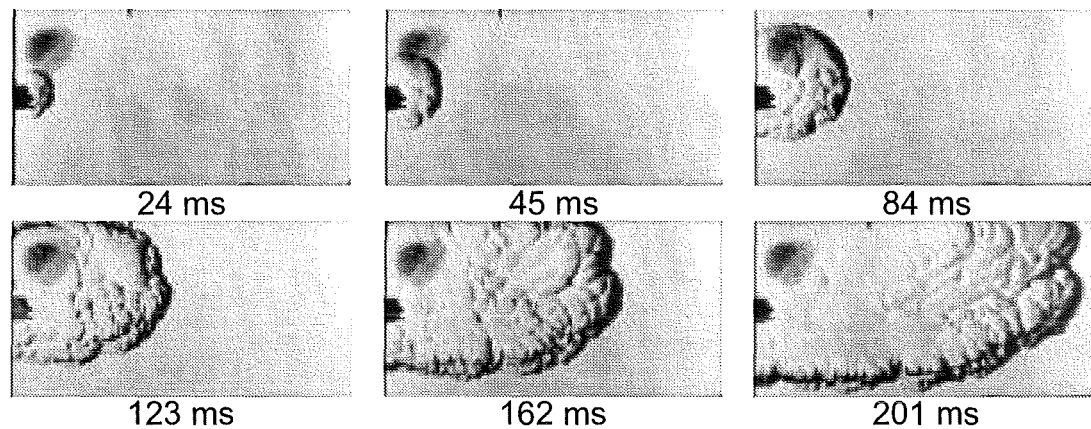


Figure 2.52: Schlieren cinematograph of experiment G20. Hydrogen concentration  $9.9\text{Vol.\%}$ ,  $p_0 = 1028\text{mbar}$ ,  $T_0 = 20.0^\circ\text{C}$

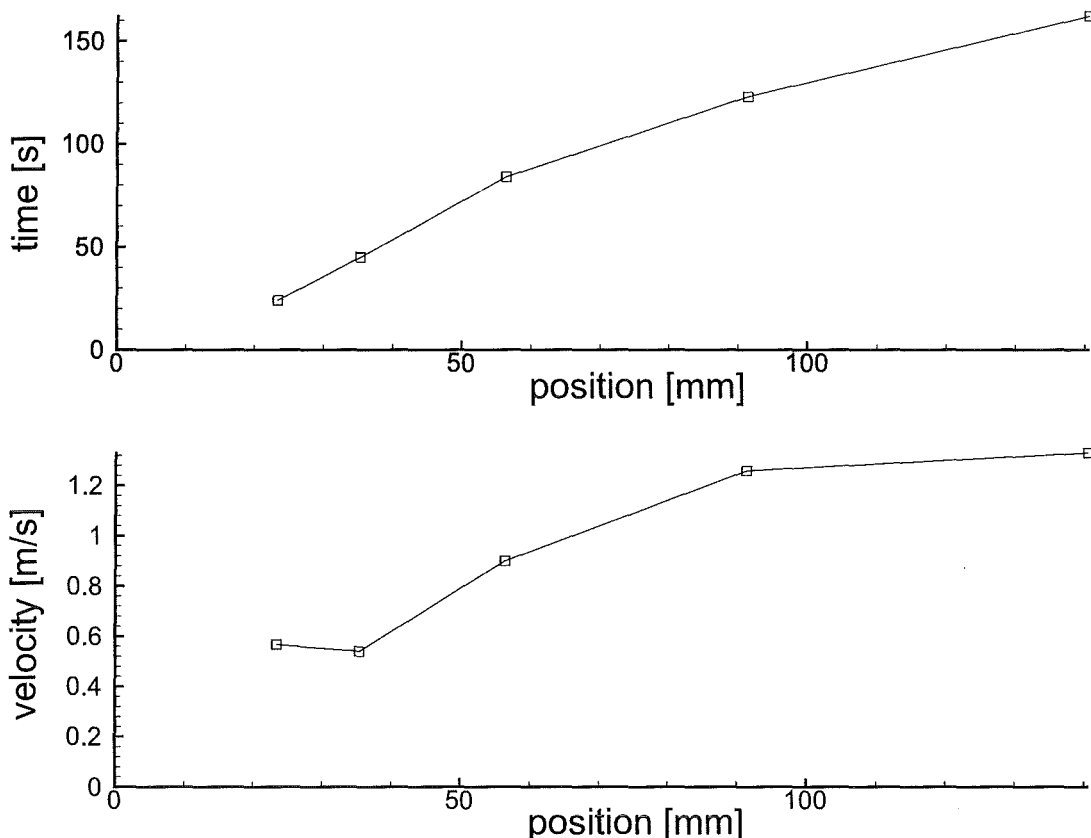


Figure 2.53: Position and velocity of the flame, experiment G20. Hydrogen concentration  $9.9\text{Vol.\%}$ ,  $p_0 = 1028\text{mbar}$ ,  $T_0 = 20.0^\circ\text{C}$

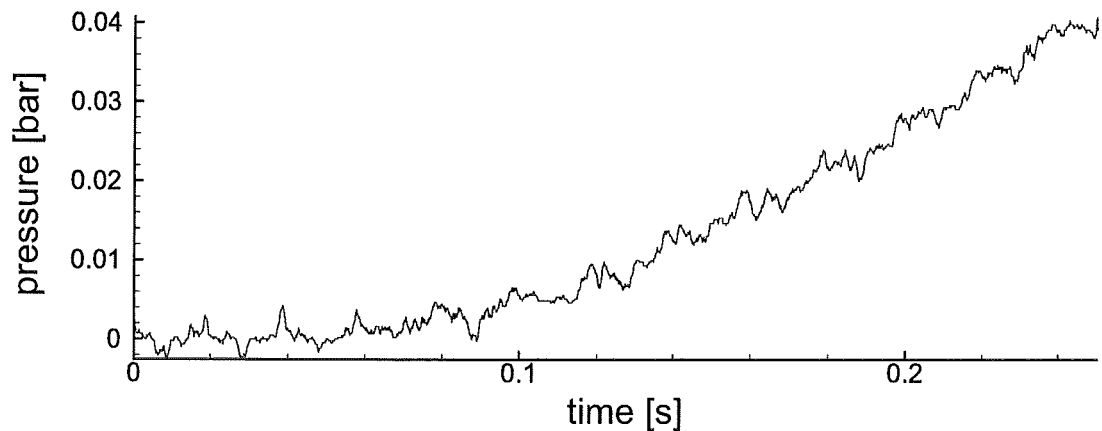


Figure 2.54: Pressure, experiment G20. Hydrogen concentration  $9.9\text{Vol.\%}$ ,  $p_0 = 1028\text{mbar}$ ,  $T_0 = 20.0^\circ\text{C}$

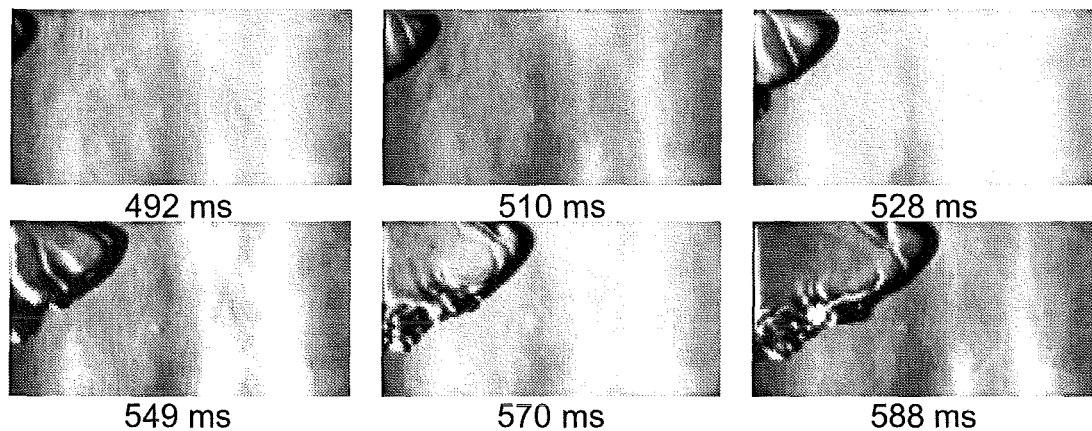


Figure 2.55: Schlieren cinematograph of experiment G50. Hydrogen concentration  $10.0\text{Vol.}\%$ ,  $p_0 = 1048\text{mbar}$ ,  $T_0 = 28.1^\circ\text{C}$

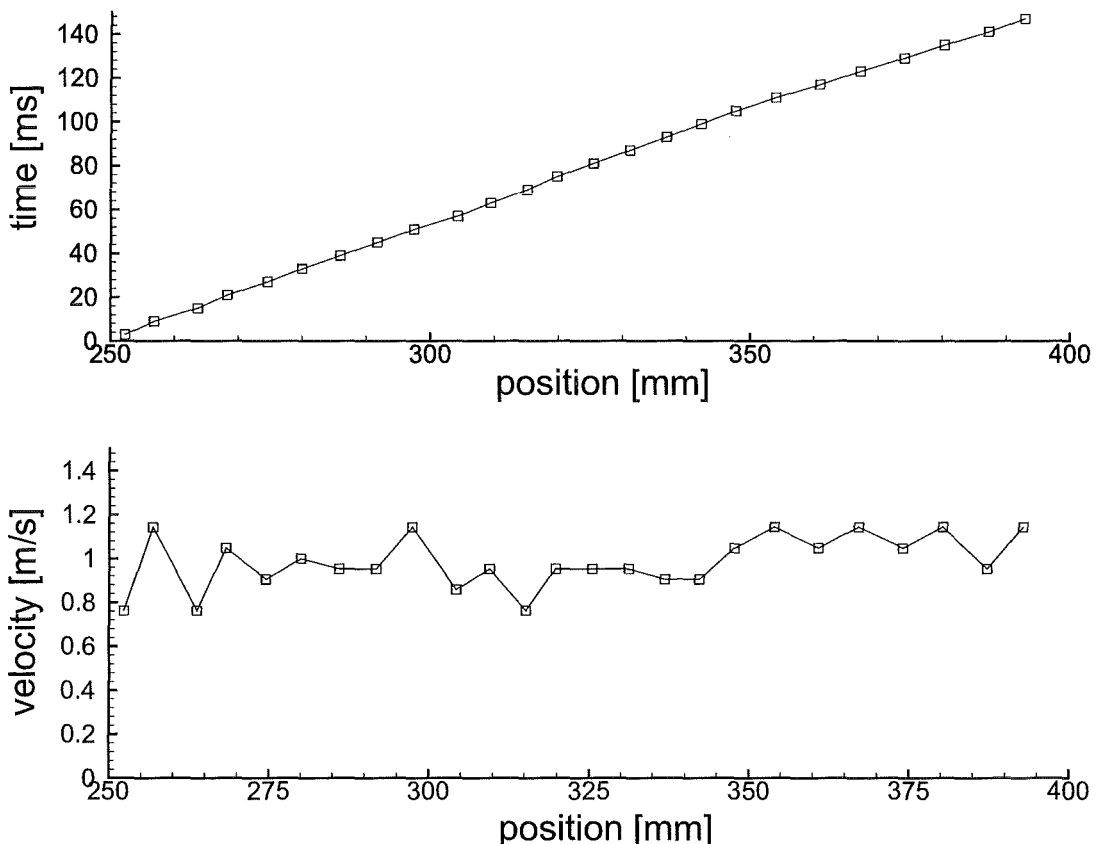


Figure 2.56: Position and velocity of the flame, experiment G50. Hydrogen concentration  $10.0\text{Vol.}\%$ ,  $p_0 = 1048\text{mbar}$ ,  $T_0 = 28.1^\circ\text{C}$ , time  $t = t - 490\text{ms}$

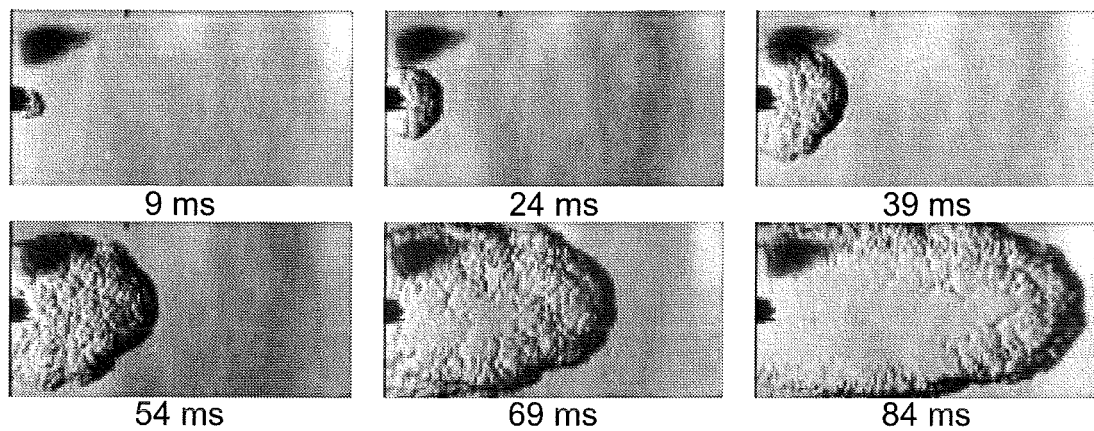


Figure 2.57: Schlieren cinematograph of experiment G22. Hydrogen concentration  $11.1\text{Vol.\%}$ ,  $p_0 = 1023\text{mbar}$ ,  $T_0 = 21.0^\circ\text{C}$

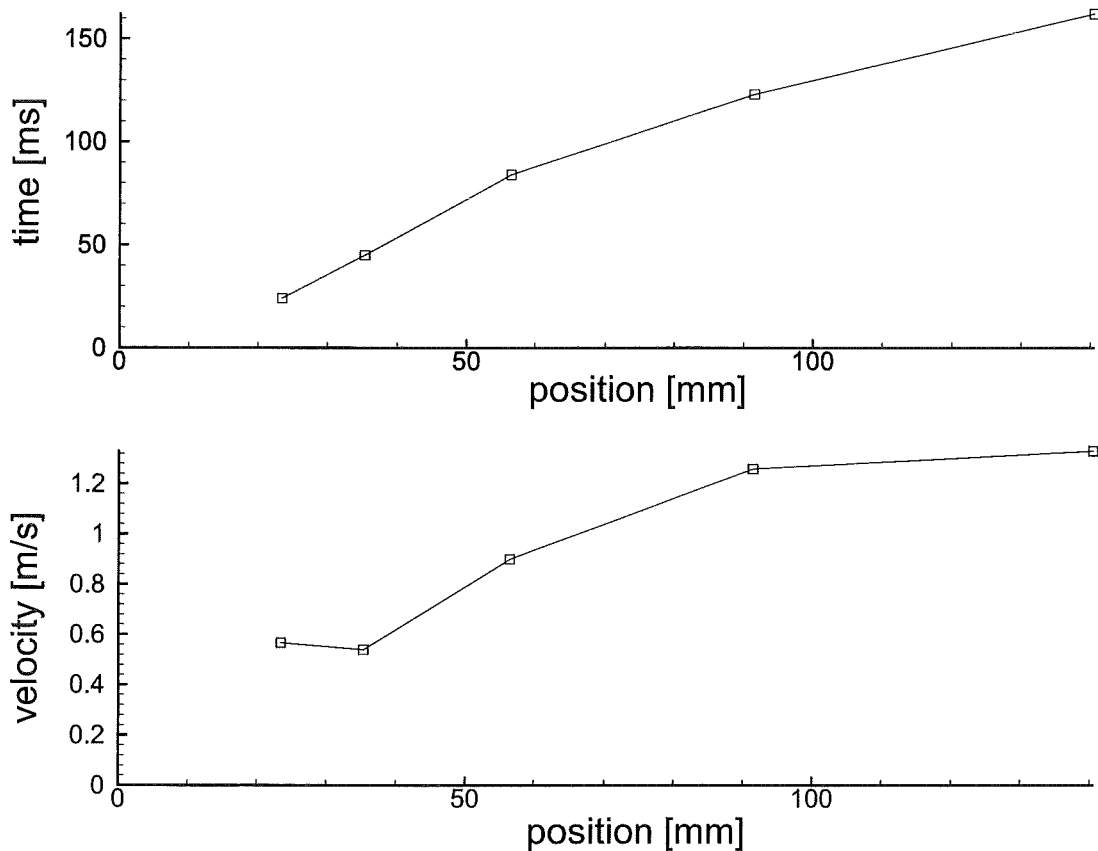


Figure 2.58: Position and velocity of the flame, experiment G22. Hydrogen concentration  $11.1\text{Vol.\%}$ ,  $p_0 = 1023\text{mbar}$ ,  $T_0 = 21.0^\circ\text{C}$

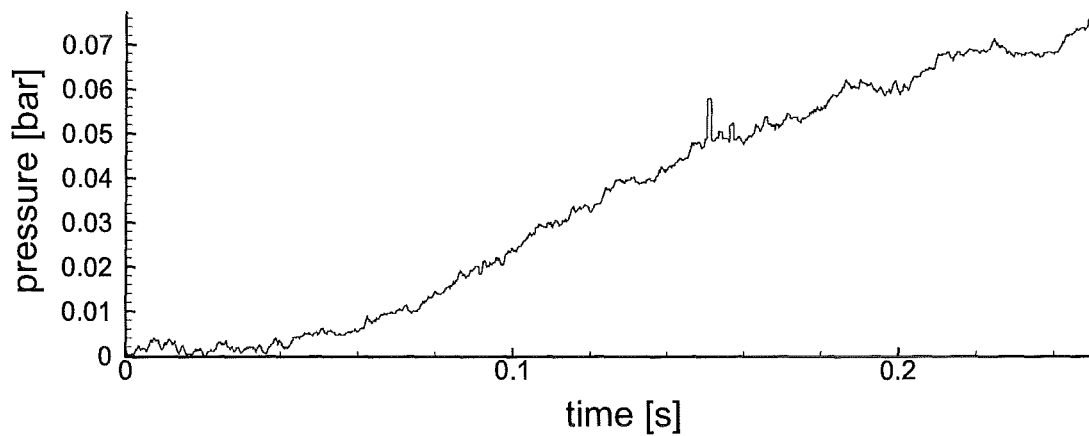


Figure 2.59: Pressure, experiment G22. Hydrogen concentration 11.1 Vol.%,  $p_0 = 1023\text{mbar}$ ,  $T_0 = 21.0^\circ\text{C}$

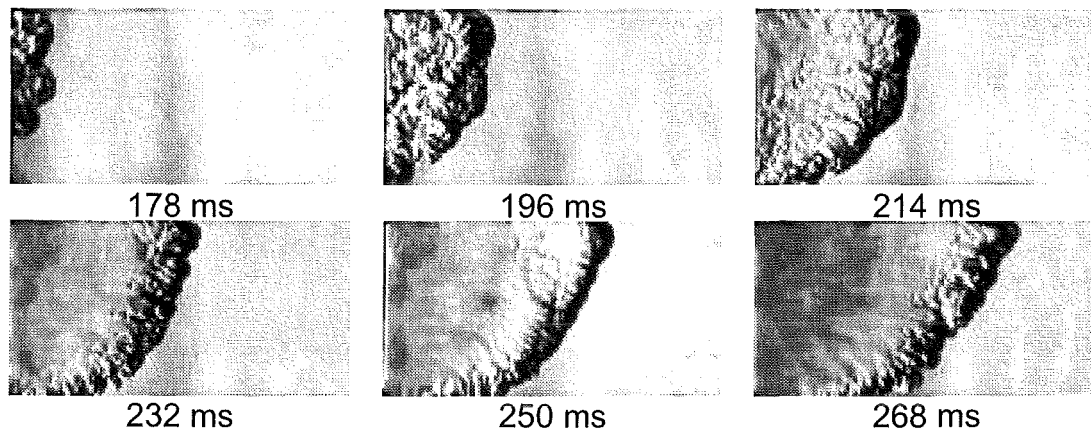


Figure 2.60: Schlieren cinematograph of experiment G51. Hydrogen concentration 11.1 Vol.%,  $p_0 = 1030\text{mbar}$ ,  $T_0 = 27.3^\circ\text{C}$

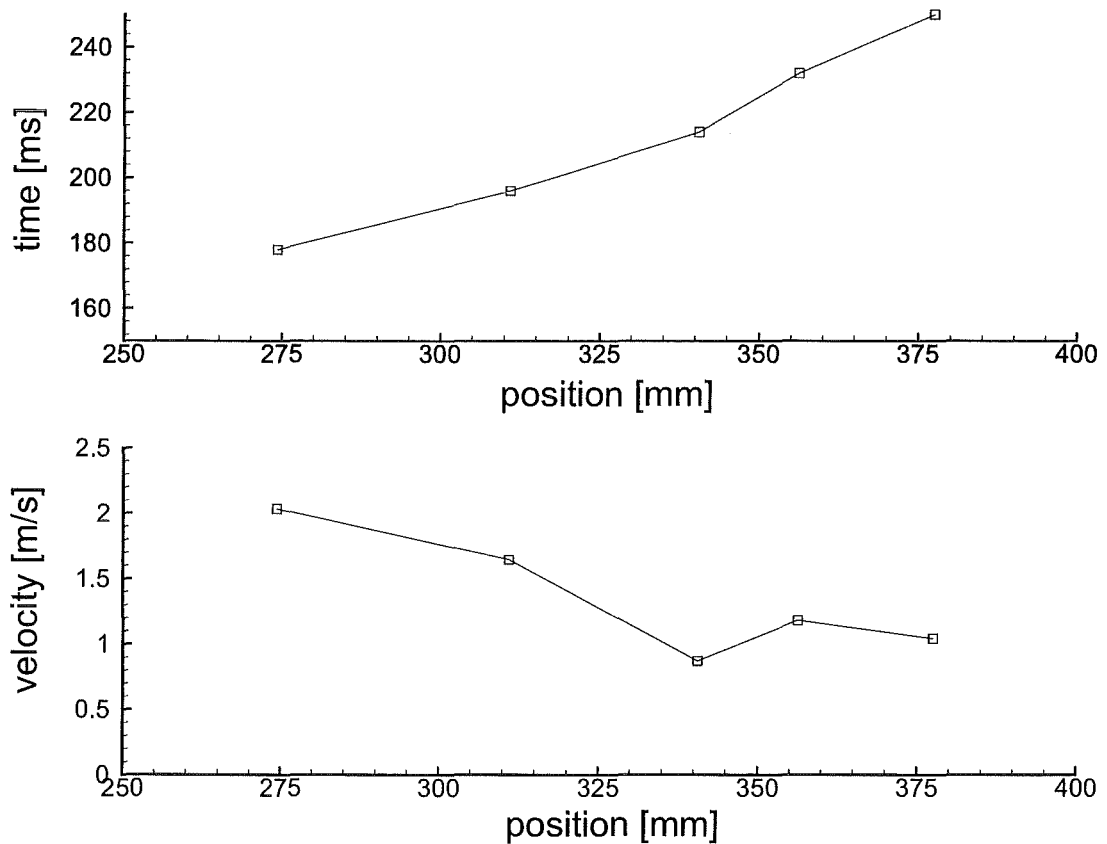


Figure 2.61: Position and velocity of the flame, experiment G51. Hydrogen concentration 11.1 Vol.%,  $p_0 = 1030\text{mbar}$ ,  $T_0 = 27.3^\circ\text{C}$

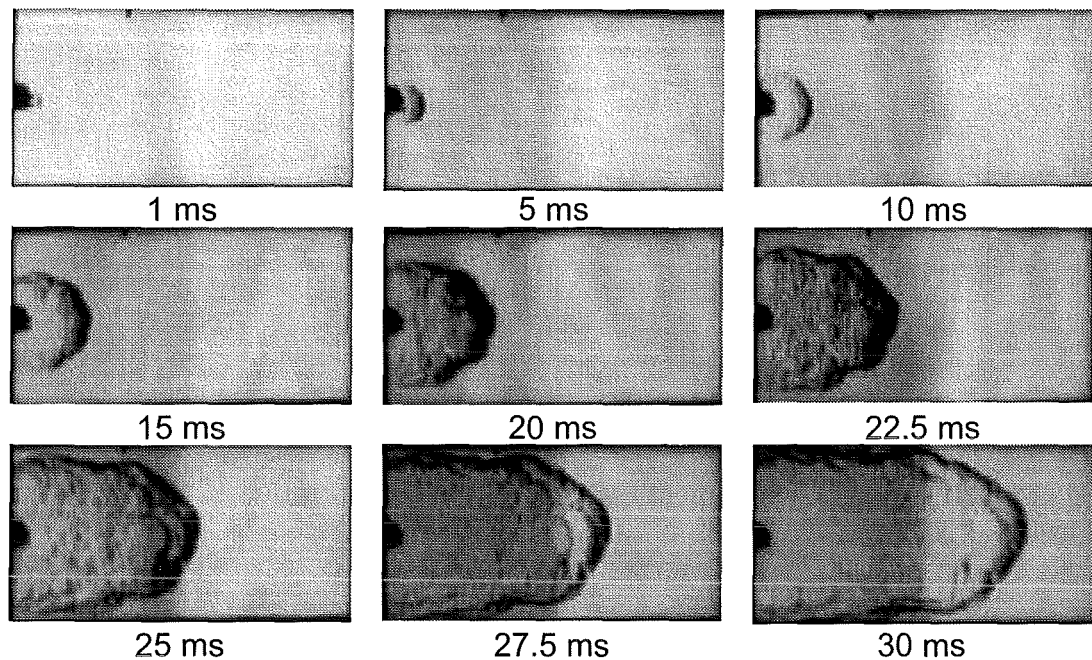


Figure 2.62: Schlieren cinematograph of experiment G26. Hydrogen concentration  $13.2\text{Vol.}\%$ ,  $p_0 = 1028\text{mbar}$ ,  $T_0 = 21.4^\circ\text{C}$

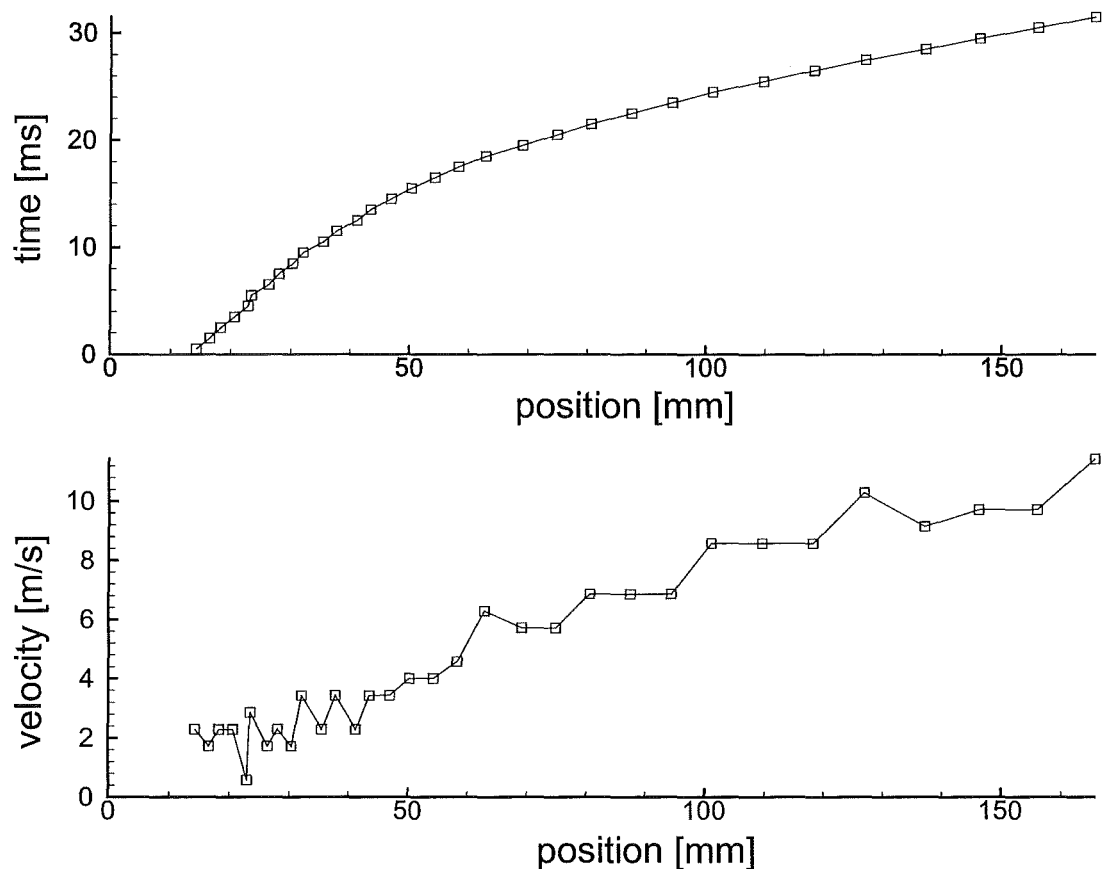


Figure 2.63: Position and velocity of the flame, experiment G26. Hydrogen concentration  $13.2\text{Vol.}\%$ ,  $p_0 = 1028\text{mbar}$ ,  $T_0 = 21.4^\circ\text{C}$

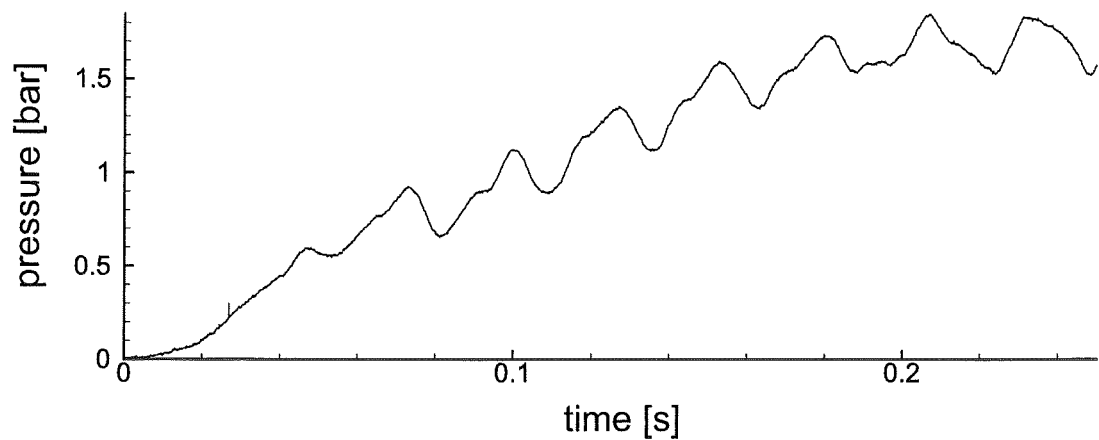


Figure 2.64: Pressure, experiment G26. Hydrogen concentration 13.2 Vol.%,  $p_0 = 1028\text{mbar}$ ,  $T_0 = 21.4^\circ\text{C}$

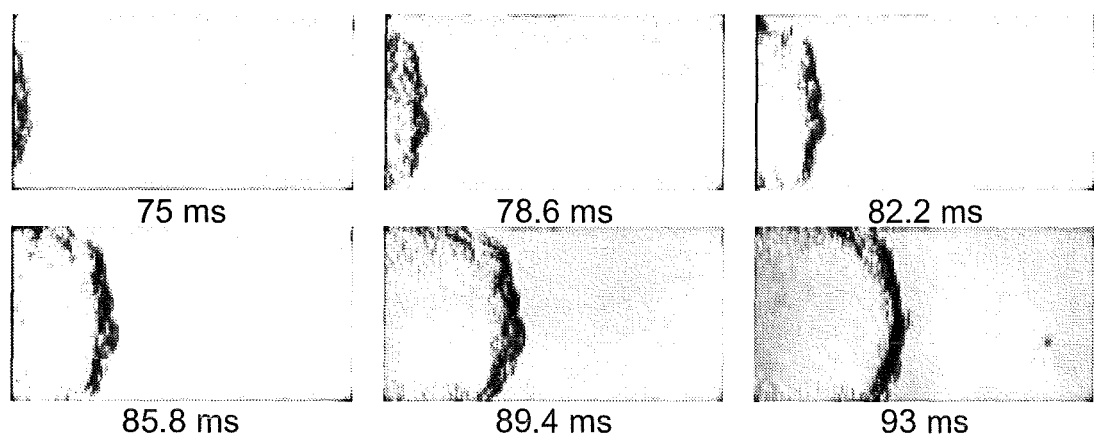


Figure 2.65: Schlieren cinematograph of experiment G48. Hydrogen concentration  $13.0\text{Vol.}\%$ ,  $p_0 = 1040\text{mbar}$ ,  $T_0 = 27.9^\circ\text{C}$

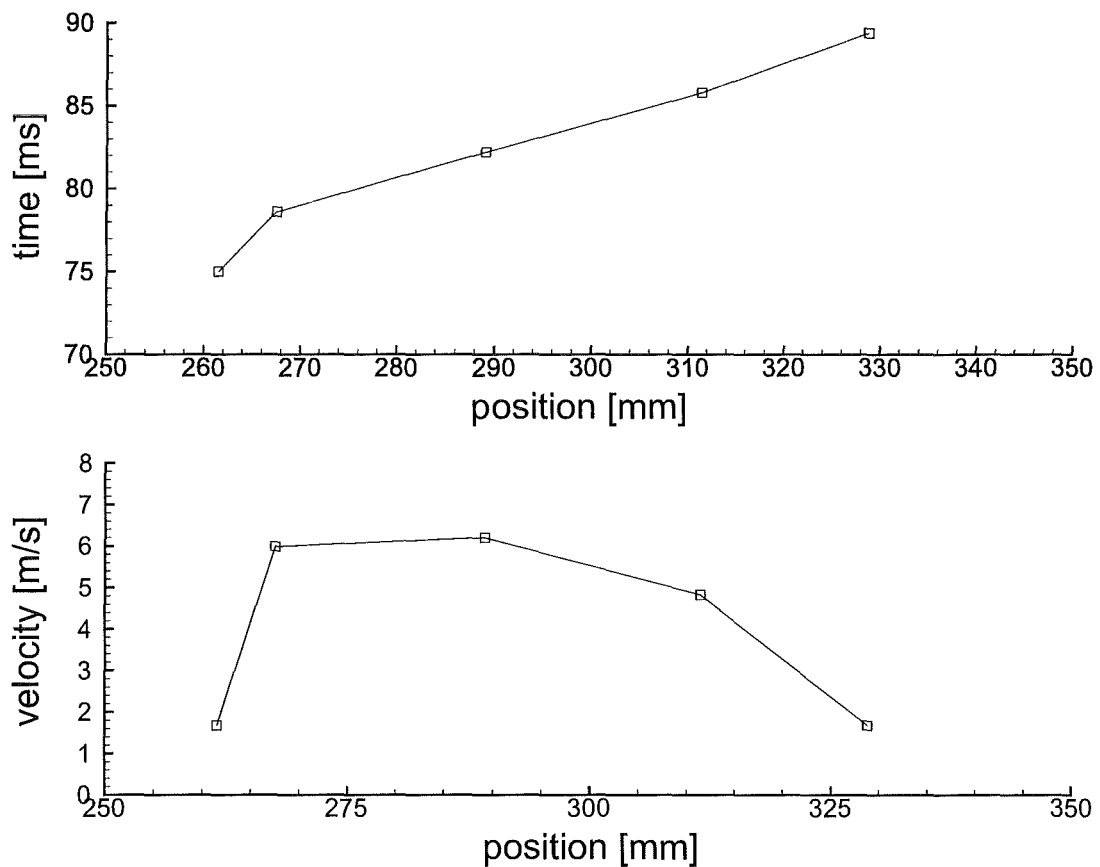


Figure 2.66: Position and velocity of the flame, experiment G48. Hydrogen concentration  $13.0\text{Vol.}\%$ ,  $p_0 = 1040\text{mbar}$ ,  $T_0 = 27.9^\circ\text{C}$

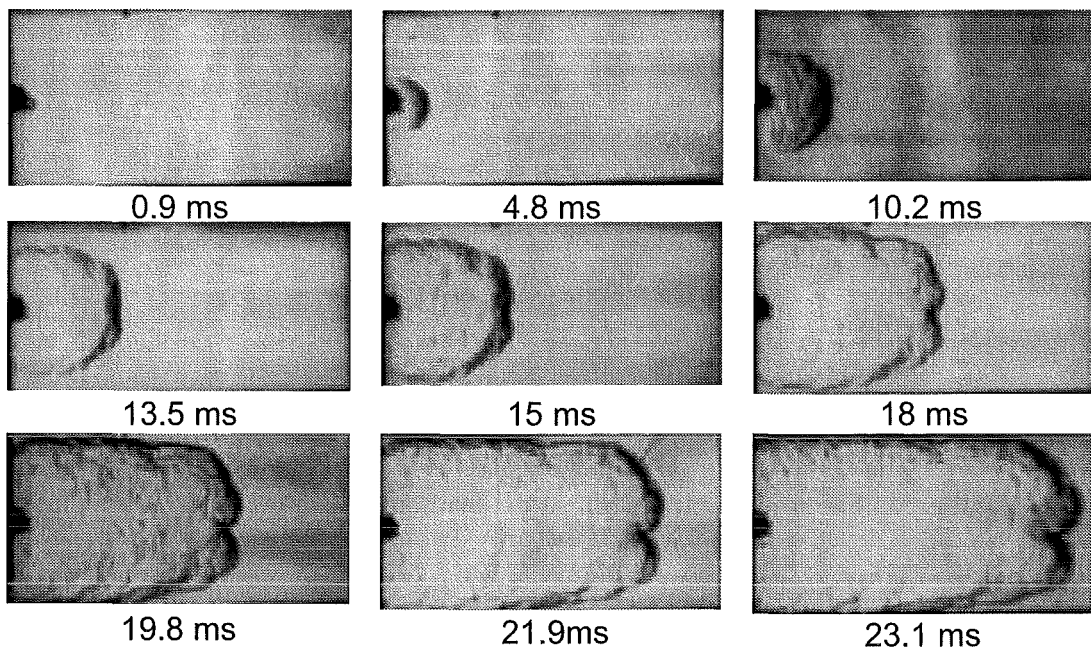


Figure 2.67: Schlieren cinematograph of experiment G28. Hydrogen concentration 15.2 Vol.%,  $p_0 = 1028 \text{ mbar}$ ,  $T_0 = 24.4^\circ\text{C}$

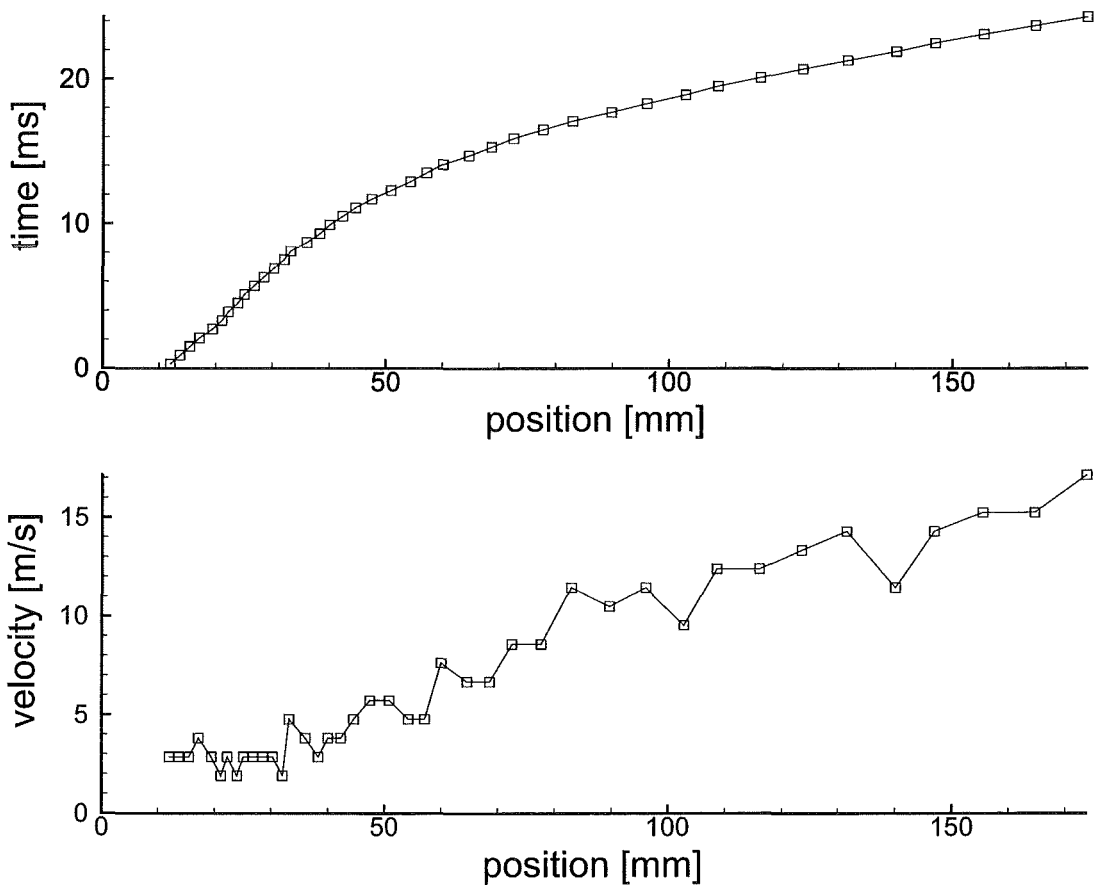


Figure 2.68: Position and velocity of the flame, experiment G28. Hydrogen concentration 15.2 Vol.%,  $p_0 = 1028 \text{ mbar}$ ,  $T_0 = 24.4^\circ\text{C}$

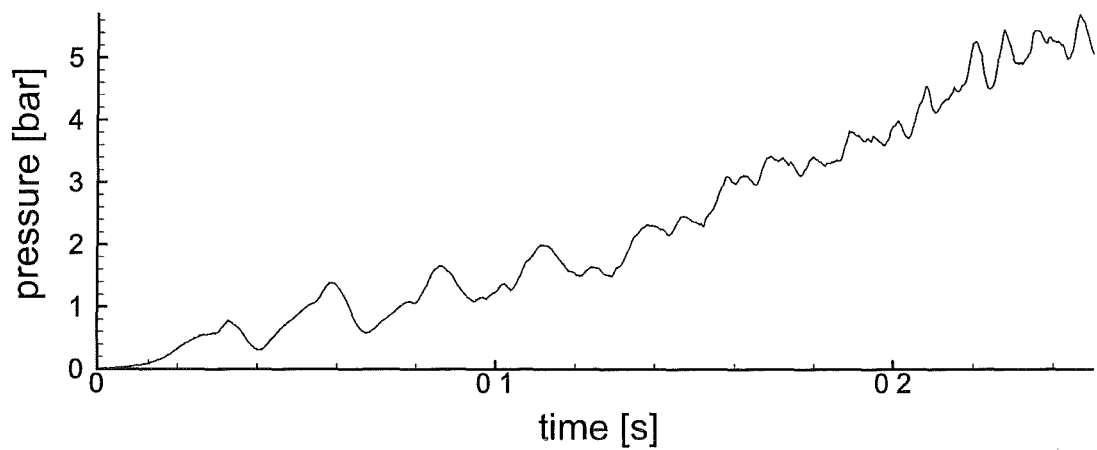


Figure 2.69: Pressure, experiment G28. Hydrogen concentration 15.2 Vol.%,  $p_0 = 1028\text{mbar}$ ,  $T_0 = 24.4^\circ\text{C}$

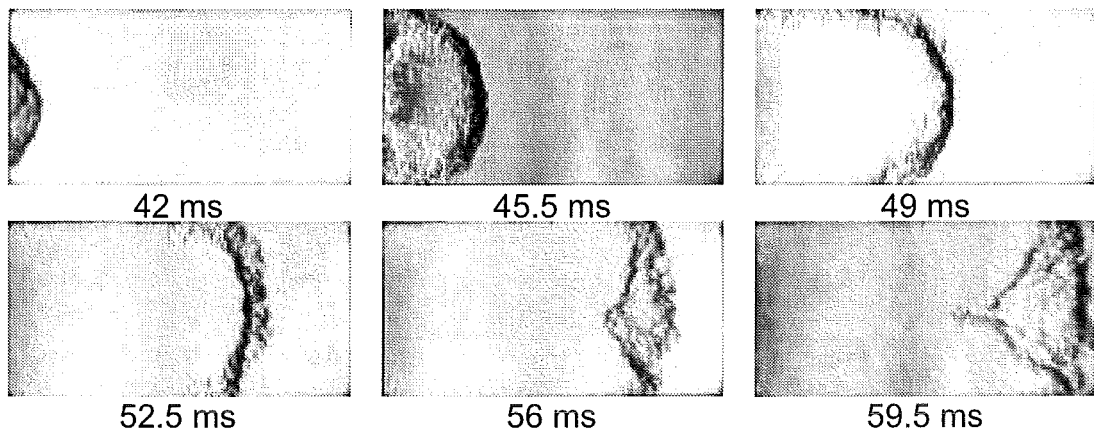


Figure 2.70: Schlieren cinematograph of experiment G47. Hydrogen concentration 15.0 Vol.%,  $p_0 = 1035\text{mbar}$ ,  $T_0 = 27.5^\circ\text{C}$

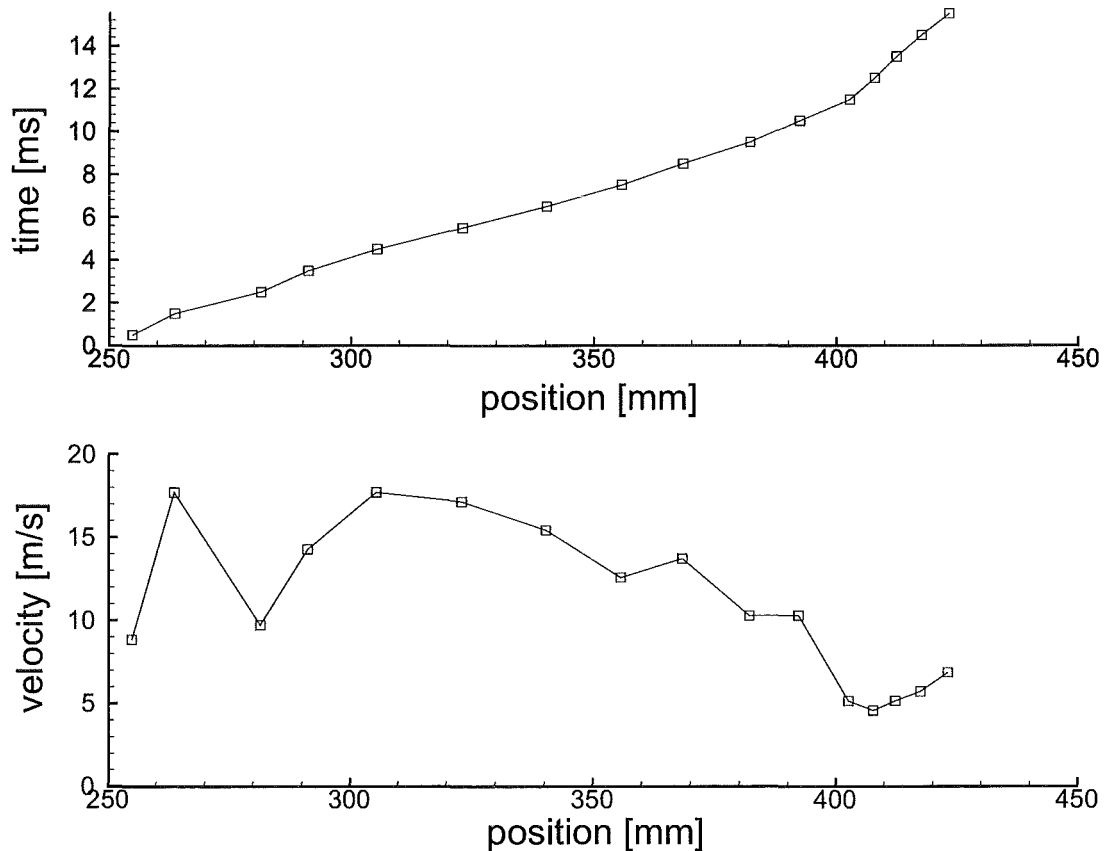


Figure 2.71: Position and velocity of the flame, experiment G47. Hydrogen concentration 15.0 Vol.%,  $p_0 = 1035\text{mbar}$ ,  $T_0 = 27.5^\circ\text{C}$ , time  $t = t - 40.5\text{ms}$

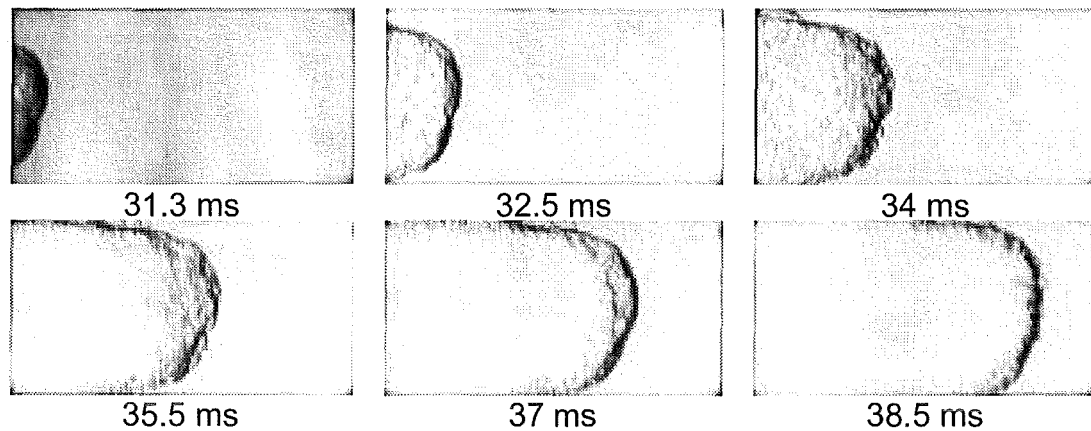


Figure 2.72: Schlieren cinematograph of experiment G46. Hydrogen concentration  $16.9\text{Vol.\%}$ ,  $p_0 = 1039\text{mbar}$ ,  $T_0 = 27.0^\circ\text{C}$

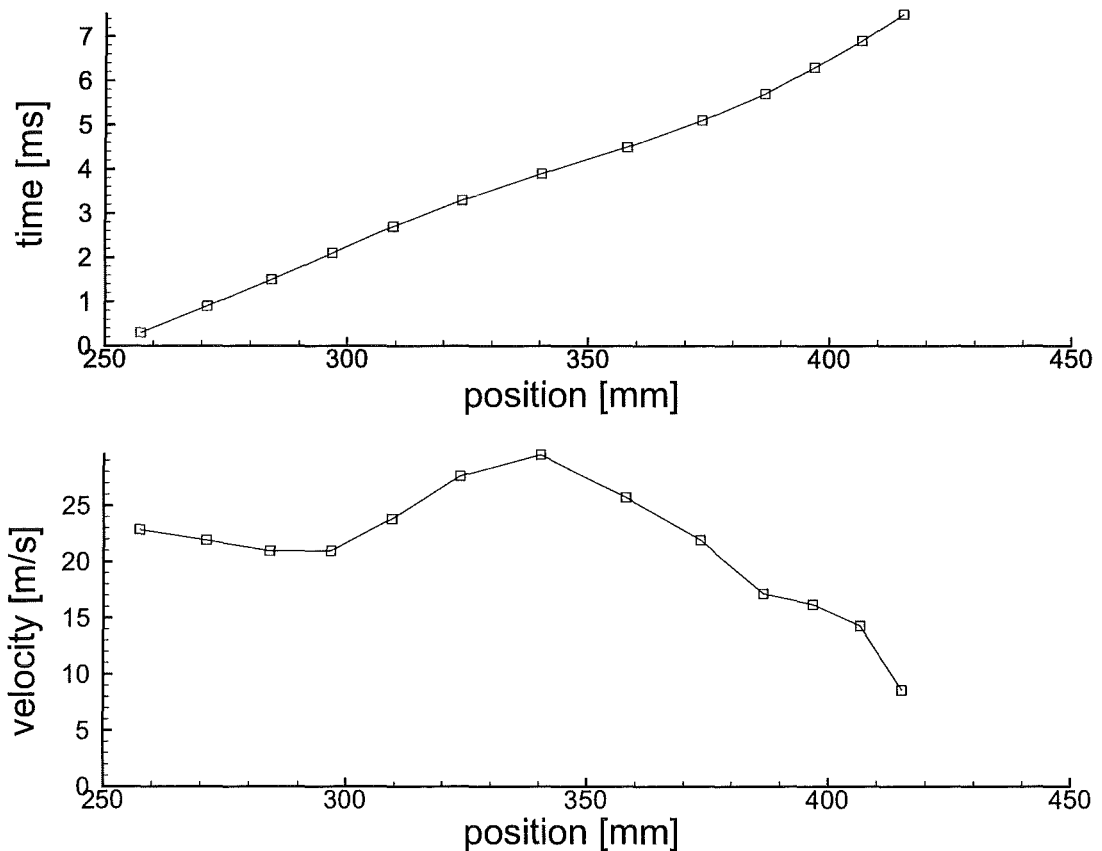


Figure 2.73: Position and velocity of the flame, experiment G46. Hydrogen concentration  $16.9\text{Vol.\%}$ ,  $p_0 = 1039\text{mbar}$ ,  $T_0 = 27.0^\circ\text{C}$ , time  $t = t - 31\text{ms}$

### 2.4.2 Data of the LDV-measurements in a single obstacle configuration

experiment	$H_2$ conc. [ Vol%]	obstacle	meas. position	meas. plane
phd 1 184	9.93	orifice 60%	middle	1
phd 1 150	9.89	orifice 60%	middle	2
phd 1 1	9.92	orifice 60%	middle	3
phd 1 260	10.22	-	middle	4
phd 1 278	11.51	orifice 60%	middle	1
phd 1 243	11.44	orifice 60%	middle	2
phd 1 123	11.61	orifice 60%	middle	3
phd 1 280	11.51	-	middle	4
phd 1 236	12.99	orifice 60%	middle	1
phd 1 244	13.02	orifice 60%	middle	2
phd 1 129	13.03	orifice 60%	middle	3
phd 1 288	13.12	-	middle	4
phd 1 252	16.09	orifice 60%	middle	2
phd 1 142	15.94	orifice 60%	middle	10 mm behind orifice
phd 1 132	15.81	orifice 60%	middle	3
phd 1 295	15.91	-	middle	4

Table 2.7: Initial conditions and configuration of the experiments below.

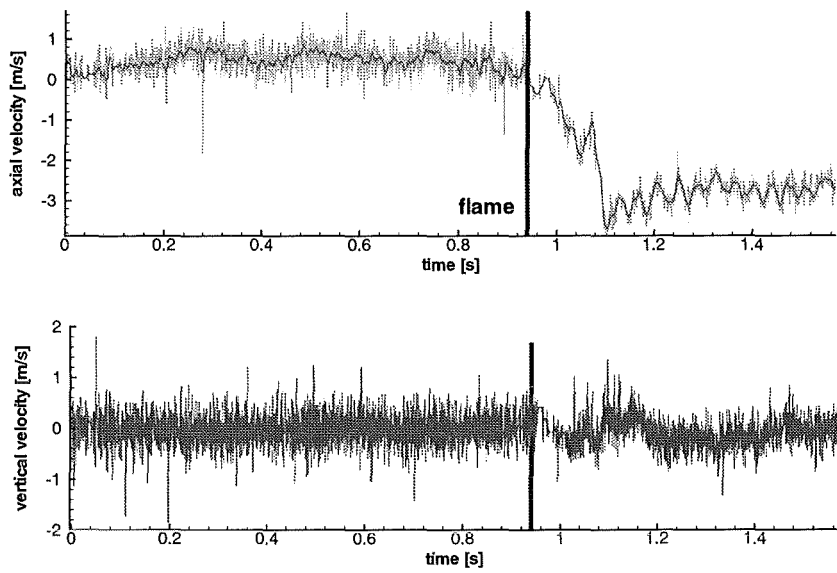


Figure 2.74: Measured horizontal and vertical velocity component in the PHD-tube with a single orifice with a blockage ratio of 60%. Measurement position: plane 1 middle, hydrogen concentration: 9.93Vol.%.  $t = 0s$  corresponds to 2000ms after ignition. Experiment phd 1 184.

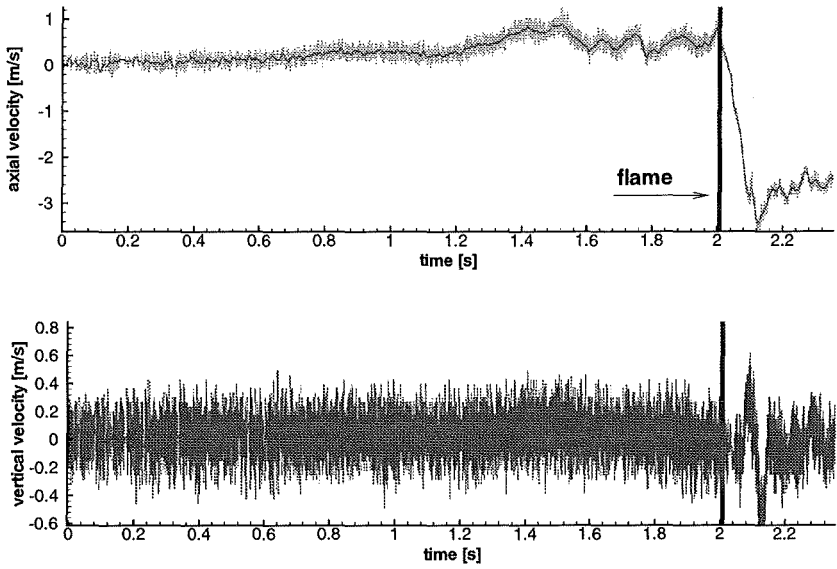


Figure 2.75: Measured horizontal and vertical velocity component in the PHD-tube with a single orifice with a blockage ratio of 60%. Measurement position: plane 2 middle, hydrogen concentration: 9.89Vol.%.  $t = 0s$  corresponds to 1500ms after ignition. Experiment phd 1 150

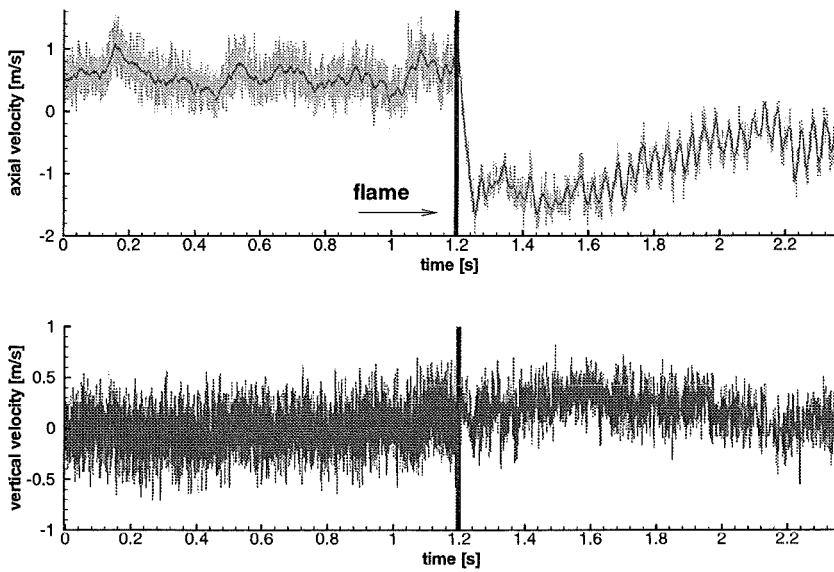


Figure 2.76: Measured horizontal and vertical velocity component in the PHD-tube with a single orifice with a blockage ratio of 60%. Measurement position: plane 3 middle, hydrogen concentration: 9.92 Vol.%.  $t = 0s$  corresponds to 1500ms after ignition. Experiment phd 1 1.

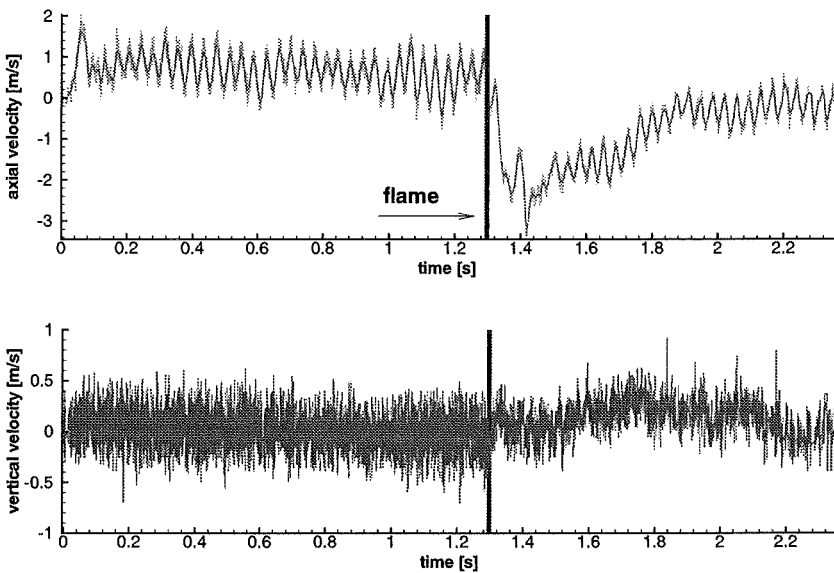


Figure 2.77: Measured horizontal and vertical velocity component in the PHD-tube without obstacle. Measurement position: plane 4 middle, hydrogen concentration: 10.22 Vol.%.  $t = 0s$  corresponds to 0ms after ignition. Experiment phd 1 260.

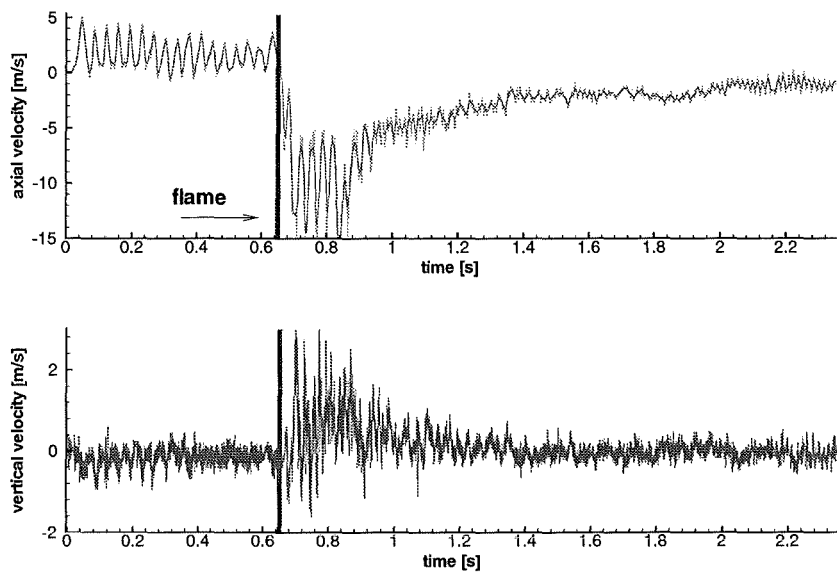


Figure 2.78: Measured horizontal and vertical velocity component in the PHD-tube with a single orifice with a blockage ratio of 60%. Measurement position: plane 1 middle, hydrogen concentration: 11.5 Vol.%.  $t = 0s$  corresponds to 0ms after ignition. Experiment phd 1 278.

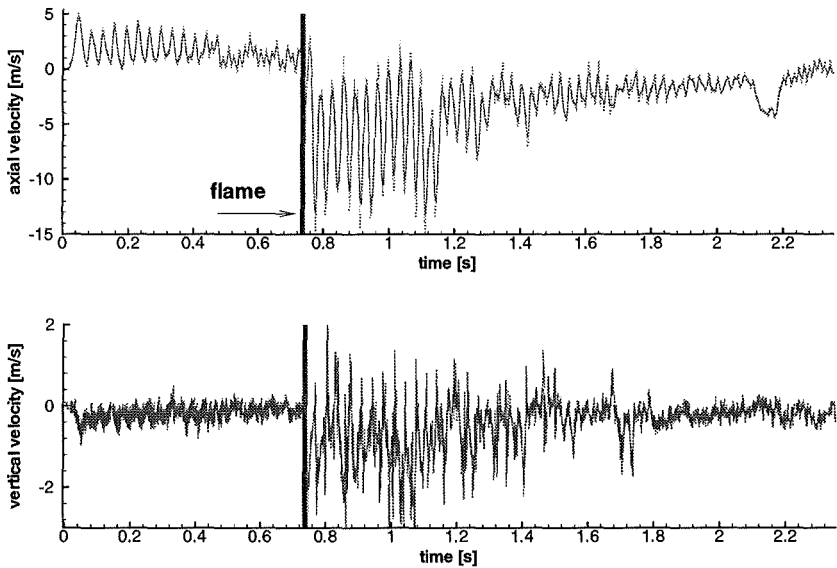


Figure 2.79: Measured horizontal and vertical velocity component in the PHD-tube with a single orifice with a blockage ratio of 60%. Measurement position: plane 2 middle, hydrogen concentration: 11.44 Vol.%.  $t = 0s$  corresponds to 0ms after ignition. Experiment phd 1 243.

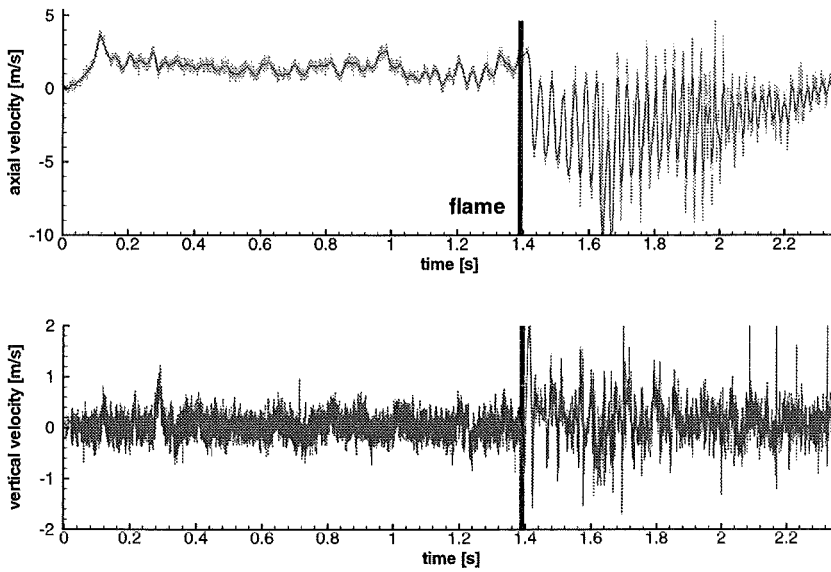


Figure 2.80: Measured horizontal and vertical velocity component in the PHD-tube with a single orifice with a blockage ratio of 60%. Measurement position: plane 3 middle, hydrogen concentration:  $11.61\text{Vol.\%}$ .  $t = 0\text{s}$  corresponds to  $0\text{ms}$  after ignition. Experiment phd 1 123.

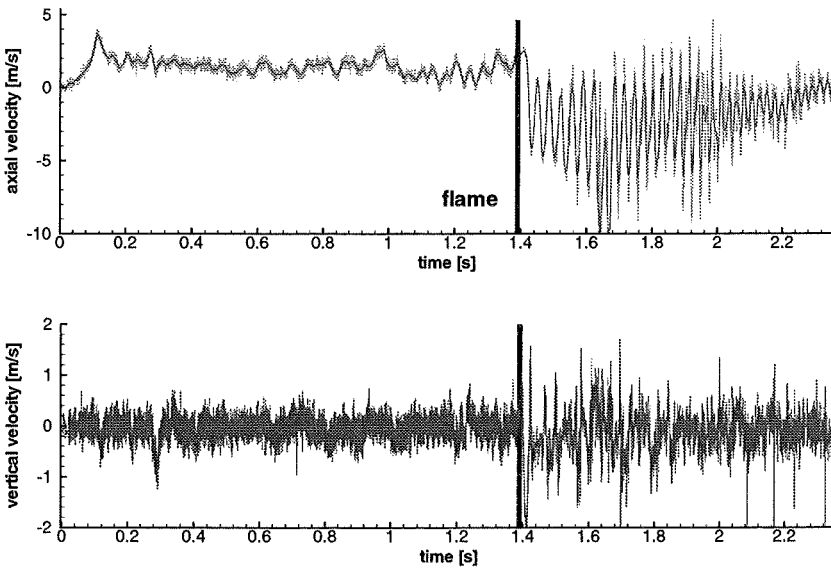


Figure 2.81: Measured horizontal and vertical velocity component in the PHD-tube without obstacle. Measurement position: plane 4 middle, hydrogen concentration:  $11.51\text{Vol.\%}$ .  $t = 0\text{s}$  corresponds to  $0\text{ms}$  after ignition. Experiment phd 1 280.

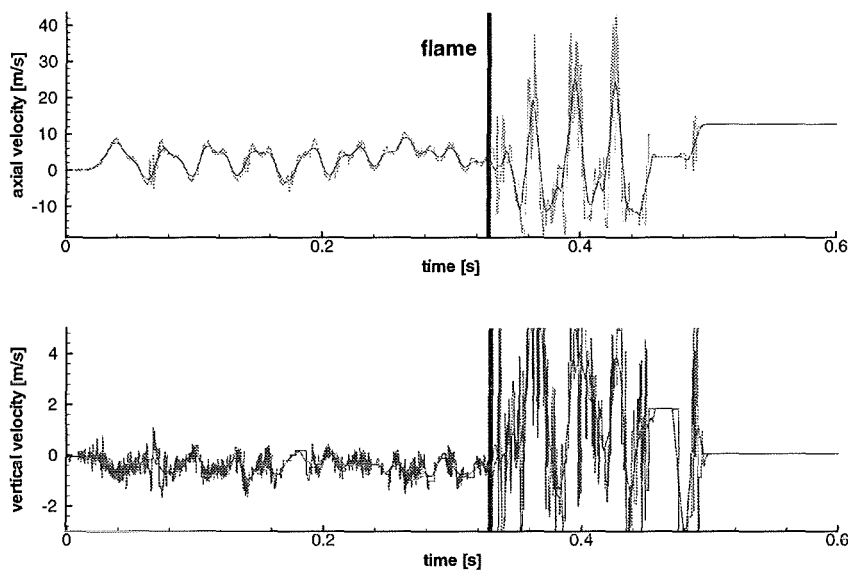


Figure 2.82: Measured horizontal and vertical velocity component in the PHD-tube with a single orifice with a blockage ratio of 60%. Measurement position: plane 1 middle, hydrogen concentration:  $12.99\text{Vol.}\%$ .  $t = 0\text{s}$  corresponds to  $0\text{ms}$  after ignition. Experiment phd 1 236.

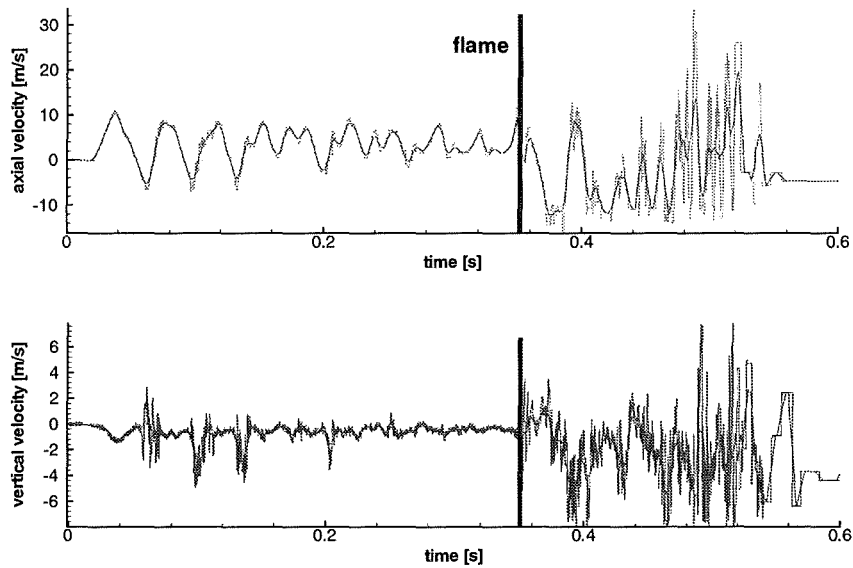


Figure 2.83: Measured horizontal and vertical velocity component in the PHD-tube with a single orifice with a blockage ratio of 60%. Measurement position: plane 2 middle, hydrogen concentration:  $13.02\text{Vol.}\%$ .  $t = 0\text{s}$  corresponds to  $0\text{ms}$  after ignition. Experiment phd 1 244.

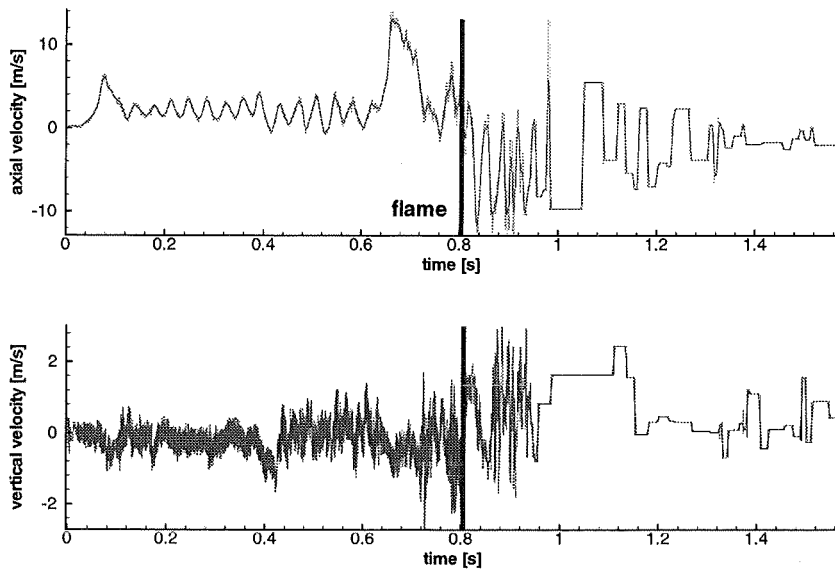


Figure 2.84: Measured horizontal and vertical velocity component in the PHD-tube with a single orifice with a blockage ratio of 60%. Measurement position: plane 3 middle, hydrogen concentration:  $13.03\text{Vol.}\%$ .  $t = 0\text{s}$  corresponds to  $0\text{ms}$  after ignition. Experiment phd 1 129.

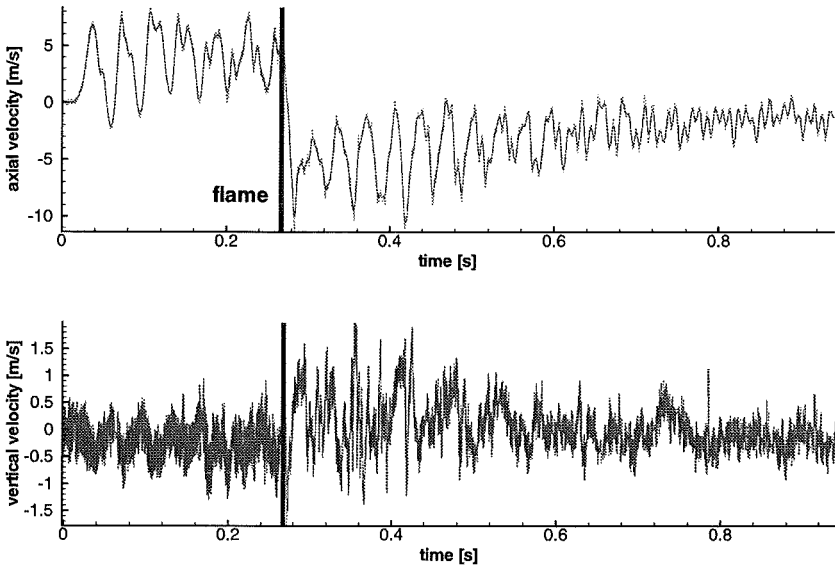


Figure 2.85: Measured horizontal and vertical velocity component in the PHD-tube without obstacle. Measurement position: plane 4 middle, hydrogen concentration:  $13.12\text{Vol.}\%$ .  $t = 0\text{s}$  corresponds to  $0\text{ms}$  after ignition. Experiment phd 1 288.

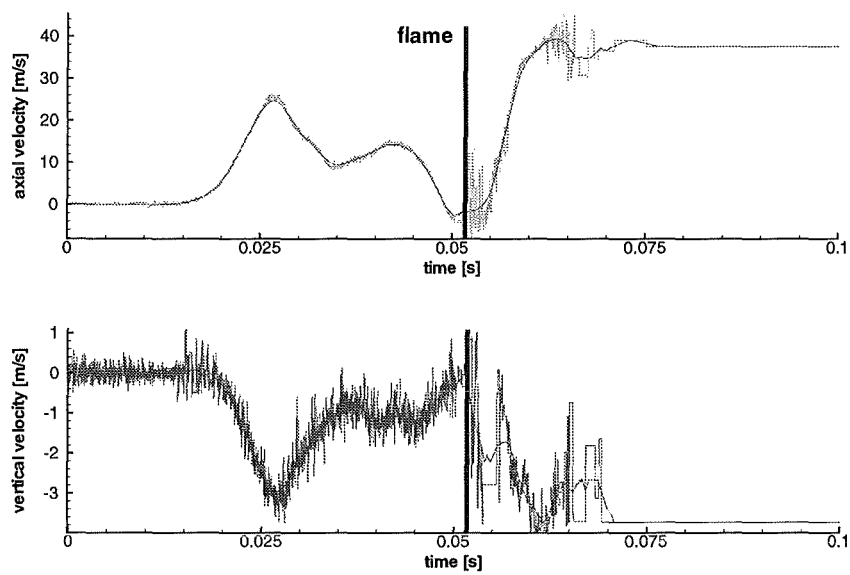


Figure 2.86: Measured horizontal and vertical velocity component in the PHD-tube with a single orifice with a blockage ratio of 60%. Measurement position: plane 2 middle, hydrogen concentration: 16.09 Vol.%.  $t = 0s$  corresponds to 0ms after ignition. Experiment phd 1 252.

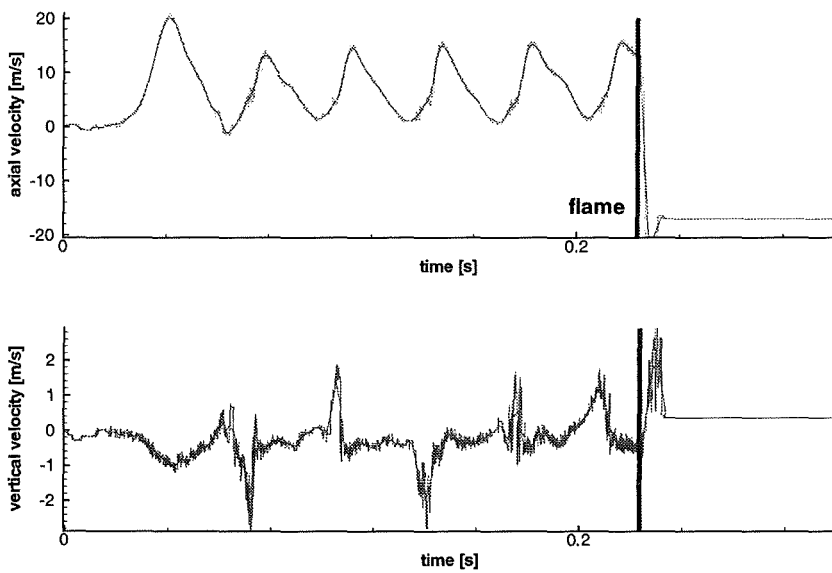


Figure 2.87: Measured horizontal and vertical velocity component in the PHD-tube with a single orifice with a blockage ratio of 60%. Measurement position: 10mm behind obstacle, middle, hydrogen concentration: 15.94 Vol.%.  $t = 0s$  corresponds to 0ms after ignition. Experiment phd 1 142.

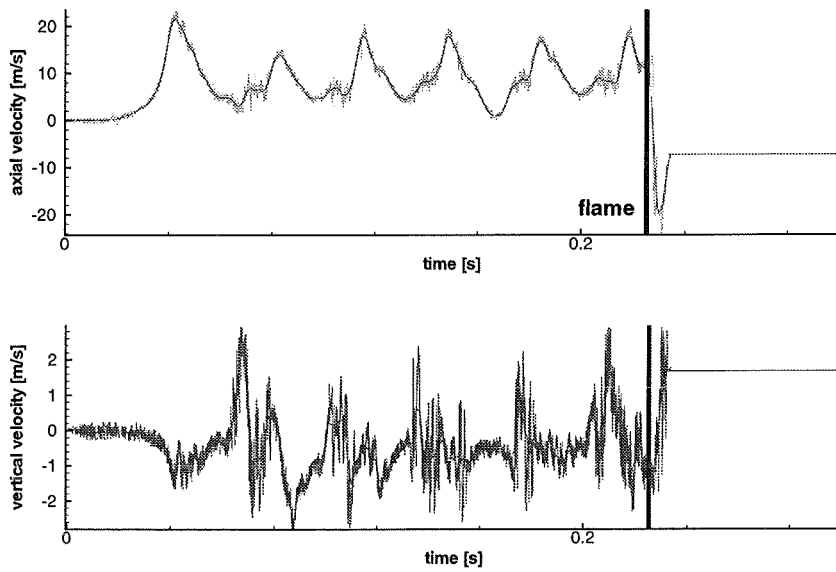


Figure 2.88: Measured horizontal and vertical velocity component in the PHD-tube with a single orifice with a blockage ratio of 60%. Measurement position: plane 3 middle, hydrogen concentration: 15.81 Vol.%.  $t = 0s$  corresponds to 0ms after ignition. Experiment phd 1 132.

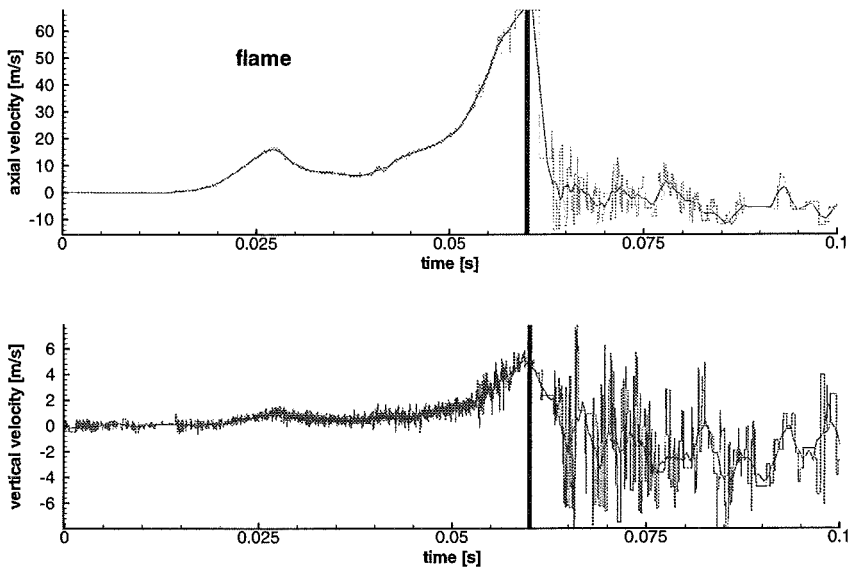


Figure 2.89: Measured horizontal and vertical velocity component in the PHD-tube without obstacle. Measurement position: plane 4 middle, hydrogen concentration: 15.91 Vol.%.  $t = 0s$  corresponds to 0ms after ignition. Experiment phd 1 295.

### 2.4.3 Data of experiments without obstacle in the PHD-tube

experiment	hydrogen concentration [ Vol%]
phd o 479	9.9
phd o 480	11.07
phd o 482	12.03
phd o 484	12.85
phd o 487	14.14
phd o 492	15.99

Table 2.8: Initial conditions of the experiments without obstacles.

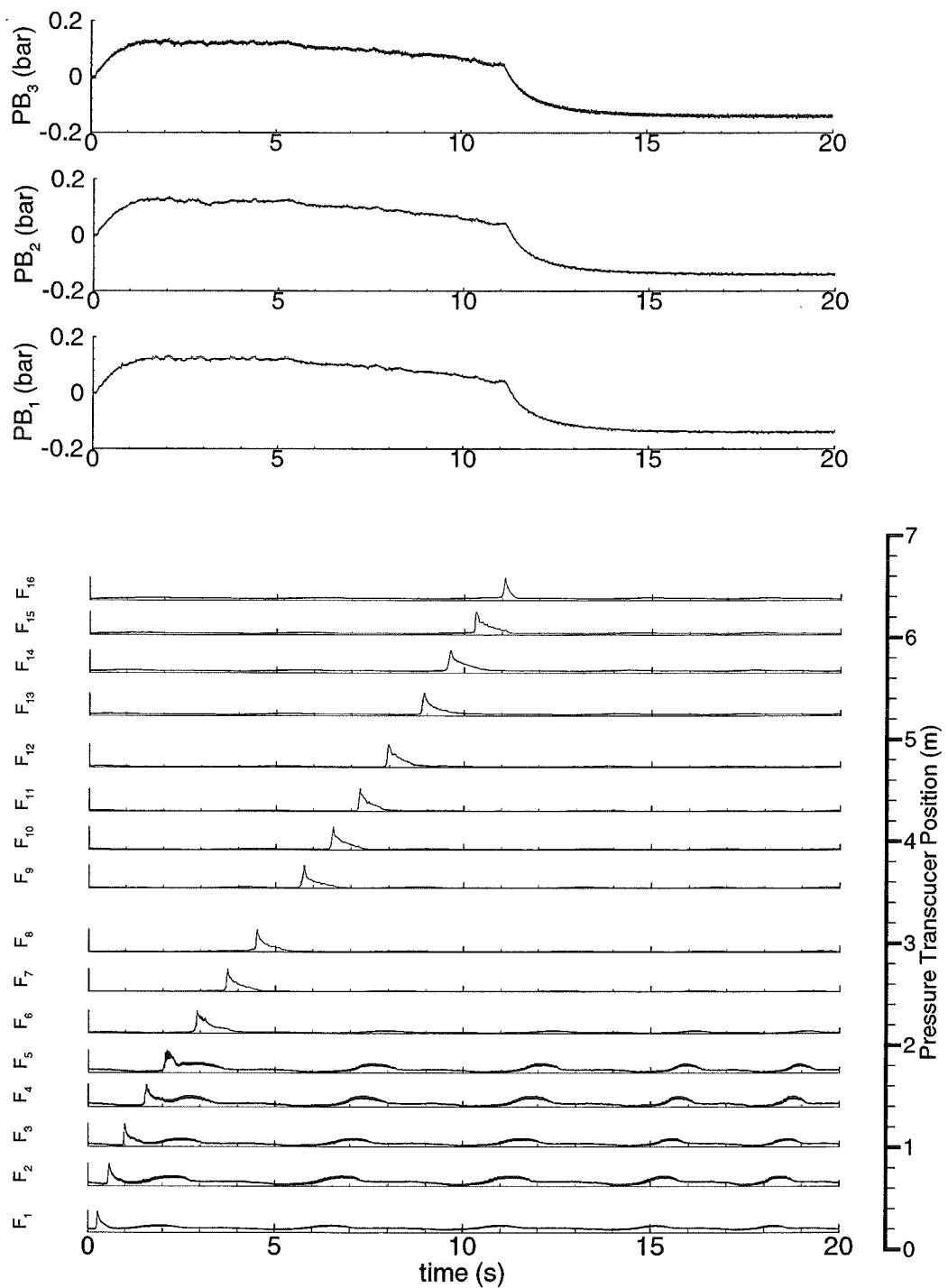


Figure 2.90: Pressure traces and flame position of experiment phd o 479. Initial conditions: 9.9 % hydrogen, 0.990 bar initial pressure, 20.0° C.

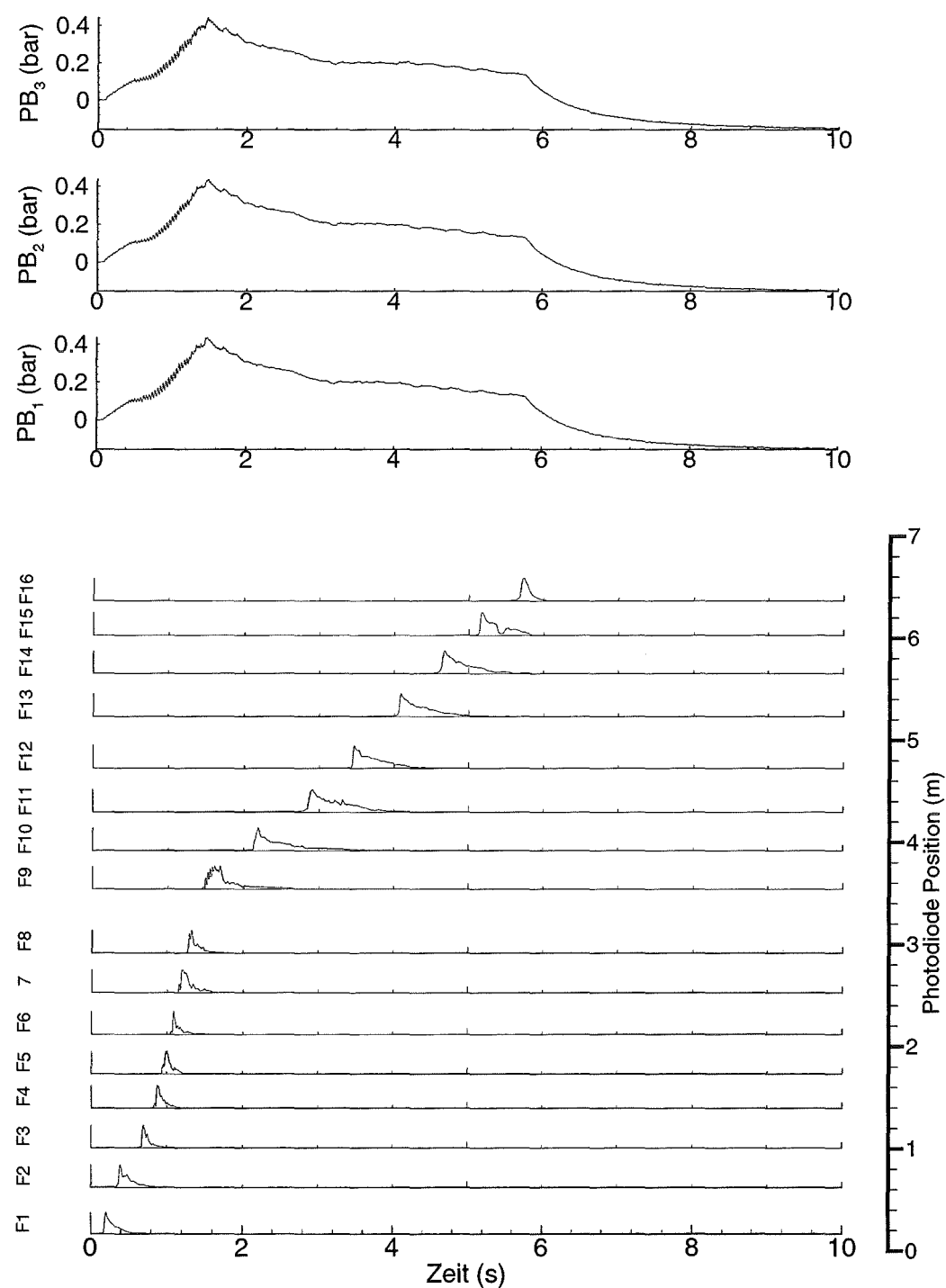


Figure 2.91: Pressure traces and flame position of experiment phd o 480. Initial conditions: 11.07 % hydrogen, 0.988 bar initial pressure, 20.1° C.

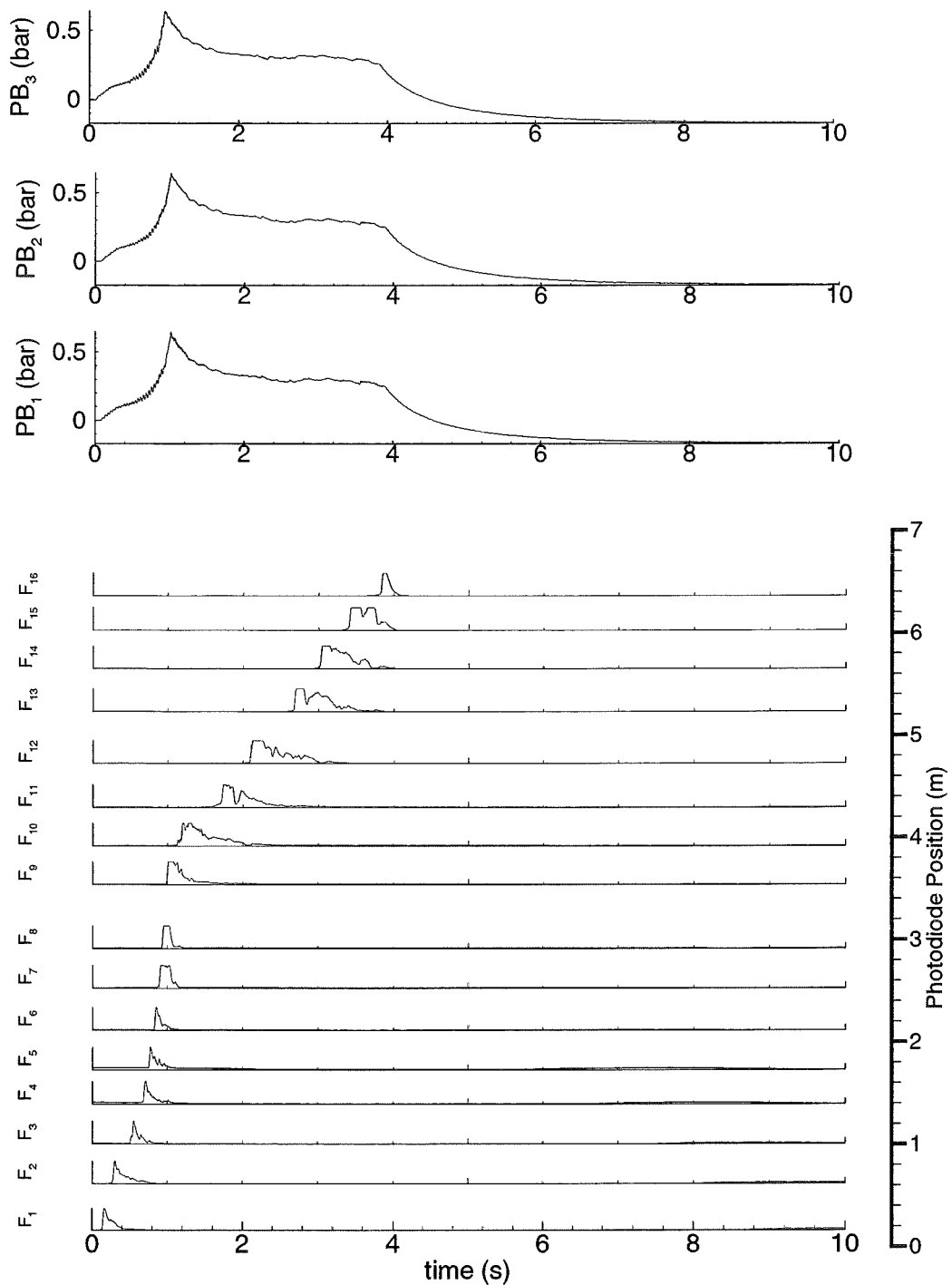


Figure 2.92: Pressure traces and flame position of experiment phd o 482. Initial conditions: 12.03 % hydrogen, 0.990 bar initial pressure, 20.5° C.

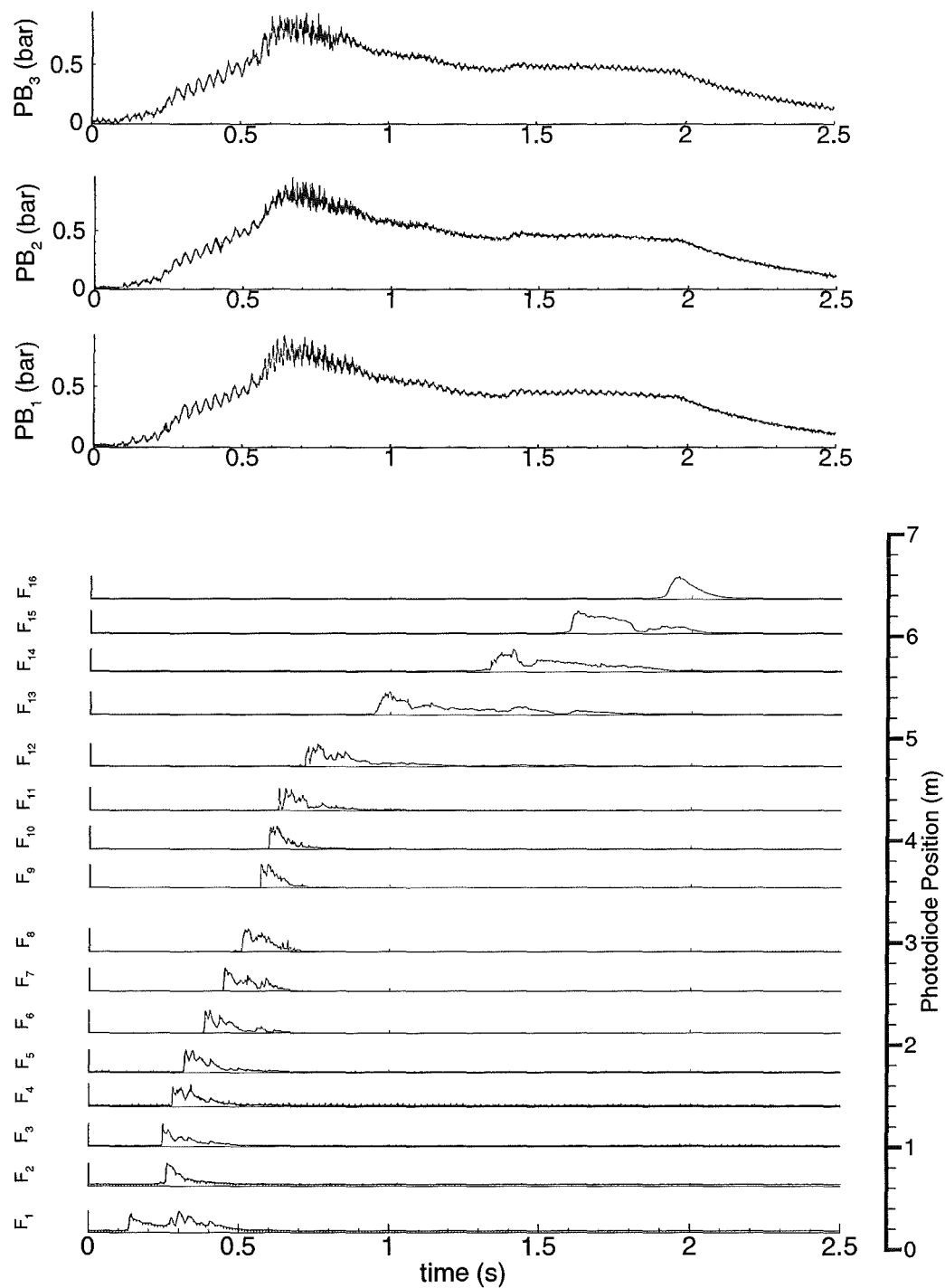


Figure 2.93: Pressure traces and flame position of experiment phd o 484. Initial conditions: 12.85 % hydrogen, 1.000 bar initial pressure, 21.0° C.

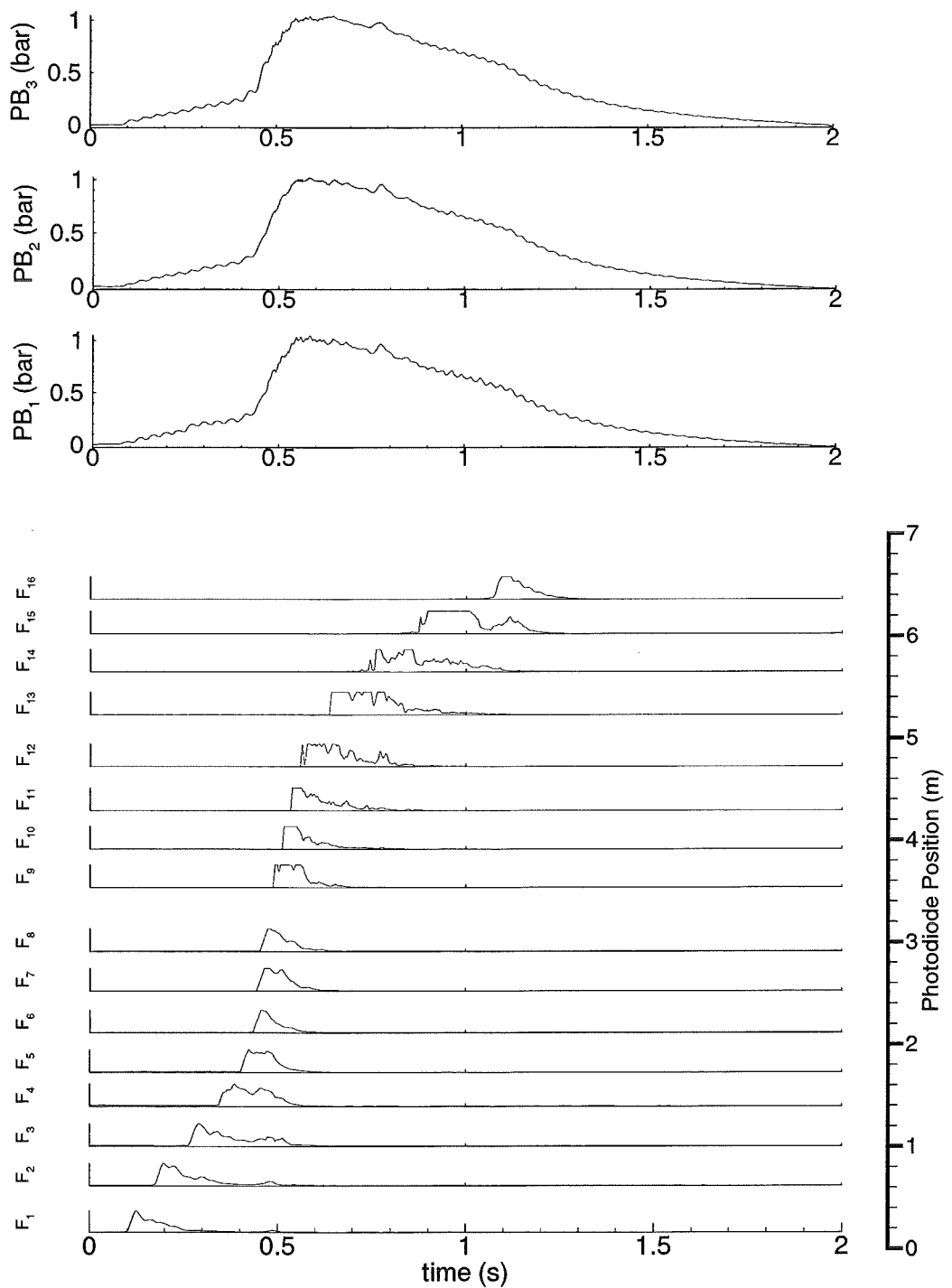


Figure 2.94: Pressure traces and flame position of experiment phd o 487. Initial conditions: 14.14 % hydrogen, 0.992 bar initial pressure, 21.3° C.

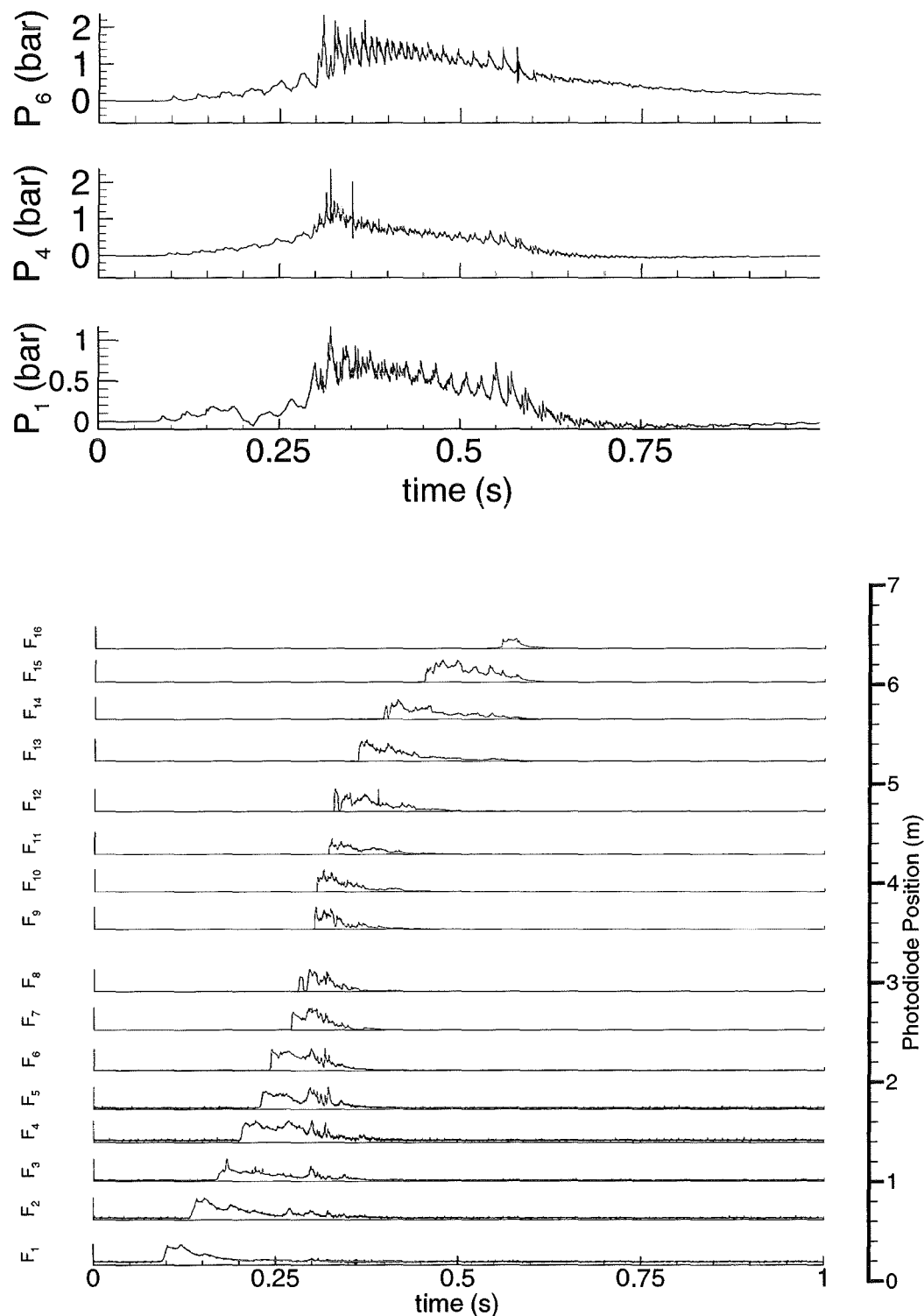


Figure 2.95: Pressure traces and flame position of experiment phd o 492. Initial conditions: 15.99 % hydrogen, 1.002 bar initial pressure, 22.0° C.

## 2.5 Inert test in the FZK tubes

The aim of these tests was to verify the turbulence and the hydrodynamic models of the different codes (FZK, JRC Ispra, TU Munich) under inert conditions, without interference from a combustion process.

### 2.5.1 Theory

A defined volume is separated in two sections by a membrane. One section is filled with gas to a defined initial pressure (lower than in section 2). The other section is filled with helium until the membrane bursts. Figure 2.96 shows the initial conditions before the membrane bursts. After the membrane bursted a shock wave propagates into the low pressure section, while an expansion wave propagates backwards into the high pressure section. Figure 2.97 illustrates the course of these tests, the levels of pressure, flow velocity and density. The pressure ratio is determined by the nonlinear shock tube theory, given in equation 2.36.

$$\frac{p_1}{p_4} = \frac{\left[1 - \frac{\gamma_4 - 1}{\gamma_1 + 1} \frac{c_1}{c_4} \frac{M_s^2 - 1}{M_s}\right]^{\frac{2\gamma_4}{\gamma_4 - 1}}}{1 + \frac{2\gamma_1}{\gamma_1 + 1} (M_s^2 - 1)} \quad (2.36)$$

Where:

$p_1$  = high pressure

$p_4$  = low pressure

$\gamma_1$  = ratio of specific heats in LPS

$\gamma_4$  = ratio of specific heats in HPS

### 2.5.2 Experiments

#### 2.5.2.1 Inert tests in FZK 12m-tube

##### 2.5.2.1.1 Tests for verification of turbulence models

The 12m-FZK tube was modified to allow inert tests in a shock tube mode, and in which a three m long section can be pressurised. After bursting of the membrane a shock wave travels into the remaining section which is initially at a low pressure ( $p_1 = 1$  bar) and contains circular orifices as obstacles (12 rings, 30% BR, 50 cm apart). The shock wave loses velocity and pressure amplitude by partial reflection and turbulence generation. The measured pressure signals at different locations can then be compared to numerical simulations using different

turbulence models. These data allow to verify the turbulence modelling under inert conditions, without interference from a combustion process. Four experiments (Table 2.9) were performed in the inert shock-tube mode. Figure 2.98 shows one example for the measured pressure decay as the wave proceeds into the obstacle region. These results are compared to the calculations with the different codes in the benchmark section of this report.

Table 2.9: Inert tests in FZK 12m-tube for verification of turbulence models

Experiment	Pressure in HPS $p_1$ [bar]	Pressure in LPS $p_4$ [bar]	Initial temperature [K]	Membrane thickness [mm]
R1096_00	2.35	1.0	283	0.2
R1096_01	3.7	1.0	283	0.4
R1096_02	5.1	1.0	283	0.6
R1096_03	5.05	1.0	283	0.6

### 2.5.2.1.2 Adaptive mesh refinement tests

The 3m tube was modified to allow inert tests in a shock tube mode where a 1.8m section can be pressurized. After bursting of the membrane the shock wave

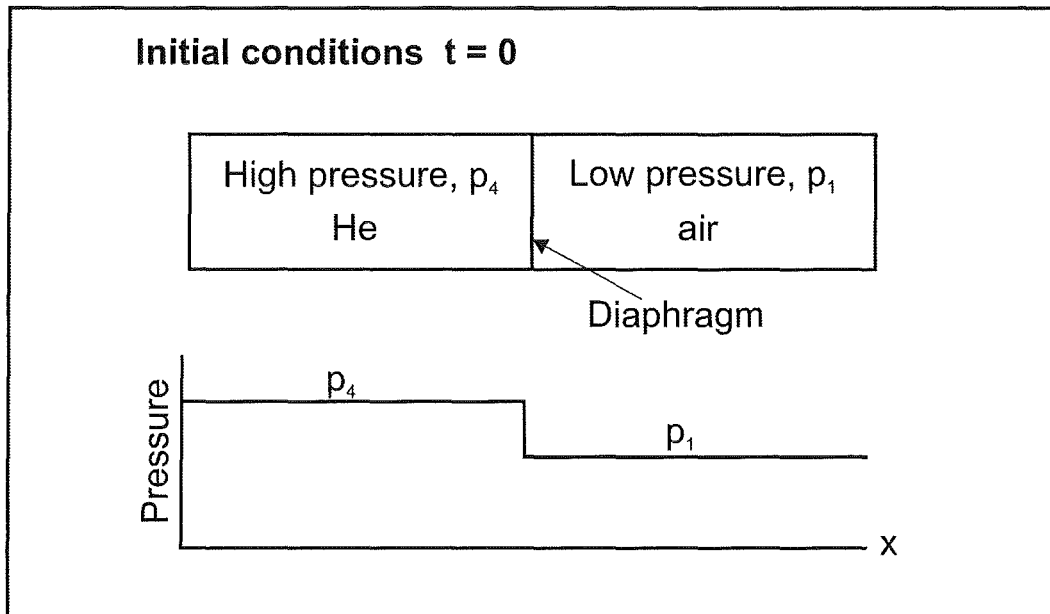


Figure 2.96: Initial conditions in shock tube experiments

travels into the remaining section which is initially at low pressure and contains a cube of 5 cm x 5 cm x 5 cm. The measured pressure signals at different locations can then be compared to numerical simulations. These data allow to verify the AMR-models under inert conditions, without interference from a combustion process. Fig. 2.99 shows one example of the measured pressure history.

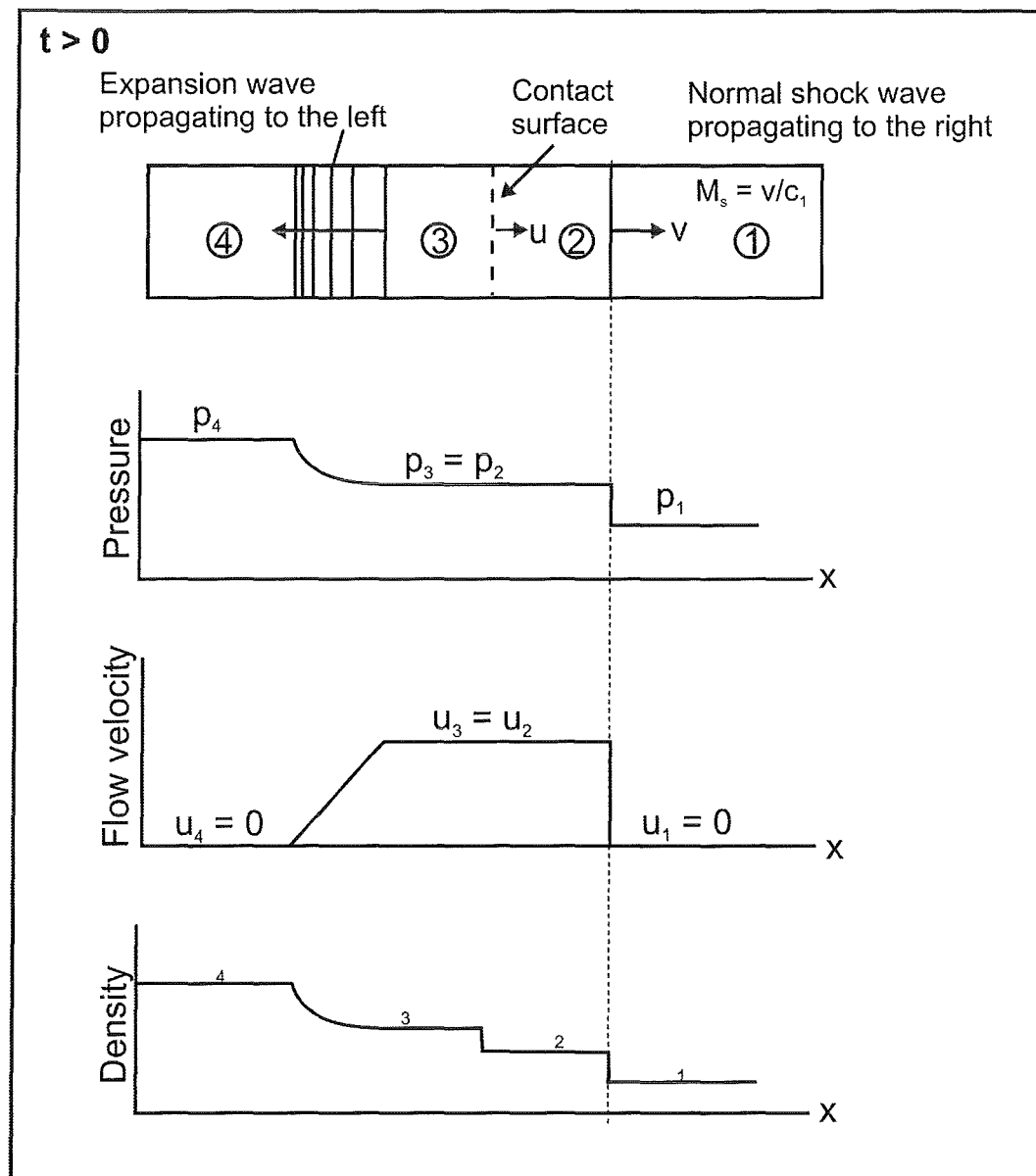


Figure 2.97: Schematic diagram of wave propagation in a shock tube

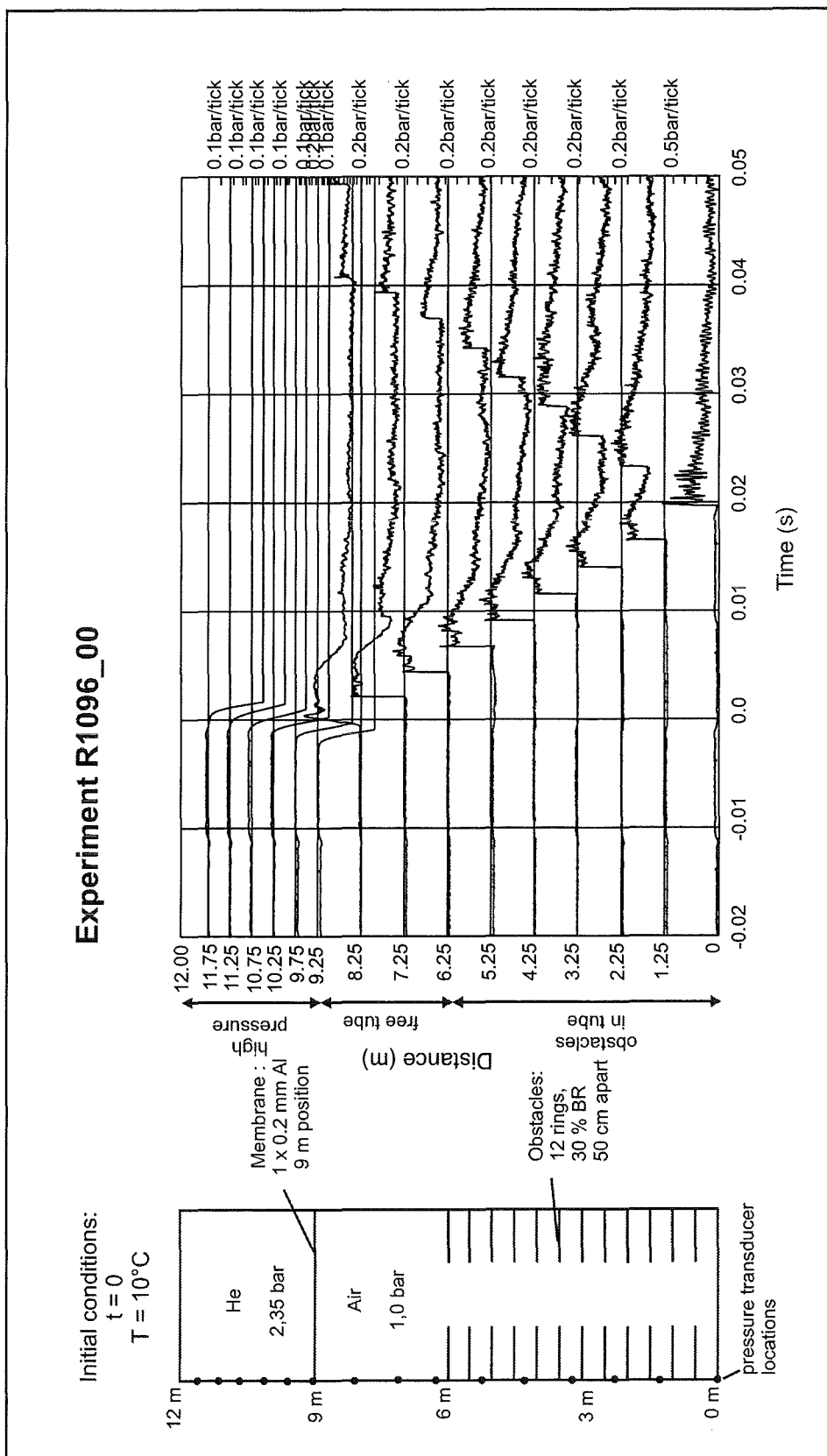


Figure 2.98: Inert shock-tube experiment in 12m-FZK-tube. The measured pressure data contain information about turbulence generation and dissipation without combustion

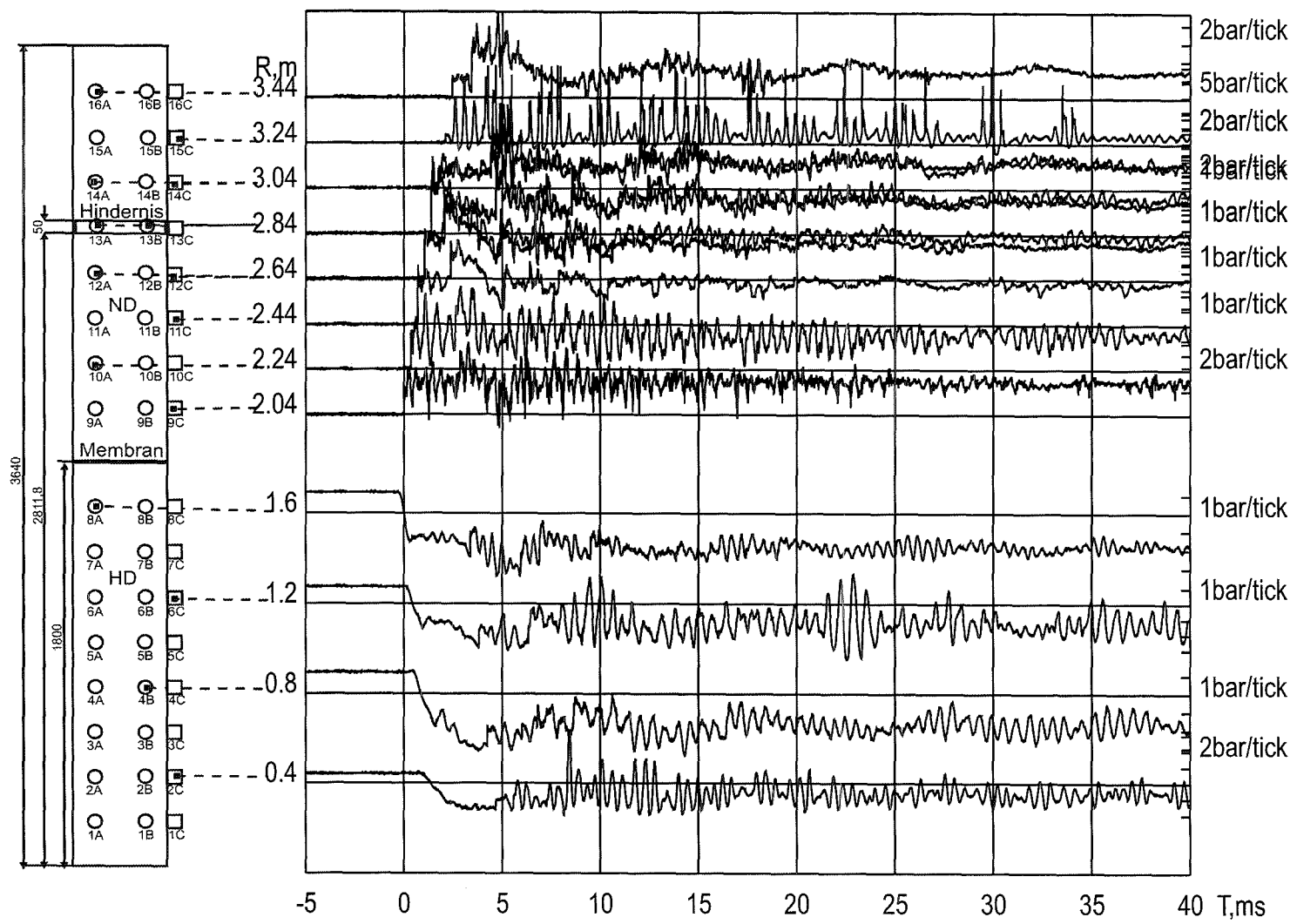


Figure 2.99: Measured pressure signals of experiment R1397\_03

## 2.6 FZK 12m-Tube

### 2.6.1 Theory of premixed turbulent combustion

In severe reactor accidents different  $H_2$ - combustion modes are possible. They are not only influenced by the mixture parameters (e.g.  $H_2$  or steam concentration in air) but also by the geometrical parameters like obstacles and surrounding geometry. A close relationship exists between hydrodynamics and chemistry.

Figure 2.100 shows Schlieren pictures of different combustion modes in  $H_2$ -air mixtures. High density gradients are represented by dark areas.

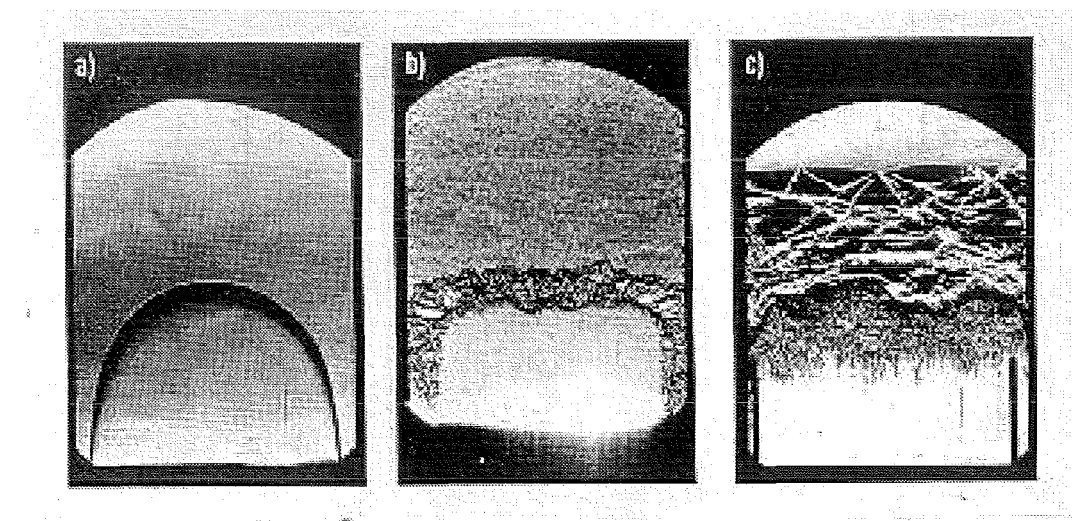


Figure 2.100: Schlieren pictures of a laminar deflagration (a), turbulent deflagration (b) and quasi- detonation (c) (F.-J. Wetzel, DLR, 1993)

Picture 8 shows a laminar flame in which unburned and burned gas are separated by a smooth, very thin flame surface. The flame travels with a constant velocity to the top. The continuous combustion is maintained by diffusion of heat and radicals. The transport and the detailed chemistry can be well described by numerical models with sufficient space resolution. Picture 8b shows a typical fast turbulent flame. A continuous flame surface is not existing, pockets of unburned and burned gas are surrounded by the respective other medium. The heat and mass transport are governed by turbulence, not by molecular diffusion. The turbulent combustion velocity  $S_t$  may often be described by the laminar combustion velocity  $S_L$  and the turbulent fluctuation velocity  $u'$  according to:

$$S_t/S_L = 1 + u'/S_L (u'/S_L < 40) \quad (2.37)$$

$u'$  is a measure for the mean turbulent kinetic energy per mass  $k$ . At very high turbulence loads quenching causes a decrease of the turbulent combustion

velocity. Picture 8c shows an even faster combustion form, a so-called quasi-detonation. The flame front is so fast that the leading pressure wave of heats the unburned gas above its ignition temperature. The pressure waves were created by the rapid expansion of the burned and compressed gas. Transversal shock waves formed by overlapping local temperature gradients which ignite the preheated gas. This complex of fast flame and pressure waves reaches in lean  $H_2$ -air mixtures velocities of about 1300 m/s (15 %  $H_2$ ). Well developed stable detonations in which flame and shock are coupled reach about 2000 m/s in stoichiometric  $H_2$ -air mixtures. Fast turbulent flames and detonations generate high dynamic loads and are therefore of considerable interest for the reactor safety.

In recent publications turbulent combustion processes are classified according to the turbulent fluctuation velocity  $u'$  and the turbulent macro length  $L_t$  of the flow. The so- called Borghi diagram is shown in Figure 2.101.

$u'$  and  $L_t$  are scaled by the velocity and length scale of the laminar combustion, namely laminar velocity  $S_L$  and flame thickness  $d_L$ .  $S_L$  and  $d_L$  only depend on the gas mixture but not on the hydodynamic flow parameters. The so defined parameter range for the turbulent combustion is divided by the three dimensionless numbers in five characteristic regimes. If the turbulent Reynolds number  $R_t = u'L_t/\nu$  is smaller than 1 the combustion is quasi-laminar ( $\nu$ = viscosity). The other regimes in Figure 2.101 are defined by the turbulent Karlovitz number and Damköhler number. The Karlovitz number describes the ratio of laminar reaction time ( $d_L/S_L$ ) to turbulent transport time of the smallest eddies ( $I_k/u'_k$ ).

$$Ka = (d_L/S_L)/(I_k/u'_k) \quad (2.38)$$

The turbulent Damköhler number describes the ratio of the largest turbulent transport time ( $L_t/u'$ ) and the laminar combustion time ( $d_L/S_L$ ).

$$Da = (L_t/u')/(d_L/S_L) \quad (2.39)$$

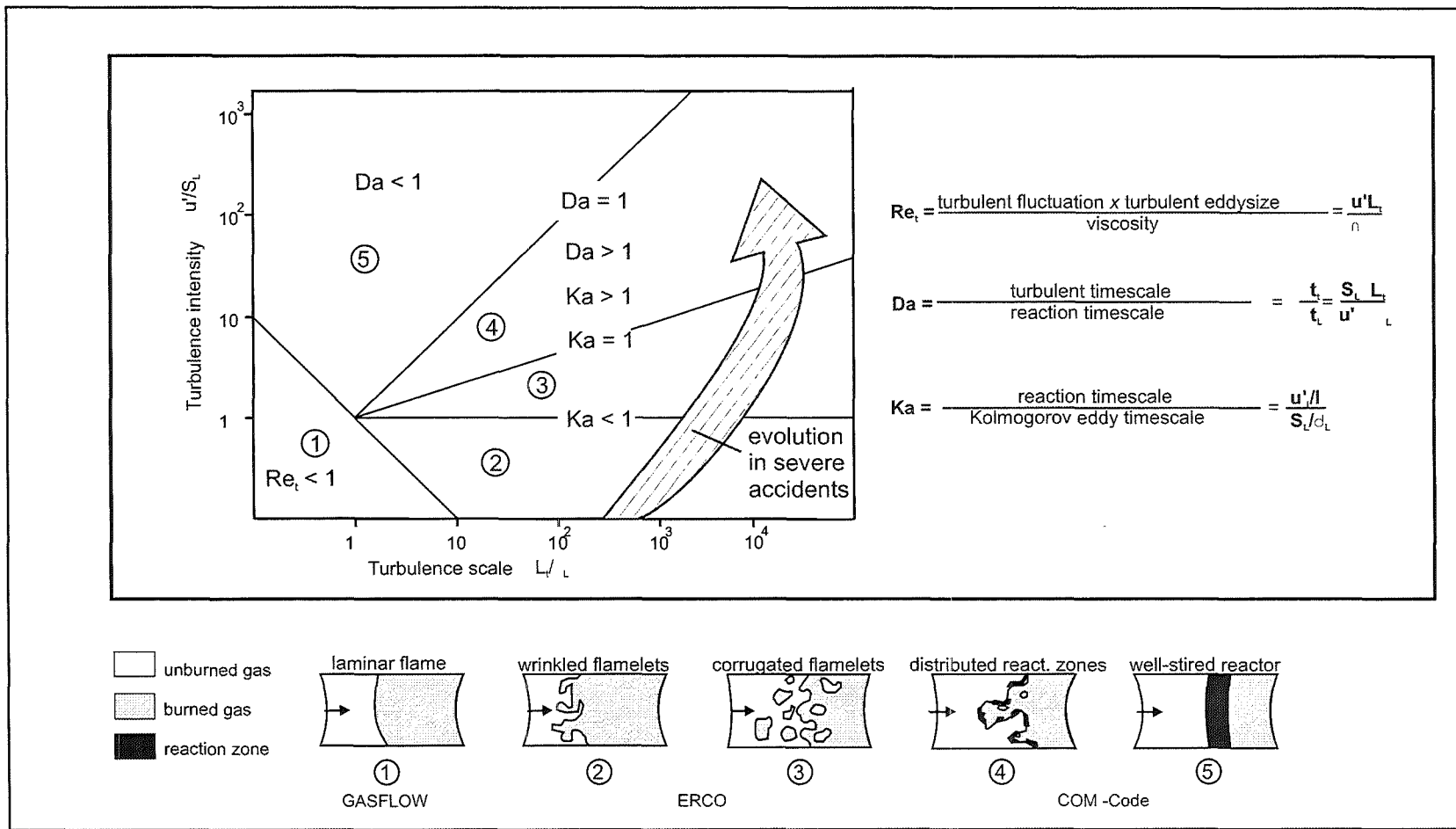
The size of the turbulent eddies ranges from macro length scale to the micro length scale of the smallest eddies, the so-called Kolmogorov length  $l_K$ . In regime 2 of figure 2.101 the turbulent fluctuation velocity is smaller than the laminar flame velocity. There are only slightly wrinkled but in their inner structure still laminar flames observable.

In regime three the turbulence eddies are already capable to slow down or to accelerate the flame front locally. These folded flames also have a local laminar structure, but burn because of wrinkling and stretching effects with different velocities.

In regime 4 the smallest eddies can penetrate the flame front and change its thin and laminar structure to a thickened flame front. In contrast to the regimes 2 and 3, where the combustion velocity becomes higher because of wrinkles and the expansion of the laminar flame surface, the combustion velocity in regime 4 increases mainly because of the faster turbulent transport within the flame zone.

With increasing  $u'$  the heat and mass transport in the flame can be accelerated due to increasing eddy sizes. Along the line  $Da = 1$  the turbulent transport has the same time scale as the chemical reaction. With the further acceleration of the turbulent transport ( $Da < 1$ ) extended volumes of the reactive gas are brought rapidly to ignition conditions by mixing of burned and unburned gas before then the burn proceeds in a relatively slow reaction. The combustion rate is now determined by the reaction kinetics and no longer by mixing processes between burned and unburned gas.

Figure 2.101: Classification of turbulent premixed deflagration regimes (Borghesi diagramm) and typical evolution of combustion regime in severe accidents



## 2.6.2 Experimental details

A large variety of experiments was performed during the reported period. A summary of the different test issues is shown in figure 2.102 The test issues are listed as follows:

- turbulence models
- adaptive mesh refinement tests
- flame quenching
- flame acceleration

In the present report detailed information about the experiments and results obtained will be described.

### 2.6.2.1 Test facility

Two combustion tubes (12 m long, 35 cm inner diameter (Figure 2.103) and 3 m long, 10 cm cross section) were designed and constructed at FZK.

### 2.6.2.2 Instrumentation

Since the objective is to investigate combustion processes, fast pressure transducers and Germanium photodiodes were selected and installed along the tubes.

#### 2.6.2.2.1 Pressure transducers

To measure combustion generated dynamic loads to structures, fast pressure transducers were selected as one part of instrumentation. The used gauges (PCB models 113A22 and 113A24) have rated resonance frequencies of 500 kHz and measuring ranges of 70 and 350 bar, respectively. A special shock tube was designed, fabricated and used to calibrate the pressure transducers for shockwave applications. Sensitivity coefficients were measured by comparing the gauge output (Volts) with pressure steps calculated from ideal shock tube theory. The measured sensitivities agreed well with the suppliers data up to the specified pressure limit of the gauge. For higher pressures the gauge's response becomes strongly nonlinear, so that extrapolation of measured pressure is not reliable above about 130 % of the rated pressure range. The pressure gauges were installed along the whole length of the combustion tube. The gauge output was recorded on transient digitizers with 4 *mus* sampling rate.

### 2.6.2.2.2 Photodiodes

To determine local and integral flame velocities photodiodes were used (J16-18A- R01M-HS). These detectors are high quality Germanium photodiodes designed for the 800 to 1800 nm wavelength range. The equivalent circuit for a Germanium photodiode (Figure 2.104) is a photon generated current source with shunt resistance RD, parallel capacitance CD and series resistance RS. The value RS is very small compared to RD and can be disregarded except at high power levels (more than 10 MW). A Germanium photodiode generates a current across the p-n or p-i-n junction when photons of sufficient energy are absorbed within the active region. The responsivity (Amps/Watt) is a function of wavelength and detected temperature. The photodiodes were installed along the length of the combustion tube. The gauge output was recorded on transient digitizers with 4 *mus* sampling intervals.

### 2.6.2.2.3 Test procedure

Figure 2.105 shows the standard scheme and data recording of the performed combustion experiments, which used the following standard procedure: The air filled combustion tube is evacuated with three vacuum pumps to about 1 mbar. The evacuated tube is filled with a  $H_2$ /air mixture of defined composition (mass flow controllers) to the chosen initial pressure. The mixture is ignited at one end of the tube by a glow plug. During the combustion process the signals of the pressure transducers and the photodiodes are recorded by a transient recorder. In combustion processes the composition of the gas mixture has to be determined precisely. Therefore a smaller test tube (standing upright to provide complete combustion) is connected to the combustion tube and filled simultaneously together with it. After the filling process, the smaller tube is disconnected and the initial pressure and temperature inside this smaller tube are measured. The mixture inside the smaller tube is ignited and allowed to cool down to the initial temperature. Then again the pressure is measured. With the partial pressure theory it is possible to calculate the hydrogen concentration composition of the mixture by using equation 2.40.

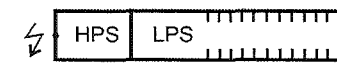
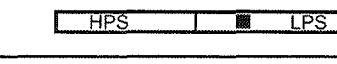
$$[H_2] = 2/3[(p_0 - p_1 + p_s(T))/p_0] \quad (2.40)$$

$p_0$  = initial pressure (mbar)

$p_1$  = pressure after combustion (mbar) and temperature equilibration

$p_s(T)$  = saturated pressure of water vapor (mbar)

Figure 2.102: Schematic of different experimental set-ups

TEST ISSUE medium scale	Mixture composition	EXPERIMENTAL VARIABLES				TUBE CONFIGURATION
		Pressure $p_0$ (bar)	Type	%BR	Spacing (m)	
Turbulence Models	He/air	HPS=3-5 LPS=1-2	- rings	60	0.35	
AMR Tests	$H_2$ /air, He/air, air/air	HPS=3-5 LPS=1	5 cm cube	25	—	
Flame Quenching	lean $H_2$ -air, 8-12 % $H_2$	0.5-4	- rectangle - rings	30 45 60 75 90	0.25 0.5 1.0 2.0	 0.35 m Anlauf s 0.1 m
Flame Acceleration	$H_2$ /air $H_2$ / $O_2$ / $N_2$ $H_2$ / $O_2$ / $Ar$ $H_2$ / $O_2$ / $He$ $H_2$ / $O_2$ / $CO_2$ $H_2$ /air/ $CO_2$	1	- rings	60	0.35	

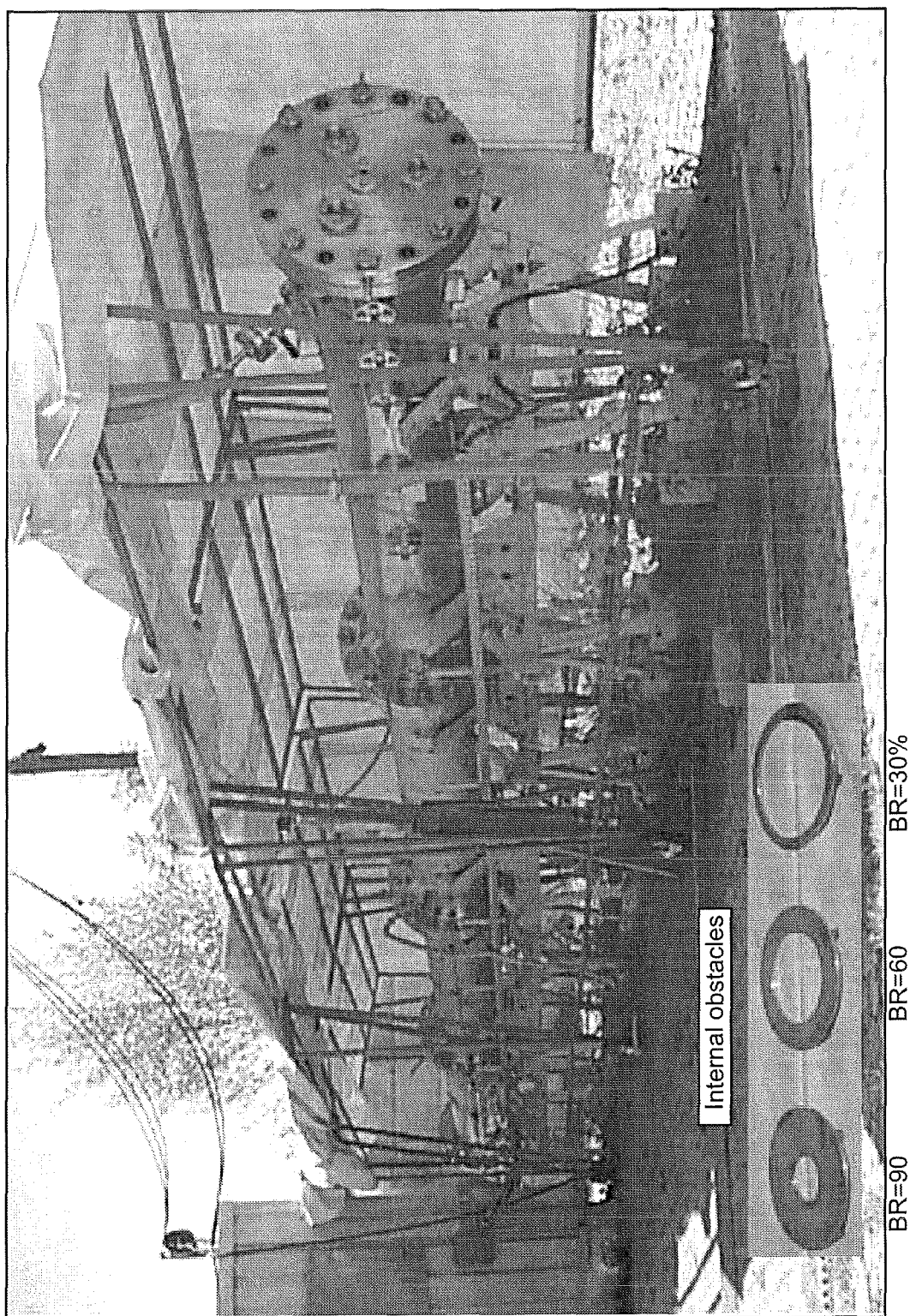
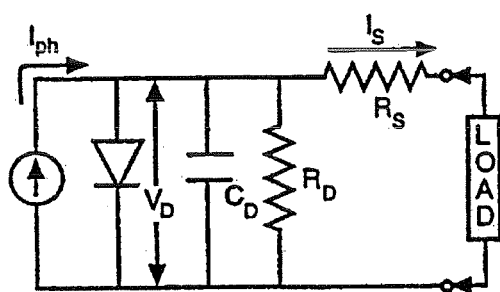


Figure 2.103: FZK 12m-tube



$I_{ph}$  = Current generated by incident photons  
 $V_D$  = Actual voltage across diode junction  
 $C_D$  = Detector junction capacitance  
 $R_D$  = Detector shunt resistance  
 $R_S$  = Detector series resistance  
 $I_S$  = Output signal current

Figure 2.104: Germanium photodiode equivalent circuit

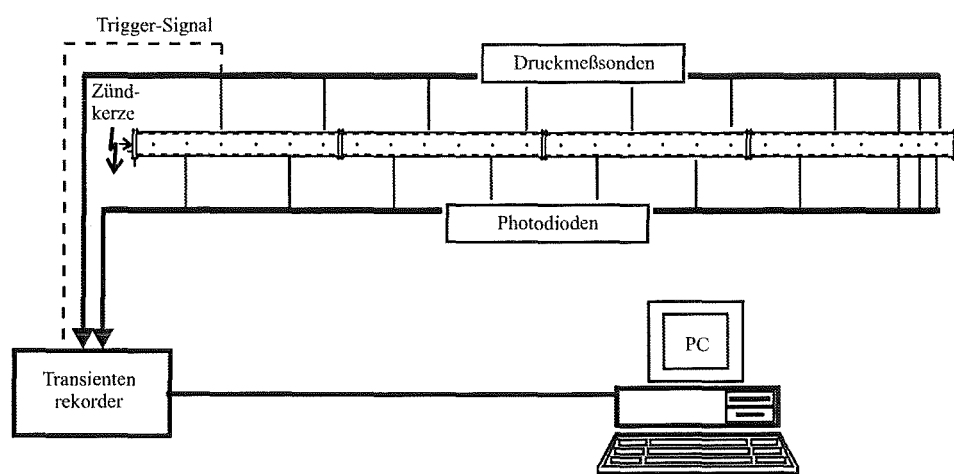
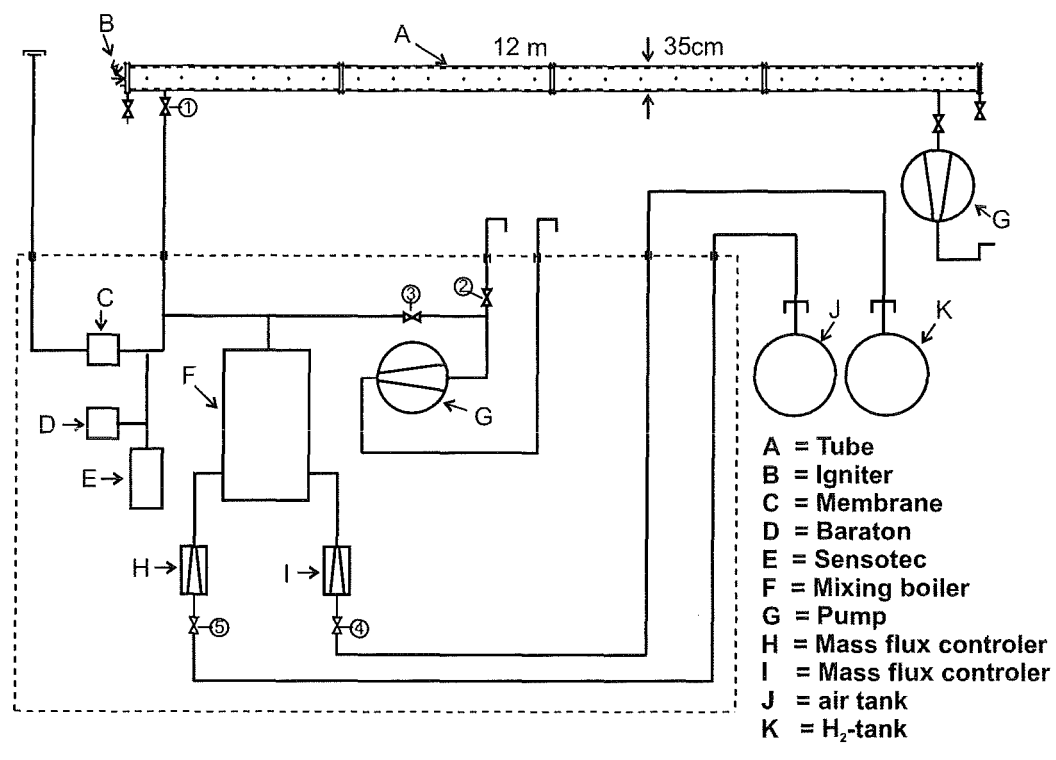


Figure 2.105: Experimental scheme and data recording

### 2.6.3 Quenching experiments

To derive criteria for quenching and to generate an adequate data base for code evaluation many tests on different scales (FZK: 12 m x 0.35 m, KI: 0.17m x 12 m, 0.52 m x 30 m) in obstructed tubes were performed. The evaluation of the experiments is not yet completed but preliminary results were already obtained for FZK-12-m-tube.

The experiments done so far were performed with a blockage ratio (BR) of 90 % a fixed initialisation part of obstacles (2 x BR 30 %, 2 x BR 60 %), obstacle spacing  $\Delta x$  from 25 to 200 cm, initial pressures from 0.5 to 4 bar and mixture compositions from 8 to 11 % hydrogen in air.

All experiments that were performed so far are listed in Table 2.10.

The typical results obtained in the measurements, are described by using few examples.

Figure 2.106 summarizes the results of experiment R0597\_00 as an R-t-diagram of measured pressure and measured photodiodes signals. The test parameters used in this experiment were 11 % hydrogen in air with an initial pressure of 1 bar and an obstacle spacing of 25 cm. In this test the flame accelerated up to the end of the tube to a terminal velocity of about 260 m/s. No quenching was observed in this case.

Experiment R0597\_04 was performed by changing the initial pressure from 1 bar to 3 bar but with the same hydrogen concentration and obstacle spacing as in experiment R0597\_00. The measured pressure and light signals of this experiment are given in Figure 2.107. The photodiode at the position 5.75 m shows no signal and the pressure gauges in this area show a distinct pressure fluctuation. These two effects are a sign for local quenching. Experiment R0597\_05 was performed with 10.5 % hydrogen in air with an initial pressure of 1 bar and an obstacle spacing of 25 cm. The R-t-diagrams of this experiment are shown in Figure 2.108. In this test the flame accelerates during the first 6 m to a velocity of about 100 m/s. Beyond 9 m no light emission was detected, which indicates quenching of the flame. The pressure gauges give signals up to the 11 m position because the burned gas compresses the unburned gas between the obstacles which causes an elevation of pressure.

The R-t-diagram of experiment R0597\_03 is given in Figure 2.109. This experiment was performed with the same test parameters as experiment R0597\_05, except that the initial pressure was raised from 1 bar to 2 bar. Signals of the photodiodes and pressure gauges were only detected up to 3.5 m. This shows that the flame was quenched in this area near the initial part of the tube (global quenching).

The other experiments, which were using the same obstacle configuration, showed the same behaviour in pressure and concentration dependence as these four described examples. Figure 2.110. shows the results of all performed experiments for different obstacle spacings. A white point indicates that the flame was

quenched during this experiment, while a black point represents an experiment which burned through to the end of the tube. Additionally for each points three numbers are given. The first number specifies the experiment, the second refers to the measured burn- out in % hydrogen, and the third refers to the burned tube length. The data points are grouped into three regimes:

- completely burned (white)
- incompletely burned up to 9 m from ignition point (light grey)
- incompletely burned up to 4 m from ignition point (dark grey).

Furthermore a dependence on the initial pressure is observable.

Table 2.10: Test matrix of quench experiments

Experiment	BR [%]	$p_0$ [bar]	$[H_2]$ [%]	Obstacle spacing
R0497_00	90	0.5	10	$\Delta x = 50\text{cm}$
R0497_01	90	1.0	10	$\Delta x = 50\text{cm}$
R0497_02	90	0.75	10	$\Delta x = 50\text{cm}$
R0497_03	90	1.0	11	$\Delta x = 50\text{cm}$
R0497_04	90	2.0	11	$\Delta x = 50\text{cm}$
R0497_05	90	3.0	11	$\Delta x = 50\text{cm}$
R0597_06	90	0.75	9	$\Delta x = 50\text{cm}$
R0497_07	90	1.0	9	$\Delta x = 50\text{cm}$
R0497_08	90	1.0	10	$\Delta x = 50\text{cm}$
R0497_09	90	1.0	9	$\Delta x = 50\text{cm}$
R0497_10	90	2.0	9	$\Delta x = 50\text{cm}$
R0597_00	90	1	11	$\Delta x = 25\text{cm}$
R0597_01	90	1	10	$\Delta x = 25\text{cm}$
R0597_02	90	1	10,5	$\Delta x = 25\text{cm}$
R0597_03	90	2	10,5	$\Delta x = 25\text{cm}$
R0597_04	90	3	11	$\Delta x = 25\text{cm}$
R0597_05	90	1	10,5	$\Delta x = 25\text{cm}$
R0597_06	90	1	11	$\Delta x = 100\text{cm}$
R0597_07	90	1	10	$\Delta x = 100\text{cm}$
R0597_08	90	0.5	9	$\Delta x = 100\text{cm}$
R0597_09	90	1	9	$\Delta x = 100\text{cm}$
R0597_10	90	0.5	8	$\Delta x = 100\text{cm}$
R0597_11	90	0.5	8.5	$\Delta x = 100\text{cm}$
R0597_12	90	1.5	9	$\Delta x = 100\text{cm}$
R0597_13	90	1.5	9	$\Delta x = 100\text{cm}$
R0597_14	90	1.5	9	$\Delta x = 100\text{cm}$
R0597_15	90	1.5	9.5	$\Delta x = 100\text{cm}$
R0597_16	90	2	10	$\Delta x = 100\text{cm}$
R0597_17	90	2	9.5	$\Delta x = 100\text{cm}$
R0597_18	90	2	9.5	$\Delta x = 100\text{cm}$
R0697_00	90	1	11	$\Delta x = 200\text{cm}$

Table 2.11: Test matrix of quench experiments

Experiment	BR [%]	$p_0$ [bar]	[ $H_2$ ] [%]	Obstacle spacing
R0697_01	90	1	10	$\Delta x = 200\text{cm}$
R0697_02	90	1	9	$\Delta x = 200\text{cm}$
R0697_03	90	2	10	$\Delta x = 200\text{cm}$
R0697_04	90	0.5	9	$\Delta x = 200\text{cm}$
R0697_05	90	3	11	$\Delta x = 200\text{cm}$
R0697_06	90	1.5	10	$\Delta x = 200\text{cm}$
R0697_07	90	1	9.5	$\Delta x = 200\text{cm}$
R0697_08	90	0.5	9.5	$\Delta x = 200\text{cm}$
R0697_09	90	2	10.5	$\Delta x = 200\text{cm}$
R0697_10	90	0.5	9.5	$\Delta x = 200\text{cm}$
R0697_11	90	0.5	8.5	$\Delta x = 200\text{cm}$
R0697_12	90	0.5	8.5	$\Delta x = 200\text{cm}$
R0697_13	90	0.5	9.5	$\Delta x = 200\text{cm}$
R0697_14	90	0.5	9.5	$\Delta x = 200\text{cm}$
R0697_15	90	1	9.5	$\Delta x = 200\text{cm}$
R0697_16	90	2	9.5	$\Delta x = 200\text{cm}$
R0697_17	90	2	10.5	$\Delta x = 200\text{cm}$
R0697_18	90	4	10.5	$\Delta x = 200\text{cm}$
R0697_19	90	2	11	$\Delta x = 200\text{cm}$
R0697_20	90	3	10	$\Delta x = 100\text{cm}$
R0697_21	90	2	10.5	$\Delta x = 100\text{cm}$
R0697_22	90	3	10.5	$\Delta x = 100\text{cm}$
R0697_23	90	3	11	$\Delta x = 100\text{cm}$

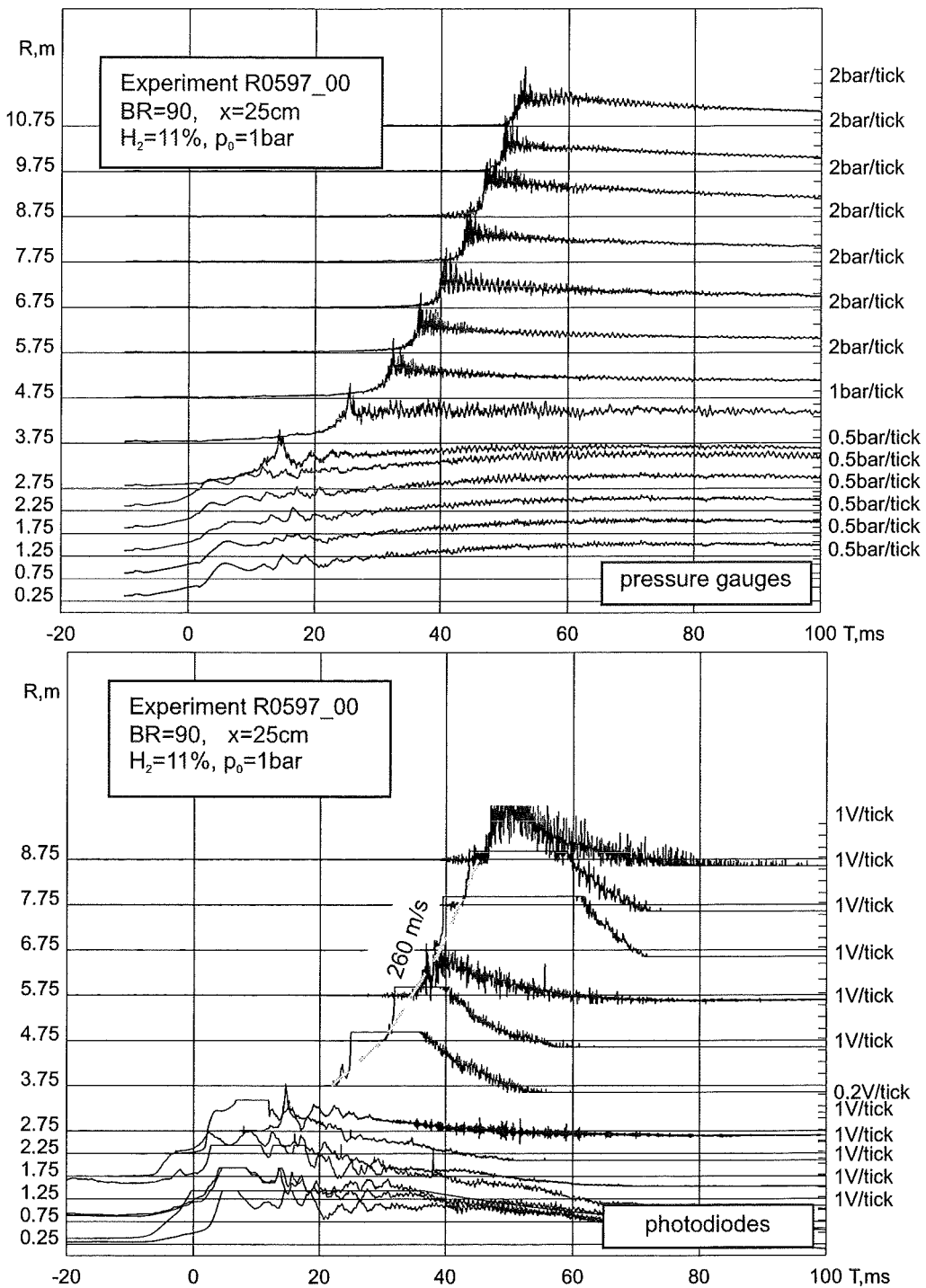


Figure 2.106: Measured pressure and photodiode signals for experiment R0597\_00

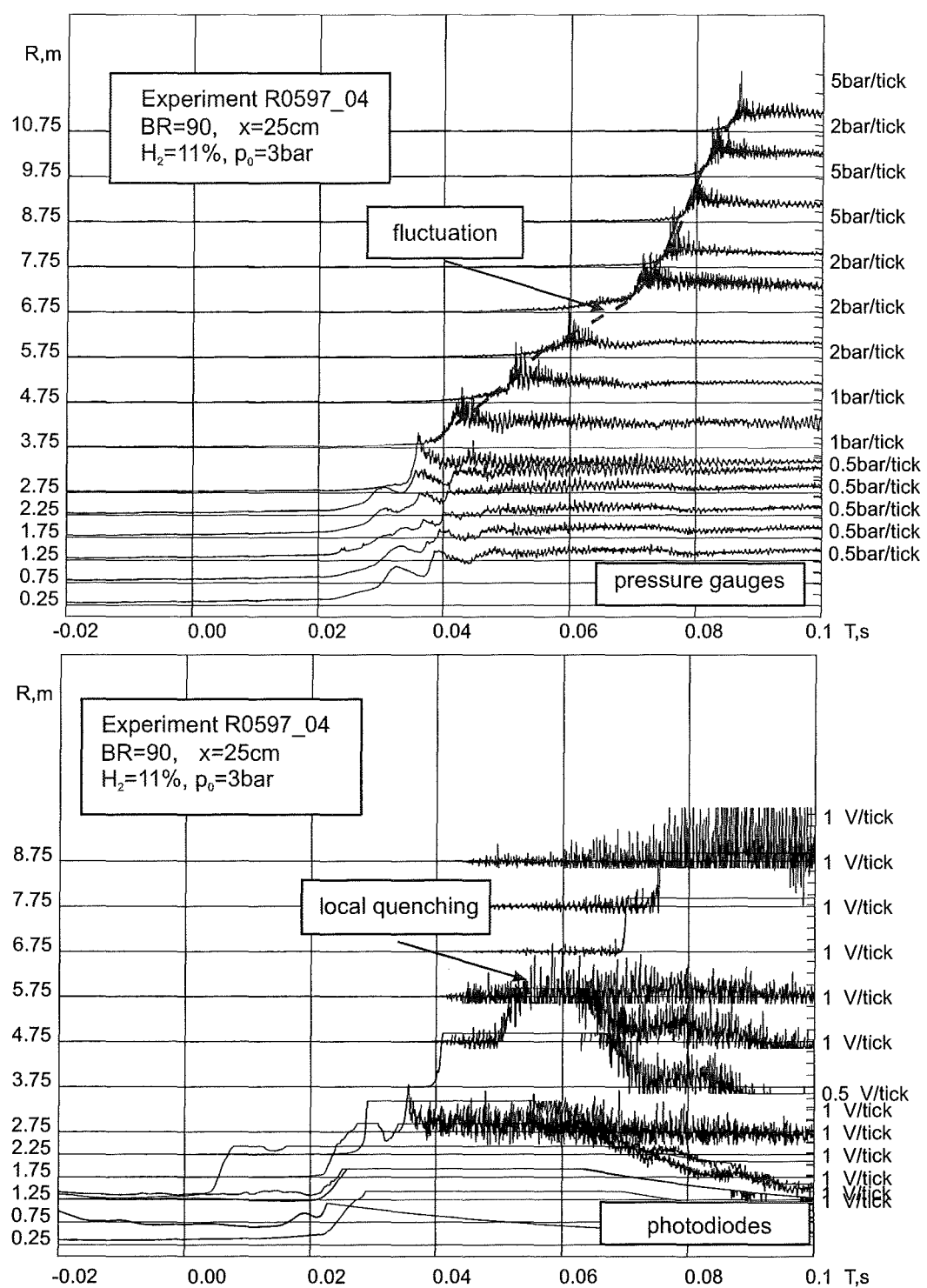


Figure 2.107: Measured pressure and photodiode signals for experiment R0597\_04

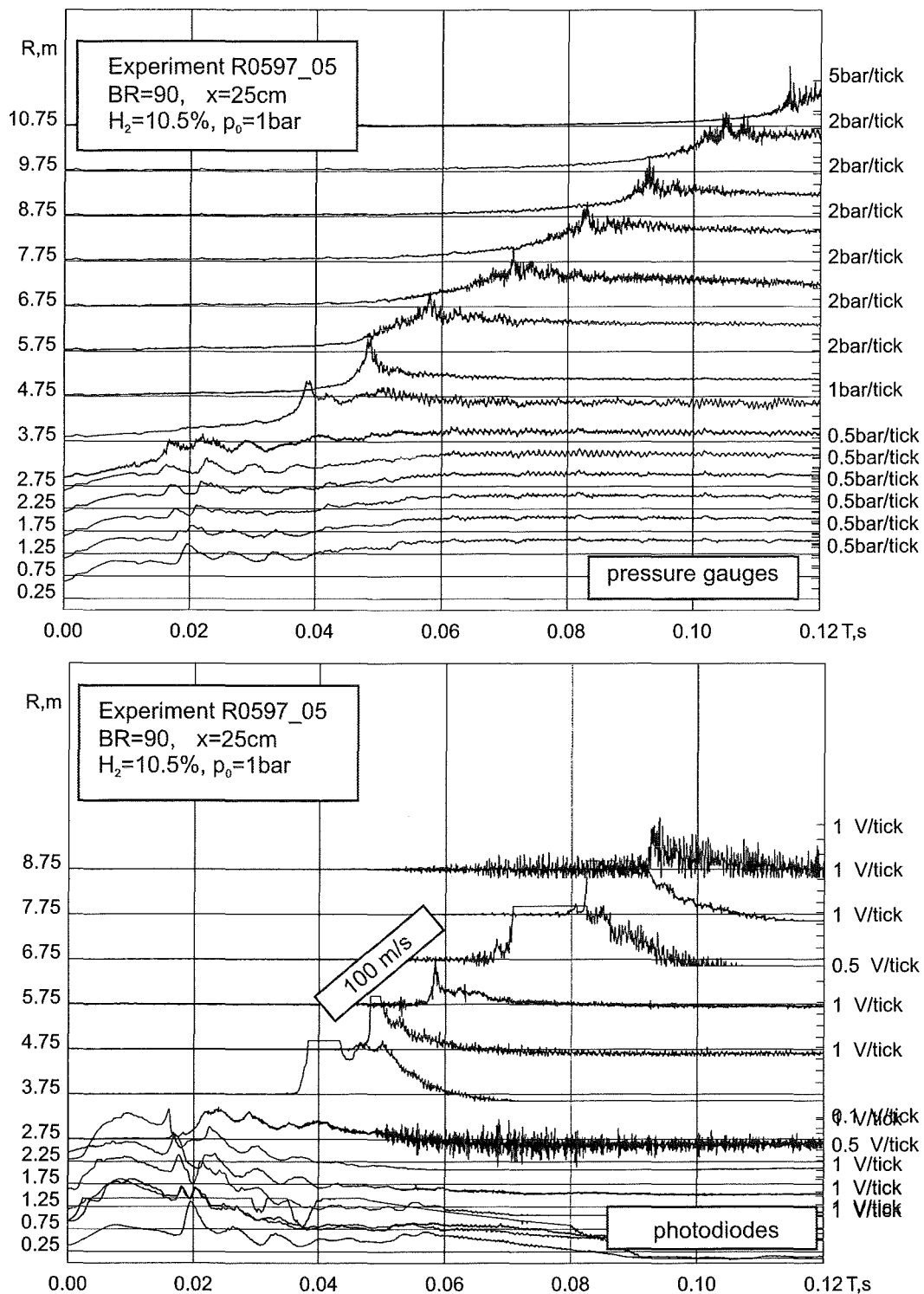


Figure 2.108: Measured pressure and photodiode signals for experiment R0597\_05

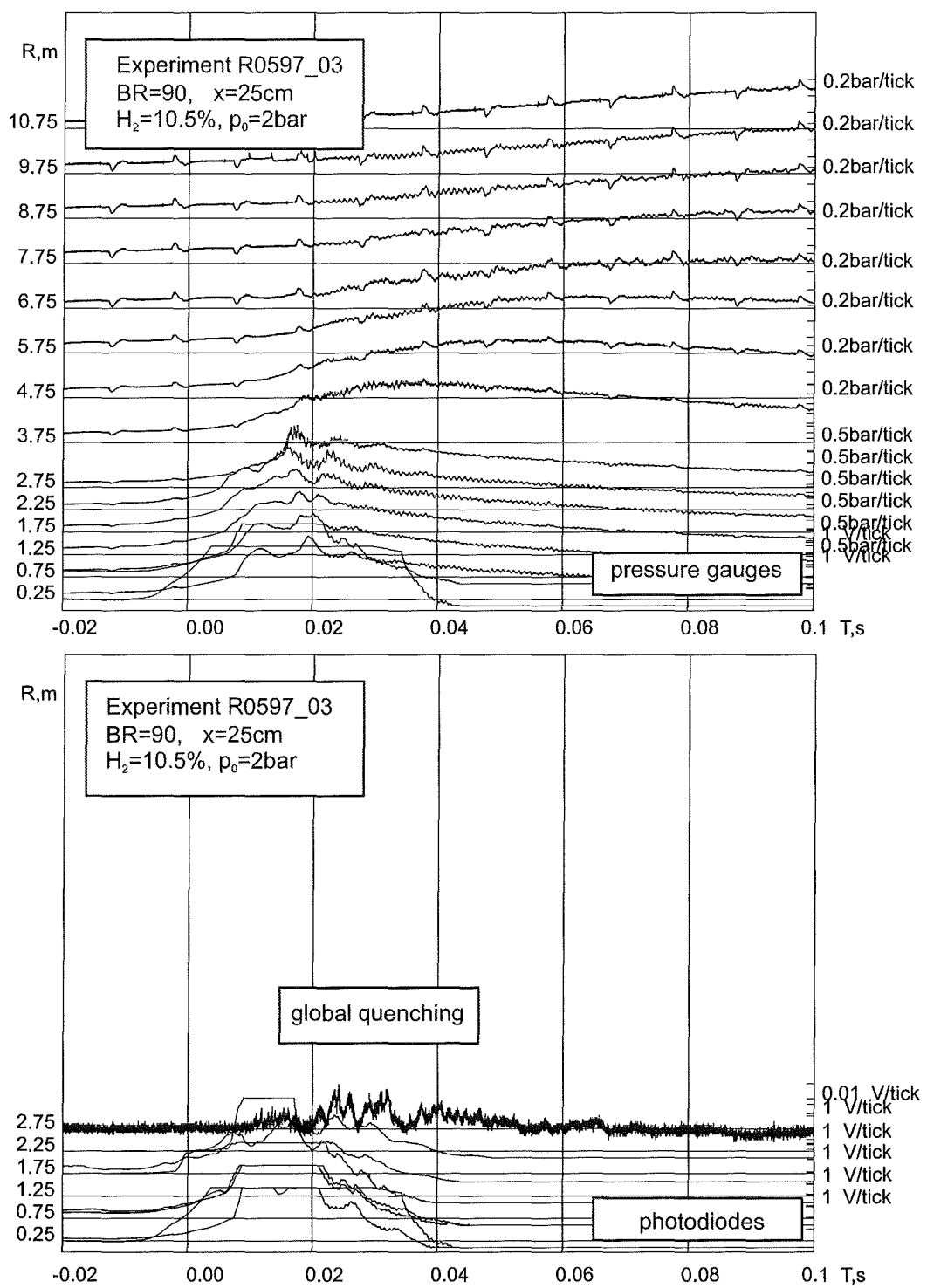
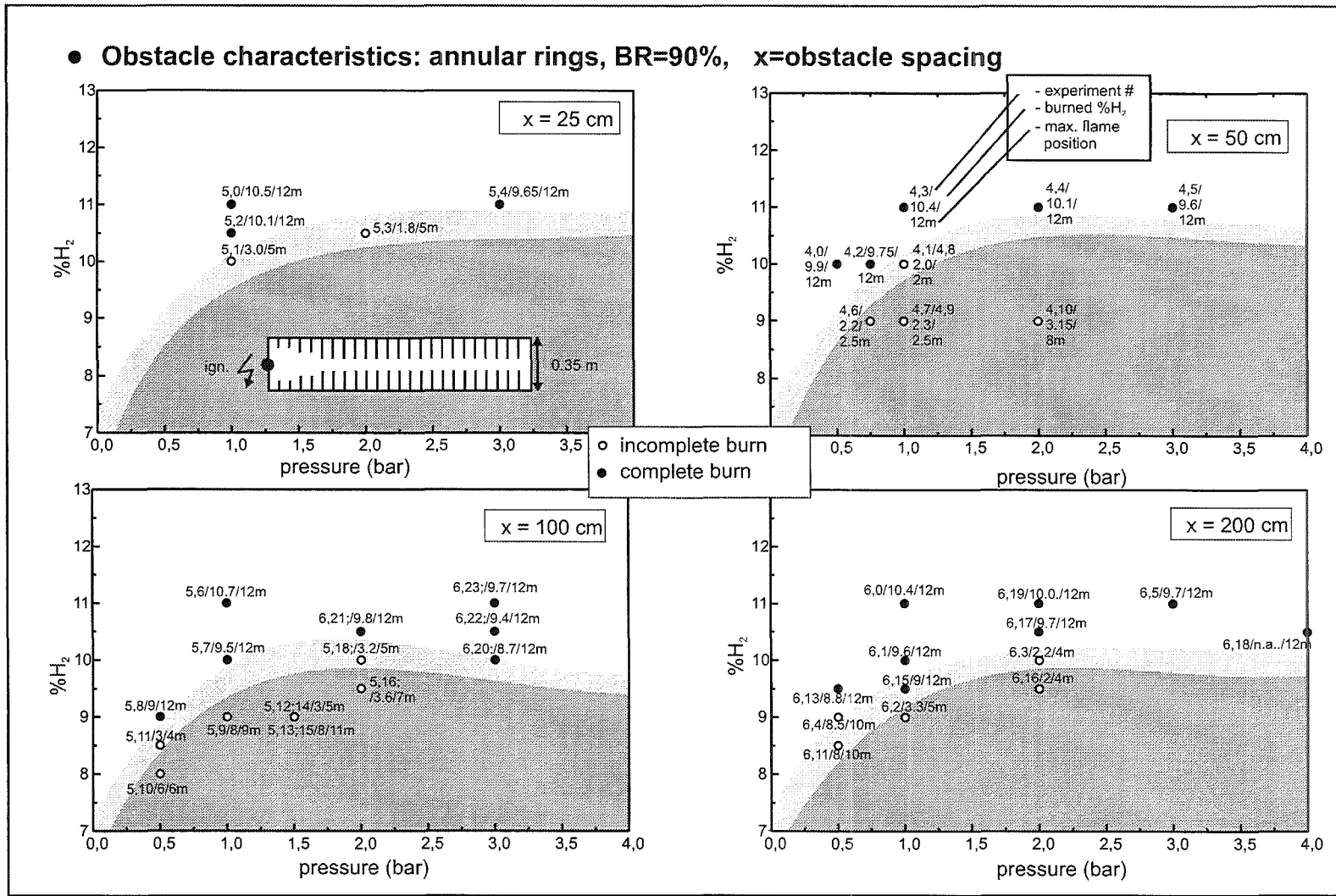


Figure 2.109: Measured pressure and photodiode signals for experiment R0597\_03

Figure 2.110: Summary of results of quench experiments in FZK 12m-tube



## 2.6.4 Flame acceleration experiments

### 2.6.4.1 $H_2$ /air mixtures

The most damaging accidental gaseous explosions occur in obstructed areas with significant degree of confinement. Interactions of the flow, produced by expansion of the combustion products, with the flame itself provide the most effective means for flame acceleration. The laminar flame propagates initially from the ignition source. It becomes turbulent at a certain stage due to flame instabilities. The flame generates the flow ahead which appears to be turbulent due to the large enough characteristic sizes of the enclosure. A higher burning rate generates a higher level of turbulence. The flame acceleration is a result of the interaction of the flame produced flow with the flame itself (positive feedback).

To derive a conservative criteria for flame acceleration, optimum conditions have to be created. Tests were performed on different scales (FZK: 12 m x 0.35 m, KI: 0.17m x 12 m, 0.52 m x 30 m, 2.5m x 34 m) in an obstructed tube. The evaluation of the experiments is not yet completed, but preliminary results were already obtained for the FZK-12-m-tube.

All experiments done so far were performed with a BR of 60 %, a constant obstacle spacing of 0.35 m and an initial pressure of 1 bar. The parameter changed was the mixture composition. Different inert components ( $O_2$ ,  $N_2$ ,  $Ar$ ,  $He$ ,  $CO_2$ ) were added to hydrogen air mixtures.

### 2.6.4.2 $H_2$ - $O_2$ -diluent mixtures

Characteristic combustion sequences for  $H_2$ - $O_2$ -diluent mixtures are presented in this section. All experiments with  $N_2$ ,  $Ar$  and  $He$  diluent were performed with a constant equivalence ratio of  $\Phi = 1$ . The following mixtures were considered:

- $\alpha H_2 + \text{air}$ ,
- $2H_2 + O_2 + \beta N_2$ ,
- $2H_2 + O_2 + \beta Ar$ ,
- $2H_2 + O_2 + \beta He$

The values of  $\alpha$ ,  $\beta$  are assumed to be variables.

The acceleration experiments, with hydrogen in air are listed in Table 2.12. Mixtures close to the lean and rich flammability limits were investigated.

Table 2.12: Test matrix of acceleration experiments with  $H_2$ /air mixtures

Experiment	[ $H_2$ ] Vol%	[Air] Vol%
R0897_00	9	91
R0897_01	9	91
R0897_02	9	91
R0897_03	10	90
R0897_04	11	89
R0897_05	70	30
R0897_06	72	28
R0897_07	75	25

Figure 2.111 compares the measured pressure and light signals as a function of time for experiments R0897\_01, R0897\_03 and R0897\_04. The hydrogen concentration was varied in these experiments from 9-11%. A hydrogen concentration of 9% (experiment R0897\_01) leads to a slow combustion with a fluctuating flame. An increase of the hydrogen concentration from 9 to 10 % (experiment R0897\_03) and 11% (R0897\_04) shows another behaviour of the flame. The flame moves slow at first, but it then accelerated very fast up to 347 m/s (experiment R0897\_03) and 494 m/s (experiment R0897\_04) respectively.

All acceleration experiments, performed with a mixture of hydrogen, oxygen and, nitrogen are listed in Table 2.13.

Table 2.13: Test matrix of acceleration experiments with  $H_2/O_2/N_2$  mixtures

Experiment	[ $H_2$ ]	[ $O_2$ ]	[ $N_2$ ]
R0897_08	11	18.69	70.31
R0897_09	11	8.5	83.5
R0897_10	12	18.48	69.52
R0897_11	12	6	82
R0997_00	11	18.69	70.31
R0997_01	11	5.5	82.5
R0997_02	12	6	82
R0997_03	12	6	82
R0997_06	10	5	85
R0997_07	10	5	85

The R-t diagram of experiment R0997\_01 with a  $H_2/O_2/N_2$  mixture ( $H_2=11\%$ ,  $O_2=5.5\%$ ,  $N_2=83.5\%$ ) is shown in Figure 2.112. The flame starts slow and then accelerates to a terminal velocity of 473 m/s.

Table 2.14 shows the experimental matrix performed for all acceleration experiments with a mixture of hydrogen, oxygen and argon.

Table 2.14: Test matrix of acceleration experiments with  $H_2/O_2/Ar$  mixtures.

Experiments	[ $H_2$ ]	[ $O_2$ ]	[Ar]
R0897_12	8	4	88
R0897_13	8	4	88
R0897_14	9	4.5	86.5
R0997_12	6.67	3.33	90
no ignition:			
	5	2.5	92.5
	5.5	2.75	91.75
	6	3.0	91
	4.23	2.09	93.68

All experiments with a concentration of argon  $\geq 91\%$  were not ignitable with the used glow plug. The reduction of the argon concentration to 90% (experiment R0997\_12:  $H_2=6.67\%$ ,  $O_2=3.33\%$ , Ar=90%) leads to a combustion, that starts slow but still accelerates to a maximum velocity of 473 m/s. A further reduction of the Argon concentration to 86.5% (experiment R0897\_14:  $H_2=9\%$ ,  $O_2=4.5\%$ , Ar=86.5%) causes a fast combustion with a maximum velocity of 1079 m/s, which is close to DDT. The R-t-diagrams of these two experiments are given in Figure 2.113.

Table 2.15 shows the experimental matrix performed for all acceleration experiments done so far with a mixture of hydrogen, oxygen and helium.

All experiments with a concentration of helium  $\geq 88\%$  were inignitable. The reduction of the helium concentration to 87.25% (experiment R0997\_10:  $H_2=8.5\%$ ,  $O_2=4.25\%$ , He=87.25) very close together. The flame burns slowly for about 7 m but then rapidly accelerates to a maximum velocity of 1200 m/s. Figure 2.114 shows the R-t-diagram of this experiment.

The experiments with argon and helium as diluent do not show a regime of slow combustion which is detected in lean hydrogen/air mixtures.

The measured flame propagations of all experiments are given in Figure 2.115.

Table 2.15: Test matrix of acceleration experiments with  $H_2/O_2/He$  mixtures

Experiment	[ $H_2$ ]	[ $O_2$ ]	[ $He$ ]
R0897_15	12	6	82
R0897_16	13.5	6.75	79.75
R0997_04	11	6.43	82
R0997_05	11.68	5.79	82.52
R0997_08	10	5	85
R0997_09	9	4.5	86.5
R0997_10	8.5	4.25	87.25
R0997_11	12	6	82
no ignition:			
	8	4	88
	8	4	88
	6.5	3.24	90.2
	7.47	3.7	88.83
	6.55	3.24	90.2
	6.42	10.8	82.78

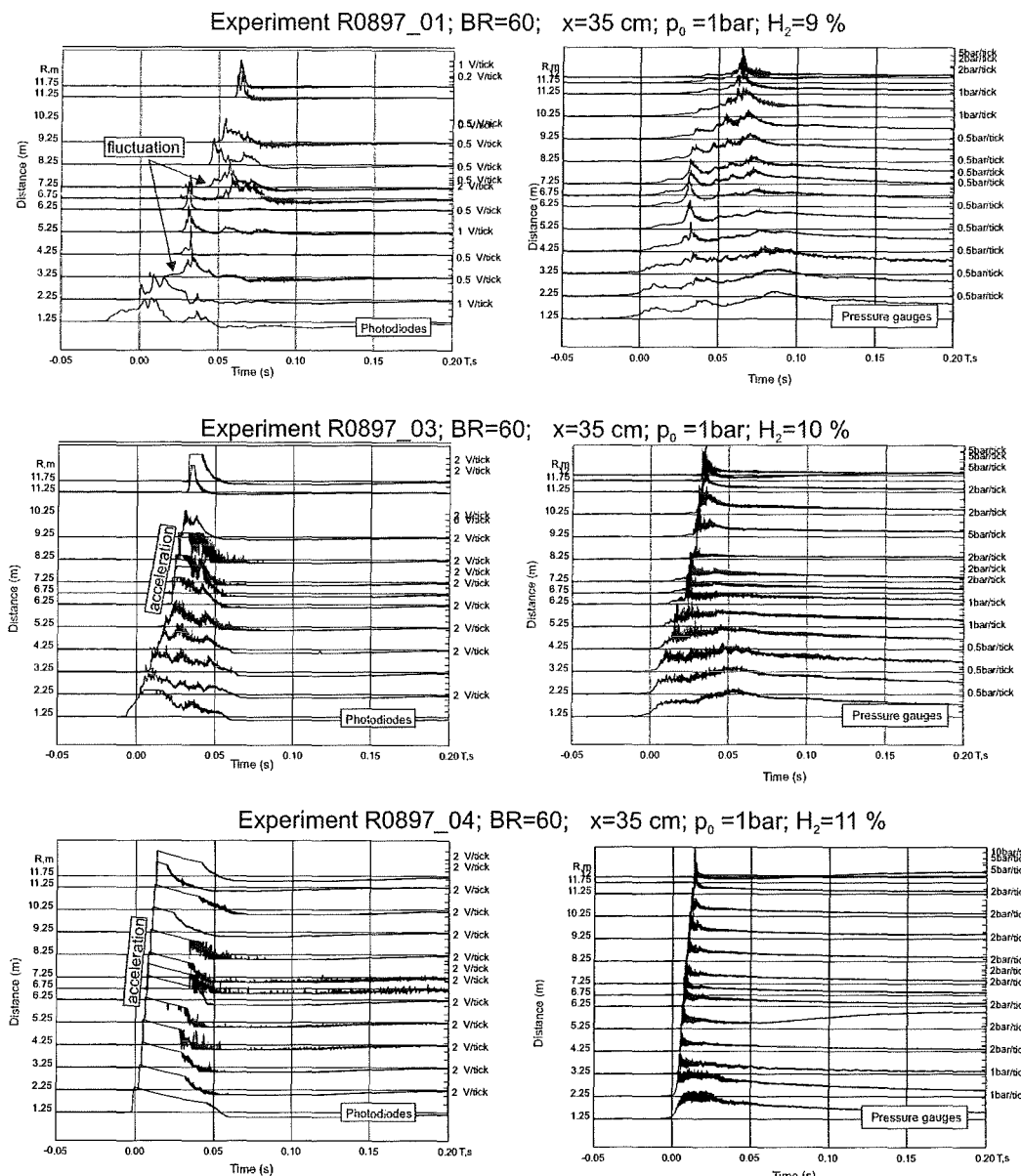


Figure 2.111: Measured pressure and photodiode signals for experiments R0897\_01, R0897\_03, and R0897\_04.

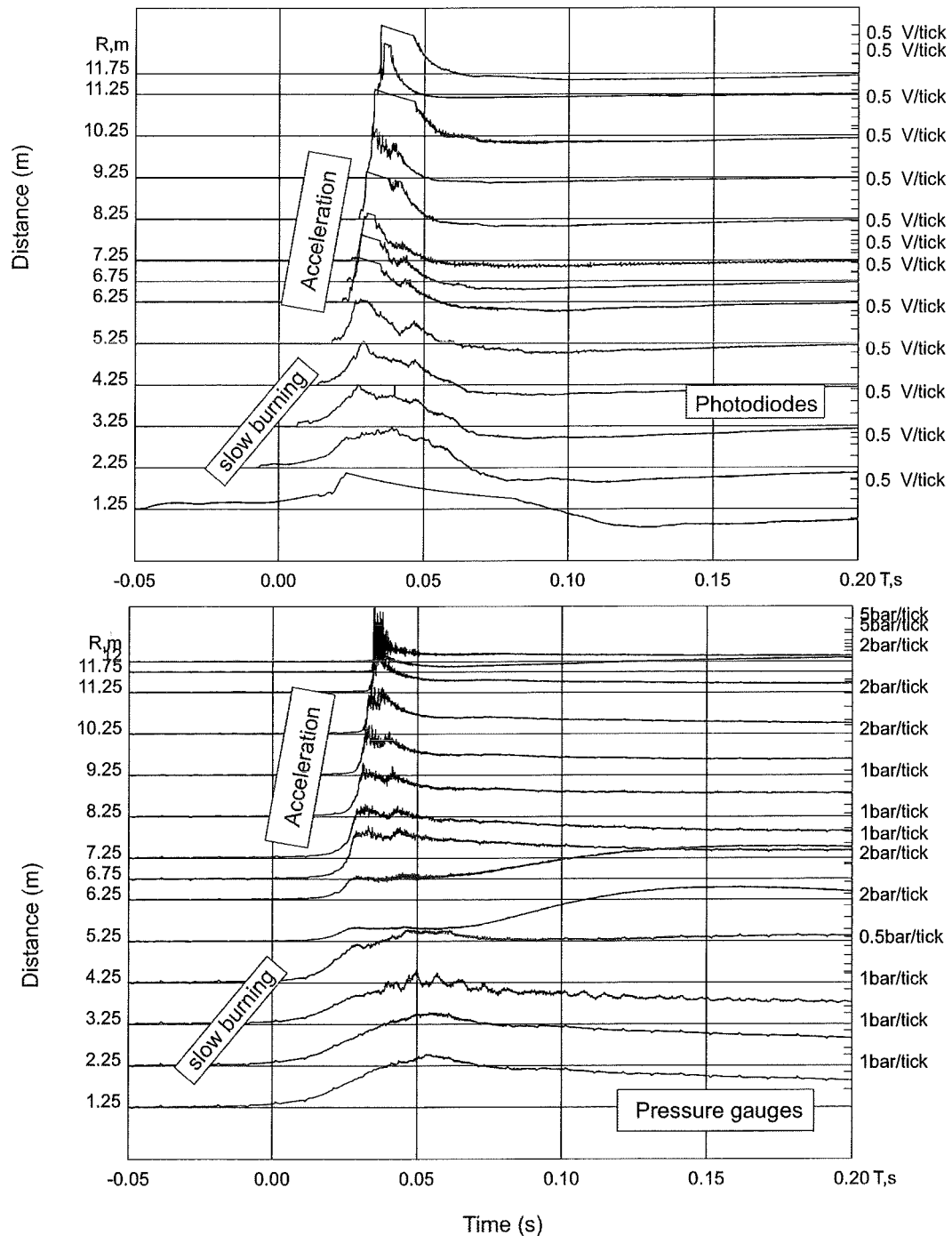
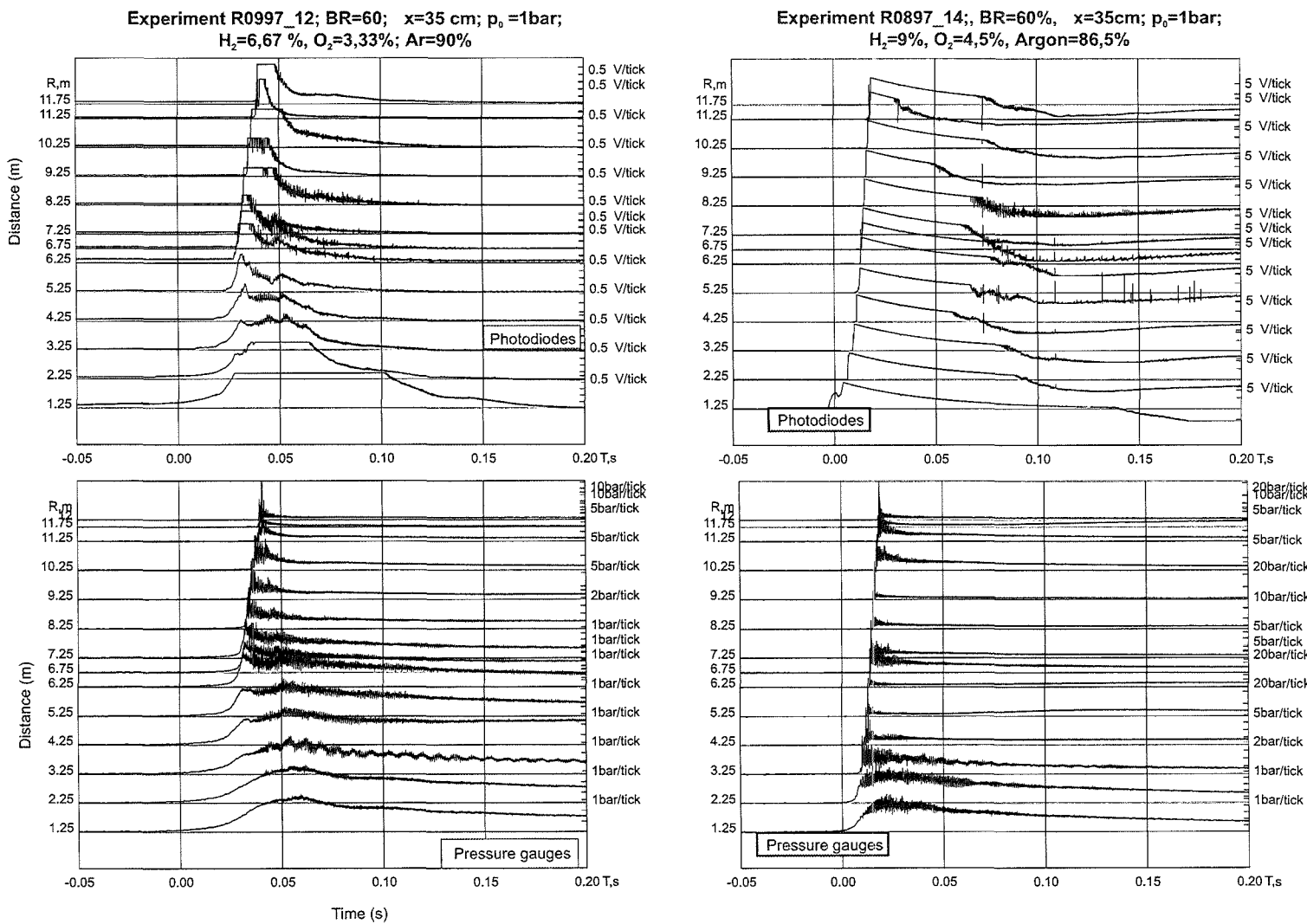


Figure 2.112: Measured pressure and photodiode signals for experiments R0997\_17

Figure 2.113: Measured pressure and photodiode signals for experiments R0997\_12 and R0897\_14



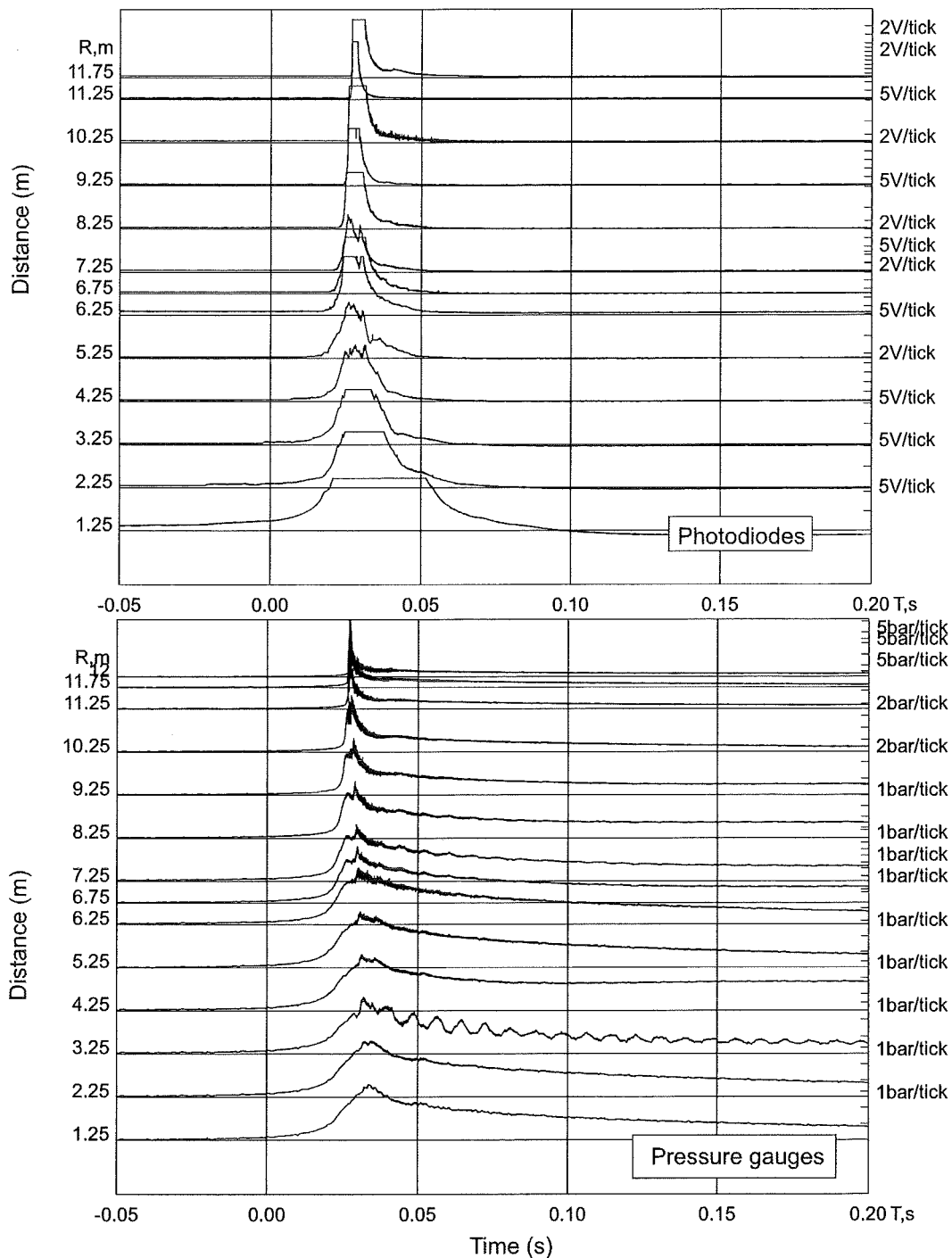
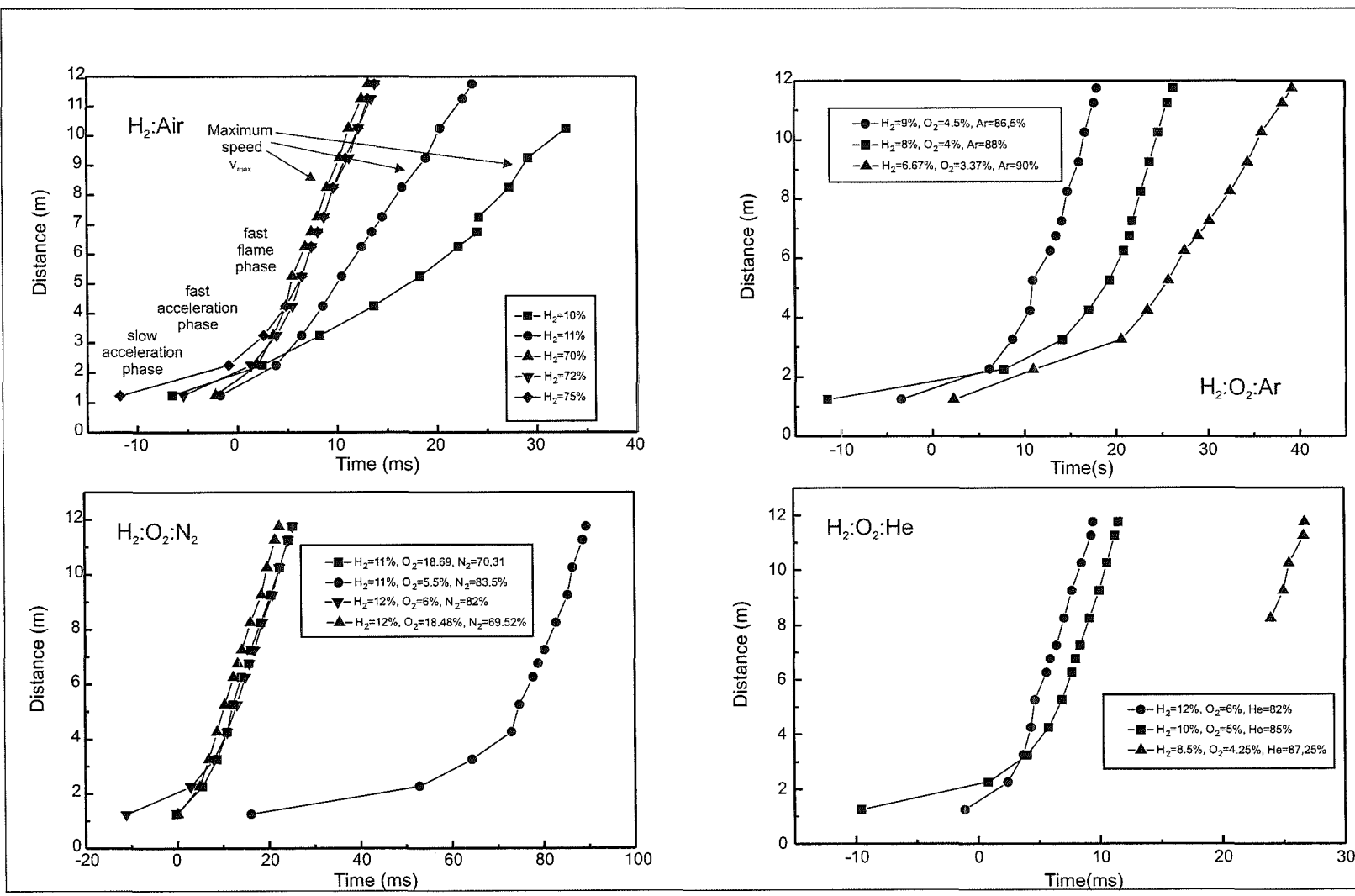


Figure 2.114: Measured pressure and photodiode signals for experiments R0997\_10

Figure 2.115: Summary of results of flame acceleration experiments in FZK 12m-tube



### 2.6.4.3 Hydrogen-air- $CO_2$ mixtures

In an accident scenario with core/concrete interaction  $CO_2$  appears as a part of the mixture. Therefore it is also necessary to study the flame behaviour and the acceleration limits of  $CO_2$  containing mixtures. In addition the effectiveness of  $CO_2$  to suppress fast combustion modes is of interest for mitigation studies. By changing the equivalence ratio ( $\Phi=0.25, 0.5, 1.0, 2.0, 4.0$ ) a large number of experiments were performed. These experiments are listed in Table 2.16.

As an example the flame propagation of all experiments with  $\Phi = 1$  are given in Figure 2.116. The maximum flame velocities calculated from these flame trajectories are presented as a function of the  $CO_2$  concentration in Figure 2.117. The following regimes have been distinguished:

- inert regime (no ignition)
- slow burn regime ( $v_{max} < 250$  m/s)
- acceleration or chocked flow regime ( $250$  m/s  $< v_{max} < 900$  m/s)
- quasidetonation regime ( $v_{max} > 900$  m/s)

The experiments with  $\Phi=1,2$  and 4 shows a fast transition from inert behaviour to an accelerated flame within a narrow range of  $CO_2$  concentrations. This is an important result because the velocity of a combustion in a containment should not be higher than 100 m/s, because of the resulting pressure waves.

The current conclusion from the acceleration experiments is that all investigated rich mixtures, with one-, two- and three-atomic dilutents, have only a small safety margin between the flammability limit and rapidly accelerating combustion. Currently there is no final explanation for this observation. It appears difficult to control rich mixtures, which means that large and extended hydrogen accumulations to  $\Phi > 1$  should be avoided by early ignition or by recombiners.

Table 2.16: Test matrix of hydrogen/air/ $CO_2$ -experiments. Part 1

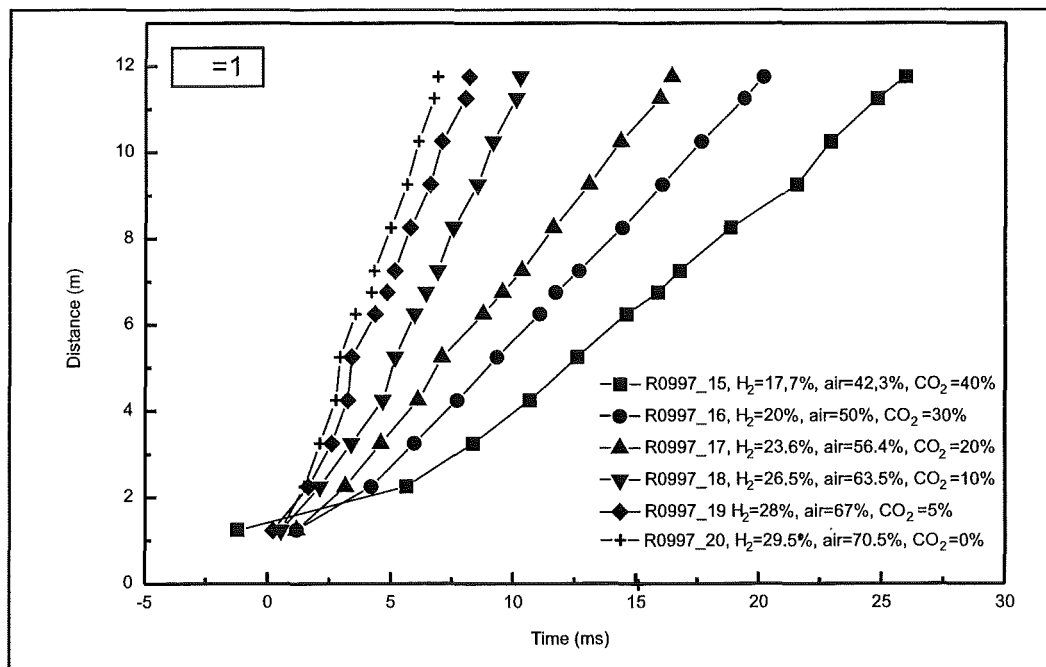
Equivalence ratio $\Phi = 1$			
Experiment	[ $H_2$ ]	[ $CO_2$ ]	[air]
R0997_12	12	0	88
R0997_14	14.8	35.	2 50
R0997_15	17.7	40	42.3
R0997_16	20	30	50
R0997_17	23.6	20	56.4
R0997_18	26.5	10	63.5
R0997_19	28	5	67
R0997_20	29.5	0	70.3
R1097_00	25	15	60
R1097_01	19.19	35	45.81
R1097_02	16.8	43	40.2
R1097_03	15.6	47	37.4
R1097_04	26	12.5	61.5
R0997_05	15.2	48.5	36.3
R0997_21	20	70	10
R0997_22	30	55	15
R0997_23	30	0	70 %Luft
R0997_24	18	73	9
R0997_25	16	76	8
R0997_26	17	74.5	8.5
no ignition:			
	14	79	7
	10	85	5
	11.8	60	28.2
	13.3	55	31.7
Equivalence ratio $\Phi = 0.25$			
Experiment	[ $H_2$ ]	[ $CO_2$ ]	[air]
R1197_06	9.5	0	90.5
R1097_11	48.5	22.5	29
R1097_12	47.75	23.75	28.5

Table 2.17: Test matrix of hydrogen/air/ $CO_2$ -experiments. Part 2

Equivalence ratio $\Phi = 0.5$			
Experiment	$[H_2]$	$[CO_2]$	[air]
R1197_11	10.39	40	49.61
R1197_12	11.26	35	53.74
R1197_13	12.12	30	57.88
R1197_14	12.12	30	57.88
R1197_15	12.99	25	62.01
R1197_16	13.86	20	66.14
R1197_17	14.72	15	70.28
R1197_18	15.59	10	74.41
R1197_19	16.45	5	78.55
R1197_20	17.31	0	82.69
R1197_21	17.31	0	82.69
R1197_22	14.72	15	70.28
R1197_23	16.89	2.5	80.61
R1197_25	16.89	2.5	80.61
R1197_26	17.31	0	82.69
R1197_28	12.56	27.5	59.94
Equivalence ratio $\Phi = 2.0$			
Experiment	$[H_2]$	$[CO_2]$	[air]
R1197_01	41	10	49
R1197_02	36.5	20	43.5
R1197_03	31.91	30	38.09
R1197_04	27.35	40	32.65
R1197_05	45.59	0	54.41
R1197_07	29.63	35	35.37
R1197_08	28.49	37.5	34
R1197_09	43.31	5	51.69
R1197_10	44.45	2.5	53.03
R1197_24	42.88	3.75	52.37
R1197_27	26.21	42.5	31.29

Table 2.18: Test matrix of hydrogen/air/ $CO_2$ -experiments. Part 3

Equivalence ratio $\Phi = 4.0$			
Experiment	[ $H_2$ ]	[ $CO_2$ ]	[air]
R1097_06	50	20	30
R1097_07	56	10	34
R1097_08	53.2	15	31.8
R1097_09	59.5	5	40.45
R1097_10	62.62	37.38	
R1097_11	48.5	22.5	29
R1097_12	47.75	23.75	28.5
no ignition:			
	44	30	26
	38	40	22

Figure 2.116: Flame propagation in experiments with  $\Phi = 1$

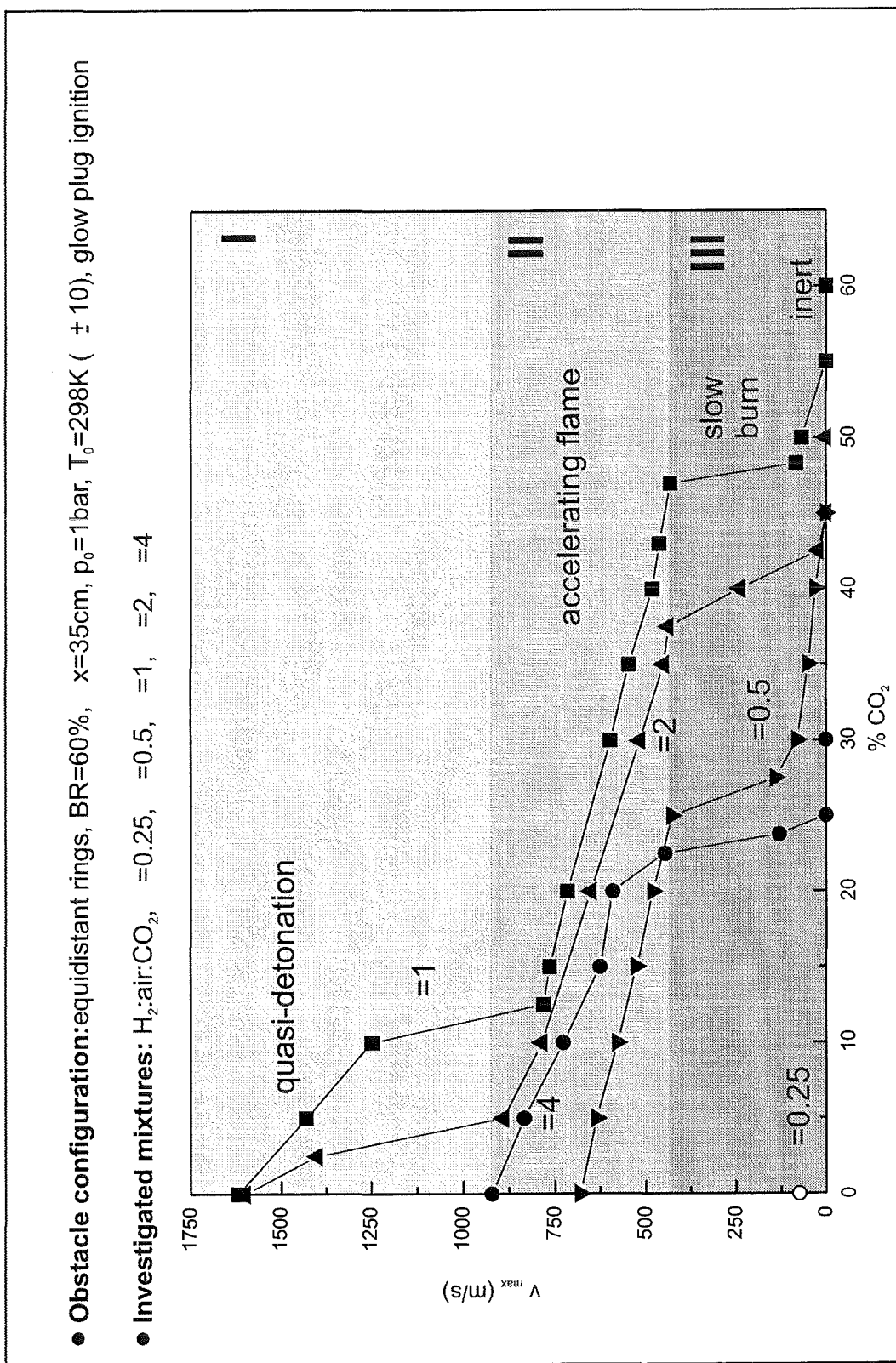


Figure 2.117: Summary of results of flame acceleration experiments in hydrogen/air/ $CO_2$

# Bibliography

[AbBr81] **Abdel-Gayed R.G., Bradley D.:**  
*A Two-Eddy Theory of Premixed Turbulent Flame Propagation*  
Philosophical Transaction of The Royal Society of London, Vol. 301, no. A, pp.1-25,1981

[ABL75] **Andrews G.E., Bradley D., Lwakabamba S.B.:**  
*Combustion Regimes and the Straining of Turbulent Premixed Flames, Short Communication*  
Combustion and Flame, Vol. 76, pp. 213-218, 1989

[ABL89] **Abdel-Gayed R.G., Bradley D., Lung F.K.-K.:**  
*Turbulence and Turbulent Flame Propagation-A Critical Appraisal*  
Combustion and Flame, Vol. 24, pp. 285-304, 1975

[ArMa98] **Ardey N., Mayinger F.:**  
*Einfluß Containment-typischer Strömungshindernisse auf die Ausbreitung von Wasserstoff-Luft-Flammen*  
Abschlußbericht zum Forschungsvorhaben BMBF Nr. 1500957, TU-München, vol.1, 1998

[Ard98] **Ardey N.:**  
*Struktur und Beschleunigung turbulenter Wasserstoff-Luft-Flammen in Räumen mit Hindernissen*  
Dissertation, Technische Universität München, 1998

[AMD95] **Ardey N., Mayinger F., Durst B.:**  
*Influence of Transportphenomena on the Structure of Lean Premixed Hydrogen Air Flames*  
Proceedings of the 1995-ANS Winter Meeting, Thermal Hydraulics of Severe Accidents, San Francisco and ANS-Transactions Vol. 73, TANSAO 73 1-522(1995), ISSN:0003-018X,1995

[Bea94] **Beauvais R.:**  
*Brennverhalten vorgemischter, turbulenter Wasserstoff-Luft-Flammen in einem Explosionsrohr*  
Dissertation TU-München, 1994

[BeMa94] **Beauvais R., Mayinger F.:**  
*Einfluß der Strömungsstruktur auf die Ausbreitung von Wasserstoff-Luft-Flammen*  
 Abschlußbericht zum Forschungsvorhaben BMBF Nr. 1500810, TU-München, 1994

[Bor64] **Borghi R.:**  
*On the structure of Turbulent Premixed Flames; Recent Advances in Aeronautical Science*  
 Pergamon Press, 1984

[Bra71] **Bradshaw P.:**  
*Introduction to Turbulence and its Measurement*  
 Pergamon Press Ltd., Oxford, 1971

[Bre88] **Brehm N., Mayinger F.:**  
*Grenze für den Übergang von der Deflagration in die Detonation in Wasserdampf-Luft-Gemischen*  
 Abschlußbericht Förderkennzeichen 15007124, Bundesministerium für Forschung und Technologie

[Cha95] **Chan C.K.:**  
*Collision of a Shock Wave with Obstacles in a Combustible Mixture*  
 Combustion and Flame 100: 341-348 (1995)

[Cho79] **Chomiak J.:**  
*Basic Considerations in the Turbulent Flame Propagation in Premixed Gases*  
 Prog. Energy Combust. Sci., Vol. 5, pp.207-221, Pergamon Press Ltd., 1979

[DAM96] **Durst B., Ardey N., Mayinger F.:**  
*Interaction of Turbulent Deflagrations with Representative Flow Obstacles*  
 Proceedings of the OECD/NEA/CSNI Workshop on the Implementation of Hydrogen Mitigation Techniques, Winnipeg, Manitoba, pp. 433-447, May 13-15, 1996

[DAM97] **Durst B., Ardey N., Mayinger F.:**  
*Higly Resolved Measurements of Flame Turbulence and Implications for Numerical Simulation*  
 Proceedings of the Int. Cooperative Exchange Meeting on Hydrogen in Reactor Safety, Toronto, Canada, June 1997

[Dar41] **Darrieus G.:**  
*Propagation d'un front de flamme Essai de theorie des vitesses anomalies de deflagration par developpement spontane de la turbulence.*  
 La mecanique de fluides. Quelques progres recents, Dunod, Paris, 1941

[DMW87] **Durst F., Melling A., Whitelaw J.H.:**  
*Theorie und Praxis der Laser-Doppler-Anemometrie*  
 Karlsruhe Braun, 1987

[Dun85] **Dunn-Rankin D., Sawyer R.F.:**  
*LDA Study of the Unburned Gas Motion Induced by Nonsteady Flame Propagation in a Constant Volume Duct.*  
 Joint Technical Meeting, Central States Section/Western States Section/The Combustion Institute, San Antonio, TX, April 22-23.  
 Lawrence Berkeley Laboratory Report LBL-19165.

[Ell28] **Ellis**  
 J. Fuel Science 7:502-508 (1928)

[FrMo77] **Frost W., Moulden T.H.:**  
*Handbook of Turbulence*  
 Plenum Press, New York, 1977

[Gon92] **Gonzalez M., Borghi R., Saouab A.**  
*Interaction of a Flame Front with its Self-Generated Flow in an Enclosure: The Tulip Flame Phenomenon*  
 Combustion and Flame 88:201-220 (1992)

[Gue64] **Guénoche, H.:**  
*Flame Propagation in Tubes and in Closed Vessels,*  
 IN: G.H. Markstein (Ed.), *Nonsteady Flame Propagation* Pergamon Press. New York, 1964

[Hin59] **Hinze J.O.:**  
*Turbulence*  
 McGraw-Hill, New York, 1959

[JAM98] **Jordan M., Ardey N., Mayinger F.:**  
*Effects of Molecular and Turbulent Transport on Flame Acceleration within Confinements*  
 Proceedings of the 11th International Heat Transfer Conference, Vol. 7, August 23-28, 1998, Kyongju, Korea, Ed.: J.S. Lee, pp.295-300

[Jor99] **Jordan M.:**  
*Zündung und Verbrennung in vorgemischten turbulenten Freistrahlen*  
 Dissertation, Lehrstuhl A für Thermodynamik, TU München, 1999

[Kuo86] **Kuo K.K.:**  
*Principles of Combustion*  
 John Wiley & Sons, New York, 1986

[LeMa77] **Leyer J.C., Manson N.:**  
*Development of vibratory flame propagation in short closed tubes and vessels*  
 13th Symposium (Int.) on Combustion, 1970, pp.551-558

[Lew61] **Lewis B., von Elbe G.:**  
*Combustion, Flames, and Explosions of Gases*  
 Academic, New York, 1961

[Mar64] **Markstein G.H.:**  
*Nonsteady Flame Propagation*  
 Pergamon Press, Oxford, 1964

[MMM87] **Makhviladze G.M., Melikhov V.I., Melikhov O.I.:**  
*Flame Propagation in an Enclosed Channel*  
 Plenum Publishing Corporation, 1987

[Opp83] **Oppenheim A.K., Ghoniem A.F.:**  
 Twenty-First Aerospace Sciences Meeting, AIAA, Reno, 1983

[Pet86] **Peters N.:**  
*Laminar Flamelet Concepts in Turbulent Combustion*  
 21st Symposium (Int.) on Combustion, 1986, pp. 1231-1250

[Philips] **Thermocoax:**  
*Produktinformation: Mantelthermoelemente, Auswahl und Anwendung*  
 Philips IE Deutschland GmbH, Meiendorfstraße 205, 22145 Hamburg

[Rey74] **Reynolds A. J.:**  
*Turbulent Flows in Engineering*  
 John Wiley & Sons, London, 1974

[Rot72] **Rotta J.C.:**  
*Turbulente Strömungen*  
 Leitfäden der angewandten Mathematik und Mechanik, Bd.15,  
 Teubner-Verlag Stuttgart, 1972

[Ruc90] **Ruck B.:**  
*Lasermethoden in der Strömungsmeßtechnik*  
 At Fachverlag, 1990

[Sta86] **Starke R., Roth P.**  
*An Experimental Investigation of Flame Behaviour During Cylindrical Vessel Explosions*  
Combustion and Flame 66: 249-259 (1986)

[Sch34] **Schardin H.**  
*Das Toeplersche Schlierenverfahren*  
VDI Forschungsheft 367, VDI-Verlag GmbH, Berlin 1934

[Tay35] **Taylor G.I.:**  
*Statistical Theory of Turbulence Part I/II*  
Proceedings of the Royal Society of London, Vol.873, no. A, pp.421-464, 1935

[TeKa95] **Tenschert J., Kanzleiter T.:**  
*Wasserstoff-Deflagrations-Experimente in einer kleinmaßstäblichen Versuchsanlage DN400*  
Technischer Fachbericht BF-R68.145-302 zum BMBF-Vorhaben 1500954, Eschborn, 1995

[TeLa87] **Tennekes H., Lumley J.L.:**  
*A First Course in Turbulence*  
The MIT Press, Cambridge, Massachusetts and London, Englandm no. 11, 1987

[Toe64] **Toepler A.:**  
*Beobachtungen nach einer neuen Methode*  
Max Cohen und Sohn, Bonn, 1864

[Kra96] **Kratzel Th.:**  
*Modellierung turbulenter Prozesse am Beispiel der Wasserstoff-Luft Verbrennung*  
Fortschr. Ber. VDI Reihe 7 Nr.290, VDI-Verlag Düsseldorf, 1996



# Chapter 3

## Model development and code implementation : synthesis

This section is devoted to model comparison between different computer codes involved in this EU Project (COM3D-FZK, REACFLOW-JRC ISPRA, CFX4.2-TUM Munich and TONUS-CEA [3]). The following tables will summarize and compare as far as possible the models implemented in each computer code previously described.

Concerning TONUS models, the first column deals with Low Mach Number Flow solver [2] [4] and the second one with Compressible flow solver [1]. Concerning TUM developments, models are implemented in the commercial code CFX4.2.

### 3.1 Equations

#### 3.1.1 Hydrodynamic

The following table compares the models implemented in the different computer codes. Most of the computer codes are fully compressible flow solver except TONUS which is more dedicated to low Mach number flows but is not able to cover all the Mach number range between slow deflagration and detonation. Conservation equations are classical Favre-averaged Navier-Stokes equations for compressible and reactive mixtures:

- Favre-averaged quantities are the velocity  $u$ , the species mass fraction  $Y$ , the temperature  $T$ , the enthalpy  $H$ , the energy  $E$ , the turbulent kinetic energy  $k$  and the turbulent dissipation rate  $\varepsilon$ ;
- Time averaged quantities are the density  $\rho$  and the pressure  $p$ .

COM3D has a maximum number of terms in all the conservation equations. Viscous stress tensor  $M_{ij}$  contains many terms and conservation of total energy is assumed without any simplifications:  $\epsilon$  and turbulent correlation terms between

velocity fluctuations and mean pressure gradient  $B$  (turbulent pressure work) are taken into account.

TONUS (Low Mach Number) uses some simplifications according to slow flame velocity and mixture composition. Viscous stress tensor  $M'_{ij}$  is restricted to velocity gradients because  $(u_r)_{x_r}$  is supposed to be small and  $k$  is usually neglected versus  $p'$  (some tentatives have been mentioned to take this term into account). Regarding energy equation, only the internal energy is taken into account because for slow flames, kinetic energy and turbulent kinetic energy are smaller than internal energy. To simplify  $C_p$  is assumed to be constant: for hydrogen/air, the mixture is mainly composed of nitrogen but temperature dependence needs to be implemented.

REACFLOW hydrodynamic equations are quite similar to COM3D equations except for energy equation energy which does not include turbulent pressure work term and turbulent dissipation rate.

In CFX4.2-TUM, the hydrodynamic equations are expressed in terms of modified pressure  $p''$ : additional terms involved in the viscous stress tensor (due to compressibility) are implemented in the modified pressure gradient.

All the 3 fully compressible codes (COM3D, REACFLOW and CFX4.2-TUM) are not dealing with low Mach number flows and so the first stage of combustion behavior will be poorly modeled but fast flame phenomena will have a good description.

For all the codes, closure of the equation are using classical gradient-diffusion hypothesis associated to turbulence model ( $k$ ,  $\varepsilon$  and  $\mu_{turb}$ ). No counter-gradient diffusion is taken into account in the following models.

ITEM	COM3D
Mass eq.	$(\rho)_t + (\rho u_i)_{x_i} = 0$
Momentum eq. (j=1,2,3)	$(\rho u_j)_t + (\rho u_i u_j)_{x_i} = \rho g_j$ $- p_{x_j}$ $+ M_{ij,x_i}$
Energy eq.	$(\rho e)_t + ((\rho e + p)u_i)_{x_i} = \rho g_i u_i$ $+ u_j M_{ij,x_i}$ $+ (\frac{\mu + \mu_{turb}}{C_h} (e - \frac{1}{2} u_j u_j + \frac{p}{\rho})_{x_i})_{x_i}$ $+ \frac{\mu + \mu_{turb}}{C_\rho} \frac{1}{\rho^2} \rho_{x_r} p_{x_r}$ $+ \rho \varepsilon$
Species eq.	$(\rho Y_\ell)_t + (\rho Y_\ell u_i)_{x_i} = \dot{\omega}_\ell$ $+ ((\frac{\mu + \mu_{turb}}{C_{f\ell}}) Y_{\ell,x_i})_{x_i}$

ITEM	REACFLOW
Mass eq.	$(\rho)_t + (\rho u_i)_{x_i} = 0$
Momentum eq. (j=1,2,3)	$(\rho u_j)_t + (\rho u_i u_j)_{x_i} = \rho g_j$ $- p_{x_j}$ $+ M_{ij,x_i}$
Energy eq.	$(\rho E)_t + ((\rho E + p)u_i)_{x_i} = \rho g_i u_i$ $+ (\sum_{\ell=1}^N h_\ell D_\ell (\rho Y_\ell)_{x_i})_{x_i}$ $+ (\tau_{ij} u_i)_{x_i}$ $+ (\lambda(T)_{x_i})_{x_i}$ $+ \sum_{\ell=1}^N \omega_\ell \Delta h_\ell^f$
Species eq.	$(\rho Y_\ell)_t + (\rho Y_\ell u_i)_{x_i} = \dot{\omega}_\ell$ $+ (D'_\ell Y_{\ell,x_i})_{x_i}$

ITEM	CFX4.2
Mass eq.	$(\rho)_t + (\rho u_i)_{x_i} = 0$
Momentum eq. (j=1,2,3)	$(\rho u_j)_t + (\rho u_i u_j)_{x_i} = (\rho - \bar{\rho}) g_j$ $- p''_{x_j}$ $+ M'_{ij, x_i}$
Energy eq.	$(\rho H)_t + (\rho H u_i)_{x_i} = (p)_t$ $+ ((\frac{\lambda}{C_p} + \frac{\mu_{turb}}{\sigma_t}) h_{x_i})_{x_i}$ $+ \sum_{\ell=1}^N \dot{\omega}_\ell \Delta_\ell$
Species eq.	$(\rho Y_\ell)_t + (\rho Y_\ell u_i)_{x_i} = \dot{\omega}_\ell$ $+ (\rho D_\ell + \frac{\mu_{turb}}{S_{ct}} Y_{\ell, x_i})_{x_i}$

ITEM	TONUS
Mass eq.	$\Delta p' = \frac{1}{\Delta t} [\rho (\frac{1}{P} \frac{dP}{dt} - \frac{1}{RT} \frac{dRT}{dt}) + \nabla \cdot (\rho \bar{u})]$ $+ \nabla \cdot ((\rho - \bar{\rho}) \bar{g}$ $+ \nabla \cdot (\bar{\tau} + \bar{\tau}_t)$ $- \nabla \cdot (\rho \bar{u} \otimes \bar{u})]$ $(\rho)_t + (\rho u_i)_{x_i} = 0$
Momentum eq. (j=1,2,3)	$(\rho u_j)_t + (\rho u_i u_j)_{x_i} = (\rho - \bar{\rho}) g_j$ $- p'_{x_j}$ $+ M'_{ij, x_i}$ $(\rho u_j)_t + (\rho u_i u_j)_{x_i} = - p_{x_j}$
Energy eq.	$(T)_t + (T u_i)_{x_i} - \frac{1}{\rho c_p} \frac{dP}{dt} = ((\frac{\lambda}{\rho c_p} + \frac{\nu_t}{P r_t}) (T)_{x_i})_{x_i}$ $+ \frac{1}{\rho c_p} \Omega$ $= (c_p T Q)_{jet}$ $- \oint_{\partial V} \bar{q} \cdot d\bar{n}$ $+ \iint_V \Omega dV$ $(\rho E)_t + (\rho u_i H)_{x_i} = Q$
Species eq.	$(Y_\ell)_t + (Y_\ell u_i)_{x_i} = ((D_\ell + \frac{\nu_t}{S_{ct}}) (Y_\ell)_{x_i})_{x_i}$ $+ \dot{r}_\ell$ $(\rho Y_\ell)_t + (\rho Y_\ell u_i)_{x_i} = \dot{r}_\ell$

Some additional definitions are needed to understand the preceding tables:

Stress tensor:

$$M_{ij} = -\frac{2}{3} \delta_{ij} (\rho k + (\mu + \mu_{turb})(u_r)_{x_r}) + (\mu + \mu_{turb})(u_{j, x_i} + u_{i, x_j})$$

$$M'_{ij, x_i} = (\mu + \mu_{turb})(u_{i, x_j} + u_{j, x_i})$$

Energy:

$$e = \sum_{\ell=1}^N \frac{f_\ell}{\mu_\ell} (h_\ell + \Delta h_\ell^0 - RT) + \frac{1}{2} u_j u_i$$

$E$  = internal energy + kinetic energy

Enthalpy:

$$H = \sum_{\ell=1}^N Y_\ell h_\ell + \frac{1}{2} u_i^2$$

Pressure:

$$p'' = p + \frac{2}{3}\rho k + \left(\frac{2}{3}(\mu + \mu_{turb}) - \zeta\right)(u_r)_{x_r} - \bar{\rho}g_j x_j$$

Species transport:

$$\begin{aligned} f_\ell &= \frac{\rho_\ell}{\rho} \\ \rho_\ell &= \rho Y_\ell \\ D'_\ell &= \rho D_\ell + \frac{\mu_{turb}}{Sc_t} \end{aligned}$$

Bulk viscosity:  $\zeta$

### 3.1.2 Turbulence

All the codes are using 2 equations  $k - \epsilon$  turbulence model (except TONUS fully compressible flow solver which has up to now no turbulence model). RNG  $k - \epsilon$  turbulence models are implemented in COM3D and in TONUS but there are not used for these combustion calculations. Also second moment turbulent closures have also not been implemented in the partners computer codes. The models are mainly standard  $k - \epsilon$  models but some production/destruction terms are added: buoyancy or mean pressure gradient terms.

If one looks at the real  $k$  equation [7] many terms appear and need to be modeled to deal with turbulent combustion.

$$\begin{aligned} \bar{\rho} \frac{\partial k}{\partial t} + \bar{\rho} \bar{u}_j \frac{\partial k}{\partial x_j} &= -\frac{1}{2} \overline{\frac{\partial \rho u''_i u''_j u''_j}{\partial x_j}} \\ &\quad - \overline{u''_i \frac{\partial p''}{\partial x_i}} \\ &\quad + \overline{u''_i \frac{\partial \tau_{ij}}{\partial x_j}} \\ &\quad - \overline{\rho u''_i u''_j \frac{\partial \bar{u}_i}{\partial x_j}} \\ &\quad - \overline{u''_i \frac{\partial \bar{\rho}}{\partial x_i}} \\ &\quad - \overline{u''_i F_i} \end{aligned}$$

Signification of terms are as follow:

- terms 1 and 2 : rate of change of kinetic energy of turbulence
- term 3 : diffusion of fluctuation energy
- term 4 : power developed by pressure fluctuations
- term 5 : work of viscous stresses due to fluctuation motion
- term 6 : production of turbulent energy

- term 7 : production of turbulent energy due to correlations between density-velocity and mean pressure gradient
- term 8 : production due body forces  $\mathbf{F}$

After some manipulations and classical gradient-diffusion hypothesis, term 3, part of term 4 and part of term 5 define the diffusion term of turbulent kinetic energy. Rest of term 4 is usually neglected or added to rest of term 5 to create the dissipation of turbulent kinetic energy  $\varepsilon$ . The following discussion will be more concentrated around models for terms 7 and 8.

Mean pressure gradient term are non zero in variable density flow only. This term represents the preferential effect of mean pressure gradient acting on light and heavy gases. The pressure gradient will tend to produce a larger acceleration of the light gas relative to the heavy and provides an additional mechanism for turbulent transport. This term is also part of the counter-gradient diffusion effect observed by Bray and Libby. Mean pressure gradient terms seems to be a key term for compressible and so for turbulent combustion calculation because this term seems to be the only thing to add to a constant density turbulence model to obtain acceptable accuracy. The first idea is that this term will be of importance for high velocity turbulent combustion when the pressure gradients become steep (complex precursor shock wave system behind the flame front). In the present computer codes, this term has only been implemented in the COM3D code using the simplest gradient-diffusion hypothesis. Some tests have also been performed in the TONUS low-Mach number flow solver but only qualitative effects have been observed.

Regarding buoyancy term, implementation has been performed in the CFX4.2-TUM and TONUS code. TONUS uses formulation coming from non reactive formulation and CFX4.2 rewrites this contribution with the Boussinesq buoyancy approximation.

Except mean pressure gradient or buoyancy terms, the others terms (diffusion, production/destruction...) are quite the same in all the computer codes.

ITEM	COM3D
$k$ equation	$(\rho k)_t + (\rho k u_i)_{x_i} = S - \rho \varepsilon + \left( \frac{\mu + \mu_{turb}}{C_k} k_{x_i} \right)_{x_i}$
$\varepsilon$ equation	$(\rho \varepsilon)_t + (\rho \varepsilon u_i)_{x_i} = \frac{\varepsilon}{k} (C_1 S - C_2 \rho \varepsilon) + \left( \frac{\mu + \mu_{turb}}{C_k} \varepsilon_{x_i} \right)_{x_i}$
Prod./destr. terms	$S = u_{j,x_i} M_{ij} - B$ $B = \frac{\mu + \mu_{turb}}{C_\rho} \frac{1}{\rho^2} \rho_{x_r} p_{x_r}$ $\mu_{turb} = C_\mu \rho \frac{k^2}{\varepsilon}$
Constants	$C_k = \text{classical}$ $C_1 = \text{classical}$ $C_2 = \text{classical}$ $C_\rho = \text{classical}$ $C_h = 1.3$ $C_{f_t} = 0.7$ $C_\mu = \text{classical}$

ITEM	REACFLOW
$k$ equation	$(\rho k)_t + (\rho k u_i)_{x_i} = \mu_{turb} S' - \rho \varepsilon - \frac{2}{3} \rho k (u_r)_{x_r} + \left( \frac{\mu_{turb}}{Pr_k} k_{x_i} \right)_{x_i}$
$\varepsilon$ equation	$(\rho \varepsilon)_t + (\rho \varepsilon u_i)_{x_i} = \frac{\varepsilon}{k} (C_1 (\mu_{turb} S' - \frac{2}{3} \rho k (u_r)_{x_r}) - C_2 \rho \varepsilon) + \left( \frac{\mu_{turb}}{Pr_\varepsilon} \varepsilon_{x_i} \right)_{x_i}$
Prod./destr. terms	$S' = [(u_{j,x_i} (u_{i,x_j} + u_{j,x_i})) - \frac{2}{3} ((u_r)_{x_r})^2]$ $\mu_{turb} = C_\mu \rho \frac{k^2}{\varepsilon}$
Constants	$Pr_k = 0.87$ $C_1 = 1.47$ $C_2 = 1.92$ $C_\mu = 0.09$ $Pr_\varepsilon = 1.30$

ITEM	CFX4.2
$k$ equation	$(\rho k)_t + (\rho k u_i)_{x_i} = P + G - \rho \varepsilon + ((\mu + \frac{\mu_{turb}}{\sigma_k}) k_{x_i})_{x_i}$
$\varepsilon$ equation	$(\rho \varepsilon)_t + (\rho \varepsilon u_i)_{x_i} = \frac{\varepsilon}{k} (C_1 (P + C_3 \max(0, G)) - C_2 \rho \varepsilon) + (\mu + \frac{\mu_{turb}}{\sigma_\varepsilon} \varepsilon_{x_i})_{x_i}$
Prod./destr. terms	$P = (\mu + \mu_{turb}) [(u_{j,x_i} (u_{i,x_j} + u_{j,x_i})) - \frac{2}{3} ((u_r)_{x_r})^2]$ $G = -\frac{2}{3} \rho k (u_r)_{x_r}$ $\mu_{turb} = C_\mu \rho \frac{k^2}{\varepsilon}$
Constants	$\sigma_k = 1.0$ $\sigma_\varepsilon = 1.21743$ $C_1 = 1.44$ $C_2 = 1.92$ $C_3 = 1.$ $\sigma_t = 0.9$ $Sc_t = 0.9$ $\alpha, \beta = CFX$ $C_\mu = 0.09$

ITEM	TONUS	
$k$ equation	$(\rho k)_t + (\rho k u_i)_{x_i} = ((\mu + \frac{\mu_{turb}}{Sc_k}) k_{x_i})_{x_i} - \rho \varepsilon + H_k$	Not implemented
$\varepsilon$ equation	$(\rho \varepsilon)_t + (\rho \varepsilon u_i)_{x_i} = ((\mu + \frac{\mu_{turb}}{Sc_\varepsilon}) \varepsilon_{x_i})_{x_i} + H_\varepsilon$	Not implemented
Prod./destr. terms	$H_k = P + G - \rho \varepsilon$ $H_\varepsilon = C_{1\varepsilon} (P + (1 - C_{3\varepsilon}) G) \frac{\varepsilon}{k}$ $- \rho C_{2\varepsilon} \frac{\varepsilon^2}{k}$ $P = \mu_{turb} [(u_{j,x_i} (u_{i,x_j} + u_{j,x_i})) - \frac{2}{3} ((u_r)_{x_r})^2]$ $- \frac{2}{3} \rho k (u_r)_{x_r}$ $G = - \frac{\mu_{turb}}{\sigma_t} \bar{g}(\rho)_{x_i}$ $\mu_{turb} = \rho C_\mu \frac{k^2}{\varepsilon}$	Not implemented
Constants	$Sc_k = 1.0$ $Sc_\varepsilon = 1.3$ $C_{1\varepsilon} = 1.44$ $C_{2\varepsilon} = 1.92$ $C_{3\varepsilon} = 1. \quad if \quad G < 0$ $0. \quad if \quad G > 0$ $\sigma_t = 0.7$ $C_\mu = 0.09$	Not implemented

Regarding the constants used in the different models, there are some slight differences between each model. If one looks for example at recommended values by [5] or [6]:

- $C_\mu = 0.09$  : everybody use this standard value;
- $C_{1\varepsilon} = 1.44$  : the same value is used in each model except REACFLOW which uses 1.47;
- $C_{2\varepsilon} = 1.92$  : everybody use this standard value;
- turbulent Prandtl or Schmidt number for  $k$   $\sigma_k = 1.0$  : used values vary from 0.87 to 1.0;
- turbulent Prandtl or Schmidt number for  $\varepsilon$   $\sigma_\varepsilon = 1.3$  : used values vary from 1.21743 to 1.3;
- turbulent Prandtl number  $\sigma_t = 0.7$  : used values vary from 0.7 to 0.9;

Regarding the three last constants, differences are small and are mainly coming from the user experience with the  $k - \varepsilon$  model verification (mainly non reactive test cases).

### 3.1.3 Closure and properties

For the state equation, models usually consider perfect gases. TONUS has a low Mach number flow solver which involves only the thermodynamical pressure  $P(t)$  ('lumped' parameter pressure) in the state equation (acoustic waves are filtered by the model).

Properties are mainly dependent on temperature and polynomial approximations are used.

The boundary conditions mean inflow, outflow, symmetry and solid surfaces conditions. Wall-bounded calculations in this project are mainly performed with slip conditions at walls. The main problem is the validity of standard wall function in transient turbulent combustion calculations. There are mainly developed and adjusted for stationary flows but also directly extended to combustion processes.

ITEM	COM3D
Equation of State	$p = \rho \cdot RT$
Properties of gases	JANAF Tables, $H(T)$ $C_v(T)$
Boundary conditions	slip conditions

ITEM	REACFLOW
Equation of State	$p = \rho \cdot RT$
Properties of gases	$C_v(T)$ 3rd order polynomials
Boundary conditions	slip conditions

ITEM	CFX4.2
Equation of State	$p = \rho \cdot RT$
Properties of gases	databases of CFX and CHEMKIN ( $C_p$ )
Boundary conditions	slip and standard Wall function

ITEM	TONUS	
Equation of State	$\rho = P(t)/RT$	$p = \rho \cdot RT$
Properties of gases	$C_v(T)$	polynomials versus T
Boundary conditions	Slip and Standard Wall function	Not implemented

### 3.1.4 Chemistry

#### 3.1.4.1 Turbulent combustion models

Most of the computer codes use Eddy Break-Up (EBU), Eddy dissipation (EDC) or Arrhenius models to describe hydrogen/oxygen combustion. Only CFX4.2 is dealing with PDF (see description below) to model combustion behavior (Eddy Break-Up could be considered as a simplified PDF model). For each partner, it seems that Said and Borghi correlations give better results for EBU or EDC constants but calculations are very sensitive to these constants.

Transition regimes are often expressed in terms of critical Damköhler number (transition regime for COM3D and up to now damping factor for TONUS). Nobody uses Karlovitz number to express transition regime like in the Borghi-Peters Diagram (transition between flamelets and thin reaction zone regimes).

The first stage of combustion process is calculated via Arrhenius reaction rate (TONUS) or directly via EBU or EDC models (COM3D or REACFLOW). This initial process is deliberately poorly modeled and other specific models are needed if attention must be paid to this initial stage of combustion behavior.

Concerning REACFLOW EDC model, extinction criteria have been added regarding to large chemical characteristic time scale ( $\tau_{ch}$ ).

ITEM	COM3D
Low turbulence intensity	$Da > 1$ $\dot{\omega} = -C_{EBU} \frac{\varepsilon}{k} \omega (1 - \omega)$
High turbulence intensity	$Da < 1$ $\dot{\omega} = -k\omega \exp(-E_a/RT)$
Constant definitions	$C_{EBU} = C_{EBU}^o \left(1 + \frac{4.4}{1+3.2\sqrt{k/S_L}}\right)$ $Da = \frac{k\omega \exp(-E_a/RT)k}{\varepsilon}$ $C_{EBU}^o = \text{adjusted}$

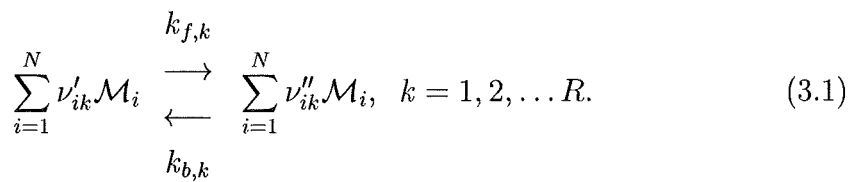
$\omega$  represents the fuel mass fraction.

ITEM	REACFLOW
Low turbulence intensity	$\tau_{ch} < \tau_{turb}$ $\dot{\rho}_{H_2} = -C_f \rho \frac{\varepsilon}{k} \rho_{lim}$
High turbulence intensity	extinction criteria
Constant definitions	$C_f = 4.0 - 4.65$ $\tau_{ch} = A_{ch} e^{\frac{E}{RT}} (\rho Y_{H_2})^a (\rho Y_{O_2})^b$ $\tau_{turb} = \frac{k}{\varepsilon}$ $\rho_{lim}$ = <i>limiting density</i> $A_{ch} = 2.25 \cdot 10^{-11}$ $a = 0$ $b = -1$

ITEM	TONUS	
Low turbulence intensity	$\dot{\rho}_{H_2} = -C \rho^2 Y_{H_2} Y_{O_2} \exp(-T_a/T)$	not implemented
High turbulence intensity	$\dot{\rho}_{H_2} = -C_{EBU} \rho \frac{\varepsilon}{k} Y_{H_2} [1 - \frac{Y_{H_2}}{Y_{H_2,a}}]$	$\dot{\omega} = A \rho^3 Y_{H_2}^2 Y_{O_2} T^{-b} \exp(-T_a/T)$
Constant definitions	$C = 2.06 \cdot 10^7 m^3/s/kg$ $C_{EBU} = C_{EBU}^0 (1 + \frac{4.4}{1+3.2\sqrt{k}/S_L})$ $C_{EBU}^0$ = <i>adjusted</i>	$A = 1.1725 \cdot 10^{14}$ $T_a = 8310 K$ $b = 0.91$

### 3.1.4.2 Chemical reaction rate

Any combustion process consists of many elementary reactions. In general a reacting system consisting of  $N$  components and  $R$  elementary reactions can be described by



$\mathcal{M}_i$  is the chemical symbol of the component  $i$ ,  $\nu'_{ik}$  and  $\nu''_{ik}$  the whole-numbered stoichiometric coefficients of the reactants and products of the  $k$ 'th reaction. The quantities  $k_{f,k}$  and  $k_{b,k}$  are the forward and reverse rate coefficients. The rate coefficients depend on the temperature and can be expressed by the generalised Arrhenius relation:

$$k_k = A_k T^{n_k} \exp\left(-\frac{E_k}{R_m T}\right), \tag{3.2}$$

where  $A_k$  is the frequency factor,  $n_k$  the exponent of temperature,  $E_k$  the activation energy of the  $k$ 'th reaction and  $R_m$  the gas constant. In general the

temperature dependency of the preexponential factor is small compared to the exponential dependence and, therefore, the exponent  $n_k$  can be set to 0.

In the energy and the mass fraction conservation equations of the combustion model, the chemical reaction rate  $w_i$  for each species  $i$  has to be determined. The reaction rate  $w_i$  determines the mass for the species  $i$  produced in a specific time and volume. The instantaneous reaction rate can be calculated by:

$$w_i = M_i \sum_{k=1}^R \left\{ (\nu''_{ik} - \nu'_{ik}) \left[ k_{f,k}(T) \prod_{j=1}^N \left( \frac{\rho Y_j}{M_j} \right)^{\nu'_{jk}} - k_{b,k}(T) \prod_{j=1}^N \left( \frac{\rho Y_j}{M_j} \right)^{\nu''_{jk}} \right] \right\}. \quad (3.3)$$

The chemical reaction mechanism for hydrogen air flames can be expressed by 37 elementary reactions (see [23]). In order to consider all elementary reactions and to solve the transport equations for all intermediate species tremendous computational effort is required. Therefore, the reduction of the kinetic mechanism is an important task if combustion problems are solved numerically.

### 3.1.4.3 Reduction of the thermochemical state

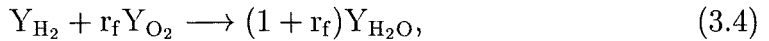
**3.1.4.3.1 COM-3D** The chemical characteristic time  $\tau_{ch} = \frac{1}{k\omega \exp(-E_a/T)}$  is determined from adiabatic induction time  $\tau_{ind}$ . Using CHEMKIN code with detailed chemical kinetics, Arrhenius laws are built for the adiabatic induction time  $\tau_{ind} = k' \exp(E_a/T)$ . Then, chemical characteristic time is computed through:

$$\tau_{ch} = \frac{T_{eff}^2 C_v^{reac}}{E_a Q k'} \exp(E_a/T_{max})$$

where  $Q$  is the combustion heat,  $T_{max} = \frac{C_v^{prod} T_{eff} + \omega Q}{C_v^{prod}}$  and  $T_{eff}$  is the effective temperature for chemistry.

**3.1.4.3.2 REACFLOW and TONUS** Both codes use very simplified reduction of the kinetic mechanism i.e. a simple Arrhenius law with constant coefficients (see table above).

**3.1.4.3.3 CFX4.2-TUM** In this application the proposed combustion model along the lines of Bray [15] is based on the following single step irreversible reaction:



where  $Y_i$  is the mass fraction of the species  $i$  and  $r_f$  is the stoichiometric ratio

$$r_f = \frac{M_{O_2} \nu'_{O_2}}{M_{H_2} \nu'_{H_2}} \approx 8. \quad (3.5)$$

Under the assumption, that the considered species have equal Schmidt numbers  $Sc_i = \frac{\nu}{D_i} = const.$ , which is valid in turbulent flows, it is possible to relate all species concentrations of the fluid to one progress variable

$$c = \frac{Y_{H_2O}}{Y_{H_2O,\infty}}, \quad (3.6)$$

with the mass fraction  $Y_{H_2O,\infty}$  of the product in the completely burned gas. Thus,  $c = 1$  when combustion is complete, while  $c = 0$  in the unburned mixture. The initial mixture is expected to contain no products, i.e. steam which can occur in a severe reactor accident is not taken into account. For a given initial condition, expressed by the index 0, the species concentrations are in dependency of  $c$ :

$$Y_{H_2} = Y_{H_2,0} - \frac{1}{1+r_f} c Y_{H_2O,\infty}, \quad (3.7)$$

$$Y_{O_2} = Y_{O_2,0} - \frac{r_f}{1+r_f} c Y_{H_2O,\infty}. \quad (3.8)$$

Due to the reduction of the kinetic scheme to one progress variable, it is sufficient to solve a single scalar transport equation to express the instantaneous state of the combustion process:

$$\frac{\partial}{\partial t} (\varrho c) + \frac{\partial}{\partial x_k} (\varrho u_k c) = \frac{\partial}{\partial x_k} \left( \Gamma_c \frac{\partial c}{\partial x_k} \right) + w_c, \quad (3.9)$$

with the production rate  $w_c$  of the scalar  $c$  and the molecular diffusion coefficient  $\Gamma_c$ . The production rate  $w_c$  can be expressed in terms of the chemical reaction rate  $w_{H_2O}$ :

$$w_c = \frac{w_{H_2O}}{Y_{H_2O,\infty}} \quad (3.10)$$

In the turbulent case, the molecular diffusion coefficient  $\Gamma_c$  in equation 3.9 is replaced by a turbulent diffusion formulation, and does, therefore, not have to be determined.

The motion in a turbulent flow is random, irregular and has a wide range of length scales. In order to obtain theoretical solutions for a turbulent flame by solving three-dimensional, transient equations huge computational effort is necessary to resolve the occurring scales in time and length. Numerical simulations trying to regard for the smallest time and length scales - referred to as Direct Numerical Simulation (DNS) - are not practicable for huge geometries like reactor containments. Up to now, the numerical solution is, therefore, limited to a chosen time and spatial resolution. In order to derive a discrete set of equations, which take into account the effects of turbulence, an averaging procedure has to be performed. In the case of the numerical simulation of combustion phenomena,

mass-weighted averaging - referred to as Favre averaging - is preferred to the conventional time averaging - referred to as Reynolds averaging -. By applying Favre averaging a considered quantity  $\phi$  in the concerning transport equation is replaced by

$$\phi = \tilde{\phi} + \phi'', \quad (3.11)$$

where the favre averaged value is

$$\tilde{\phi} = \frac{\bar{\rho}\phi}{\bar{\rho}} \quad (3.12)$$

and  $\phi''$  is the fluctuation around that average. In a second step the all the terms of the transport equation are time averaged. Using Favre averaging the transport equation for  $c$  and the modelling of the occurring scalar flux by a gradient diffusion approximation, Eq. 3.9 can be transformed to:

$$\frac{\partial}{\partial t} (\bar{\rho}\tilde{c}) + \frac{\partial}{\partial x_k} (\bar{\rho}\tilde{u}_k\tilde{c}) = \frac{\partial}{\partial x_k} \left( \frac{\eta_t}{Sc_t} \frac{\partial \tilde{c}}{\partial x_k} \right) + \bar{w}_c. \quad (3.13)$$

Due to the fact that the production rate  $\bar{w}_c$  is a highly nonlinear function of  $c$ ,  $\rho$  and  $T$ , Favre averaging leads to a closure problem (see [17]). Thus  $\bar{w}_c$  can not easily be determined. In order to overcome this problem and to regard for the influences of fluctuations on the mean production rate, the use of a Probability Density Function (PDF) model is an appropriate method for the fluctuating variables (see Sect. 3.1.5). The computational effort increases exponentially with the number of scalars for which a PDF formulation is performed. Therefore, in this approach, a further simplification is achieved by meeting the requirement of a low Mach number flow in the flame front region. Beside the species mass fractions, also the temperature and the density can be expressed in terms of  $c$ . Hence the production rate is only a function of  $c$ .

The fractional rise of the temperature, that would result from all the mechanical energy being converted into heat, can be approximated by

$$\frac{\Delta T}{T} \approx \frac{\frac{1}{2}U^2}{c_P T} \approx Ma^2 \frac{1}{2}(\kappa - 1). \quad (3.14)$$

As can be seen, for low Mach numbers the transfer of mechanical energy to heat can be neglected. If, in addition to that, the combustion process is considered as adiabatic and the Sorret effect is not taken into account, then the energy equation is formally identical to a common scalar transport equation. In a turbulent flow, heat and mass transfer based on diffusive processes is small compared to the apparent diffusivity due to turbulent convection processes. Therefore, a Lewis number  $Le = \frac{a}{D} = \frac{Sc}{Pr} \approx 1$  is a good assumption for the molecular transport mechanism of heat and species. In this case, heat is transported in the turbulent flame region analogous to the progress variable  $c$  (see Eq. 3.13). Under

this assumption both instantaneous quantities, the reaction progress  $c$  and the temperature  $T$  can be related together if an initial temperature  $T_0$  is given:

$$\int_{T_0}^T c_p dT = \Delta_{H_2O} c Y_{H_2O,\infty}, \quad (3.15)$$

where  $\Delta_{H_2O}$  is the heat of reaction. Thus when  $c = 0$  it follows  $T = T_0$  and when  $c = 1$  the temperature corresponds to the adiabatic flame temperature  $T = T_{ad}$ . Solving the integral by determining an averaged specific heat capacity in the considered temperature range, Eq. 3.15 can be written

$$T = T_0(1 + \bar{\tau}c), \quad (3.16)$$

where  $\bar{\tau}$  is the heat release parameter defined as

$$\bar{\tau} = \frac{\Delta_{H_2O} Y_{H_2O,\infty}}{\bar{c}_p T_0}. \quad (3.17)$$

It should be noted that Eq. 3.16 does not change when Favre averaging is applied.

To be able to determine a relationship between the density and the reaction progress  $c$  the combustion is assumed to occur at a constant pressure level. Pressure fluctuations occurring due to turbulent fluctuations can be estimated to be of the magnitude

$$\frac{\Delta p}{p} \propto Ma^2 \quad (3.18)$$

(see [16]) and can be neglected in low Mach number flows. Thus, using the equation of state

$$p = \bar{p} = \frac{\varrho R_m T}{\bar{M}}, \quad (3.19)$$

where  $\bar{M}$  is a constant mean molecular weight, and replacing  $T$  by Eq. 3.16 we get an expression for the density:

$$\varrho = \frac{\varrho_0}{1 + \tau c}. \quad (3.20)$$

By applying the suggested relations to Eq. 3.3, the reaction rate for the product can be expressed by

$$\begin{aligned} w_{H_2O}(c) &= M_{H_2O} \nu''_{H_2O} A e^{\frac{-E}{R_m T_0(1+\tau c)}} \left( \frac{\varrho_0}{1 + \tau c} \right)^{\nu'_{H_2} + \nu'_{O_2}} \frac{1}{M_{H_2}^{\nu'_{H_2}}} \frac{1}{M_{O_2}^{\nu'_{O_2}}} \\ &\quad \left( Y_{H_2,0} - \frac{1}{1 + r_f} c Y_{H_2O,\infty} \right)^{\nu'_{H_2}} \left( Y_{O_2,0} - \frac{r_f}{1 + r_f} c Y_{H_2O,\infty} \right)^{\nu'_{O_2}} \end{aligned} \quad (3.21)$$

The function  $w_{H_2O}(c)$  is hence referenced as 'laminar' reaction rate, though being derived with some assumptions only valid for turbulent flames. The classification 'laminar' is still valid, because up to this point the influences of turbulent fluctuations are not taken into account.

### Determination of the 'laminar' reaction rate

By reducing the elementary chemical kinetics of a hydrogen-air reaction mechanism to a single-step, irreversible reaction, the chemical reaction rate can be expressed in terms of the reaction progress (Eq. 3.21). For simplification Bray [15] suggests, the following equation:

$$w_{H_2O}(c) = B w_{max} (1 - c)^3 \exp\left(-E^* \frac{1 - c}{c}\right) Y_{H_2O,\infty}, \quad (3.22)$$

where  $B$  is a normalizing constant. The parameters are assumed to be  $E^* = 5$  and  $\tau = 5$ . But the problem is to find an appropriate value for the maximum occurring reaction rate  $w_{max}$ . This value strongly depends on the initial hydrogen-air mixture.

Due to the fact that the whole combustion simulation using the PDF model is very sensitive to the choice of the reaction rate  $w_c(c)$  in this approach it is attempted to find the exact chemical reaction rate for a given mixture. Therefore, for Eq. 3.21 the parameters

- preexponential factor A
- activation energy E
- order of reaction of water  $\nu'_{H_2}$  and oxygen  $\nu'_{O_2}$

have to be determined. In contrast to elementary reactions there is no obvious choice of these parameters for a complex reaction. Several authors, e.g. Varma et al. [20], Marathe et al. [21] and Coffee et al. [22] have investigated premixed laminar flames in order to derive a set of parameters for the global kinetic model. They succeeded in the determination of parameters, which guarantee a good agreement between a calculation of a laminar propagating flame based on a detailed reaction scheme and a calculation done with a reduced set of reactions. A comparison to experimental data, considering flame speed and flame thickness also revealed good results. The suggested parameters by Varma and Coffee vary with the initial mixture fraction of hydrogen, in contrast to Marathe, who suggests constant parameters for all cases. Since the parameters  $A$  and  $E$ , suggested by Varma and Coffee, are limited to discrete hydrogen concentrations, interpolation or even extrapolation in the lean fuel cases was necessary to get values for specific hydrogen concentrations. Linear interpolation procedures revealed to be too crude to get appropriate results. Therefore Durst [18] suggested a curve

fitting procedure for the determination of these two parameters. As an example the values of  $A$  and  $E$  for a 13vol%- $H_2$  in air mixture are listed in Table 3.1.4.3.3. It should be emphasized that the orders of the reaction  $\nu'_{H_2}$  and  $\nu'_{O_2}$  can differ

author	$A$	$E$	$\nu'_{H_2}$	$\nu'_{O_2}$	unit for A
Coffee et al.	5.6e12	74.09e3	2.0	1.0	$kmol^{-2.0}m^{6.0}s^{-1}$
Varma et al.	8.61e8	33.622e3	1.1	1.1	$kmol^{-1.2}m^{3.6}s^{-1}$
Marathe et al.	5.14e8	57.767e3	1.0	0.92	$kmol^{-0.92}m^{2.76}s^{-1}$

from whole-numbered values. Therefore, to keep the unit of the reaction rate the unit of  $A$  has to be adjusted.

As shown in Fig. 3.1 the different approaches lead to significant differences. All calculations were performed starting from an initialization of  $T_0 = 293.15$  K and  $p_0 = 1$  atm. The reason for the differences might be, that in the derivation of the function  $w_{H_2O}(c)$  some simplifying assumptions were made, with the consequence that the suggested sets of parameters are not appropriate anymore.

Since the results for other hydrogen-air mixtures (e.g. 9%, 12%) showed the same deviations (see [18]), it was not possible to choose an appropriate global kinetic scheme. To overcome this problem a detailed calculation of a freely propagating premixed laminar flame by the chemical kinetic code Insfla (programmed by Maas [24] and [25]) under consideration of all occurring elementary reactions was performed. The program accounts for finite rate chemical kinetics and exact molecular transport mechanisms. As a result, starting from the same initialization as for the global kinetic models, the laminar profiles of all involved species over the flame front can be calculated. For example  $H_2$ ,  $O_2$ ,  $H_2O$  and the temperature, are printed in Fig. 3.2. Further it is possible to extract for discrete water concentrations the affiliated reaction rate and relate it to the progress variable  $c$ .

By comparing the curves of Insfla with the curves calculated with the Arrhenius law it is observed, that the reaction rate calculated with Insfla is much smaller in the region of low reaction progress, i.e. for small values of  $c$ . Accordingly the maximum reaction rate is located at a higher reaction progress (at about  $c = 0.87$ ). This behaviour originates from the fact that the detailed calculation with Insfla is based on exact molecular transport mechanisms. Therefore the assumption of  $Le = 1$ , which was made by determining the reaction rate in dependence of  $c$  (Eq. 3.21), is not complied with. Due to the fact, that in this case ( $Le = 1$ ), the molecular transport in the flame front is expected to be small in comparison to the transport through turbulent fluctuations, a different approach for the determination of  $w_{H_2O}(c)$  is necessary. It has to be emphasized at this point, that this consideration is valid if combustion processes are investigated, which occur at Karlovitz numbers  $Ka > 1$ , i.e. combustion takes not place within

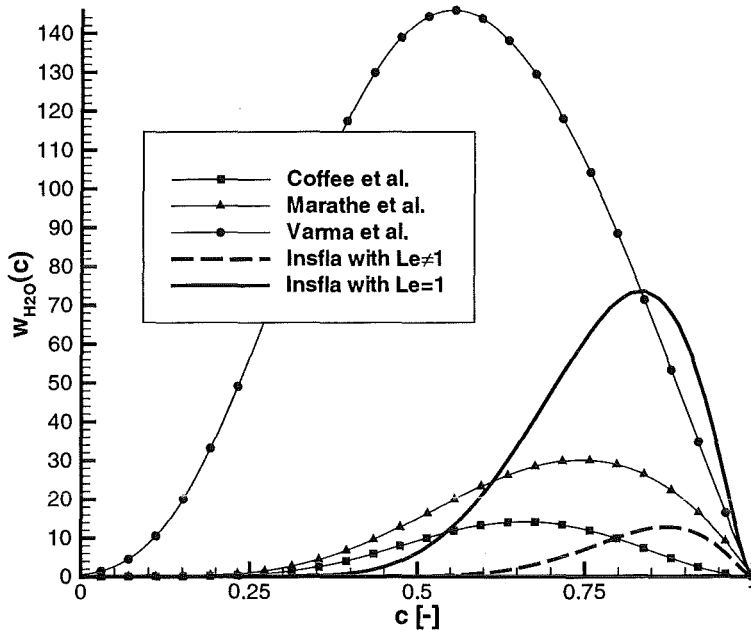


Figure 3.1: Different approaches for the determination of the 'laminar' reaction rate for a 13 vol-%  $H_2$  in air mixture

an asymptotically thin layer embedded in the turbulent flow - referred to as laminar flamelet concept - (see [28]). The Karlovitz number is a measure for the interaction of turbulent fluctuations at the Kolmogorov length scale  $l_K$  and the combustion:

$$Ka = \frac{l_f^2}{l_K^2} \quad (3.23)$$

By  $Ka = 1$  the smallest eddies are expected to be of the same magnitude as the flame thickness  $l_f$ . For higher values of  $Ka$  the smallest eddies can enter into the flame structure since  $l_K < l_f$ .

In order to derive an appropriate 'laminar' reaction rate  $w_{H_2O}(c)$  a calculation with Insfla under the default of  $Le = 1$  was performed. In this case all the binary diffusion coefficients of the involved species  $D_i$  are determined from

$$D_i = \frac{\nu}{Sc} = \frac{\nu}{Pr} = a \quad (3.24)$$

As shown in Fig. 3.1 this leads to a higher maximum reaction rate and enables higher reaction rates at lower reaction progress. But, in comparison to the curves

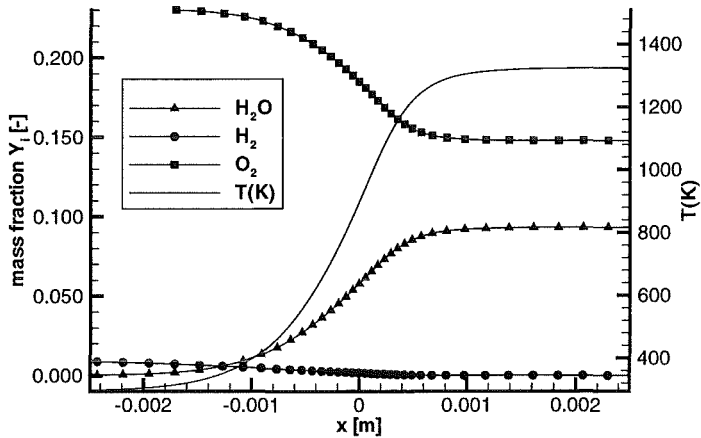


Figure 3.2: Profiles of a laminar propagating flame

calculated with the Arrhenius law it can be seen that no agreement with a selected curve is achieved, and that no obvious choice of a global chemical kinetic scheme is possible. It is therefore suggested to use, as a basis for the calculations with the PDF model, the extracted reaction rate of the detailed calculation with Insfla under the default of  $Le = 1$ .

### 3.1.5 The 'presumed PDF' method

In the previous section the instantaneous 'laminar' reaction rate for a global kinetic model was derived. The basic problem in turbulent combustion simulations is the determination of the time averaged reaction rate. It is not possible to calculate the reaction rate in dependence of time averaged quantities. It can be shown that:

$$\overline{w_c(c)} \neq w_c(\bar{c}), \quad (3.25)$$

whereas the values can vary by orders of magnitude.

One way to overcome this problem and to take into account the influence of the fluctuations  $c''$  on the reaction rate is the application of PDF methods (see [16]). In this formulation the time average for any thermodynamic state-variable  $\phi$  (which can be expressed in terms of  $c$ ) can be calculated by solving the following integral -referred to as folding integral -.

$$\bar{\phi} = \int_{-\infty}^{\infty} \phi(c) P(c; \mathbf{x}, t) dc \quad (3.26)$$

where,  $P(c; \mathbf{x}, t)$  represents the instantaneous probability density function of  $c$ . This function has to satisfy the condition

$$\int_{-\infty}^{\infty} P(c; \mathbf{x}, t) dc = 1. \quad (3.27)$$

Favre averaged variables, which are applied in the present work, can be determined by solving the following equation:

$$\tilde{\phi} = \frac{1}{\bar{\varrho}(\mathbf{x}, t)} \int_{-\infty}^{\infty} \varrho(c) \phi(c) P(c; \mathbf{x}, t) dc, \quad (3.28)$$

with the time averaged density

$$\bar{\varrho}(\mathbf{x}, t) = \varrho_0 \int_0^1 \frac{P(c; \mathbf{x}, t)}{1 + \bar{\tau}(c)c} dc. \quad (3.29)$$

The use of a 'presumed PDF' has the advantage of the 'moment's approach', which does not require the computation of the PDF. In the case of a presumed PDF it is necessary to adopt a shape for the the presumed distribution of the considered fluctuating variable, depending on certain parameters, e.g. the expected value or the variance of the variable. The parameters can change with the flow field and have to be computed based on transport equations for the moments of the random variable  $c$ . A lot of different shapes have been suggested in the literature for the PDF eg. uniform, rectangular, triangular, two delta and  $\beta$ -functions. In the applied approach a clipped gaussian shape following Lockwood and Naguib [19] has been chosen for the PDF:

$$P(c; \mathbf{x}, t) = \begin{cases} \int_{-\infty}^0 \frac{1}{\sigma\sqrt{2\pi}} \exp\left[-\frac{1}{2} \left(\frac{c-\mu}{\sigma}\right)^2\right] dc & \text{if } c = 0 \\ \frac{1}{\sigma\sqrt{2\pi}} \exp\left[-\frac{1}{2} \left(\frac{c-\mu}{\sigma}\right)^2\right] & \text{if } 0 < c < 1 \\ \int_1^{\infty} \frac{1}{\sigma\sqrt{2\pi}} \exp\left[-\frac{1}{2} \left(\frac{c-\mu}{\sigma}\right)^2\right] dc & \text{if } c = 1 \end{cases}$$

The course of  $P(c; \mathbf{x}, t)$ , shown in Fig. 3.3, is represented by a Gaussian distribution for the range  $0 < c < 1$ , whereas the tails of the function are represented by  $\delta$ -functions at  $c = 0$  and  $c = 1$ . The parameters  $\mu$  and  $\sigma$  can be determined by solving:

$$\tilde{c}(\mathbf{x}, t) = \frac{1}{\bar{\varrho}(\mathbf{x}, t)} \int_0^1 \varrho(c) c P(c; \mathbf{x}, t) dc, \quad (3.30)$$

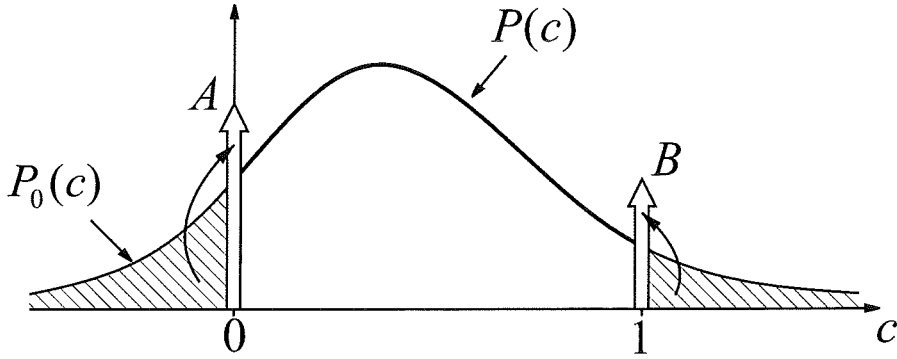


Figure 3.3: Clipped gaussian distribution of the reaction progress variable  $c$  clipped at  $c = 0$  and  $c = 1$

for the first moment, and

$$\widetilde{c''^2}(\mathbf{x}, t) = \frac{1}{\bar{\varrho}(\mathbf{x}, t)} \int_0^1 \varrho(c) (c - \tilde{c}(\mathbf{x}, t))^2 P(c; \mathbf{x}, t) dc, \quad (3.31)$$

for the second central moment of the random variable  $c$ . It is obvious that explicit expressions for  $\mu$  and  $\sigma$  cannot be obtained. The values must be calculated iteratively from the implicit Eqs. 3.30 and 3.31.

In addition to the transport equation for the mean value  $\tilde{c}$  (Eq. 3.13) a partial equation for  $\widetilde{c''^2}$  has to be solved.

$$\begin{aligned} \frac{\partial}{\partial t} (\bar{\varrho} \widetilde{c''^2}) + \frac{\partial}{\partial x_k} (\bar{\varrho} \tilde{u}_k \widetilde{c''^2}) &= \frac{\partial}{\partial x_k} \left( \frac{\eta_t}{Sc_c} \frac{\partial \widetilde{c''^2}}{\partial x_k} \right) + 2 \frac{\eta_t}{Sc_c} \left( \frac{\partial \tilde{c}}{\partial x_k} \right)^2 \\ &\quad - c_c \bar{\varrho} \frac{\epsilon}{k} \widetilde{c''^2} + 2 \overline{c'' w_c}. \end{aligned} \quad (3.32)$$

It should be noted that for the derivation of Eqs. 3.13 and 3.32 modelling was necessary for closure of the equation system. The constants in these equations are  $Sc_c = 0.9$  and  $c_c = 2.0$  (see [16] for details).

### 3.1.5.1 Calculation of the 'pdf reaction rate'

As shown above it is possible to determine time averaged quantities by solving the folding integral of the PDF and the concerning quantity. Analogous the time averaged reaction rate can be calculated from (see Fig. 3.4):

$$\overline{w_c}(\mathbf{x}, t) = \int_0^1 w_c(c) P(c; \mathbf{x}, t) dc, \quad (3.33)$$

Due to the fact that  $P(c; \mathbf{x}, t)$  is a clipped gaussian function the integration limits

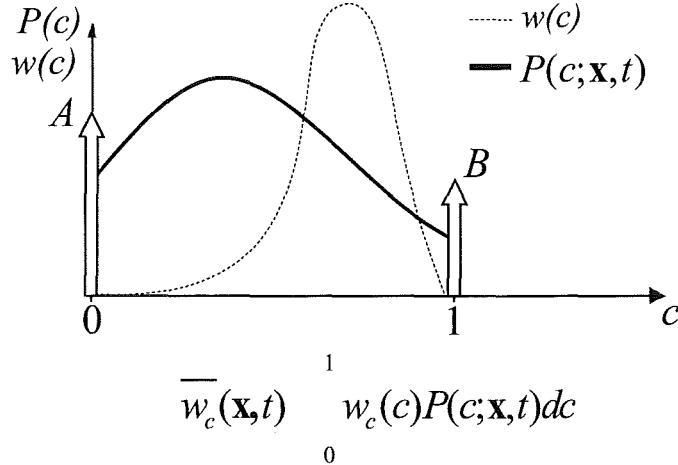


Figure 3.4: Calculation of the 'pdf reaction rate'

reduce to 0 for the lower and 1 for the upper value of  $c$ . As mentioned above, the Eqs. (3.30) and (3.31) can be solved for  $\mu$  and  $\sigma$  if  $\tilde{c}$  and  $\tilde{c}^{\prime\prime 2}$  are known, and the PDF can be determined. The thereby applied iterative Newton-Raphson method for nonlinear systems of equations (see [29]) is very time consuming. In order to reduce computational effort, the process of calculating the mean reaction rate is done before a combustion simulation is performed and a table look-up procedure is employed. The table is calculated a priori for discrete values of  $\tilde{c}$  and  $\tilde{c}^{\prime\prime 2}$ .

Because the variance  $\tilde{c}^{\prime\prime 2}$  only can be in the range  $0 \leq \tilde{c}^{\prime\prime 2} \leq \tilde{c}(1 - \tilde{c})$ , a normalized variance

$$g = \frac{\tilde{c}^{\prime\prime 2}}{\tilde{c}(1 - \tilde{c})} \quad (3.34)$$

is introduced with the range  $0 \leq g \leq 1$ .

In Fig. 3.5 a table containing the probability density weighted reaction rates - referred to as 'pdf reaction rates' - for a 13vol%- $H_2$  in air mixture is shown. It can be seen that for low fluctuations  $\tilde{c}^{\prime\prime 2} \approx 0$  the pdf reaction rate is close to the 'laminar' reaction rate. This region corresponds to a combustion process which is limited through chemical processes and therefore to regions with a small Damkhler number. Higher fluctuations of  $c$ , i.e. higher values of  $\tilde{c}^{\prime\prime 2}$ , lead to a decreasing of the maximum reaction rate and to higher reaction rates for smaller values of  $\tilde{c}$ . This originates from the fact that more and more unmixed regions with unburned or fully burned pockets arise which are represented through the two delta peaks of the clipped gaussian probability density function. As shown in

Fig. 3.4 the peaks do not contribute to the averaged reaction rate by calculating the folding integral, because the 'laminar' reaction rate is zero at  $c = 0$  respectively  $c = 1$ . In this case the combustion takes place in the 'distributed reaction zone' regime (see Fig. 3.7). Finally if the fluctuations reach their maximum, the PDF only consists of the two delta peaks and therefore the pdf reaction rate tends to small values. This behaviour corresponds to the mixing limited case of a turbulent combustion in which the flame is expected to burn in flamelets. The influence of the chemical reaction rate on the pdf reaction rate vanishes.

It should be noted, that also the source term  $\overline{c''w_c}$  in Eq. 3.32 has to be calculated and stored in a table. Again a complex iterative method is necessary where

$$\overline{c''w_c} = \int_0^1 w_c(c)cP(c; \mathbf{x}, t)dc - \tilde{c} \int_0^1 w_c(c)P(c; \mathbf{x}, t)dc, \quad (3.35)$$

is solved for the same discrete values  $\tilde{c}$  and  $\tilde{c''}$  as for the pdf reaction rate. The term  $\overline{c''w_{H_2O}}$  easily can be determined by

$$\overline{c''w_{H_2O}} = \overline{c''w_c} \cdot Y_{H_2O,\infty}. \quad (3.36)$$

The result is shown in Fig. 3.6.

### 3.1.5.2 Valid range of the PDF model

In turbulent combustion processes various types of flames occur, which are shown in Fig. 3.7 (see [26] and [28]). As can be seen, each of the combustion models covers only a specific region in which full model validity is given. Due to the fact that it is not always possible to verify exactly which combustion regime is relevant and that the regimes can change during a combustion process, the derivation of a combustion model which covers all regimes is an ambitious aim. Borghi [17] pointed out that the PDF combustion model can be used for all flame types if different shapes for the PDF are chosen. In our case the shape of the PDF does not change during a combustion simulation. Since a clipped gaussian shape has been chosen for the whole combustion process, the applied PDF model is only full valid in regions where the Karlovitz number  $Ka > 1$ . Furthermore the PDF model is optimized for the regions of the Borghi diagram marked out in Fig. 3.7 through the applied determination of the 'laminar' reaction rate  $w_{H_2O}(c)$  (see Sect. 3.1.4.3.3). It has to be emphasized that the applied PDF approach is also applicable for the flamelet region but might be not so accurate as the flamelet (see [28]) or the eddy dissipation combustion models (see [30]). To overcome this problem it is suggested in the literature (e.g. [27]) to couple the PDF combustion model with one of the models for fast chemistry, which is not used in terms of this project.

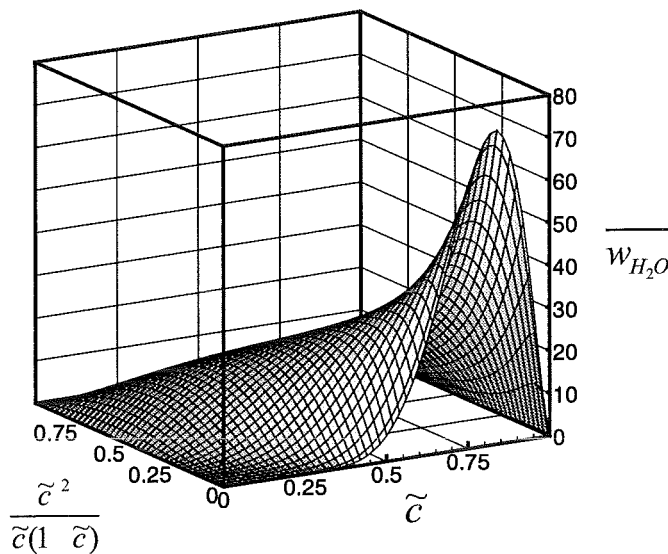


Figure 3.5: pdf reaction rate for 13vol%- $H_2$  in air

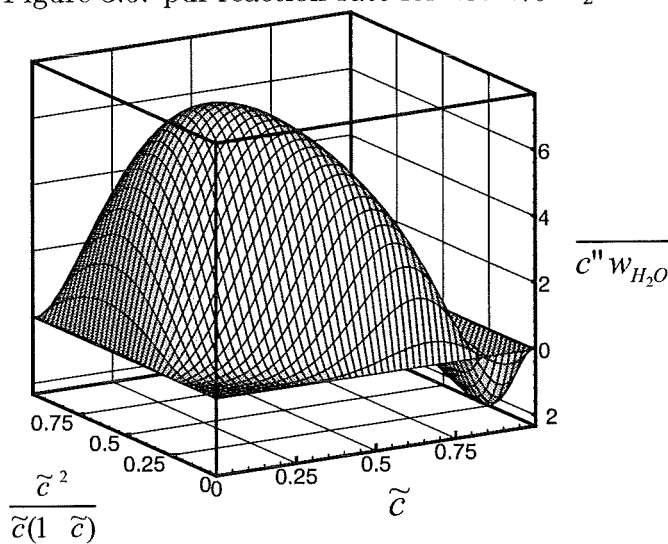


Figure 3.6: Source term for the variance due to chemical reaction for 13vol%- $H_2$  in air

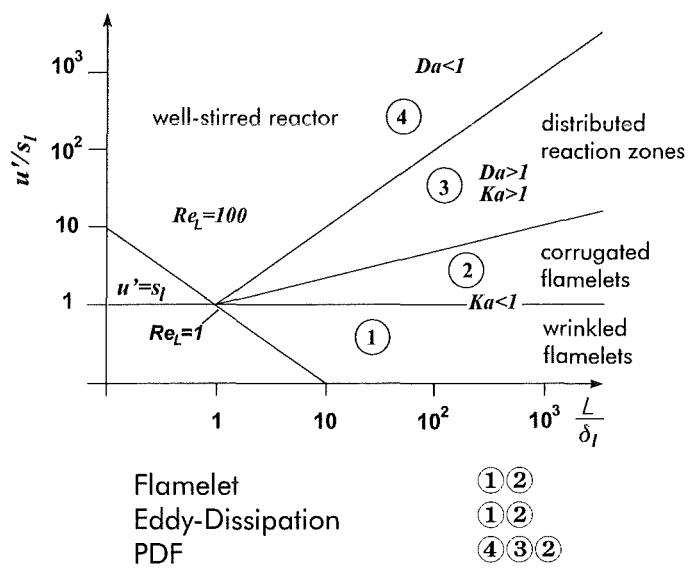


Figure 3.7: Borghi diagram with a classification of existing combustion models

### 3.1.6 Recombiner models

A micro-recombiner model has been developed by Siemens. This model is mainly based on two-dimensional viscous and compressible partial differential equation model of a multi-component gas mixture boundary layer. A detailed description of this model is provided in Annex A.

Other simplified model of catalytic recombiners have been developed in CFD tools.

TONUS has a simplified recombiner model which is available for the lumped parameter and the multi-dimensional formulation. This sort of "black box" has inlet and outlet conditions connected to the global geometry. The unknowns of the problem are outlet mass flow-rate, outlet concentrations of each component of the mixture, catalytic plate temperature and outlet temperature. Incompressibility is assumed for the gaseous mixture. The following set of equation is solved:

Item	Equation
Mass Balance	$\dot{m}_{inlet} = \dot{m}_{outlet}$
Momentum Balance	$(\frac{1}{2}K^{inlet} + \frac{1}{2}k\frac{L_c}{D_h} + \frac{1}{2}K^{outlet})\frac{\dot{m}^2}{\rho^m s^2} = g((\rho^{ext} - \rho^m)L_c + (\rho^{ext} - \rho^{out})L_{ch})$
Energy (Catalytic plates)	$\dot{m}_{H_2}\Delta H = m_c C p_c \frac{dT_c}{dt} + S_{ch}(T_c - T_{inlet})$
Energy (Gas mixture)	$\dot{m} C p^m (T_{outlet} - T_{inlet}) = S_c(h + h_r)(T_c - T_{outlet})$

where:

$\dot{m}$ : mass flow-rate

$m$ : mass

$K$ : pressure losses

$k$ : friction coefficient

$\rho$ : density

$L$ : length

$S$ : area

$Cp$ : heat capacity

$D_h$ : hydraulic diameter of the plates

$h$ : convective heat transfer (Elenbaas)

$h_r$ : radiative heat transfer

$s$ : cross section of the plates

$T$ : temperature

$\Delta H$ : heat release of catalytic combustion

$c$ : catalytic plates

$m$ : mean value in the recombiner

$_{ext}$ : value outside the recombiner

$\dot{m}_{H_2}$  is defined using global correlation developed by the industry for each type of catalytic recombiner. This model have been successfully validated on KALI and H2PAR experiments.

## 3.2 Model implementation and numerical scheme

### 3.2.1 Grid definition

For the mesh processing, several strategies have been adopted in the different codes.

Some codes are limited to structured mesh : in COM3D, structured cubic mesh is used while in CFX a block-structured body fitted strategy is adopted. For the latter, two space grids are considered : a computational space grid and a physical space grid. In computational space, a multi-block grid is considered. It is a set of sub-grid or block. Each block is a uniform grid in some transformed coordinate system. The computational space transforms into a grid in physical space in which block remains topologically cubic : it retains the connectivity of the computational space grid but may be distorted into an arbitrary shape [8].

Others consider unstructured mesh : TONUS and REACFLOW. As the former is strongly linked to the finite element community, all classical polygonal elements can be used in two and three space coordinates. The different elements can be mixed in an unstructured fashion in the same mesh. For REACFLOW, due to the numerical method used for the convective fluxes evaluation, only triangles in 2D and tetrahedra in 3D are accepted. Nevertheless, REACFLOW is the only code where adapted grid can be performed. New nodes can be added or removed based on an evaluation of the local variation of some flow field variables (for example pressure, temperature, density or one of the conservative variables). The original grid points cannot be removed and a number of different criteria for the refinement/coarsening decisions have been implemented : simple difference between neighbors, norm of the gradient in each element or local evaluation of the interpolation error. New nodes are inserted by bisection of an element edge between two existing nodes, thus dividing all the element touching that edge. This method closely related that of Rivera and Levin [9].

ITEM	COM3D
Type of mesh	structured
Type of element	cubes
Grid refinement	Not available

ITEM	CFX4.2
Type of mesh	block-structured body fitted
Type of element	hexahedron
Grid refinement	Not available

ITEM	TONUS
Type of mesh	unstructured
Type of element	all finite element polygons
Grid refinement	Not available

ITEM	REACFLOW
Type of mesh	unstructured
Type of element	triangles in 2D, tetrahedra in 3D
Grid refinement	Available

### 3.2.2 Numerical methods

In order to perform 3D calculation with large geometrical length scale, low diffusive schemes appear to be essential. Convective terms usually represent the main difficulty. As spurious oscillations can occur if space central second order discretization is used, upwinding is necessary. To limit artificial viscosity, several techniques can be used depending on the way in dealing with convective fluxes and algorithm for the resolution of the Navier-Stokes equation.

One approach is a pressure-based approach. The well-known semi-implicit ICE method [12] may perhaps be recognized as one of the first methods able to simulate both incompressible and low Mach number flows. The scheme, which uses pressure and not density as a main variable, is based on an elaborate operator splitting procedure to handle the pressure-velocity coupling and on the implicit treatment of the density in both the continuity equation and the equation of state to effectively remove the acoustic speed stability condition. The PISO method also uses pressure and velocity as dependent variables, but relies on a non-iterative fully implicit discretization of the equations. SIMPLE, SIMPLER and SIMPLEC methods belong to the same class of formulation. TONUS low Mach number formulation [11] and CFX use numerical methods coming from this point of view.

In TONUS, a finite element method is used. Artificial viscosity is added when necessary using a streamline upwind Petrov-Galerkin procedure (SUPG). For each element the pressure is at the cell center and the velocity is at the cell vertices. In CFX a finite volume approach has been developed. As all the variables are colocated at the cell center, for advective terms Rhie-Chow interpolation formula are employed to transport quantities at the cell interfaces. Some modification has

been done to the original SIMPLE algorithm in order to perform computation for high-speed compressible flow. Numerous discretization methods are available in order to limit the numerical viscosity : upwind first order differencing, quadratic upwind differencing or MUSCL approach can be selected.

On the other way, methods coming from the resolution of compressible inviscid Navier-Stokes equations (Euler equations) are used in COM3D and REACFLOW codes.

Convective fluxes are evaluated through the total variation diminishing scheme of Harten in COM3D [13] while an approximate Riemann solver is used in REACFLOW [10]. These schemes involve the resolution at the cell interfaces of a one dimensional Riemann problem where the right state and the left state are constituted by the averaged values of the primitive variables cell by cell. Second order accuracy can be achieved with those scheme when the solution is smooth.

TONUS code use a similar approach in the compressible flow solver [14].

ITEM	COM3D
Spatial discretization	finite volume
Time discretization	explicit
Low Mach preconditioning	no information
Convective terms	TVD approach

ITEM	REACFLOW
Spatial discretization	finite volume
Time discretization	implicit or explicit
Low Mach preconditioning	not implemented
Convective terms	approximate Riemann solver
Positivity of $k$ and $\epsilon$	assumed

ITEM	CFX4.2
Spatial discretization	finite volume
Time discretization	implicit
Low Mach preconditioning	not necessary if selected
Convective terms	upwinding
Positivity of $k$ and $\epsilon$	assumed

ITEM	TONUS	
Spatial discretization	finite element	finite volume
Time discretization	implicit for pressure, explicit unless	explicit
Low Mach preconditioning	not necessary	not implemented
Convective terms	SUPG	Riemann solver
Positivity of $k$ and $\epsilon$	filter design	not implemented

# Bibliography

- [1] A. Beccantini and H. Paillère. A two-dimensional high-order unstructured grid solver for unsteady shock propagation problems CEA internal report 1998.
- [2] H. Paillère, S. Clerc, C. Viozat, I. Toumi and J.-P. Magnaud. Numerical Methods for Low Mach Number Thermal-Hydraulic Flows. ECCOMAS 98.
- [3] E. Studer CEA/IPSN, H. Paillère, A. Beccantini, A. Faix and F. Dabbene CEA/DRN. Multi-dimensional simulation of hydrogen distribution and combustion in severe accident - CEA contribution (IPSN and DRN) Final Report 1998 Contract No FI4S-CT-95-0001.
- [4] H. Paillère, L. Dada, F. Dabbene, J.-P. Magnaud, and J. Gauvain. Development of hydrogen distribution and combustion models for the multi-dimensional/lumped-parameter TONUS code. Paper Log No. 230, 8th International Meeting on Nuclear Thermal-Hydraulics NURETH-8, Kyoto, September 1997.
- [5] K. K. Kuo. Principles of combustion. Wiley Interscience Edition.
- [6] W. Rodi. Turbulent Models and their application in hydraulics. IAHR Monograph.
- [7] B. Mohammadi and O. Pironneau. Analysis of the  $k - \epsilon$  turbulence model, Research in applied mathematics. Masson Edition.
- [8] CFX-F3D, Version 4.1 : user manual.
- [9] Rivara M.-C. and C. Levin, A 3-D refinement algorithm suitable for adaptive and multi-grid techniques, *comm. in appl. num. meth.*, vol 8, pp 281-290, 1992.
- [10] Nkonga B. and H. Guillard, Godunov type method on non-structured meshes for three-dimensional moving boundary problems, *Comput. Methods Appl. Mech. Engrg.*, **113**, pp 183-204, 1994.

- [11] Paillre H. and J.-P. Magnaud, A finite element elliptic flow solver for low mach number compressible flows, *proc. 10th Int. Conf. on Finite Elements in Fluids*, Tucson, Arizona, Jan. 5-8, 1998.
- [12] Harlow F.H. and A.A. Amsden, A numerical fluid dynamics calculation for all flow speeds, *J. Comput. Phys.*, **8**, pp 197-213, 1971.
- [13] Harten A., High resolution schemes for hyperbolic conservation laws, *J. Comput. Phys.*, **49**, pp 357-393, 1983.
- [14] Beccantini A., H. Paillre, R. Morel and F. Dabbene, Multi-dimensional simulation of shock-induced hydrogen detonations, *17th Int. Colloquium on the dynamics of explosions and reactive systems*, Heidelberg, Germany, July 25-30, 1990.
- [15] K. N. C. Bray and J. B. Moss. A unified statistical model of the premixed turbulent flame. *Acta Astronautica*, 4:291-319,1977.
- [16] S. B. Pope . The statistical theory of turbulent flames. *Transactions of the Royal Society of London*, 291:529-568, 1978
- [17] R. Borghi. Turbulent combustion modelling. *Prog. Energy Combust. Sci.*,14:245-292, 1988.
- [18] B. Durst. Messungen und Simulationen zur Wechselwirkung zwischen Turbulenz und vorgemischten Flammen. München, Techn. Univ.,Diss.,2000.
- [19] F. C. Lockwood and A. S. Naguib. The prediction of the fluctuations in the properties of free, round-jet, turbulent diffusion flames. *Combust. and flame*,24:109-124,1975.
- [20] A. K. Varma, A. U. Chatwani and F.V. Bracco. Studies of premixed laminar hydrogen-air flames using elementary and global kinetics models. *Combust. and flame*, 64:233-236,1986.
- [21] A. G. Marathe, H. S. Mukunda and V. K. Jain. Some studies on hydrogen-oxygen diffusion flame. *Combust. Sci. and Tech.*,13:49-64,1977
- [22] T. P. Coffee, A. J. Kotlar and M. S. Miller, The overall reaction concept in premixed laminar steady state flames,54:155-169,1983.
- [23] J. Warnatz and U. Maas, *Technische Verbrennung*, Springer Verlag, Berlin Heidelberg 1993
- [24] U. Maas, *Mathematische Modellierung instationärer Verbrennungsprozesse unter Verwendung detaillierter Reaktionsmechanismen*, Dissertation Universität Heidelberg,1988

- [25] U. Maas J. Warnatz, Ignition Processes in Hydrogen-Oxygen Mixtures, *Combust. and Flame*, 74:53, 1988
- [26] R. Borghi, On the structure of turbulent premixed flames, *Recent Advances in Aeronautical Science*, Eds.:Bruno C.,Casci C.,Pergamon Press, 1984.
- [27] R.Borghi, Application of a "Presumed p.d.f." model of turbulent combustion to reciprocating engines. *Proc. 21st. Symposium (Int.) on Combustion*, The Combustion Institute, pp. 1591-1599, Pittsburgh, USA, 1986.
- [28] N. Peters, Laminar flamelet concepts in turbulent combustion, *Proc. 21st. Symposium (Int.) on Combustion*, The Combustion Institute pp. 1231-1250, Pittsburgh, USA, 1986.
- [29] W. H. Press, B.P. Flannery, S.A. Teukolsky and W.T. Vetterling, *Numerical recipes*, Cambridge Univ. Press, Cambridge, 1989
- [30] B. F. Magnussen and B. H. Hjertager. On mathematical modeling of turbulent combustion with special emphasis on soot formation and combustion. *17'th Symposium (Int.) on Combustion*. The Combustion Institute, pp. 719-729,Pittsburgh, USA.

# Chapter 4

## Code and Model verification

Within the framework of this program various models and software programs, which have been described in chapter 3, were used by the different partners. In the following sections the procedures used to verify each of these codes will be discussed. Results of test calculations and comparisons with experimental or analytical data are presented. At the end of this chapter results of direct code comparisons are discussed. In these benchmarks the same test problems are calculated with different codes and the results are compared.

## 4.1 GASFLOW Code and Model Validation

GASFLOW has been developed to simulate steam/hydrogen distribution in complex 3D containment geometries. A large effort during the code development was put in defining simple GASFLOW test problems for which an analytical solution existed and to verify the agreement of the GASFLOW results with the analytical solutions. Most of the test problems are simple 1D simulations that are narrowly focused, but exact. The following table summarizes the analytical test problems, which have been developed and which are all documented in the assessment manual of GASFLOW [1]. The right column gives the purpose of each test problem.

All simple test problems agreed well with the analytical solutions, in particular the laminar flow between parallel plates and the transient diffusion in stagnant fluid showed good agreement. The only significant finding revealed by testing GASFLOW with these problems was that the boundary condition specification can change the results in GASFLOW. If the fluid speed is specified at the inlet, for example, the momentum flux is not calculated. This is characteristic for a finite volume differencing scheme. Specification of the velocity as a boundary condition implies that the momentum equation solution is replaced with the velocity boundary-condition specification and that the calculation of the momentum flux at the boundary is not necessary.

Table 4.1: Analytical Assessment of GASFLOW with simple test problems

Problem Description	What is Tested
1. Laminar startup between parallel plates.	Gravity and momentum diffusion (shear stresses).
2. Transient diffusion in stagnant fluid.	Mass diffusion term.
3. Flow past a rectangular block.	Test van Leer differencing scheme.
4. Steady flow through a smooth area change (a nozzle).	Momentum flux (convection, advection) and pressure gradient terms.
5. Steady flow through an abrupt area change (contraction).	Momentum flux and pressure gradient.
6. Steady flow in a constant-area channel with wall friction.	Wall friction and pressure gradient.
7. Steady flow in a constant-area change with wall friction with inlet velocity fixed.	Wall friction and pressure gradient with inlet velocity fixed.
8. One-dimensional flow through an orifice.	Momentum flux, orifice loss model, and pressure gradient terms.
9. Uniform energy source in two 3D blocks with one connecting duct.	Volumetric energy source and time rate of change of energy.
10. Mass-flow-rate boundary condition specification.	Tests boundary condition specification by use of time-dependent function.
11. Test filter model with turbulent flow losses.	Test filter model.
12. Test filter model with laminar flow losses.	Test filter model.
13. Test filter model with both laminar and turbulent flow losses.	Test filter model.
14. Steady-state conduction through a plain wall.	Conduction equation solution and heat-transfer-coefficient evaluation.
15. Vapor condensation from bulk in mixture of air and water vapor.	Tests p-v work term and transient energy equation.

## 4.2 Tonus (Distribution and combustion code from CEA)

### 4.2.1 Low Mach number flow solver verification

In this section, numerical verifications of TONUS low Mach number flow solver are given [3]. This approach is compared to solutions of the compressible equations using preconditioned fluxes in a finite volume setting [4] [5].

Three test cases involving low Mach number flows are selected: the flow over a smooth sine-shape channel, the lid-driven cavity test-case and the buoyant flow in a differential heated square cavity. Details of these test-cases can be found in [3] and here only some results are presented.

#### 4.2.1.1 Flow over a sine-shaped bump

The inviscid flow at different Mach numbers (between 0.001 and 0.5) in a channel with a sine-shaped lower wall has been simulated using the Low Mach Number solver (LMS), the original and the preconditioned Roe solver (PRS2). Figure 4.1 shows the Mach iso-lines obtained with the original, unpreconditioned Roe solver for the case  $Ma = 0.001$ , and illustrates how the accuracy of the solver degrades severely at very low Mach number. When the flux function is modified via preconditioning, the accuracy is restored as shown in figure 4.2. The solution obtained using the Low Mach number solver is shown in figure 4.3, and resembles closely that produced by the preconditioned solver.

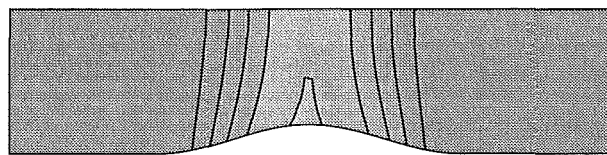


Figure 4.1: Mach number iso-lines ( $M_{inlet} = 0.001$ ) obtained with unpreconditioned Roe solver

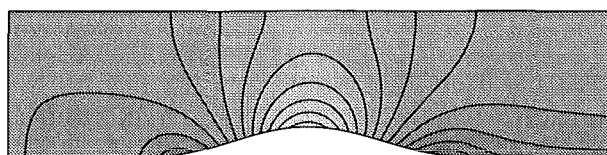


Figure 4.2: Mach number iso-lines ( $M_{inlet} = 0.001$ ) obtained with PRS2

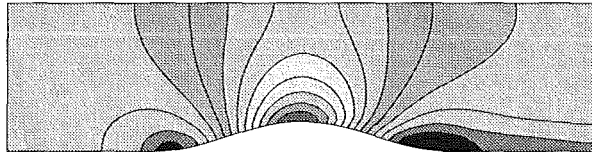


Figure 4.3: Mach number iso-lines ( $M_{inlet} = 0.001$ ) obtained with LMS

With an inlet Mach number of 0.5 compressibility effects become important. The Mach number distributions along the top and the bottom walls are clearly underestimated by the Low Mach Number solver (figure 4.4) compared to the preconditioned Roe solver.

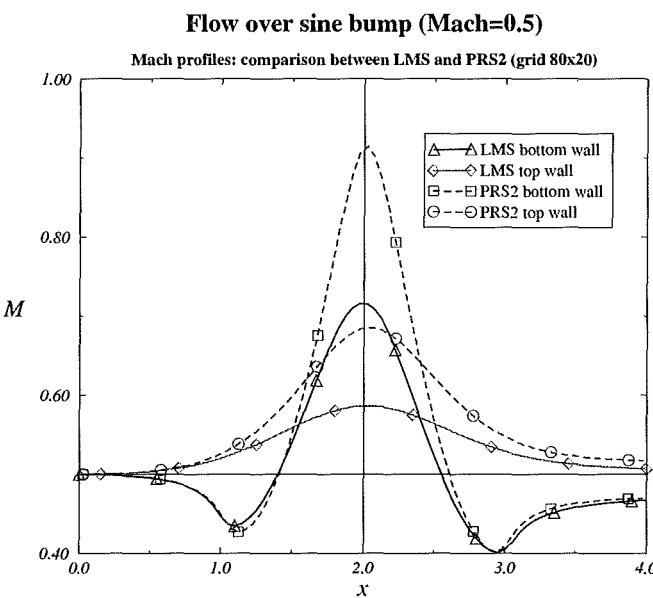


Figure 4.4: Comparison of Mach number distributions ( $M_{inlet} = 0.5$ ) along the walls obtained with LMS and PRS2

#### 4.2.1.2 Lid-driven cavity at $Re = 1000$

The second test-case is the well known lid-driven cavity flow. The flow at Reynolds number 1000 is characterized by a primary vortex in the centre of the cavity and two secondary vortices in the lower right and left corners. Our results will be compared to the benchmark solution obtained by Ghia et al. [6] and the highly accurate results obtained recently by Botella and Peyret [7].

For example, the profile of the horizontal velocity at  $x = 0.5$  is shown in figure 4.5. For the LMS, the most accurate solution has been obtained by using a central discretization, switching off the SUPG stabilizing terms.

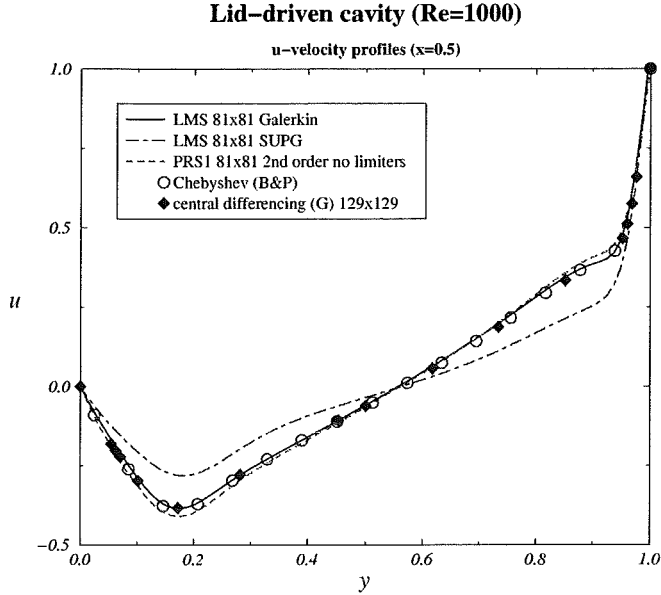


Figure 4.5: Comparison of horizontal velocity profiles at  $x = 0.5$

#### 4.2.1.3 Differential heated square cavity

This test-case is a square cavity ( $L = 0.04m$ ) with differentially heated vertical walls and thermally insulated horizontal walls. The fluid is air, the cold wall temperature is set at  $T_c = 300K$  and the hot wall temperature  $T_h = T_c + \Delta T$ . If  $\Delta T$  is small enough, the incompressible Boussinesq approximation may be used.

Results are shown for both a small temperature difference  $\Delta T = 15K$  and a large temperature difference  $\Delta T = 150K$ , for which the Boussinesq approximation is no longer valid. The Nusselt number distributions along the hot and cold walls (figure 4.6) show that for large temperature differences, the compressible flow results obtained with the LMS are asymmetrical (this is confirmed by experiments) whereas the Boussinesq approximation yields identical distributions on the left and right walls.

#### 4.2.1.4 Conclusions on Low Mach Number Flow solver

The preceding test-cases show good behavior of our Low Mach number flow solver, especially for a reduction to the incompressible flow equations as  $Ma \rightarrow 0$ . However, this flow solver is by construction limited to subsonic flows. As neglected terms are of the order of  $O(Ma^2)$  in the following applications the maximum Mach number is less than 0.3.

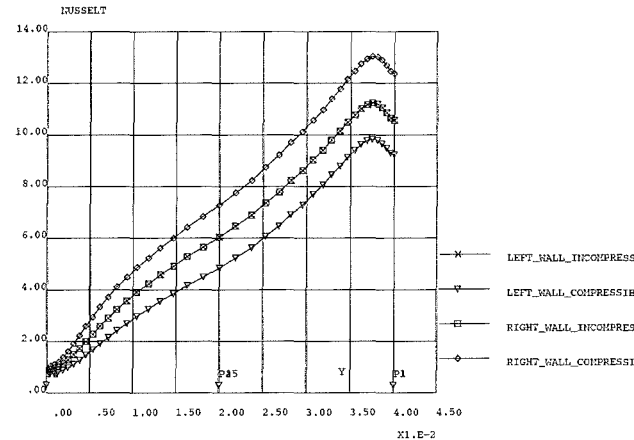


Figure 4.6: Nusselt distributions on left and right walls computed using incompressible Boussinesq approximation and compressible low Mach number approximation (large temperature difference  $\Delta T = 150K$ )

## 4.2.2 Compressible flow solver verification

### 4.2.2.1 Non reactive test cases

In this section we analyze the phenomenon of shock reflection on oblique rigid walls. Such phenomenon can generate stationary flows or *pseudo-stationary* flows (i.e. flows that are “locally” stationary in a particular frame).

The numerical computation of such flows is very interesting because it allows to test the ability of a numerical method to capture multidimensional shocks and contact discontinuities (i.e. we can test both the robustness and accuracy of a numerical scheme).

In Section 4.2.2.1.1 a description of the physical phenomenon is given; further comparisons between different numerical upwind schemes for different shock-reflection problems are then presented.

#### 4.2.2.1.1 The phenomenon of oblique shock reflection

##### Oblique stationary shock

Let us consider the stationary shock represented in Figure 4.7. Following [19, 13], by imposing the continuity of the flux of mass, normal and tangential momentum and enthalpy (i.e. the continuity of the vector flux in the  $(n, t)$ -reference), we see that for each fixed state (1) ahead of the shock front S (with  $M_1 > 1$ ), there is a one-parameter family of states (2) behind the shock. In particular the relation between  $\beta$ , the shock angle, and  $\theta$ , the flow deflection angle, is given by

$$\tan \theta = 2 \cot \beta \frac{M_1^2 \sin^2 \beta - 1}{M_1^2 (\gamma + \cot 2\beta) + 2} \quad (4.1)$$

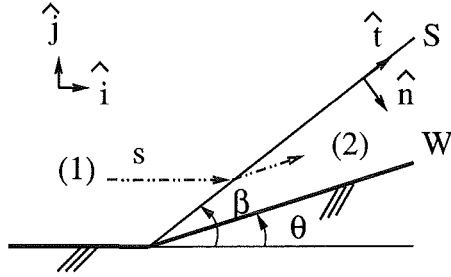


Figure 4.7: A stationary shock wave  $S$ , attached to the corner of a deflected rigid wall  $W$ . (1) is the flow ahead the shock, (2) is the flow behind the shock,  $\theta$  is the deflection angle of the wall and of the flow passing through the shock (see the streamline  $s$ ),  $\beta$  is the inclination angle of the shock  $S$ ,  $(\hat{n}, \hat{t})$  is a frame whose directions are normal and tangential to the shock  $S$ .

with

$$\gamma = \frac{c_p}{c_v}$$

$$\arcsin \frac{1}{M_1} \leq \beta \leq 90^\circ$$

and it is represented in Figure 4.8 for different values of  $M_1$ . Other interesting diagrams that represent the one parameter family of states behind the shock are the so-called “Folium of Descartes” (or  $(u, v)$  shock polar, see [13]) and the  $(p, \theta)$  shock polar (Figure 4.9). The latter is given in parametric form by:

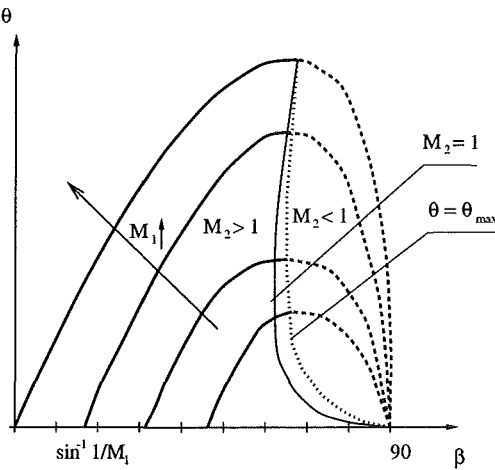


Figure 4.8: Relationship between the flow deflection angle  $\theta$  and the shock inclination angle  $\beta$  for different values of the Mach number  $M_1$ .

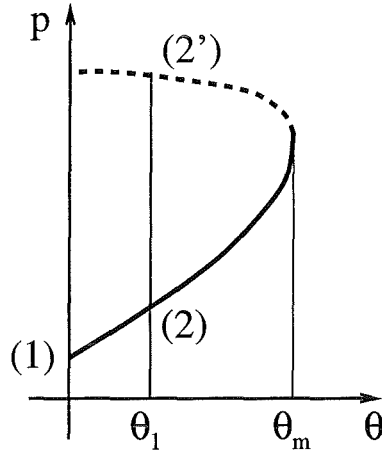


Figure 4.9:  $(p, \theta)$  shock polar. For the deflection angle  $\theta_1$  there are two possible solutions, the weak shock reflection (2) and the strong shock reflection (2'); but only (2) would seem to be physical.

$$p_2 - p_1 = \rho_2 u_2 (u_1 - u_2)$$

$$\tan \theta = \frac{u_1 - u_2}{u_2} \sqrt{\frac{u_2 - \tilde{u}}{U - u_2}}$$

where

$$\tilde{u} = \left( \mu^2 + \frac{1 - \mu^2}{M_1^2} \right) u_1$$

$$U = (1 - \mu^2) u_1 + \tilde{u}$$

$$\mu^2 = \frac{\gamma - 1}{\gamma + 1}$$

$$\tilde{u} \leq u_2 \leq u_1$$

Note that  $\tilde{u}$  is the velocity of the flow behind the shock in the case of a normal shock ( $\theta = 0, \beta = 90^\circ$ )

In Figures 4.8 and 4.9 we can observe that for a fixed state ahead of the shock, there exists a maximum deflection angle,  $\theta_m$ , such that for  $\theta > \theta_m$ , this stationary shock configuration cannot exist. Conversely, for  $\theta \leq \theta_m$  two possible configurations are possible:

- the *strong shock reflection*, with the flow behind the shock subsonic (i.e.  $M_2 < 1$ );

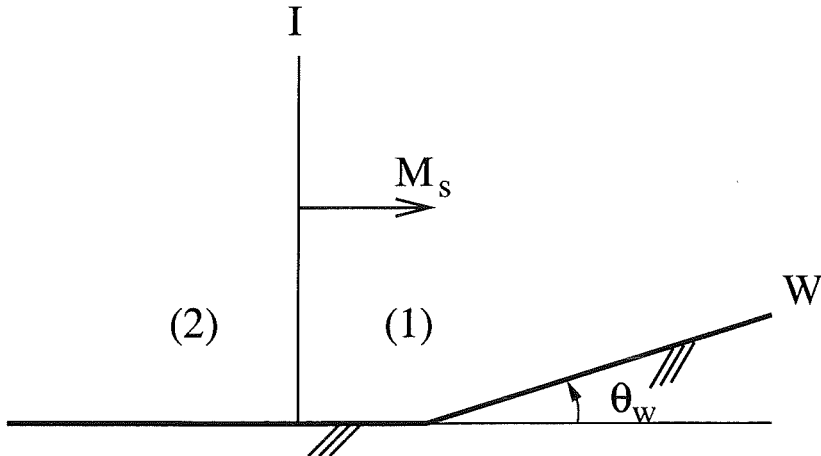


Figure 4.10: A shock wave I traveling towards an oblique rigid wall W at a Mach number  $M_s$  in a fluid at rest (1). Note that  $M_s$  (the ratio between the shock speed and the sound speed of the fluid ahead the shock) is equal to  $M_1$  in the shock frame; thus  $M_s > 1$ .

- the *weak shock reflection*.

In the past, it has frequently been stated that the strong solution is unstable; only recently Li [18] has shown that, if  $\theta \neq 0$ , only the weak shock reflection is physical because the strong one does not obey the principle of minimum entropy production.

### Oblique shock reflection

Let us consider a shock wave traveling towards an oblique rigid wall into a fluid initially at rest (Figure 4.10). What happens to the shock when it encounters the wall? First of all, we can distinguish between two possible configurations: *regular reflection* (RR, Figure 4.11) and *Mach reflection* (MR). The latter phenomenon was first observed by Mach at the end of nineteenth century and was first studied analytically by von Neumann (1945).

Following [16], MR can be classified into 3 different regimes: single Mach reflection (SMR, Figure 4.12), transitional Mach reflection (TMR, Figure 4.14) and double Mach reflection (DMR, Figure 4.15).

Let us consider the regular reflection represented in Figure 4.11 (a). I is the incident shock, R is the reflected shock, P is the attached point at the wall W. The flow is not stationary but it is said to be pseudo-stationary, i.e. in a frame fixed with the point P, a region close to P can be considered stationary. Such a region is represented in Figure 4.11 (b) in the frame  $(\hat{i}, \hat{j})$ , that is fixed with P. In this frame we have:

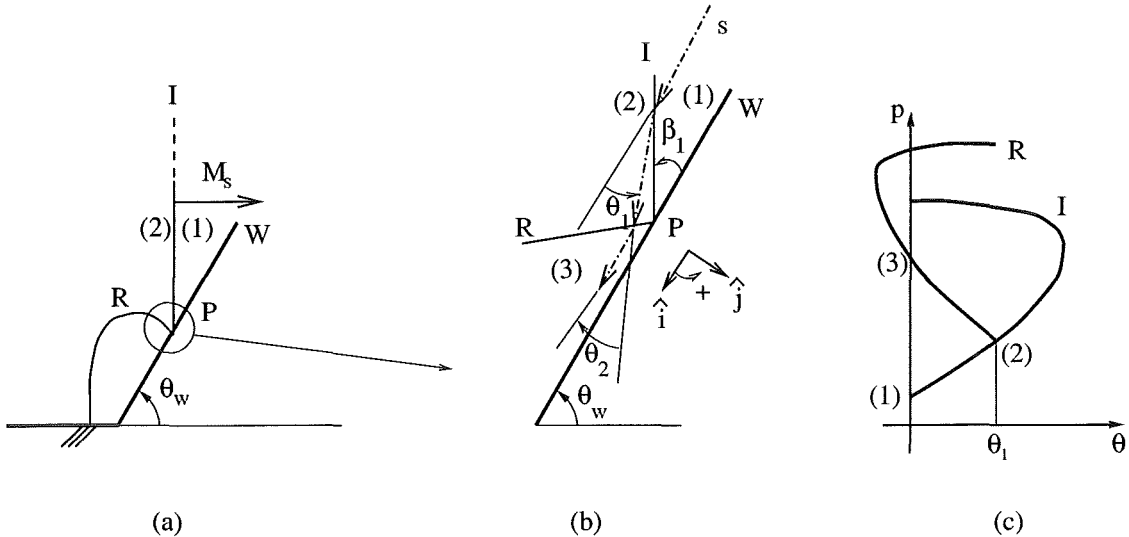


Figure 4.11: (a) Regular reflection of a traveling shock on an oblique rigid wall; (b) the locally stationary flow in the P frame (the dotted-dashed line s represents a streamline of the flow); (c) the shock polar of the incident shock I and the reflected shock R in the P frame.

$$\begin{aligned}
 u_1 &= \frac{M_s a_1}{\cos \theta_w} \leftrightarrow M_1 = \frac{M_s}{\cos \theta_w} \\
 v_1 &= 0 \\
 \beta_1 &= 90^\circ - \theta_w
 \end{aligned} \tag{4.2}$$

$\beta_1$  being the angle of inclination of I. So we can plot the shock polar relative to I (Figure 4.11 (c)).

The state (2) is already known in the laboratory system: it is the state behind the incident shock (it is determined by imposing the Rankine-Hugoniot for the traveling shock I); thus it is known in the P-reference and we can trace the shock polar relative to R. The state (3) is determined by imposing

$$\theta_1 + \theta_2 = 0$$

Note that in this case the shock polar R does not intersect the I polar but intersects the p-axis in two points (we have only indicated the physical solution). Now let us decrease the wall angle  $\theta_w$ ; from Equations (4.2) it is clear that  $M_1$  decreases and  $\beta_1$  increases; the same is true for  $M_2$  (note that in the P frame the component of the velocity of (1) and (2) normal to the shock are initial conditions and decreasing  $\theta_w$  we decrease only their tangential component). For the sake of simplicity, in order to keep the same shock polar for I (i.e. the same  $M_1$  in the P

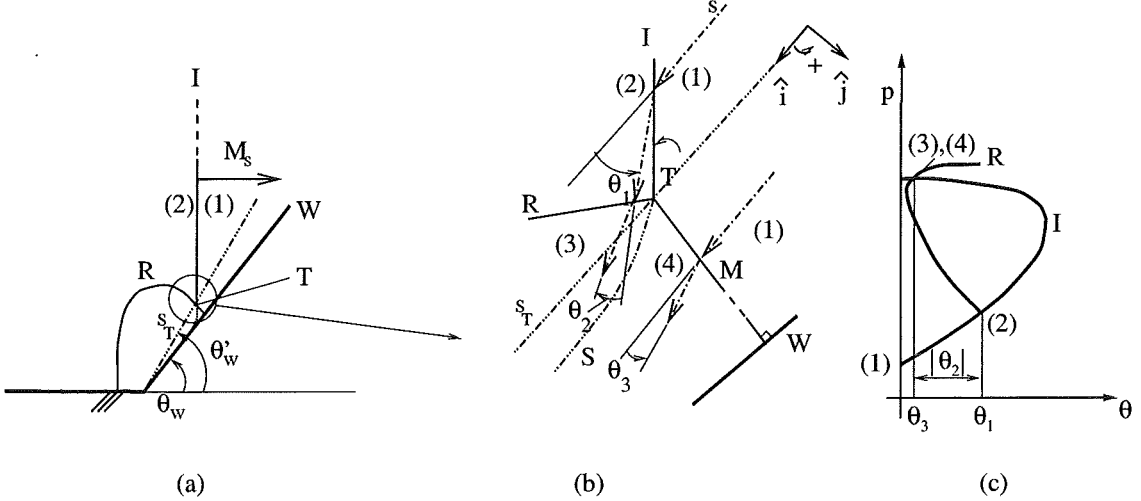


Figure 4.12: (a) Single Mach reflection; (b) the locally stationary flow in the T frame. (c) the shock polar of the incident shock I and the reflected shock R in the T frame

frame), we increase also the strength of the incident shock, i.e.  $M_s$ .

For a large decrease of  $\theta_w$ , a possible regime that can develop is the one shown in Figure 4.12. In this case we have the formation of a triple point (T), where the incident shock I, the reflected shock R, a third shock (the Mach stem M), and a slipstream (S) converge. The trajectory of T is a straight line ( $s_T$ ), starting from the corner of the wedge, and it moves with a constant velocity

$$u_T = \frac{M_s a_1}{\cos \theta'_w}$$

In this case R, M and S are curved. As in the RR, the problem is not stationary but pseudo-stationary; in Figure 4.12 (b) we have represented a region close to T in the T frame (note that the x-axis is parallel to the T trajectory); in Figure 4.12 (c) we have represented the shock polar I and R in this frame. Note that the shock polar R does not intersect the p-axis; so the total deviation of the flow passing through I and R is not zero (see the streamline s); i.e.

$$\theta_1 + \theta_2 \neq 0$$

The Mach stem is a strong shock transition from the state (1) to the state (4); close to the slipstream is

$$\theta_1 + \theta_2 = \theta_3$$

$$p_3 = p_4$$

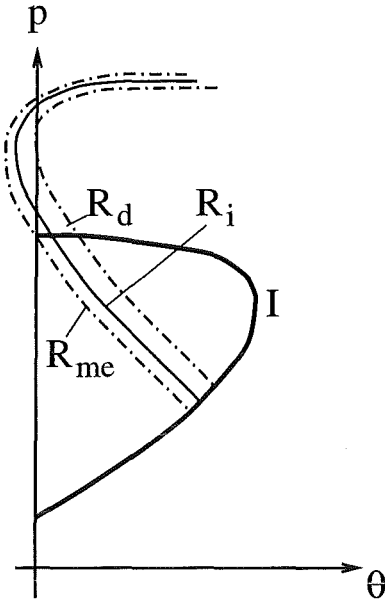


Figure 4.13: The criteria for RR  $\rightarrow$  MR transition. The shock polar  $R_d$  represents the limit situation in the detachment criterion; the shock polar  $R_{me}$  represents the limit situation in the mechanical equilibrium criterion. These curves are obtained by decreasing the wall inclination  $\theta_w$ , and by increasing the strength of the shock in order to keep  $M_1$  constant in the frame fixed to the locally stationary domain (i.e. the shock polar I does not change). We remind that if the deflection of the wall  $\theta_w$  decreases, the flow deflection in shock transition (1)  $\rightarrow$  (2) increases.

Note that:

- the state (4) is on the shock polar I and the state (3) is on the shock polar  $R$ ; but they have the same pressure and the same velocity direction, thus they have the same position in the  $(p, \theta)$  diagram;
- in the case considered, (3) is subsonic in the T frame.

Here we have considered two extreme cases: in the former (Figure 4.11) the shock polar  $R$  intersects the p-axis but does not intersect the shock polar I while in the latter (Figure 4.12) the shock polar  $R$  intersects the shock polar I but not the p-axis. Let us consider Figure 4.13: a possible configuration that we can have is the shock polar  $R_i$  that intersects the I polar and the p-axis; the same is true for all the shock polars  $R_i$  between  $R_{me}$  and  $R_d$  (we remind that all the shock polars have been obtained by decreasing  $\theta_w$  and by increasing the shock strength of the incident shock I, in order to keep  $M_1$  constant in the frame fixed with the pseudo-stationary flow). The transition RR  $\rightarrow$  MR is not yet well understood; two possible criteria have been proposed:

- the *detachment criterion* (introduced by von Neumann), i.e. if the shock polar I has an intersection with the p-axis, we have a RR reflection; conversely we have a MR reflection (the limit curve is represented in  $R_d$ );
- the *mechanical equilibrium criterion* (introduced by Henderson and Lozzi in 1975, but also considered by von Neumann), i.e. if the shock polar I has a weaker intersection with the I polar, we have MR reflection (the limit curve is represented in  $R_{me}$ ); note that if this criterion is not satisfied, in the transition RR  $\rightarrow$  MR the Mach stem has immediately a non-zero length and the flow regime changes discontinuously.

There is also another criterion, the sonic criterion, but it is very close to the detachment criterion [16].

Recently it has been shown experimentally [14] and theoretically [18] that in the region between  $R_d$  and  $R_{me}$  both RR and MR can exist; it seems to depend also on the global geometry of the flow (in the analysis followed here, only the local geometry of the system has been considered and no characteristic lengths have been defined) and on the history of the flow (i.e. how it reaches the stationary state). See for example [17].

In Figure 4.12 we have considered a possible regime of MR; this happens when the flow in (3) is always subsonic in the T frame. Note that the reflected shock R is curved and the flow in (3) is not in a constant state. Conversely, if for the flow behind the shock there is a supersonic region, a possible configuration is shown in Figure 4.14. In this case the reflected shock R is straight when the flow behind it is supersonic and is curved when the flow is subsonic; we have the formation of a kink point K ( $M_{3,K} = 1$  in the T frame), whose trajectory is a straight line starting from the wall corner ( $s_K$ ). There is a compression wave between (3) and (6), and a weak slipstream between (5) and (6). If the flow in (3) is supersonic with respect to the kink K, the compression wave (3)  $\rightarrow$  (6) becomes a shock wave and the kink K becomes a second triple point  $T_1$  (see Figure 4.15).

In Figure 4.16 a qualitative representation of the possible different flow regimes is shown.

We want to underline that, as stated in [13], “All statements made here are conjectures so far”, i.e. the problem of the development of such flows is still an open problem.

#### 4.2.2.1.2 Oblique Shock Waves reflexion: Double Mach Reflexion Regime

In this test-case, proposed in [21], we compute the reflection of a Mach 10 shock wave traveling in a flow at rest towards a rigid wall with an inclination angle of 30°: this originates a Double Mach Reflection. The **purpose** is the study of the behavior of the schemes in computing the Mach stem in the DMR regime;

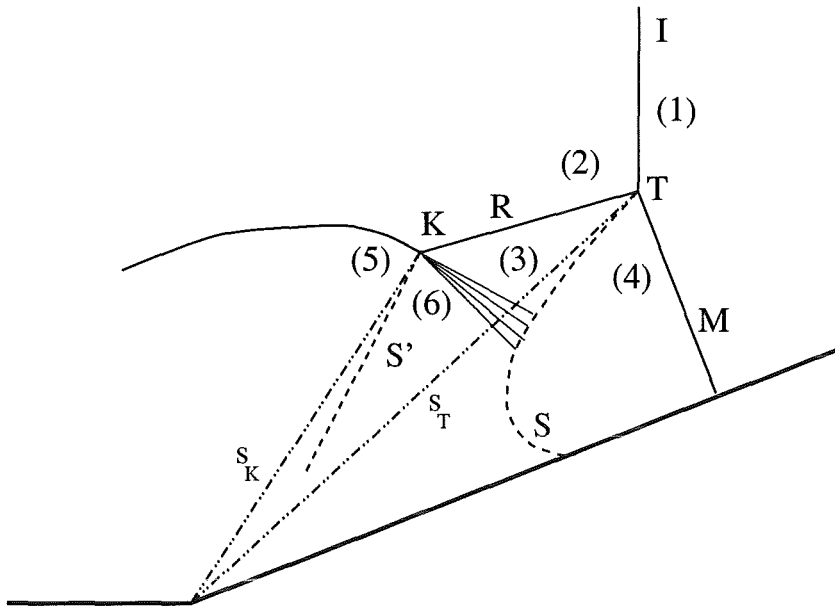


Figure 4.14: Transitional Mach reflection.

in fact it is well known that numerical solutions of a DMR present sometimes a pathological behavior: the strongest Mach stem in unphysically kinked [20]. Moreover, the second Mach stem is very weak and very difficult to compute; this allows us to do some considerations on the accuracy of the numerical schemes.

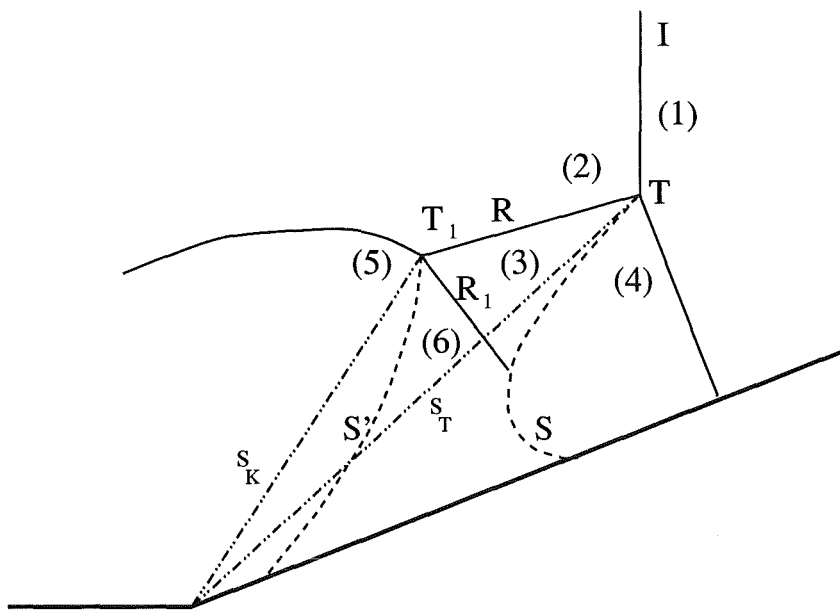


Figure 4.15: Double Mach reflection.

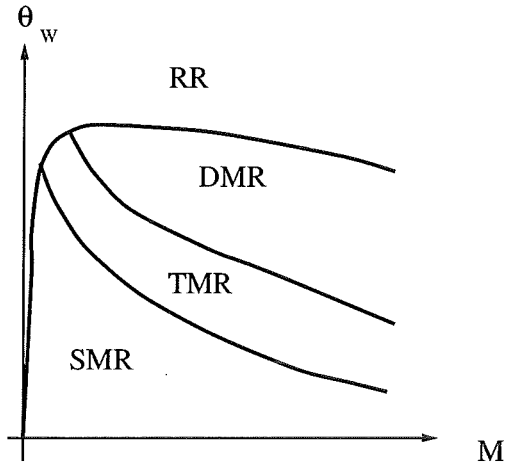


Figure 4.16: A qualitative representation of the different shock reflection regimes.

As far as the **initial conditions** are concerned, the state ahead the shock (state (2)) is given by

$$\begin{aligned}\rho_2 &= 1.4 \\ p_2 &= 1 \\ u_2 = v_2 &= 0\end{aligned}$$

The state behind the shock (state (1)) is then determined by imposing the Rankine-Hugoniot conditions for the traveling shock wave S. We compute the solution at  $t = 2.0026 \cdot 10^{-1}$ .

In Figure 4.17 we have represented two possible **computational domains**: in the one bounded by a solid line, we can impose a wall condition on the top boundary (very easy to treat); conversely the other one, bounded by a dashed line (and almost identical to the one presented in [21]), is smaller and allows a more accurate study of the Mach stems.

In Figure 4.18 we have represented the internal domain and the ghost cells, where we impose the following **boundary conditions**:

- wall boundary condition on the bottom;
- inlet supersonic boundary condition on the left;
- constant state (2) on the right (as we will see, shocks do not reach this zone at  $t = 2.0026 \cdot 10^{-1}$ );
- the exact motion of the shock on the top.

We have considered **3 different structured grids**: a coarse grid, with  $96 \times 30$  cells; i.e. in the region above the oblique wall ( $x > 1/6$ ) we have  $Dx = Dy =$

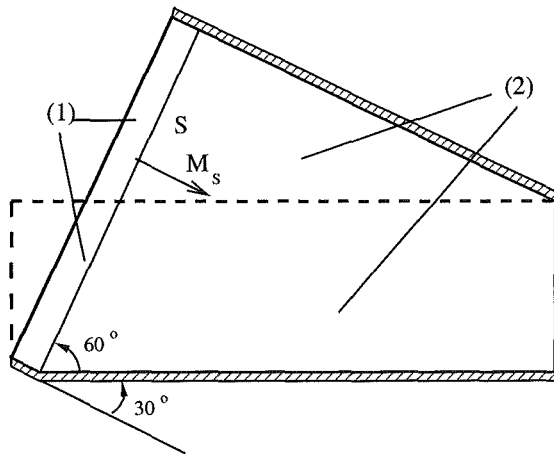


Figure 4.17: DMR: possible computational domains. S is the shock wave at  $t = 0$ , (1) is the state behind the shock, (2) is the state ahead. The domain bounded by a dotted line is the one we have considered.

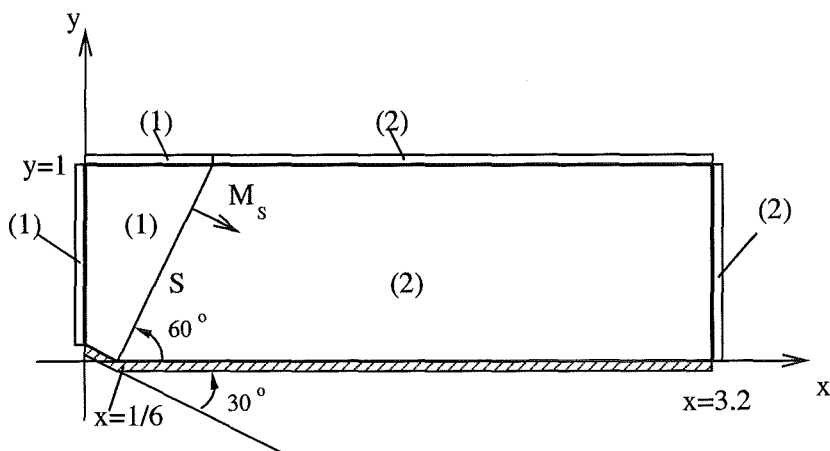


Figure 4.18: DMR: initial and boundary conditions. Here we have represented the domain and the ghost cells with the relative boundary conditions. On the top boundary we have imposed the exact motion of the shock.

$1/30$ . In the medium grid, in the same region, it is  $Dx = Dy = 1/60$  and in the fine one it is  $Dx = Dy = 1/120$ . The CFL coefficient has always been chosen equal to 0.8.

As far as the **Godunov** method is concerned, in Figure 4.19 we have represented the “second order” numerical solution computed in the fine grid, Figure 4.20 represents the “first order” computation on the same grid, while in Figure 4.21 we have just plotted the density on the medium and on the coarse grids (“second order” computations). We can observe that:

- on the coarse grid all the discontinuities are completely spread;
- the “second order” computation on the medium grid is more accurate than the “first order” computation on the fine grid;
- the strongest Mach stem is kinked; moreover comparing first order and second order computations on the fine grid, we can say that this pathological behavior is more evident in the former one.

In Figures 4.22 and 4.23 we have represented the numerical solutions obtained with **HUS** scheme; as in Godunov method the strongest Mach stem is kinked. Comparing the results obtained by these two schemes, we can say that there are no sensible differences.

Finally, the numerical results obtained with the **van Leer Flux Vector Splitting** scheme are shown in Figures 4.24 and 4.25; these are the best ones because we have no kink in the strongest Mach stem; moreover, the contact discontinuities are so spread as by the other numerical schemes.

In [15], Gressier *et al.* have tested other upwind schemes on a (different) DMR computation and with a different disposition of the grid (here the grid is almost aligned with the strongest Mach stem while in [15] meshes are aligned with the incident shock). Summarizing they have obtained the following results:

- Osher schemes (in natural and in the reversal order decomposition), Roe scheme and AUSM present a kinked Mach stem;
- EFM (a kinetic scheme, i.e. a Flux Vector Splitting scheme) is not affected by this pathological problem.

**Concluding**, we can say that

- the upwind schemes that exactly capture stationary contact discontinuities (i.e. Godunov, HUS, AUSM, Roe and Osher schemes) do not compute correctly the strongest Mach stem while FVS schemes (i.e. Van Leer and EFM) do;

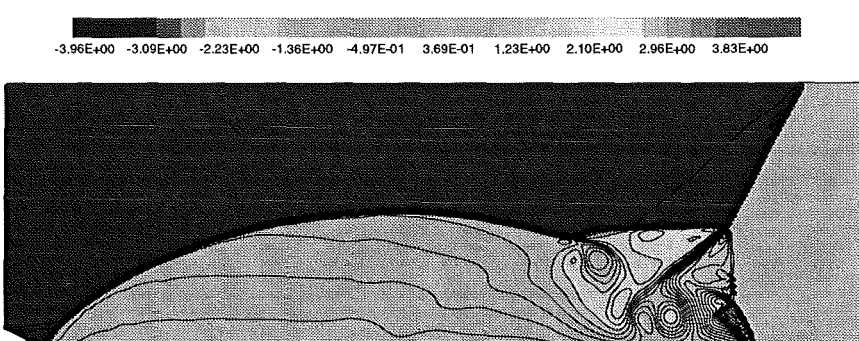
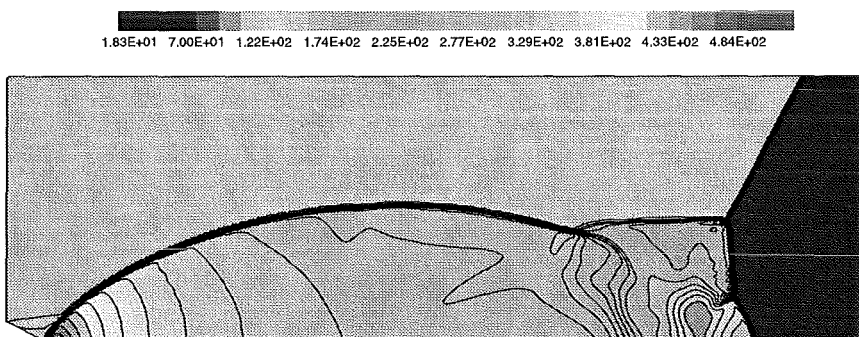
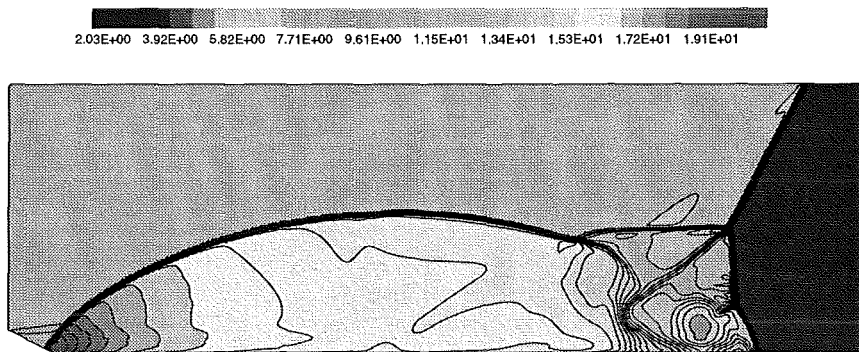
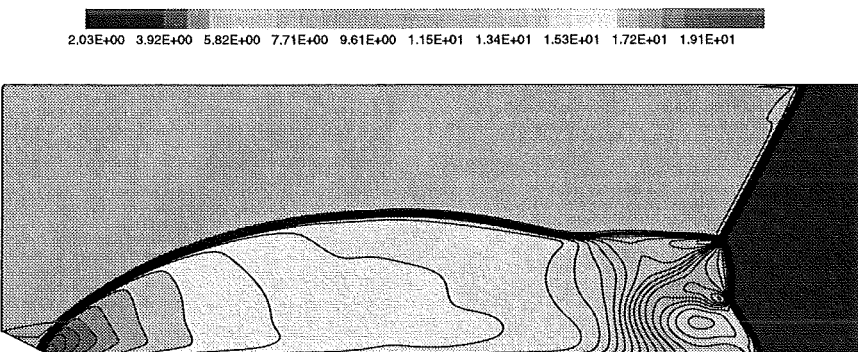
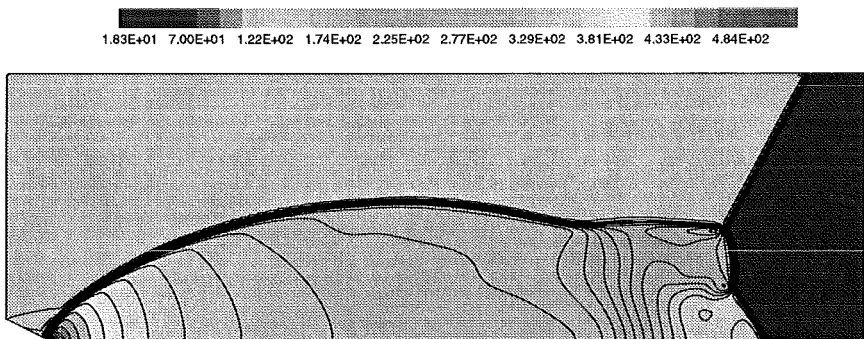


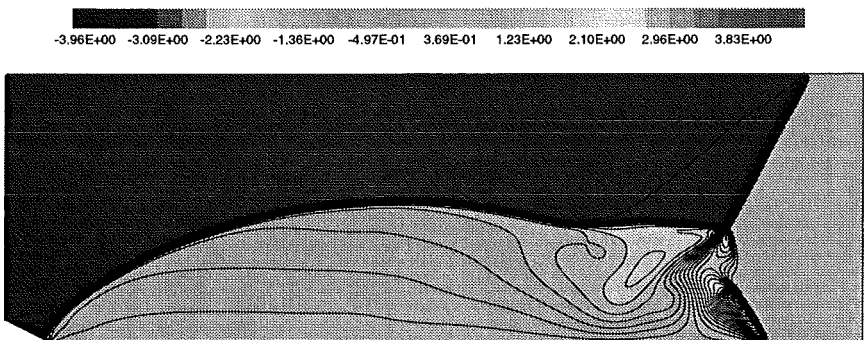
Figure 4.19: DMR numerical simulation, Godunov (predictor-corrector approach): density, pressure and velocity component along the  $y$ -axis.



**Density at  $t = 2.026E-1$ :** min = 1.400 max = 21.95  
**Godunov, SO = TO = 1, DX = DY = 1/120**  
**30 isolines: min = 2.031 max = 21.64**

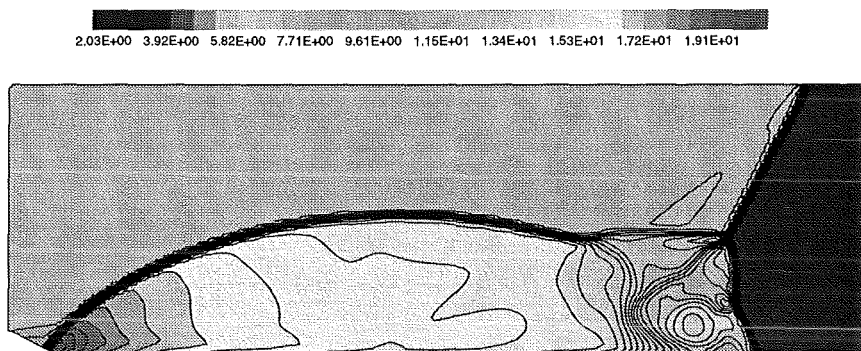


**Pressure at  $t = 2.026E-1$ :** min = 1.000 max = 534.5  
**Godunov, SO = TO = 1, DX = DY = 1/120**  
**30 isolines: min = 18.26 max = 518.9**

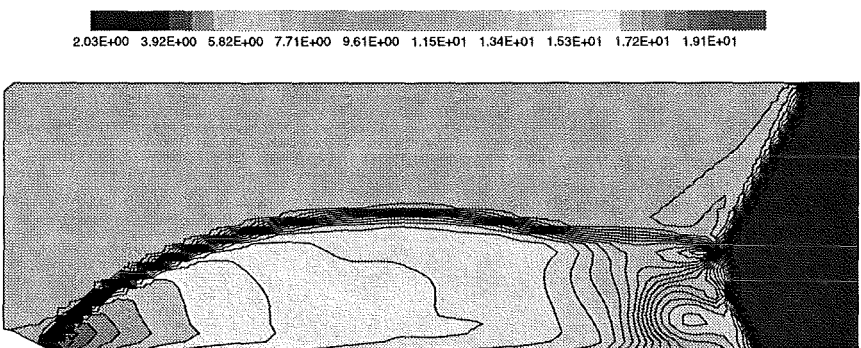


**UY at  $t = 2.026E-1$ :** min = -4.443 max = 4.428  
**Godunov, SO = TO = 1, DX = DY = 1/120**  
**30 isolines: min = -3.958 max = 4.407**

Figure 4.20: DMR numerical simulation, Godunov (“first order”): density, pressure and velocity component along the  $y$ -axis.

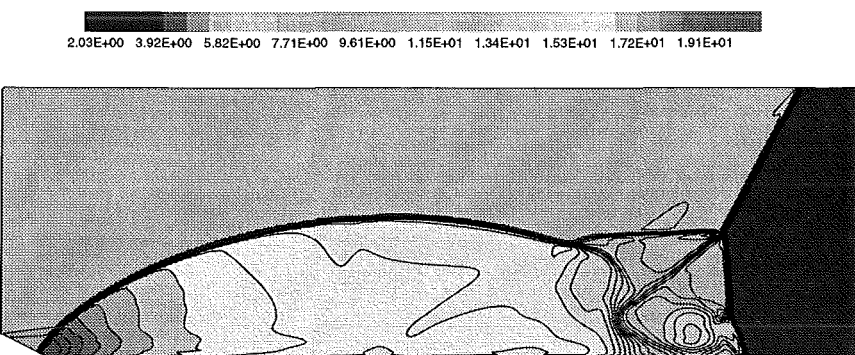


**Density at  $t = 2.026E-1$ :** min = 1.400 max = 21.83  
**Godunov, SO = TO = 2, DX = DY = 1/60**  
**30 isolines: min = 2.031 max = 20.34**

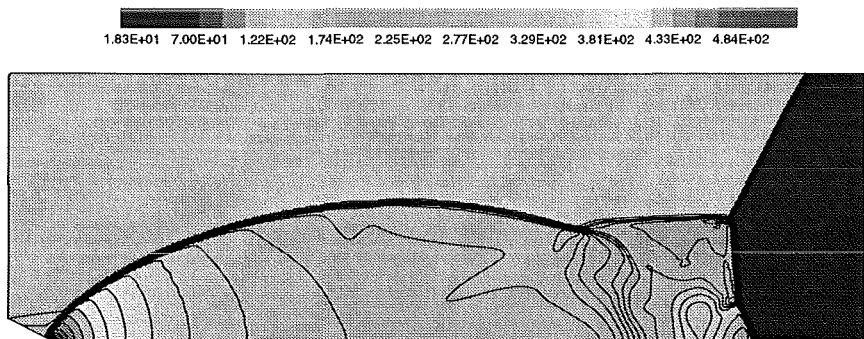


**Density at  $t = 2.026E-1$ :** min = 1.400 max = 20.96  
**Godunov, SO = TO = 2, DX = DY = 1/30**  
**30 isolines: min = 2.031 max = 20.34**

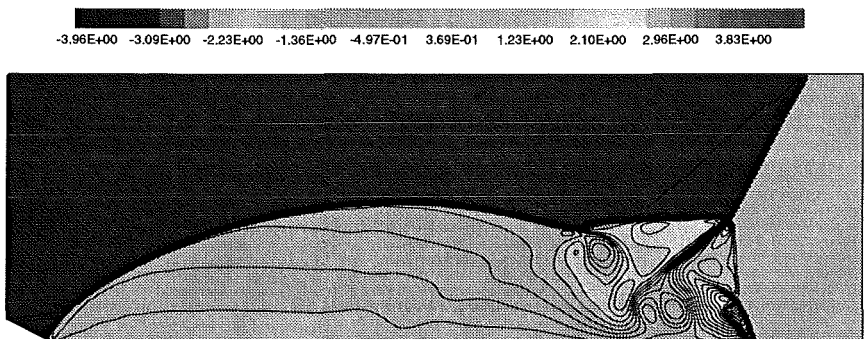
Figure 4.21: DMR numerical simulation, Godunov (predictor-corrector approach): density on the medium (top) and coarse (bottom) grid.



**Density at  $t = 2.026E-1$ :** min = 1.400 max = 22.62  
**HUS, SO = TO = 2, DX = DY = 1/120**  
**30 isolines: min = 2.031 max = 20.34**



**Pressure at  $t = 2.026E-1$ :** min = 1.000 max = 545.6  
**HUS, SO = TO = 2, DX = DY = 1/120**  
**30 isolines: min = 18.26 max = 518.9**



**UY at  $t = 2.026E-1$ :** min = -4.184 max = 4.097  
**HUS, SO = TO = 2, DX = DY = 1/120**  
**30 isolines: min = -3.958 max = 4.407**

Figure 4.22: DMR numerical simulation, HUS (predictor-corrector approach): density, pressure and velocity component along the  $y$ -axis.

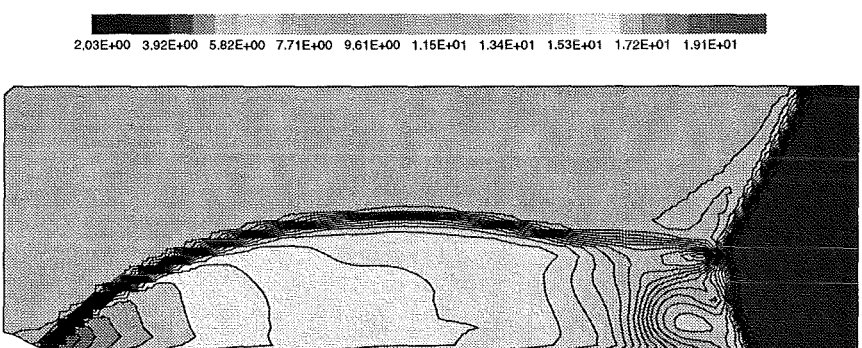
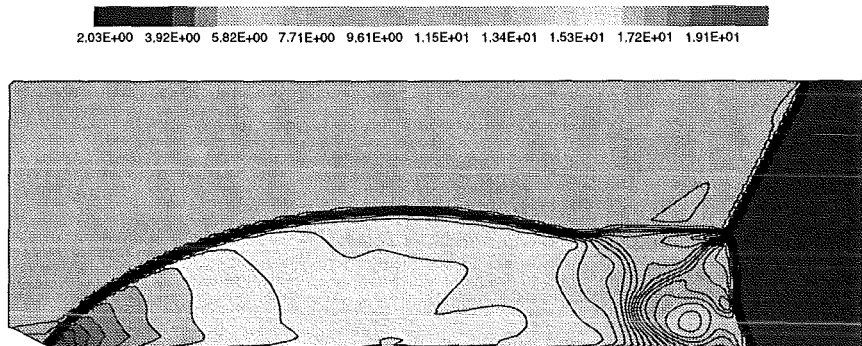
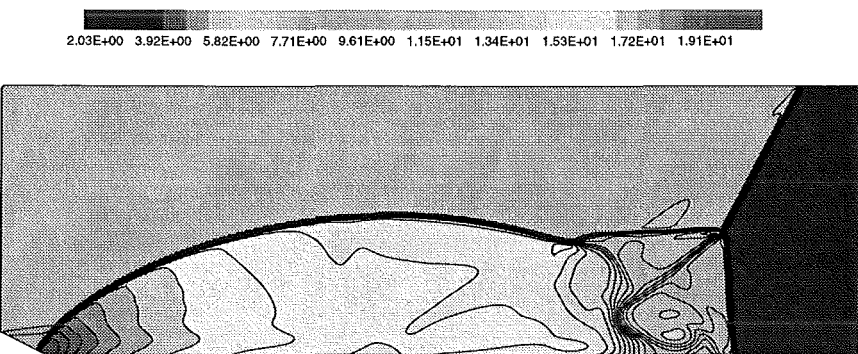
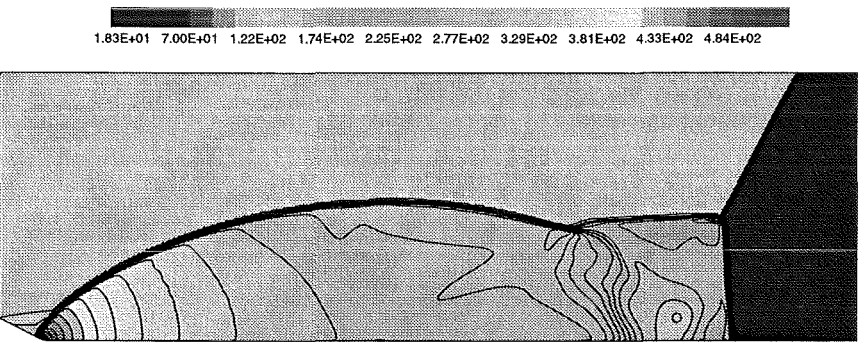


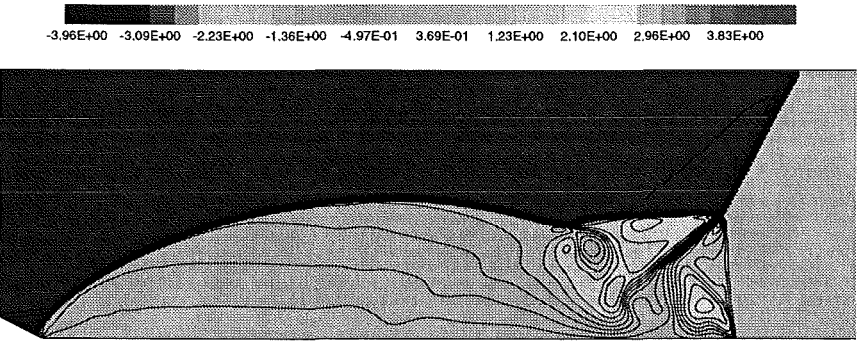
Figure 4.23: DMR numerical simulation, HUS (predictor-corrector approach): density on the medium (top) and coarse (bottom) grid.



**Density at  $t = 2.026E-1$ :** min = 1.400 max = 23.15  
 VL-FVS, SO = TO = 2, DX = DY = 1/120  
 30 isolines: min = 2.031 max = 20.34

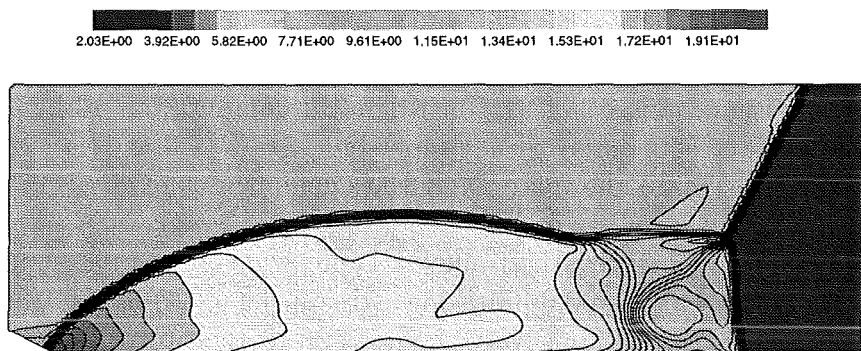


**Pressure at  $t = 2.026E-1$ :** min = 1.000 max = 563.2  
 VL-FVS, SO = TO = 2, DX = DY = 1/120  
 30 isolines: min = 18.26 max = 518.9

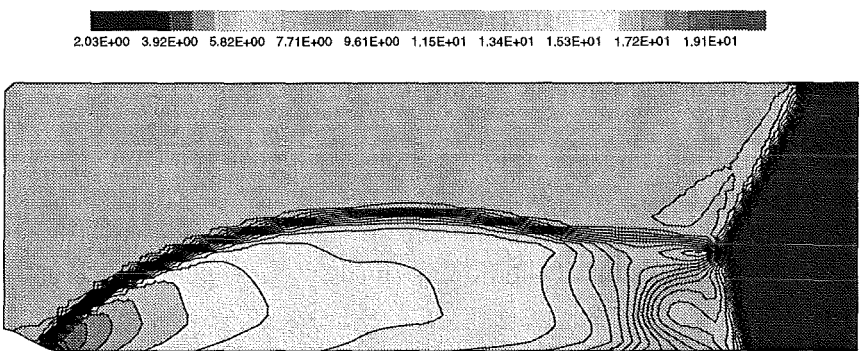


**UY at  $t = 2.026E-1$ :** min = -4.184 max = 2.260  
 VL-FVS, SO = TO = 2, DX = DY = 1/120  
 30 isolines: min = -3.958 max = 4.407

Figure 4.24: DMR numerical simulation, VL-FVS (predictor-corrector approach): density, pressure and velocity component along the  $y$ -axis.



**Density at  $t = 2.026E-1$ : min = 1.400 max = 22.78**  
**VL-FVS, SO = TO = 2,  $DX = DY = 1/60$**   
**30 isolines: min = 2.031 max = 20.34**



**Density at  $t = 2.026E-1$ : min = 1.400 max = 21.90**  
**VL-FVS, SO = TO = 2,  $DX = DY = 1/30$**   
**30 isolines: min = 2.031 max = 20.34**

Figure 4.25: DMR numerical simulation, VL-FVS (predictor-corrector approach): density on the medium (top) and coarse (bottom) grid.

- the contact discontinuity of the strongest Mach stem, that is not aligned with the grid, is captured with the same accuracy by all the schemes tested here;
- the computations obtained with the predictor-corrector scheme are more accurate than the “first-order” ones.

#### 4.2.2.1.3 Forward facing step

This test-case, proposed in [21], consists in the computation of the interaction between a forward facing step with a supersonic  $Ma = 3$  flow (see Figure 4.26); our main **target** is still the analysis of the capability of numerical schemes in capturing the Mach stem.

In non-dimensional variables, the tunnel is 1 unit wide and 3 units long; the step is 0.2 units high and located 0.6 units downstream the inlet. At the beginning we have a supersonic  $Ma = 3$  flow everywhere; as far as the **boundary conditions** are concerned, we have

- wall boundary condition on the top and on the bottom boundaries;
- inlet supersonic boundary condition on the left, i.e. we impose the state (1)  $(\rho, p, u, v) = (1.0, 1.4, 3.0, 0.0)$ ;
- outlet supersonic boundary condition on the right.

We have computed the solution at the non-dimensional time  $t = 4.0$ ; here the flow is non-stationary.

At the beginning we have the formation of a shock wave, traveling to the left, generated by the interaction of the flow with the step. Such a shock wave interacts

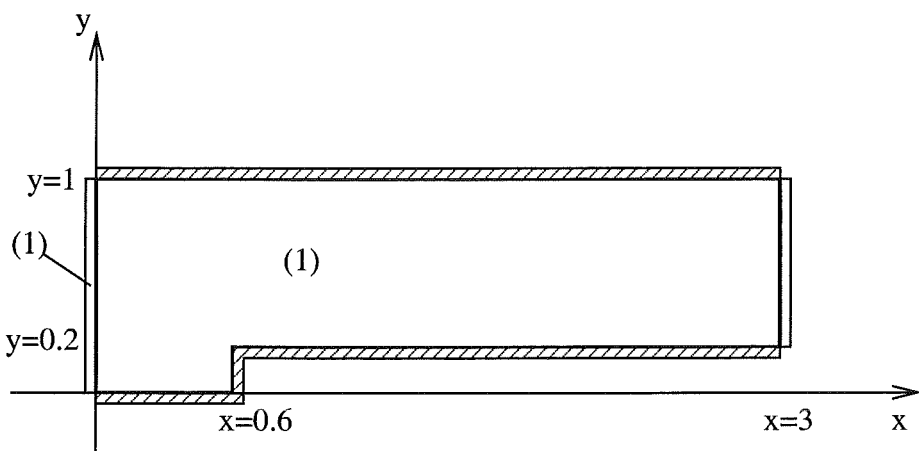


Figure 4.26: Forward facing step: domain, ghost cells and initial conditions.

with the top wall and it originates a Mach stem; the reflected wave of the Mach stem, attenuated by the rarefaction wave centered in the corner (Prandtl-Meyer expansion) interacts with the top wall of the step (RR regime). Finally we have another shock reflection on the top of the wall.

In Figure 4.27 we have represented the numerical solution computed by **HUS** scheme, in a grid with  $Dx = Dy = 1/80$ . Note that on the top wall of the step we have a typical configuration of *shock-boundary layer interaction* (with an adverse pressure gradient that caused the detachment of the boundary layer, see [12]). In Figure 4.28 the detachment zone behind the incident shock is well evident. But here the boundary layer is just a *numerical phenomenon* generated by the vertex of the step (singular point), that slows down the fluid on the opposite mesh. In order to avoid this phenomenon, the general thing to do is to put more cells around a singular point; here it is not necessary because we know that such point is the center of a rarefaction wave (and we also know the flow direction in this rarefaction wave); thus we have imposed in a zone around the corner the constancy of the total enthalpy and of the entropy, as suggested in [21].

In Figures 4.29 and 4.30 we have computed the solution, with this additional boundary condition, with the same numerical scheme: although the grid is coarser ( $Dx = Dy = 1/40$ ), this numerical phenomenon disappears and the entropy production is drastically lower (see Table 4.2). Conversely, another numerical phenomenon appears: an unphysical Mach stem appears on the top wall of the corner. In Figure 4.30 we have also shown the Mach number in order to show that the right boundary is a supersonic outlet.

In Figures 4.31 and 4.32 the numerical solutions are computed with the **Godunov** scheme and the FVS scheme of **Van Leer**.

Comparing all these figures, we can observe that

- the Mach stem is captured by all the methods; but its slipstream, which is almost stationary and aligned to the grid, is more evident in the computation with the Godunov and HUS schemes (that conserves stationary contact discontinuities) and spread by the VL-FVS (well evident in the entropy solution);
- in [21], in the solution relative to Godunov method (“first order”), the author observes the presence of an unphysical expansion shock next to the corner of the step; in our opinion it is the typical glitch phenomenon of transonic rarefaction waves, a phenomenon that tends to disappear if we use a predictor-corrector approach; thus we have no glitch in all the computation of such centered rarefaction waves;
- the phenomenon of noise behind the first reflected shock (the one generated by the flow-step interaction) and behind the Mach stem is well-evident in the solutions computed with Godunov and HUS schemes, while VL-

Numerical Scheme	Entropy $p/\rho^\gamma$	
	Maximum	Integral
HUS (I)	2.449	2.324
HUS (II)	1.365	2.251
Godunov	1.392	2.251
VL-FVS	1.251	2.253

Table 4.2: The entropy, comparison of the different method. By HUS (I) we means the computation performed without the additional boundary condition on the corner of the step; note that the entropy production is larger, even if the cell dimension is two times finer.

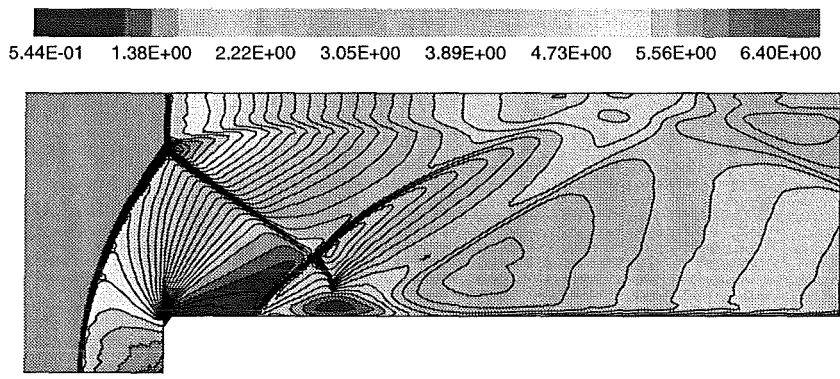
FVS dissipates such noise; thus the Mach stem captured by VL-FVS is unperturbed by such noise, i.e. perfectly normal to the wall;

- all the schemes compared capture a numerical Mach stem in the top of the step wall; in VL-FVS it is less evident because the Mach stem is quasi-stationary and its slipstream is almost aligned with the grid (and FVS schemes spread stationary contact discontinuities).

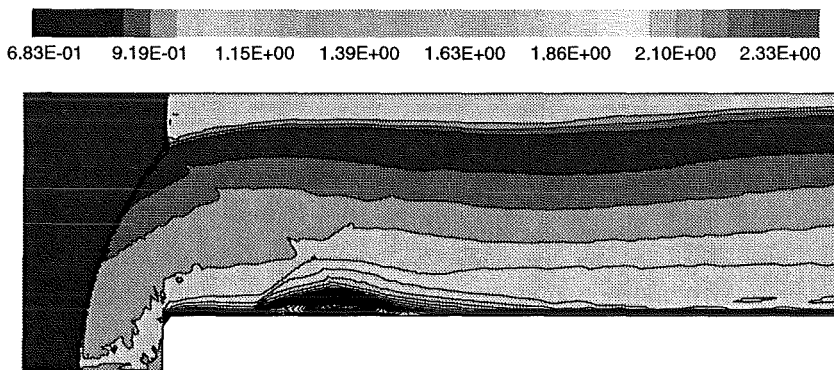
In Table 4.2 we have represented two important parameters: the maximum of the entropy and its integral on the domain. Note that the entropy reaches its maximum behind the second (numerical) Mach stem; that's why in the van Leer method it is lower (it spreads this almost stationary contact discontinuity); conversely the integral of the entropy is biggest in the VL-FVS computation (and this is due to the fact that it is the most diffusive method).

## Conclusion

- Godunov and HUS schemes capture the slipstream of the Mach stem more accurately than Van Leer schemes;
- conversely the Van Leer scheme does not present oscillations behind the first reflected shock, being less sensible to numerical noise, while other schemes do.



**Density at  $t = 4.0$ :** min = 0.3354 max = 6.816  
**HUS, SO = IO = 2, DX = DY = 1/80**  
**30 isolines: min = 0.5445 max = 6.607**



**Entropy at  $t = 4.0$ :** min = 0.6243 max = 2.449  
**HUS, SO = IO = 2, DX = DY = 1/80**  
**30 isolines: min = 0.6832 max = 2.391**

Figure 4.27: Forward facing step: the shock-numerical boundary layer interaction.

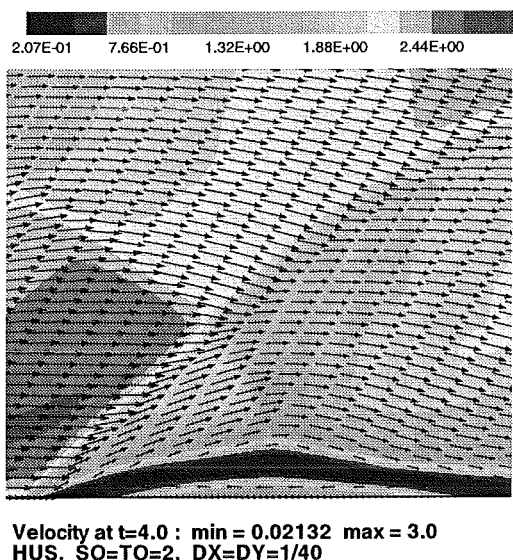


Figure 4.28: Forward facing step: the shock-numerical boundary layer interaction. The detachment zone.

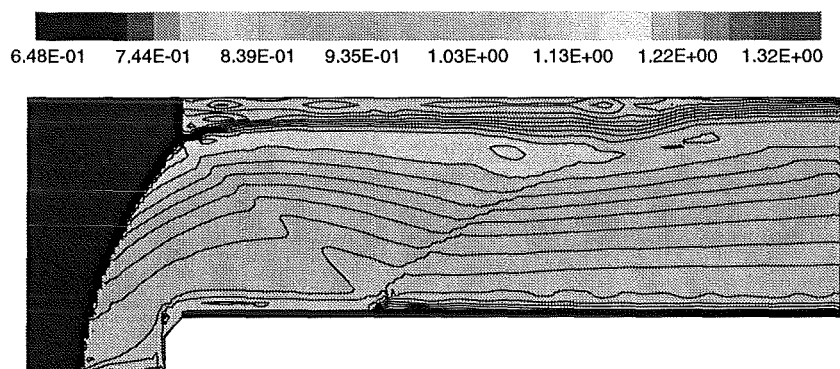
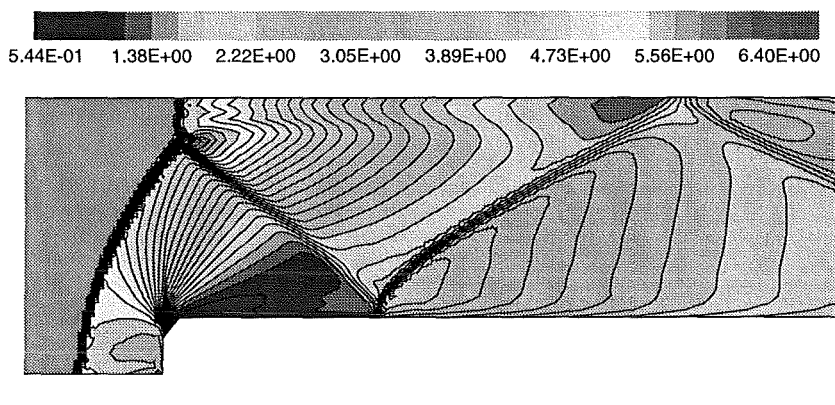
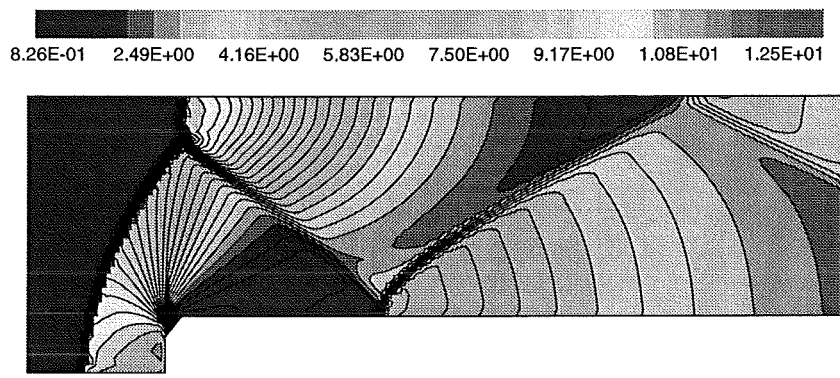
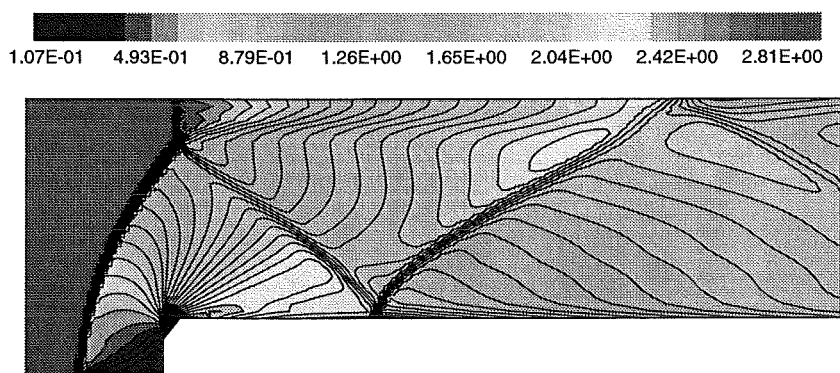


Figure 4.29: Forward facing step: HUS (predictor-corrector approach), density and entropy.

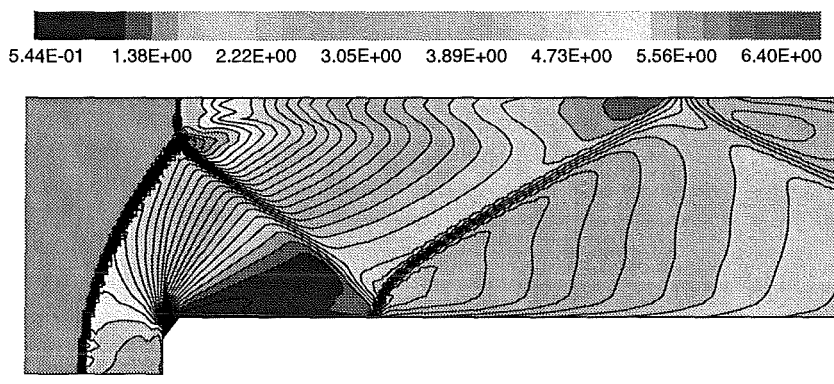


**Pressure at  $t = 4.0$ :** min = 0.4094 max = 13.34  
HUS, SO = IO = 2, DX = DY = 1/40  
30 isolines: min = 0.8265 max = 12.92

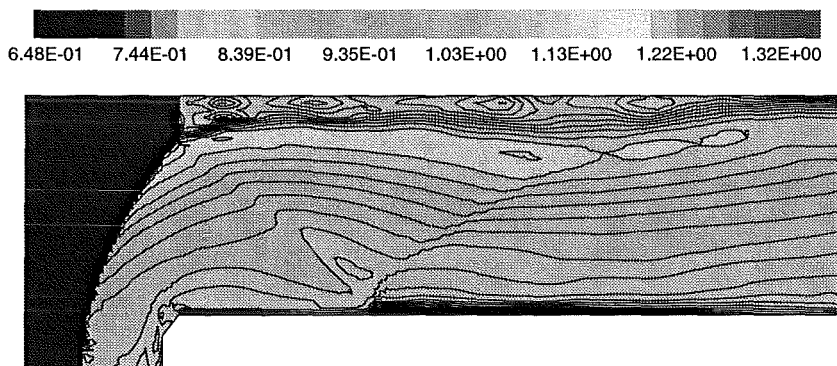


**Mach number at  $t = 4.0$ :** min = 0.01105 max = 3  
HUS, SO = IO = 2, DX = DY = 1/40  
30 isolines: min = 0.1075 max = 2.904

Figure 4.30: Forward facing step: HUS (predictor-corrector approach), pressure and Mach number.



**Density at  $t = 4.0$ :** min = 0.4597 max = 6.850  
**Godunov, SO = IO = 2, DX = DY = 1/40**  
**30 isolines:** min = 0.5445 max = 6.607



**Entropy at  $t = 4.0$ :** min = 0.6243 max = 1.3918  
**Godunov, SO = IO = 2, DX = DY = 1/40**  
**30 isolines:** min = 0.6482 max = 1.341

Figure 4.31: Forward facing step: Godunov (predictor-corrector approach), density and entropy.

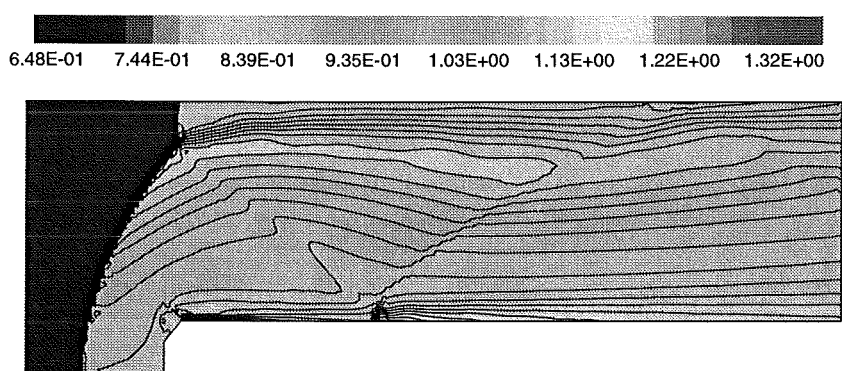
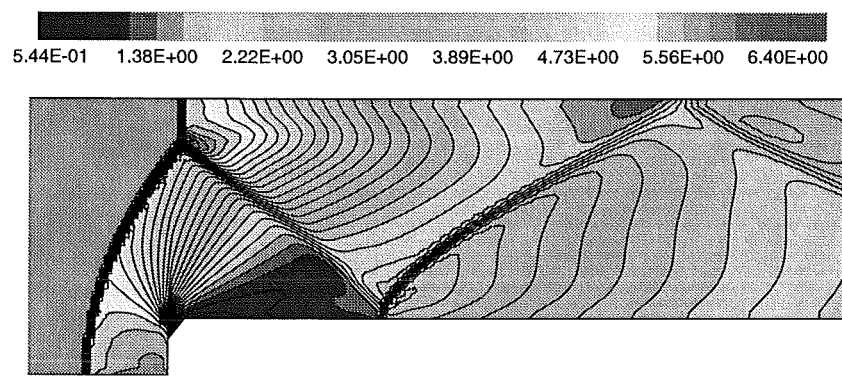


Figure 4.32: Forward facing step: VL-FVS (predictor-corrector approach), density and entropy.

#### 4.2.2.2 Reactive test cases

As mentioned above, reactive test cases are up to now restricted to detonation phenomena. Extensions to flame phenomena are planned but not within this project. This needs further investigations like for example low Mach number preconditioning, Navier-Stokes equations and turbulence models. For these reasons, the following paragraph is restricted to 1D detonation test cases.

##### 4.2.2.2.1 1D Detonation tube

This reactive test case has been first implemented for calorically perfect gases where the heat capacities  $C_{v_i}$  were evaluated at a given temperature called the reference temperature  $T_{ref}$ . This test case has shown large discrepancies between the calculated and measured detonation properties (mainly pressure and velocity) and the implementation of thermally perfect gases has been performed to obtain more accurate results. Heat capacities of each gas depend now on temperature with a 4th order polynomial regression of JANAF data in the range of 200 to 6000 K.

Initial conditions for the test case are as follows: mixture is composed of stoichiometric hydrogen/air with an initial temperature of 285 K and initial pressure of 0.965 bar. The explosion tube length is about 12 meters. The following table 4.3 gives the initial conditions for the three numerical calculations.

Comparison between numerical, analytical and experimental data are given in tables 4.4 and 4.5. If one looks at Case C, the Chapman-Jouguet velocity is quite well reproduced compared to analytical results or experiments and the maximum pressure is between Chapman-Jouguet and Von-Neuman pressure.

##### 4.2.2.3 Conclusions on Compressible Flow solver

After the computation of the different test cases, we can conclude that:

- the van Leer Flux Vector Splitting scheme is the most diffusive scheme in dealing with contact discontinuities, especially when they are aligned with the mesh; conversely it is very robust for computing shock waves;
- Godunov and HUS schemes are less diffusive than the Van Leer Flux Vector Splitting; conversely they have shown some problems in dealing with shocks in multidimensional domains.

As far as the computation of reactive flows in DDT regime is concerned, Van Leer FVS is probably the most suitable candidate, being the most efficient in dealing with the unsteady propagation of shocks.

Extension to multi-component mixtures with chemistry has been performed and

Case	hypothesis	$C_{v_i}$
Case A	calorically perfect	$T_{ref} = 3000K$
Case B	calorically perfect	$T_{ref} = 600K$
Case C	thermally perfect	4-th order pol.

Table 4.3: Different test-cases 1D detonation calculation

Analytical	$D_{CJ}$	$P_{CJ}$	$P_{VN}$
Case A	1958 m/s	15.6 bar	-
Case B	2371 m/s	21.4 bar	-
STANJAN (Therm. perf. gas)	1980 m/s	15.9 bar	28.3 bar

Table 4.4: 1D detonation: Analytical results

Numerical	D	$P_{max}(t_{fin})$
Case A (HUS)	1935 m/s	15.8 bar
Case B (HUS)	2250 m/s	20 bar
Case C (VLH)	2000 m/s	19.5 bar
Experiment [2]	1941 m/s	-

Table 4.5: 1D detonation numerical results and experiments

thermally perfect gases are necessary requirements to obtain a good representation of stable detonation properties. Future work will mainly deal with:

- the study of shock-focusing phenomena in large geometries (like RUT geometry);
- extension of the reactive flow solver to flame phenomena.

#### 4.2.3 Combustion model verification

In this section, verifications of TONUS low Mach number flow solver associated with hydrogen combustion models are presented. First, flame shapes are computed using TUM glass tube experiments in order to test the codes ability to reproduce different effects observed during experiments (self acceleration). Flame acceleration by repeated obstacles is addressed in a later section on benchmark calculations.

Due to low Mach number restrictions  $Ma < 0.3$ , only slow flames are addressed in this section. This range of flame velocity is of interest in reactor scale applications because it represents the first stage of combustion behavior. This work

is complementary to the other models involved in the project which are more restricted to higher Mach number flows.

#### 4.2.3.1 Flame shapes

As observed in TUM glass tube experiments, flame shapes can be very different when the hydrogen content of the mixture is increased. For lean mixtures (9 volume percent of hydrogen in dry air - Test 14), buoyancy effects are predominant and the flame reaches first the highest part of the tube before propagating. For richer mixtures (13.2 volume percent of hydrogen in air - Test 26), the flame behavior is completely different. The flame generates small scale turbulence and buoyancy effects are neglectable. For this mixture, the flame is strongly accelerated along the axis. If the hydrogen content is increased to 14.8 volume percent a so-called "tulip flame" can be observed in the second part of the glass windows. According to these phenomena, these test-cases have been simulated with the TONUS combustion models.

##### 4.2.3.1.1 Flame with buoyancy effects - Test 14

"Eddy Break-Up" combustion models have two types of restrictions for their application. The first one is that the fluctuation velocity  $u'$  is greater than the laminar burning velocity  $S_L$  and the second one is that the minimum turbulent length scale (Kolmogorov length scale) is greater than the laminar thickness of the flame (fast chemistry). In the glass tube test 14 these two conditions for such a combustion model failed near the ignition point. For this reason, first calculations have been performed with the so-called Arrhenius combustion model associated with the standard  $k - \epsilon$  turbulence model.

Ignition is made by imposing a temperature peak in the igniter region and slip conditions are considered at wall. In figure 4.33 the flame position is defined by the progress variable  $1 - \frac{Y_{H_2}}{Y_{H_2,u}}$  being higher than a minimum value of 0.01. In the calculation, the whole glass tube length is simulated but the results are plotted only in the first 50 cm (which represents the two glass windows). The results show the buoyancy effects, the flame rises first to the top of the tube and then travels at the top. The flame velocity is quite the same as the experimental result. Only the downward propagation near the ignition point due to shear stresses near the wall is not reproduced by the model.

The same test case has also been calculated with the "Eddy Break-Up" model described above, but the mixture is ignited via initial hydrogen mass depletion in the igniter region or via first initial steps with the Arrhenius Law model and the switching to the EBU model. Concerning the EBU constant the Said and Borghi correlation [11] is used with  $C_{EBU}^o = 1.0$ . This value has been chosen after some preliminary tests and this is consistent with Said and Borghi suggestions (values between 1.0 and 3.0). In figure 4.34, the flame also travels at the top of the tube

and the flame speed is quite the same as in figure 4.33. Slight differences can be observed like a more efficient downward propagation of the flame but the results are mainly the same.

This validation work shows that the model is adequate to simulate such flame propagation and it is possible to start the calculation directly with the EBU model.

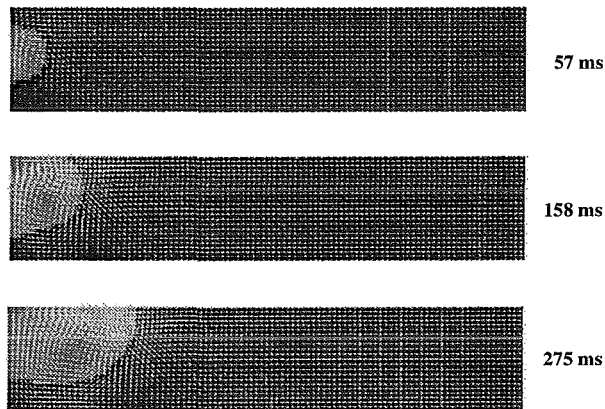


Figure 4.33: Glass tube - Test 14 - Flame shapes - TONUS 'Arrhenius' combustion model

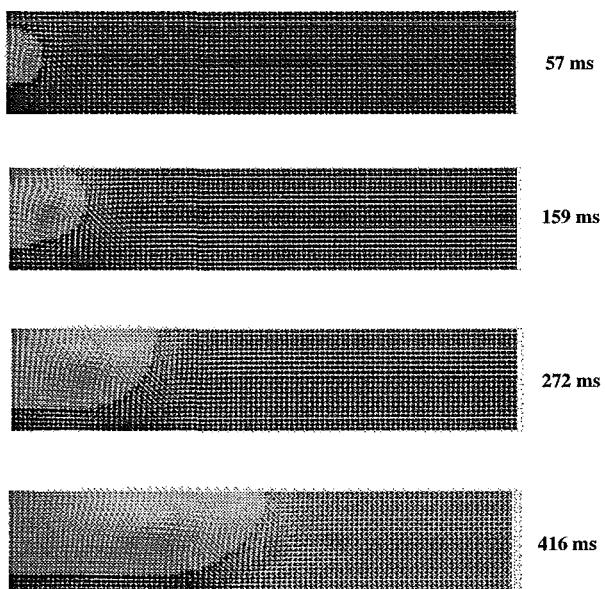


Figure 4.34: Glass tube - Test 14 - Flame shapes - TONUS 'EBU' combustion model

#### 4.2.3.1.2 Accelerated flame - Test 26

For this range of initial hydrogen concentration, the phenomena are quite different and the flame is no longer affected by buoyancy and small scale turbulence creates a large acceleration along the tube axis.

After preliminary tests with the model used for Test14 (same EBU constant and same turbulence model), it has been observed that the model can not reproduce this kind of phenomena: the flame is always affected by buoyancy and the strong axis acceleration can not be computed. Different reasons can explain this problem. If one looks at the momentum equation, the buoyancy term  $(\rho - \bar{\rho})\bar{g}$  is balanced by pressure gradients  $-\nabla p'$  and the divergence of the viscous and turbulent stress tensor. The divergence of the turbulent stress tensor could be approximated by  $-\frac{2}{3}\nabla k$ . If the change of flame shape with increase of hydrogen content could be explained by turbulence, the buoyancy term could be damped by  $k$  production in front of the flame. This transition regime concerning flame propagation can be explained in terms of a critical Froude Number ( $Fr$ ). If the Froude number is lower than a critical value the buoyancy effect takes place and creates a "rising" flame. In the other case, the flame is more spherical and is not affected by buoyancy. At the present time, this critical value of Froude Number is not well defined.

Coming back to the equations, our turbulence model (described in chapter 3) has only production/destruction terms related to the velocity field and to buoyancy. No terms are related to pressure gradients. The buoyancy terms are introduced to deal with stratification. This means that no turbulence is produced for stable stratification (hot gases in the upper part and cold gases in the lower part). Regarding flames, this  $G$  term in  $k$  equation needs to be damped by Froude number: if  $Fr < Fr_{critical}$ ,  $G < 0$  and if  $Fr > Fr_{critical}$ ,  $G > 0$ . So, the following formula has been assumed for the  $G$  term:  $G = (Fr - Fr_{critical})\frac{\mu_t}{\sigma_t}g\nabla\rho$ .

Concerning pressure gradients, if one looks at the real  $k$  equation [8] many terms appear and are neglected in our model which is mainly based on an extension of non-compressible models.

$$\bar{\rho}\frac{\partial k}{\partial t} + \bar{\rho}\tilde{u}_j\frac{\partial k}{\partial x_j} = -\frac{1}{2}\frac{\partial \rho u''_i u''_i u''_j}{\partial x_j} \quad (4.3)$$

$$-u''_i \frac{\partial p''}{\partial x_i} \quad (4.4)$$

$$+u''_i \frac{\partial \tau_{ij}}{\partial x_j} \quad (4.5)$$

$$-\rho u''_i u''_j \frac{\partial \tilde{u}_i}{\partial x_j} \quad (4.6)$$

$$-\overline{u''_i} \frac{\partial \bar{p}}{\partial x_i} \quad (4.7)$$

Term (2) is usually neglected in many modelings but it seems that term (5) needs to be modeled to deal with  $k$  production due to compressible flow. One

difficulty is that in our Low Mach Number flow solver, the pressure is divided in two parts and we have only dynamic pressure  $p'$  depending on space. According to the gradient hypothesis, term (5) could be modeled as  $-\frac{\nu_t}{\rho\sigma_T}\nabla\rho\nabla p'$ . Other authors [9] propose to link this term to the pressure and progress variable ( $c$ ) gradients  $\frac{\tau\nu_t}{\rho_r\sigma_T}\nabla c\nabla p'$ . This last formula is interesting because the mixture effect is integrated through  $\tau = \frac{T_p - T_r}{T_p}$  and  $\rho_r$  where  $r$  means reactant and  $p$  product.

Test Number	$\tau$	$\frac{\tau}{\rho_r}$
Test G14	3.26	2.97
Test G26	4.54	4.27

These differences could perhaps explain the different behavior in the combustion front propagation by different source terms for  $k$  equation.

These preceding modifications have been implemented and tested in the TONUS low Mach number turbulent deflagration model. The test consists in a square box (20 cm long) filled with hydrogen/air mixtures (same as test-14 or test-26) and ignited in the center. In the figure 4.35, differences between standard  $k - \epsilon$  and modified  $k - \epsilon$  models can be seen in terms of flame shapes. The buoyancy effect is still present at 9.2 volume percent of hydrogen and it's less important at 13.2 volume percent. The flame is also more spherical using the modified  $k - \epsilon$  model. These results can only be considered as preliminary results because while the flame shapes seem more in agreement with experimental behavior, the time schedule is far from the experimental results for 13.2 volume percent of hydrogen (acceleration is not so strong). This could perhaps be achieved by adjustment of the constant in the turbulence model, for example  $\sigma_T$  or  $\sigma_t$  or decoupling between  $k$  and  $\epsilon$  equations.

At present time, the model is not adequate to simulate "self-acceleration" of the hydrogen/air flame front. This problem is not trivial and not well understood. For our model (low Mach number flow solver) many questions remain open, like: effect of Lewis number (our model assumes that the Lewis number is equal to one, which is not true for hydrogen), effect of acoustic waves filtering (especially in the burned gases where the sonic speed is the highest), effect of turbulence model (some recent publications use low a Reynolds number  $k - \epsilon$  turbulence model [10]). Much work has been performed, but a lot of work remains to be performed on combustion at low Mach number.

#### 4.2.3.2 Conclusions of combustion models verification

Validation work has shown some good capabilities of TONUS turbulent combustion model especially for low hydrogen concentration. Turbulence/combustion interaction is a complex problem and the present model is not able to deal with all the phenomena observed experimentally. For example, the following open

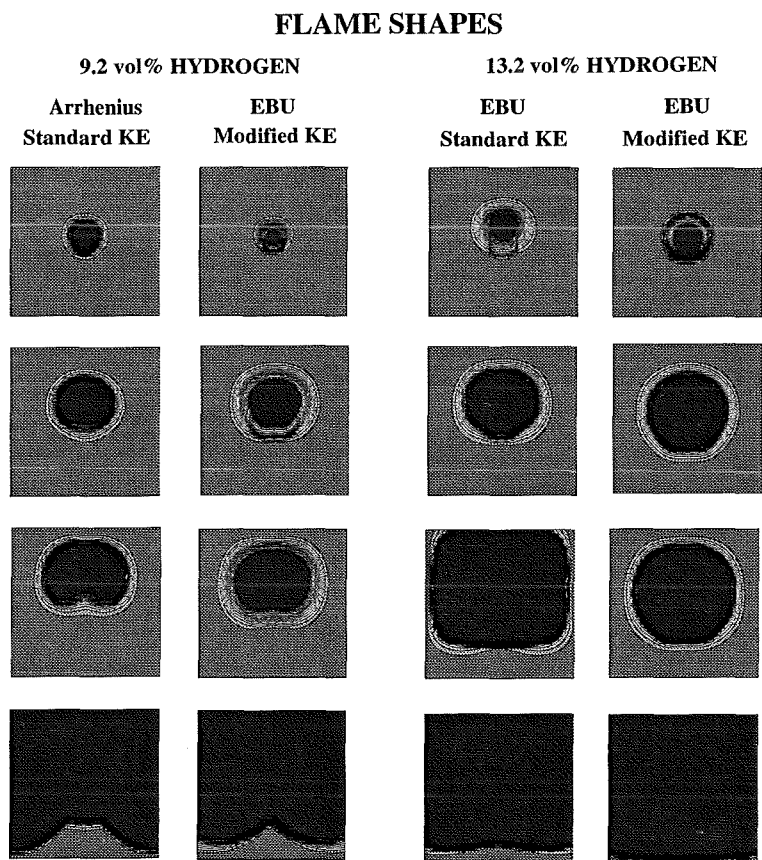


Figure 4.35: Square box - Flame shapes - TONUS turbulent combustion model

points remain after the present verification work.

- "Self-acceleration" of an hydrogen flame front needs further investigations in our modeling. This entails a better understanding of flame-turbulence interaction and a higher level of modeling especially for turbulence creation in front of the flame.
- Adjustment of the EBU constant is an important problem, especially for the foreseen applications on Nuclear Power Plants. The EBU model is a very simplified and easy to implement combustion model but the physics inside is quite poor. Many authors have tried to enhance the physics in the EBU model by adding terms in the EBU constant (Said and Borghi correlations is one example). More work is needed in this field to ensure that the "EBU constant" is not dependent on geometrical size or mixture composition mainly for low hydrogen concentration (9 to 12 volume percent).
- Concerning model implementation, an important thing that was not investigated in the present study is the convergence of the results with the grid size. In the foreseen applications, the grid size used will be very coarse and this could be an important problem for combustion modeling if no good adaptive mesh is available.

## 4.3 COM3D (combustion code from FZK)

### 4.3.1 Test of thermodynamic model

The computer code COM3D uses the polynomial fits given in table 4.6 to calculate the enthalpy of the mixture and the heat capacity. An important first test for the computer code has to prove that these polynomial fits give correct results for the pressure and temperature range of interest.

Table 4.6: Thermodynamic parameters used in COM3D

	Hydrogen H <sub>2</sub>	Oxygen O <sub>2</sub>	Nitrogen N <sub>2</sub>	Steam H <sub>2</sub> O
Molecular weight	2.0160·10 <sup>-3</sup>	3.2000·10 <sup>-2</sup>	2.8013·10 <sup>-2</sup>	1.8016·10 <sup>-2</sup>
Enthalpy of formation	0.0000·10 <sup>+0</sup>	0.0000·10 <sup>+0</sup>	0.0000·10 <sup>+0</sup>	-2.3900·10 <sup>+5</sup>
Polynomial coefficients				
$c_0$	2.3314·10 <sup>+01</sup>	3.0000·10 <sup>+01</sup>	3.1255·10 <sup>+01</sup>	3.4021·10 <sup>+01</sup>
$c_1$	3.1871·10 <sup>-02</sup>	-1.3554·10 <sup>-02</sup>	-1.9106·10 <sup>-02</sup>	-8.9246·10 <sup>-03</sup>
$c_2$	-7.0165·10 <sup>-05</sup>	5.8690·10 <sup>-05</sup>	5.0961·10 <sup>-05</sup>	3.2019·10 <sup>-05</sup>
$c_3$	8.1860·10 <sup>-08</sup>	-7.4377·10 <sup>-08</sup>	-5.0938·10 <sup>-08</sup>	-2.1678·10 <sup>-08</sup>
$c_4$	-5.2914·10 <sup>-11</sup>	4.9546·10 <sup>-11</sup>	2.8403·10 <sup>-11</sup>	6.9461·10 <sup>-12</sup>
$c_5$	2.0487·10 <sup>-14</sup>	-1.9506·10 <sup>-14</sup>	-9.7408·10 <sup>-15</sup>	-9.7708·10 <sup>-16</sup>
$c_6$	-4.8821·10 <sup>-18</sup>	4.6982·10 <sup>-18</sup>	2.1017·10 <sup>-18</sup>	-2.8390·10 <sup>-20</sup>
$c_7$	7.0237·10 <sup>-22</sup>	-6.8066·10 <sup>-22</sup>	-2.7826·10 <sup>-22</sup>	2.9077·10 <sup>-23</sup>
$c_8$	-5.5985·10 <sup>-26</sup>	5.4504·10 <sup>-26</sup>	2.0662·10 <sup>-26</sup>	-3.6943·10 <sup>-27</sup>
$c_9$	1.8989·10 <sup>-30</sup>	-1.8542·10 <sup>-30</sup>	-6.5892·10 <sup>-31</sup>	1.5870·10 <sup>-31</sup>
$h_0$	-846.56	-2258.9	-2399.9	-5031.2
$h_1$	28.917	33.189	32.705	39.85
$h_2$	0.001251	0.0010451	0.000604	0.0025366

Here enthalpy  $h(T)$  and heat capacity  $C_p(T)$  are given by polynomial approximations ([23]):

$$h(T) = h_0 + h_1 T + h_2 T^2 \text{ and } C_p(T) = c_0 + c_1 T + \dots + c_9 T^9;$$

units: enthalpy and enthalpy of formation [J/mole], heat capacity [J/mole/K], molecular weights [kg/mole].

Here we present results for the constant volume combustion of a 15 % hydrogen air mixture which corresponds to a composition of H<sub>2</sub>/O<sub>2</sub>/N<sub>2</sub> of .84 : 1 : 3.76 at ambient conditions. Figure 4.36 shows the verbatim output produced with STANJAN [22]

In table 4.7 these results from STANJAN are compared to the output from COM3D. The agreement between the two computed thermodynamic states is fairly good.

```

CASE NO. 1 RUN AT 16 4.28 ON 6-22-1998

Computed properties

atoms      population
H          1.68000000E+00
O          2.00000000E+00
N          7.52000000E+00

Reactants at P = 1.000E+00 atmospheres
species      mol fraction    mol fraction    mass fraction    mols*
            in the phase    in mixture    in mixture
phase 1: molal mass = 24.825 kg/kmol T = 298.15 K
H2          .15000E+00    .15000E+00    .12181E-01    8.40000E-01
O2          .17857E+00    .17857E+00    .23017E+00    1.00000E+00
N2          .67143E+00    .67143E+00    .75765E+00    3.76000E+00

Calculations made using frozen composition.

* Species mols for the atom populations in mols.

Mixture properties: molal mass = 24.825 kg/kmol
P = 1.0133E+05 Pa      V = 9.8548E-01 m**3/kg
U = -.9985E+05 J/kg    H = .7228E-02 J/kg    S = .7731E+04 J/kg-K
Made 0 (T,P) iterations; 0 equilibrium iterations; v 3.95 JES-PC

Computed properties
Independent      population      element
atom            population      potential
            potential
H          1.68000000E+00    -14.4146
O          2.00000000E+00    -14.4264
N          7.52000000E+00    -12.5896

Products at T = 1800.20 K P = 5.585E+00 atmospheres
species      mol fraction    mol fraction    mass fraction    mols*
            in the phase    in mixture    in mixture

phase 1: molal mass = 26.838 kg/kmol
O2          .11197E+00    .11197E+00    .13350E+00    5.80000E-01
N2          .72587E+00    .72587E+00    .75765E+00    3.76000E+00
H2O         .16216E+00    .16216E+00    .10886E+00    8.40000E-01

* Species mols for the atom populations in mols.

Mixture properties: molal mass = 26.838 kg/kmol
T = 1800.20 K      P = 5.6590E+05 Pa      V = 9.8548E-01 m**3/kg
U = -.9985E+05 J/kg    H = .4578E+06 J/kg    S = .9090E+04 J/kg-K
Made 4 (T,P) iterations; 11 equilibrium iterations; v 3.95 JES-PC

```

Figure 4.36: Reference output from STANJAN

Table 4.7: Comparison of Results from STANJAN and COM3D

	COM3D	STANJAN
Pressure	$5.42 \cdot 10^5 \text{ Pa}$	$5.66 \cdot 10^5 \text{ Pa}$
Temperature	$1725 \text{ K}$	$1800 \text{ K}$
Density	$1.0144 \text{ kg/m}^3$	$1.0147 \text{ kg/m}^3$

### 4.3.2 Flow over forward facing step

One standard test case for cfd codes is the flow over a forward facing step [21]. This test case was calculated for a nitrogen flow with an entry Mach number of 3. The initial conditions were  $p_0 = 1.013 \cdot 10^5$  Pa and  $T = 298.15$  K, the thermodynamic data for N<sub>2</sub> is based on the JANAF tables as specified in the previous section. The duct width  $L$  is equal to 1, its length is 3, and the step of height 0.2 is located at distance 0.6 from the entrance.

This test problem has also been calculated by many other authors and ample results can be found in the literature. The correct solution to this problem is well known. The same test was also performed with the Tonus code (see section 4.2) and with REACFLOW (see section 4.4).

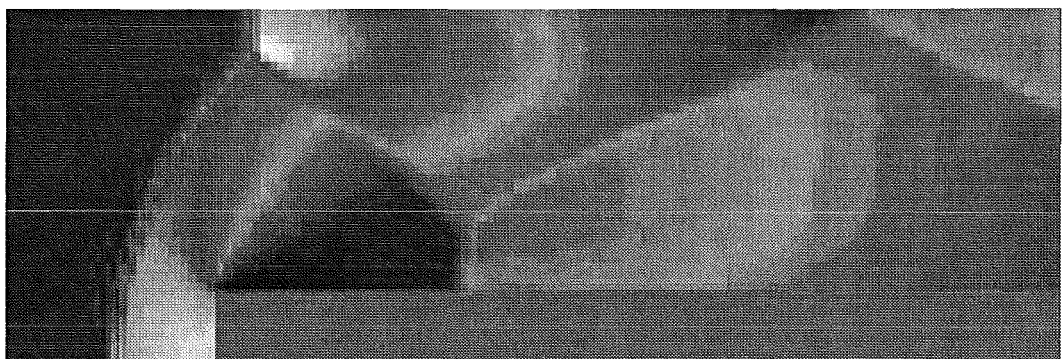
Figure 4.37 shows the density distribution at time  $tC_s/L = 4$  for three different grid resolutions. For the finest grid of 100 x 300 cells the results are very similar to the Tonus results discussed in section 4.2.

Critical points in the evaluation of numerical solutions for this test problem include stagnation pressure, angle of bow shock, shear layer position and the downstream shock pattern. A closer inspection of the COM3D results showed that all these features were reproduced with good agreement to the other known results. This test case also demonstrates that the TVD scheme used in COM3D preserves shock fronts very well.

$20 \times 60$  cells



$40 \times 120$  cells



$100 \times 300$  cells



Figure 4.37: Flow over forward facing step with Mach number 3 at dimensionless time  $t/C_s = 4$

### 4.3.3 Flow in RRCKI CHANNEL

At the Russian Research Centre Kurchatov Institute experiments were performed in a small scale channel with obstacles. The height of the rectangular channel was 80 mm and the length of the tube was 5280 mm. The interesting feature of these CHANNEL experiments is the possibility to take high speed schlieren pictures of the propagating flame at different locations along the flame. This allows to get pictorial information of the propagating flame along the complete tube from a sequence of repeated experiments [24].

In Figure 4.38 the initial phase of a propagating flame passing through the first two obstacles of the CHANNEL setup is shown in the left column. The blockage ratio in the channel was 0.3 and a mixture with 10 %  $H_2$  in air was used. From the very beginning the flame has a cellular structure, as is to be expected for mixtures with Lewis numbers  $Le < 1$  (The Lewis number of this mixture is  $Le = 0.352$  ).

Due to the resolution of the COM3D calculation shown in the right column of Figure 4.38 the cellular structure is not resolved in the calculation. However, the global shape of the propagating flame is reproduced remarkably well. Initially the flame brush expands spherically from the ignition location (second picture from top). Then the flame preferentially propagates in the axial direction. The flame reaches the first obstacle with a blunt tip and the top and bottom walls near the end wall at about the same time. This is also shown in the calculated flame shape. Behind the first obstacle the flame expands and reaches the tube walls rather quickly. A similar behavior is also observed in the last picture of the calculation. It seems that in the calculation the axial propagation is a little bit faster than the radial propagation as compared to the experimental data.

Such direct comparisons of flame shapes provide a good insight into the capabilities of the numerical model as the schlieren pictures provide more detailed information than is available from pressure measurements alone.

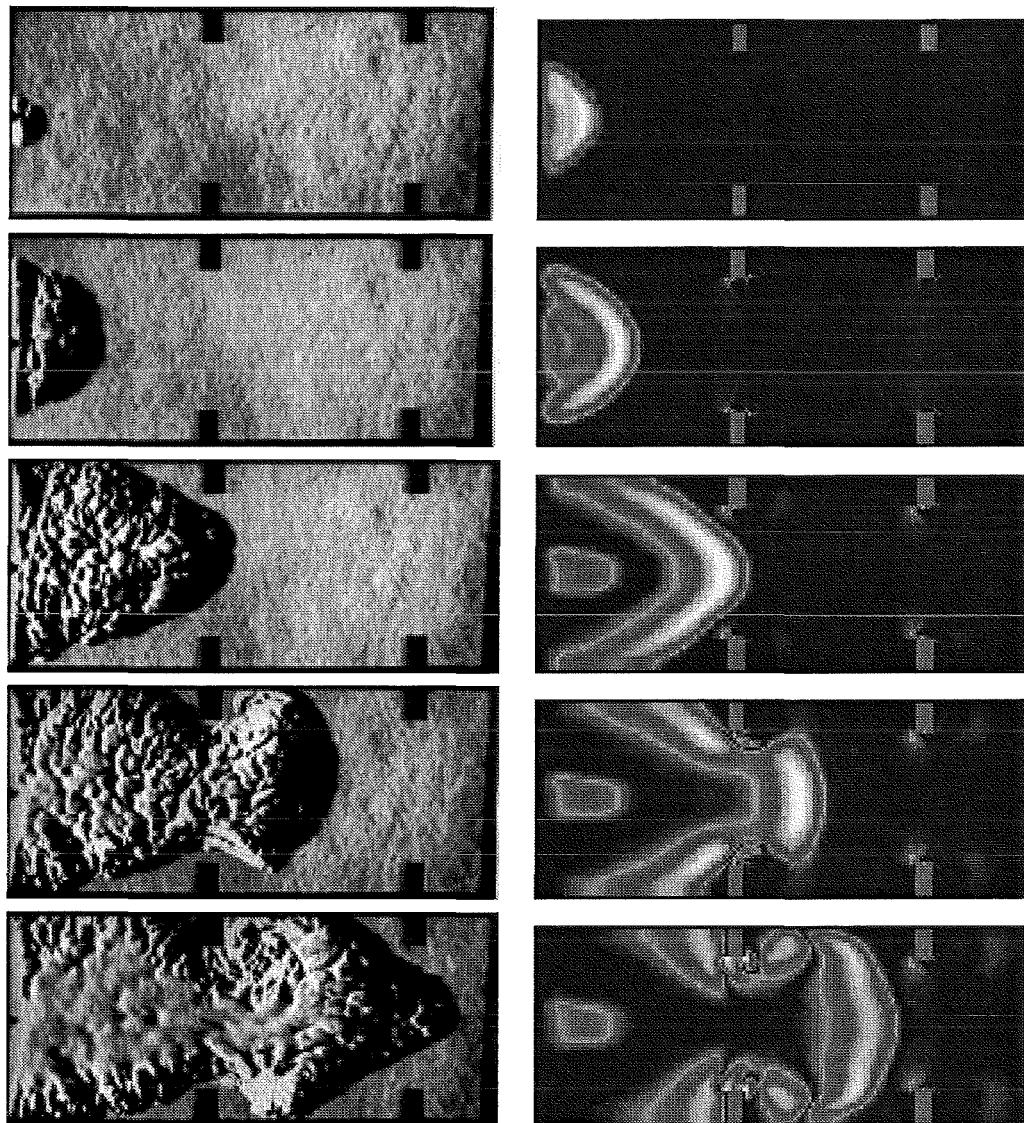


Figure 4.38: Flame propagation in obstructed channel of Kurchatov Institute, Comparison of simulation with Schlieren pictures

#### 4.3.4 Calculations of FZK-tube experiments

The main verification of COM3D was performed on the results from the FZK tube as these data were readily available and the experimental conditions were well defined. The set up modeled with COM3D is depicted in Figure 4.39. In the calculations only one quarter of the tube cross section was calculated due to symmetry conditions.

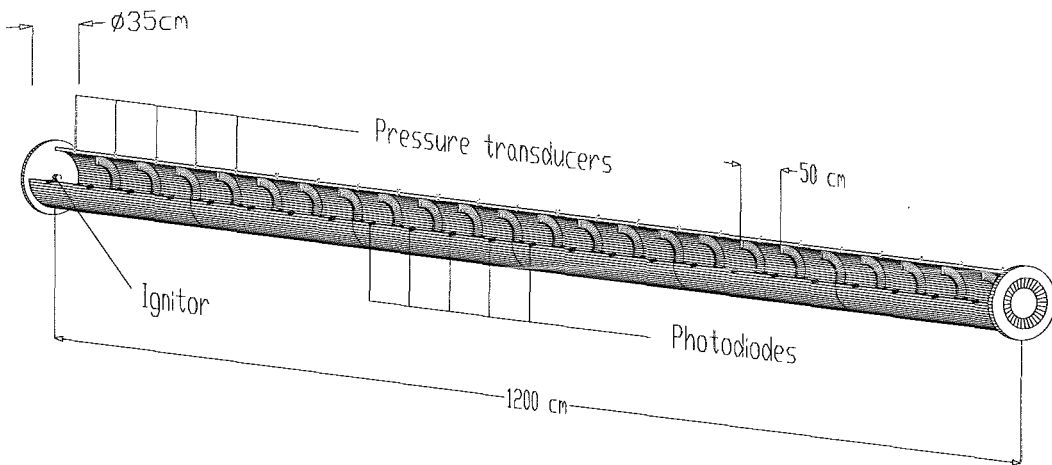


Figure 4.39: Schematic of the 12 m FZK tube

As an example results for experiment R0498\_09 are presented in Figure 4.39. In this experiment the hydrogen concentration was 15 % by volume and the blockage ratio was 0.3. At the top the measured and calculated pressure histories at the 14 probe locations are shown. The numerical results are shifted by a constant offset to account for uncertainties in the start up phase. The agreement between measured and calculated values is excellent. In the second plot the light emission as seen by photodiodes in the tube is compared to the corresponding data from the calculation. The calculated curves are again shifted by the same time offset as the pressure data. The peak which indicates the arrival of the flame at each measurement location is reproduced very well by the computation.

Experimental data from the FZK tube is available for blockage ratios from 0.3 to 0.9 and for hydrogen concentrations from 11 % to 20 % by volume. This data base is ideal to calibrate and check the constants in the eddy break-up model. For the conditions listed in table 4.8 numerical simulations with different values of the model constant were performed. For each set of initial conditions the value that gave the best agreement with the experimental data was selected. The values for the eddy break-up constant are listed in table 4.8. It can be seen that these values do not vary too much with the experimental conditions investigated. This point is an important indication for the predictive capabilities of COM3D.

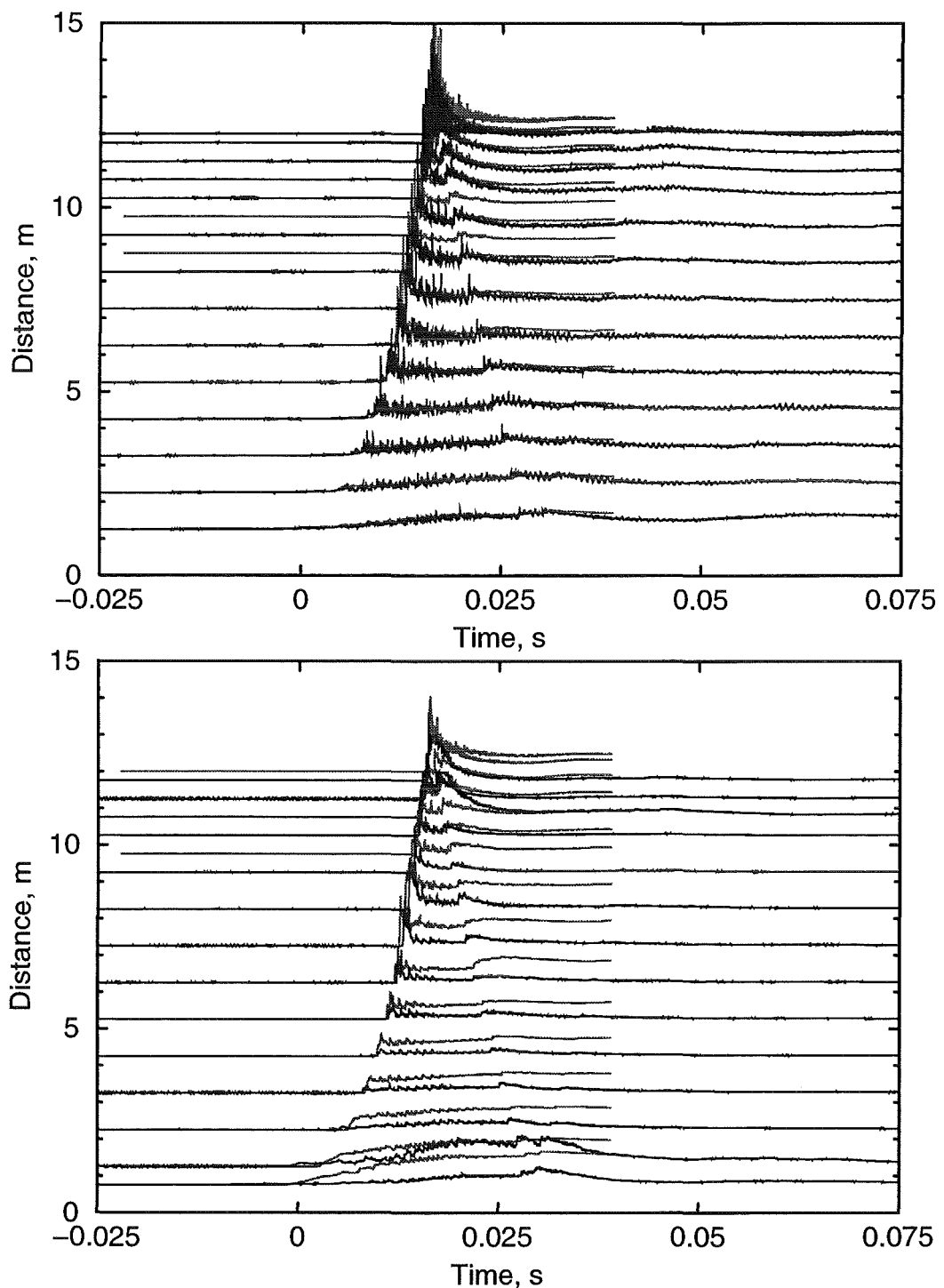


Figure 4.40: Measured and calculated pressure histories (top) and flame positions (bottom) for R0498\_09 - 15 %  $H_2$ , blockage ratio 0.3

Table 4.8: Model parameter of eddy break-up model for the calculations performed with COM3D

BR	20% $H_2$	15% $H_2$	12% $H_2$	11% $H_2$
0.30	6.0	6.0	4.9	5.5
0.45	6.0	6.0	5.0	5.5
0.60	6.0	6.0		
0.90		8.0	7.0	7.0

### 4.3.5 Large scale test in RUT facility

The eddy break-up combustion model without Said-Borghi extension [11] in the COM3D code contains a reaction rate constant  $c_f$  which must be determined empirically from experimental results. In the previously discussed series of calculations for turbulent combustion experiments in the 12 m tube a  $c_f$ -value of  $6 \pm 1$  gave good agreement with the test data for quite different experimental conditions, provided the mixture burned completely in the test.

A second series of calculations was performed for large scale RUT experiments in order to determine the optimum  $c_f$ -value for larger, more reactor typical geometric scales. The geometry of the RUT facility is schematically shown in Figure 4.41. Table 4.9 summarizes the turbulent combustion tests for which COM3D calculations were performed, together with the optimum  $c_f$ -values, necessary to produce good agreement with the test results (flame speed, overpressure). These tests were selected because they resulted in turbulent flame propagation (no DDT) and because they provided the detailed measured data. The experimental parameters cover a wide range of initial conditions ( $p_0$ ,  $T_0$ ,  $H_2$  concentration, steam concentration), geometrical configurations ( $S_1$  - opening from first channel to canyon,  $S_2$  - vent opening of second channel, BR - blockage ratio of installed obstacles) and maximum flame speeds in the first channel ( $v_{max}$ ).

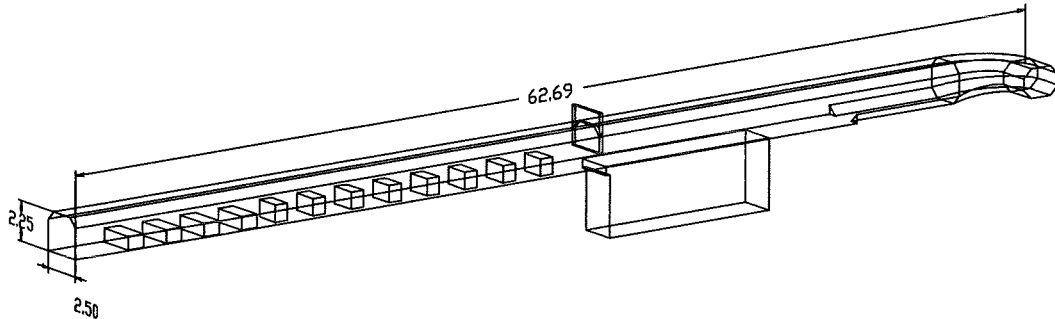


Figure 4.41: Schematic view of RUT facility, consisting of first channel (equipped with obstacles), large cavity, and second channel leading to exit. All dimensions are shown on same scale.

Figure 4.42 compares measured and calculated positions of the flame front as it accelerates along the obstructed first channel. Ignition was near the 1.4 m position by a weak spark. It is remarkable that despite of the quite different initial conditions (%  $H_2$ ) and geometries ( $S_1$ ,  $S_2$ , BR), the flame path can be modeled well with a nearly constant  $c_f$  value (6 or 7). The maximum flame speeds varied significantly (factor 3). The calculations were done with a numerical grid size of 12.5 cm ( $44 \times 50 \times 50 \approx 1.100.000$  grid cells).

In test 19 without obstacles the optimum  $c_f$  value differed noticeably from tests 13, 17, 21 and 23. The most likely reason is that the calculated turbulence

Table 4.9: Experimental conditions of simulated RUT tests and resulting eddy break-up coefficient  $c_f$  giving the best agreement with measured data.

Test	$p_0$ [bar]	$T_0$ [K]	$H_2$ %	$H_2O$ %	$S_1$ [ $m^2$ ]	$S_2$ [ $m^2$ ]	BR %	$v_{max}$ [m/s]	Optimum $c_f$ value
13	1	280	11.0	-	2.0	0	30	210	7
17	1	280	11.0	-	5.6	2.5	30	440	6
19	1	280	12.5	-	5.6	2.5	0	35	9
21	1	280	12.5	-	5.6	2.5	60	650	7
23	1	280	11.2	-	5.6	2.5	60	340	6
stm2	1	370	14.7 (dry)	14.7	5.6	2.5	30	680	10
stm7	1	370	17.5 (dry)	25.7	5.6	2.5	30	680	10

level is too low for two reasons:

- the  $k-\varepsilon$  model does not include turbulence generation at the walls
- small obstacles in the channel (crane, instrumentation and cable piping) are not included in the geometrical COM3D model.

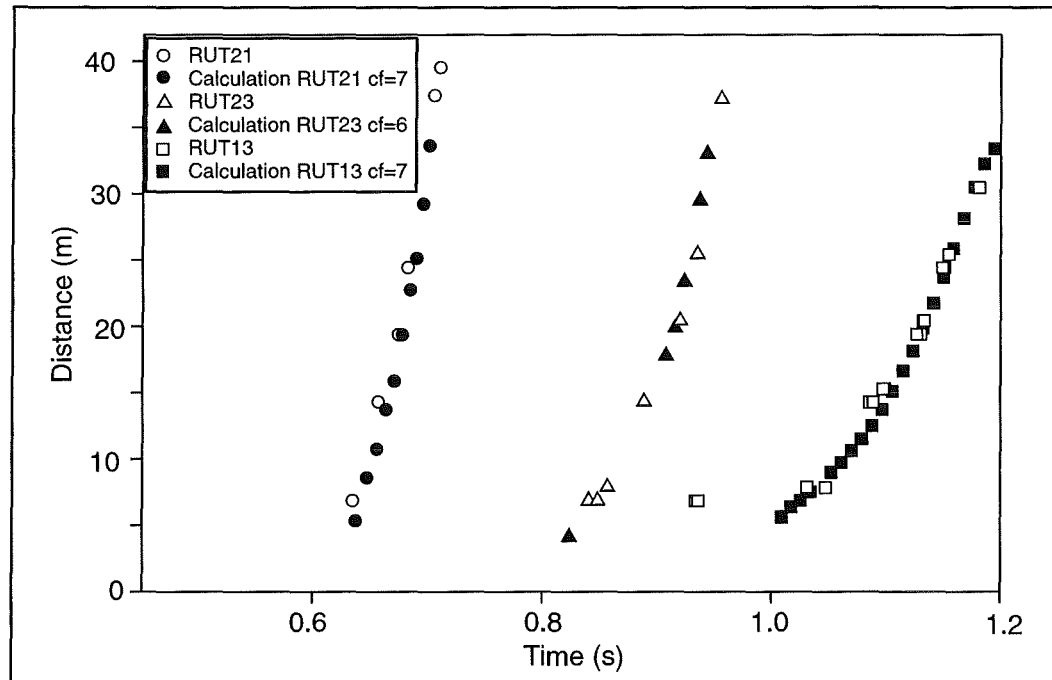


Figure 4.42: Comparison of measured and calculated flame front trajectories in the first channel of the RUT facility (0 - 34 m).

In experiments with large obstacles (BR = 30 % and 60 %) the turbulence generation from the walls and secondary small flow resistances is neglectable compared to that from the large obstacles.

A comparison of the measured and calculated pressure histories in the RUT facility (Figure 4.43) shows good agreement for the integral combustion development and local pressure loads. All major peaks in the experiments can be identified in the calculation, showing that the simulation captures the essential wave propagation phenomena in the complex 3-D enclosure. At later times the calculated pressures exceed the test data because the late venting of the facility was not simulated.

For the simulation of the  $H_2$ -air-steam tests (stm2 and stm7) a relatively high  $c_f$  value (10) was needed to obtain acceptable agreement. This is very likely due to the fact that the heating tubes and other additional equipment, which was installed for heating the RUT facility to about 100° C, were neglected in the COM3D geometry model. This results in too low calculated turbulence generation and requires an artificially high  $c_f$  value for compensation, similar to test 19.

Figure 4.44 shows the flame propagation through the RUT facility for test 23. Shown are five different instances of the propagating flame. For each instance three perpendicular cuts through the computational domain are shown. The flame is initiated near the left end wall of the RUT facility. The flame passes through the gaps in the obstacles and moves as a jet into the next empty space between obstacles. At the upstream side of the obstacles remain pockets of unburned gas that are only slowly burning. At 137 ms the flame has almost reached the end of the first channel. But unburned gas is still burning at all obstacles. At 164 ms the flame has moved halfway through the large cavity. At that time there is still some reaction near the last obstacles. In the last picture the flame has reached the second channel and moves rather fast through that part of the RUT facility. At the same time the flame propagation is much slower in the cavity. At the bottom of figure 4.44 two closeups of the flame are shown. It is clearly seen how the flame passes through the gaps between obstacle and wall and then expands into the next open space. The figure at 137 ms shows a jet like structure between the obstacles.

In summary the observed  $c_f$  variation can be interpreted in terms of model approximations. It appears important that the dominant turbulence generation processes are captured in order to obtain reliable results from an eddy break-up combustion model. For instance in large empty rooms it may be necessary to include wall functions in the turbulence model.

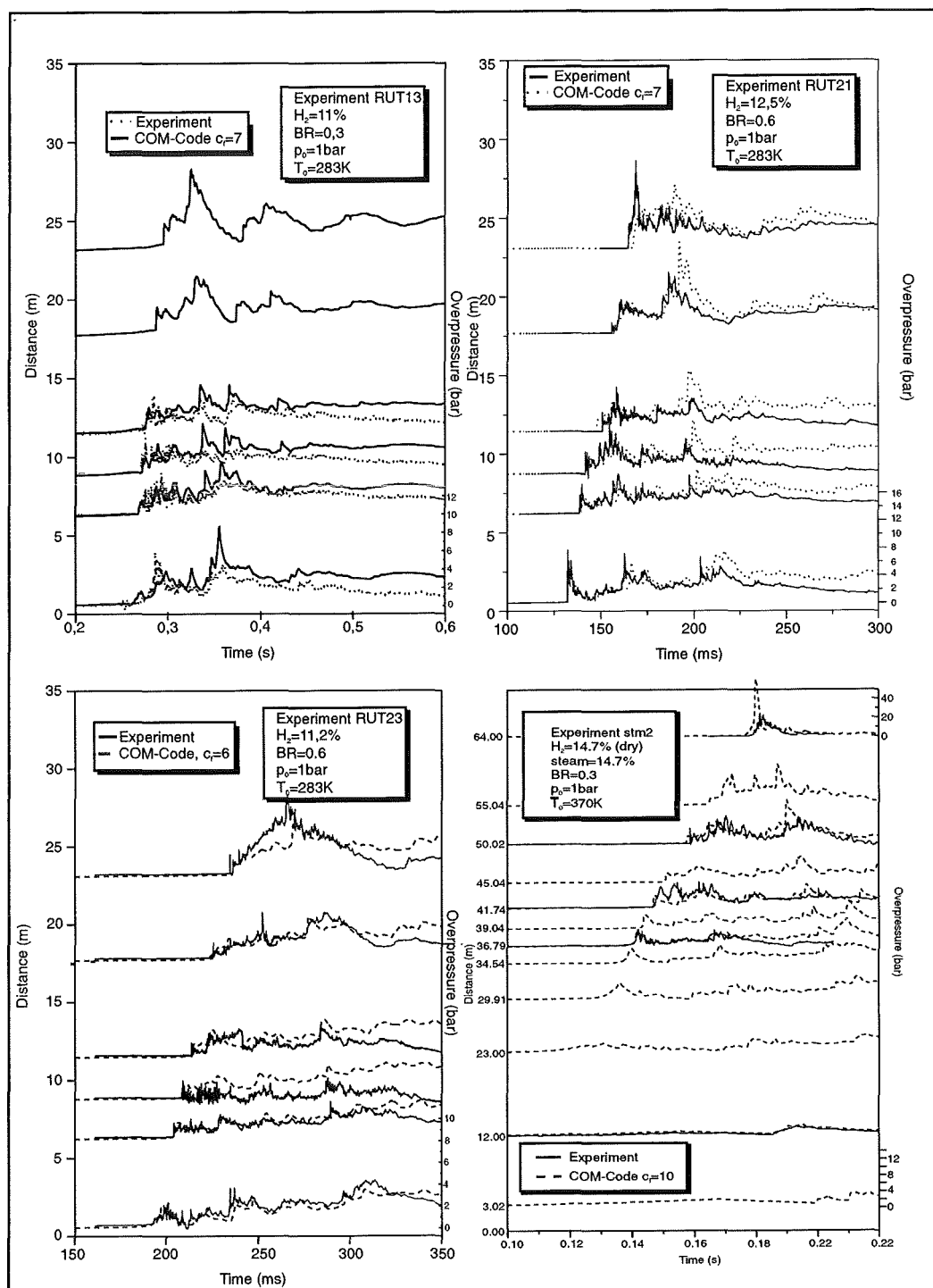


Figure 4.43: Numerical simulation of large scale RUT experiments with hydrogen-air and hydrogen-air-steam mixtures. Pressure histories for R0498\_09

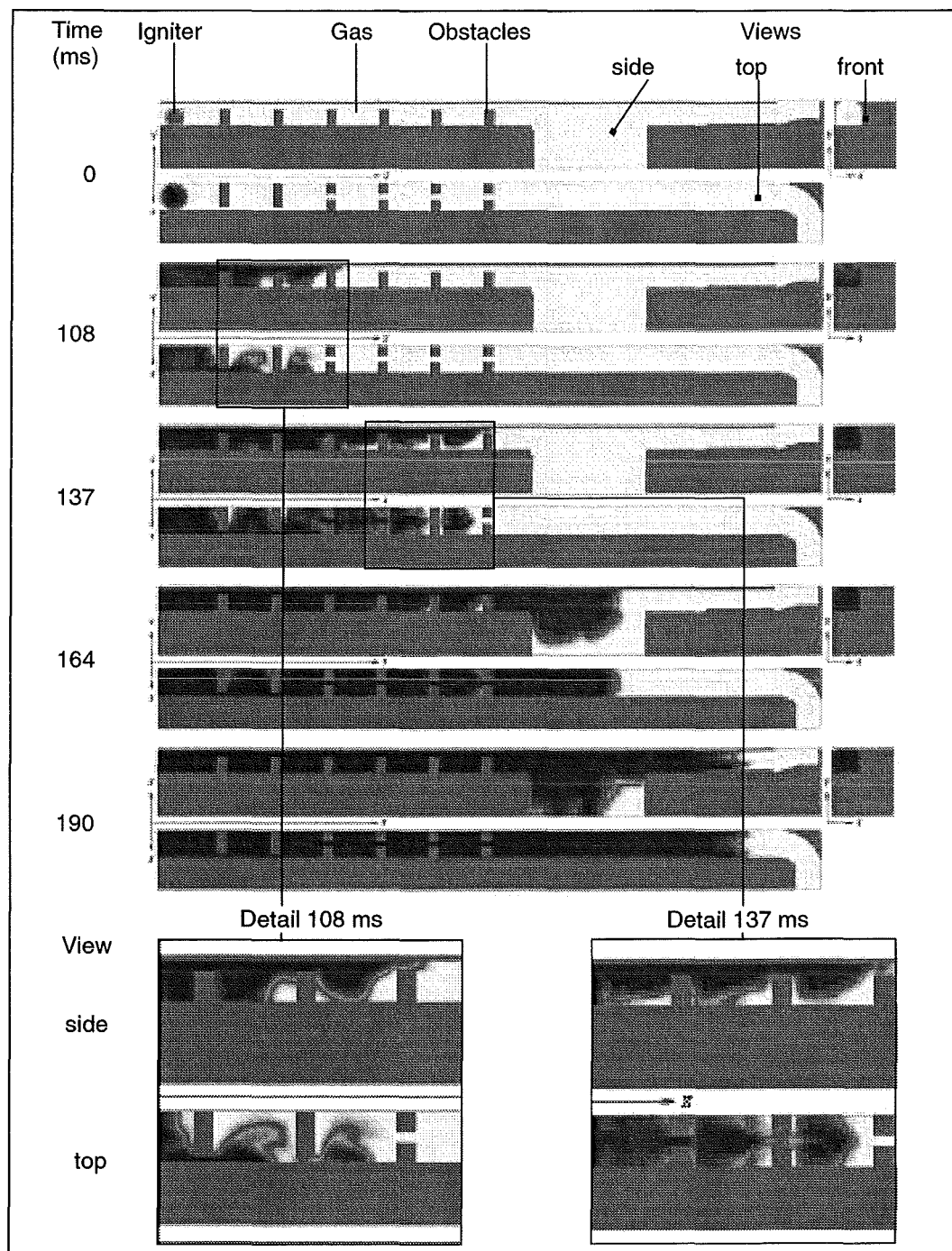


Figure 4.44: RUT facility test 23. Calculated flame shapes for different instances in time

## 4.4 REACFLOW (combustion code from JRC)

In this section we first describe four numerical test cases performed with REACFLOW. The first three cases are non-reactive, but they are known as challenging test cases for Euler solvers. These cases include the standard shock-tube problem, the forward facing step problem and a shock diffraction over a sudden expansion. These test cases cover physical phenomena relevant to studies of chemical explosions. Although these examples have only physically 1- and 2-D nature they are simulated using the 3-D solver of REACFLOW, as described previously.

The last test case is a reactive case, a detonation simulation of a 3-D experiment the large scale RUT facility [25, 26].

### 4.4.1 Shock tube problem

A simple but quite revealing test for the grid adaptation consists of a shock tube. The problem is essentially one-dimensional, as the initial state does not vary across the tube. The computational domain is a short tube of square cross-section, with dimensions  $0.05 \times 0.5 \times 0.05$ m. At time  $t = 0$ s one half of the tube is filled with gas (a mixture of air and hydrogen) at  $p = 5$ atm. The other half has  $p = 1$ atm. Initial composition and temperature are uniform, with  $T = 293$ K. The initial grid has nodes spaced uniformly along the coordinate axes with equal grid spacing in the 3 directions.

The following results are all data taken from along the second axis, in the middle of the tube. Only the original grid points are shown in the figures, even when adaptation was used.

The effect of grid resolution is clearly seen in Fig. 4.45, top. Here we show the density profile along the tube at time  $t = 4 \cdot 10^{-4}$ s after the release of the high-pressure region. Results are shown for three different grid resolutions, of  $\Delta x = 0.025$ m,  $\Delta x = 0.01$ m and  $\Delta x = 0.005$ m, respectively, using the 2nd order method. With the fine resolution we easily see, from bottom to left, the shock front, the contact discontinuity and the expansion fan. With the coarse resolution, these regions are so smeared out that they actually overlap. However, the fine resolution result is obtained using almost 70 times more grid points than the coarsest resolution.

In order to obtain good resolution of the shock and contact discontinuity with fewer grid points the grid adaptation system may be used. A result is shown in Fig. 4.45, bottom. Here, the results from a fine grid and a coarser grid without adaptation are compared with a result using the coarser grid and grid adaptation. The adaptation method uses absolute differences of density. (For this problem, density is the best adaptation criterion. Using pressure, for instance, the contact discontinuity would not be well resolved.) The smallest allowed grid point distance during the calculation was about 0.002m. During the calculation the number of grid points increased from the original 1836 nodes to close to 8000

before settling back to around 5500 nodes.

From the results we see that the grid adaptation method gives essentially the same result as the calculation on the finer static grid with 12221 grid points. Yet during most of the calculation the adaptive calculation uses less than half as many grid points as the fine static grid. Even so, most of the inserted grid points were placed in the expansion fan. If a good resolution is not needed here it would probably be possible to tweak the adaptation thresholds to significantly reduce the number of grid points while keeping the good resolution at the shock front and contact discontinuity.

#### 4.4.2 Supersonic flow over a forward-facing step

This problem is described in detail by Woodward and Colella [21]. In non dimensional variables the channel is 1 unit high, 3 units long and 0.4 units wide. The step is 0.2 units high and is located 0.6 units downstream. Initial flow conditions correspond to a uniform flow at Mach 3.

The initial mesh has 2506 nodes and 10902 elements. As adaptation criterion the difference between density at neighboring nodes was used. Refinement was possible down to a minimum resolution of about 0.025.

Fig. 4.46 shows 3-D and 2-D iso colors and contour plots of the density at  $t = 0.5, 2.0, 4.0$ , respectively. Density varies between 1 and 6. The 3-D plots show in addition the mesh. The 2-D contour plot, which is a cut through the center plane of the channel, has 30 iso-lines for the same density range.

Starting from the initial conditions a shock detached from the step has developed ( $t = 0.5$ ); when this shock reaches the upper channel wall, it moves there upstream ( $t = 2.0$ ) and forms a Mach stem with a lambda-configuration as can be seen at ( $t = 4.0$ ). Behind the lambda-shock a contact discontinuity is formed. This contact discontinuity is much weaker than in the reference, because the minimum resolution of this calculation is still twice as coarse as in the reference case.

The corner (edge) of the step is a geometric singularity for the numerical scheme. Here spurious entropy is generated and convected downstream in the expansion fan behind the corner and interacts with the oblique shock from the Mach stem. By this a so-called numerical boundary layer is formed.

#### 4.4.3 Shock wave diffraction over a backward facing step

This problem is a well known test problem for supersonic flows including shocks and expansion waves. It has been studied extensively in the literature e.g. by Quirk [20].

In non dimensional variables the channel is 1.1 units high, 1.5 units long and 0.4 units wide. The step is 0.6 units high and is located 0.2 units downstream. The fluid is at rest initially. The inflow pressure ratio is 30.0 and the density

ratio is 5. This results then in a shock wave moving at Mach 5 which can be determined from the Rankine–Hugoniot relations.

The initial grid has 2269 nodes and 10167 elements. As adaptation criterion the absolute difference between density at neighboring nodes was used. Refinement was possible down to a minimum resolution of 0.0125.

Fig. 4.47 shows 3–D and 2–D contour plots of the density at  $t = 0.75$ . Density varies between 0.25 and 6. The 3–D plot shows in addition the mesh (113543 nodes and 592733 elements). The 2–D contour plot, which is cut through the center plane of the channel, contains 22 iso-lines for the same density range.

As we use an unstructured grid no odd-even decoupling was found, as was described by Quirk. In addition, no unphysical expansion shocks were observed at the corner of the backward facing step.

#### 4.4.4 Code verification for combustion modeling

Experiment i13 performed in the Munich–PHD tube was chosen as one experiment for validating the combustion model in REACFLOW. The experiment was made with 11.32 Vol.% hydrogen in air with 16 orifices with 60% blockage ratio consisting of transverse baffles spaced 185mm apart.

Fig. 4.48 (left) shows flame position versus time for the experiment and the simulation using different values for  $c_f$  in the turbulent combustion model. The initial flame acceleration is not calculated very well for all  $c_f$ -values chosen. This is caused by the fact that the eddy-dissipation model can not describe the initial flame, as it assumes burning is governed by the turbulent mixing rate in the flame. This assumption is only valid for a highly turbulent flame.

The 16 orifices are placed in the first 3m of the tube followed by a free section where the flame decelerates. This is observed in the experiment as well in the simulation. A remarkable observation is that although no orifices for turbulence generation are present in the tube between 3m and 6.5m, the flame stays at a rather high flame speed. This is caused by the fact that the flame itself generates strong turbulence.

In general, higher values of  $c_f$  cause higher flame speeds as the turbulent burning rate is proportional to  $c_f$ .

Fig. 4.48 (right) shows a comparison of pressure for experiment and simulation using a value of  $c_f = 3.75$ . As the flame accelerates to flame speeds much higher than the sound velocity in the unburned gas, high pressure peaks in front of the flame are generated. This can be seen in the experiment as well as in the simulation.

#### 4.4.5 Large scale detonation modeling

The last test-case we consider is a large scale true 3–D detonation simulation of the Russian RUT Facility located near Moscow. The facility has a total volume

of about  $263\text{m}^3$  in the present configuration. The volume has compartments of different size. There is a large volume, the so called canyon, followed by a long channel. The facility has a total length of 28m. Details of the geometry and the experiments performed can be found in [25].

For the simulation we chose test **hyd5** with a uniform hydrogen concentration of 20% hydrogen (by volume) in air at ambient conditions. The detonation was initiated by 200g of high explosives at a low position inside the canyon near the end wall. Experimental data were recorded by pressure transducers at various positions in the test facility.

The chemical source terms were calculated using the Finite-Rate scheme. We used a scheme with 8 elementary chemical reactions [27]. To avoid the well-known problem of numerical detonation speeds, we added a cutoff temperature for the chemical source terms below which no reactions take place, as suggested by Klein et al. [28]. The cutoff temperature was chosen as  $T = 1200\text{K}$ . This means only high temperature chemistry is taken into account, which is sufficient assumption for detonation modeling, because the detonation process is driven by the heat release due to chemical reaction. Heat release mainly occurs in the high temperature regime.

For the simulation with REACFLOW we used an initial grid with 3615 nodes and 15592 elements. The mesh distribution is nearly uniform. This corresponds to an initial resolution of  $\Delta x \simeq 0.5\text{m}$ . In the simulation the detonation was initiated by imposing a high temperature and pressure value for the nodes around the experimental ignition point. For the grid adaptation criterion the difference between pressure at neighboring nodes were used. Nodes were added down to a minimum resolution of 0.1m and, as a reference, to 0.075m. During the calculation nodes were added and removed up to a maximum of 70000 nodes for the coarse grid and 115000 nodes for the finer grid. Both calculations showed nearly the same results, so general grid convergence could be assumed. Results are shown for the weaker refinement.

Fig. 4.49 shows 3-D and 2-D contour plots of the pressure at  $t = 9\text{ms}$ . Pressure varies between 0.1MPa and 1.75MPa. The 3-D plot shows in addition the mesh (56024 nodes and 287099 elements). The 2-D contour plot, which is cut through the center plane of the channel, contains 22 iso-lines for the same pressure range. At this time the detonation has proceeded through the whole canyon and propagated 23m down the second part of the test facility. The reflected pressure waves at the end wall of the former can be seen clearly, especially in the upper part of the canyon. The detonation front which is running down the second part of the facility is clearly seen at this time, when the grid has 56024 nodes and 287099 elements. Nodes are added at positions of large pressure gradients. These are mainly found at the system of reflected shock waves and at the detonation front. Everywhere else the mesh is close to the initial mesh, as the nodes previously added have been removed.

Fig. 4.50 shows comparisons between experimental and simulated pressure

time history plots at 2 different positions in the canyon. The detonation velocity is 1750m/s in the experiment as well as in the simulation. At the position at which the data in Fig. 4.50 (lower) have been taken, the incoming shock wave propagates nearly perpendicular to the surface; therefore the peak pressure here is larger than in a case where the shock wave moves parallel to the surface (Fig. 4.50 upper). This can be seen in the experiment as well as in the simulated results. In general the peak pressures are under predicted due to the coarse resolution chosen. The thickness of the detonation wave itself is about two orders of magnitude smaller than the finest possible resolution in the adaptation. But in general the pressure peak itself does not contribute much to the impulse load on the confining structures, because of the short time-duration of the pressure peak.

Other pressure peaks are generated by reflected shock waves between the side walls. These pressure peaks arise due to the fact that the detonation at first propagates freely with a spherical shape, then this spherical detonation interacts with the confining walls of the facility. By this mechanism reflected waves are formed. It is a little surprising that not all reflected waves are found in the simulation. This may be because the detonation was initiated in the simulation by high initial pressure and temperature at a node point near the physical ignition point including also all the neighbors of this node point. This is a rather coarse representation of a real point ignition by a high explosive.

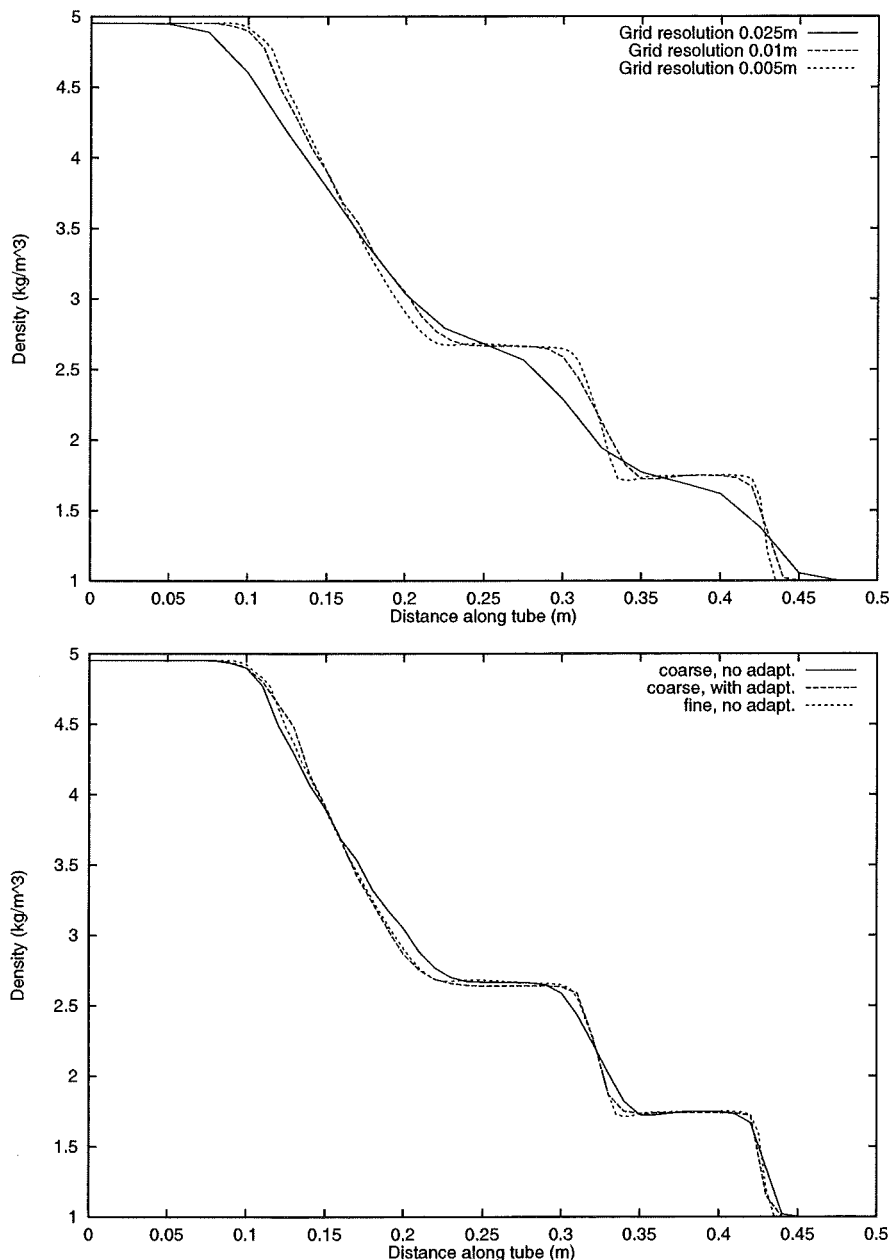
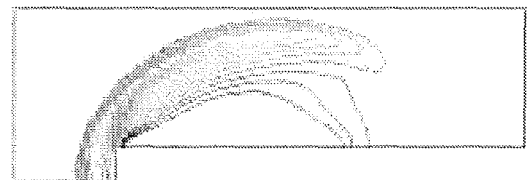
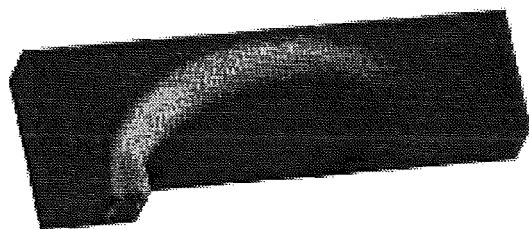
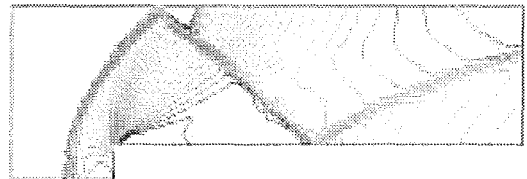
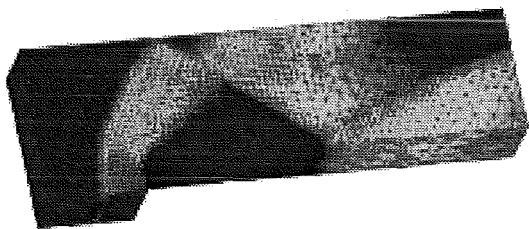


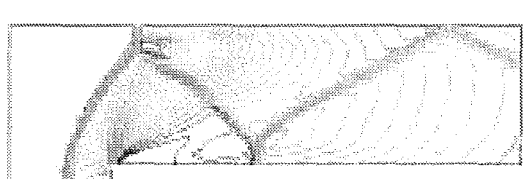
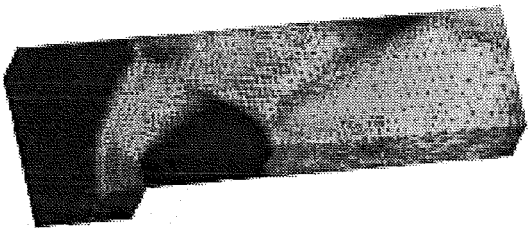
Figure 4.45: Density profile in the shock tube at time  $t = 4 \cdot 10^{-4}$ s after the release of the shock. Upper: profiles for three different grid resolutions using everywhere the 2nd order convective solver without grid adaptation. Lower: A comparison between results on two different fixed grids (with, respectively,  $\Delta x = 0.01$ m and  $\Delta x = 0.005$ m) and a result using the coarser grid and grid adaptation.



$t=0.5$  27693 nodes and 140735 elements



$t=2.0$  39065 nodes and 198542 elements



$t=4.0$  43510 nodes and 220403 elements

Figure 4.46: Supersonic flow over a forward-facing step. 3-D calculation with 2nd order convective scheme and grid adaptation. Left figures show the surface iso colors and the surface grid. Right figures show iso-lines for a 2-D cut through the channel.

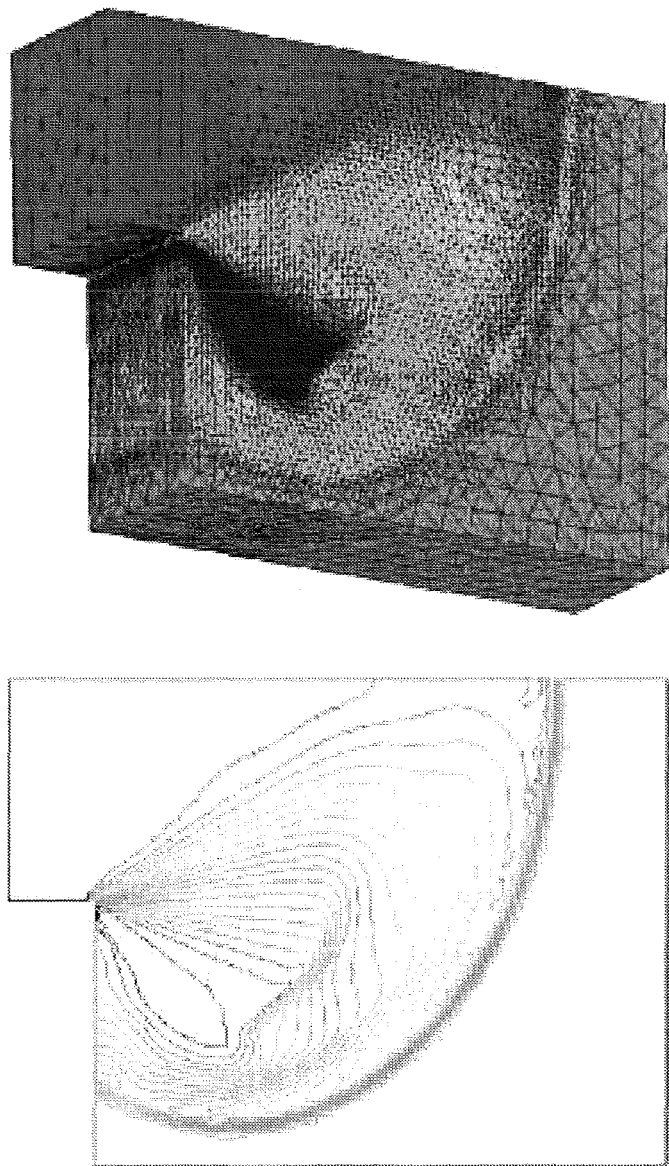


Figure 4.47: Supersonic diffraction over a backward-facing step. 3-D calculation with 2nd order convective scheme and grid adaptation. Upper figure shows the surface iso colors and the surface grid. Lower figure shows iso-lines for a 2-D cut through the channel.

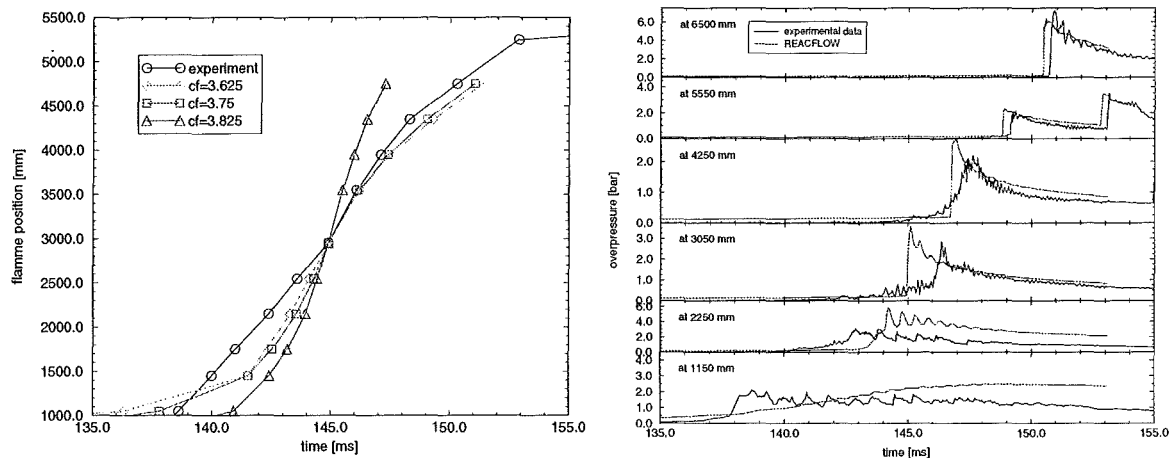


Figure 4.48: Comparison of experimental and simulated data for 11.32 Vol.% hydrogen in air. Flame-position versus time (left) and pressure at different positions along the tube versus time (right) with  $c_f = 3.75$  for the simulated data.

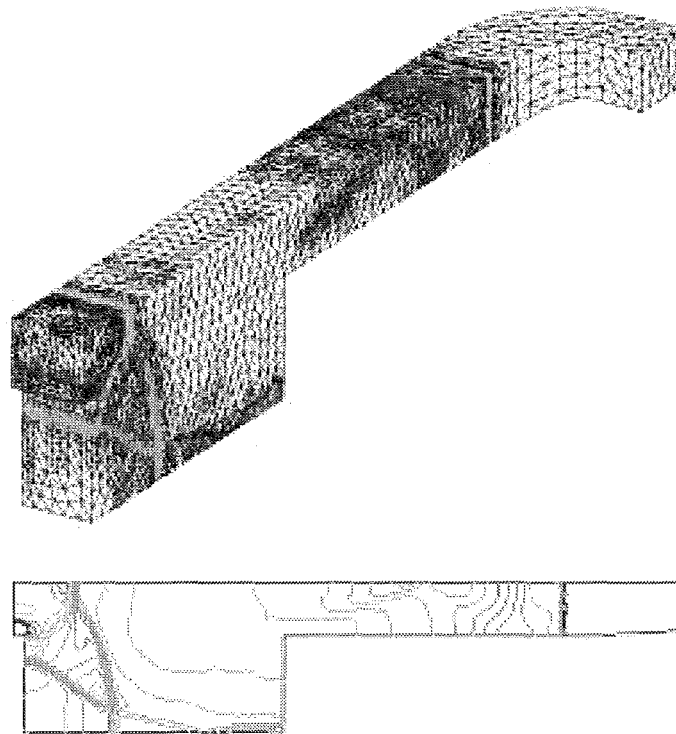


Figure 4.49: RUT detonation. Pressure iso-lines and surface grid at time  $t = 9\text{ms}$  after ignition.

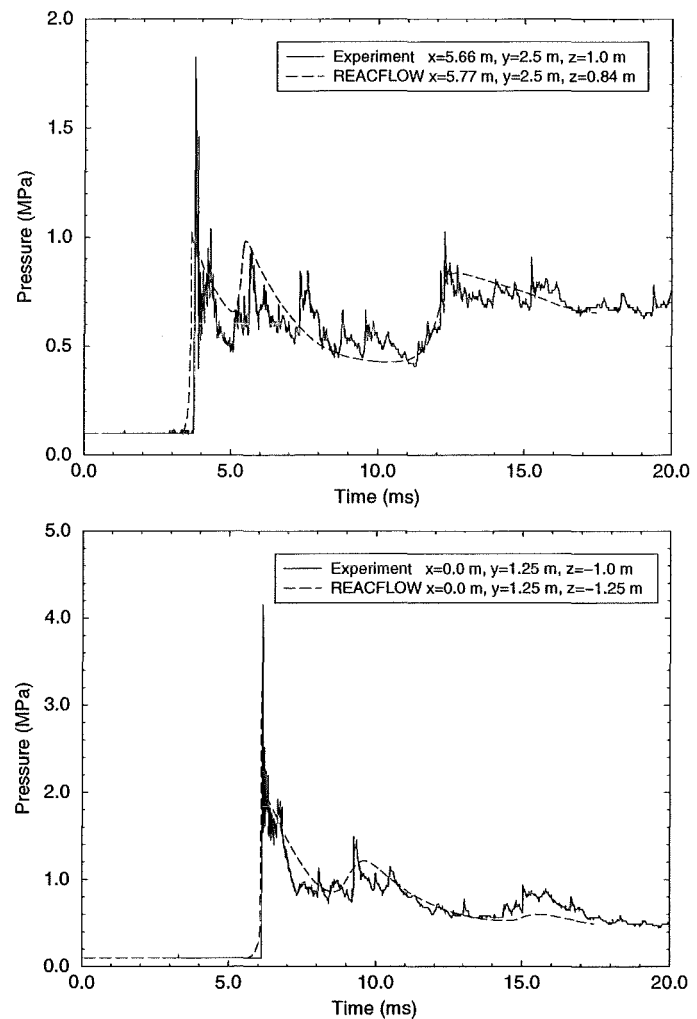


Figure 4.50: Hydrogen detonation in the RUT facility. Pressure versus time for two positions inside the canyon (upper is a sidewall, lower is an end wall position).

## 4.5 Combustion code from TUM

### 4.5.1 Geometry

The applied PDF combustion model is verified with agreed benchmark test cases. These benchmark experiments have been carried out in the PHD-tube (15 obstacles with 60% blockage ratio) and the FZK 12m combustion tube (23 obstacles with 30% blockage ratio), which were described in section 2. The meshes for the tubes used by the numerical simulations are based on a blockstructured topology.

In Fig. 4.51, the mesh of the PHD-tube, used for the benchmark test calculations is shown. This mesh consists of about 6700 control volumes. In order to avoid degenerated cells in the center of the tube, a butterfly topology has been used, i.e. an H-grid topology in the center of the mesh is connected to a surrounded O-grid topology (see Fig. 4.51). Due to the symmetry of the investigated problem only one half of the tube is considered. A further reduction is not possible as buoyancy effects have to be taken into account for the investigated combustion regime. In the region where the mixture is ignited the grid is refined. Since the obstacles are placed only in the first half of the tube, a coarser grid resolution is used behind the last obstacle.

The mesh of the FZK 12m combustion tube is generated in a different way to the mesh for the PHD tube. In order to achieve a better spatial resolution in the direction in which the flame propagates a two dimensional grid based on cylindrical coordinates is used for the combustion calculations. The mesh consists of about 35000 cells.

### 4.5.2 Boundary conditions and initialization

At the walls slip conditions are defined for the momentum equation. The use of slip boundary conditions is valid in the considered combustion processes, because the expansion flow passing through the obstacles placed in the tubes dominates the turbulence production. Therefore, shear stress at the walls serving as a turbulence promotor can be neglected.

Concerning the energy equation an adiabatic boundary conditions is set. Test calculations revealed that the use of a constant ambient wall temperature, which is suggested by Ardey [46], has no significant influence on the combustion simulation.

It is often suggested when doing combustion simulations in closed facilities to use an ignition model (e.g. [32]) in order to get a good approximation of the start up process, and to overcome the problem of the initialization of an existing flame front and the concerning flow field. Within this project an ignition

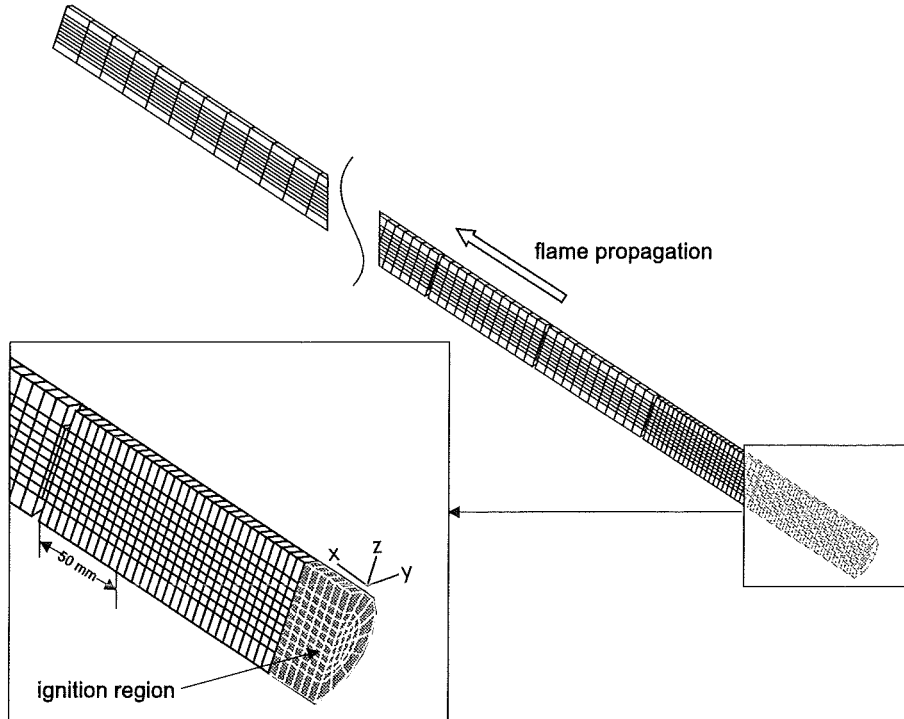


Figure 4.51: Mesh for the PHD tube

model based on a hemispherical laminar flame propagating from the ignition point has been implemented. In the further verification process and the comparison to the experimental data, the ignition process has been found out to be not significant for the investigated geometries. In order to simplify and to speed up the whole calculation the ignition model is not used for the tube geometries but it is available for other geometries, in which the ignition process gets important. For the initialization of the combustion process, a preburned area in the ignition region (see Fig. 4.51) is defined. In this region the value for the reaction process is set to  $\tilde{c} = 1.0$  (fully burned) and the temperature to the corresponding value. In order to push the flame in this state and to avoid an extinction a slightly higher pressure is set in the ignition region. Because the flow is also expected to be turbulent an initial guess for the values for  $k$  and  $\epsilon$  has to be set in the ignition area. It has to be emphasized that the calculation revealed not to be sensitive on the initial choice of  $k$  and  $\epsilon$ . With the applied initialization strategy for the benchmark tests, the combustion simulation is expected to overpredict the flame speed in the very early stages of the combustion process. After passing the first obstacles no influence of the ignition process on the flame propagation is observed.

### 4.5.3 Numerical control

In principle the time resolution should be chosen in a way that it is possible to resolve the occurring pressure waves. With respect to the grid resolution the time step should be of the magnitude

$$\Delta t < \frac{\Delta x}{a_0}, \quad (4.8)$$

where  $a_0$  is the speed of sound in front of the flame (unburned gas). In combustion simulations pressure waves occur, which possibly propagate much faster than the speed of sound  $a_0$ . The time step has to be adjusted taking into account the expected propagation speed of the pressure wave and the flame front. This is an absolute necessity if the numerical solution of the flow field is calculated explicitly for reasons of the stability of the solution process. In the case of an implicitly calculated flow field the time step can be set higher with the consequence that pressure waves are not clearly resolved.

In the performed combustion simulations the following time steps have been chosen:

- PHD tube:  $\Delta t = 2 \cdot 10^{-5}$ s
- FZK tube:  $\Delta t = 2 \cdot 10^{-5}$ s

#### 4.5.3.1 PDF reaction rate

The basis of the applied PDF combustion model is the definition of the production rate  $w_c(c)$ . As pointed out previously this can be done by evaluating the results of a detailed calculation of a premixed laminar propagating hydrogen-air flame. For this calculation the chemical kinetic code Insfla (programmed by Maas [39] and [40]) is used. The production rate  $w_c(c)$  strongly depends on the initial conditions of the hydrogen-air mixture, i.e., the hydrogen concentration, the pressure and the temperature. For the verification of the combustion model by means of the experiments a mixture of 13vol%  $H_2$  in air for the PHD tube and a mixture of 11vol%  $H_2$  in air for FZK tube was chosen as a reference example. The initial condition for the pressure  $p_0 = 1$  atm and for the temperature  $T_0 = 293.0$  K were defined.

For a given production rate  $w_c(c)$ , the PDF reaction rate is calculated by solving the folding integral of the production rate with the PDF (see Sect. 3.1.5). Additionally, the source term  $\widetilde{c''w_c}$  used in the transport equation for the variance  $\widetilde{c''^2}$  is calculated. These calculations are performed before the PDF combustion simulation and the results are stored in tables (see Fig. 4.52 and Fig. 4.53 for 13vol%  $H_2$  in air and Fig. 4.54 and Fig. 4.55 for 11vol%  $H_2$  in air). The numerical simulation is performed by applying a table-lookup procedure.

#### 4.5.4 Combustion simulation

The experimental results allow two possibilities for the verification of the numerical simulations. The first is the comparison of the flame propagation, i.e., the location of the flame front in the tube in dependence of time. The second possibility is the comparison of the pressure distribution at a certain position over the time.

By comparing the flame propagation, the flame position is determined from the numerical simulation by detecting the isoline of the progress variable (see section 3) of  $\tilde{c} = 0.5$  along the line placed in the middle of the tube for each time step. With this method, it is possible to extract the flame position in dependence of the time. For a better comparison, this curve is shifted in time in a way that the measured and the calculated curve have a common outset. In case of the the benchmark calculations concerning the PHD tube, this is done by defining the point at which the flame front in the experiment has passed the tube-length of  $z = 0,4$  m as reference point. The common outset for the benchmark calculations in the FZK tube is placed at the point  $z = 0,7$  m. This procedure is necessary, as the ignition and the start-up processes are not calculated. Due to the applied initialization, a short acceleration of the flame followed by a deceleration is observed in the very beginning of the combustion simulation. Starting from the reference point no more influence of the performed initialization can be seen.

In order to compare the pressure distribution with the experimental data, the calculated curve is shifted in time by the same value as for the flame propagation curve.

##### 4.5.4.1 Comparison of calculation and experiment concerning the PHD tube

A comparison between the flame propagation measured in the experiments and the calculation revealed a significant difference, which is shown in Fig. 4.60. The calculated flame speed is considerable slower compared to the measurement. The difference can be explained by having a closer look at the flame propagation: The maximum measured flame speed is of the magnitude of 600 m/s. By the fact that this is a supersonic propagation related to the initial mixture, a direct interaction of the flame front and the induced pressure wave is taking place. In the case of the 13vol%  $H_2$  in air combustion process in the PHD tube it can be found that after the ignition process and the passing of the first obstacles the flame front is coupled to the pressure wave due to the strong acceleration of the flame in this region. In Fig. 4.56 the described coupling is shown at a position of  $x = 2.25$  m. After passing the last obstacle the flame decelerates and a decoupling of the

pressure wave occurs. This behaviour can be seen in the lower picture of Fig. 4.56 where the flame front and the pressure distribution is shown over time at the position  $x = 4.25$  m, which is located in the second half of the tube.

The coupling of the flame front and the pressure wave has the consequence that the flame is burning into a mixture with a thermodynamic state, which is different from the initial conditions of  $T_0 = 293.0$  K and  $p_0 \approx 1$  atm. In this case the combustion takes place in an area which is due to the compressing effect of the shock wave characterised by a higher pressure and enthalpy level, which causes significant higher reaction rates. A comparison between the ‘laminar’ reaction rates in dependence of  $\tilde{c}$  ( $w_{H_2O}(c)$ ) starting from two different initial conditions is shown in Fig. 4.57. For the initialization with a higher pressure and enthalpy level a pressure of  $p_0 = 6$  bar and a temperature of  $T_0 = 488$  K has been chosen. The pressure level is extracted from the measurements and the temperature is calculated by assuming an isentropic change of the thermodynamic state. As can be seen in Fig. 4.57 the reaction rates vary by orders of magnitude. It has to be emphasized that the change of the ‘laminar’ reaction rate  $w_{H_2O}(c)$  has of course a strong influence on the PDF reaction rates.

As the consideration of changes of the enthalpy and pressure level during one calculation is not yet implemented in the applied PDF model, the following approach is applied: In order to improve the numerical simulation in the part of the tube where the flame is accelerated to its maximum speed, the calculation is performed with a PDF reaction rate based on the actually occurring pressure and temperature level. It has to be emphasized that the definition of these levels is a very rough approximation but is appropriate enough to prove the assumptions. Of course, this strategy will lead to an overestimation of the reaction rate during the start up process and the end of the combustion process, but will be a good approximation if the flame front is coupled to the pressure wave. In Fig. 4.58 and Fig. 4.59 the tables containing the new PDF reaction rates are shown.

In Fig. 4.60 the calculated flame propagation based on the modified PDF reaction rates is shown. It can be seen that within the start up process the flame speed is overestimated. This originates on the one hand due to the initialization and on the other hand due to the earlier described overestimation of the reaction rate in this region. Comparing the region from 1 m to 3 m distance from the ignition point, a good agreement between the calculation and the experiment can be seen. The maximum flame speed is well predicted with the calculation. In this region the assumption of the coupling of the flame front and the pressure wave is valid. After passing the last obstacle (at  $x = 3$  m) the calculated PDF reaction rate overestimates the real reaction rate and, therefore, the flame speed is not predicted accurately. The simulation was performed up to the time when the flame front reached the end of the tube.

For the comparison of the pressure distribution over the time of the calculation and the experiment, the position  $x = 2.25$  m is chosen. As mentioned above

the pressure trace is shifted in time by the same value as the flame propagation curve. Therefore, the calculated pressure wave is arriving earlier than the measured one. As can be seen in Fig. 4.61 the pressure level and distribution behind the maximum peak is well predicted. But the calculation is not able to predict the maximum pressure peak, as the chosen resolution in time (time step size of  $\Delta t = 2 \cdot 10^{-5}$  s) and space ( $\Delta x \approx 0.04$  m) is not accurate enough.

In Fig. 4.62 the flame front and the concerning turbulence field are depicted in the range of  $2.5 \text{ m} \leq x \leq 3.0 \text{ m}$  of the PHD-tube during the combustion process. It can be seen that due to the propagation of the flame front with a velocity faster than the speed of sound of the initial mixture, the turbulence field is induced together with the arrival of flame front.

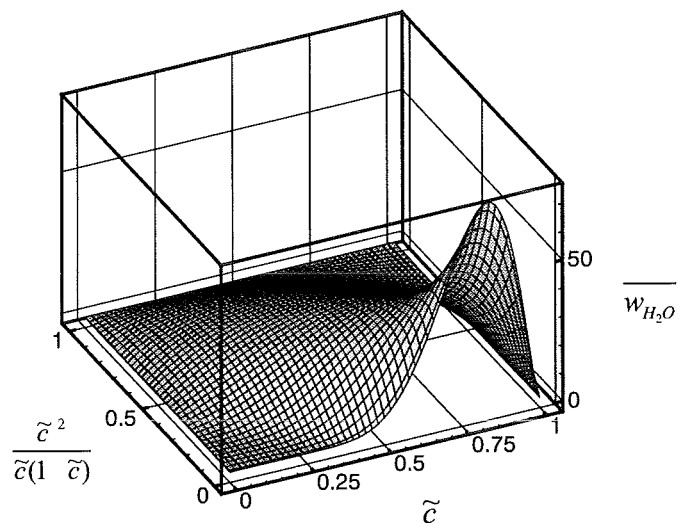


Figure 4.52: PDF reaction rate for 13vol%- $H_2$  in air

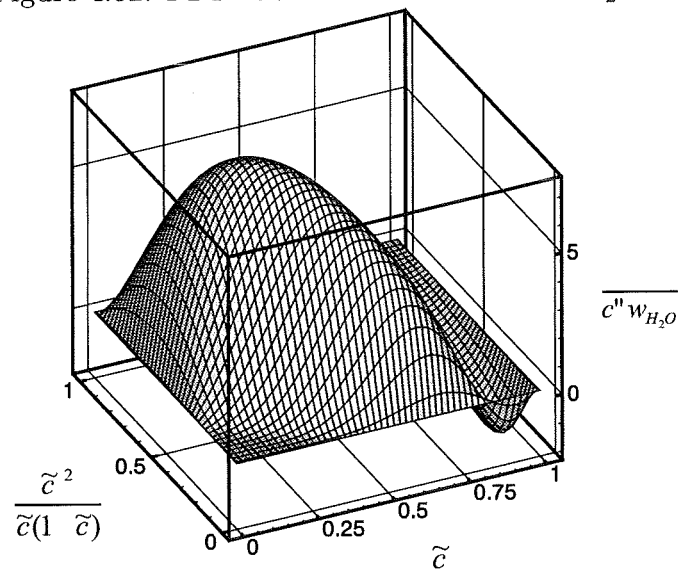


Figure 4.53: Source term for the variance due to the chemical reaction for 13vol%- $H_2$  in air

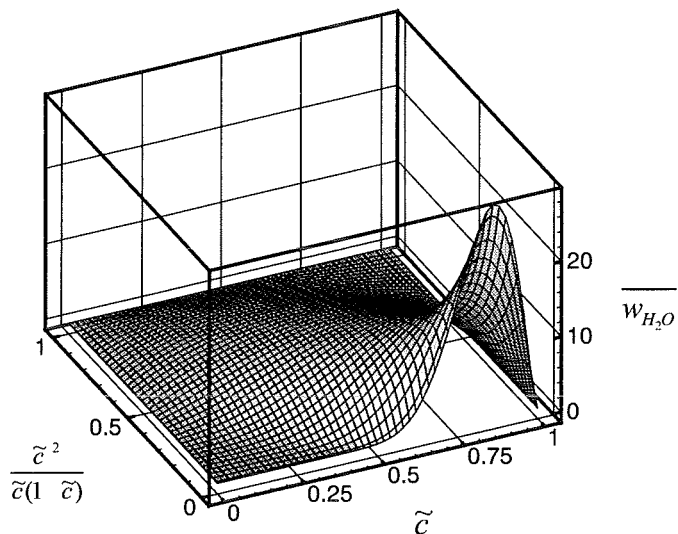


Figure 4.54: PDF reaction rate for 11 vol%  $H_2$  in air

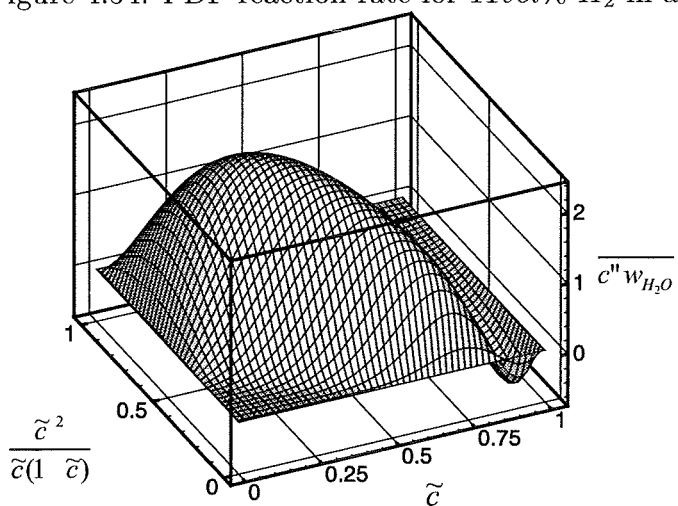


Figure 4.55: Source term for the variance due to the chemical reaction for 11 vol%  $H_2$  in air

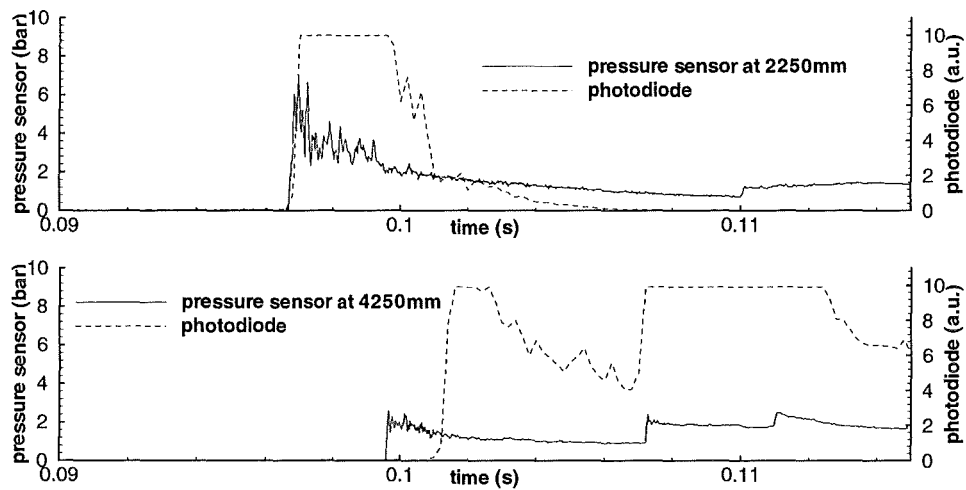


Figure 4.56: Flame front and pressure wave interaction in the PhD-tube (13vol%  $H_2$  in air combustion process)

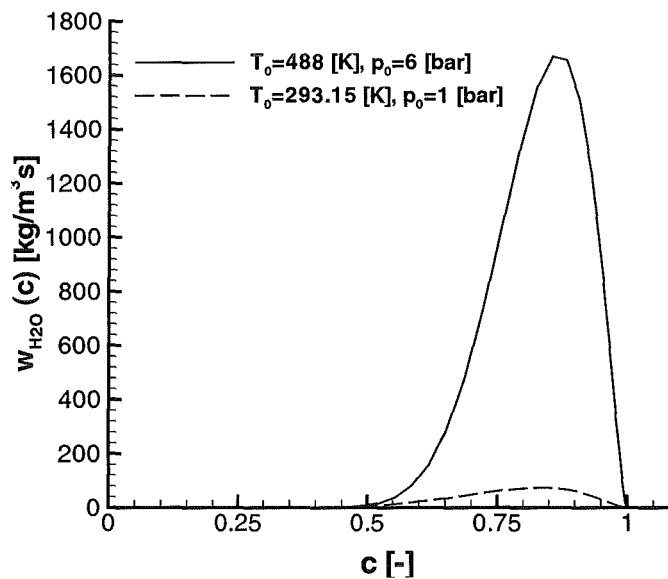


Figure 4.57: Reaction rates for 13vol%  $H_2$  in air in dependence of  $\tilde{c}$ , starting from different initial conditions

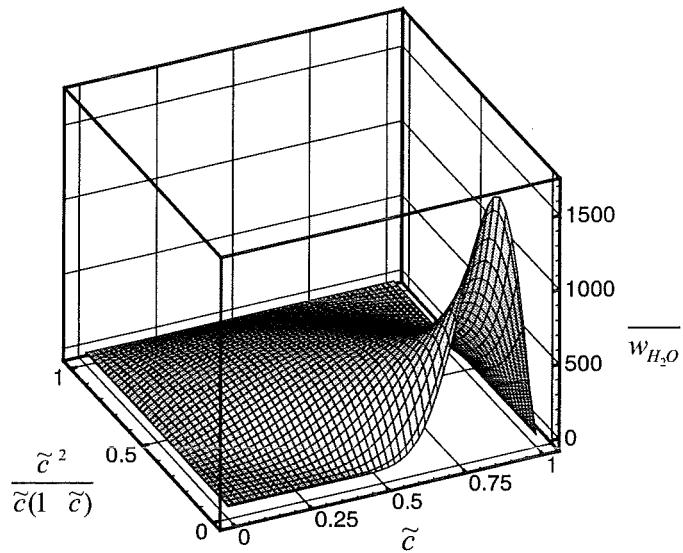


Figure 4.58: PDF reaction rate for 13vol%- $H_2$  in air starting from a higher pressure and enthalpy level ( $p_0 = 6$ ,  $T_0 = 488$ )

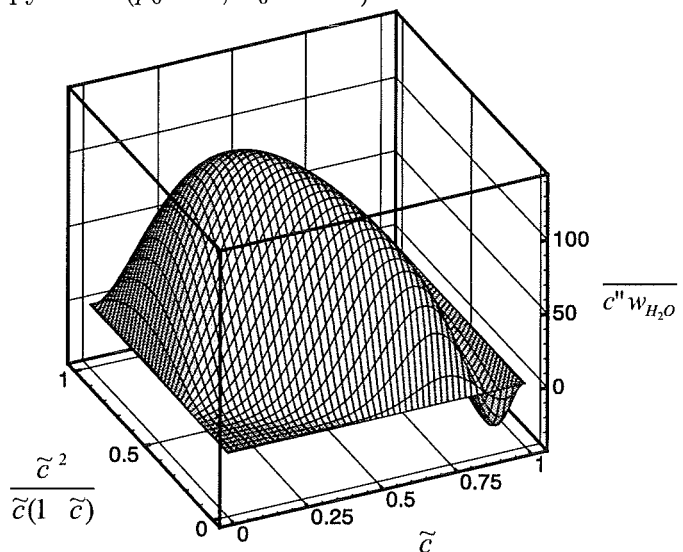


Figure 4.59: Source term for the variance due to chemical reaction for 13vol%- $H_2$  in air starting from a higher pressure and enthalpy level ( $p_0 = 6$ ,  $T_0 = 488$ )

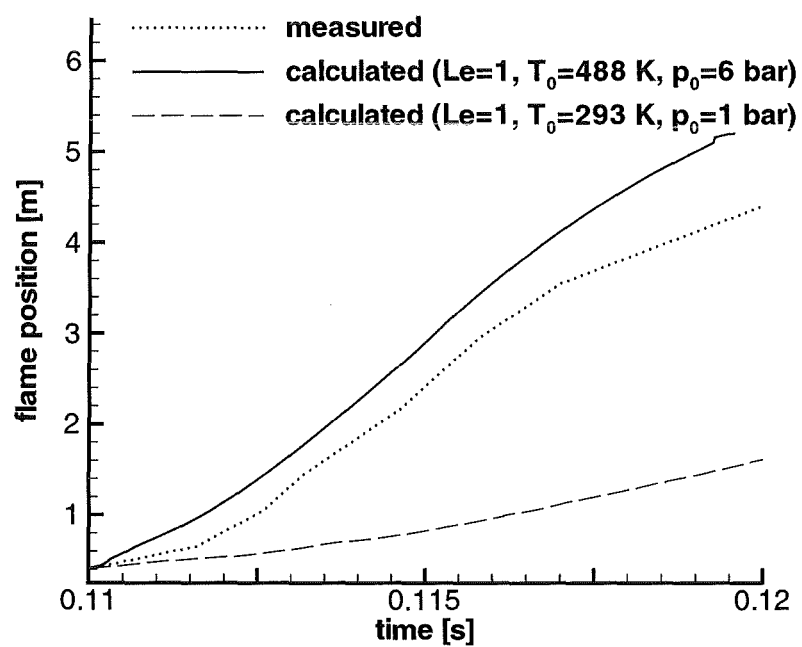


Figure 4.60: Comparison of experimentally determined data with numerical calculations of the flame propagation in the PHD tube for a 13vol%- $H_2$  in air mixture

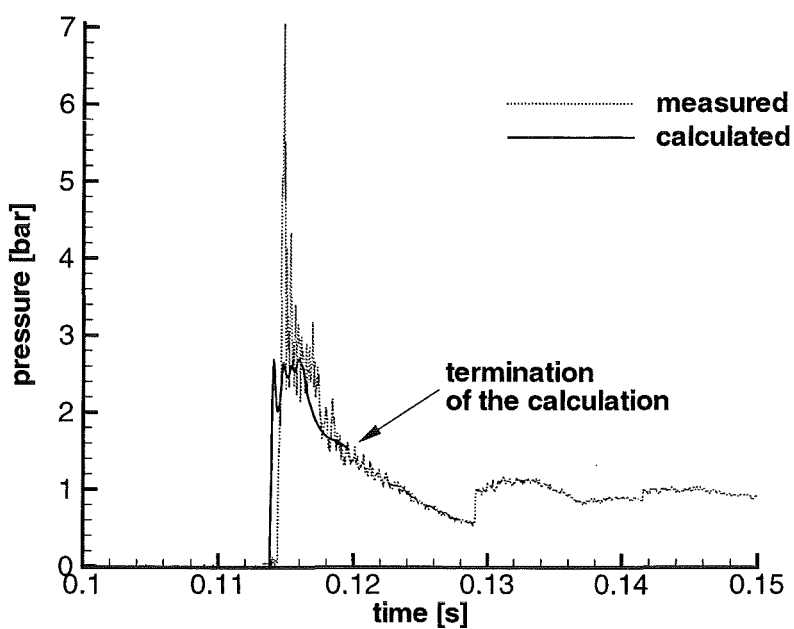


Figure 4.61: Comparison of the pressure distribution between experiment and calculation

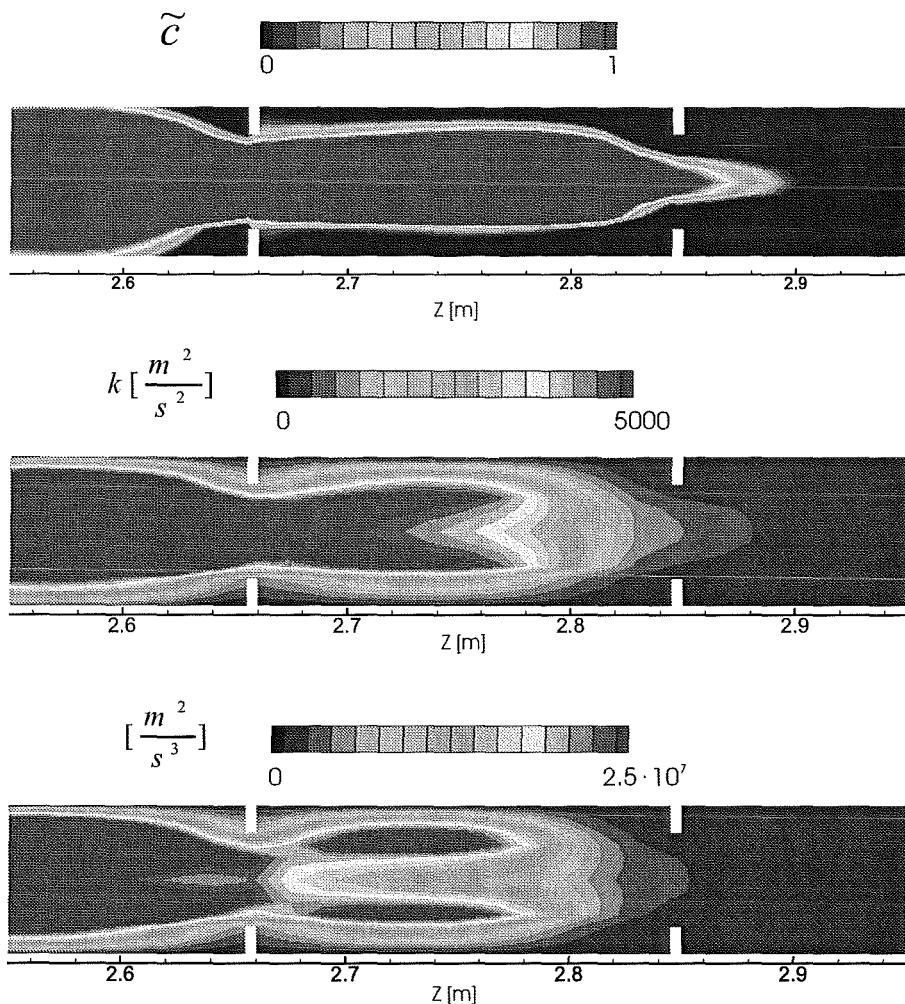


Figure 4.62: Flame front and the turbulence field during the combustion process in the PHD tube (13 vol%  $H_2$  in air)

## 4.6 Benchmark calculations

For a direct comparison of the different numerical codes a set of experiments was selected. Due to the different restrictions of the different codes not all benchmarks could be calculated with all codes. Here we only discuss test cases that were calculated by at least two partners. The selected experiments are listed in table 4.10.

Table 4.10: Benchmark calculations for code comparison

Experiment	Description	Participants
FZK-TUBE R1096-03	inert shock tube test, BR = 0.3	FZK, JRC
TUM PHD-tube i16	12.94 % $H_2$ , BR = 0.6	JRC, TUM
TUM PHD-tube i15	14.89 % $H_2$ , BR = 0.6	FZK, JRC
FZK-Tube R0498_07	10 % $H_2$ , BR = 0.3	CEA, JRC
FZK-Tube R0498_02	11 % $H_2$ , BR = 0.3	FZK, JRC, TUM
FZK-Tube R0498_05	12 % $H_2$ , BR = 0.3	FZK, JRC

### 4.6.1 Helium shock tube test as benchmark for the numerical solver

As a benchmark test case of the numerical solvers involved in this project, experiment R1096\_03 from the experiments performed in the FZK-Shock-Tube was used. The details of the experiment are described in the experimental part of the report (see chapter 2).

For the benchmark numerical results from COM3D and REACFLOW are compared with experimental results. Two different calculations using COM3D and three different using REACFLOW were made.

For both COM3D calculations a 3-D grid with a constant resolution of 1cm was used. For the first simulation standard  $k - \epsilon$  turbulence model was used, for the second simulation the RNG-turbulence model was used.

For the REACFLOW calculations two different 2-D grids were used for the axisymmetric version of REACFLOW. The first grid has non-constant resolution. Around the obstacles the resolution was 1cm, everywhere else the resolution was about 2.5cm. Simulations using this grid were always made using the adaptive grid refinement method of REACFLOW, as it was described before. During the simulations the number of grid nodes increased from 5000 nodes of the initial grid up to 11000 nodes maximum. For the evaluation of the grid effects a reference simulation was made on an a fine constant grid with 27600 nodes and a resolution of 1cm everywhere.

For the first simulation using the adaptive grid turbulence was modeled using REACFLOWS standard  $k - \epsilon$  turbulence model. The second simulation was done using the same turbulence model, but using the constant fine grid. The third simulation is done without any turbulence modelling at all, using only REACFLOWS convective solver.

Figures 4.63 to 4.71 show comparisons between experimental pressure data and calculated pressure for various positions in the low pressure section of the tube against time. The time behavior is very well represented (565m/s velocity for the incoming shock wave). The pressure peaks are sometimes a little under- or over-predicted, but are very similar for all simulations.

Starting from the 9m position, the shock moves toward the first obstacle, as can be seen in Figures 4.63 – 4.65. At the same time an expansion wave runs from the 9m position towards the end of the tube (12m). At 6m part of the shock is reflected at the first obstacle, as can be seen from fig. 4.65. This reflected shock travels back towards the high pressure section of the tube (figures 4.64,4.63).

Part of the shock, which has passed the first obstacle, is reflected again at the next obstacle, but this does not generate a new shock-wave, because this shock-wave will interact with the expansion wave in the wake of the obstacle before. Therefore only one single shock will reach the end-wall at 0m, which can be seen in fig. 4.71.

Overall the calculations indicate, that for this test case turbulence does not have a great influence, as results do not differ very much, when using different turbulence models, or no turbulence model at all. Also, there is no significant difference between adaptive and constant fine grid.

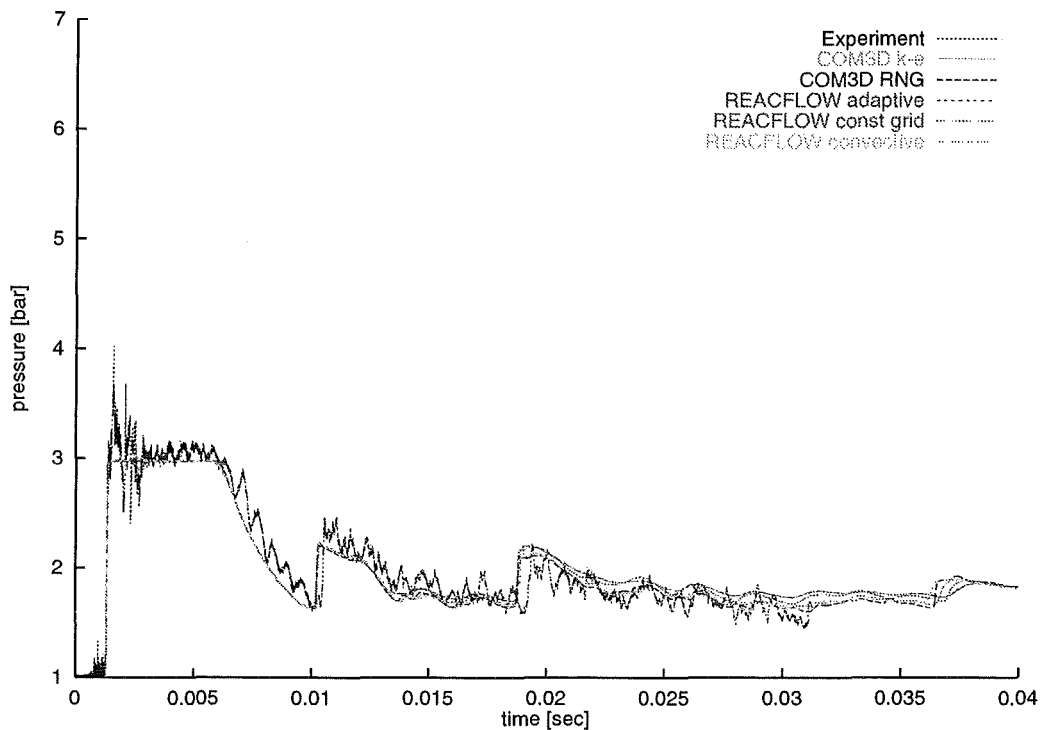


Figure 4.63: Pressure histories for test case R1096\_03 at position 8.25 m

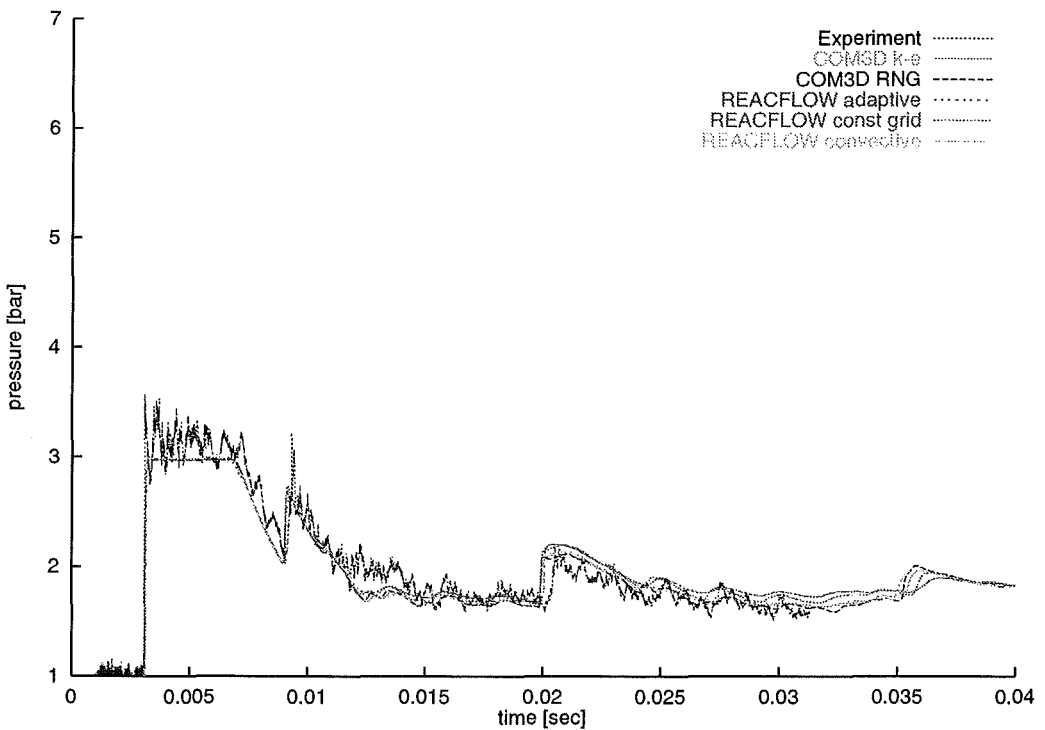


Figure 4.64: Pressure histories for test case R1096\_03 at position 7.25 m

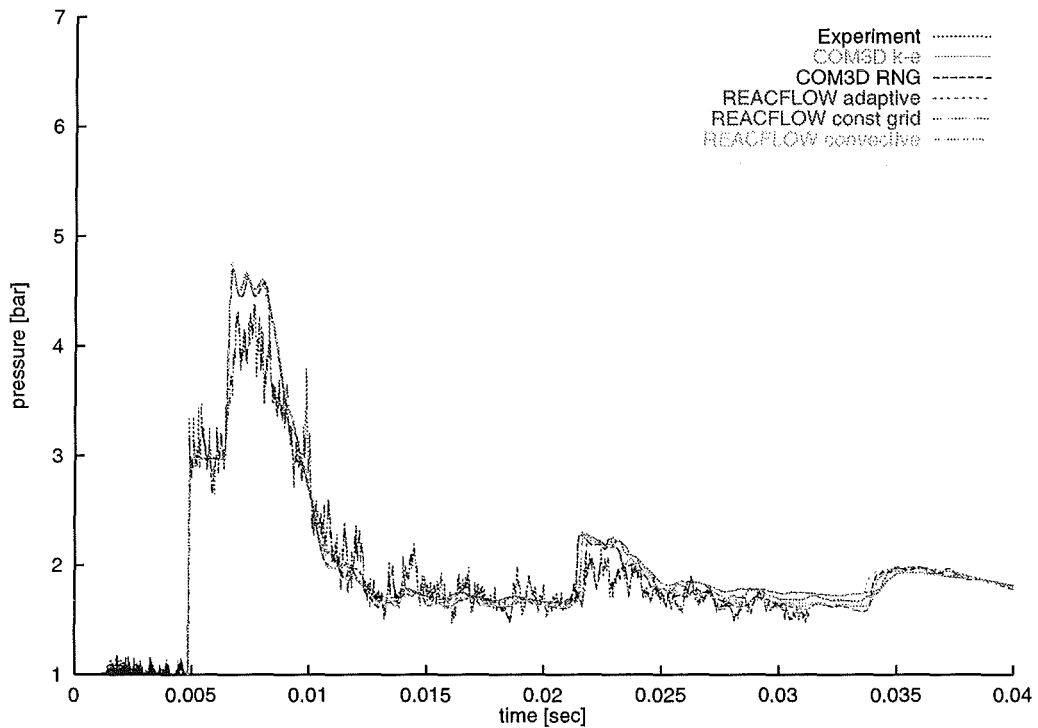


Figure 4.65: Pressure histories for test case R1096\_03 at position 6.25 m

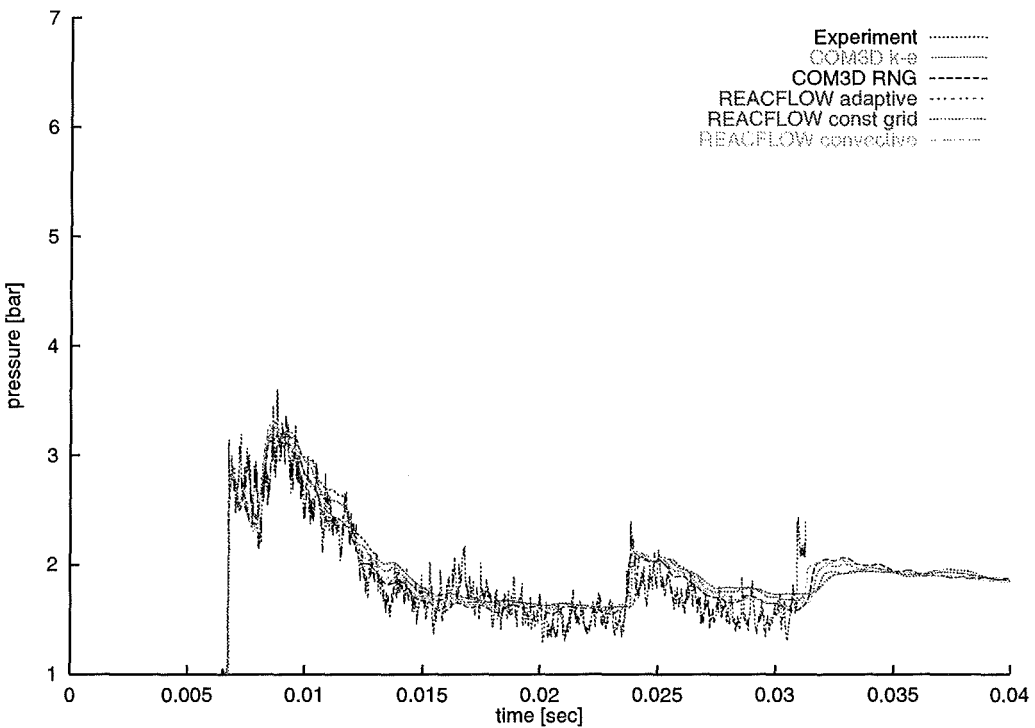


Figure 4.66: Pressure histories for test case R1096\_03 at position 5.25 m

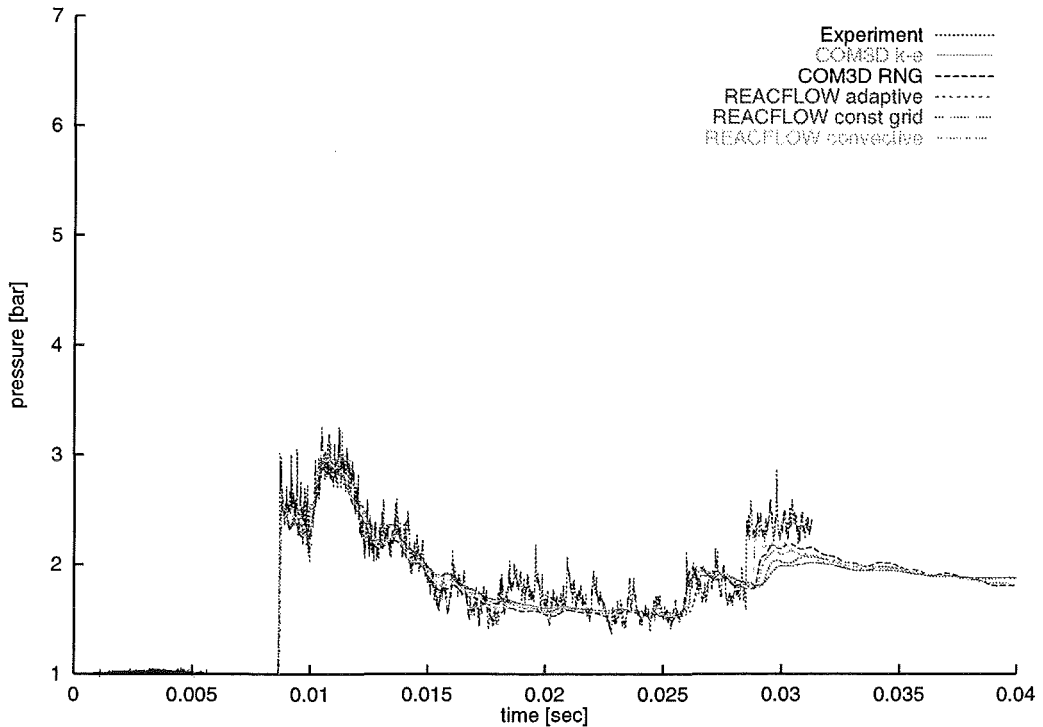


Figure 4.67: Pressure histories for test case R1096\_03 at position 4.25 m

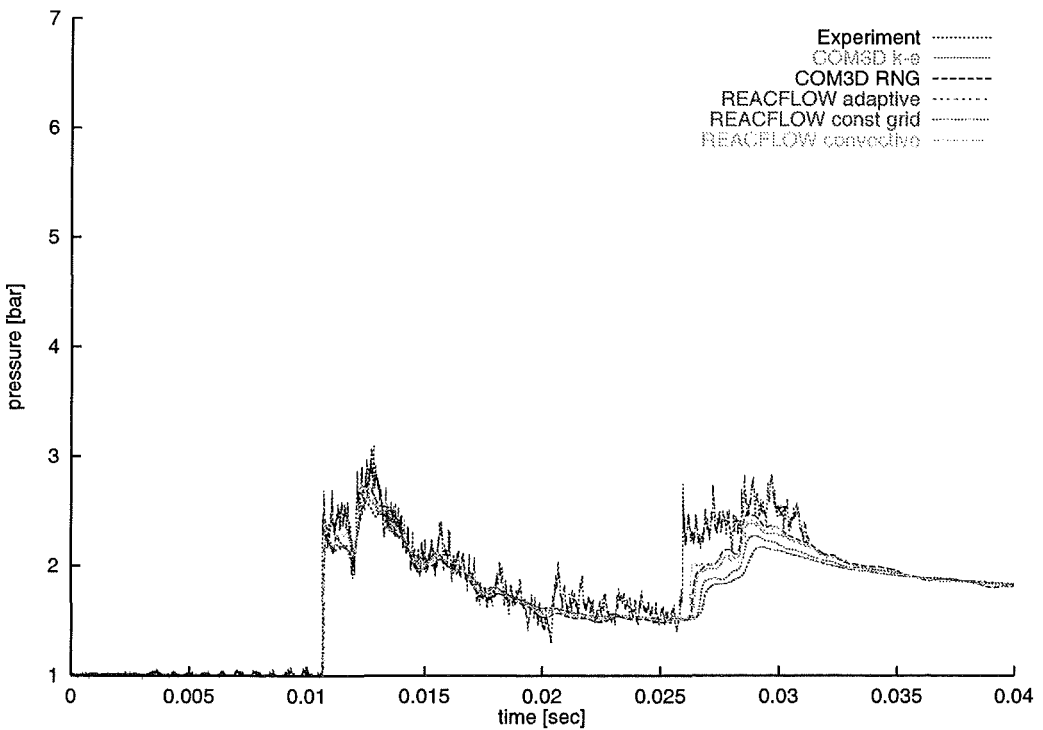


Figure 4.68: Pressure histories for test case R1096\_03 at position 3.25 m

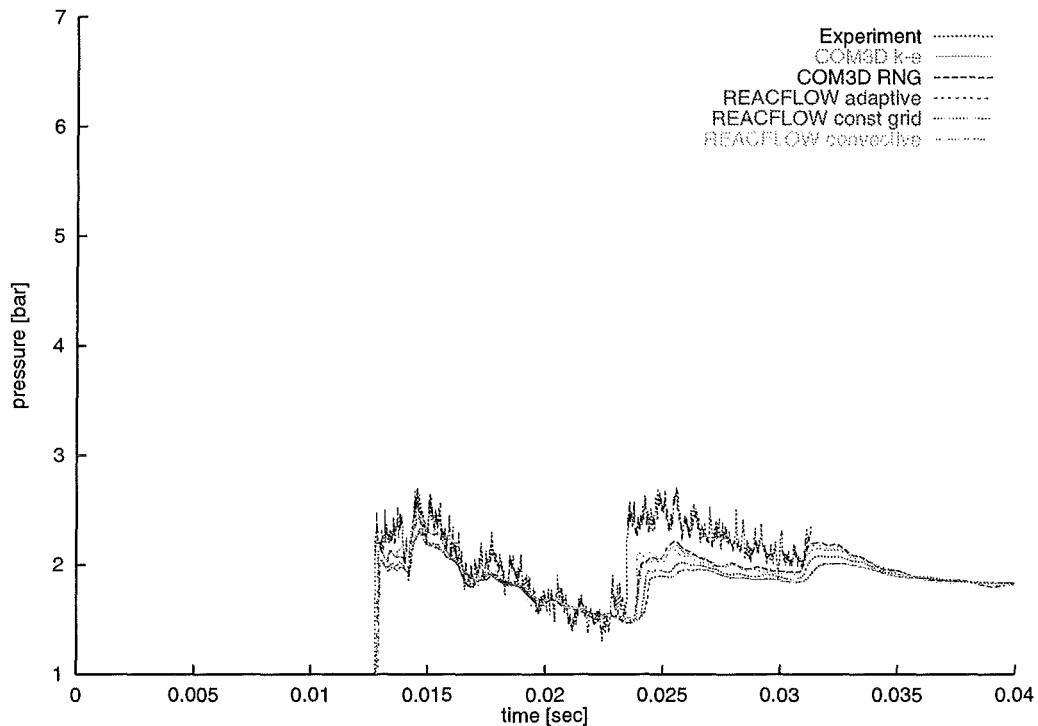


Figure 4.69: Pressure histories for test case R1096\_03 at position 2.25 m

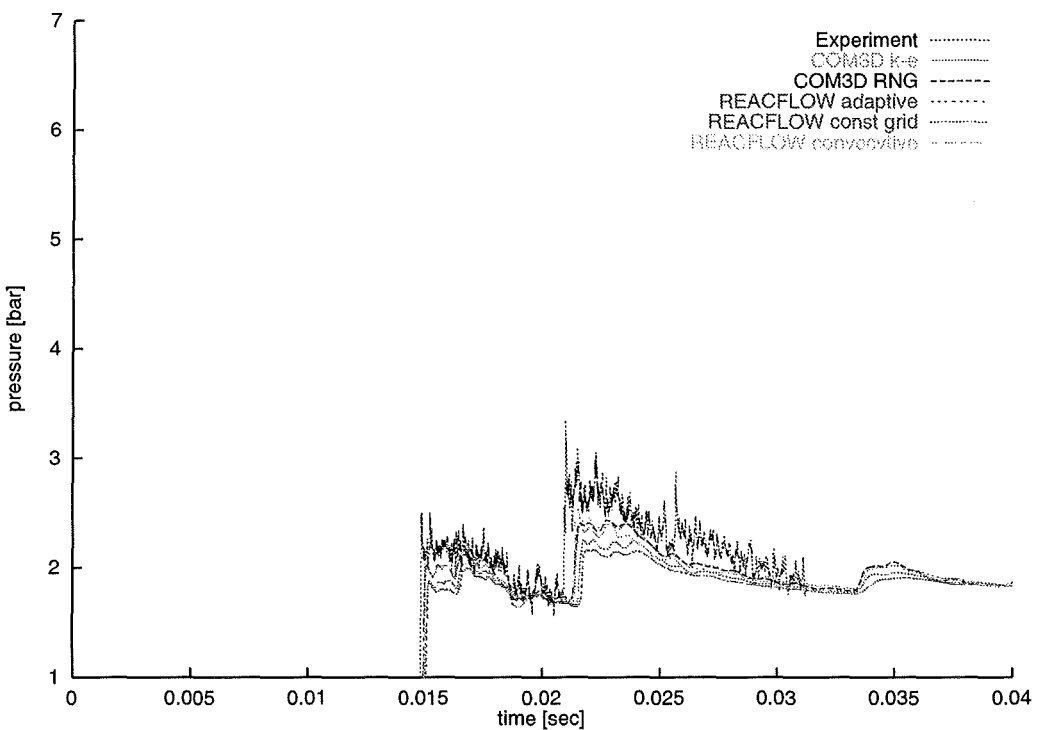


Figure 4.70: Pressure histories for test case R1096\_03 at position 1.25 m

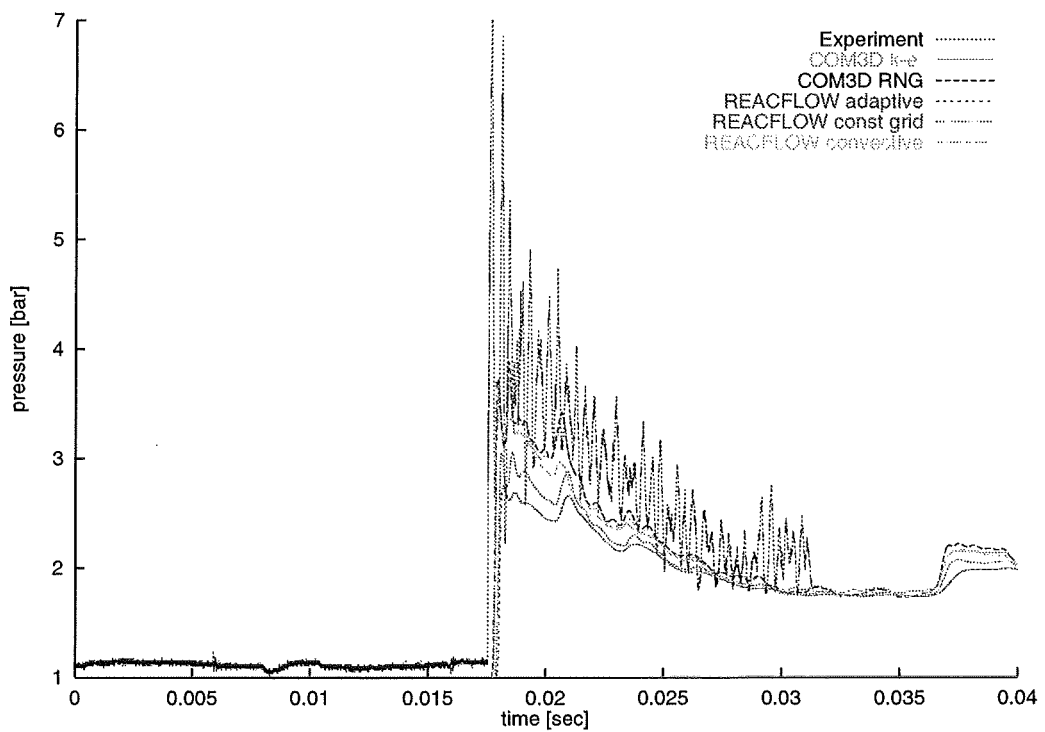


Figure 4.71: Pressure histories for test case R1096\_03 at position 0.0 m

### 4.6.2 Small scale tests in PHD-tube

In chapter 2 the experiments performed by TUM in the PHD tube were discussed in detail. With a tube length of 6.5 m and a tube diameter of 66 mm the experiments are on the smallest scale considered in the numerical simulations. For the benchmark calculations two of these experiments were selected. Both experiments have a blockage ratio of 0.6 and an obstacle spacing of 296 mm. The difference between the two test cases is the mixture composition. Case I16 with 12.94 %  $H_2$  by volume is a relatively slow combustion process, while Case I15 with 14.89 %  $H_2$  resulted in a rather fast flame propagation.

#### 4.6.2.1 Test case I16 - 12.94 % $H_2$ by volume

The initial conditions for this test case in the experiment were  $p_0 = 1.002\text{bar}$  and  $T_0 = 294.28\text{K}$ . The test case was calculated by TUM and JRC. Due to the different combustion models used by the two codes the presentation of the numerical results is somewhat different. The results of the TUM calculation are given in section 4.5 as example for a model verification calculation. Thus only the results from JRC are discussed here.

##### 4.6.2.1.1 Results from JRC

Test case I16 was also calculated with REACFLOW. Figure 4.72 shows the flame front position as function of time for three different values of the constant  $c_f$  in the eddy break-up model together with the experimental data. It is obvious that the calculation does not cover the initial phase of the experiment well. The flame propagation is much to slow in this phase. Therefore the calculated flame front positions are shifted in time to give good agreement during the phase were the highest flame velocities are observed, that is between 1.5 and 3.0 m. For all three values of  $c_f$  the agreement between experiment and calculation is rather good while there are no differences between the different calculations. Behind the obstacles the flame decelerates and now an effect of the different  $c_f$  values becomes evident. For the larger  $c_f$  values the flame decelerates not fast enough. The best agreement between experiment and calculation is achieved for  $c_f = 3.5$ , where the calculated flame front position is in good agreement with the experimental data up to 5.0 m. Note that the differences in the  $c_f$  values are rather small. This indicates that careful selection of the  $c_f$  value is necessary for good agreement with the experiment.

Figure 4.73 gives the pressure histories at the 6 probe locations in the PHD tube. At 1.15 m the experimental data shows a pressure peak that is not reproduced with the numerical calculation. As has already been discussed the initial phase is not reproduced well in the calculation. At 2.25 m the agreement between numerical model and experiment becomes better. The peak pressure is well re-

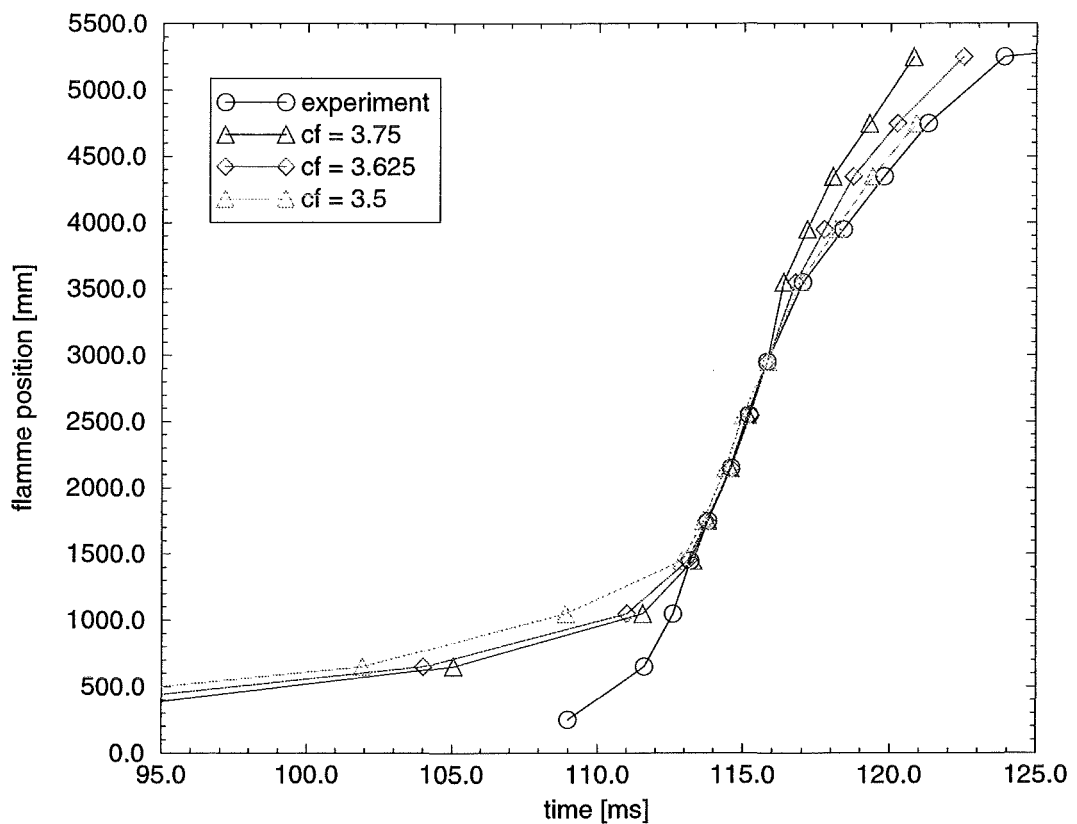


Figure 4.72: Flame front position as function of time for different runs of REACFLOW

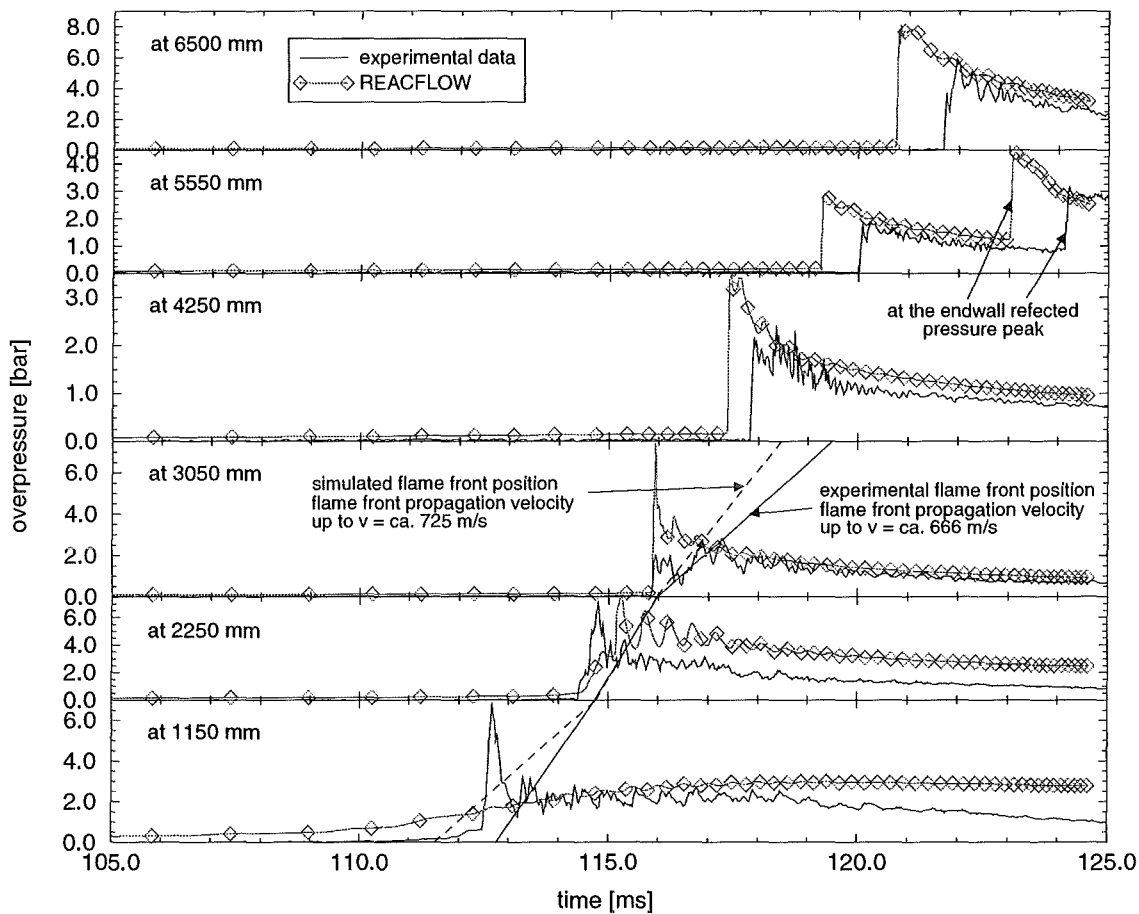


Figure 4.73: Pressure histories as function of time. Comparison of calculation with REACFLOW and experimental data

produced but the time of this pressure peak is to late in the calculation. At 3.05 m the timing is perfect as this position is used to determine the offset between calculation and experiment. Here the calculation gives a higher peak pressure than the experiment. For the pressure histories at the later three positions it can be seen that the flame is to fast in the calculation during this phase. The time difference between calculation and experiment increases. However, the peak pressure is covered reasonably well, the calculated values being somewhat higher than the experimental values. At the last two probe positions the reflected shock can be clearly seen.

Fig. 4.74 gives a detailed qualitative comparison between experiment and simulation. Pictures show a state when the flame has passed by the last orifice. The leading shock system of fast propagating turbulent flames as well as the flame contour is determined by means of the schlieren-technique as can be seen on the

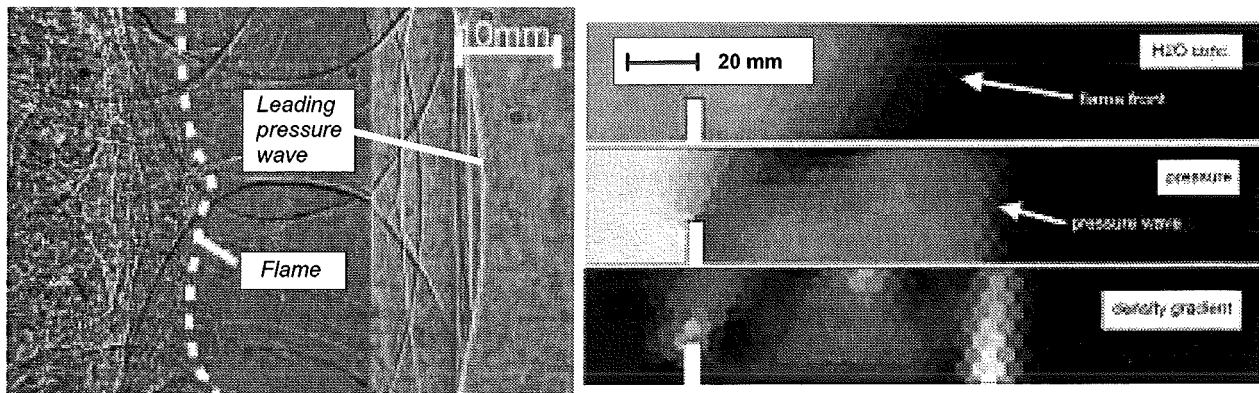


Figure 4.74: Comparison of experimental schlieren optics (left) and simulated isocolour plots (right) ( $c_f = 3.625$ ) for  $\text{H}_2\text{O}$  Vol. concentration, pressure and density gradient for 12.94 Vol.% hydrogen in air.

left. As the schlieren-signal is proportional to the density gradient, caused by the leading shock and the combustion process, on the right isocolourplots for  $\text{H}_2\text{O}$  Vol. concentration, pressure and density gradient are shown. Here the reaction zone and the leading pressure wave can be seen as well. In general the flame thickness is overpredicted.

#### 4.6.2.2 I15 - 14.89 % $H_2$

Compared to the previous benchmark the higher hydrogen concentration in this test case results in faster flame propagation. Results for this benchmark are presented from FZK and JRC.

Figures 4.75 to 4.80 show the pressure histories at six locations along the tube. In the first probe position at a run length of 1150 mm (Fig: 4.75) shows already a fast flame. In the experiment a sharp peak is followed by a constant pressure plateau and later by a slow decrease of the pressure. The peak as well as the constant pressure are predicted by COM3D (FZK). However, the predicted peak pressure is to low, and the constant pressure plateau is to high. The high pressure for the later is expected since heat losses are not included in the calculations. The high peak pressure at this location in the experiment (higher than at the following locations) could indicate a local explosion which is not predicted by the numerical model. Another explanation is an insufficient time resolution in the simulation. The REACFLOW code (JRC) predicts for this probe position a relatively slow pressure increase, followed by a decay similar to the COM3D results.

At 2250 mm the flame has reached its maximum velocity and the pressure peak has achieved a triangular shape (see Fig. 4.76). Both codes give good agreement in the peak pressure and the following decay. The pressure calculated by REACFLOW at later stages is somewhat higher than the one calculated by COM3D. The timing of both calculations is quite good. For COM3D the reflected shock from the end wall arrives at the correct time at this probe position.

Figure 4.77 shows the pressure histories just behind the last obstacle. The flame is now moving in an unobstructed area. As can be seen from the following Figures 4.78 and 4.79 the flame is decelerating and the observed peak pressures decrease. Again the agreement between both calculations and the experiment is good. At both locations, 3050 mm (Fig. 4.77) and 4250 mm (Fig. 4.78), the peak pressure in the calculations is a bit higher than the experiment. REACFLOW consistently predicts higher pressures in the decay phase after the first peak than COM3D. The later code also predicts the later stages of the wave reflection correctly. The REACFLOW calculation was stopped before the reflection.

Figures 4.79 and 4.80 show the pressure histories near the end wall at 5550 mm and at the end wall (6500 mm) respectively. Both codes predict the high peak pressure at the shock reflection. In figure 4.79 the incoming and the reflected shock can be clearly distinguished. And again the calculations show good agreement with the experiment.

At this point it should be noted that the COM3D calculation was performed with a  $c_f$  value of 3.0. This value is different from the  $c_f$ -value used for blockage ratios than 60 %. This indicates a problem with the standard turbulence model. Since the  $c_f$ -value must be reduced for this geometry it can be concluded that the turbulence intensity is overestimated. It seems that for intermediate blockage ratios the boundary conditions for the flow calcualtion become more important

than for very low or very high blockage ratios, where the flow is either relatively slow or concentrated to a region far away from the boundary. At the moment slip boundary conditions are used in COM3D. And this topic clearly needs further investigation.

For the REACFLOW additional information is plotted in Figures 4.81 to 4.84. Figure 4.81 gives the flame position as function of time for REACFLOW calculations with different values for the constant  $c_f$  in the eddy-break-up model. For the pressure histories discussed before a value of 3.125 has been used. Thus also REACFLOW needs a comparatively small  $c_f$ -value for this test case.

Figure 4.82 shows the species concentration of  $H_2O$  and  $H_2$ , the pressure and temperature fields and the distribution of the turbulent kinetic energy and dissipation rate in the middle of the obstacle range. The flame is propagating from left to right and the shock has just reached the second last obstacle to the right. The leading edge of the reaction zone follows closely behind this shock. All distributions are essentially one dimensional with gradients only in axial direction. Small disturbances are observed only at the obstacles. Only the turbulence data shows some radial variations. At the obstacles close to the shock high values of the turbulent kinetic energy and of the dissipation rate are observed. The region of high turbulence is spreading downstream of the obstacle.

In Figure 4.83 the same variables are shown but at a different location in the tube. Here the last obstacles of the obstructed section are shown. The shock leaves the obstructed section and the flame is already decoupling from the shock. A shock reflection at the third obstacle from the right causes high pressures at that obstacle and results in high turbulence production. The pressure and temperature fields now show more radial variations.

The unobstructed section of the tube is shown in Figure 4.84. The leading shock has already been reflected from the end wall and can now be observed at the right boundary moving upstream. This reflected shock has not yet reached the downward moving flame. As the flow velocities are smaller in this part of the tube the turbulence levels are also smaller. Again the species concentrations show only minor radial variations.

The radial distribution of the species concentration, the flame shape, is predicted differently by the different codes (see also the results of test case R0498\_02). But at the present time no experimental data to verify the code predictions of the flame shape is available. For further evaluation of the numerical codes a visualization of the propagating flame would be necessary.

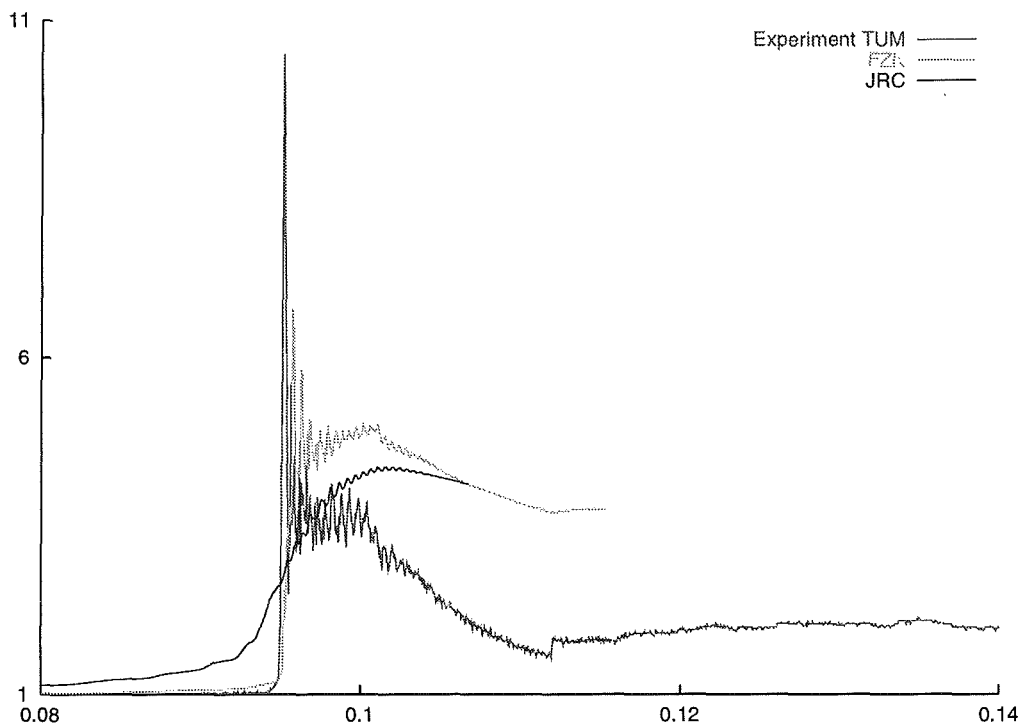


Figure 4.75: Pressure histories for test case I15 at position 1150 mm

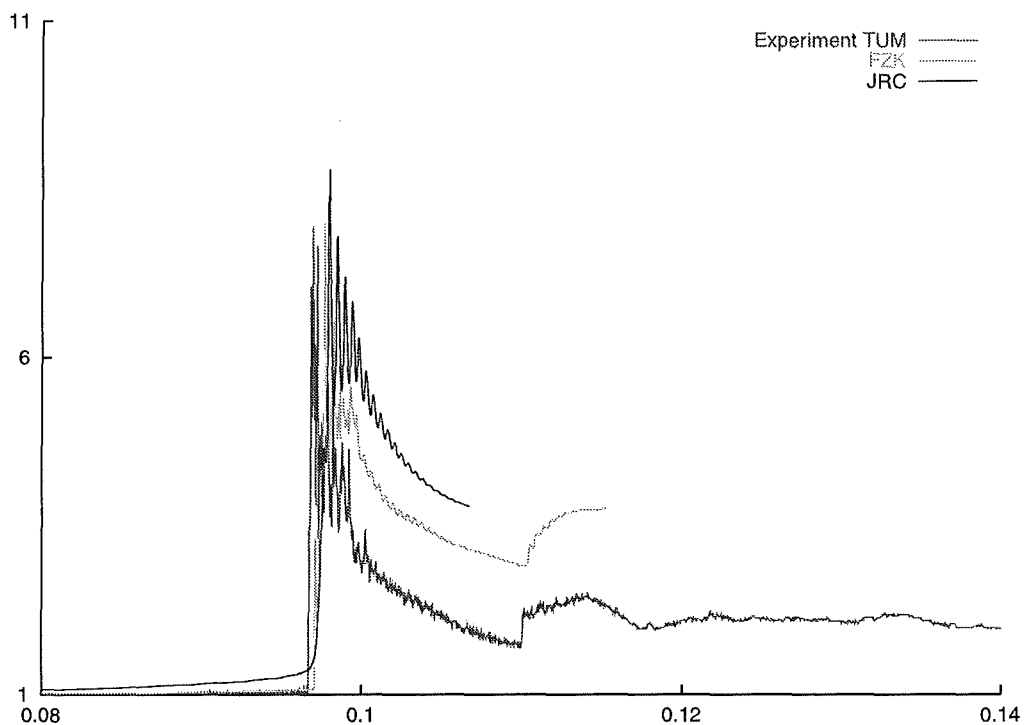


Figure 4.76: Pressure histories for test case I15 at position 2250 mm

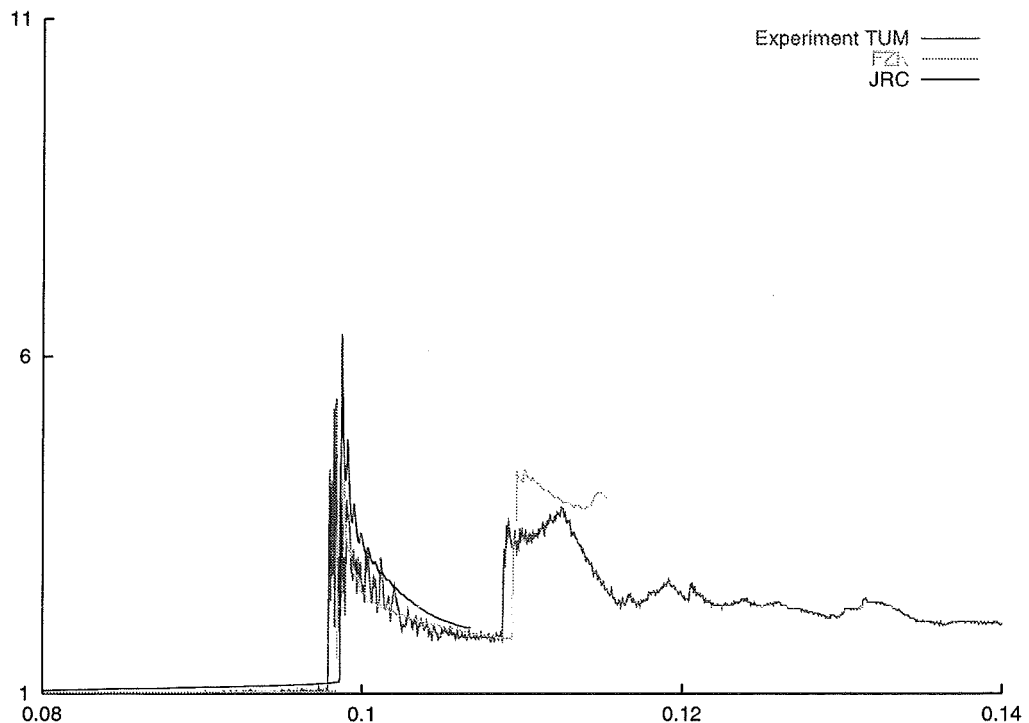


Figure 4.77: Pressure histories for test case I15 at position 3050 mm

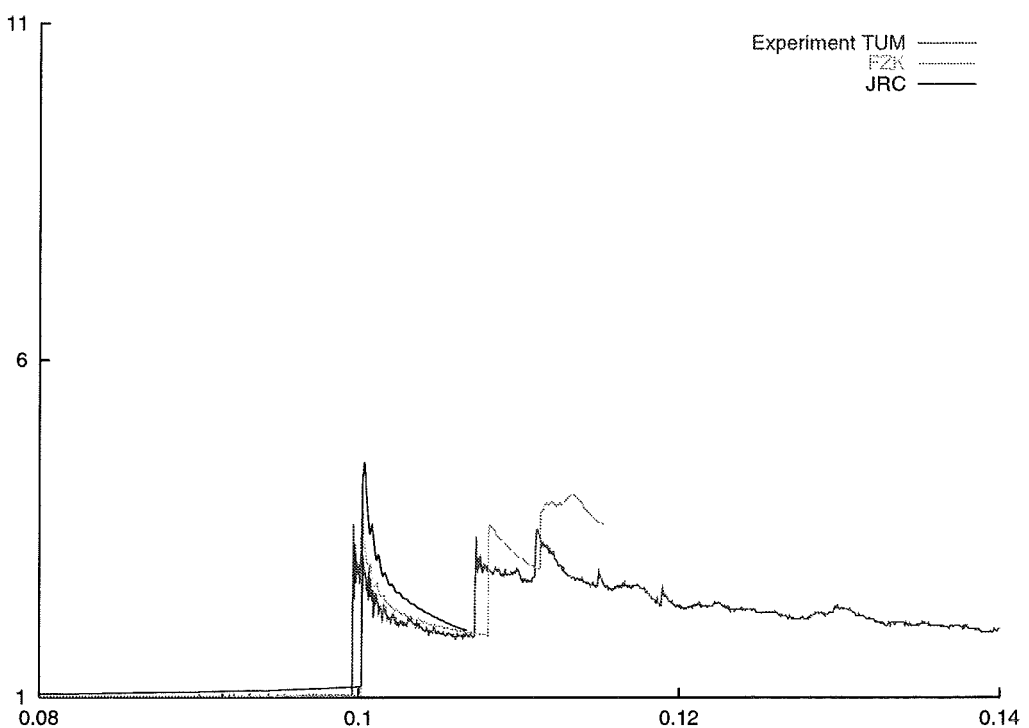


Figure 4.78: Pressure histories for test case I15 at position 4250 mm

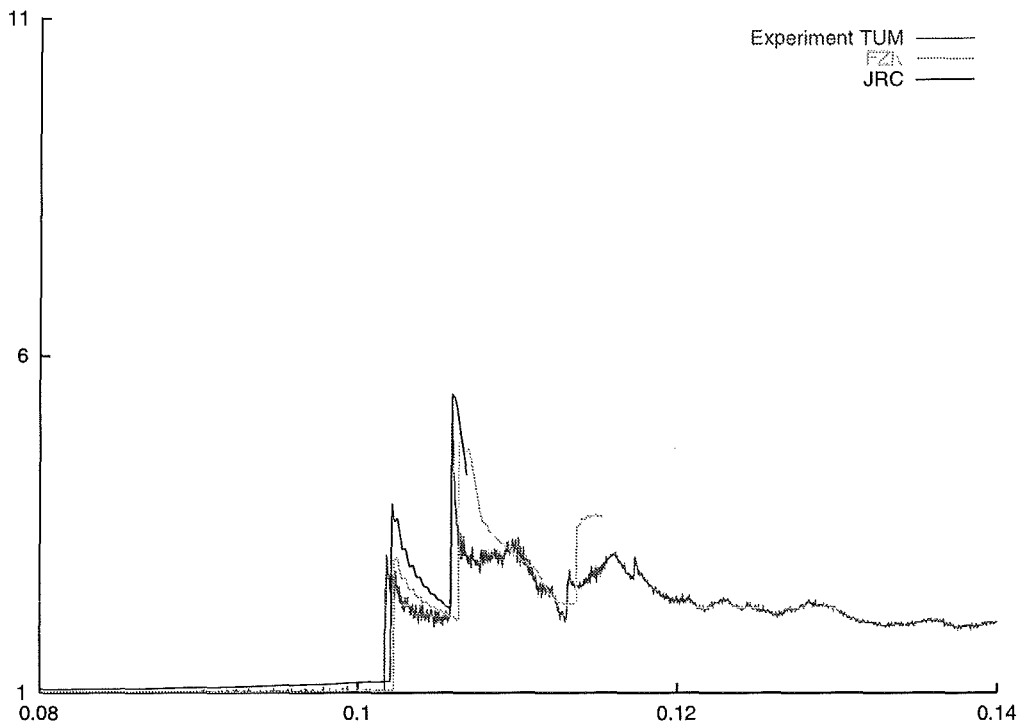


Figure 4.79: Pressure histories for test case I15 at position 5550 mm

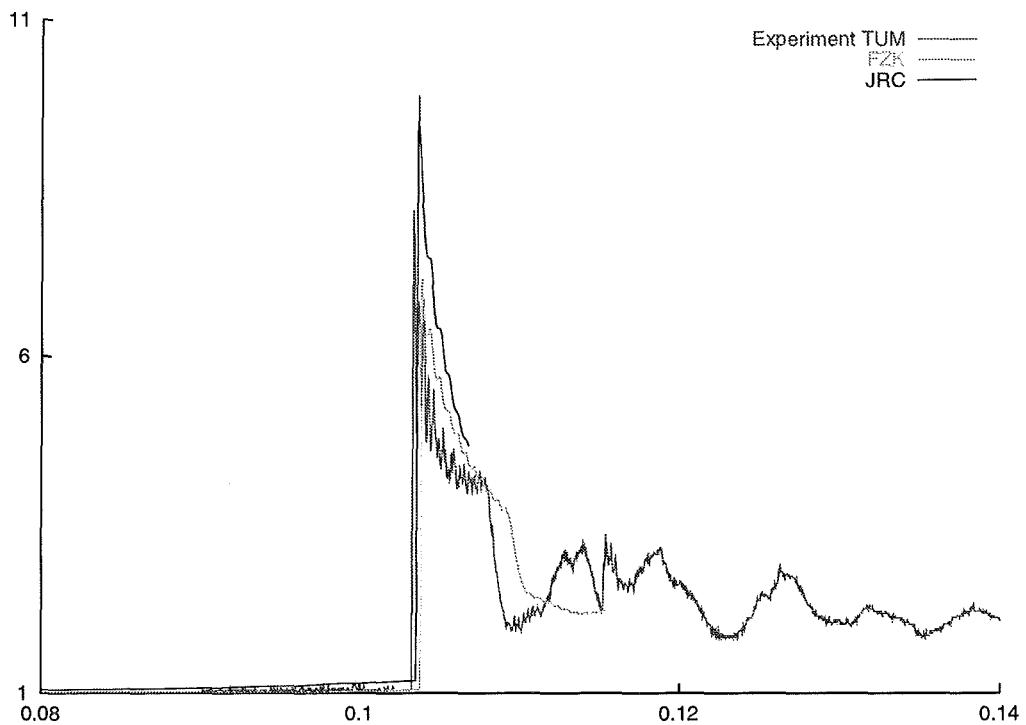


Figure 4.80: Pressure histories for test case I15 at position 6500 mm

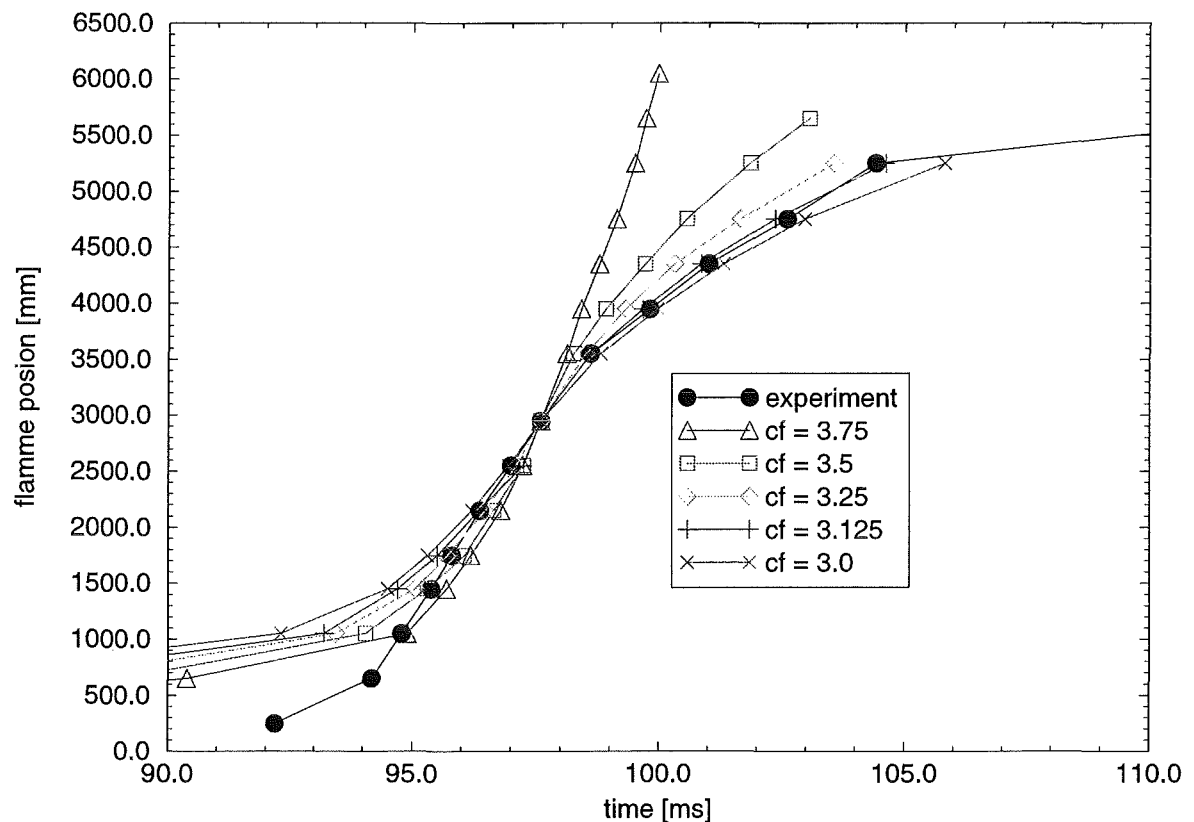


Figure 4.81: JRC

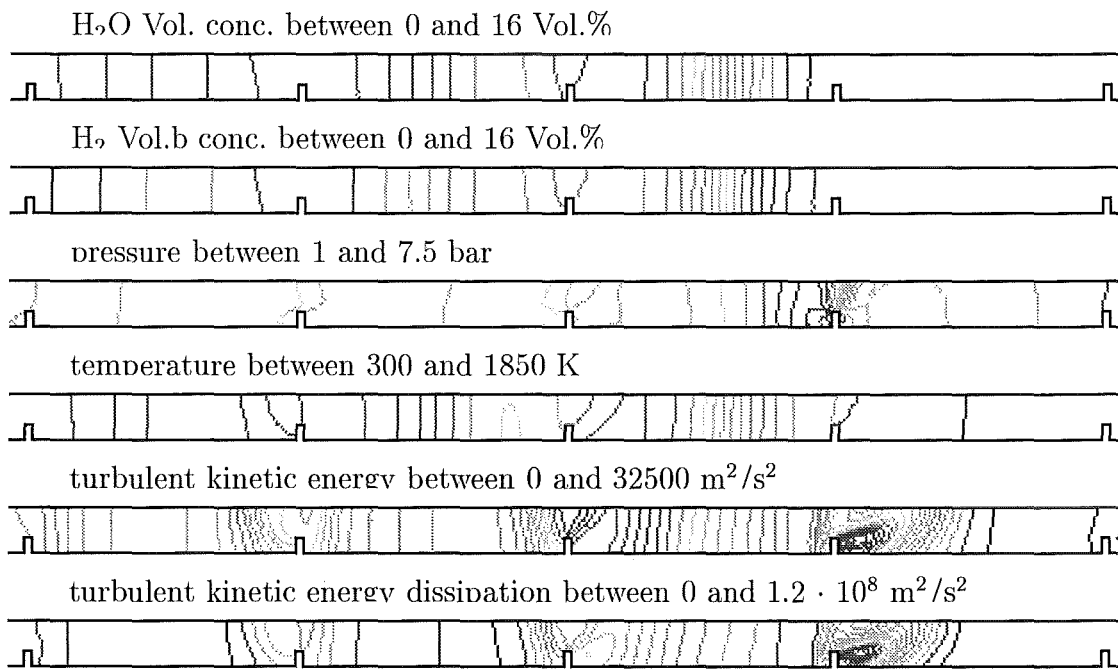


Figure 4.82: Flame position at 1.945 m. 20 iso-lines from blue to red between min. and max. value in every plot.

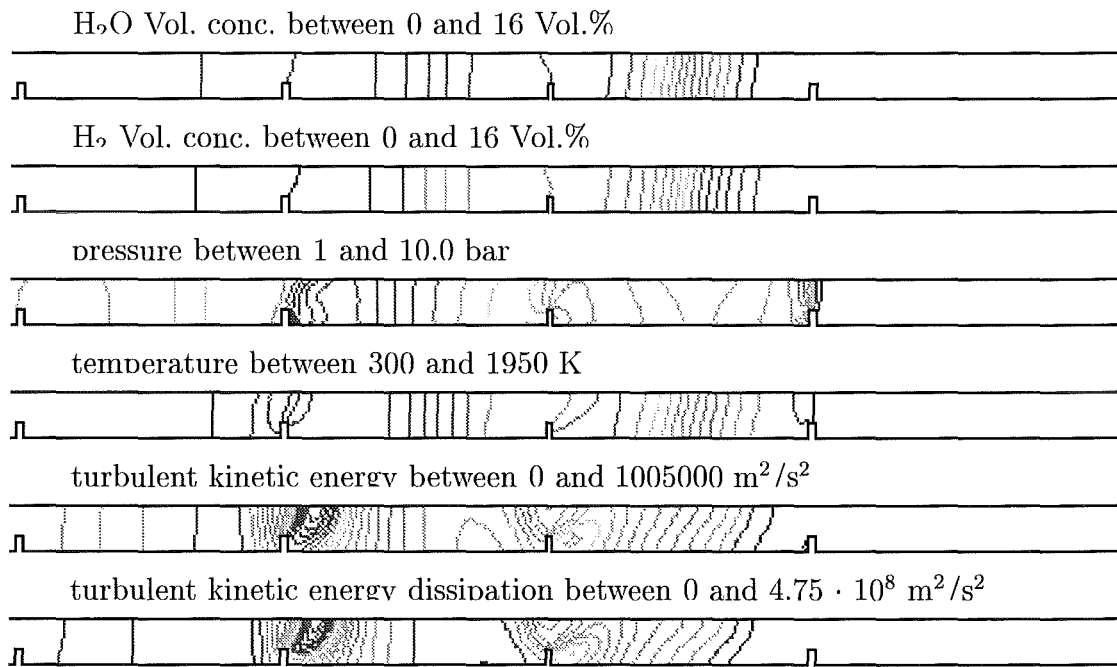


Figure 4.83: Flame position at 2.85 m. 20 iso-lines from blue to red between min. and max. value in every plot.

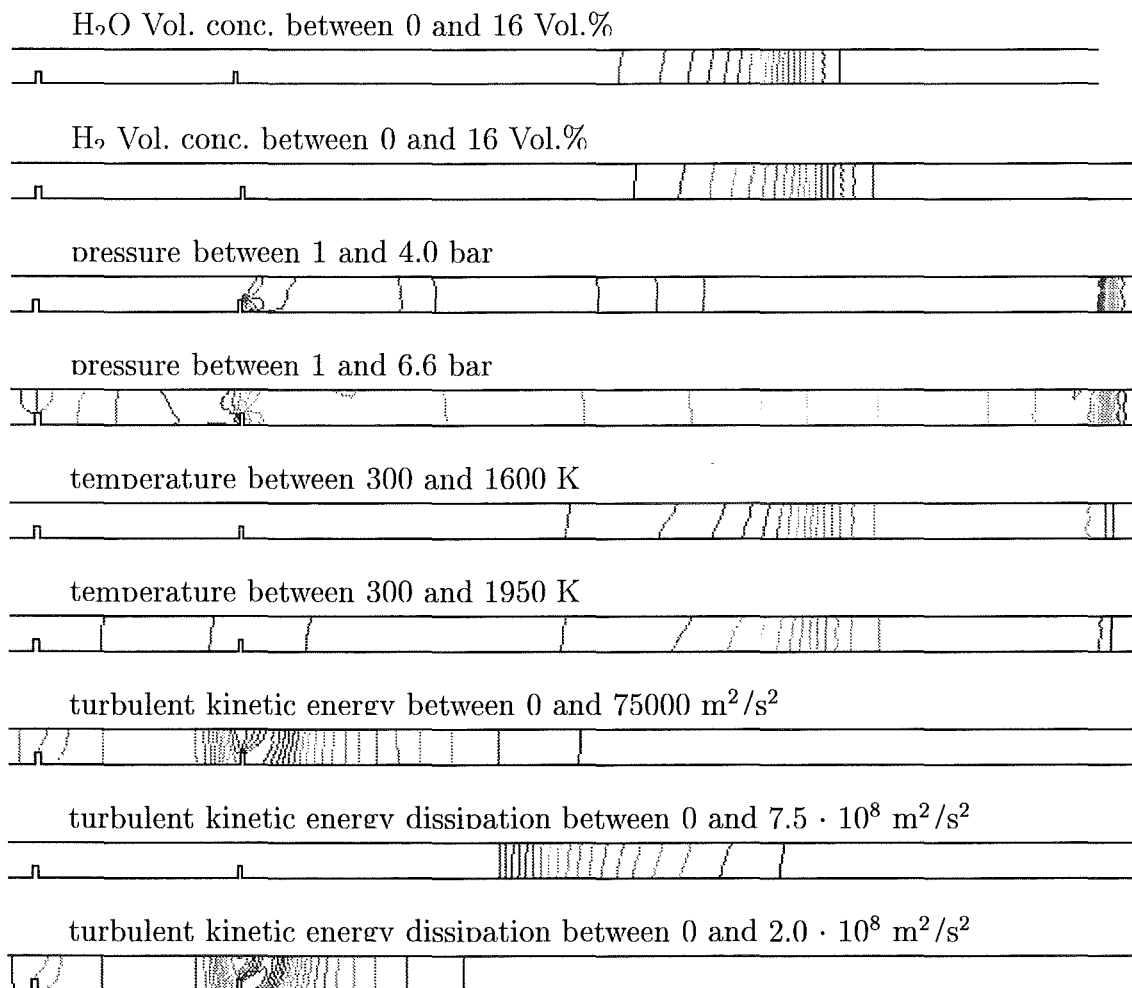


Figure 4.84: Flame position at 3.5 m. 20 iso-lines from blue to red between min. and max. value in every plot.

### 4.6.3 Medium scale test in FZK-tube

The FZK tube is 12 m long and has a diameter of 350 mm. Thus this experimental setup represents the intermediate length scale in our benchmark matrix. All experiments selected as benchmarks have a blockage ratio of 0.3 and were performed at ambient initial conditions. The distance between the obstacles is 500 mm throughout the whole tube. Three different hydrogen air mixtures with 10 %, 11 % and 12 % hydrogen by volume were selected. The results for each of these test cases will be discussed in the sections.

#### 4.6.3.1 R0498\_07 - 10 % $H_2$ in air

##### 4.6.3.1.1 Calculation with Tonus (CEA)

Due to the previously described restrictions of the CEA model this test is the only benchmark calculation in which the TONUS computer code took part. Compared to the previously discussed TUM tests, this test case is more related to turbulence-flame interaction. The flow field ahead of the flame interacts with obstacles and creates turbulence. Then the flame arrives in this turbulent flow field and accelerates.

The calculations have been performed on a 2D axisymmetric grid with a typical mesh size of 1 cm. Buoyancy terms were neglected. The standard  $k - \epsilon$  model of TONUS has been used. A comparison of the experimental and the calculated flame front position is shown in figure 4.85.

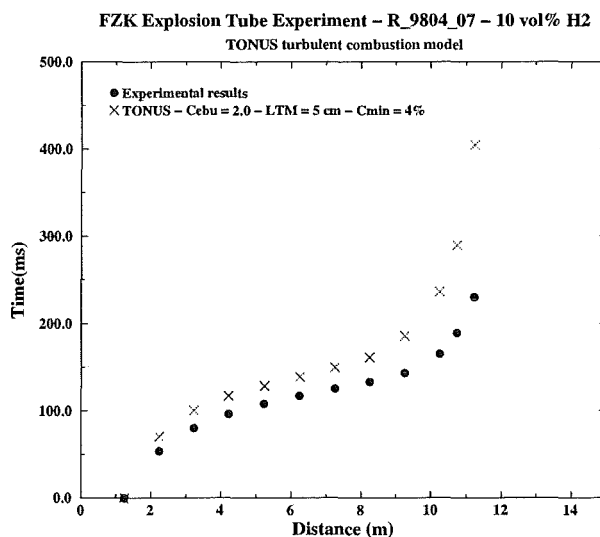


Figure 4.85: FZK Explosion Tube Experiment - 10 volume percent hydrogen -  $Br=0.3$  - TONUS turbulent combustion model

The experimental results show that the flame accelerates in the first half of

the tube (6 m). Then, the flame velocity is quite constant until 8 m and finally, the flame decelerates at the end of the tube.

In the calculation adjustments of the model constants were performed to obtain the results in figure 4.85. The model parameters are mainly the EBU constant  $C_{EBU}^0$ , the turbulent integral length scale  $L_{tm}$ , the critical Damköhler number and the minimum progress variable  $C_{min}$ . These values have been chosen to obtain the best fit to the experiment results:  $L_{tm}$  corresponds to the obstacle height and  $D_{critical}$  corresponds to the transition between flamelet regime and well-stirred reactor. According to this fit a good acceleration profile is obtained along the tube. Just at the end of the tube, due to low compressibility and perhaps poor  $k - \epsilon$  model, the flame is affected by the end of the tube earlier in the calculation compared to experimental results.

It's also interesting to compare the transient pressure in the experiment and in the calculation (figure 4.86). In the experiment all pressure gauges have the same response due to the fact that the flame velocity is small compared to the sonic velocity. This corresponds to the assumption of TONUS low Mach number flow solver where the thermodynamical pressure  $P$  depends only on time. In the calculation, after a synchronization with the first gauge flame arrival time, the shapes of the pressure response are the same as the experimental results. Oscillations are higher in the calculation than in the experiment. This is perhaps due to the fact that in the calculation the Mach number is close to the maximum Mach number allowed by the model (0.3). Despite this the results are in quite good agreement with the experimental results. At the end the pressure increases in the calculation. This corresponds to the heat losses that are not modeled in the calculation.

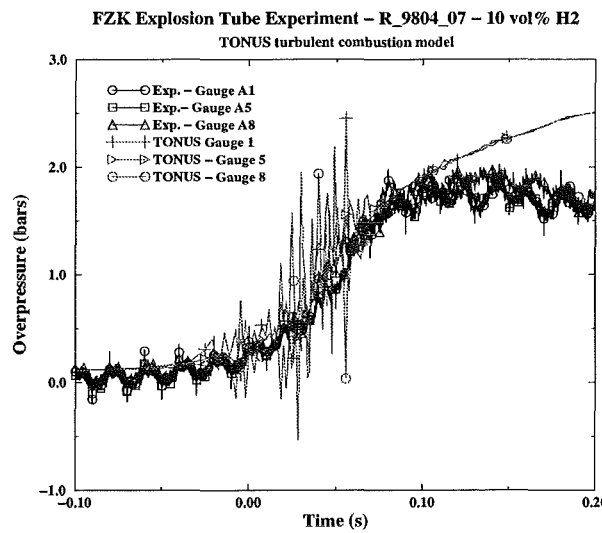


Figure 4.86: FZK Explosion Tube Experiment - 10 volume percent hydrogen -  $Br=0.3$  - TONUS turbulent combustion model

Additional information on the turbulence were obtained in the calculation. Figures 4.88 to 4.90 show turbulence data near the 13th obstacle.  $k$ ,  $\varepsilon$  and the characteristic turbulent time scale  $\tau_t = \frac{\varepsilon}{k}$  are plotted for the positions given in figure 4.87. The first peak corresponds to the flame arrival near the obstacle (the highest level of  $k$  is obtained just after the obstacle at 6.55-R/2). The second peak corresponds to the flame arrival at the end of the tube: when the flame arrives at the end of the tube, a reverse flow is created due to compressibility effects and this flow creates turbulence around the obstacles (the highest level of  $k$  is obtained before the obstacle 6.25-D/2).

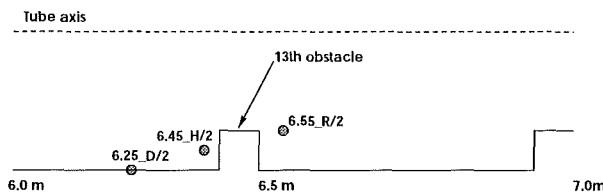


Figure 4.87: FZK Explosion Tube Experiment - 10 volume percent hydrogen -  $Br=0.3$  - Turbulent measurement location

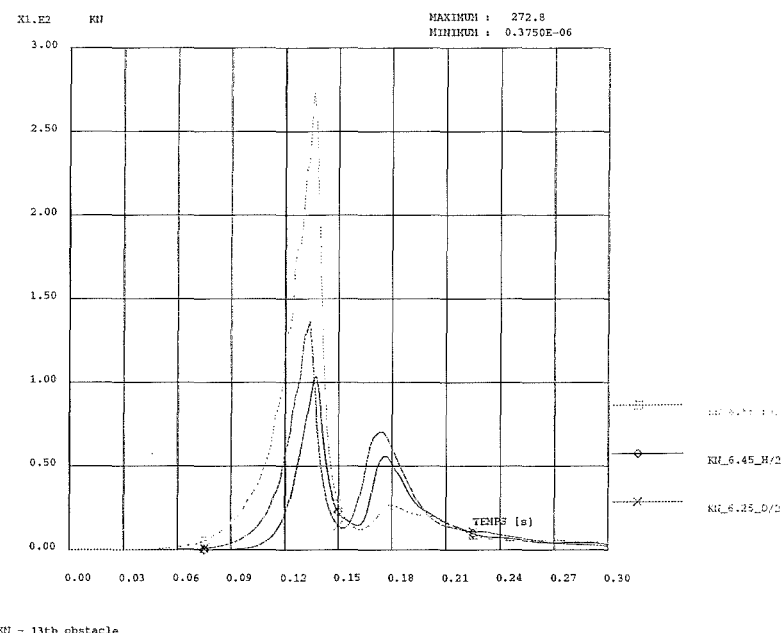


Figure 4.88: FZK Explosion Tube Experiment - Turbulent kinetic energy

The flame has been visualized at different times during the calculation. In figure 4.91 the flame front (Hydrogen mole fraction iso values) is plotted for 3 characteristic times: 86 ms, 134 ms and 170 ms. For this low blockage ratio 0.3,

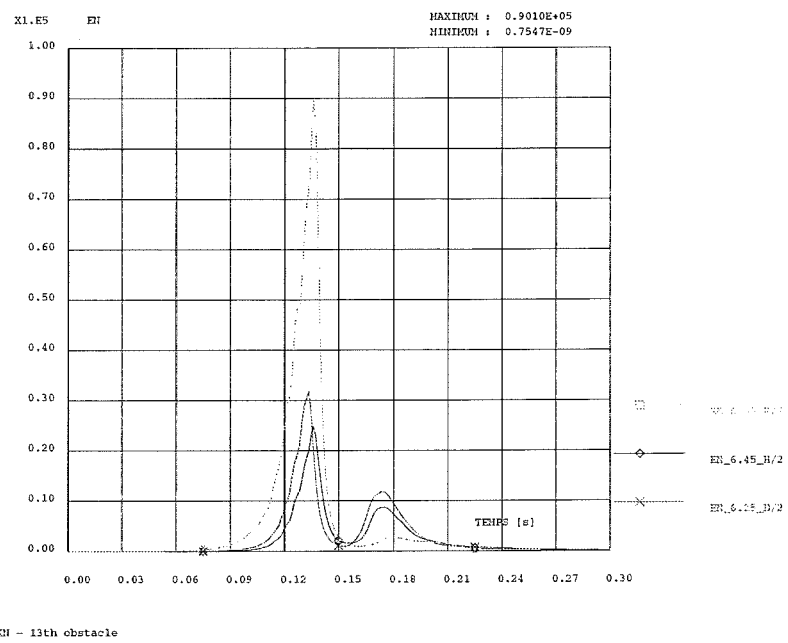


Figure 4.89: FZK Explosion Tube Experiment - Turbulent dissipation

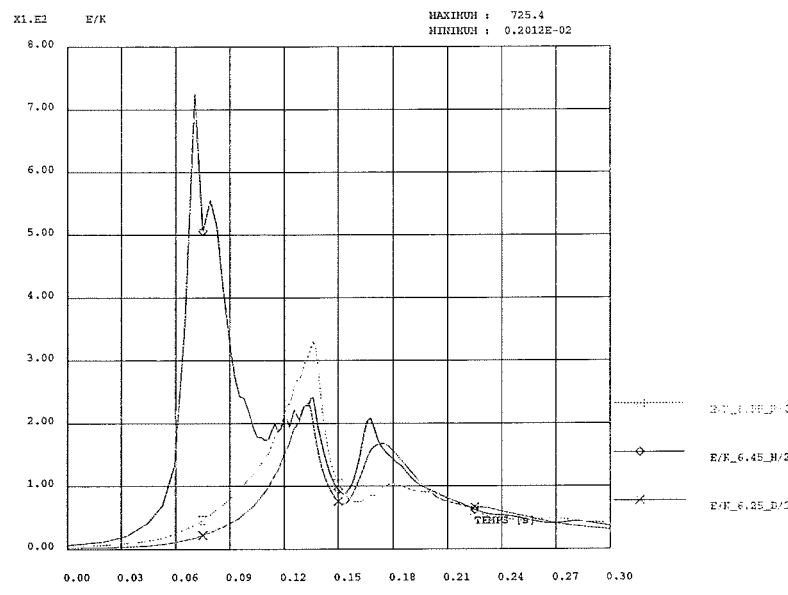


Figure 4.90: FZK Explosion Tube Experiment - Characteristic time scale  $\frac{\varepsilon}{k}$

the flame is distended along several obstacles. Due to the flame deceleration at the end of the tube the flame becomes "thinner" in the last picture.

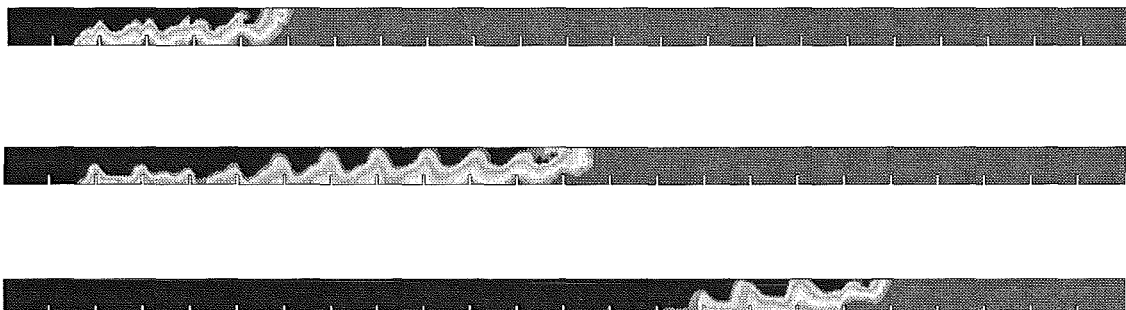


Figure 4.91: FZK Explosion Tube Experiment - 10 volume percent hydrogen -  $Br=0.3$  - Flame profile

#### 4.6.3.1.2 Calculation with REACFLOW (JRC)

The test case with a 10 % hydrogen air mixture was also calculated with REACFLOW by JRC. However, only the pressure histories for this calculation are available and are presented in Figure 4.92. The calculated pressure values show a slow increase corresponding to the experimental observation that only minor pressure waves are created and that the combustion process is dominated by the mean combustion pressure. The calculated values are consistently higher than the experimental data. In the initial phase the difference between measured and calculated values is constant indicating that the initial data in the computation might have been too high. In the later stage of the combustion process the difference increases. This indicates that heat losses to the wall, which have been neglected in the computations, become increasingly important.

The calculated pressure curves are smoother than the experimental values. Oscillations as were observed in the TONUS calculation do not develop. The small pressure variations in the experimental data which are probably caused by transverse waves are not reproduced by the numerical calculation.

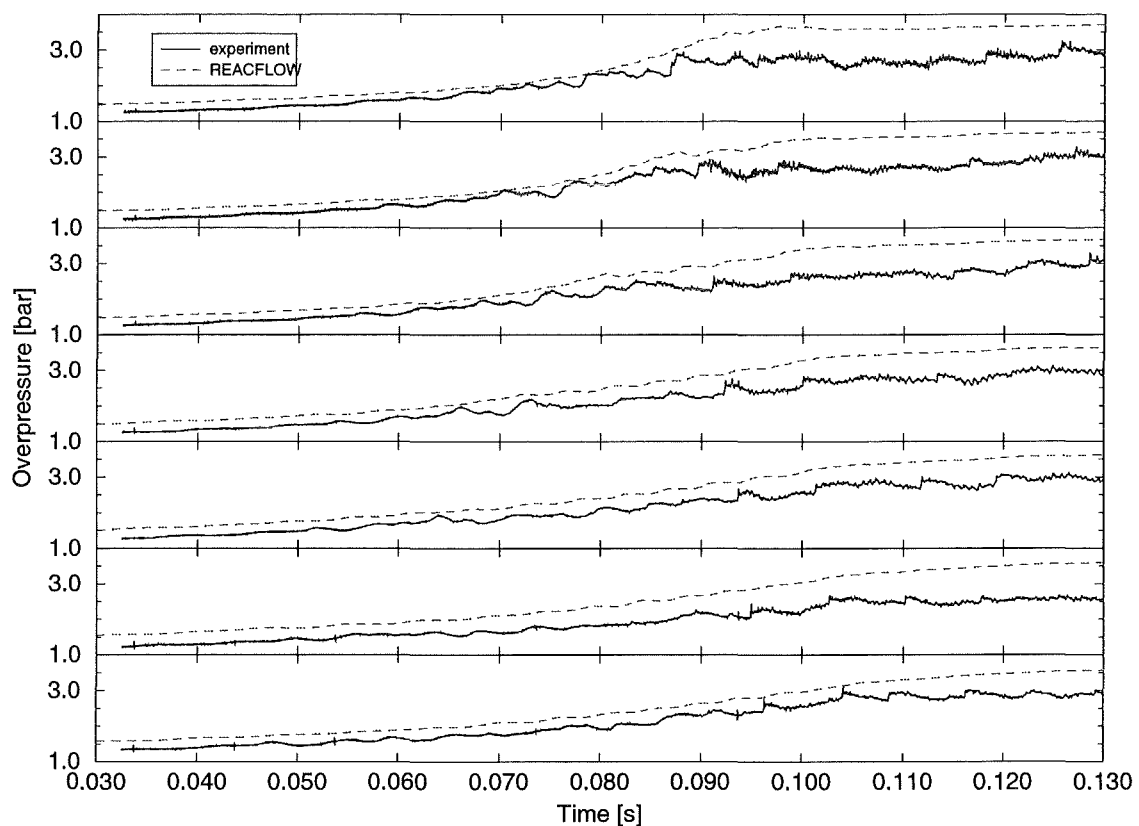


Figure 4.92: JRC

#### 4.6.3.2 R0498\_02 - 11 % $H_2$

For the benchmark in the FZK tube with an 11 % hydrogen air mixture results were contributed from FZK, JRC and TUM. The unique feature of this benchmark is that detailed information about the calculated turbulence field is available for the three codes used. First the results from FZK and JRC are compared in the following sections. In Section 4.6.3.2.4 the results from TUM will be discussed separately.

##### 4.6.3.2.1 Pressure histories

In the experiment pressure histories were measured at 14 positions along the tube axis. Figures 4.93 to 4.106 compare the measured and the calculated pressure histories at all of these 14 locations. Shown are results from FZK and JRC together with the experimental values. In all figures a constant time offset was applied to the numerical results to account for the initial delay at ignition not covered in the calculations. This offset was determined for each calculation by fitting the pressure peak at the end wall.

From the experimental data it can be seen that the maximum pressure as well as the amplitude of the pressure oscillations increase from the ignition end to the downstream end of the tube. The flame accelerates, a shock develops (see figures 4.100 and 4.101), the flame probably couples to the shock forming a detonation (see figure 4.102), and finally the shock is reflected at the end wall (see figures 4.105 and 4.106) and travels back through the tube.

At the first three probe locations (1.25 m, 2.25 m and 3.25 m, figures 4.93 to 4.95) only a slow pressure rise is observed in the experiment. Both numerical calculations (FZK and JRC) cover this slow pressure rise very well. The calculation from JRC starts from a somewhat higher pressure level than the FZK calculation and the experiment. Otherwise the two numerical models give virtually the same results. At approximately 0.06 s pressure waves returning from the downstream side of the tube arrive at the probe positions. These waves are not reproduced by the numerical models. Consequently the predicted pressures at this locations are too low in this phase. At later stages the computations both predict a higher pressure level than was observed in the experiments. This is again due to the fact that heat losses to the walls were not accounted for in the calculations.

At a probe position 4.25 m downstream from the ignition location both numerical models produce a small pressure jump between 0.05 and 0.06 s. This jump corresponds to a wave traveling upstream becoming weaker as it approaches the upstream end of the tube. The JRC calculation predicts this jump a little bit later than the FZK calculation. However, both predictions agree well with a pressure maximum observed in the experiment.

The oscillations in the experimental data become more pronounced downstream from this position and it seems not clear whether these oscillations in the

experiment are partially caused by resonances in the measurement equipment. The numerical calculations do not predict the peak pressures of the experiment, but seem to describe the mean pressure of these oscillations.

Starting at 5.25 m (Figure 4.97) and continuing to the end of the tube the calculation from JRC predicts consistently higher pressures than the FZK calculation. However, the general behavior of the two models is quite similar. They both predict pressure peaks appearing at the same times in good agreement with the experimental data.

As the flame accelerates between position 5.25 m and 8.25 m (see figures 4.97 to 4.100) a second pressure peak becomes observable. This small pressure maximum is first seen at 7.25 m (figure 4.99). As this pressure maximum travels downstream its maximum value increases and it becomes more visible in the downstream locations. The JRC calculations predicts this maximum a little bit earlier than the FZK calculation. But the difference is small compared to the width of the experimentally observed pressure peak.

While the observed pressures are well below 10 bar for the measurement locations up to 8.25 m, much higher pressures occur in the remaining part of the tube. At 9.25 m (figure reffig:p9) a pressure peak well above 15 bar appears in the reflected shock. At 10.25 m (figure 4.102) pressures above 20 bar are observed in the incident and the reflected shock, the values in the former being higher. Both calculations predict pressures near 10 bar for this stage of the combustion process. At 11.75 m (figure 4.105) the JRC calculation predicts about 15 bar and the FZK calculation about 11 bar maximum pressure. The experimentally observed peak pressure is 25 bar at that position.

The measured peak pressure at the end wall is only about 5 bar. The difference between the measured pressure histories at the end wall and at a location 250 mm before the end wall support the opinion that resonance effects in the pressure transducers magnify the measured peak pressures. At the end wall (figure 4.106) the calculated pressures are much higher than the measured values. Both numerical models predict similar peak pressures. This peak pressures are in accordance with what should be expected for a shock reflection on a plain end wall. While the pressure probes in the numerical simulation see an ideal shock reflection, this is not true for the experiment. Here the pressure transducer averages over some spatial area.

Summarizing the results from figures 4.93 to 4.106 it can be said, that both numerical models describe the acceleration of the flame very well with remarkably small differences between the two models.

#### 4.6.3.2.2 Turbulence field data

For each of the three codes participating in this benchmark turbulence field data have been collected for three different instances in time. The first set of

data gives the turbulence field when the flame is between obstacles 5 and 6 that is at approximately 2.75 m from the ignition end. As was discussed previously the flame is still rather slow at that instance. The second set of data gives the turbulence field when the flame is between obstacles 12 and 13 (approximately at 6.25 m). It is here that the first pressure waves are initiated and the flame starts to accelerate to sonic speeds. A third set of plots shows the turbulence field at a later stage, when the flame has passed the 18th obstacle (approximately at 9.25 m). Here the flame has already reached its maximum velocity.

Figures 4.107 to 4.109 give the turbulence data for the calculation with COM3D from FZK. In each figure hydrogen concentration, turbulent kinetic energy and turbulent kinetic energy dissipation are shown from top to bottom. The upper half of each plot shows a vertical cut and the lower half a horizontal cut through the 3D computational domain which consisted due to symmetry conditions of only a quarter of the tube.

In Figure 4.107 at the early stage of combustion the flame is just passing through obstacle 5 as can be seen from the hydrogen concentration. The flame moves faster in the center of the tube and is stretched downstream of the obstacle. It has a blunt leading edge. While the core region of the flame has already passed the obstacle the trailing edges are still attached to the wall between obstacles 4 and 5. In this pocket between the obstacles the flame is slowly burning outward. The plot of the turbulent kinetic energy shows that the highest values occur ahead of the flame near the downstream corners of the obstacles where vortices are shed from the sharp corners. The highest values are seen at obstacle 6 clearly ahead of the flame. The turbulence production in the displacement flow ahead of the flame stretches over at least 6 obstacles. The dissipation of turbulent kinetic energy shown in the lower plot is closely coupled to the turbulent kinetic energy itself and shows a similar distribution.

At the transition state shown in Figure 4.107 the flame appears to be somewhat thinner. The leading edge at the center of the tube and the trailing edges near the wall are closer together. Now the maximum of the turbulent kinetic energy appears at the obstacle the flame is just passing. It is also interesting to note that higher values of the turbulent kinetic energy are also observed far upstream of the flame near obstacles. From this figure it seems that the turbulent kinetic energy is highest on the right side of the obstacles and is then transported to the left. This indicates that a flow reversal has occurred and that the gas is moving to the left in this region of the tube. The dissipation of turbulent kinetic energy occurs mainly near the flame. At the upstream obstacles no significant dissipation is observed.

Figure 4.109 shows the turbulence field once the flame has reached the end of the tube. The pressure wave has already been reflected from the end wall and is now moving upstream. The position of this pressure wave can be deduced from the turbulent kinetic energy. Near obstacles 18 and 19 high values of the turbulent kinetic energy are seen to the left of the obstacles. This again is an

indication of the gas moving to the left behind the reflected shock.

Figures 4.110 to 4.112 show similar data from the REACFLOW calculation of JRC. Shown are for the half of the tube iso-lines of  $H_2O$  concentration,  $H_2$  concentration, pressure, temperature, turbulent kinetic energy and turbulent kinetic energy dissipation rate.

For the initial stage (see figure 4.110) the flame has a similar shape than in the FZK calculation. The flame is rather blunt at the leading edge. It is stretched through the obstacle and is oriented almost parallel to the wall behind the last obstacle it passed. The flame thickness appears to be somewhat larger than in the FZK calculation. The turbulent kinetic energy reaches maximum values near the downstream edges of the obstacles close to but downstream of the flame. The distribution of the dissipation rate of the turbulent kinetic energy is similar to the turbulent kinetic energy distribution.

At the intermediate state (see figure 4.111 the flame has become rather flat. It is quite thick, but the iso-lines of the concentrations are almost perpendicular to the tube axis. This flame shape is different from the one observed in the FZK calculation. Turbulent kinetic energy and dissipation rate reach their maximum near the closest obstacle ahead of the flame. Again these maxima are convected downstream of the obstacles. The differences between the turbulent kinetic energy distributions at an early stage and at this intermediate stage are not as pronounced as they were in the FZK calculation.

Figure 4.112 shows the flame at the 18th obstacle. This is earlier than the last picture from FZK (figure 4.109). Here maxima of the turbulent kinetic energy and of the dissipation rate appear on both sides of the flame. Close to the flame front on the unburned side and about to obstacles behind the flame on the burned side. Again the form of the maxima indicates that the flow is to the left behind the flame.

#### 4.6.3.2.3 Time histories of turbulence data

For the three locations near obstacle 13 the turbulent kinetic energy and the dissipation rate of the turbulent kinetic energy were sampled for each time step. These data are shown in Figures 4.113 to 4.115.

Figure 4.113 gives the data for a position in the undisturbed flow near obstacle 13. The COM3D calculation from FZK predicts for both turbulent kinetic energy and dissipation rate a small maximum followed by a much larger maximum. The REACFLOW calculation from JRC gives a similar prediction. The first maximum is predicted higher and a little later but the second peak is almost identical to the FZK calculation. The curves are quite similar indicating the similarity of the models used in both codes. The values in the  $k-\varepsilon$ -model are calculated using a gradient assumption. Thus a coarser grid automatically means also smaller gradients and thus different production and destruction rates in the turbulence

model.

Data from the stagnation region before obstacle 13 is plotted in Figure 4.114. The curves are similar to figure 4.113. Again there is a small peak followed by a much larger one. However, the first peak is more pronounced in the FZK model than in the JRC model. The second peak is almost identical in both models. The absolute values are somewhat higher at this position.

The third position of interest is behind obstacle 13 in the region where vortices are expected to be created. The data is shown in figure 4.115. The values are even higher than at the previous location. While the FZK model predicts now peaks of similar height, the JRC model still calculates a small first and a large second peak.

From the results can be deduced that the turbulence models in COM3D and REACFLOW are similar and give similar predictions. In order to further compare the quality of these predictions additional experimental data on the turbulence field is required.

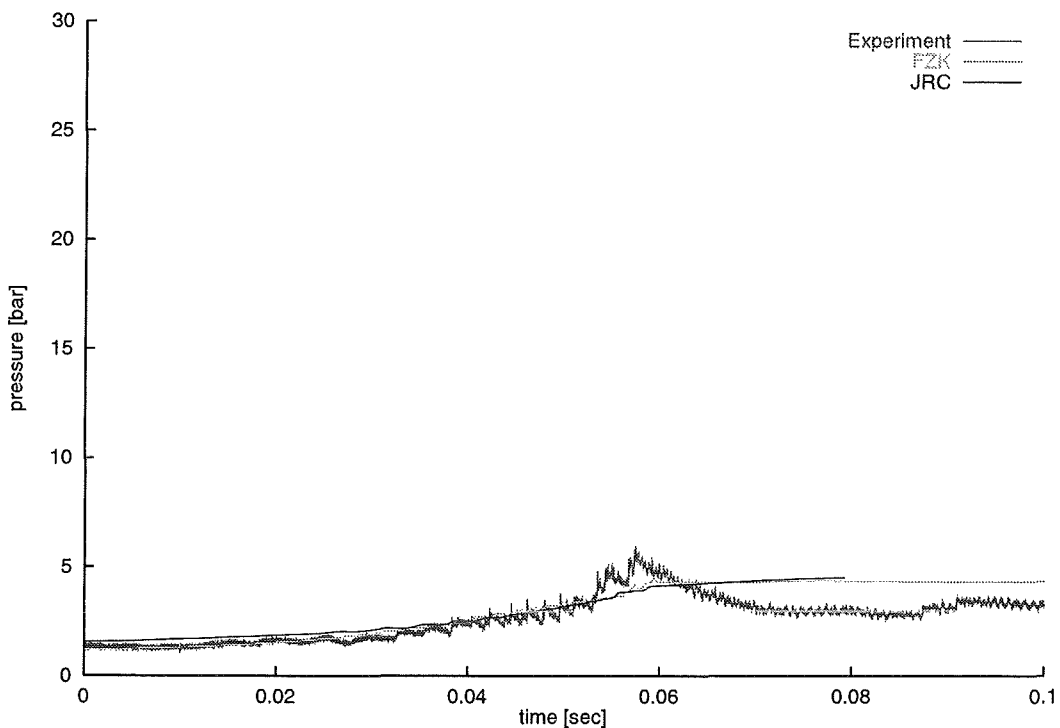


Figure 4.93: Pressure histories at position 1.25 m

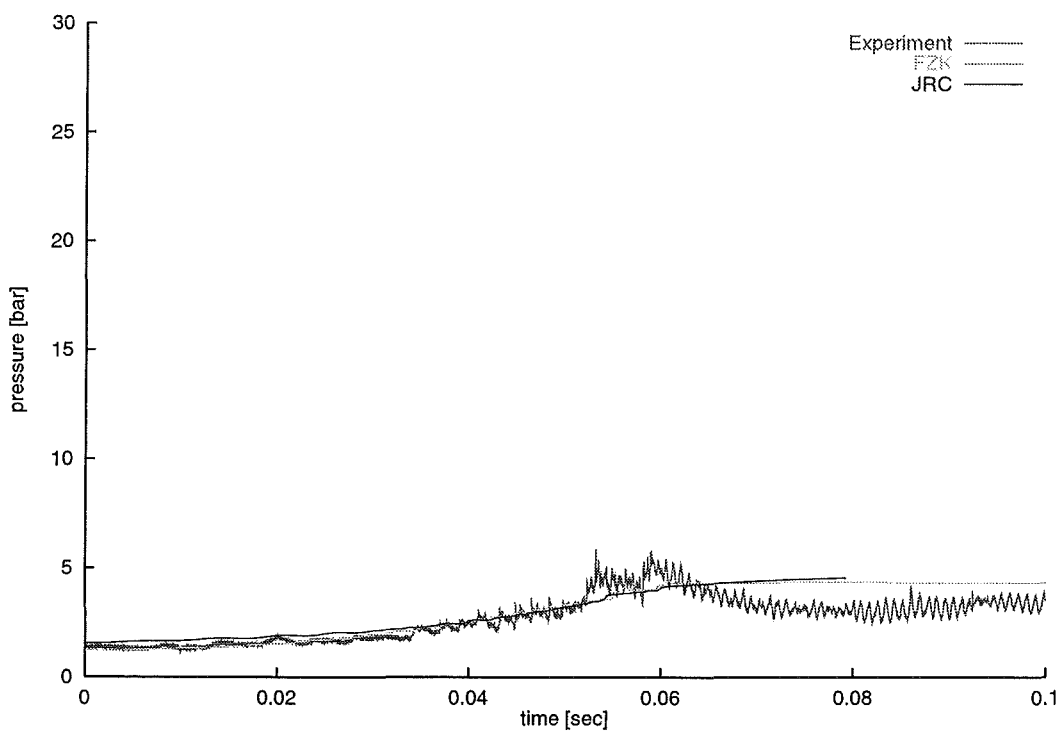


Figure 4.94: Pressure histories at position 2.25 m

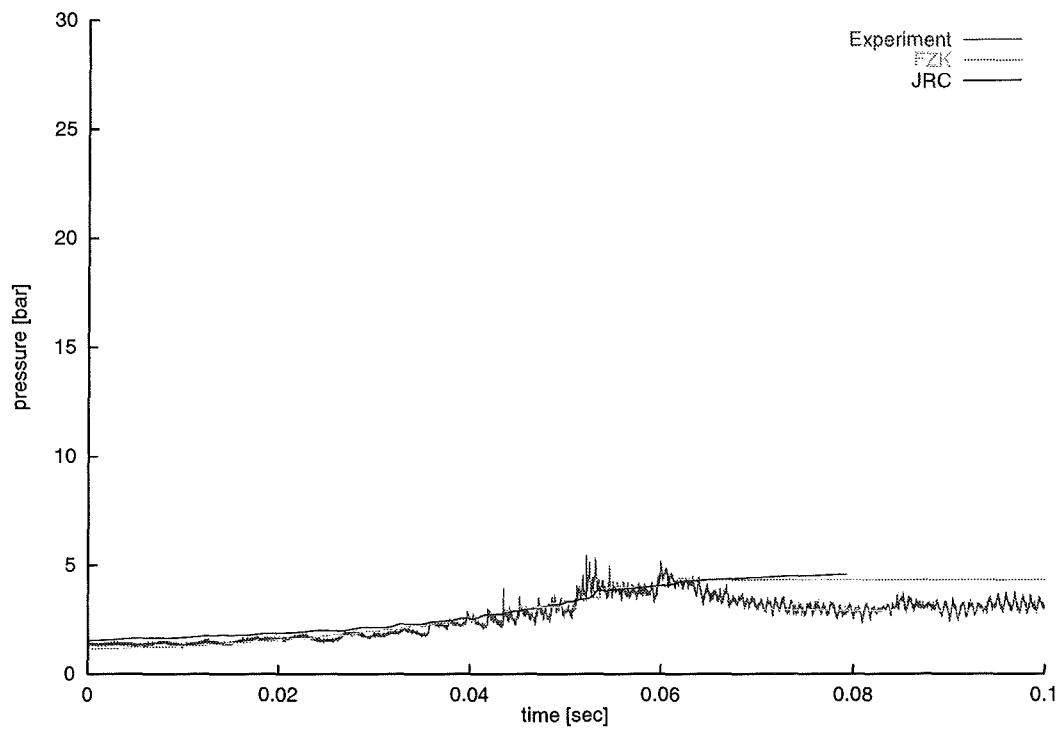


Figure 4.95: Pressure histories at position 3.25 m

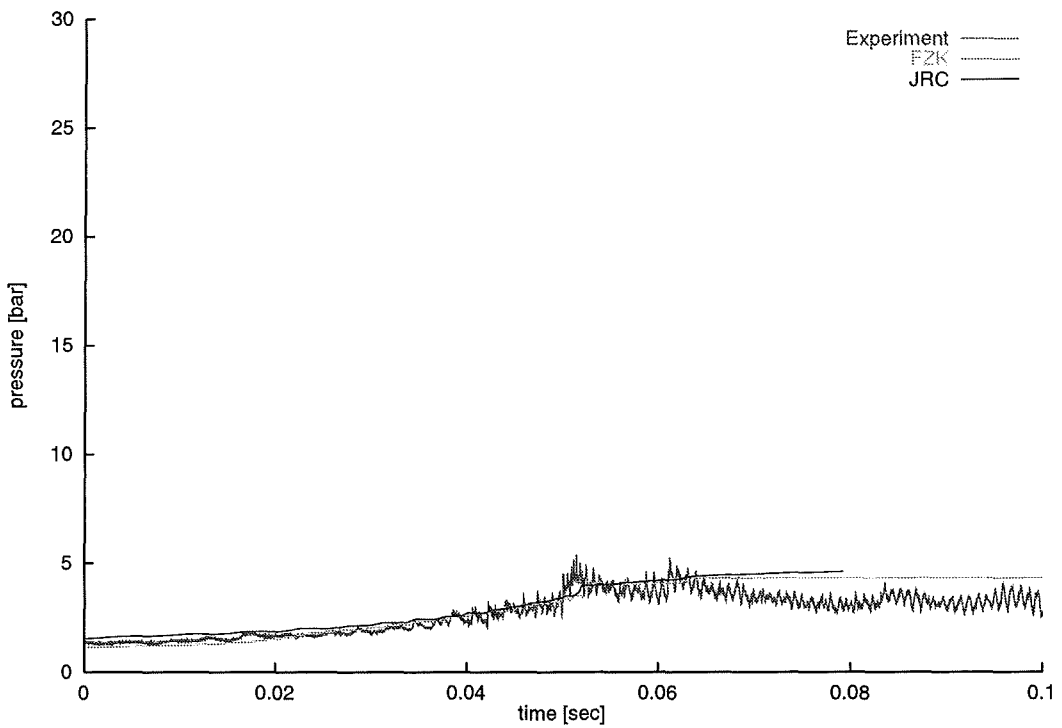


Figure 4.96: Pressure histories at position 4.25 m

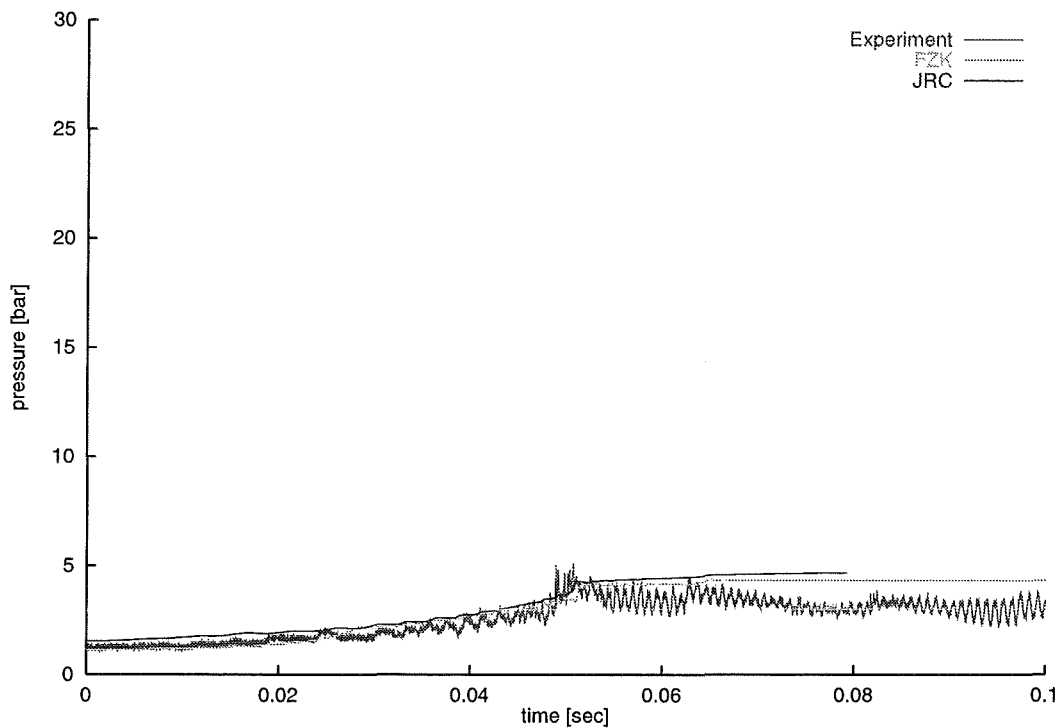


Figure 4.97: Pressure histories at position 5.25 m

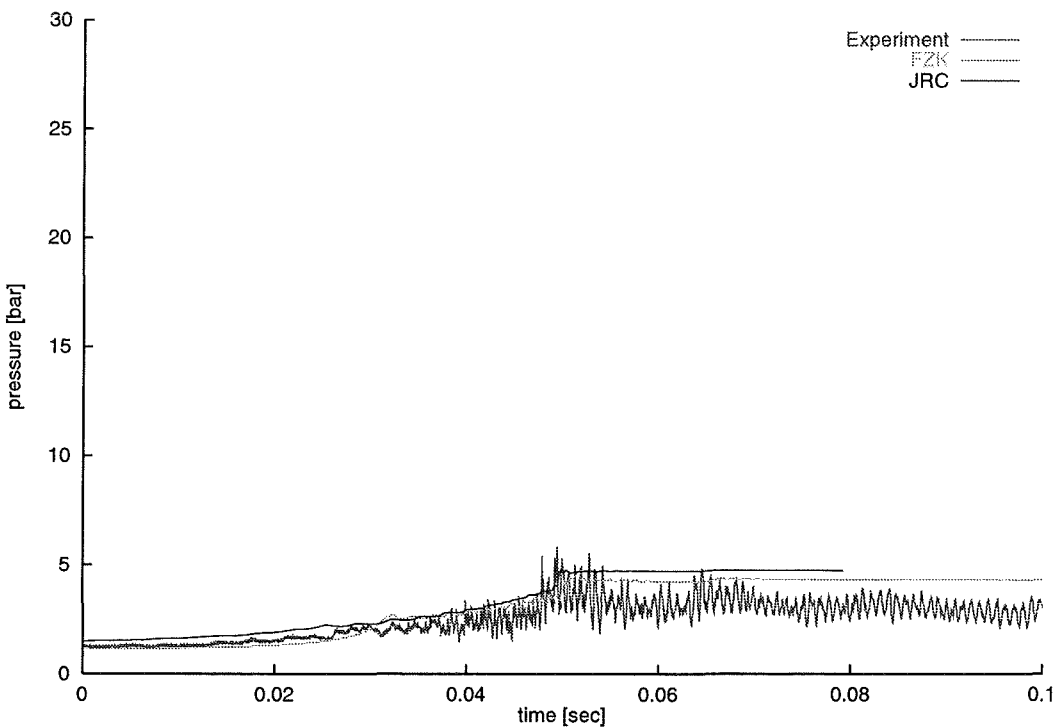


Figure 4.98: Pressure histories at position 6.25 m

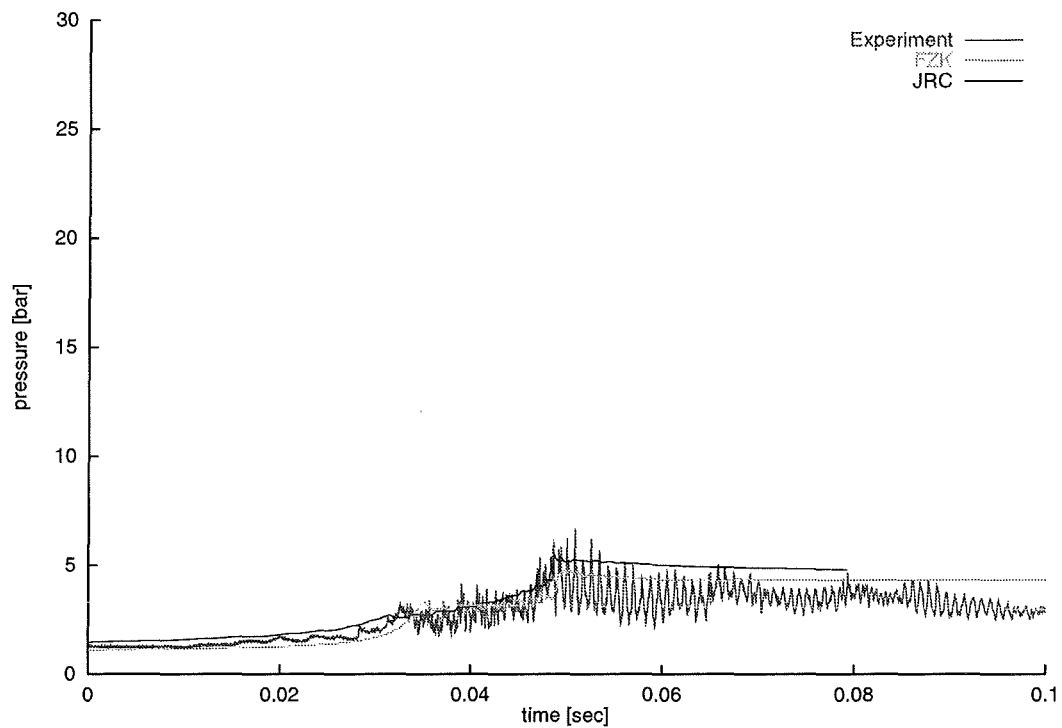


Figure 4.99: Pressure histories at position 7.25 m

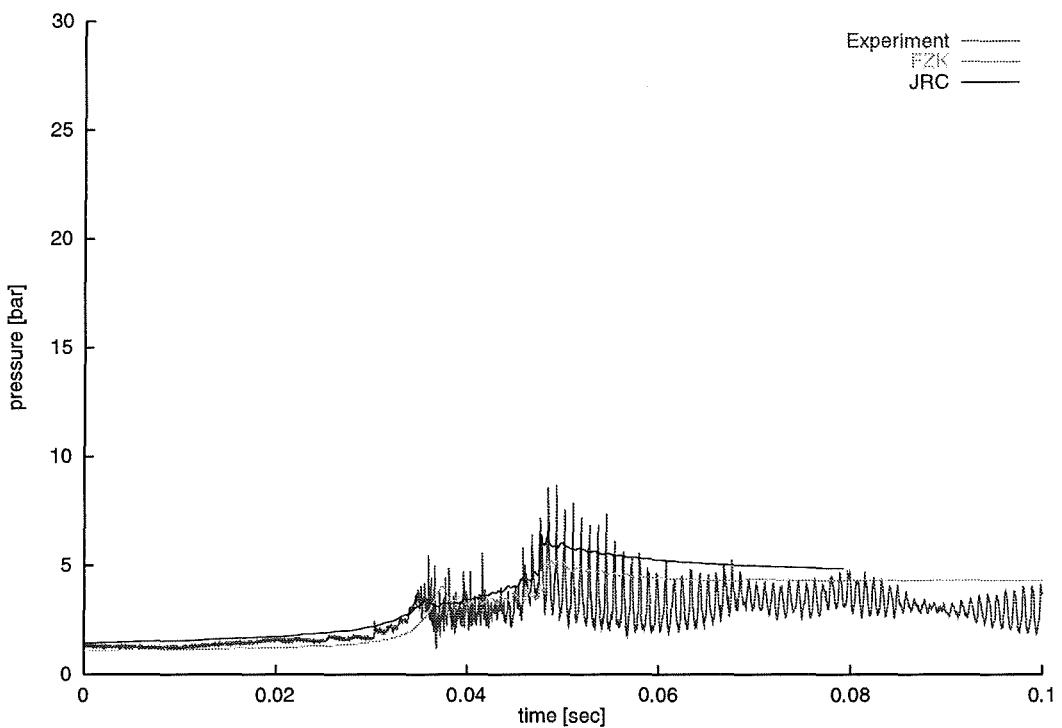


Figure 4.100: Pressure histories at position 8.25 m

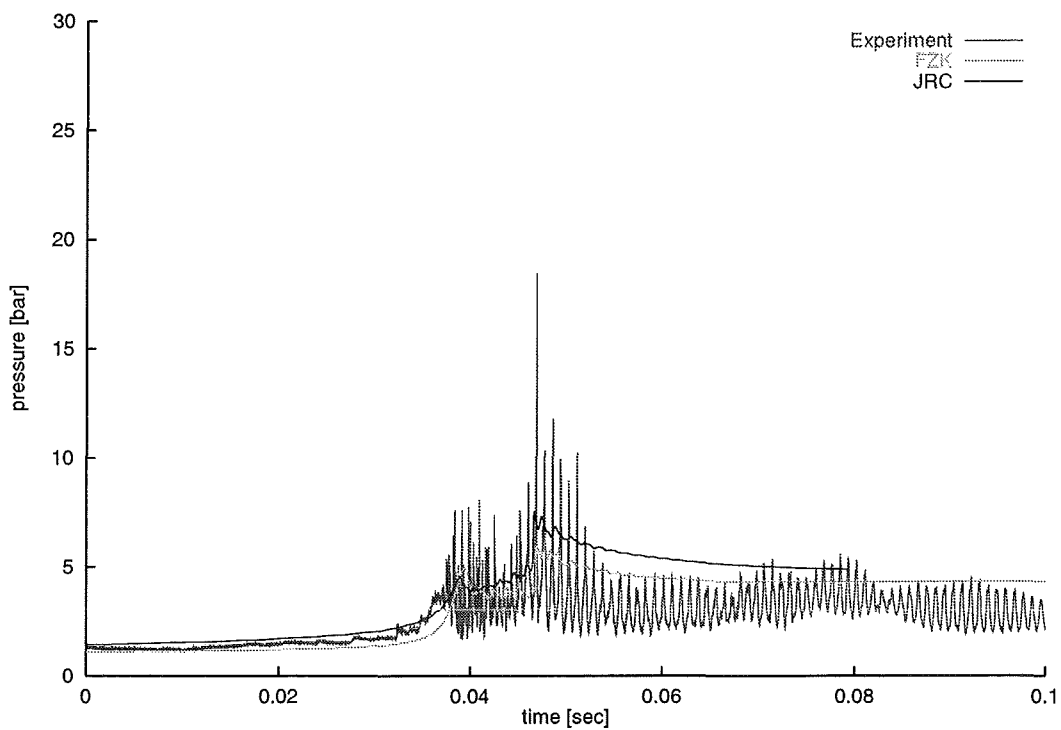


Figure 4.101: Pressure histories at position 9.25 m

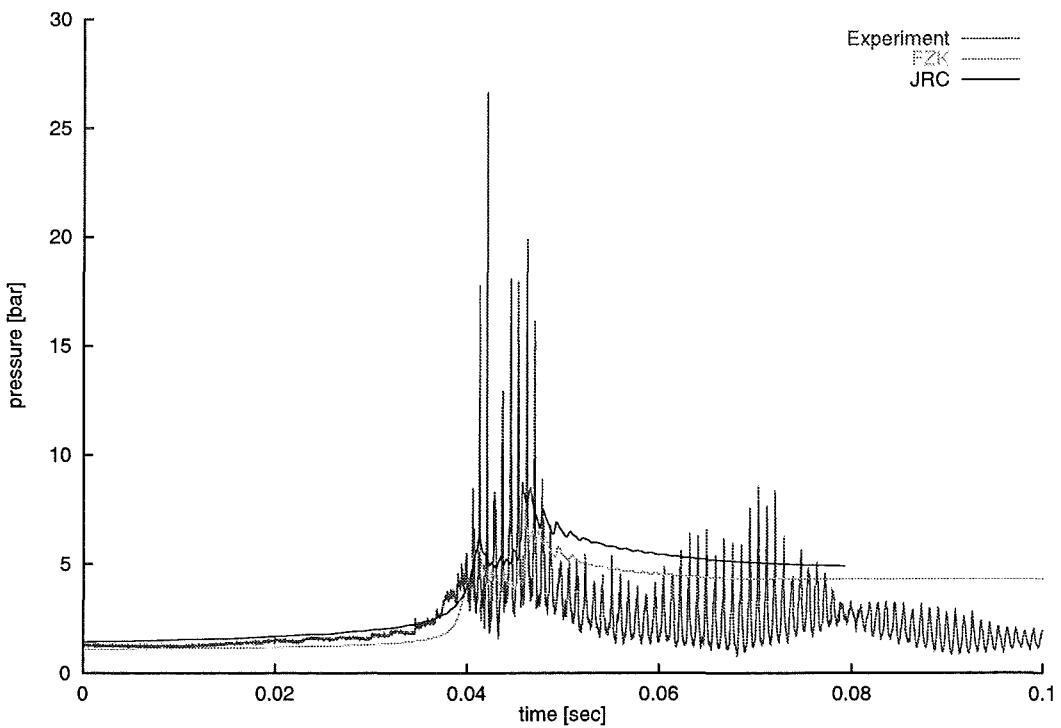


Figure 4.102: Pressure histories at position 10.25 m

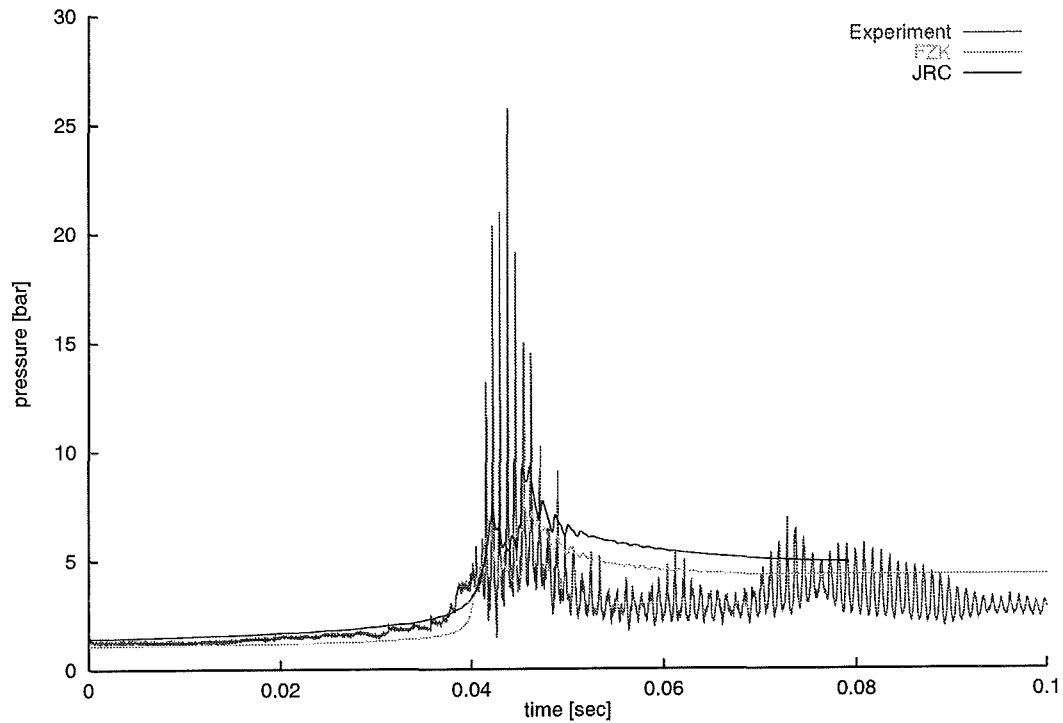


Figure 4.103: Pressure histories at position 10.75 m

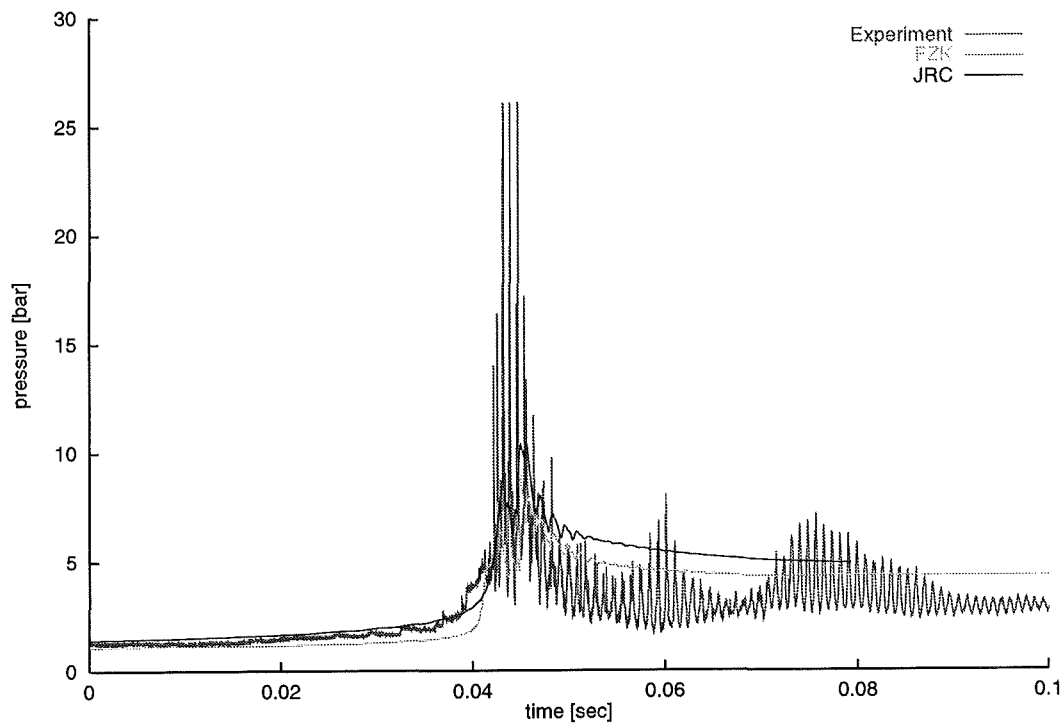
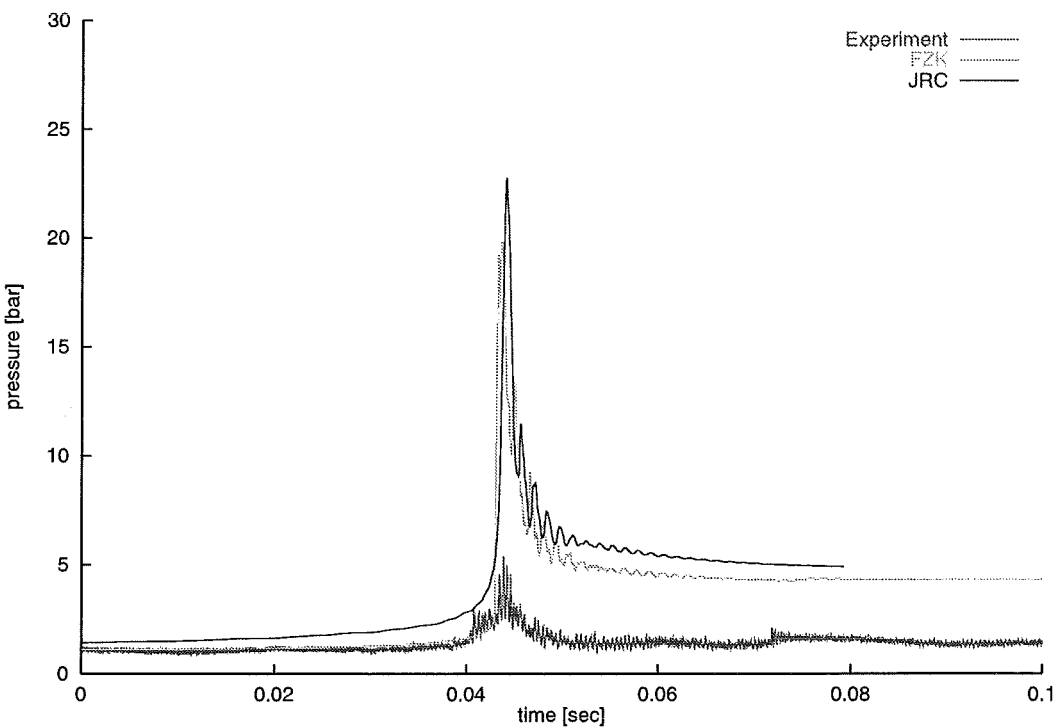
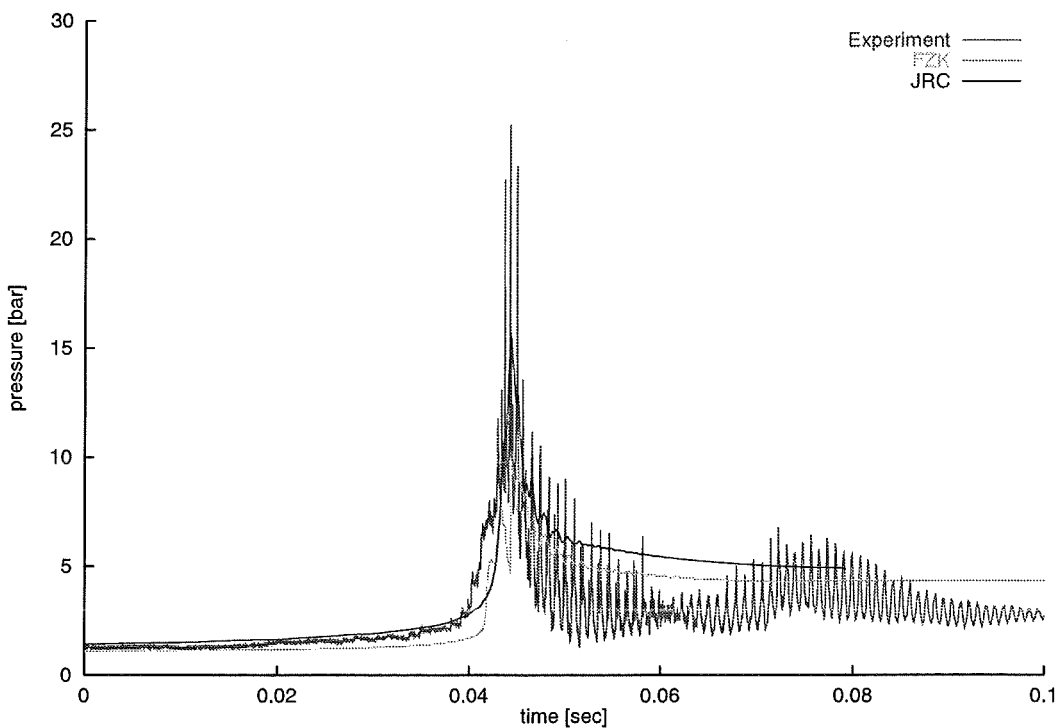


Figure 4.104: Pressure histories at position 11.25 m



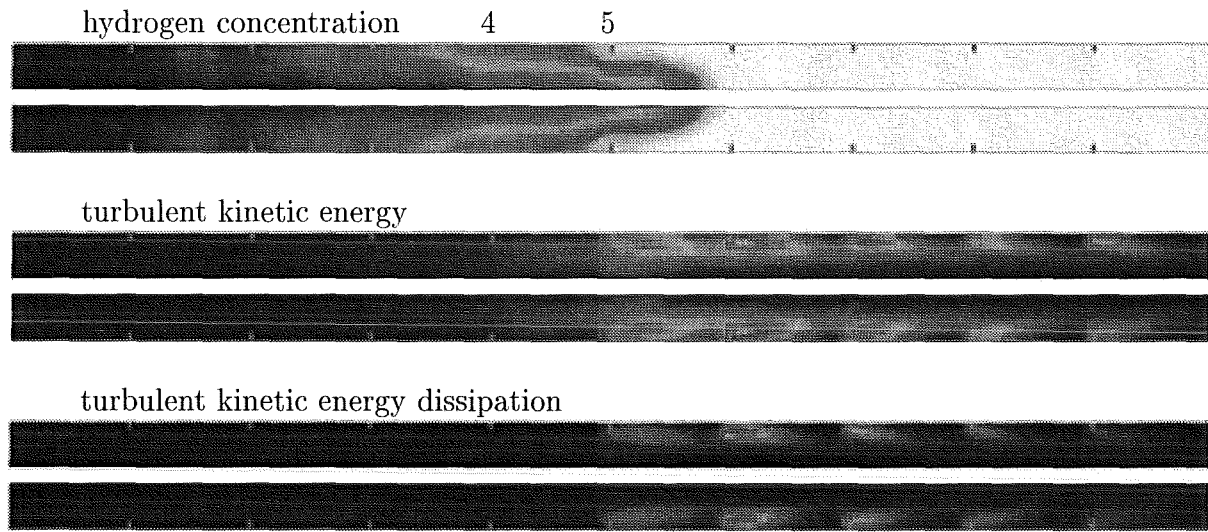


Figure 4.107: COM3D field data: flame between obstacles 5 and 6

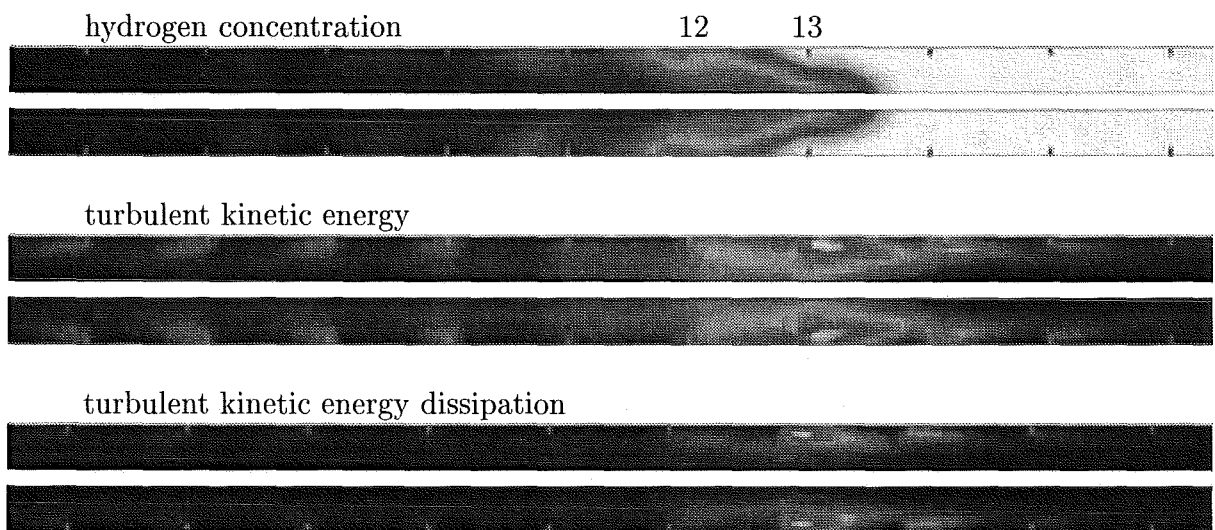


Figure 4.108: COM3D field data: flame between obstacles 12 and 13

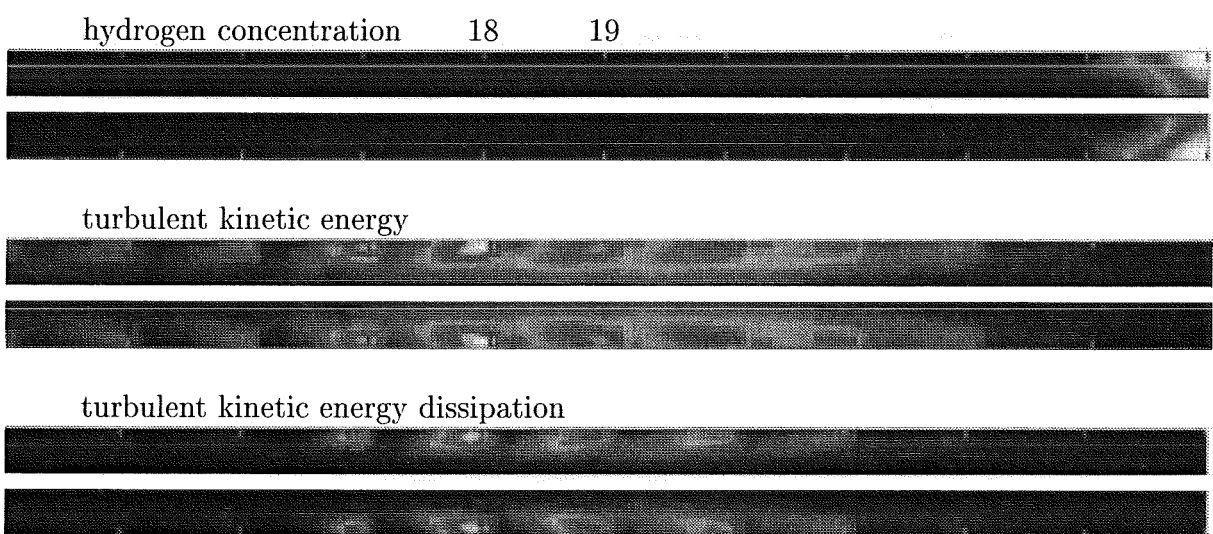


Figure 4.109: COM3D field data: flame close to the end wall

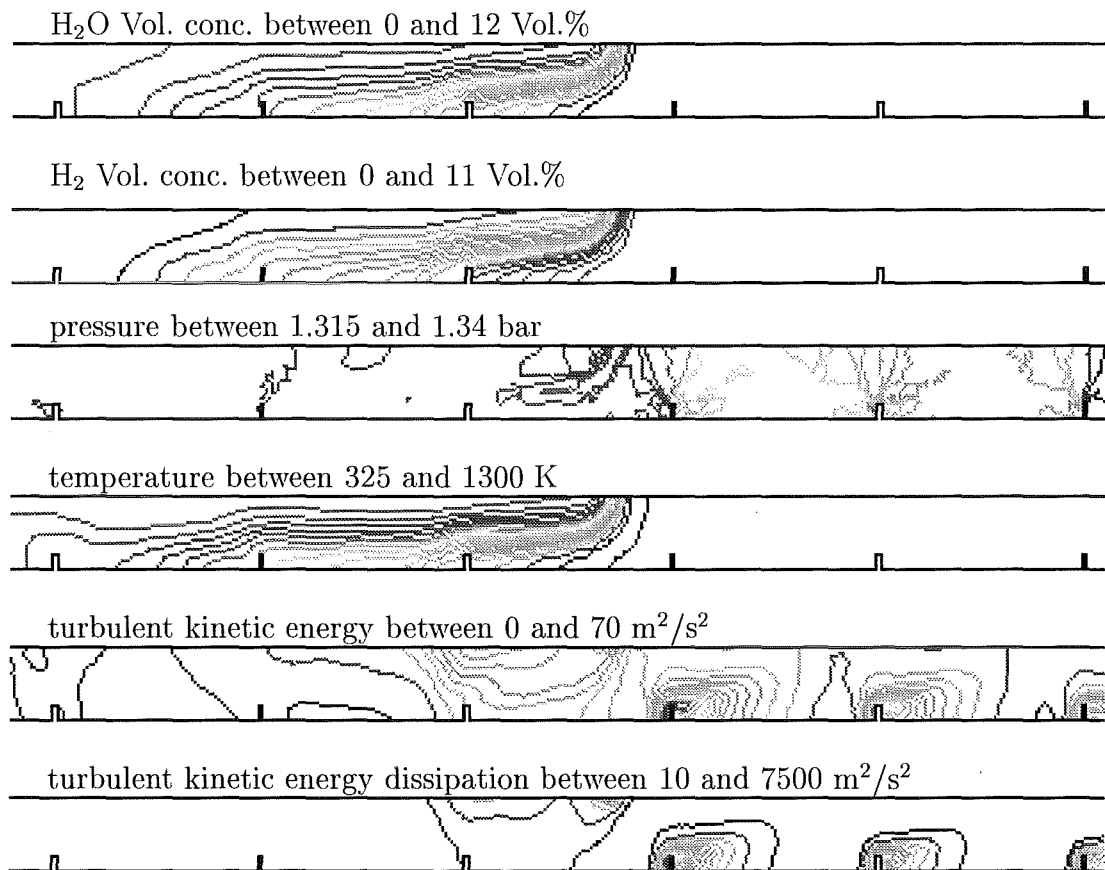


Figure 4.110: REACFLOW: Flame position at 2.75 m. 20 iso-lines from blue to red between min. and max. value in every plot.

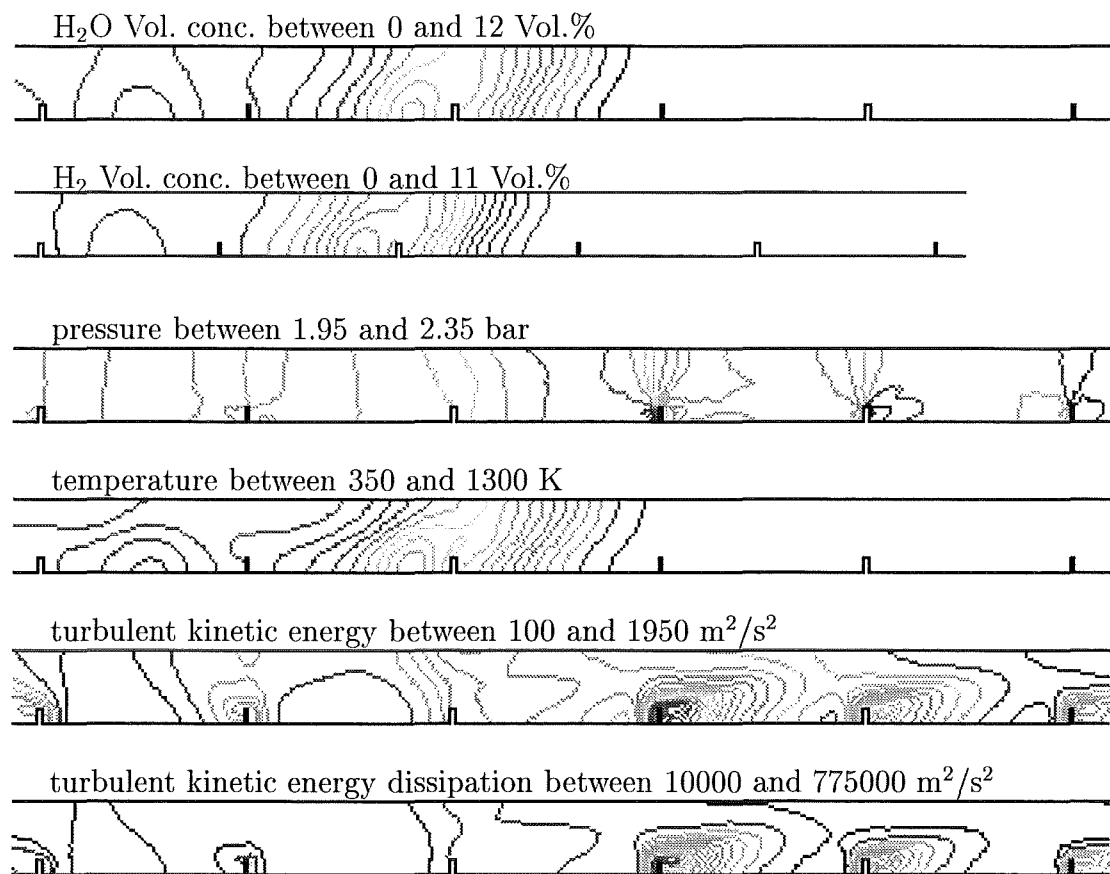


Figure 4.111: REACFLOW: Flame position at 6.25 m. 20 iso-lines from blue to red between min. and max. value in every plot.

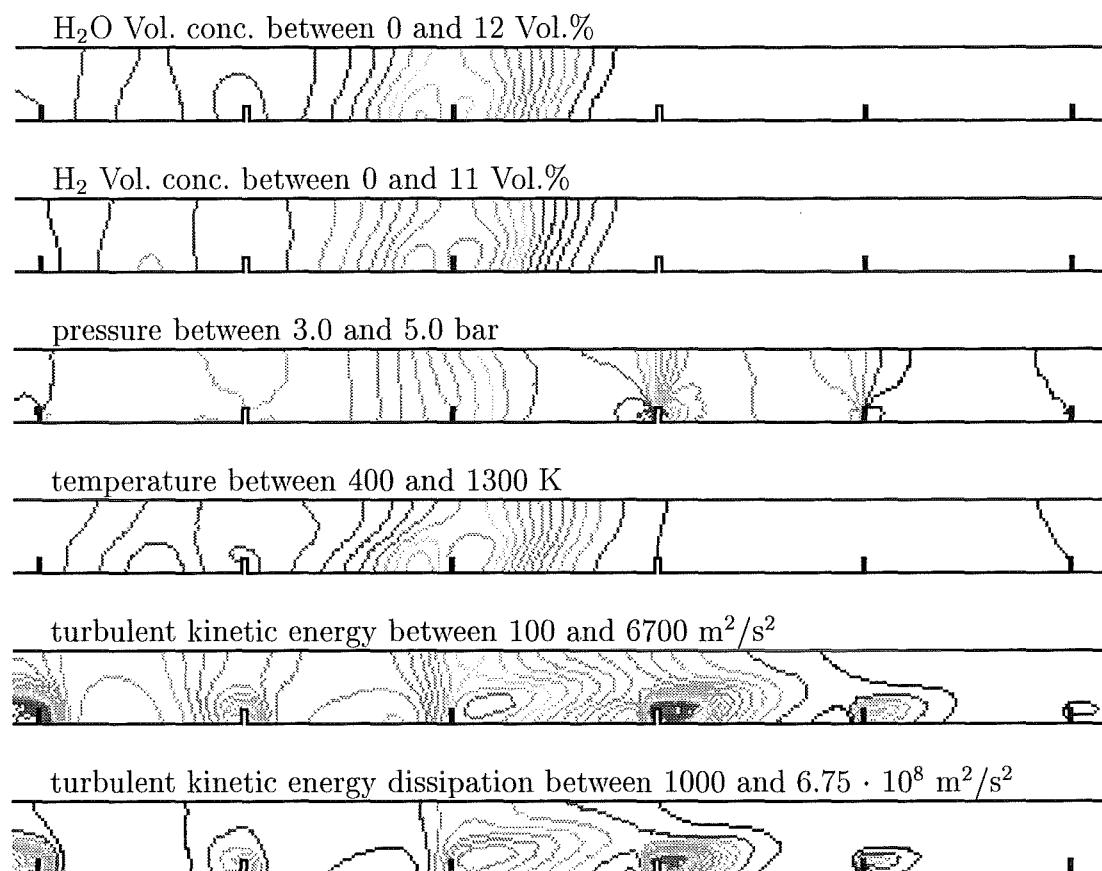


Figure 4.112: REACFLOW: Flame position at 9.25 m. 20 iso-lines from blue to red between min. and max. value in every plot.

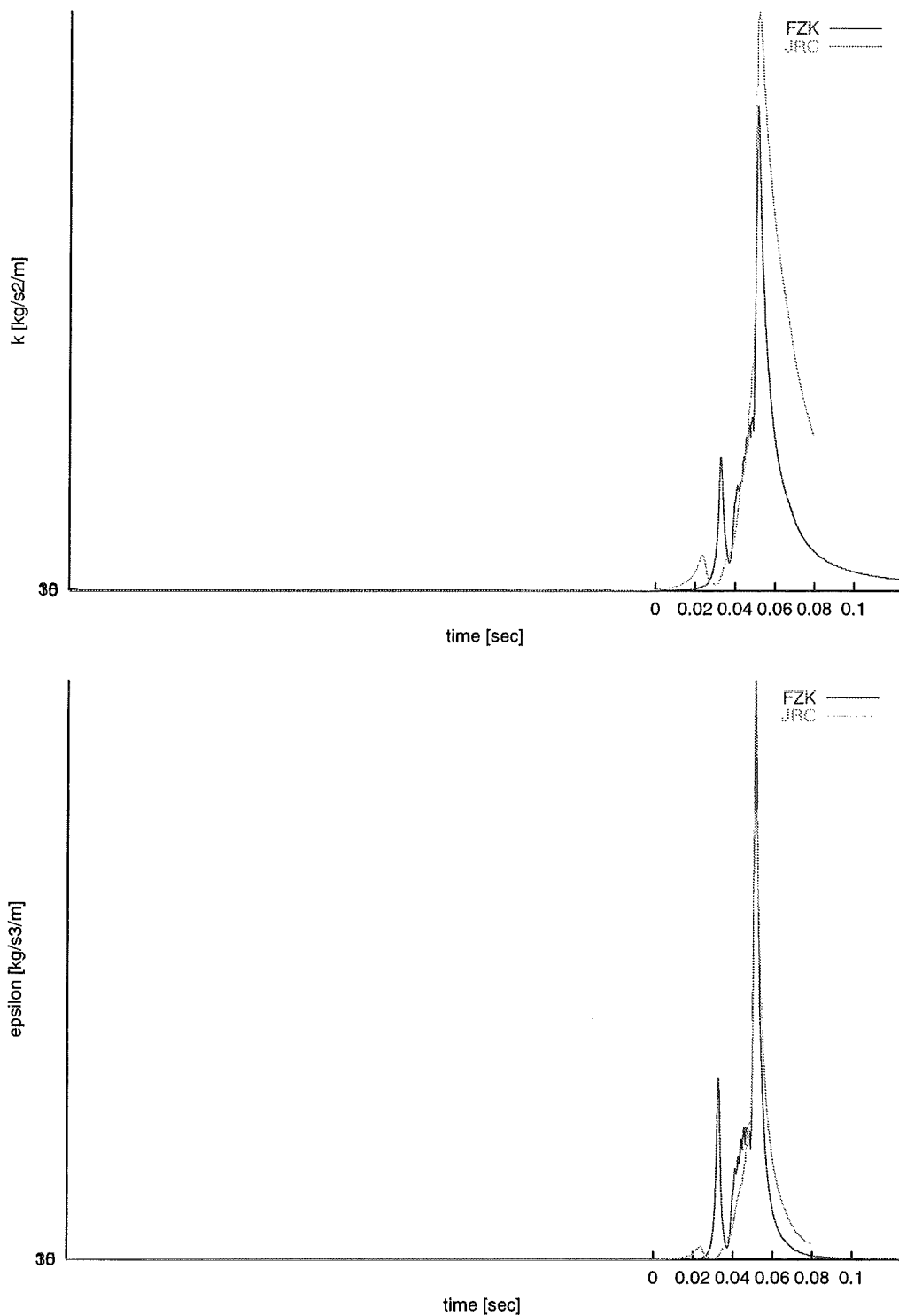


Figure 4.113: Turbulence data near obstacle 13 (6.5 m): free flow upstream of obstacle

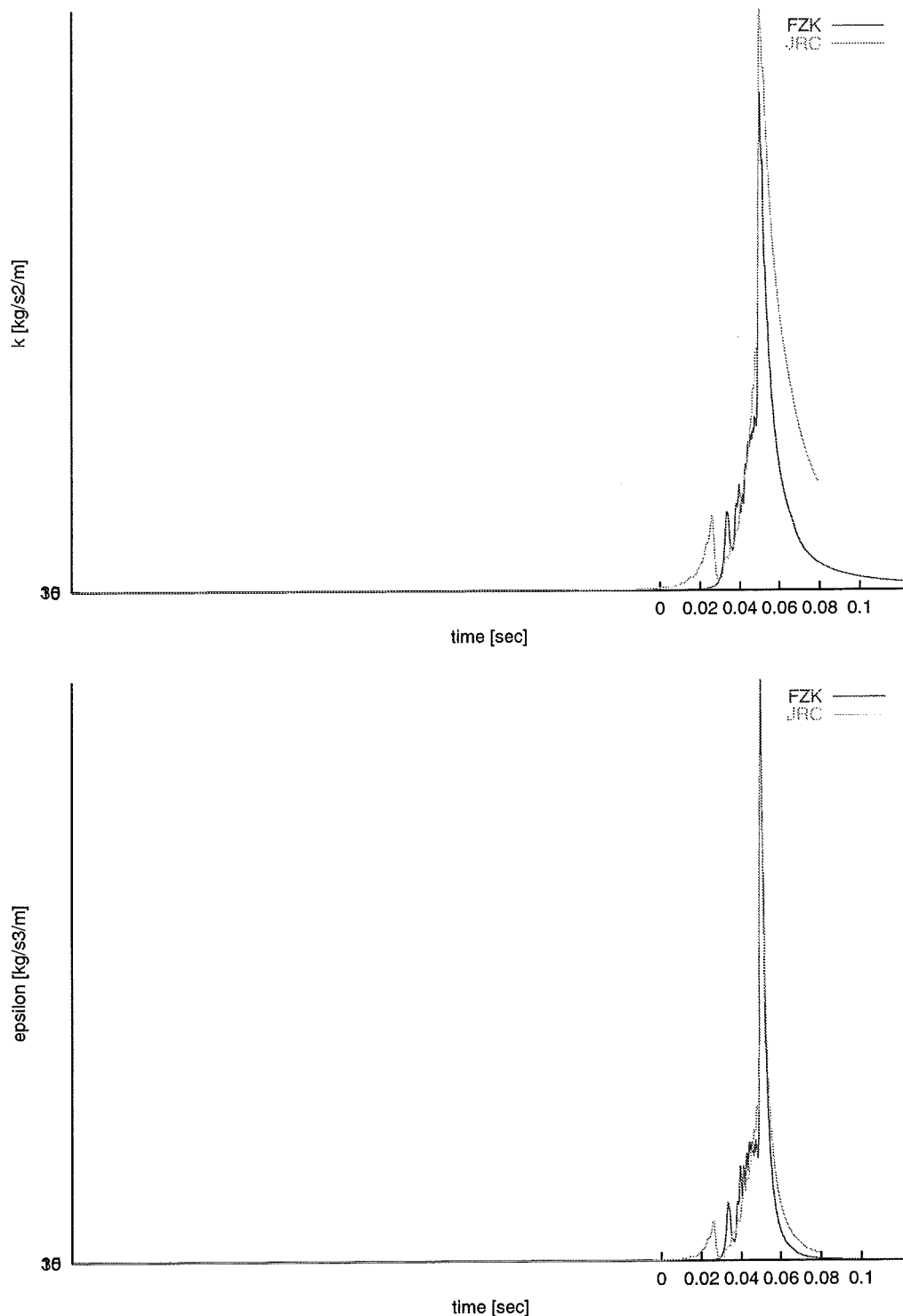


Figure 4.114: Turbulence data near obstacle 13 (6.5 m): stagnation region upstream of obstacle

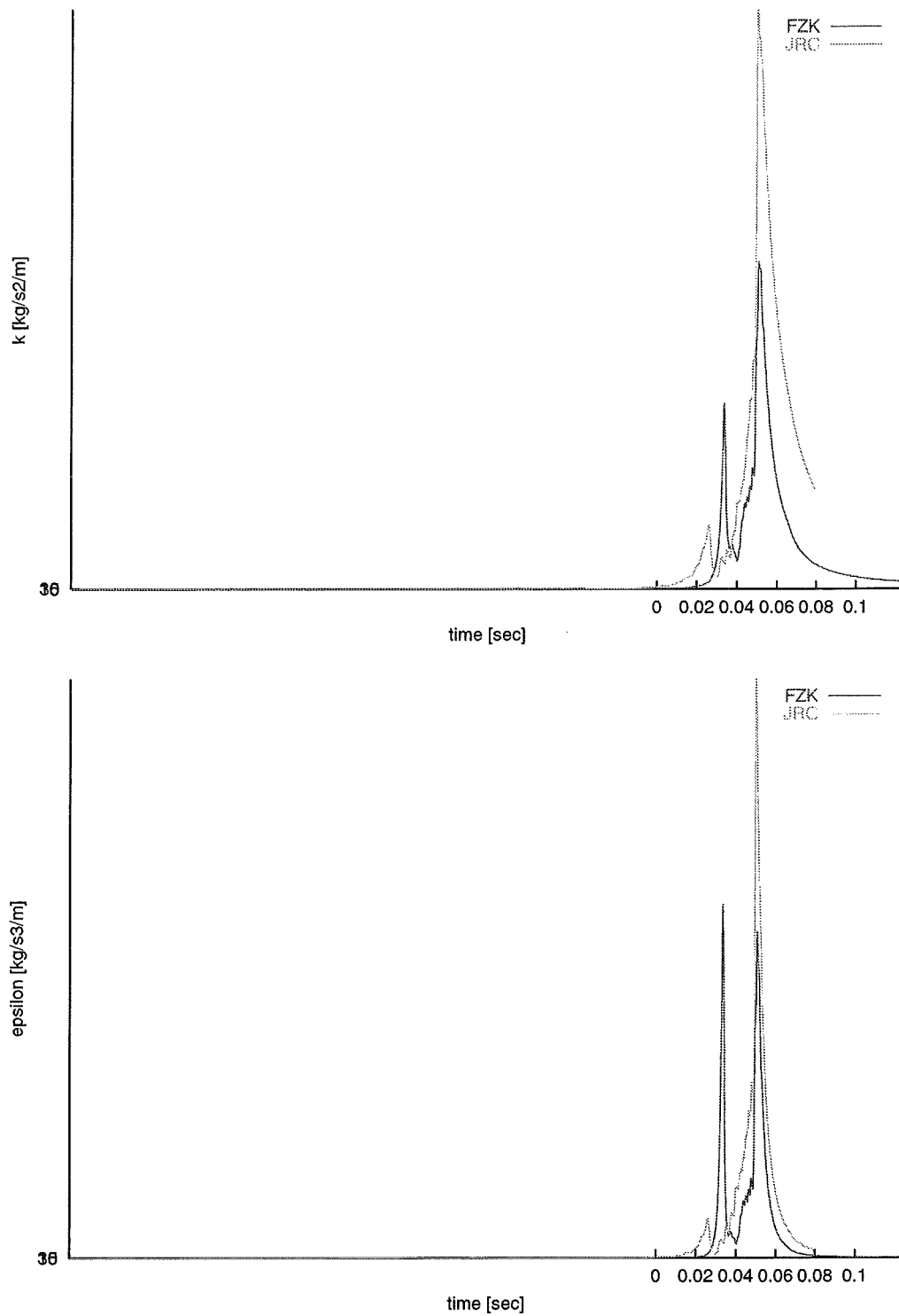


Figure 4.115: Turbulence data near obstacle 13 (6.5 m): shear layer downstream of obstacle

#### 4.6.3.2.4 Discussion of PDF calculations

The comparison between the flame propagation measured in the experiment and the calculation shows a very good agreement in the first third of the tube (see Fig. 4.116). The flame propagation-velocity and, therefore, the acceleration of the flame due to the obstacle path is well predicted. With progressing combustion process the calculation shows an increasing deviation from the measurement. This can be explained by an enhanced coupling of the flame front and the precursor pressure wave. Due to this coupling the flame is burning into a region in which the thermodynamic state has changed significantly from the initial state. As already mentioned in Sect. 4.5.4.1 the chemical reaction rate and accordingly the PDF reaction rate are strongly depending on a predefined thermodynamic state. Therefore, it is not possible to predict the strong acceleration of the flame with the applied PDF model based on one reaction progress variable. As a consequence the pressure development and the pressure peaks, which were measured in the experiment (see Fig. 4.93 to Fig. 4.106), can not be predicted. Furthermore the expansion flow in front of the flame is underestimated and, therefore, the induced turbulence field. Based on this knowledge the calculation is considered for verification (see Sect. 4.6.3.2.4.1) only in the first part of the FZK tube.

In Fig. 4.117, the flame front and the turbulence field is shown in the region  $0,9\text{m} < z < 3,4\text{m}$ . The flame is identified by the reaction progress variable  $\tilde{c}$ , where  $\tilde{c} = 0$  represents the unburnt, and  $\tilde{c} = 1$  the fully burnt mixture. The second picture points out that turbulence is mainly induced in front of the flame. Due to the fact that the turbulent kinetic energy at this stage of the combustion process is located to a great extent in large eddies near the walls between the obstacles, the flame is accelerated by the turbulent influence beneath the middle axis. Therefore, the flame shape is folded in the middle of the tube.

##### 4.6.3.2.4.1 Discussion of the PDF model by means of the combustion simulation in the FZK tube

Since the combustion process in the FZK tube is well predicted by the PDF model in the first third of the tube, the most important variables are evaluated at the position  $z = 3,25\text{ m}$  as a function of time. In order to point out the influence of turbulence the position is located near to the wall between two obstacles where a higher turbulence level is expected. See Fig. 4.118 for the location of the tracer.

The upper tracer in Fig. 4.120 shows the reaction progress and the concerning reaction rate  $w_{H_2O}(c)$ . The flame is identified by the progress variable  $\tilde{c}$  progressing from 0 to 1. Since the reaction rate is depending on the reaction progress  $\tilde{c}$  and on the variance  $\tilde{c}''^2$  the development of the variance is depicted in the second picture of Fig. 4.120. As an outer limit the dashed line shows the maximal possible variance

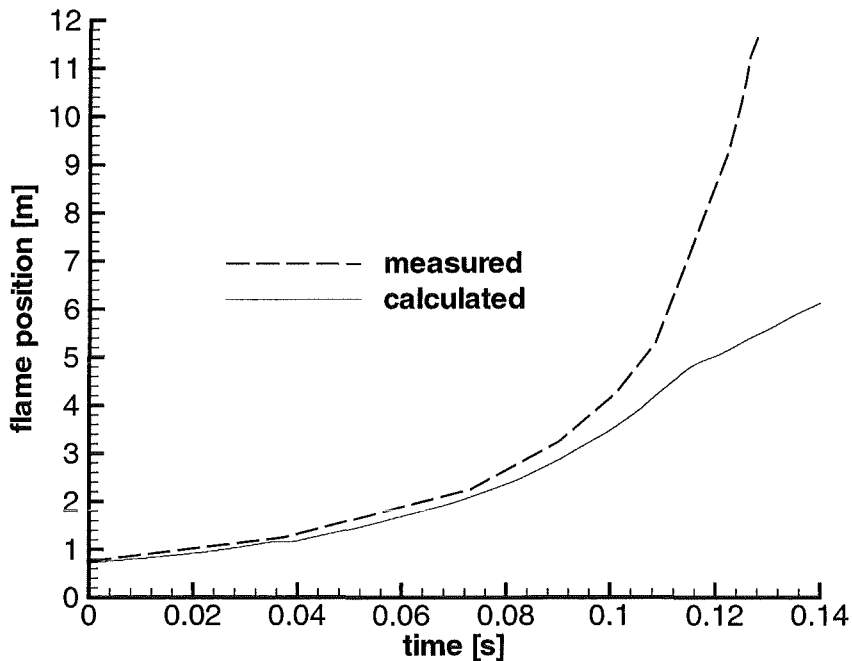


Figure 4.116: Comparison of experimentally determined data with numerical calculations of the flame propagation in the FZK tube for a 11vol%- $H_2$  in air mixture

$$\widetilde{c''^2_{max}} = \tilde{c}(1 - \tilde{c}). \quad (4.9)$$

The variance has a strong influence on the reaction rate and, in addition to that, it provides an information about the approxiamted shape of the flame. As can be seen in Fig. 4.119 the maximum reaction rate tends to a lower reaction progress if the variance tends to be maximal, i.e., if the normalised variance tends to be one. In this case the flame is considered to burn in a very thin flame front and the combustion process is expected to be limited by turbulent mixing. Due to the high variance the clipped gaussian PDF consists mainly of two peaks at 0 and 1 and, therefore, the folding with the laminar reaction rate leads to a smaller PDF reaction rate. If the variance reaches its maximum no reaction takes place and the mixture is considered to be seperated in unburnt and fully burnt regions. On the other hand if the variance tends to zero the clipped gaussian PDF consists mainly of the gaussian distribution between 0 and 1 and the PDF reaction rate becomes more and more chemical limited. In this case the combustion process is supposed to proceed in a very thick flame front. Finally, if the variance is 0, the reaction rate is corresponding to the chemical limited reaction rate (also

referred to as 'laminar' reaction rate).

At the considered location, the variance reaches a maximum value of  $\widetilde{c''^2} = 0.185$ . Hence it can be concluded that the flame is burning in a thickened flame front. Because the variance plays an important role in the PDF combustion simulation the determination of the variance has to be considered. The progress of the variance is determined by solving a scalar transport equation for  $\widetilde{c''^2}$ . This transport equation is mainly influenced by three source terms which are printed over the time in the fourth picture of Fig. 4.120. The three source terms are:

- $svar_{grad}$ : gradient production:

$$2 \frac{\eta_t}{Sc_e} \left( \frac{\partial \tilde{c}}{\partial x_k} \right)^2 \quad (4.10)$$

- $svar_{skd}$ : scalar dissipation:

$$-c_c \bar{\varrho} \frac{\epsilon}{\bar{k}} \widetilde{c''^2} \quad (4.11)$$

- $svar_{cw}$ : reactive term:

$$2 \overline{c'' w_c} \quad (4.12)$$

The term  $svar_{skd}$  is always a negative source and, therefore, reduces the variance. In contrary the term  $svar_{grad}$  is always positive and increase the variance. The reactive term is mainly positive and pushes the PDF model to higher values of the variance. As can be seen, the source term  $svar_{grad}$  (by modeling  $\eta_t$  with  $k$  and  $\epsilon$ ) and the scalar dissipation term are strongly influenced by the turbulence field. It has to be emphasized that the mentioned interaction of the turbulence field and the variance production represents the main way in which turbulence effects the PDF combustion simulation. Besides the turbulence effects the numerical simulation by modeling the turbulent diffusivities in all transport equations based on the information of the turbulent kinetic energy  $k$  and the dissipation rate  $\epsilon$ .

It can be observed in the fourth picture of Fig. 4.120, that the turbulence increases considerably before the flame front is crossing the considered position. With an increasing velocity of the expansion flow  $u_{ex}$  (see lowest picture of Fig. 4.120) the turbulent kinetic energy  $k$  and the dissipation rate  $\epsilon$  are reaching their maximum and are decreasing as the combustion proceeds. The axial velocity becomes even negative as the flame front has passed at this point. The short velocity peak and the following disturbance of the velocity  $u_{ex}$  (as marked in the picture) are originating from the performed initialization of the combustion simulation. It clearly can be seen that the initialization exerts no influence on the flame front passing the reference point.

The pressure trace shown in the lowest picture of Fig. 4.120 reveals that no pressure peak is induced by the flame front, and that the pressure level is steadily increased as was measured in the experiment at this stage of the combustion process.

#### 4.6.3.2.4.2 Conclusions

Within this project a presumed PDF combustion model based on the idea of Bray [29] was implemented in the commercial code CFX4.2. The PDF model has been adjusted in a way, that it was possible to calculate combustion processes with different premixed hydrogen-air mixtures.

For the verification of the calculations, experiments were performed in the PhD-facility at the TU Munich and the FZK combustion tube, measuring the flame with photo diodes and pressure transducers for flames in different hydrogen-air mixtures. In order to investigate the effect of turbulence on the flame propagation, two different experimental set-ups were chosen:

- PhD tube with 15 obstacles with a blockage ratio of 60 % and a mixture of 13% $H_2$  in air.
- FZK tube with 23 obstacles with a blockage ratio of 30 % and a mixture of 11% $H_2$  in air.

The calculations revealed a basic problem of the applied PDF model. Due to the fact that the reaction rate calculated with the PDF model is based on a predefined initial guess the simulation can not account for enthalpy changes of the combustible mixture. This change has to be considered if the flame front propagates with a velocity faster than the speed of sound of the initial mixture. In this case a direct interaction of the flame front and the precursor shock wave takes place with the consequence that much higher reaction rates, due to the different thermodynamic state in which the flame is burning, can occur.

In order to overcome this problem the calculation for the PhD tube was performed with PDF reaction rates based on an increased temperature and pressure level (extracted from the measurements). With this approximation the numerical simulation showed a good agreement with the measurements concerning the maximum flame speed and the pressure development.

In the case of the combustion simulations based on the FZK set-up a very good agreement between the calculation and the measurements can be observed up to the point where the flame is accelerated strongly due to the coupling of the flame front and the precursor shock wave.

From the obtained results it can be concluded that for flames propagating at low Mach numbers the PDF model based on one progress variable is able to predict the propagation velocity. In the case of a strong acceleration of the flame and a propagation velocity at a high Mach number the applied PDF model has

to be extended with PDF reaction rates which account for enthalpy changes. A simple way to realize this is to calculate the PDF reaction rates for different initial guesses and interpolate the pressure and temperature dependent exact PDF reaction rates. In order to account for the temperature fluctuations an additional progress variable which is based on the temperature information has to be introduced. This has the consequence that two additional scalar transport equations (variance of the progress variable for temperature and the covariance) have to be solved.

A further improvement could be the use of a more detailed chemical reaction scheme instead of using a complex reaction for the hydrogen combustion. The reaction rate based on this extended information could be determined using ILDM methods by Maas [39].

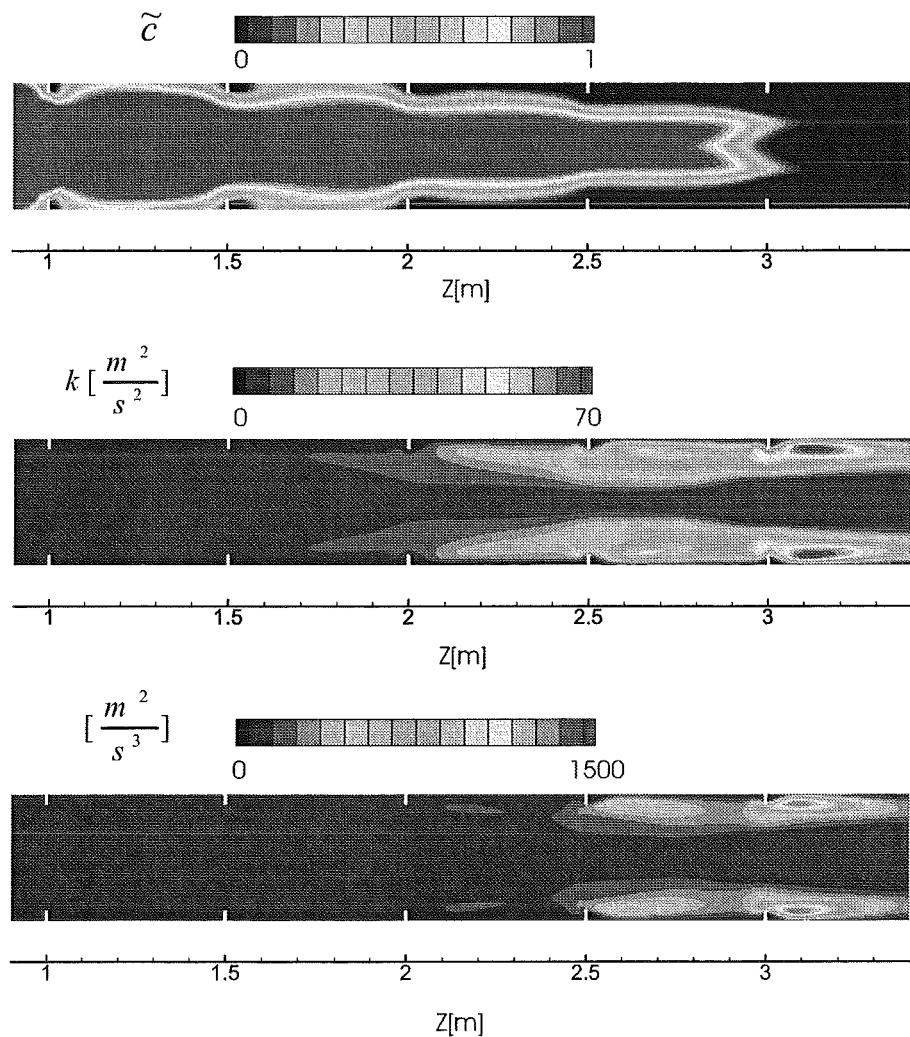


Figure 4.117: Flame front and the turbulence field during the combustion process in the FZK tube (11 vol%  $H_2$  in air)

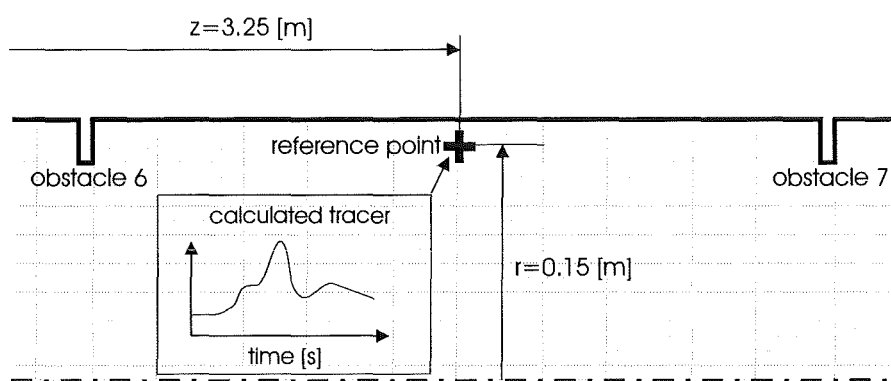


Figure 4.118: Location of the reference point in the FZK tube

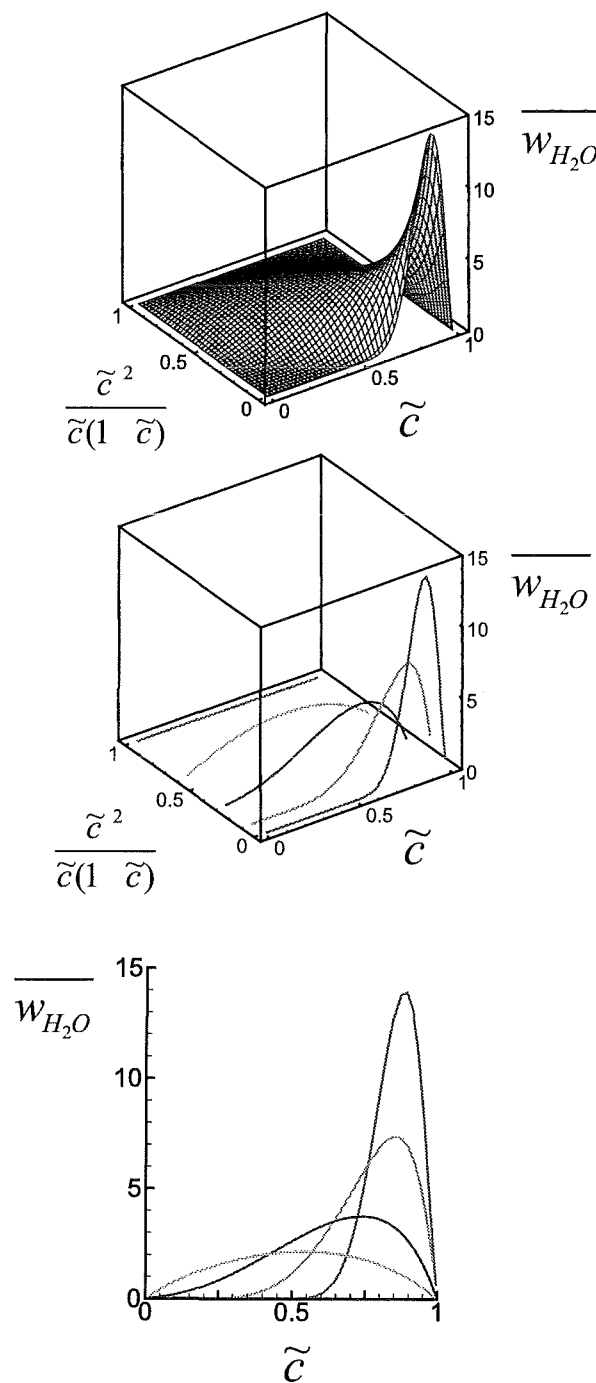


Figure 4.119: The influence of the normalised variance on the PDF reaction rate

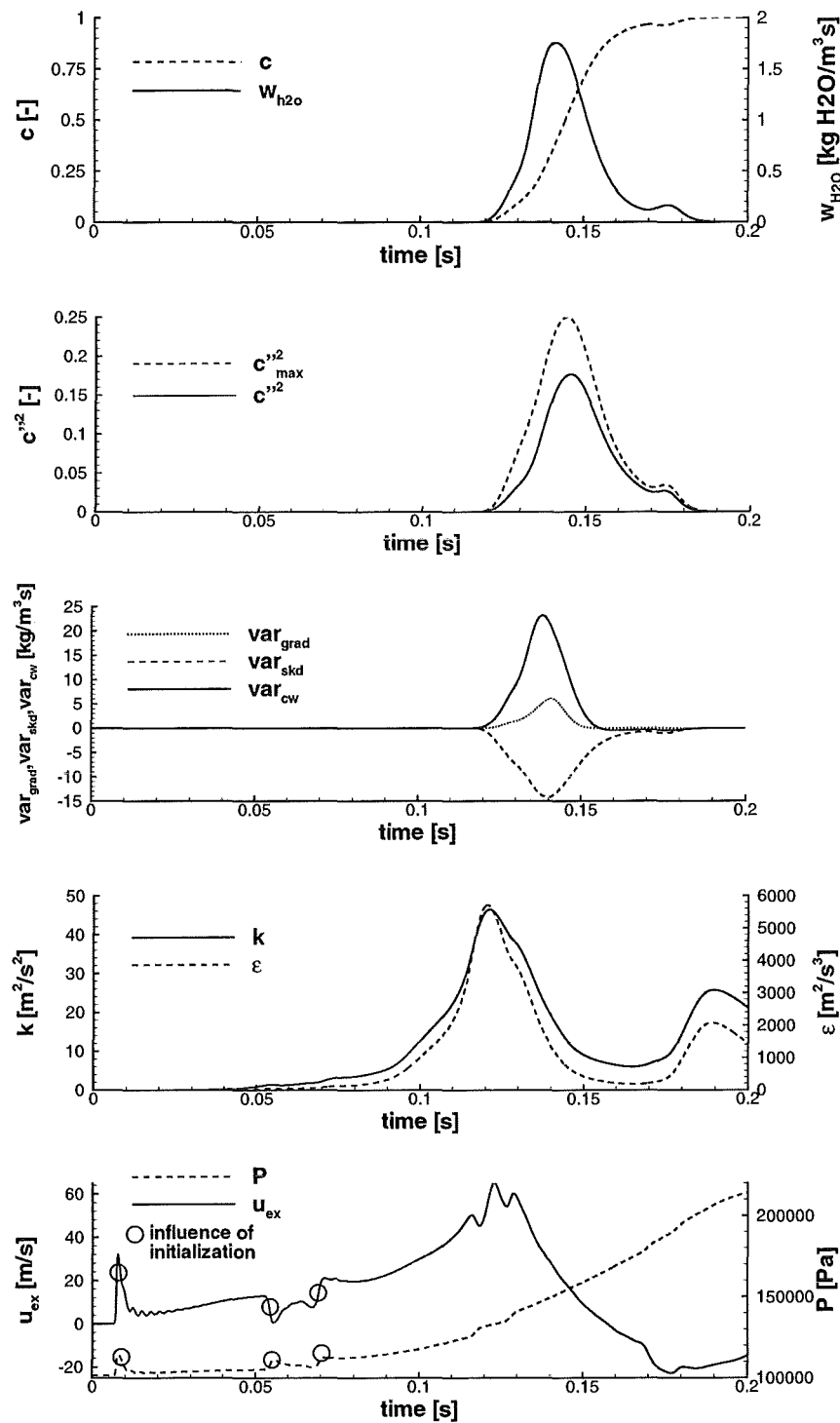


Figure 4.120: Time development of PDF model variables at the position  $z = 3.25$  m in the middle of the FZK tube

#### 4.6.3.3 R0498\_05 - 12 % $H_2$

A 12 % hydrogen air mixture was selected as a third benchmark in the FZK tube. Calculations for this experiment were performed by FZK and JRC. Pressure histories of the COM3D calculation are compared in Figure 4.121 to the experimental values for all 14 available probe positions. Figure 4.122 shows similar data for the REACFLOW calculation. Here only 6 selected positions in the second half of the tube are displayed.

Due to the higher hydrogen concentration compared to the previously discussed benchmark the combustion proceeds faster. However the general behavior is similar. Both codes predict the flame propagation throughout the tube fairly good.

#### 4.6.4 Summary of benchmark calculations

In this section benchmark calculations with four different codes were compared. Due to limitations in the different codes not all benchmarks could successfully be calculated with all codes. Still it is not possible to select one code as superior to all others in all situations.

The Tonus Code from CEA is specifically designed for low Mach number flow. Therefore it has advantages for dilute mixtures with low hydrogen concentrations where only slow flames can develop.

The REACFLOW code from JRC and the COM3D code from FZK cover a wide range of combustion regimes. The COM3D code is the only fully 3D code in the tests, but has some limitations for very low hydrogen concentrations (below 10 % by volume). While REACFLOW and COM3D have quite different grid representations, their basic models are similar and thus the calculated results are also close to each other.

The code developed by TUM uses the most advanced combustion model. However, at present the achievable grid resolution seems not to be sufficient when compared to the other codes.

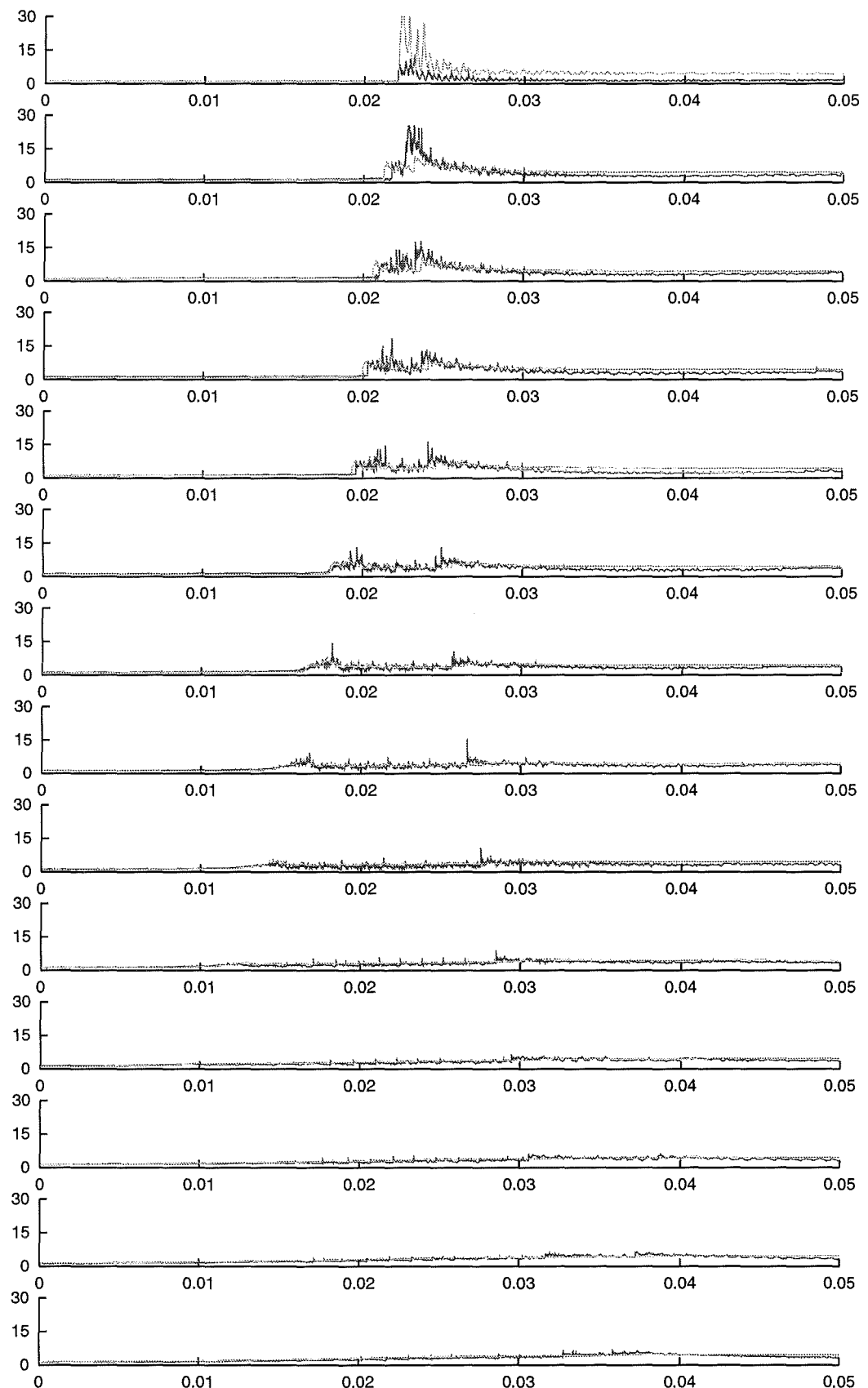


Figure 4.121: Pressure histories for R0498\_05

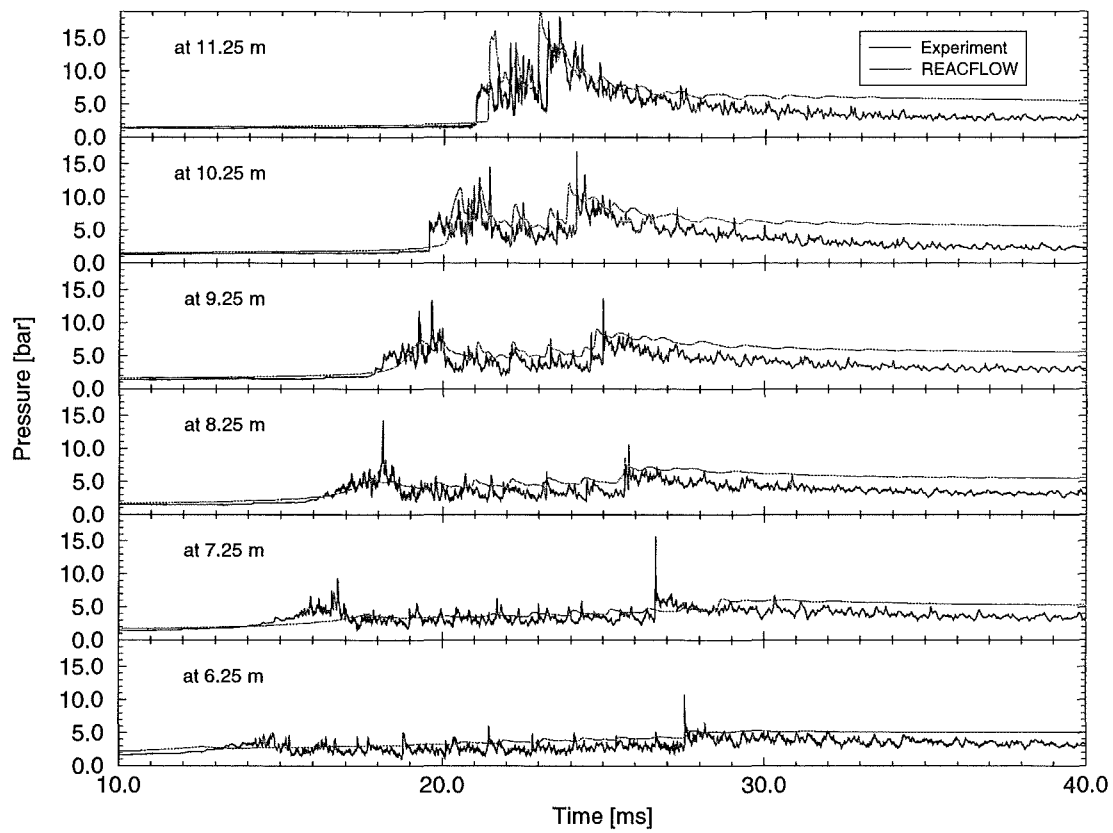


Figure 4.122: JRC

# Bibliography

- [1] J. Spore, P. Royl, J.R. Travis et al.. GASFLOW: A Computational Fluid Dynamics Code for Gases, Aerosols and Combustion. Report LA-13357-M and FZKA-5995, Vol III Assessment Manual, Oct. 1998.
- [2] W. Breitung and al. Hydrogen-Air detonation experiments in complex geometry and their analysis with different codes FISA 1995.
- [3] H. Paillère, S. Clerc, C. Viozat, I. Toumi and J.-P. Magnaud. Numerical Methods for Low Mach Number Thermal-Hydraulic Flows. ECCOMAS 98.
- [4] C. Viozat. Implicit Upwind Schemes for Low Mach Number Compressible Flows, Technical Report, INRIA, (1997), report 3084.
- [5] S. Clerc. Etude de schémas décentrés implicites pour le calcul numérique en mécanique des fluides. Résolution par décomposition de domaines. Ph.D. dissertation, Université Paris VI, 1997.
- [6] U. Ghia, K.N. Ghia, and C.T. Shin. High-Re Solutions for Incompressible flow using the Navier-stokes Equations and Multigrid Method, Journal of computational Physics, 48, 387-411, (1982).
- [7] O. Botella and R. Peyret. Benchmark spectral results on the lid-driven cavity flow, Computers and Fluids, 17(1), 1-12, (1989).
- [8] B. Mohammadi and O. Pironneau. Analysis of the  $k - \epsilon$  turbulence model, Research in applied mathematics. Masson Edition.
- [9] D. Karmé, H. Lahjaily, P. Brûlé and M. Champion. Influence of the Turbulent Damköhler Number on the Structure of Premixed Flames in a Stagnation Flow, Combustion Science and Technology, vol 113-114, 351-365, (1996).
- [10] P. Brûlé, D. Karmé and M. Champion. A Pseudo-Compressibility Method for Reactive Flows at Zero Mach Number, International Journal of Computational Fluid Dynamics, vol 7, 291-310, (1996).

- [11] R. Saïd and R. Borghi. A Simulation with a “Cellular Automaton” for Turbulent Combustion Modelling. pages 569–577. The Combustion Institute, Pittsburgh, 1988. Proc. of 22nd Symposium (Int.) on Combustion.
- [12] J. D. Anderson. *Hypersonic and High Temperature Gasdynamics*. McGraw-Hill, New York, 1989.
- [13] R. Courant and K.O. Friedrichs. *Supersonic Flow and Shock Waves*. Interscience Publishers, New York, 1948.
- [14] A. Chpoun, D. Passerel, H. Li, and G. Ben-Dor. Reconsideration of oblique shock wave reflections in steady flows. Part 1. Experimental investigation. *Journal of Fluid Mechanics*, 301:19–35, 1995.
- [15] J. Gressier and J. M. Moschetta. On the Pathological Behavior of Upwind Schemes. 1998. AIAA-98-0110.
- [16] I. I. Glass and J. P. Sislian. *Nonstationary Flows and Shock Waves*. Clarendon Press, Oxford, 1994.
- [17] H. Li and G. Ben-Dor. A parametric study of Mach reflection in steady flow. *Journal of Fluid Mechanics*, 341:101–125, 1997.
- [18] H. Li. *Reconsideration and Modification of Analytical Models of Shock and Detonation Wave Reflections*. PhD thesis, Dept. Mech Eng, Ben-Gurion University of the Negev, 1995.
- [19] H.W. Liepmann and A. Roshko. *Elements of Gasdynamics*. John Wiley & Sons, New York, 1957.
- [20] J.J. Quirk. A Contribution to The Great Riemann Solver Debate. *International Journal for Numerical Methods In Fluids*, 18:555–574, 1994.
- [21] P.R. Woodward and P. Colella. The Numerical Simulation of 2D Fluid Flows with Strong Shocks. *Journal of Computational Physics*, 54:115–173, 1984.
- [22] Reynolds, WC. The element potential method for chemical equilibrium analysis: Implementation in the interactive program STANJAN Version 3. Dept. of Mechanical Engineering, Stanford University, Palo Alto, CA, USA. 1986.
- [23] R. Redlinger. Private Communications, 1996.
- [24] I. Matsukov, M. Kuznetsov, V. Alekseev, and S. Dorofeev. Photographic Study of the Characteristic Regimes of Turbulent Flame Propagation, Local and Global Quenching in Obstructed Areas. Report from Russian Research Centre Kurchatov Institute for FZK-INR, 1998.

- [25] Breitung, W., Dorofeev, S. B., Efimenko, A. A., Kochurko, A. S., Redlinger, R. and Sidorov, V. P., 1994, "Large Scale Experiments on Hydrogen-Air Detonation Loads and their Numerical Simulation," Proc. Int. Topical Meeting on Advanced Reactor Safety (ARS '94), Pittsburgh, USA, Vol. 2, pp. 733-745.
- [26] Dorofeev, S. B., Sidorov, V. P., Velmakin, S. M. and Zhernov A. V., 1993, "Large Scale Hydrogen-Air Detonation Experiments. The Effect of Ignition Location and Hydrogen Concentration on Loads," Report Russian Research Center, Kurchatov Institute, RRCKI-80-05/59, 123182 Moscow, Russia.
- [27] Evans, J. S. and Schexnayder, C. J. Jr., 1980, "Influence of Chemical Kinetics and Unmixedness on Burning in Supersonic Hydrogen Flames," AIAA Journal, **18**, pp. 188-193.
- [28] Klein, R., Breitung, W., Rehm, W., Olivier, H., He, L., Armand, P. and Ang, M., 1997, "Models and Criteria for Prediction of Deflagration-To-Detonation Transition (DDT) in Hydrogen-Air-Steam Systems under Severe Accident Conditions," Proc. FISA-97, Comm. Eur. Union, EUR 18258 EN, pp. 360-370.
- [29] K. N. C. Bray and J. B. Moss. A unified statistical model of the premixed turbulent flame. *Acta Astronautica*, 4:291-319, 1977.
- [30] S. B. Pope . The statistical theory of turbulent flames. *Transactions of the Royal Society of London*, 291:529-568, 1978.
- [31] R. Borghi. Turbulent combustion modelling. *Prog. Energy Combust. Sci.*,14:245-292, 1988.
- [32] B. Durst. Messungen und Simulationen zur Wechselwirkung zwischen Turbulenz und vorgemischten Flammen. München, Techn. Univ., Diss.,2000.
- [33] F. C. Lockwood and A. S. Naguib. The prediction of the fluctuations in the properties of free, round-jet, turbulent diffusion flames. *Combust. and flame*,24:109-124, 1975.
- [34] A. K. Varma, A. U. Chatwani and F.V. Bracco. Studies of premixed laminar hydrogen-air flames using elementary and global kinetics models. *Combust. and flame*, 64:233-236, 1986.
- [35] A. G. Marathe, H. S. Mukunda and V. K. Jain. Some studies on hydrogen-oxygen diffusion flame. *Combust. Sci. and Tech.*,13:49-64, 1977.
- [36] T. P. Coffee, A. J. Kotlar and M. S. Miller, The overall reaction concept in premixed laminar steady state flames,54:155-169, 1983.

- [37] S. S. Girimaji, Assumed  $\beta$ --pdf model for turbulent mixing: validation and extension to multiple scalar mixing. *Combust. Sci. and Tech.*, 78:177-196, 1991.
- [38] J. Warnatz and U. Maas, *Technische Verbrennung*, Springer Verlag, Berlin Heidelberg, 1993.
- [39] U. Maas, *Mathematische Modellierung instationärer Verbrennungsprozesse unter Verwendung detaillierter Reaktionsmechanismen*, Dissertation Universität Heidelberg, 1988
- [40] U. Maas J. Warnatz, Ignition Processes in Hydrogen-Oxygen Mixtures, *Combust. and Flame*, 74:53, 1988.
- [41] On the structure of turbulent premixed flames, *Recent Advances in Aeronautical Science*, Eds.:Bruno C.,Cascl C.,Pergamon Press, 1984.
- [42] Application of a "Presumed p.d.f." model of turbulent combustion to reciprocating engines. *Proc. 21st. Symposium (Int.) on Combustion*, The Combustion Institutue, pp. 1591-1599, Pittsburgh, USA, 1986.
- [43] Laminar flamelet concepts in turbulent combustion, *Proc. 21st. Symposium (Int.) on Combustion*, The Combustion Institutue, pp. 1231-1250, Pittsburgh, USA, 1986.
- [44] W. H. Press, *Numerical recipes*, Cambridge Univ. Press, Cambridge, 1989
- [45] B. F. Magnussen and B. H. Hjertager. On mathematical modeling of turbulent combustion with special emphasis on soot formation and combustion. *17'th Symposium (Int.) on Combustion*. The Combustion Institutue, pp. 719-729, Pittsburgh, USA, 1976.
- [46] N. Ardey. *Struktur und Beschleunigung turbulenter Wasserstoff-Luft-Flammen in Räumen mit Hindernissen*. PhD-thesis TU-Munich, 1998.

# Chapter 5

## Model application

### 5.1 Model applications from CEA

#### 5.1.1 Numerical simulation of hydrogen/steam injection

##### 5.1.1.1 A multi-compartment geometry

The numerical examples that are shown are based on a two-dimensional, four-compartment (labeled A to D) geometry (figure 5.1) which, although not particularly representative of any PWR design, induces non-trivial flow motion and allows us to compare the multi-compartment lumped-parameter model with a multi-dimensional field approach. The finite element mesh used for all the computations in this paper consists of 7424 quadrilateral elements and 7720 vertices. It is worthwhile emphasizing that the TONUS code, whether in its finite volume formulation [1] or in the finite element formulation described in this paper, uses unstructured meshes made of either quadrilaterals or triangles in 2D, and cubes, prisms or tetrahedra in 3D. An unstructured approach gives great flexibility to the code and allows complex geometries involving compartments, junctions or obstacles to be meshed fairly easily, using ‘frontal’ meshing techniques. As an example, figure 5.2 shows how the geometry considered in this paper can be triangulated. The velocity field obtained a few seconds after the beginning of a gas injection is also shown, illustrating how the finite element algorithm with its elliptic solver can handle meshes made of triangles only. (Note that for clarity, the velocity field is plotted onto a coarser mesh, as will be the case in the rest of the paper.)

##### 5.1.1.2 Three injection cases

Three injection cases are considered: hydrogen, steam and air at 650 K and in various proportions are injected during 20 seconds into the multi-compartment vessel described above, with initial pressure and temperature respectively equal

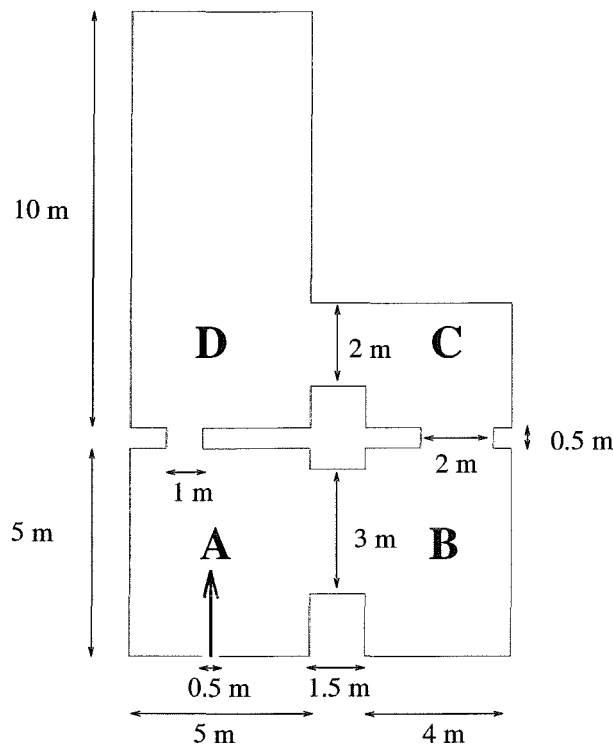


Figure 5.1: Four compartment geometry

to 1 bar and 400 K. The injection is then cut, after which only natural convection and diffusion are responsible for the mixing of the gases. Nearly steady state is obtained after approximately 160 seconds of physical time. Tables 5.1 and 5.2 give the initial and injection conditions for the 3 cases considered. Conditions are such that steam is always in a super heated state. Adiabatic wall conditions are considered, so that steam does not condensate at the walls. With these simplifications, hydrogen distribution is solely governed by mixing through natural and forced convection as well as molecular and turbulent diffusion.

### 5.1.1.3 Average hydrogen distribution per compartment

Figure 5.3 shows a comparison of average hydrogen distribution (for case 2) computed with the lumped-parameter model and the multi-dimensional model. For the latter, the mass per compartment is integrated over each compartment volume as well as over half of each junction connected to that compartment. The two distributions compare relatively well near the end of the simulation, with the multi-dimensional model predicting slightly more hydrogen in the upper compartment D. Results during the transient phase differ but this is not surprising since large time-steps were used in the case of the implicit lumped-parameter model. This information graphically illustrates the impact of the implicit parameters (not shown) and the need for fine discretization and a long simulation. The simulation results (not shown) have been compared with the lumped-parameter model results and the two are in good agreement.

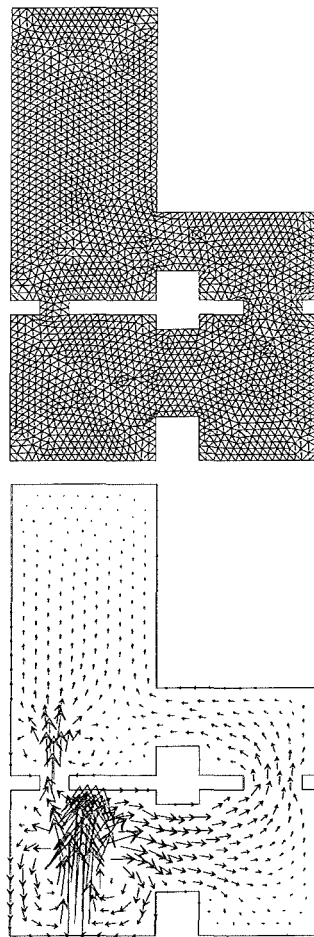


Figure 5.2: Example of an unstructured mesh made of triangles and velocity field for the multi-compartment geometry, obtained with the TONUS code

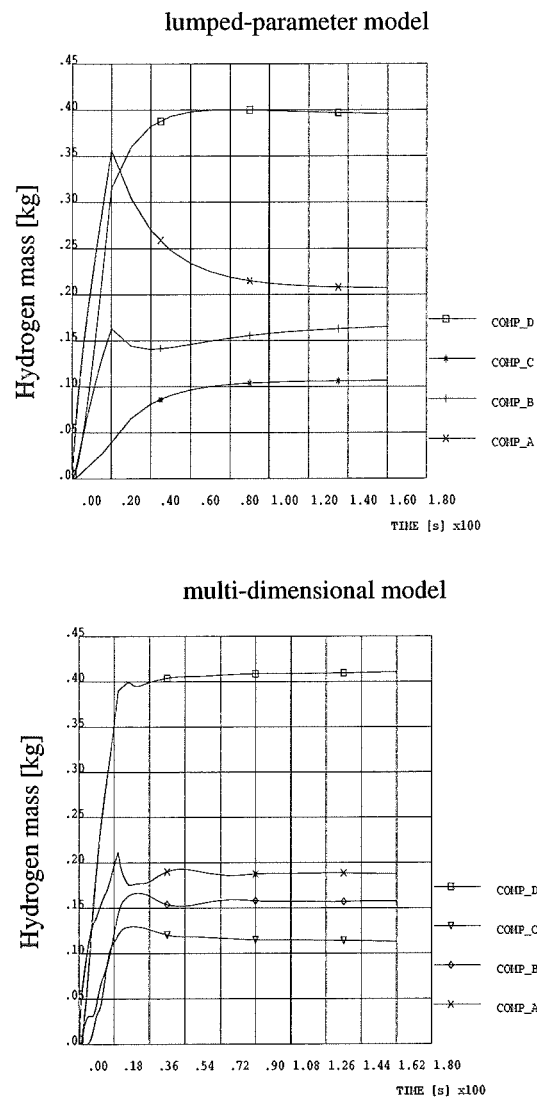


Figure 5.3: Comparison of hydrogen distribution (mass of hydrogen in kg) per compartment for case 2, obtained with the lumped-parameter (top) and multi-dimensional (bottom) models

case #	% H <sub>2</sub> vol.	% air vol.	% H <sub>2</sub> O vol.	$p_{\text{H}_2\text{O}}/p_{\text{sat}}$
1	0.	100.	0.	0.
2	0.	90.	10.	$\approx 0.04$
3	0.	70.	30.	$\approx 0.12$

Table 5.1: Initial conditions (for all three cases, pressure equals 1 bar and temperature equals 400 K)

case #	% H <sub>2</sub> vol.	% H <sub>2</sub> O vol.	% air vol.
1	10.	0.	90.
2	10.	30.	60.
3	10.	60.	30.

Table 5.2: Injection conditions (for all three cases, mass flow rate equals 5 kg/s and jet temperature equals 650 K)

obtained in all three cases. However, it is unable to reveal the precise distribution of the gases. A distribution analysis based on a multi-dimensional model is therefore mandatory.

#### 5.1.1.4 Multi-dimensional field results

Figures 5.4 and 5.5 show the velocity field and hydrogen volume fractions at times  $t = 1.2$  s,  $t = 2.6$  s,  $t = 26.7$  s and  $t \approx 160$  s, for case 2. As the vessel pressurizes, the jet velocity decreases (figure 5.7) from values close to 20 m/s at the beginning of the injection to values less than 5 m/s at the end of the injection phase. Note that the maximum velocity in the flow field is close to the jet velocity, indicating that buoyancy induced acceleration (due to the higher temperature and lighter density of the jet) remains small. During the first 20 seconds, forced convection and turbulent diffusion are the dominant mixing mechanisms. After the injection is cut, natural convection mixing is dominant, as turbulence tends to damp out. The maximum hydrogen concentration in the three cases decreases rapidly from 10% (in the jet) to levels varying between 6 and 8% (figure 5.8).

In figures 5.4 and 5.6, the concentration field at time  $t \approx 160$  s shows in all three cases a hydrogen stratification with higher concentrations situated quite understandably in the upper part of compartment D, as well as in the upper part of compartment C where the maximum concentration is located. The distribution of steam closely resembles that of hydrogen, with levels varying from 0% (case 1) to slightly more than 50% (case 3).

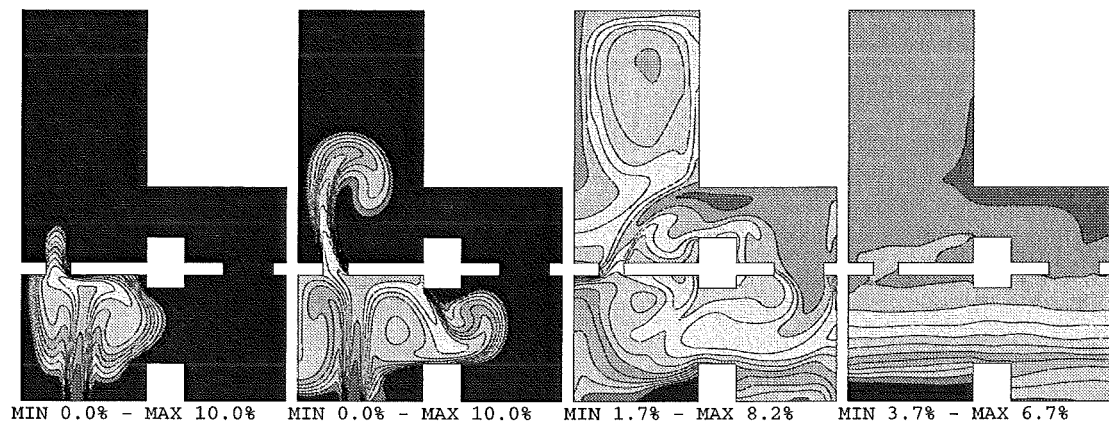


Figure 5.4: Hydrogen volume fraction at times  $t = 1.2$  s,  $t = 2.6$  s,  $t = 27.7$  s and  $t \approx 160$  s (case 2)

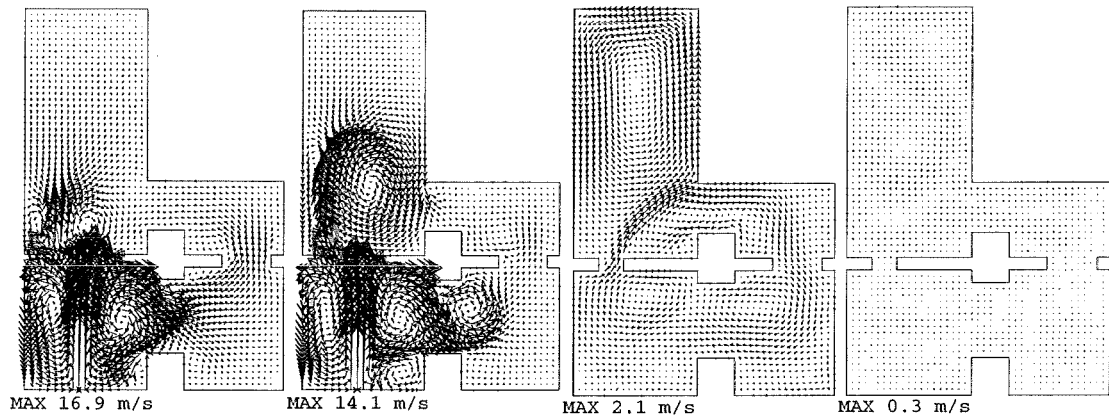


Figure 5.5: Instantaneous velocity field at times  $t = 1.2$  s,  $t = 2.6$  s,  $t = 27.7$  s and  $t \approx 160$  s (case 2)

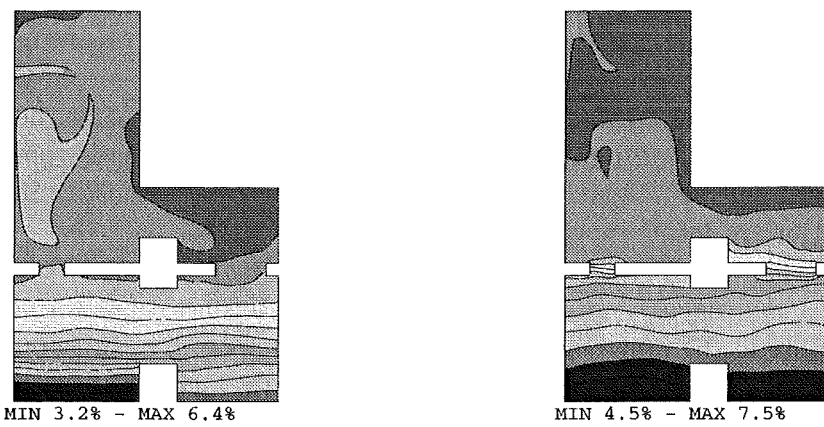


Figure 5.6: Hydrogen volume fraction at  $t \approx 160$  s (cases 1 and 3)

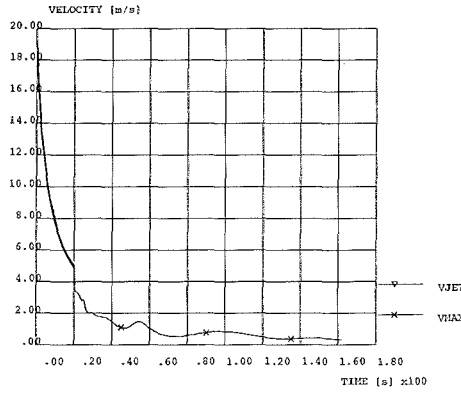


Figure 5.7: Maximum velocity in the flow and injection velocity during the first 20 s

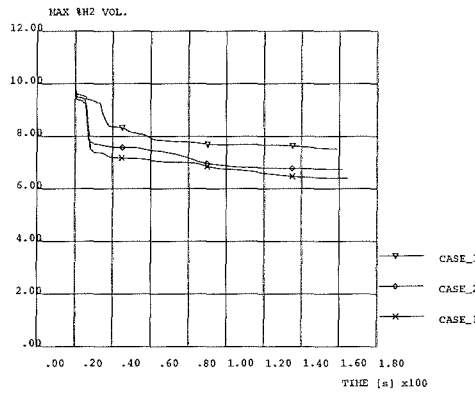


Figure 5.8: Maximum hydrogen volume fraction vs. time for the three different cases obtained with the multi-dimensional model.

### 5.1.2 Numerical simulations of hydrogen deflagrations

In this section, combustion simulations starting from the previously computed hydrogen distributions are performed. As we are interested solely in the influence of hydrogen and steam concentration on the flammability of the different gas mixtures, the pressure and the temperature have been reset to their initial values (1 bar and 400 K), keeping the volume (and mass) fractions of the different gases unchanged.

#### 5.1.2.1 Flammability diagram

The peak hydrogen concentration and the corresponding steam concentration for all three cases (at time  $t \approx 160$  s) are represented in figure 5.9, which represents the flammability limits of hydrogen, steam and air as derived by Marshall [2].

These limits have been established in conditions close to 1 bar and 400 K, in a smaller volume than the one considered here. This diagram indicates that in cases 1 and 2, the gas mixture near the peak hydrogen location lies within the flammability limits whereas in case 3, it clearly lies outside.

### 5.1.2.2 Combustion simulations

In order to try to ignite the gas mixtures, a peak of temperature has been applied near the location of the maximum hydrogen concentration (upper part of compartment C). Combustion is simulated using the 'Eddy Break-Up' model described previously. As anticipated from the flammability diagram, the mixture ignites in cases 1 and 2 but is unable to burn in case 3. Figure 5.11 shows the evolution of the volume fraction of hydrogen during the propagation of the deflagration. The initial distribution corresponds to that of case 1 (left picture in figure 5.6). The flame rapidly moves upward in compartment D, starts a swirling motion as it expands, and slowly moves downwards. Combustion is complete in just over 20 seconds. The velocity fields are shown in figure 5.12.

Figure 5.10 shows the evolution of the global pressure as a function of time in the three cases. Hydrogen in case 2 burns more slowly than in case 1, probably due to the presence of steam. On the other hand, in case 3, pressure shows only a very slight increase, indicating that the flame is unable to burn and propagate.

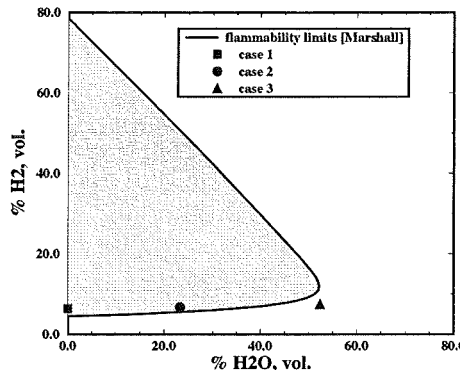


Figure 5.9: Marshall Flammability limits of air/ $H_2/H_2O$  mixtures at 0.83 bar and 383 K, and for an enclosed volume of 5.6 m<sup>3</sup> [2]. Position of peak hydrogen concentration for cases 1 to 3

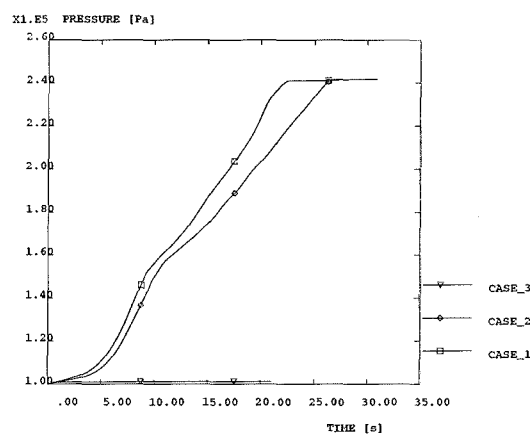


Figure 5.10: Pressure as a function of time for the three cases, with ignition point located in the upper part of compartment C

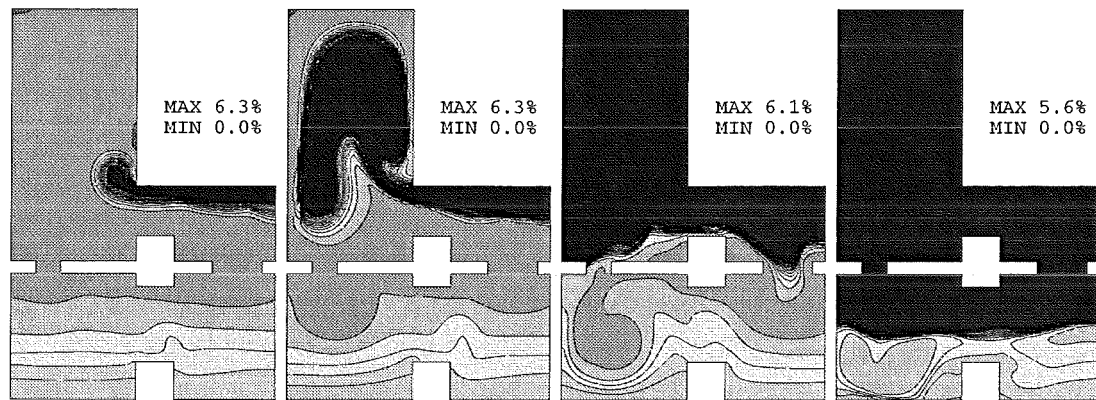


Figure 5.11: Hydrogen volume fraction at times  $t = 3.5$  s,  $t = 6.8$  s,  $t = 9.7$  s and  $t = 16.7$  s, starting from distribution corresponding to case 1

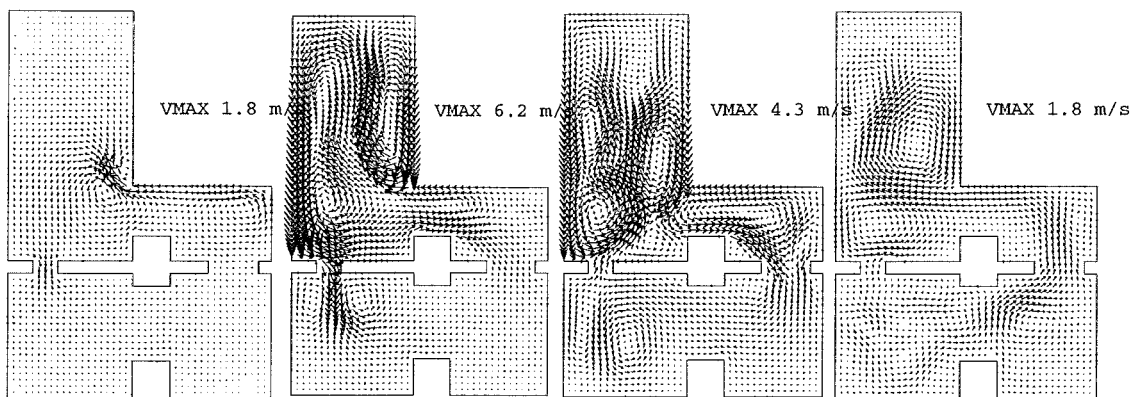


Figure 5.12: Instantaneous velocity field at times  $t = 3.5$  s,  $t = 6.8$  s,  $t = 9.7$  s and  $t = 16.7$  s, starting from distribution corresponding to case 1

## 5.2 Three dimensional GASFLOW Analysis of Steam Hydrogen Distribution with Mitigation

### 5.2.1 Introduction

During hypothetical core melt accidents, steam and hydrogen can be released into the containment of pressurized water reactors. Without counter measures, flammable mixtures may form and cause combustion loads that could threaten the integrity of the containment. Such sequences have a very low probability of occurrence and are beyond the design envelope of nuclear power plants. Measures for a risk reduction are currently being discussed to prevent an early containment failure during such beyond-design sequences. One such measure is the implementation of recombiners for the early catalytic combustion of the released hydrogen to prevent the buildup of detonable hydrogen/air mixtures in the containment atmosphere. The 3D field code GASFLOW [4] is a joint development of Forschungszentrum Karlsruhe and Los Alamos National Laboratory for the simulation of steam/hydrogen distribution and combustion in complex containment geometries. GASFLOW gives a full solution of the compressible 3D Navier-Stokes equations and has been validated by analyzing experiments that simulate the relevant aspects and integral sequences of such accidents. The newly released version 2.1 of GASFLOW that has been validated with the analysis of many integral and separate effects tests has been applied in a mechanistic 3D analysis of steam/hydrogen distribution with mitigation involving a large number of different catalytic recombiners at various locations in two types of spherical PWR containments of German design. The simulations are the first full analysis for quite complex containments. The analysis were performed after successfully predicting a buoyant helium jet and the resulting helium stratification in a blind pre-test analysis of the Battelle He-injection test Hyjet JX7 and after showing up the validity of specific recombiner models to simulate the performance of different types of recombiners in a representative containment atmosphere. The results from these 3D containment analysis show up some generic differences between similar simulations carried out in parallel by using so-called lumped parameter (LP) models [5] that represent the containment by various control volumes which are interconnected through 1D flow paths, and they identify the controlling generic effects for a scenario with a large-break loss-of-coolant accident (LOCA) in two quite different containment geometries. This final report summarizes the results from the simulation of the He injection test JX7 and from the analysis of relevant recombiner tests from the Battelle GX series that used Siemens type recombiners. Subsequently it discusses the results from the 3D containment analysis in which all these key phenomena come into play. It describes the 3D containment models, explains the applied concept of recombiner positioning, and it discusses

the results for the pressure and steam/hydrogen distribution in relation to the applied source term.

Finally the result of 3D Analysis of steam/hydrogen Distribution in Present Nuclear Reactor Containments of Siemens design will be shown.

### 5.2.2 Distribution: Blind pre-test analysis of the Battelle Hyjet He-Injection Test JX 7

In this section we describe a GASFLOW validation against the test HYJET-JX7 performed in the Battelle model containment. The objective of this test was, to have a combined jet and distribution test case. For security reasons helium instead of hydrogen was injected into the BMC. The helium was injected upwards in one of the lower Banana rooms R6 of the BMC through a 95mm nozzle. The nozzle was placed directly under an opening to an upper room R5 with an direct opening to the BMC dome. Helium was injected into the BMC for 190s at an injection flow velocity of 42m/s (in total 9.25kg helium). For a total time of 750s helium concentrations and flow velocities were measured at various positions. Details of the experiment might be found in [3].

Fig. 5.14 gives a general overview of the BMC, the helium jet, and the stratification of the jet within the dome of the BMC. In the picture a 10 vol.% helium concentration iso-surface is shown, which indicates the area of jet-entrainment and stratification within the dome area.

Fig. 5.13 shows measured and simulated helium concentrations for various position along the containment center axis. In the experimental as well as in the simulated results a clear stratification can be found. In the simulation helium concentrations are over-predicted in the upper part of the dome. This might be explained with a slightly under-prediction of the entrainment of air in the helium jet, as can be seen in Fig. 5.15 and Fig. 5.16.

Fig. 5.15 and Fig. 5.16 show a comparison between measured and simulated helium concentrations for two different times (60s and 190s after injection started). The simulation shows higher helium concentrations in the core of the jet, which is due to under-predicted entrainment into the jet. This is caused by the weakness of the algebraic turbulence used in the simulation as well as the still coarse resolution within the jet (the resolution corresponds to app. one nozzle diameter). Both simulation and experiment show a shift of the jet axis. This can be explained by some sideward openings near the jet.

Fig. 5.17 shows experimental and simulated flow velocities for two positions in the opening between room R5 and the dome of the BMC. One position was right in the jet and shows therefore an upward flow of ca. 2m/s during injection time, the other position was outside the jet but still in the same opening and shows a flow velocity of 1m/s downwards into room R5 due to entrainment/sucking of air into the jet. This is something very interesting, as in the same opening

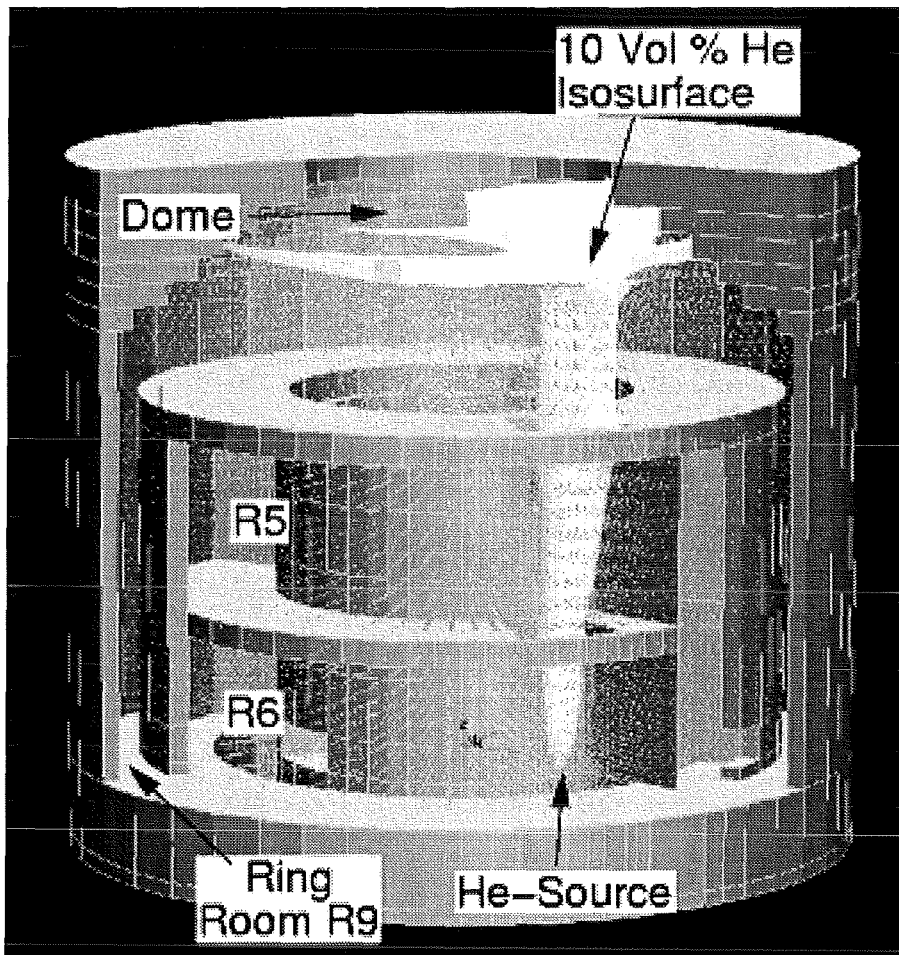


Figure 5.13: Helium jet and stratification in the BMC during HYJET JX7 test at 50s (GASFLOW-KISMET simulation)

two flow directions can be found, corresponding also to two different helium concentrations. Something like this is nearly impossible to predict with a lumped parameter code. This effect was very well predicted within the GASFLOW simulation.

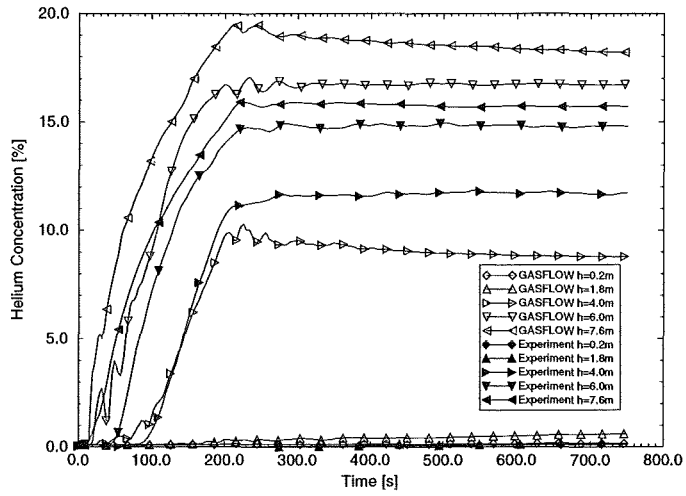


Figure 5.14: Experimental and with GASFLOW simulated helium concentrations along the BMC axis.

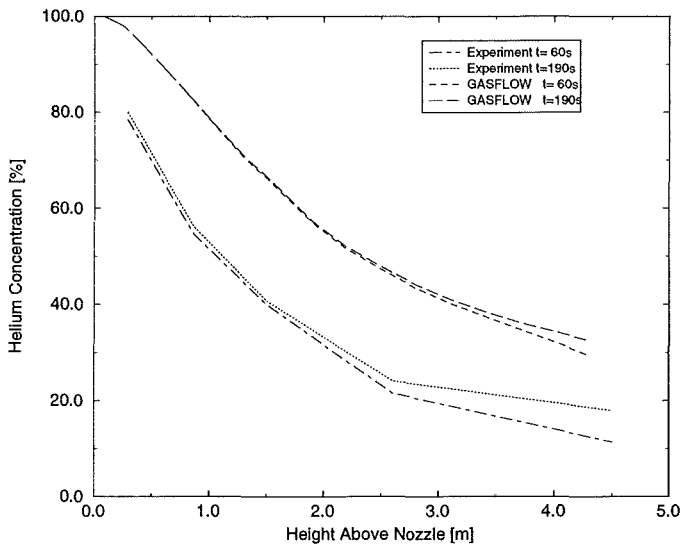


Figure 5.15: Experimental and with GASFLOW simulated helium concentrations along the jet axis at two different times.

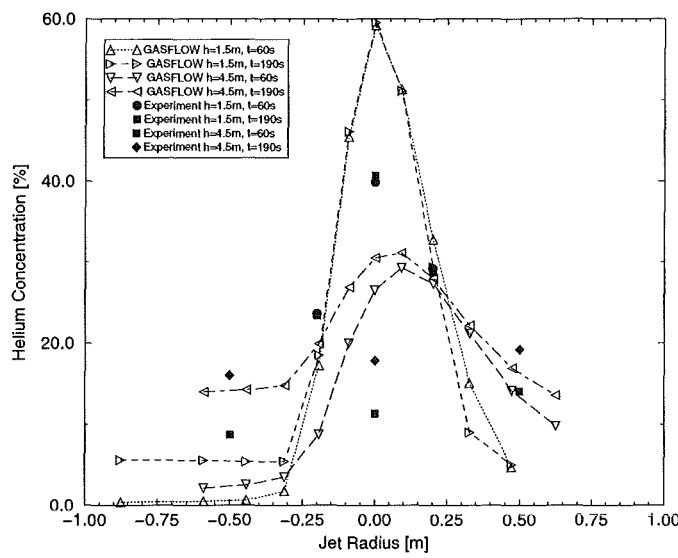


Figure 5.16: Experimental and with GASFLOW simulated helium concentrations as a function of radial position from the jet center line at two different times and two different axial positions.

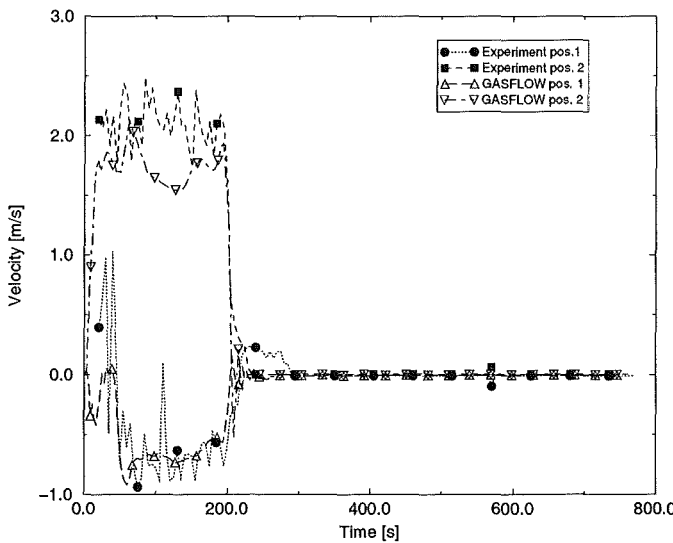


Figure 5.17: Experimental and with GASFLOW simulated flow velocities for two positions within the opening between room R5 and the dome.

### 5.2.3 Mitigation by catalytic recombiners

The installation of catalytic recombiner boxes at various locations inside the containment is considered as an option for the reduction of the hydrogen risk. Such recombiner boxes are passive devices with arrays of foils or sandwiches with granulate that are coated with a platinum containing layer. A buoyancy driven flow occurs through these boxes from the energy release of the catalytic reaction. Two different types of recombiners, the Siemens Plate and the NIS granulate recombiners are currently considered as mitigation devices. We have successfully analyzed the experiment MC3 before that tested the performance of a large prototype NIS recombiner module under conditions of steam/hydrogen release in the Battelle Model Containment [6]. During the time of the EC contract we have also successfully analyzed the GX series experiments [7] that were also performed in the Battelle Model Containment. They tested a Siemens plate recombiner box under conditions of different steam/hydrogen injections. These tests used smaller recombiner modules that were scaled from the large containment volume to the smaller test rooms of the BMC. They studied the influence of different release locations, different hydrogen release rates and different steam atmospheres. So far the GX series are the only tests that also studied the combined mitigation effect (so-called dual concept) of recombiners and igniters. We have analyzed tests GX4, GX6 with recombiners and test GX7 with recombiners and igniters using GASFLOW. Figure 5.18 gives a sketch of the test facility used for these experiments.

#### 5.2.3.1 Validation of mitigation measures with Battelle GX experiments

The Battelle Model Containment (BMC) is a cylindrical building 9 m high and 11 m in diameter (5.2.3.1). It has a free gas volume of  $625m^3$  and comprises an outer region with the dome and the annulus and an inner region with four compartments arranged in a ring, and one central compartment at two axial planes. All walls are made of concrete. The compartments can be combined in a variety of room chains by opening or closing of overflow openings.

The GX tests were performed in the annular compartments R5 to R8 ("banana rooms") and the central cylindrical room R1/R3 of the BMC. A plug on top of the central room R1/R3 and closed openings on the outside of the banana rooms sealed off this inner containment from the ring room and the dome of the BMC. The total gas volume of the participating rooms was  $209m^3$ , each banana room R5 to R8 had a gas volume of  $49m^3$ . A radial cut and the azimuthally unwrapped banana rooms (fig. 5.19) show the arrangement of the test compartments in the developed 3D cylindrical model for GASFLOW. The central compartment is closed at the top and the banana rooms can be seen on the side. On the right there are the four banana compartments in an azimuthally unwrapped representation

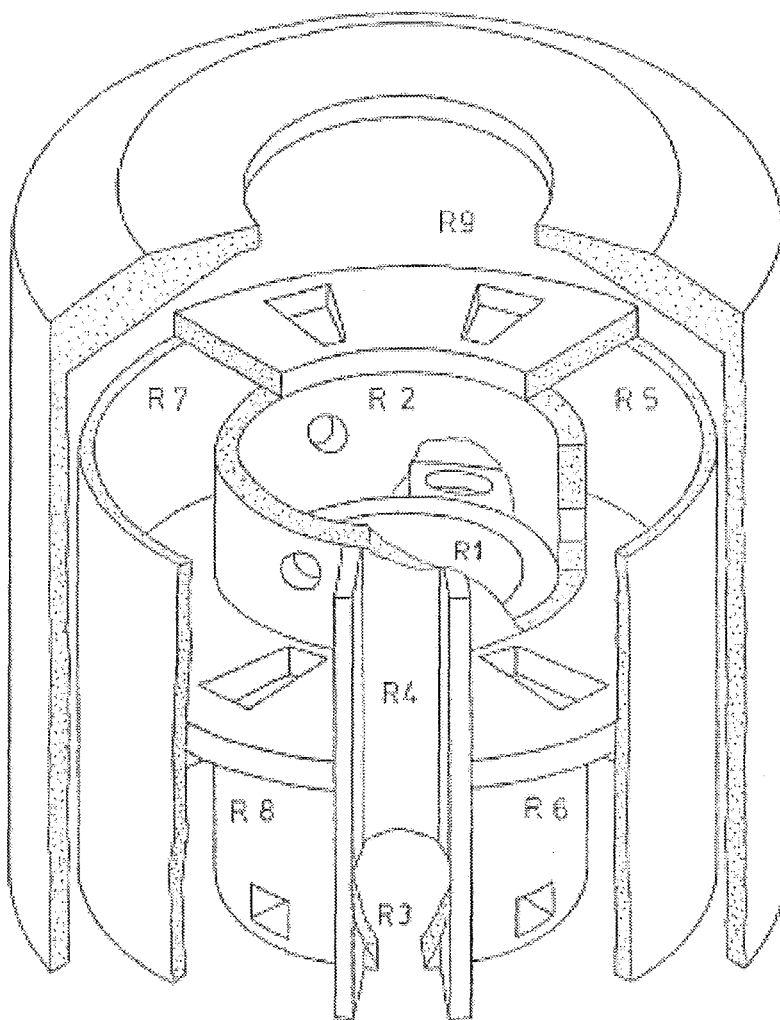


Figure 5.18: Geometry of the Battelle Model Containment

with the overflow openings linking these compartments. The inner compartments of the BMC were represented in GASFLOW by a 3D cylindrical geometry model with 5800 computational cells. The scaled recombiner box has a cross section of 11.6 cm x 16 cm, while its height of 1.6 m is that of a prototype. It is installed at the inner wall of the compartment R5, not far from the overflow opening to compartment R6. The flow passes through the box from the bottom to the top during the test. The gas heated by the recombination flows radially outward at the top into the R5 compartment.

We modeled the catalytic recombiner inside the true box size using six axial nodes (fig. 5.20) assuming the recombination energy to be released in the third node. The calculations used the measured performance data in fig. 5.20. A recombination rate was determined in dependence of the calculated hydrogen

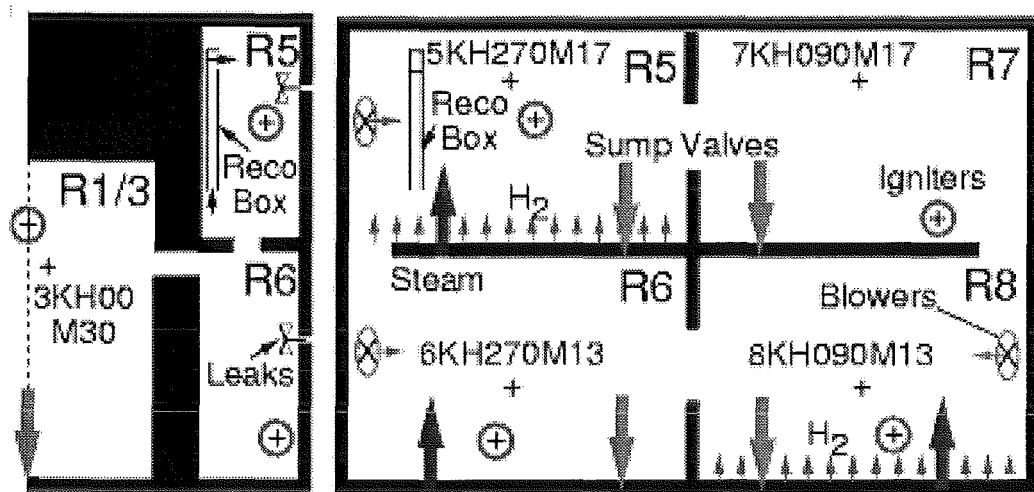


Figure 5.19: Arrangement of compartments and test setup in the Battelle model containment for the GX recombinder tests

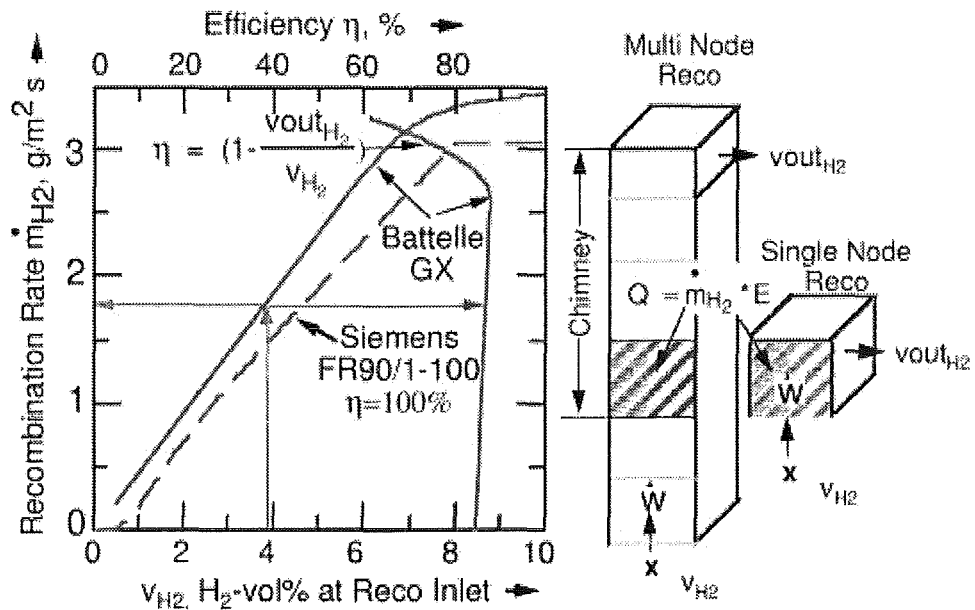


Figure 5.20: Sketch of the multi-node and single node recombinder model in GAS-FLOW

concentration at the box inlet and a forced flow boundary condition was applied at the box entrance that supplied the hydrogen and oxygen for the achievement of the measured recombination rates with the measured efficiency. For a given hydrogen concentration at the inlet to the box, the performance data define a steady state operating condition. The steady state velocity for the given hydrogen concentration is achieved with a user specified time constant. This time constant is just a few seconds for the Siemens recombiners. For other recombiners p.e. the NIS recombiners, that react with a larger thermal inertia it is in the order of 2000 s. The energy from recombining the fraction of the in-flowing hydrogen defined by the measured efficiency, heats up the entering gases and a hot exhaust flow results. When modeling the exact hydraulic resistances inside the box we could also predict the buoyancy flow from the reduction of the gas mixture density due to the recombination energy quite well with full accountance of the chimney effect that results from the differences in the density integrals on the outside and inside of the recombiner box. The simulation of the buoyancy pump from the measured recombination rate required the precise nodalization of the height of the recombiner box to capture the chimney effect. We also tested a simplified recombiner model with only a single fluid node (fig. 5.20) having an intake at the bottom and an outflow to the side. The differences were only minor [8] when using the forced ventilation option at the recombiner inlet with the measured performance data.

Such a single node representation of the recombiner box greatly enhances the flexibility for positioning of the recombiners in a complex 3D containment mesh. It avoids specific mesh adaptations for capturing the chimney effect when modeling the flow through the recombiner from the measured performance data. Most analysis of the GX tests was done with the measured performance data from fig. 5.20. But we also investigated the influence of a slightly different representation of the recombiner performance which has been suggested by Siemens [9]. We obtained a slightly reduced overall hydrogen removal with this Siemens correlation, that also included a pressure correction, but the differences were marginal.

#### 5.2.3.1.1 Test conditions

In the GX4 test, there were two periods during which hydrogen was injected, initially from a line source on the bottom of the upper banana compartment, R5, and subsequently from a line source down in the R8 compartment. Steam was injected at three locations at the bottom of R5, R6, and R8, initially for preconditioning, but then also during and between hydrogen injections. All compartments with steam injection had sump valves for pressure equilibration and also for venting the air. The valves were open during the pre-conditioning and in between hydrogen injections and briefly, due to an experimental error also while hydrogen was being injected. They were closed in time before the

hydrogen injections. The GX6 test was similar to GX4, but there was only one period in which hydrogen was injected at the bottom of R8. The GX7 test was run with considerably higher steam and hydrogen contents. At the end of the last injection period flammable conditions were reached in this test. Hydrogen was again injected in two injection periods, first in the top compartment R5 then in the bottom compartment R8. Spark igniters with a spark duration of 1 ms and a sparking interval of 7 s were installed in each compartment and were activated part of the time during the hydrogen injection in the GX7 test. This made the GX7 test the first experiment testing the combined effect of the two mitigation countermeasures provided for in the so-called "dual mitigation concept".

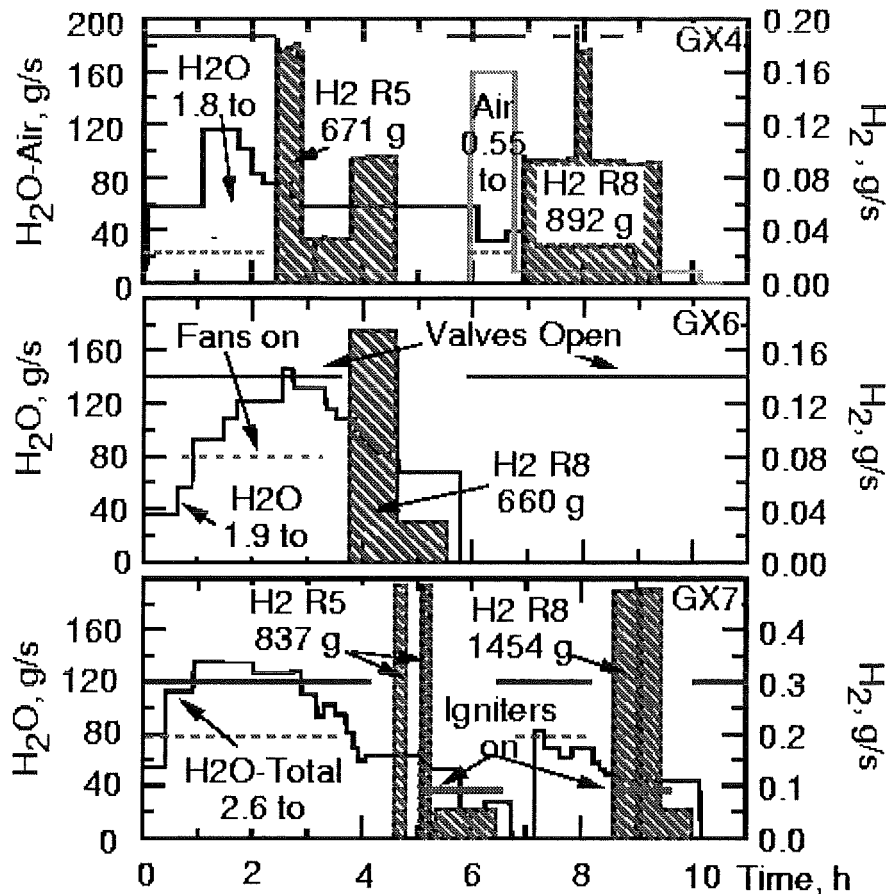


Figure 5.21: Sketch of the multi-node and single node recombining model in GAS-FLOW

The conditions of the three experiments are summarized in fig. 5.21. The dia-

gram shows the rates of steam and hydrogen injection together with the opening times of the sump valves and the periods of blower operation. For the GX7 test, also the activation times of the igniters are indicated. The analysis proved the existence of leakages. In the GX7 tests, these leakages influenced concentrations and pressure developments so much that leakage effects were simulated around the 14 instrument guide tubes penetrating the outer wall of the banana compartments. The leakage area taken into account in the analysis of GX7 totaled  $43\text{cm}^2$ , the hydraulic diameter used was 1 mm.

### 5.2.3.1.2 Results for GX4 and GX6

Calculated and measured hydrogen concentrations in the GX4 and GX6 experiments are presented in fig. 5.22. In the GX4 test, the problem time computed was 20 h, in the GX6 test, 10h. The agreement between measurements and calculations is quite good. During the second injection period of GX4 with the hydrogen source in R8 GASFLOW somewhat over-predicts hydrogen concentrations in R5 and R7 and gives a somewhat lower concentration in the low source room R8. The concentrations in GX6 are right on the measured data. The hydrogen concentration reaches a maximum of 4%. Hydrogen is distributed nearly homogeneously throughout all compartments. Minor differences occur during the second hydrogen injection in the GX4 test, while the GX6 test shows a flaw in the calculated data at 6h which disagrees with the test data. Both events are consequences of leakages not taken into account in the analysis of GX4 and GX6. The deviation in the GX4 test is a consequence of the strong decrease of the steam injection at this point in time. In the containment, which was assumed tight in the simulation, the upper compartments containing large steam volume fractions experience a pressure reduction as a result of steam condensation when the steam supply stops. At the same time, condensation of the steam adds to the hydrogen concentration in the upper compartments. The pressure sink sucks additional hydrogen from the R8 injection compartment towards the top. This results in the hydrogen concentrations being overestimated at the top and underestimated in compartment R8, compared to the measured data. In the presence of leakages, this pressure sink and the associated increase in the hydrogen volume fraction cannot occur. The flaw in the GX6 analysis is also connected with a major reduction in the steam source, but is influenced additionally by a sump valve opening in this phase. Steam reduction initially causes an increase in hydrogen concentration evident also in the measured data, albeit in an attenuated form. When the sump valve in compartment R6 opens, air is taken in in the GASFLOW analysis to offset the too strong evacuation effect. For a short period of time, this causes the hydrogen concentration to be underestimated compared to the measurement. In the presence of a leakage, and this is in agreement with the measured data, the pressure decreases only slightly as the steam source is

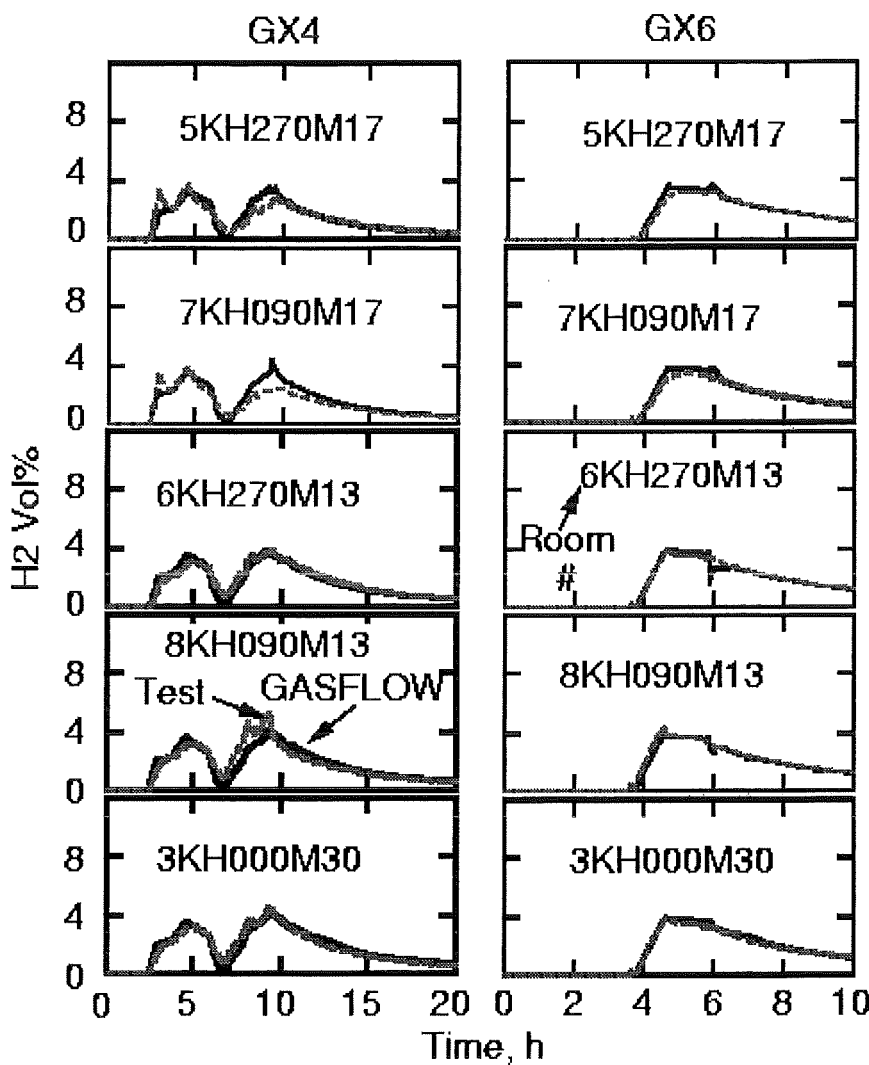


Figure 5.22: Comparison between measured and calculated hydrogen volume fractions in test GX4 and GX6

being turned off. When the sump valve in compartment R6 is opened, only a negligible brief dilution effect occurs.

#### 5.2.3.1.3 Dual concept test GX7

The concentrations calculated for the different compartments of the GX7 experiment are shown in Figure 5.23. In these analysis, leakages were taken into account from the onset of the analysis. The first hydrogen injection into the upper compartment, R5, causes pronounced stratification with maximum hydrogen concentrations of 8%. The high concentration spreads azimuthally also into the

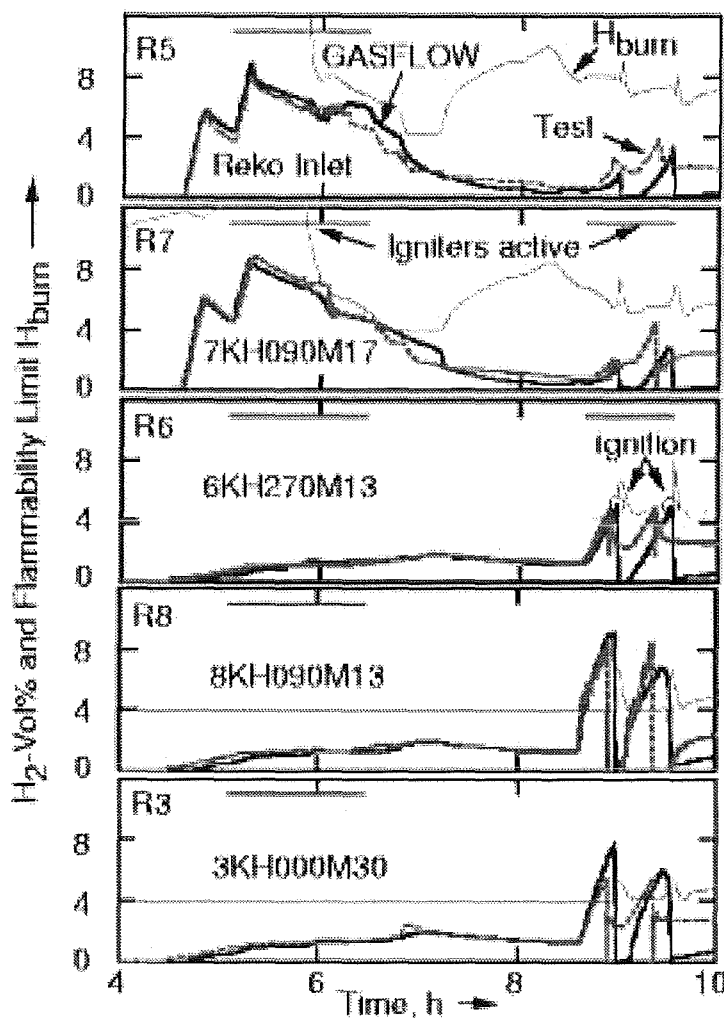


Figure 5.23: Hydrogen volume fractions, flammability limits, and ignition intervals in test GX7

adjacent compartment, R7, while concentrations in the lower compartments and in the central compartment increase only very little. This stratification is rendered well by GASFLOW. The horizontal bars in fig. 5.21 mark the activation periods of the igniters in various compartments. During the first hydrogen injection all igniters were activated. Despite the high hydrogen concentrations in the upper compartments, however, there was no ignition. The steam content was too high. The calculated ignition limit of the hydrogen/steam/air mix, according to the Shapiro diagram [10] (thin line in fig. 5.23), is above the hydrogen concentration throughout the first ignition phase. In the beginning, the atmosphere is even completely inerted by steam (steam fraction > 65 Vol%). With decreasing

steam injection the steam fraction is reduced as a result of condensation. Consequently, the ignition limit in compartments R5 and R7 approaches the hydrogen concentration. The hydrogen concentration can briefly exceed the ignition limit in compartment R7, but the igniters are no longer active at this point in time. Also in the experiment there were no ignitions during the first hydrogen injection phase. All hydrogen associated with the first injection phase is reduced solely by the catalytic recombiner, which is active far below the ignition limit. Catalytic recombination causes the hydrogen content in the upper compartments to drop even below that in the lower compartments. Also in this late phase, the analysis reflect the experimental findings quite well.

The second injection of hydrogen occurs after 8.5h from a line source near the bottom of compartment R8. Because of the low steam content in the lower compartments, the ignition limit is exceeded there very quickly. However, during the second hydrogen injection, no igniters were activated in the source compartment R8. During the second hydrogen injection, igniters were active only in the two adjacent compartments, R6 and R7. As a consequence of the hydrogen spreading out azimuthally ignition conditions are established first in the horizontally adjacent compartment, R6. Ignition was quite mild. In the simulation, flame propagation towards the source was initiated only by a continuous spark duration of 5 s, because the computational grid is rather coarse for a combustion analysis to be triggered with the real sparking time of 1 ms. The flame generated with this extended spark duration burns practically all of the hydrogen in the containment. In the experiment, only the source compartment, R8, burns out completely, while quenching goes on in all adjacent compartments so that a residual concentration of unburnt hydrogen is left. Hydrogen injection continues also after the first combustion. Again the ignition limit is exceeded in compartment R6, and there is another ignition. Because of the absence of residual hydrogen, this occurs slightly later in the GASFLOW analysis than in the experiment. In GASFLOW, again all of the available hydrogen is burnt, while residual concentrations in the adjacent compartments remain in the experiment. GASFLOW predicts the most important part of the combustion processes quite well, despite the lack of detailed models for the quenching process. A more accurate description of the combustion would require a much more refined mesh grid. The GASFLOW simulation of early ignition as a countermeasure preventing the buildup of mixes capable of detonation does not require excessive accuracy, e.g., with respect to the load potential. What is important is the local conservation of the combustion enthalpy and its impact on convection in the containment. The analysis are sufficient in quality to meet these requirements.

Some results from the GASFLOW analysis of test GX7 reveal pronounced three-dimensional effects. This is indicated by the snapshots for the conurations shown in fig. 5.24. On the left, there is the status at peak hydrogen concentration during the first hydrogen injection period; on the right the status is shown at the onset of the first ignition during the second hydrogen injection. Several

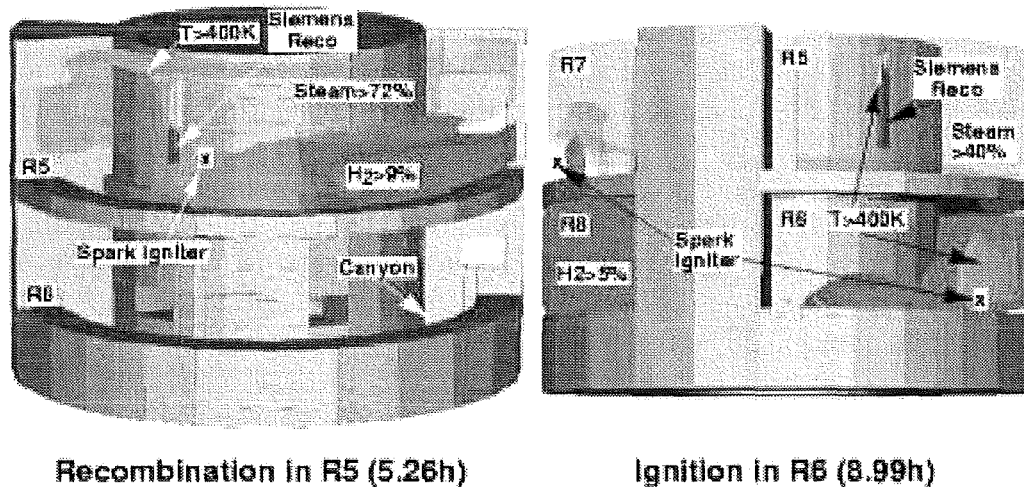


Figure 5.24: Snapshots of conditions at peak hydrogen concentration (left) and the onset of hydrogen ignition (right) in test GX7

results are superimposed in this diagram as different plumes. What is shown is the inner Battelle containment without the outer wall and the ceiling so as to provide a better view of the results. The hydrogen plume with concentrations above 9% builds up above the line source at the bottom of compartment R5. As a consequence of the continuous recombination, it is interrupted below the recombiner box. The hot exhaust gases arising as a consequence of the recombination energy are indicated by the iso-surface above the recombiner, which encompasses the hot plume with gas temperatures above 400 K. The transparent plume marks the region with steam volume percentages above 72%, indicating the steam-inerted region in which no ignition is possible. This region extends through the upper regions of the compartments R5 and R7, but not as far as to the floor. The igniter in the R5 compartment is situated fully in the region inerted with steam. If the igniter position in the R5 compartment were different, for instance, a short distance above the floor, ignitions would have been possible even during the first injection phase. Local concentrations may vary greatly even in this small compartment.

The first ignition after nine hours produces a completely different picture. The geometry model was turned slightly counterclockwise to allow the onset of ignition to be indicated and to clear the view of the R8 source compartment and the R6 ignition compartment. A hydrogen plume with hydrogen concentrations above 5% extends into the entire source compartment, R8, and, in an azimuthal direction, also into the R6 compartment. A finger of the plume in the compartment R7 indicates that hydrogen was able to penetrate locally also into the upper compartment. Another plume is generated at the lower connection between R6

and the central compartment, R3. It is produced as a result of dispersion via the central compartment. The transparent plume now marks the region with steam fractions above 40%. The steam volume fraction in the upper compartments is higher; at the overflow opening from R8 to R7, the propagating hydrogen plume has displaced the steam locally. At the onset of ignition, the steam fraction is below the inerting limit of 65 vol% everywhere. The crosses in compartments R7 and R6 indicate the positions of the two igniters active in the second hydrogen injection phase. Ignitable mixtures are produced first at the igniter in R6. The plume above the igniter marks the hot gas region at  $T > 400$  K established locally after the first ignition. The recombiner continues to operate also in this phase. Because of the much lower hydrogen concentration in the R5 compartment, its exhaust plume is only weak. After ignition, the flame propagates along the gradient of rising hydrogen concentrations. This process involves branching into an azimuthal propagation towards the source and into a flame front moving through the central compartment towards the source compartment. When the two flame fronts meet in the source compartment, there is a brief pressure peak which, compared with the measured data is overestimated in the GASFLOW analysis (narrow pressure peak of 1.9 bar as against a measured, broader peak pressure of 1.3 bar). The transient flame propagation after the ignition was recorded as a film and can be observed on a video.

### 5.2.4 Distribution and Mitigation: 3D analysis of steam/hydrogen distribution in nuclear reactor containments

#### 5.2.4.1 Containment models

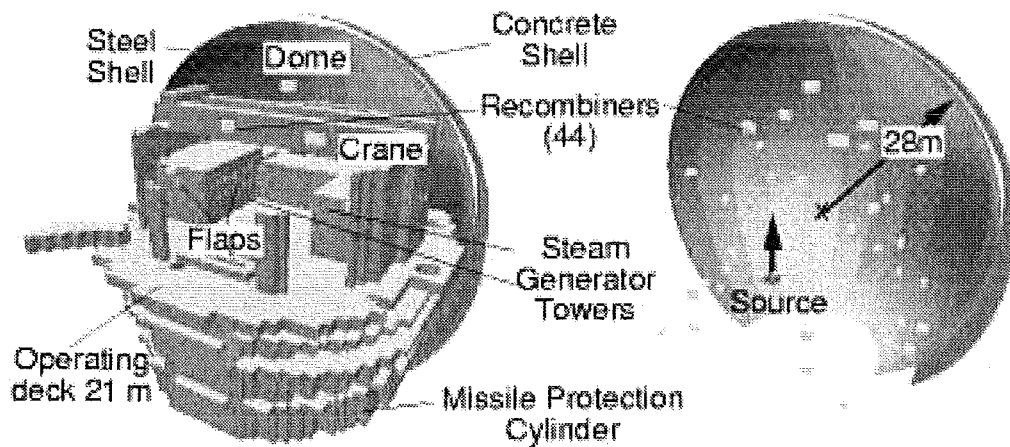


Figure 5.25: 3D GASFLOW geometry model for plant A

Two large 3D Cartesian geometry models were developed for GASFLOW. Plant A represents a spherical PWR containment of a German pre-Konvoi type, Plant B represents a current German Konvoi type PWR. Both plants have spherical containments that are bounded by a concrete shell with an annular gap of air and a steel shell around a free gas volume of ca.  $70,000\ m^3$  (fig. 5.25). GASFLOW simulates the spherical concrete shell as stair-stepped obstacles and the steel shell as stair-stepped walls in a 3D Cartesian mesh using 158,000 cells for plant A and 184,000 computational cells for plant B with an average cell volume between 1.3 and 1  $m^3$  per cell. The structures inside the steel shell are set up according to the plant layouts by defining obstacles that occupy full cell volumes, and by putting walls on cell boundaries that block the flow perpendicular to the surface. Obstacles and walls are simulated as heat absorbing structures of either concrete or steel. Their surfaces are adjusted to exactly represent the projected areas on the spherical steel and concrete shell, and they balance in total to the plant data for the internal concrete surfaces and the spherical steel shell surfaces that are given in table 1. The gas flows through the interconnected free cells not occupied by obstacles and through openings that become transiently available when the pressure difference across selected walls (defined as rupture disks or rupture flaps) exceeds a certain value (between 55 and 100 mbars) and causes the removal of this particular wall from the mesh. Figure 5.25 displays such flaps on the sides of the steam generator towers for plant A. They open connections between the operating room and the so-called component rooms with the pumps and steam generators inside. Steel shell, dome, crane, operating deck and missile protection cylinder are the relevant structures of the operating room visible in Fig. 5.25. The blow-down source is located in a component room under the left steam generator tower at a low axial location. Its location in the 3D mesh is shown on the right side of the graph which gives the geometry inside the steel sphere without the structures.

The GASFLOW analysis of plant A includes the simulation of mitigation by a total of 44 catalytic hydrogen recombiners that are placed at various locations in the operating and component rooms (fig. 5.25). The recombiners are from the NIS type [6]. About 30% of them are attached to the crane support bars and above. Each recombiner is represented by a single fluid cell that is bounded by steel walls on the sides. Gas flow occurs into and through these boxes applying an active ventilation option which determines the flow rate in dependence of the calculated local hydrogen concentration at the box entrance on basis of measured operating data. The recombiners thus operate in a 3D concentration field and reflect all effects from local stratification and sedimentation of gases. An efficiency that is defined pressure-dependent recombines a large fraction of the in-flowing hydrogen with oxygen to steam and adds the chemical energy to the gas flow, so that colder gases with hydrogen enter the boxes and hot gases of steam, nitrogen, and oxygen with only some residual amounts of hydrogen leave the boxes. For the NIS recombiners, gases leave the boxes in vertical flow. The analysis of plant

B simulates 62 recombiners of the Siemens type (fig. 5.20) that are closed at the top and open on the sides so that hot gases leave the boxes in horizontal flow. As shown before, the GASFLOW modeling of the Siemens type recombiner boxes was validated with the successful analysis of the Battelle recombiner tests GX4, GX6 and GX7, and for the NIS type recombiners with the analysis of the Battelle test MC3 [6].

#### 5.2.4.2 Results

The investigated scenario was a large-break LOCA at a low release location from a rupture of the pressure relief line from the hot leg of the primary loop to the pressurizer (surge-line LOCA). The same source was applied in the analysis of plants A and B. It was taken from a MELCOR analysis of this accident [11] and covered the in-vessel phase of this scenario with a total problem time of 7000 s. In the blow-down phase (first 700 s) a two phase mixture of 462 tons of water and 39 tons of steam gets injected. Isenthalpic expansion to the transient containment pressure adds another 50 tons of steam. The relocation of water and steam is considered in a single flow field using a homogeneous equilibrium model, from which the water is parametrically removed with a time constant of 100 s after the achievement of thermal equilibrium between water and steam. Mass and energy of the rained out water are balanced. They could be applied for the simulation of sumps, but were neglected in this analysis. Another 50 tons of super-heated steam are released after the blow-down with peak temperatures above 1000 K. Hydrogen release starts after 1500 s. Altogether 531 kg of hydrogen are added of which 120 kg are entered during a strong release peak at 5932 s due to an enhanced steam/zirconium reaction after the failure of the core support. Volatile fission products (Xenon) are also released. They carry a total decay heat of 8 MW which is released volumetrically dependent on the local Xenon density.

The applied steam/hydrogen release rates are displayed in Fig. 5.19 together with the calculated pressure transients from GASFLOW for plants A and B. Isenthalpic expansion of the blow-down source leads to an early initial pressure peak of nearly 4 bars in both containments. The further pressure development is controlled by steam condensation and release. Both containments have the same free gas volume of  $70,000 m^3$ . But because plant A is less compartmentalized than plant B and has 30% less concrete surfaces, the pressure decays less rapidly than in plant B after the blow-down, and it increases more during the further steam/hydrogen release again reaching 4 bars at the end in plant A compared to 2.7 bars in plant B. Pressure waves open most flaps and rupture disks during the first 0.5 s of the blow-down.

The released source gases of steam and hydrogen form a buoyant jet that rises through the steam generator tower above the source. The gas enters the operating room through the failed rupture disks and flaps in the steam generator tower. The openings from the failed rupture disks, which are on the roofs of the

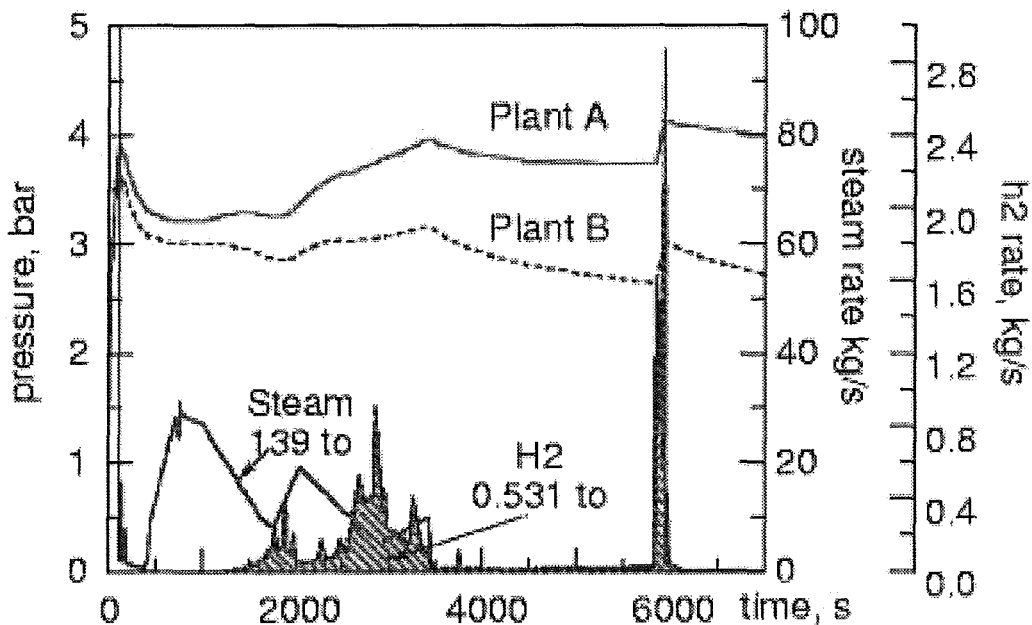


Figure 5.26: Steam/hydrogen source and pressure for the analyzed surge line LOCA in containment A and B

steam generator towers in plant B, allow a direct axial expansion of the buoyant source jet into the dome. In plant A the failed flaps are on the sides of the steam generator towers. The gas from the source jet also rises into the steam generator tower and gets injected horizontally from all sides and forms four fingers which rapidly extend deeply into the dome. Figure 5.27 shows the calculated buoyant source jets in the dome that result in Plant B (11 vol%  $H_2$ ) and plant A (7 Vol%  $H_2$ ) during the last rapid steam/hydrogen release after core support failure at 5932 s. The calculation of these jets has a good validation basis. GASFLOW could successfully predict such buoyant source jets in the blind pre-calculation of the Battelle Hyjet Helium injection test JX7 [3] and in the analysis of the Canadian Whiteshell tests with little sensitivity to the applied mesh sizes [12]. The snap shots in Fig. 5.27 also show recombiners higher up in the containment with pronounced hot exhaust gases ( $T > 650K$ ). They have little impact on the flow field and are outside the source jet in a stratified region built up after the first phase of the steam hydrogen release, while the recombiners at a lower location on the operating deck and away from the source side tower don't yet see much hydrogen at this time. The stratified region in the dome is displayed for plant B as transparent cloud ( $T > 500K$ ).

The rising source jets after the strong hydrogen release are deflected in the dome near the sphere, spread out to the side, mix within 200 s due to the vortices calculated in GASFLOW as the result of Taylor instabilities and flow diversions in the dome (Fig. 5.28) and contribute to the formation of a temporarily stratified

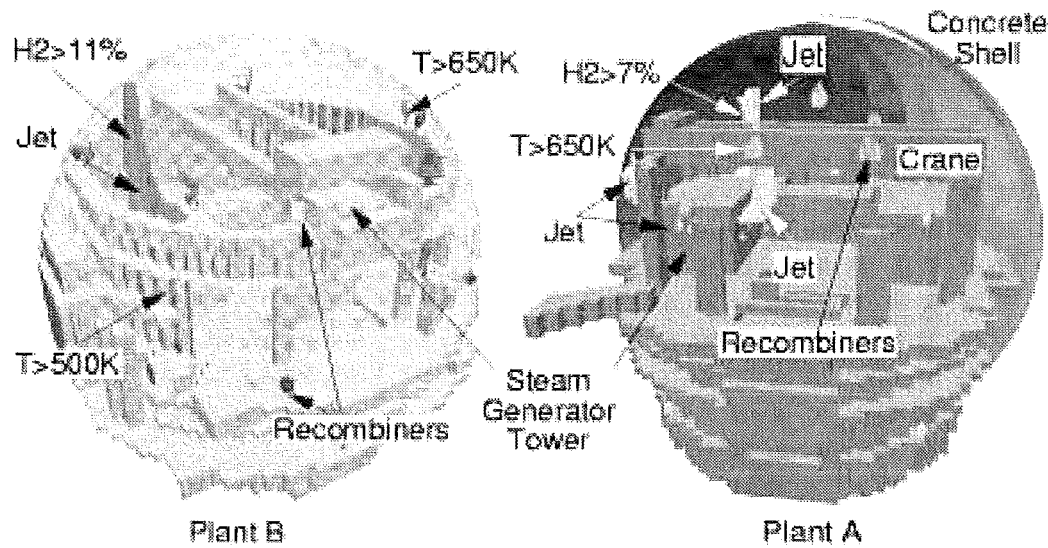


Figure 5.27: Hydrogen source jets, stratified clouds and recombination exhaust plumes, snapshot of GASFLOW results at end of  $H_2$  injection (5932 s)

cloud in the dome. On a larger time scale a secondary flow develops in a thin layer around the condensing structures when steam condensation locally leads to a dried gas with a larger hydrogen and air volume fraction and to a layer with an increased average molecular weight in which this gas sinks down along the cooled structures. This so-called condensation sedimentation effect homogenizes the stratified atmosphere in a "wet" scenario with steam. Due to the smaller structure surfaces of plant A it develops more slowly than in plant B but ultimately it is the same mechanism that is responsible for the atmospheric mixing.

Besides the spreading out of the source jet through the source side steam generator into the dome, GASFLOW also shows the buildup of a temporary circulation from a chimney effect between the steam generator towers which are heated differently on the source side and away from the source with gas flowing from the hot tower into the colder tower on the other side (see cut A-A in Fig. 5.29). A bottom-recirculation also develops through the opened flaps on the low level in cut B-B (Rohrkanal). There are significant asymmetries involved in these circulations due to a smaller failure fraction of the flaps away from the source. Parametric variations with sealed exits in the steam generator tower away from the source and sealed openings for the re-circulation in the bottom region show that these circulations do speed up the mixing for a certain time, but that they don't contribute much to the homogenization on a larger time scale which is controlled by the condensation sedimentation effect. The 3D GASFLOW results for the time development of the hydrogen and steam volume fraction and the gas temperatures in the dome of plants A and B have been averaged for a control

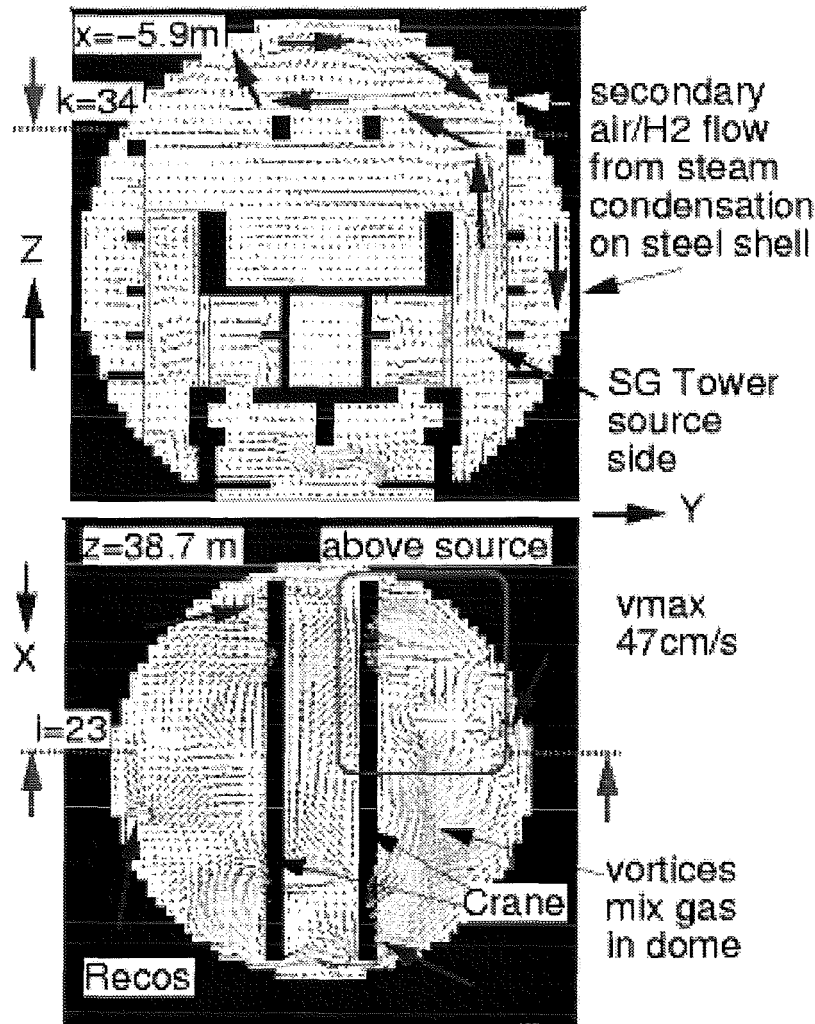


Figure 5.28: Vortex Mixing in the dome and sedimentation flow in plant B at 5932 s

volume of ca.  $2000 \text{ m}^3$  at the top of the dome which is characteristic for a control zone of the dome in a lumped parameter model of such containment, and which comprises ca. 1500 computational cells in GASFLOW. Figures 5.30 and 5.31 display these results for plants B and A. They also include the time dependent local peak hydrogen concentration and temperature occurring in the jets extending into this dome zone. For plant B the dashed lines also give the results of the same simulation without recombiners. The average  $H_2$  concentration with recombiners is 4% at the end after going through a maximum of 9% during the last hydrogen injection. The average  $H_2$  volume fraction in the dome reaches 3.5 % in plant A at 7000 s after going through a maximum of 6%. Because of the higher steam content and containment pressure it is lower in plant A in spite of an

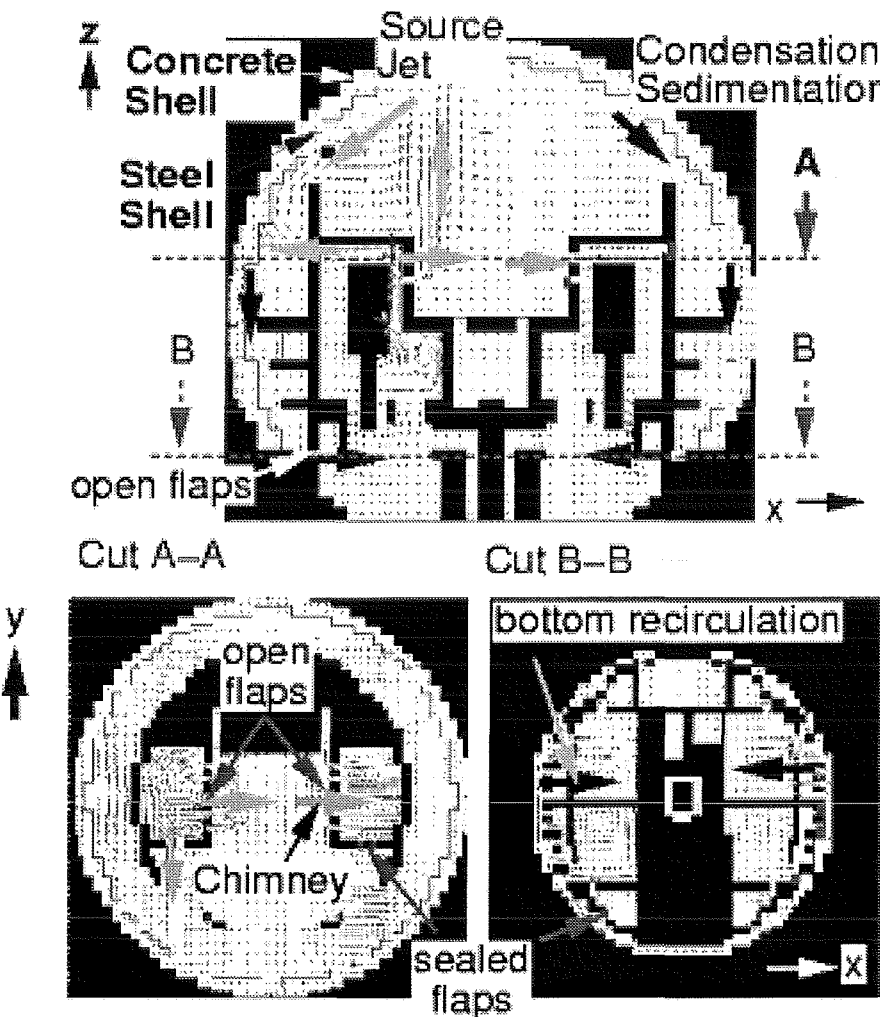


Figure 5.29: Velocity field and flow paths in plant A at 5932 s

overall higher  $H_2$  inventory calculated in plant A due to a slower  $H_2$ -removal with the installed NIS recombiners. The local peak  $H_2$  concentrations in Figs. 5.30 and 5.31 significantly exceed the average concentrations during the two periods of  $H_2$  injection when the source jets penetrate into the dome. Mixing from vortex formations dilutes the jets within some hundred seconds after each injection period so that the peak and average  $H_2$ -concentrations merge in the considered dome regions of plants A and B. The Peak  $H_2$  concentrations reach maxima of 11% and 10.5% for plant B and plant A. The lean  $H_2$ -combustion limit [10] in plant B is around 9 Vol% at this time for the steam concentration of 50 Vol% (Fig. 5.30), and for some 10 s the source jet that extends into the dome of plant B becomes flammable. Plant A has a higher lean  $H_2$ -combustion limit around 11% (Fig.5.31). The dome atmosphere has 60 Vol% steam and is inerted enough

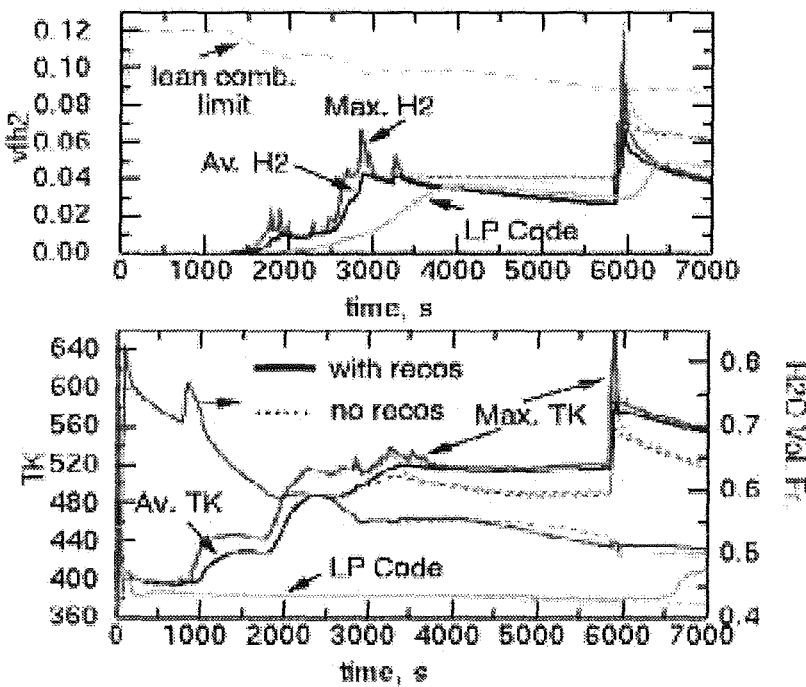


Figure 5.30: Hydrogen/steam vol. fractions and temperatures in the dome of plant B

that the source jet can never become flammable. The local peak and the average gas temperatures in the dome merge rapidly in plant B due to the mixing after each injection period. Temperatures in plant B reach peak values of 640 K and end values of 560 K. In plant A a high temperature zone develops at the top. Hot exhaust plumes from the recombiners, the decay heat from the volatile fission products that stratify together with the hydrogen and a generally reduced structure cooling effect contribute and increase the dome temperatures to 40 K higher peak gas temperatures at the end.

It is difficult to predict such local effects with LP codes even if they represent the containment by a large number of control zones. Their equations don't carry information on the 3D momentum flow which is fully conserved in GASFLOW. The integration effect of the dome control volume allows only for a relatively slow increase of temperatures and concentrations and doesn't reflect the additional heating from the source jet and the fission products which it transports. The simulation of super-heated steam together with vaporizing films on the structure in the LP results from Fig. 5.30 additionally delays the temperature increase in this large control volume. Although LP codes will calculate similarly mixed conditions at the end, they cannot conservatively predict the heterogeneous states occurring during the transition to these mixed states.

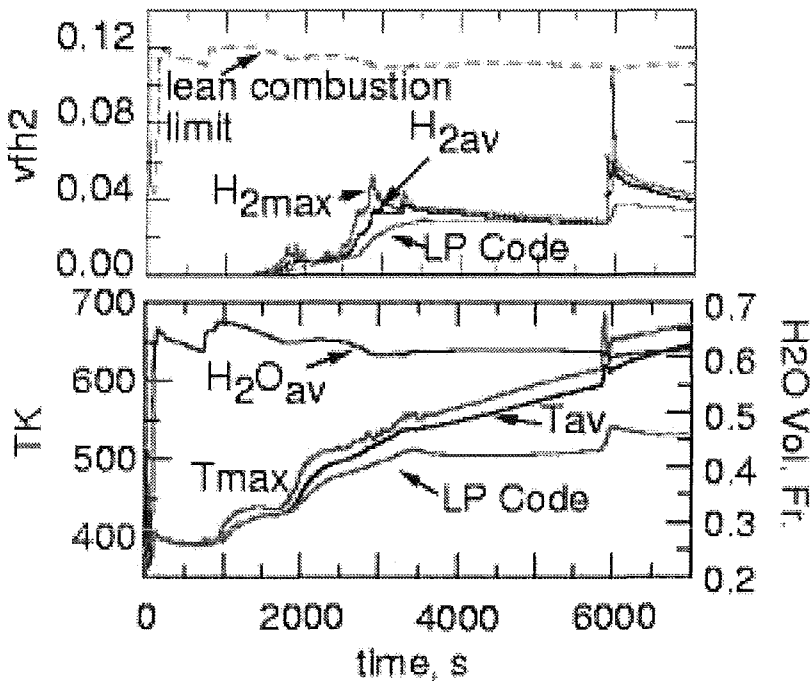


Figure 5.31: Hydrogen/steam vol. fractions and temperatures in the dome of plant A

With the simulated arrangement of the NIS and of the Siemens recombiners in plants A and B GASFLOW predicts an overall hydrogen removal of 20% and 40%, respectively (Fig. 5.32). The NIS recombiners with granulate catalysts have a higher heat capacity, start somewhat slower, and respond with larger inertia to transient loadings with hydrogen, so that they need more time in the defined arrangement for removing the same amount of hydrogen.

### 5.2.5 Application of GASFLOW to a Future Evolutionary Containment

For future reactors a further reduction of the risk associated with severe accidents including core melt is required. This implies the integrity of the containment in most of these events. As the containment could be impaired by a violent H<sub>2</sub> deflagration, means to avoid such events must be foreseen in future reactors. For a large open (weak compartmentalisation) concrete containment with a big internal water storage tank (IRWST) at the bottom a system of catalytic recombiners, distributed mainly in the equipment rooms, supported by some (spark) igniters is likely to cope with all relevant scenarios and phenomena. In order to justify this approach calculations of a series of well selected accident scenarios is necessary.

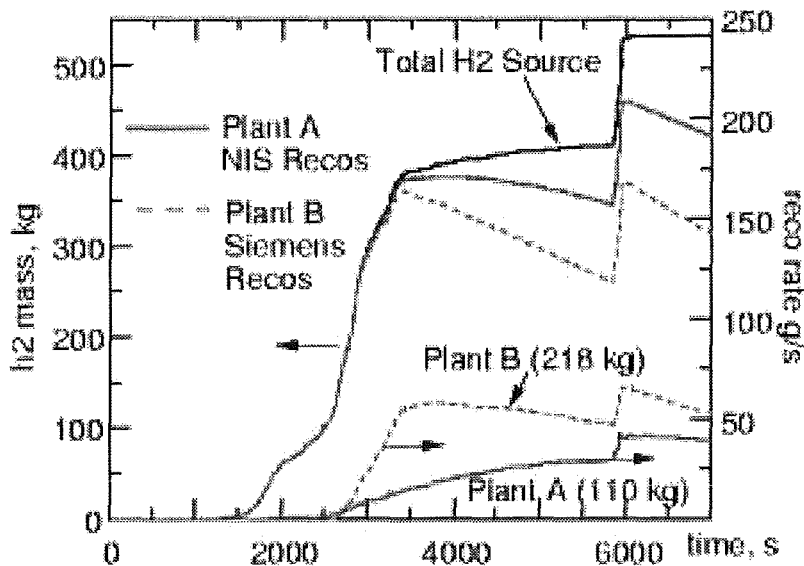


Figure 5.32: Hydrogen inventories and recombination rates the for analyzed concept of recombiner positioning in plants A and B

Concerning the analytical method a twofold approach is followed involving both

- Lumped parameter codes, as WAVCO
- CFD codes, as GASFLOW.

At present, the task of WAVCO is to address long-term and global concerns and to support the GASFLOW analysis (prediction of initial conditions, especially when hydrogen release is late in the accident). In this chapter GASFLOW analysis for two relevant scenarios is described:

- Small Break ( $20 \text{ cm}^2$ ) Loss of Coolant accident with failure of the SIS (SBLOCA), where hydrogen release is found to be highest (by performing a large number of MAAP4 calculations).
- Loss of Offsite Power (with loss of all Diesel generators) (LOOP) which leads to the release of hydrogen through the water phase of the IRWST (as a consequence of the depressurisation of the reactor coolant system) and which was found - also by many MAAP4 calculations - to be penalising with respect to release rate (reflooding of the core just before onset of melting was assumed) and atmospheric condition (little steam).

### 5.2.5.1 Plant Model for the Analysis with GASFLOW

A detailed nodalisation of the containment geometry is indispensable, since the influence of the structures, components, doors, grids, openings etc. have considerable impact on the gas transport and mixing as well as on the turbulence generation and combustion process. Thus, the containment, having a volume of  $90000\ m^3$  and concrete surfaces of  $32000\ m^2$ ) is simulated by a cylindrical coordinate system using 30 radial rings, 60 azimuthal sections and 68 axial levels, which results in 122400 cells. The subdivision in radial ( $r$ ) and vertical ( $z$ ) directions adjoins all significant structure surfaces taking into account the real surfaces on the right position. The subdivision in azimuthal ( $\Theta$ ) direction is equal and the angle amounts to  $6^\circ$ . With this approach, small cells in the equipment rooms and large cells in the dome, one can achieve a more accurate determination of the local hydrogen concentrations compared to an equal cell size in the entire containment. Because high hydrogen concentration gradients in the IRWST and the equipment room (hydrogen release location in LOOP and LOCA respectively) are expected, the cell volumes in these regions should be smaller than in regions with low hydrogen concentration gradients like the annular compartment. The smallest and largest cell sizes amount to  $0,053$  (close to the IRWST) and  $5,8\ m^3$  (close to the concrete shield in the dome) respectively. The recombiners are arranged mainly inside the equipment rooms. Since steam and hydrogen are lighter than air both gases take the same transport path from the release location to the dome. Despite the convection flow stratification of hydrogen in the dome area may occur for a period of time. Therefore, 4 additional recombiners were located in the dome region at the level of the crane. These additional 4 recombiners reduce  $H_2$ -accumulation in the dome and decrease the local pressure load due to  $H_2$  combustion.

### 5.2.5.2 Analysis of the SBLOCA scenario

The objective of this analysis was to show that the chosen distribution of recombiners is efficient to avoid DDT at any time and location. This is done by calculating the time-dependent gas distribution over the relevant time period with a good spatial resolution (more than 100000) nodes and applying a criterion for the exclusion of DDT developed by FZK which relates a geometrical information (characteristic length) with the mixture quality, expressed in terms of the detonation cell width  $\lambda$  ( $7\ \lambda$ -criterion).

For the analysis the definitive hydrogen/steam release location is determined by the relevant coordinates ( $r=9,2\ m$ ,  $\Theta = 36^\circ$ ,  $h=6,1\ m$ ) corresponding to the postulated break of a line connected to the cold leg of loop 2. Since it takes more than one day in real time for the  $20\ cm^2$  SBLOCA to develop into a severe accident, which requires time consuming calculations, the GASFLOW analysis starts at the time of hydrogen release (about 68200 s) applying the containment

conditions at that time calculated with WAVCO. The analysis was terminated 10000 s later (at 78200 s), i.e. before RPV failure. Since it was judged that the ex-vessel hydrogen production would not cause more severe conditions because of the fact that an immediate combustion of the released hydrogen would occur, this phase was not included into the present GASFLOW analysis.

The calculated maximum pressure is limited to 1.9 bar due to the condensation of steam on the structure. Due to heat input from the airborne fission products and the recombiner operation, the gas temperature in the dome atmosphere can reach a local value of 240 °C. The maximum accumulated hydrogen in the containment is limited only by the operation of the recombiners to a value of 585 kg compared to 800 kg  $H_2$  released from the reactor coolant system.

The application of the 7  $\lambda$ -criterion was simplified by defining a DDT index  $R$ , which is the ratio of the combustible cloud diameter divided by 7 times the corresponding detonation cell width  $\lambda$ .  $\lambda$  is calculated from the average hydrogen and steam concentration of the cloud. DDT can be excluded in case of  $R < 1$ .

Although the local hydrogen concentration can exceed the limit of 10 vol % at the time of maximum hydrogen release, the DDT-index inside the evaluated hydrogen cloud remains below 0.3 during the entire accident progression (Fig. 5.33).

This indicates that inside the large hydrogen cloud there is no potential risk of DDT due to the high concentration of steam, which reaches average values of about 15 vol %. Locally detonable conditions in regions with high hydrogen concentrations can not be fully excluded, however. The combustible cloud size rises up to about 43 m (Fig. 5.34) and decreases after 2 hours due to the efficient removal capacity of the recombiners. The maximal recombination rate of all recombiners amounts to 120 g/s.

The local maximum hydrogen concentration in the dome reaches 12 vol % with a corresponding steam concentration of 17 vol % (Fig. 5.35 - 5.37). Ignition of the combustible mixture cannot be excluded in the room of the break location and above the break near the dome region. It could be initiated from high outlet gas temperatures of the recombiners due to the high inlet hydrogen concentrations.

### 5.2.5.3 Analysis of the LOOP scenario

The objective of this analysis was the evaluation for need of igniters.

This scenario is characterized by the depressurization of the reactor coolant system into the water phase of the IRWST. At the end of the depressurization phase the water evaporates due to the energy release (condensation, fission products). The GASFLOW calculation starts during the boiling of the IRWST water 360 s before the start of significant  $H_2$  release (at 14500 s). Four release locations of hydrogen from the IRWST are assumed in the GASFLOW calculations. Two cases are analyzed:

- Only recombiners to show whether additional means are necessary

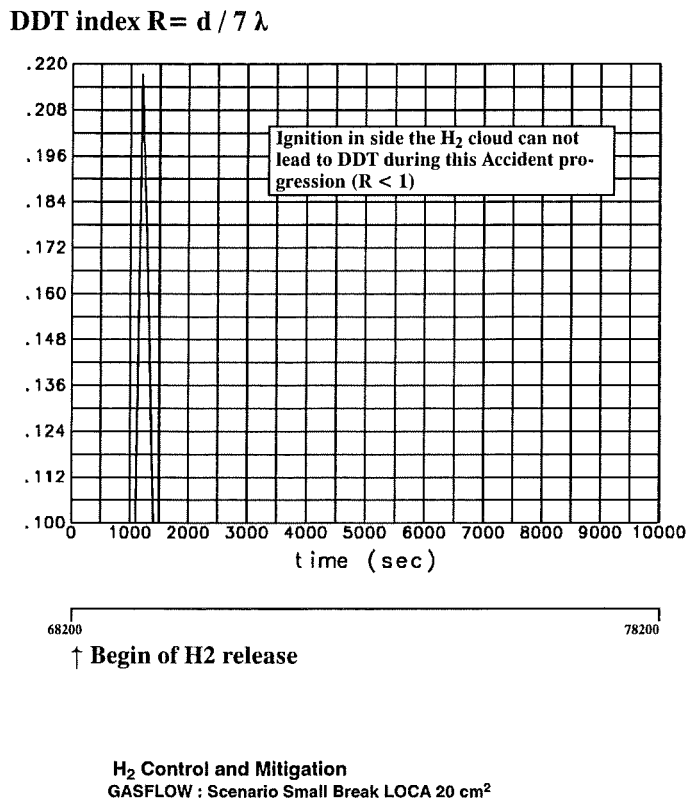


Figure 5.33: SBLOCA: DDT index as a function of time

- Recombiners + igniters at each of the 4 openings of the IRWST gas phase to the containment.

#### 5.2.5.3.1 Analysis with recombiner as the only mitigation means

Fig. 5.38 shows the mass of  $H_2$  present in the containment during accident progression. Since the recombiners are arranged mainly inside the equipment rooms the capacity of the recombiners can be used very efficiently. The maximal accumulated  $H_2$  mass amounts to 715 kg compared to the cumulative release of 900 kg. The calculated combustible cloud size can not be kept below the critical cloud size in this scenario although the removal capacity of the recombiners is up to about 125 g/s.

The index  $R$ , which indicates risk of DDT, is about 10 for less than 5 min (Fig 5.39). This means that without additional means, as igniters, DDT cannot be excluded.

Concerning the IRWST most of its gas phase is inerted and only a small part may be burnable with detonation cell length between 1 m and 5 m. The corresponding minimal critical cloud volume with regard to DDT would be 340

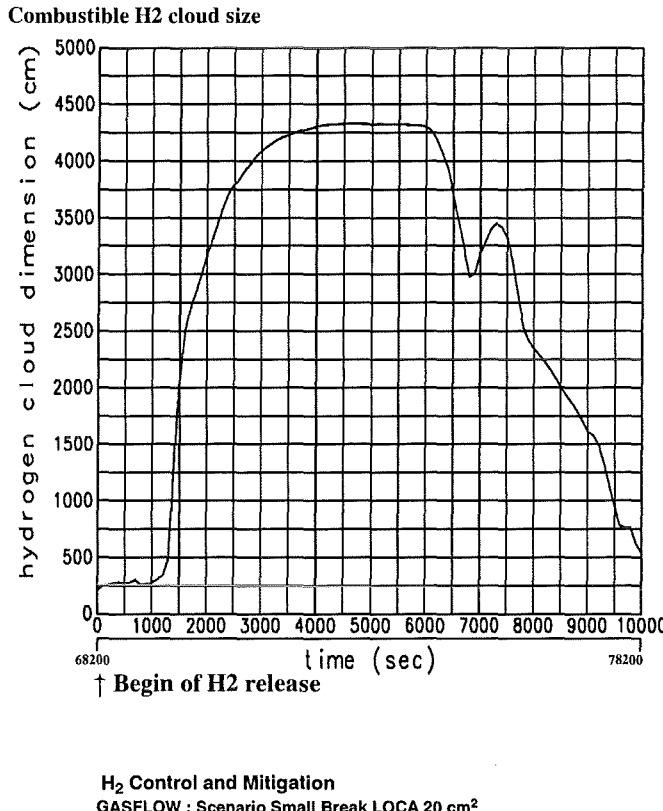


Figure 5.34: SBLOCA: Cloud size history

$m^3$ , larger than the free IRWST compartment volumes. Therefore, DDT in the IRWST can be excluded.

Fig. 5.40 shows the gas composition at the bottom of the equipment rooms in an IRWST opening. In the openings, oxygen dilution is high and thus a potential flame in the lower part of the equipment rooms is not expected to be able to propagate into the IRWST. From the conditions for ignition of the gas mixture outside the IRWST, it is expected that four standing flames in the corresponding equipment rooms can exist for about 20 min.

#### 5.2.5.3.2 Analysis with igniters as additional mitigation means

The deflagration of hydrogen close to its release locations inside the equipment rooms avoids hydrogen accumulation to high concentrations and thus it prevents the risk of DDT or fast deflagration. The calculated gas temperature in the flame is higher than the experimental measured  $H_2$ /air flame temperature (2040°C) because in the GASFLOW code currently no model for gas radiation to walls and structures is implemented. Consequently, the wall temperatures are underestimated and the gas temperatures are overestimated.

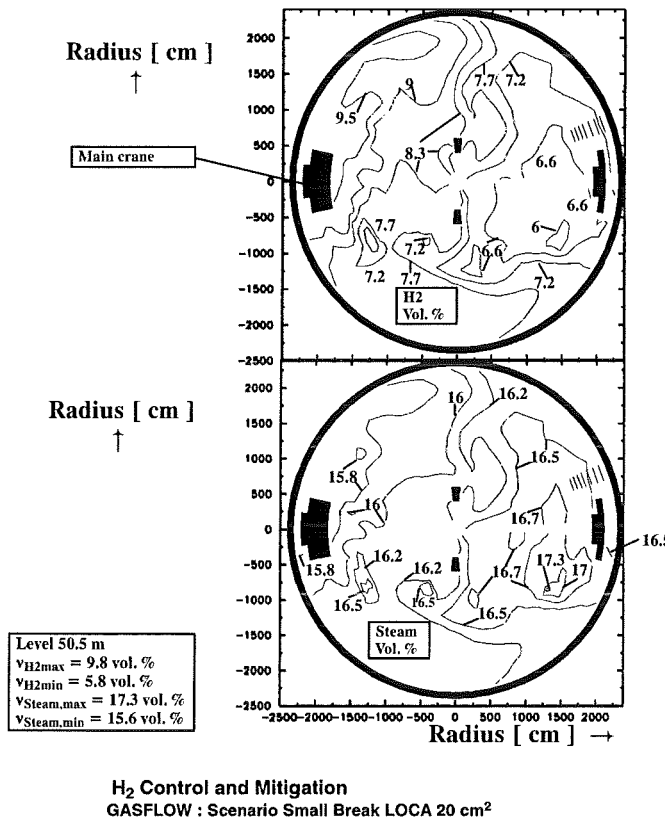


Figure 5.35: SBLOCA: Hydrogen (top) and steam (bottom) concentration in the dome (elevation of the polar crane, 40 m)

The maximum gas temperature in the dome above the loops rises locally to about 920°C whereas the average gas temperature remains below 570°C. The surface temperature of the concrete structure of the dome does not exceed 200°C.

During combustion of hydrogen strong convection flows are generated in the containment, which reach their highest velocities at the time of maximum hydrogen release (6 kg/s). The maximum flow velocity in the centerline of the flame amounts to 26 m/s (Fig 5.41). Standing flame conditions are expected to exist for a time of about 20 min, high combustion rates, corresponding to the 6 kg/s release rate, have only a duration of about 1 min.

The maximum hydrogen mass within the containment amounts to 110 kg and occurs just before the ignition.

### 5.2.6 Conclusions

The GASFLOW simulations of this scenario with a large break LOCA in the two steel containments of German design demonstrate a strong steam inertization in both containments. During the release phases with steam and hydrogen they

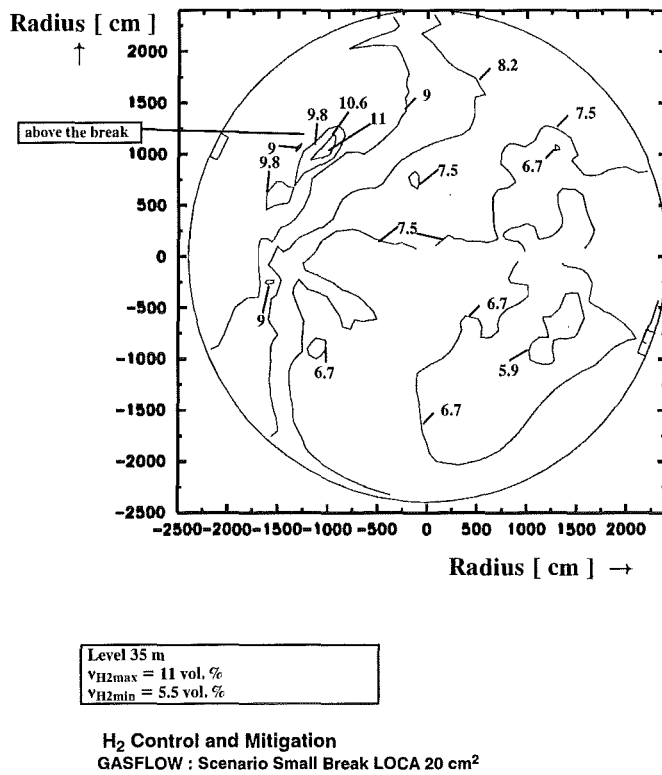


Figure 5.36: Hydrogen concentration at 35 m

predict the transient formation of a buoyant jet that extends from the source up through the steam generator towers into the dome. But there is only a short phase in which locally flammable gas mixtures develop in the dome. Vortices formed from Taylor instabilities rapidly dilute the source jet and the regions in which it is flammable. A larger stratified cloud that is inflammable forms in the dome from which a hydrogen/air mixture sinks down in a secondary flow near the structures due to the steam condensation that becomes the major mechanism for homogenizing the temporarily stratified hydrogen. This sedimentation occurs on a larger time scale in plant A which is a more open containment with smaller structure surfaces and heat capacities. Larger volume fractions of steam, reduced hydrogen volume fractions, a higher containment pressure and higher gas temperatures in the dome are the principal differences between the GASFLOW simulations for plants A and B, which are both controlled by the same mechanisms. The hydrogen recombination rate determined from the 3D concentration field is higher in the dome for some time but becomes more and more homogeneous as the hydrogen becomes mixed throughout the containment. This homogeneous removal of hydrogen is well predicted also with simple lumped parameter models which at the end predict a similar integral hydrogen removal as GASFLOW with an

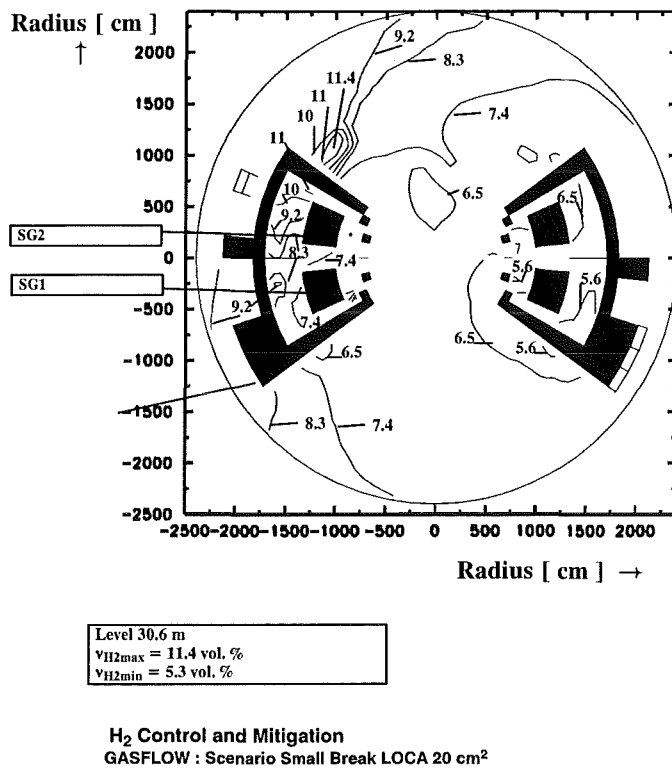


Figure 5.37: Hydrogen concentration at 30.6 m

overall hydrogen removal fraction at 7000 s of 20% and 40% for plants A and B, respectively. The principal difference is that the 3D GASFLOW simulation describes all mixing mechanisms and flow paths with a full set of mass, energy, and momentum equations. This resolves all heterogeneous states in between and confirms that the final homogeneous conditions are achieved without the occurrence of intermediate states in which combustions could develop a load potential. On a larger time scale the analyzed mitigation concept with catalytic recombiners of the Siemens and of the NIS type is demonstrated as an effective measure that prevents the formation of combustible mixtures during the ongoing slow deinertization process from steam condensation. The modeling of the recombination boxes in GASFLOW has been validated with the analysis of representative recombination tests in the Battelle Model containment. The installation of the recombiners is therefore demonstrated as an efficient measure for a further reduction of the hydrogen risk. The successful GASFLOW analysis of the recombination performance under accident specific operating conditions and the good prediction of the source jet in the Hyjet test JX7, also the successful interpretation of the Helium stratification and mixing during the outside spray phase in the HDR Test E11.2 with the simulated condensation sedimentation mechanism in GASFLOW give confidence

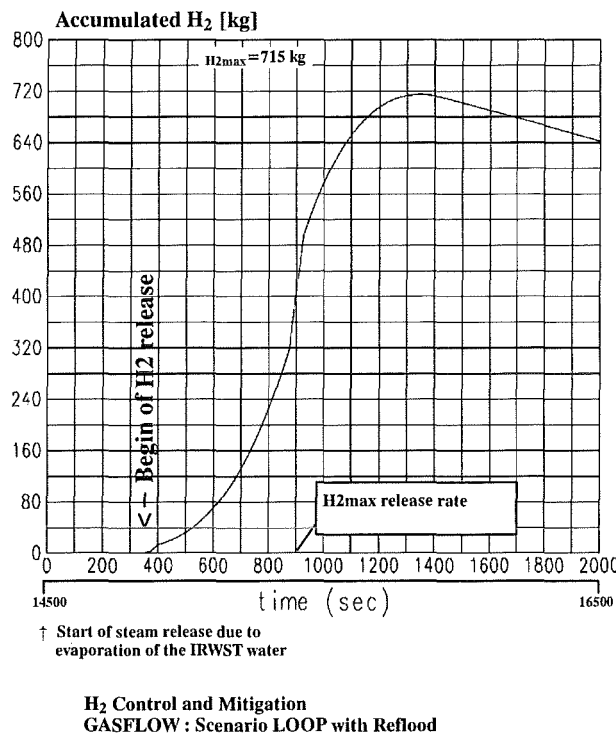
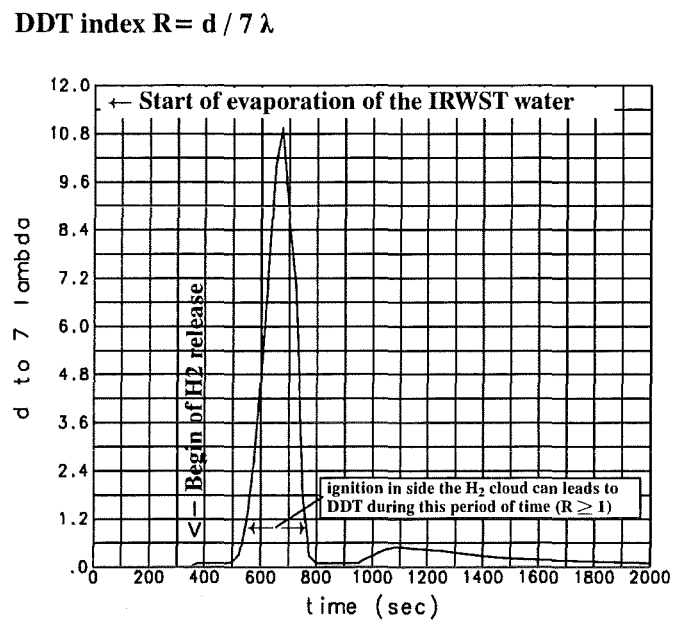


Figure 5.38: LOOP with reflood: Mass of hydrogen present in the containment (only recombiners)

in the predictive capability of GASFLOW during the before discussed scenario.

Finally the application of GASFLOW for an evolutionary containment design (large cylindrical concrete containment with water tank at the bottom) has shown that for LOCA scenarios DDT with large clouds will not occur when using well-arranged catalytic recombiners. With some additional igniters, located at the outlet of the IRWST, one can even cope with highly penalising - and unlikely - scenarios as reflood of the hot core at the most unfavourable moment.



**H<sub>2</sub> Control and Mitigation**  
**GASFLOW : Scenario LOOP with Reflood**

Figure 5.39: LOOP with reflood (without igniters): DDT index as a function of time

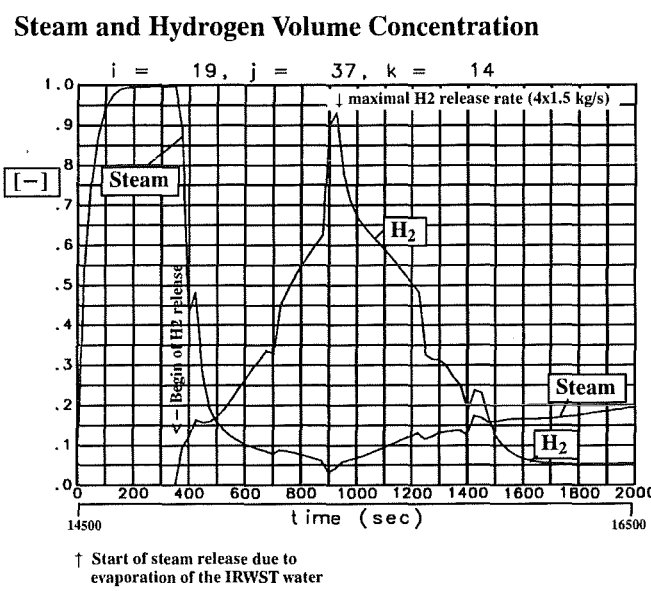


Figure 5.40: LOOP with reflood: Gas composition in the IRWST openings

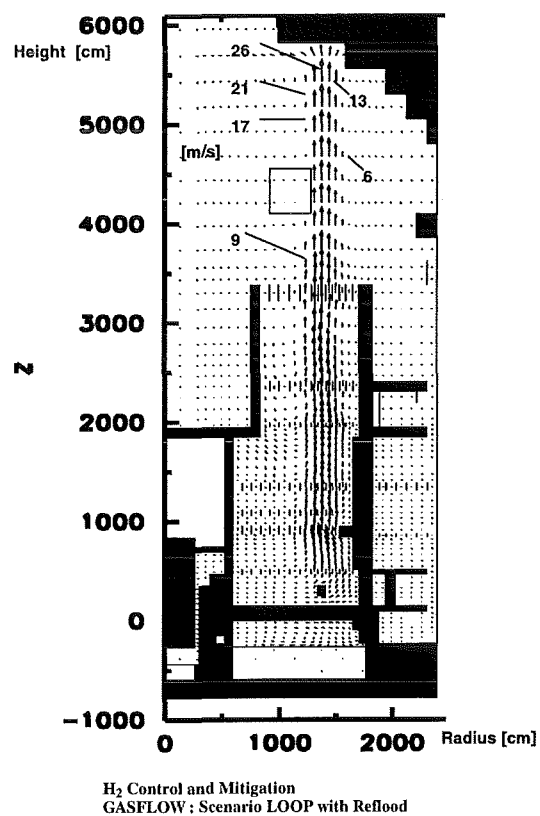


Figure 5.41: LOOP with reflood: maximum flow velocities

### 5.3 Full reactor scale turbulent combustion simulation with COM3D

The above described model development, verification and benchmark work performed for the various COM3D sub-models, resulted in sufficient predictive capabilities which allow now the analysis of turbulent  $H_2$ -air-steam deflagrations on full reactor containment scale.

Within the frame of EPR-design studies, the following problem was investigated:

- Loss-of-off-site-power scenario (LOOP) with late re-flood of the overheated core,
- calculation of hydrogen and steam sources with the MAAP code, release through IRWST,
- analysis of hydrogen/steam distribution in the EPR containment with GASFLOW,
- transfer of the gas distribution from GASFLOW to COM3D.

The investigated scenario lead to a stratified hydrogen distribution in the containment and to small steam concentrations due to the gas release through the sub-cooled IRWST pool water. The distribution was approximated in the COM3D calculation by a dry  $H_2$ -air mixture with a concentration gradient from 9 %  $H_2$  at the bottom to 13 %  $H_2$  in the upper dome.

The containment model of the COM3D code used a cubic cartesian grid with 40 cm cell size and a total of 1.1 million computational cells. 180° symmetry was assumed for the containment structures.

Fig. 5.42 shows the initial hydrogen distribution in the containment. The mixture gradient is approximated by layers with constant hydrogen concentrations (9 - 13 %). Ignition is assumed to occur in the shown pressurizer compartment. The chemical reaction is initiated by introducing hot combustion products in the dark region (no hydrogen, AICC temperature).

The early stage of the combustion is depicted in Fig. 5.43 about 0.28 seconds after ignition. Due to the low initial turbulence a relatively slow flame propagates from the ignition point. Nevertheless the expansion flow driven by the combustion products, causes high velocities in the connections between adjacent rooms (Fig. 5.44, up to 250 m/s). Such high flow velocities generate increased local turbulence levels, which then promote flame acceleration and preferential flame propagation in these space regions. At 0.412 seconds the stair cases have burned out and the flame propagates upwards into the dome at about 70 m/s and sideways into the other half of the containment at about 150 m/s (Fig. 5.45). The highest flame speed develops in the middle section of the containment, where both sufficient

hydrogen concentration and turbulence generation exist. Despite of the high hydrogen concentrations in the dome (up to 13 %), relatively low flame speeds are calculated for this region because of the un-obstructed geometry. Note that a flame velocity of 150 m/s corresponds to gases moving at about 500 km/h. A global turbulent deflagration of about 700 kg of hydrogen, as simulated in this example, would represent a very energetic event, with consequences on safety systems, needed to terminate the accident (recombiners, spray).

The highest loads to the outer containment (( 8.5 bar) developed on the containment side opposite to the ignition point, because two propagation flame fronts meet here, leading to pressure wave superposition (Fig. 5.46). The right containment wall near the ignition point is loaded quite uniformly with pressures up to about 4 bar, which corresponds to the AICC-pressure of the average mixture in the containment.

In the present example with the given hydrogen distribution and ignition location, the dynamic peak pressures reached a level of about  $2 p_{AICC}$ . The characteristic loading times of the left and right containment wall are quite different, about 50 ms and 300 ms, respectively. When compared to typical natural response times of dry PWR concrete containment ( $T_{cont}$ ), the first case represents a dynamic load ( $T_{load}/T_{cont} \ll 1$ ) and the second case a load regime which is in the transition from dynamic to quasi-static ( $T_{load}/T_{cont} \approx 1$ ). In the first domain the deformation is proportional to the wave impulse, whereas in the quasi-static domain it is proportional to the peak pressure reached.

Altogether the results of this first full scale simulation of a turbulent combustion in a reactor containment has provided important new unexpected and non-trivial results about the consequences of such an event. The example has demonstrated that 3-D CFD models are absolutely necessary to capture the complicated interaction between the flow field and the combustion rate in complex multi-compartment buildings.

From the view point of hydrogen risk management, it appears now mandatory that the accumulation of several hundred kg of hydrogen in a combustible mixture (e.g. coupled with low steam concentration) must be avoided with early acting countermeasures. The installation of recombiners alone cannot significantly reduce the early hydrogen inventory because of their slow start-up behavior. A substantial hydrogen removal by recombiners is only obtained on the time scale of hours.

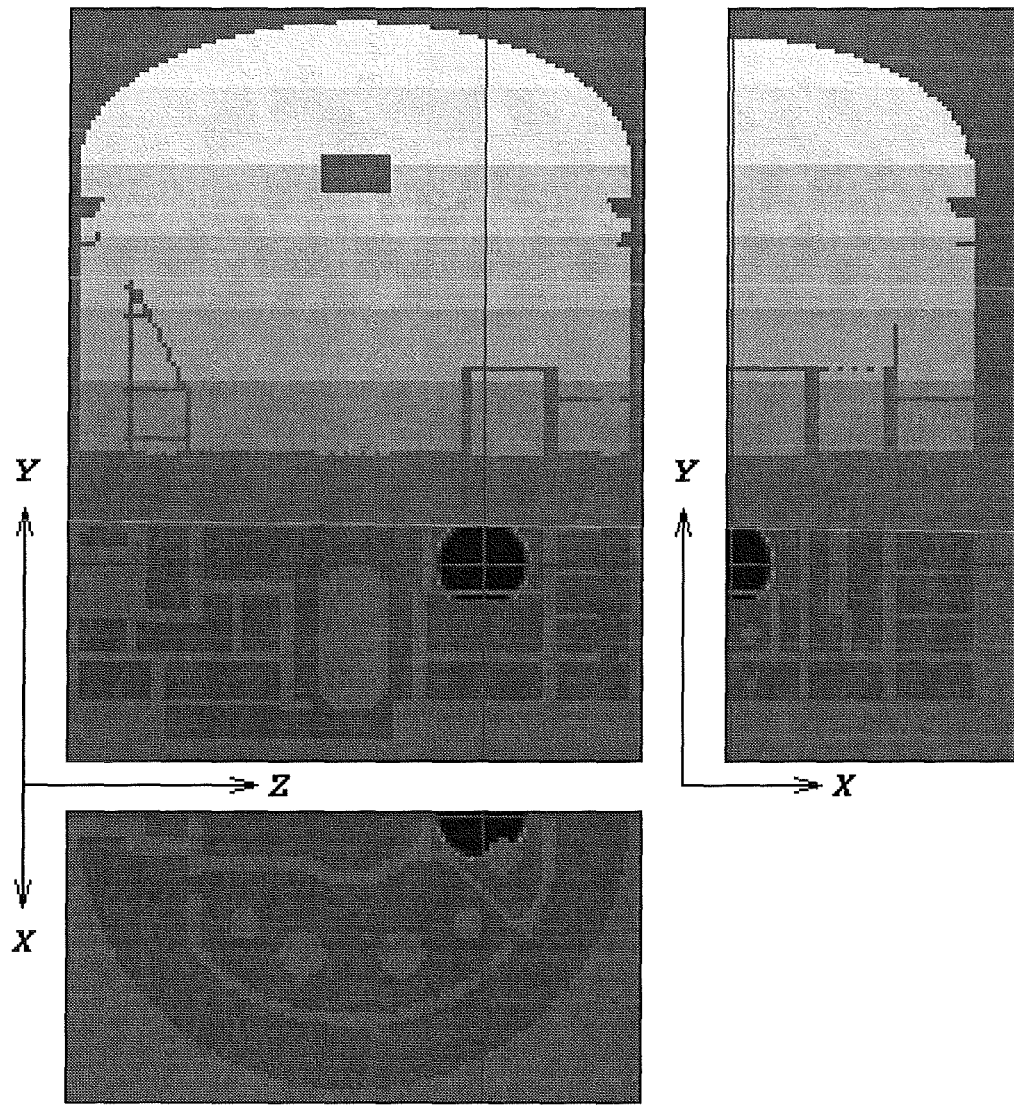


Figure 5.42: Initial hydrogen distribution in the analyzed full scale turbulent combustion case. Stratified  $H_2$ -air mixture 9 - 13 vol.%  $H_2$ , future PWR containment with  $75\ 000\ m^3$  free volume.

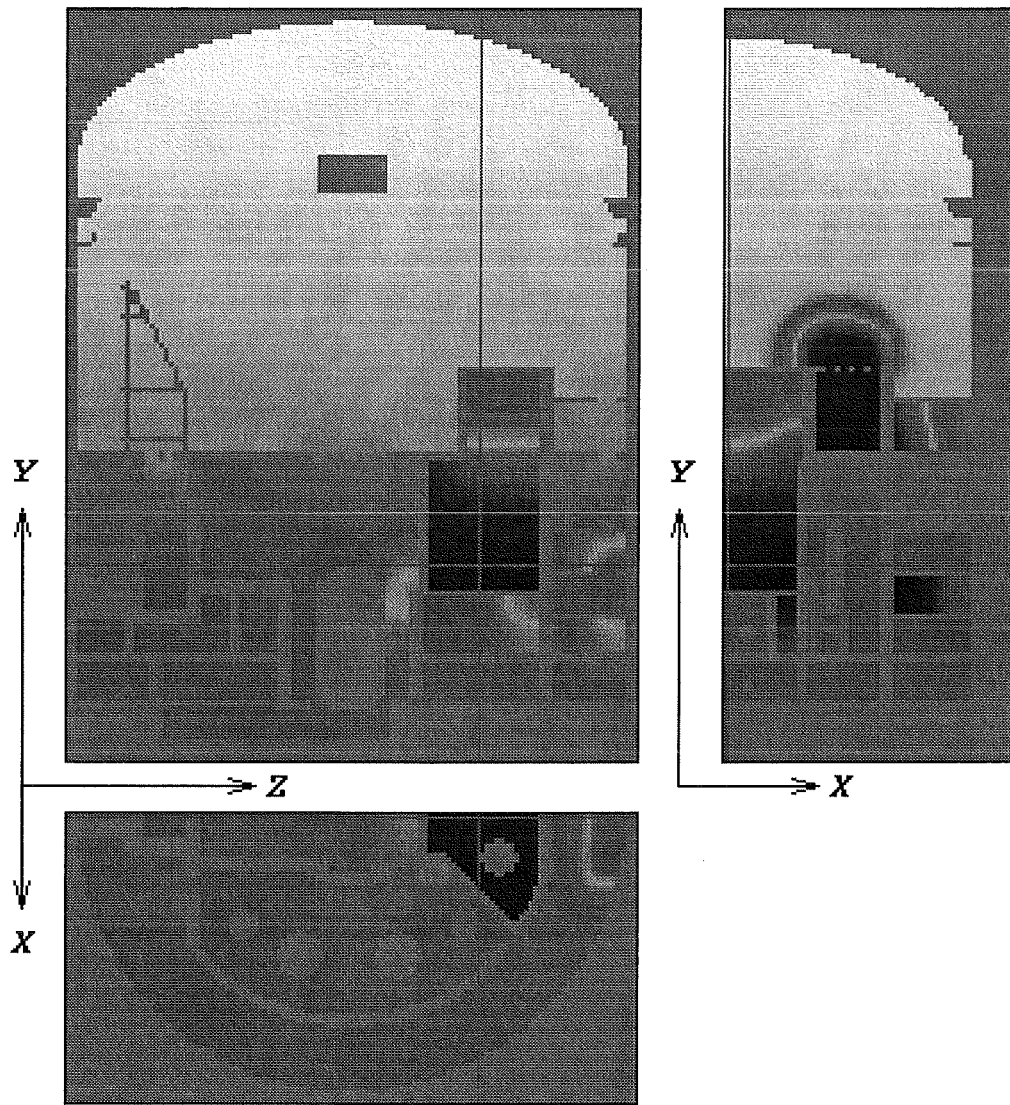


Figure 5.43: Early stage of  $H_2$ -air combustion in analyzed reactor case, 0.283 seconds after ignition.

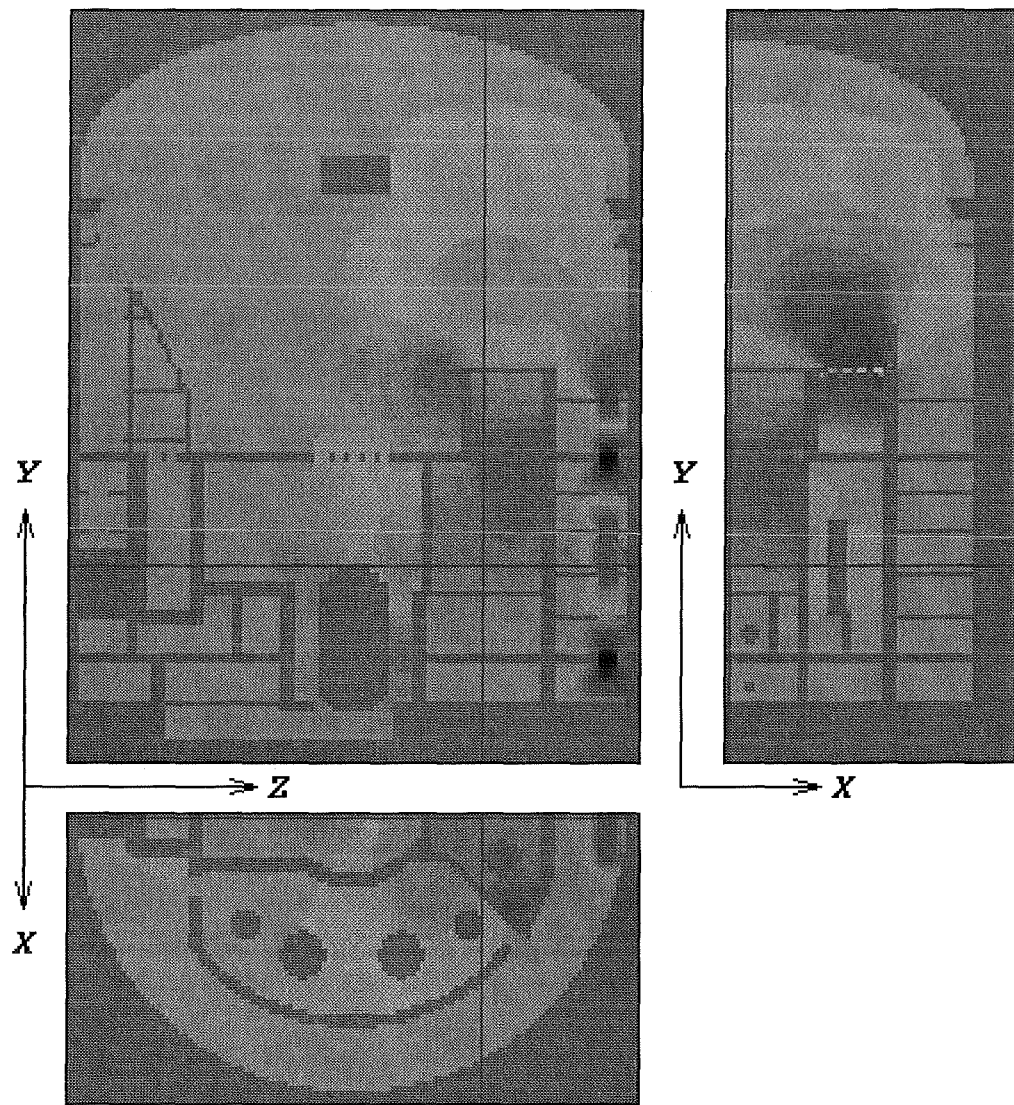


Figure 5.44: Computed vertical mass velocities during the early stage of the combustion. The shown velocity field ranges from -110 to +250 m/s, time = 0.283 seconds after ignition.

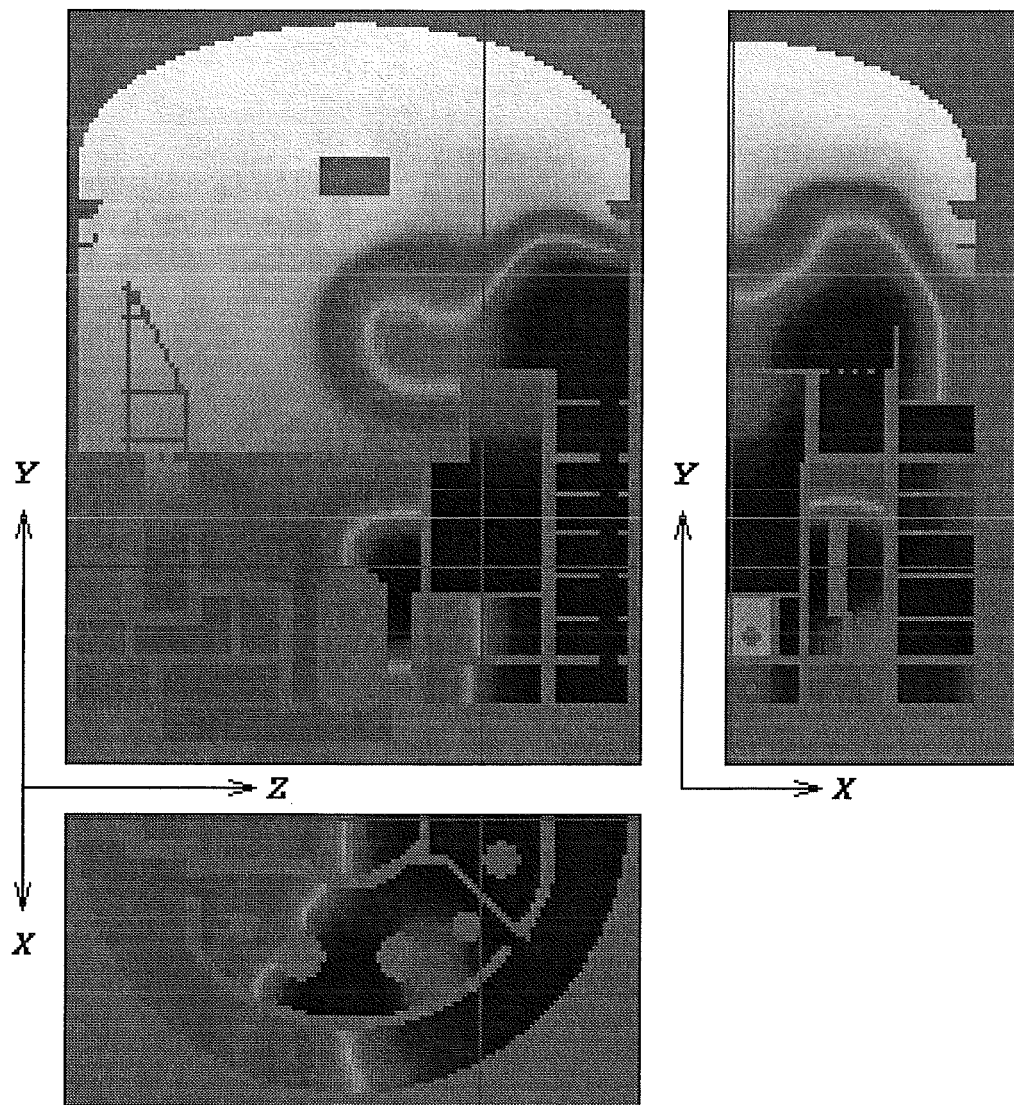


Figure 5.45: Fully developed turbulent combustion in the containment with flame speeds ranging between 70 and 150 m/s, time = 0.412 seconds after ignition.

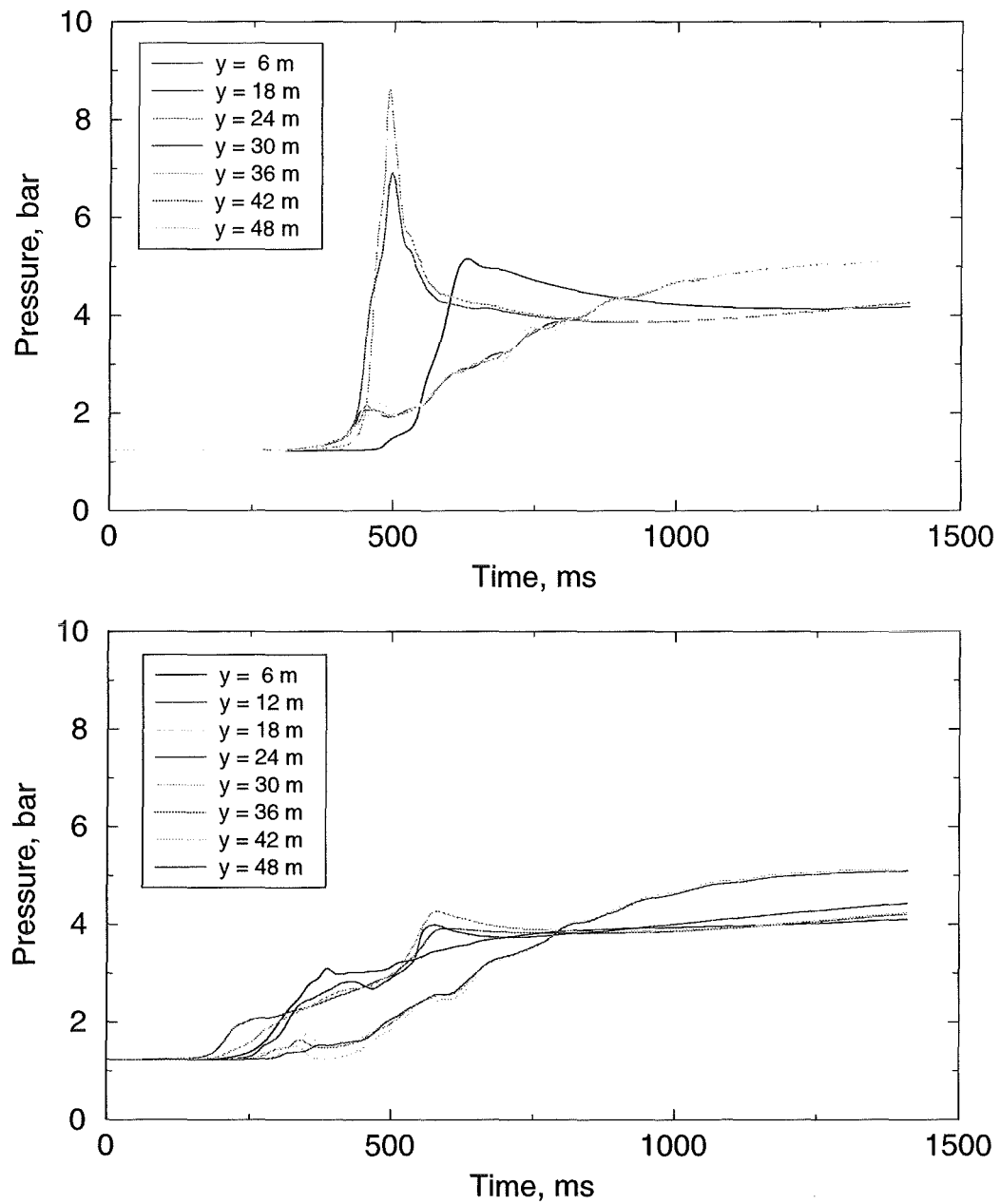


Figure 5.46: Containment pressure loads from fast turbulent combustion of about 700 kg of hydrogen in a full size containment. Top: pressure on the left containment wall, opposite from ignition point at different heights. Bottom: pressures on right containment wall near ignition point.

# Bibliography

- [1] L.V. Benet, C. Caroli, P. Cornet, N. Coulon, and J.-P. Magnaud. Modeling of Local Steam Condensation on Walls in Presence of Non-Condensable Gases. Application to a LOCA Calculation in Reactor Containment Using the Multidimensional GEYSER/TONUS code. In *NUREG/CP-0142*, pages 1443–1455. Proc. of the 7th International Meeting on Nuclear Reactor Thermal-Hydraulics NURETH-7, Saratoga Springs, New York, September 10-15, 1995.
- [2] B.W. Marshall Jr. Hydrogen:Air:Steam Flammability Limits and Combustion Characteristics in the FITS Vessel. Technical report, Sandia National Laboratories, 1986. SAND84-0383.
- [3] Kanzleiter, T., Holzbauer, H., Fischer, K., Häfner, W., Geiß, M., 1996, “HYJET-/PASCOS-Versuche im Modellcontainment”, Abschlußbericht BF-R40.075-01 für das Bundesministerium für Bildung, Wissenschaft, Forschung und Technologie, Eschborn, Germany.
- [4] J. R. Travis, J. W. Spore, P. Royl: “GASFLOW: A Computational Fluid Dynamics Code for Gases Aerosols, and Combustion”, Report LA-13357-M, FZKA-5994, Vol. I-III, October 1998.
- [5] H. Karwat et al.: “State of the Art Report SOAR on Containment Thermo-hydraulics and Hydrogen Distribution”, Report NEA/CSNI/R(99)7, Paris 1999.
- [6] P. Royl, J. R. Travis, E. A. Haytcher, and H. Wilkening, “Analysis of Mitigating Measures during Steam/Hydrogen distributions in Nuclear Reactor Containments with the 3D Field Code GASFLOW”, AECL-11762, NEA/CSNI/R(96)8, Winnipeg 1996.
- [7] P. Royl, J. R. Travis, W. Breitung, L. Seyffarth: “Simulation of Hydrogen Transport with Mitigation Using the 3D Field Code GASFLOW”, ISBN 0-89448-624-1, Orlando 1997.
- [8] P. Royl, G. Necker, J. W. Spore, J. R. Travis: “3D Analysis of Hydrogen Recombination Experiments in the Battelle Model Containment with the

GASFLOW Code", Jahrestagung Kerntechnik 98, München, 26.-28. Mai, 1998. Bonn: Inforum GmbH, 1998, S. 183-86.

[9] M. A. Movahed: "Recombiner model for lumped parameter codes, validation and application", International Workshop on Hydrogen Research for Reactor Safety, Munich 19-21 September 1994.

[10] Z. M. Shapiro, T. R. Moffette: "Hydrogen Flammability Data and Application to PWR Loss-of-Coolant Accident", WAPD-SC-545, Bettis Plant, September 1957.

[11] M. Sonnenkalb: "Unfallanalysen für DWR mit dem Integralcode Melcor 1.8.3", GRS-A-2579, June 1998.

[12] W. Baumann: "Effects of oversized jet flow areas in GASFLOW analysis- Investigations of Canadian Gas Mixing Tests", 6. Fortschrittsbericht Zusammenarbeit FZK/EVU/Siemens, März 1999.



# Chapter 6

## Conclusions and recommendations

### 6.1 Experimental investigations

Within the present project experimental investigations were performed by two partners, FZK and TUM. The purpose was to provide a common database to all partners for the validation and calibration of the numerical models that were developed within this project. The experimental database required for the calibration must cover variations of three major influence parameters: length scale, turbulence level and mixture composition. By splitting the experimental work load to two partners it was possible to perform experiments on four different length scales. At TUM experiments were performed in the TUM glass tube and in the PHD-tube to provide data on small scales. At FZK the 12m-tube was used for medium scales and RUT experiments covered reactor typical scales.

With data from four different experimental facilities the experimental database, which has been developed within the present project, is unique in its size and completeness. In addition to provide data for the validation of numerical codes the experiments also provide useful insight into the physical phenomena involved in turbulent combustion processes.

In all experimental setups a variation of the obstacle configuration allowed a variation of the turbulence parameters. Blockage ratios between 0.1 and 0.9 were employed in the tests. The smallest obstacles merely act as well defined wall surface roughness. Vortices are shed from the edges of the obstacles but the mean flow is not strongly modified by the obstacles. In this case flow and combustion are controlled by turbulence generation. Very large obstacles (or high blockage ratios) primarily limit the mass flow rates through the tube. Very high velocities and high turbulence levels are produced near the orifices, large recirculation areas exist in the corners behind the obstacles. A flame propagates in this situation very fast in a center region and pockets of unburned gas remain behind the leading

flame where they burn rather slowly. Here the combustion process is dominated by the fluid dynamics at the orifices. For intermediate blockage ratios both of these effects become equally important.

In all four experimental facilities the mixture composition of the hydrogen-steam-air mixtures was varied. In close agreement with the needs in reactor applications the experiments were focused on lean hydrogen-air mixtures and lean hydrogen-air mixtures with steam.

The experimental conditions achieved in the different tubes covered a wide range of combustion regimes, from slow propagating flames with partially flame quenching, over accelerating flames, fast accelerating flames and sonic flames, to quasi-detonations.

From the experimental work the following conclusions can be drawn.

- Incomplete combustion (flame does not reach the end of the tube) is not possible for mixtures with more than 10.5 %  $H_2$  independent of scale, obstacle configuration and initial pressure.
- For  $H_2$  concentrations lower than 10.5 % a lower initial pressure increases the probability of complete combustion (flame reaches the end of the tube).
- Results are only a weak function of obstacle spacing.
- For the mixtures under investigation ( $H_2$ -air,  $H_2$ - $O_2$ -Ar,  $H_2$ - $O_2$ - $N_2$ ,  $H_2$ - $O_2$ -He,  $H_2$ -air- $CO_2$ ) three phases in the combustion process can be distinguished. A slow acceleration phase ( $v_F < 250m/s$ ) is followed by a fast acceleration phase ( $v_F < 600m/s$ ). Later the flame propagates with a constant flame velocity in the tubes with repeated obstacles.

## 6.2 Code development

Before we summarize our results on code development and application it is useful to clarify once again the purpose what can be expected from numerical simulations.

Numerical simulations can be performed mainly for two reasons. Firstly, numerical simulations can help in analyzing experimental data. Here the calculation provides additional data not available from the experiment diagnostics. By comparing data that are available both in the experiment and the calculation the validity and quality of the numerical results is checked. Since the experimental data are readily available it is possible to perform calculations with different model parameters and select the calculation that gives the best agreement for further analysis. This approach implies that good agreement between measurement and calculations is also an indication for a good quality of the additional data produced in the calculation.

The second purpose of performing numerical simulations is to predict the behavior of systems that are not available to experimental investigation, e.g. a full scale reactor containment. Obviously the important feedback mechanism between measurement and calculation that allowed to optimize the numerical solution is no longer available. Thus the requirements on the numerical simulation are much higher. While such predictive tools would be very useful, e.g. in the design phase of new plants, the evaluation of such codes requires careful analysis.

To add the predictive capabilities described above to combustion codes several points must be checked:

- Numerical methods must be verified (e.g. solving numerical test cases)
- Model parameters must be determined and the models must be calibrated (e.g. comparison to experimental data).
- The range of validity of model parameters must be determined and the limitations of the models must be identified (e.g. calculation of different experimental data sets).
- The effects of parameter variations must be understood.

The state of the art allows combustion simulations of the first type as described above. Fully predictive calculations are not yet possible with a sufficient level of confidence.

In this project the necessary steps to use combustion codes on large scales with only limited feedback requirements were performed. This is an important step in code development toward 'blind' test calculations.

Several combustion codes have been developed and were evaluated within this project.

CEA provided the TONUS code. This code uses 2D or 3D unstructured grids, it has a specialized low Mach number solver and uses an eddy-break-up model with Said-Borghi extension as combustion model. One feature of this code is that it allows a coupling to a lumped parameter code. This allows a rapid but approximate treatment of the distribution phase of an accident scenario. The coupling makes this code a good choice for parameter studies which are too expensive in complete 3D models. However, since a low Mach number solver is used, only relatively slow combustion processes can be calculated with this code. TONUS was applied to a benchmark test with 10 % hydrogen in air and was capable to compute this test.

FZK has developed the combustion code COM3D. This is a full 3D code, that uses a structured grid and an explicit TVD solver. As combustion model an eddy-break-up model with Said-Borghi extension is used. For high turbulence intensities also an Arrhenius type burning model is available. However, it was found that all combustion simulations performed so far were within the regime of

the eddy-break-up model. Due to the structured grids and an optimized solver the code is generally very fast, but the solver is not efficient for slow combustion processes with low turbulence levels. A test case with 10 % hydrogen in the small TUM tube could not be calculated satisfactorily. However, for all other tests the code gave good results. A remarkable feature of this code is that most of the experiments could be calculated with the approximately same value of the empirical eddy-break-up constant. For many experiments a value of 6.0 gave reasonable results.

REACFLOW is the combustion code from JRC. This code uses 2D and 3D unstructured grids in combination with an eddy-break-up model for combustion. A prominent feature of this code is the possibility to perform an adaptive grid refinement. The code was successfully applied to most of the benchmark tests. It was found that the results depend strongly on the model constant in the eddy-break-up model. The option to switch between 2D and 3D and the adaptive grid refinement make this code complementary to COM3D.

At TUM a code was developed on the basis of CFX/TASCflow. This code uses 2D or 3D unstructured grids. It uses a one-dimensional PDF model for the combustion processes. This combustion model is undoubtedly more advanced from the physical point of view than the eddy-break-up model used in the other codes. However, this comes at the prize of increased computational effort. While this code seems very promising for future development, its current state seems insufficient for full scale reactor applications. It should be pointed out that most partners plan some kind of PDF model for future versions of their codes. In these versions they will profit from the experience collected at TUM.

Figure 6.1 summarizes the ranges of applicability for the different codes. This figure once again emphasizes that the codes are complementary to each other. While no single code covers the whole area of interesting combustion regimes, a combination of the different codes can describe the whole combustion process from ignition over the flame acceleration regime to fully developed detonations.

The benchmark calculations emphasized the merits and deficits of the different codes. However, it is remarkable that REACFLOW and COM3D produced very similar results in the benchmark test. Both codes use very different meshes and different solvers, but implement the governing equations in a similar way. Thus these codes demonstrate that the solutions are independent of implementation details. The agreement between the two codes can be interpreted as an important additional validation of one code by the other.

In addition to the combustion code COM3D the distribution code GASFLOW is routinely used at FZK. This code has been verified against a set of test cases and is accepted as a tool for distribution calculations in full scale containments.

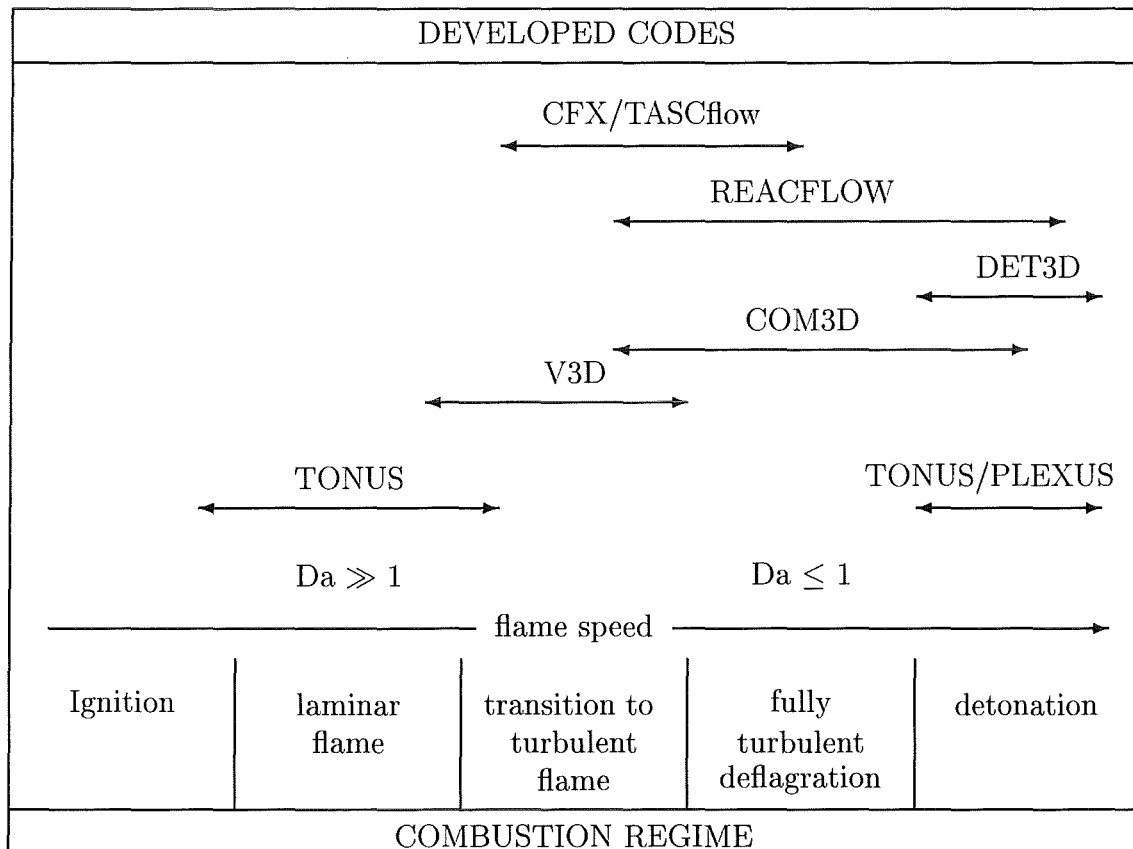


Figure 6.1: Overview of validity range of verified three-dimensional hydrogen combustion codes

### 6.3 Model application

The codes developed in this project were applied to large scale problems as far as the state of development of the codes allowed such applications.

Results of distribution calculations using GASFLOW were presented for the Battelle Hyjet tests. For these tests a comparison to the available experimental data gives good agreement. The calculations therefore strengthen the confidence in the GASFLOW code when applied to general configurations.

With GASFLOW a so called 'dry scenario' was calculated for the EPR. In this scenario the in-vessel gases are released to the containment via the IRWST. It could be shown that even with a very conservative  $H_2$ -source the combustion could be ignited safely without large pressure development if the igniter positions are chosen correctly. A DDT criterion was developed and applied for this purpose.

The efficiency of sump heating and the effect of recombiners were analyzed for a design basis accident (DBA) in Biblis A. In operation since 1974 this plant has an electric power output of 1225 MWe. The Biblis A containment was modeled with about 120000 computational cells in 3D. A large break LOCA with the DBA  $H_2$ -source was simulated. The main result was that the sump heating acts as an effective hydrogen mitigation measure by homogenizing the atmosphere. After the end of the steam injection, stratified conditions first developed. As soon as the sump temperature exceeded the temperature in the dome, a global convection loop developed in the whole containment leading to a practically uniform  $H_2$  concentration.

The effectiveness of recombiners in a DBA was confirmed for Biblis A. Four NIS recombiners were positioned in the inner containment rooms. Due to the excentric hydrogen release location the recombiners removed hydrogen with significantly different rates. The Biblis analysis has shown that realistic recombiner predictions require high spatial resolution of the flow field and a precise calculation of the local  $H_2$ -concentration at the recombiner inlet. Averaged  $H_2$ -concentrations will result only in approximate  $H_2$  removal rates.

For the TONUS code results for a set of connected rooms were presented. When the flame propagation is not too slow the combustion is described reasonably well with this code. A design study for the EPR was performed with COM3D. The results of this calculation give an impression of the importance of focusing and wave propagation effects in large 3-D geometries. The behavior of the calculated solutions looks very reasonable to the eyes of experts. Quite unexpected and non-trivial results were obtained for this full scale reactor calculation, e.g. that the maximum flame speed was not obtained in the regions of maximum  $H_2$  concentration, but rather in those containment regions were turbulence generation and  $H_2$  content together assumed peak values. However, as has been previously discussed it is difficult to judge the quality of such calculations as long as only one set of results from one code is available.

## 6.4 Recommendations

From the experimental work the limits of the different combustion regimes in tubes could be more precisely identified. However, it seems that the conditions that can be expected during a severe accident in a nuclear containment do not lie a priori in a 'safe' combustion regime. The key issue is to predict the combustion regime, because this largely determines the possible containment loads. This emphasizes the need for an accurate modeling of the combustion process as was attempted in the present project.

To determine the combustion regime that can be expected in a given situation, simple criteria, that can be easily applied and evaluated from 3-D distribution calculations, must be derived from the large set of experimental data now available. Progress on the development of such criteria has been made. These criteria help to decide, whether a given code is appropriate for the situation under investigation.

The limitations of the present combustion models do not allow fully quantitative predictions of the detailed containment loads. This once again emphasizes the importance of conservative assumptions. At the present state results on reactor scales still show uncertainty which should be accounted for with reasonably large safety margins.

In order to check the results of numerical simulations, parameter variations for a given problem should be performed. Such parameter variations must prove, that the uncertainty in the input parameters, has no significant effect on the results. This approach helps to build confidence in numerical results were a comparison to experimental data is not possible.

The work performed in this project demonstrated that it is important to consider the whole sequence of events in an accident scenario. From the experience with the different codes it is clear that no single code can cover this whole accident sequence. As a result different codes should be used for the different phases, e.g. calculation of hydrogen and steam sources, distribution and combustion. This necessitates the definition of common interfaces between different codes. Such interfaces would then allow to pass data from one computer code to another.

Furthermore the important question that needs to be addressed is to choose the appropriate tool for a given task in practical applications. For many of the every day engineering tasks it would be inefficient to employ the most advanced and complex modeling tools giving the currently best possible answers. On the other hand with increasing requirements on the precision of safety analysis a demand for detailed and sophisticated modeling exists. Therefore a good compromise seems to be the compilation of a hierarchy of models with increasing level of detail, starting from 0-D lumped parameter models to high resolution 3-D tools. The model choice is then primarily governed by the type of processes to be resolved and the required precision (see Figure 6.2).

With respect to simulations of turbulent combustion first level models neglect-

	lumped parameter	current CFD	high resolution CFD
Fluid mechanics equations	simplified mass and energy conservation  incompressible no directions	Reynolds/Favre averaged Navier-Stokes equations including momentum conservation  fully compressible	same as current CFD
Grid	0-dimensional average volume of control zone $\approx 1000 m^3$	3-dimensional average volume/cell $\approx 1 m^3$ for distribution, $\approx 0.05 m^3$ for turbulent combustion	3-dimensional high resolution grid, e.g. adaptive mesh refinement, $\approx 10^{-6} m^3$
Turbulence model	none	two equations (k- $\epsilon$ , RNG k- $\epsilon$ , k- $\omega$ , ...)	Large eddy simulation
Combustion model	empirical stretching functions (e.g. functions)	extended eddy-break-up and empirical Arrhenius  1-D PDF	multidimensional $\beta$ -PDF  ILDM reduced chemistry

Figure 6.2: Hierarchy of models for simulation of distribution and turbulent combustion in severe reactor accidents

ing momentum exchange have very restricted predictive value. The next level of computational complexity which allows representation of 3-D global unsteady, but statistically averaged flow fields, provides estimates for the influence of momentum exchange and the effects from the other previously neglected terms in the Navier-Stokes equations. This level of modeling allows realistic assessments of potential structural loads due to high speed combustion events. However, this kind of approach can still miss events that are triggered by localized processes and can then develop into global combustion events. Examples are ignition by hot spots or detonation onset through gasdynamic-reactive resonances. Reliable modeling of this kind of processes requires an even more advanced modeling level which is able to resolve the smallest flow scales, e.g. by sophisticated dynamic mesh refinement.

The main characteristics of these three levels of modeling complexity are summarized in Figure 6.2

## 6.5 Concluding remarks

Codes developed in this project allow now the investigation of reactor scale problems by experienced experts. The numerical tools can give interesting insights into the combustion processes in complex 3D geometries. But caution is necessary when interpreting the results.

The codes are not yet sufficiently validated to allow quantitative predictions of the combustion loads under all circumstances. However, the codes allow now qualitative studies of the complex turbulence/chemistry interaction processes taking place in realistic large scale 3-D geometry configurations.



# **Annex A**

## **Micro-recombiner model**

## Micro-Recombiner Model

M. A. Movahed

Siemens/KWU Offenbach Germany

### **Summary**

Passive auto-catalytic recombiner (PAR) has been used to mitigate the hydrogen risk in nuclear power plant during severe accident with core degradation and Zr steam reaction.

*Precise knowledge of the recombination process in PAR is indispensable for forecasting of the potential threat of the containment integrity due to accumulated hydrogen.*

*The quality of the simulation of the PAR in computer code is depend on the implemented recombiner model, which determines the removal capacity of the corresponding recombiner type.*

*The available empirical recombiner models consider some macro scopic thermo hydraulic parameter of the flow like pressure, temperature, hydrogen concentration at the inlet of the recombiner and some recombiner type depended specific property like size of catalytic surfaces, mass flow rate through the recombiner and pressure lost between the inlet and outlet of the recombiner as well as using an efficiency factor to take into account the incompleteness of the recombination process due to dilution of the atmosphere.*

*For the understanding of the recombination process close to the catalytic surfaces envisaging of the micro scopic phenomena of the molecular transport in the boundary layer is essential for the determination of their removal capacity and optimization of the recombiner layout.*

*The following micro scopic consideration shows us the differences between the both types of consideration.*

### **1. Introduction**

Hydrogen can accumulate in the containment of nuclear power plant during a severe accident with core degradation, which will be produced due to Zr steam reaction.

Without a suitable hydrogen removal system containment integrity can be jeopardized if the hydrogen concentration increases high enough to get DDT (Deflagration Detonation Transient) or global detonation.

For this purpose, different recombiners and igniters has been developed, optimized and qualified for the severe accident applications.

- Igniters can burn safely high amount of hydrogen at flammability limit if a deliberated arrangement of igniter can be determined and their effectiveness can be shown numerically and experimentally. Such demonstration is difficult and costly. Since the rate of hydrogen production during most of the severe accident scenario is small, a certain number of **passive auto-catalytic recombiner** (PAR) can keep hydrogen concentration below the critical limit to avoid unintentionally violent hydrogen burn which can jeopardize the containment integrity. PAR can remove hydrogen below the flammability limit even by lean oxygen as well as by diluted atmosphere by steam,  $\text{CO}_2$  or other inert gases.
- Different empirical macro-recombiner model has been developed and validated by several experiments. All these recombiners model take into account some of the thermo hydraulic parameter of the flow like pressure, temperature, hydrogen concentration at the inlet of the recombiner and some recombiner type depended specific property like size of catalytic surfaces, mass flow rate through the recombiner and pressure lost between the inlet and outlet of the recombiner and using an efficiency factor to take into account the incompleteness of the recombination process due to dilution of the atmosphere. The mentioned recombiner models don't look at molecular transport of the gas species in the boundary layer into the catalytic surface which is essential for the understanding of the recombination process and optimization of the recombiner layout as well as the determination of their removal capacity.

The present micro scopic recombiner model considers the molecular transport to the catalytic surfaces. This method promises a better understanding of the recombination process in a box recombiner (like Siemens recombiners figure 1) or a free catalytic plate in an ambient of  $\text{H}_2/\text{air}$  atmosphere. It can lead us beside the prediction of capacity of the recombiners to the significant parameters of the recombiner like:

- steady state mass flow rate
- surface temperature of catalytic plate
- outlet temperature of the gas leave the recombiner
- determination of boundary thickness
- optimization of the recombiner capacity

## 2. General basic equation

The complete system of conservation equations for a multi-component gas mixture, which is deduced from the mathematical molecular theory of non-uniform gases, according to Hirschfelder, Curtiss, Bird/1/ and Chapman, cowling/2/ can be described with the following equations

Continuity equation

$$\frac{\delta \rho}{\delta t} + \operatorname{div} \rho \vec{V} = 0 \quad (2-1)$$

Momentum equation

$$\frac{\delta \vec{V}}{\delta t} + \vec{V} \circ \nabla \vec{V} = -\frac{1}{\rho} (\nabla \circ P) + \frac{1}{\rho} \sum_i n_i \vec{X}_i \quad (2-2)$$

Equation for conservation of the i-th gas component

$$\rho \frac{\delta C_i}{\delta t} + \rho \vec{V} \circ \nabla C_i = -\nabla \circ \vec{J}_i + w_i \quad (2-3)$$

i=1,2,3,...,j-1,j+1,... N

Energy equation

$$\frac{\delta e}{\delta t} + \vec{V} \circ \nabla e = -\frac{1}{\rho} [\nabla \circ (\vec{q} + \vec{q}_R)] - \frac{1}{\rho} (P \circ \circ \nabla \vec{V}) \quad (2-4)$$

with

mass flux vector of the i-th gas component

$$\vec{J}_i = \frac{pm_i}{k^2 T^2} \sum_j m_j D_{ij} \left\{ \frac{kTC_j}{m_j} (\nabla \ln \rho + \nabla \ln T - \nabla \ln p + \nabla \ln C_j) + \left( \frac{kT}{m_j} - \frac{p}{\rho} \right) C_j \nabla \ln p \right\} - D_i^T \nabla \ln T \quad (2-5)$$

and heat flux vector in a multi-component gas mixture

$$\begin{aligned} \vec{q} = & -\lambda \nabla T + \\ & + \sum_i h_i \vec{J}_i - \sum_i D_i^T \left\{ \frac{kT}{m_i} (\nabla \ln \rho + \nabla \ln T - \nabla \ln p + \nabla \ln C_i) + \left( \frac{kT}{m_i} - \frac{p}{\rho} \right) \nabla \ln p \right\} + \\ & + \frac{k^2 T^2}{p} \nabla \ln T \sum_{i,j} \frac{C_j D_i^T}{m_i m_j D_{ij}} \left( \frac{D_j^T}{C_j} - \frac{D_i^T}{C_i} \right) \end{aligned} \quad (2-6)$$

*Heat flux vector of radiation in a multi-component gas mixture:  
(from Rosseland who defined a mean free path for the thermal radiation)*

$$\vec{q}_R = \frac{4c\lambda_R \sigma T^3}{3} \nabla T \quad (2-7)$$

As a first approximation it will be assumed that the mean-free path is constant for a gas volume between two infinite planes.

Net mass rate of production of the component  $i$  due to chemical reaction can be described as follow /3/:

$$\dot{w}_i = M_i \sum_{r=1}^R (v_{ir}^* - v_{ir}) k_{fr} \left[ \pi_{j=1}^N \left( \frac{\rho C_j}{M_j} \right)^{v_{jr}} - \frac{1}{K_{cr}} \pi_{j=1}^N \left( \frac{\rho C_j}{M_j} \right)^{v_{jr}} \right] \quad (2-8)$$

### 3. Basic boundary layer equation for a reacting gas mixture

The boundary layer equation can be deduced with application of the order analysis technique for a steady, two-dimensional, viscous, compressible flow written in Cartesian coordinates (Fig. 2):

Continuity equation

$$\frac{\delta \rho u}{\delta x} + \frac{\delta \rho v}{\delta y} = 0 \quad (3-1)$$

Momentum equation in x-direction

$$\rho \left( u \frac{\delta u}{\delta x} + v \frac{\delta u}{\delta y} \right) = \frac{\delta}{\delta y} \left( \mu \frac{\delta u}{\delta y} \right) - \frac{\delta p}{\delta x} - \rho g \quad (3-2)$$

Momentum equation in y-direction

$$\frac{\delta p}{\delta y} = 0$$

or

$$p = p(x) \quad (3-3)$$

Equation for conservation of species  $i$

$$\rho \left( u \frac{\delta C_i}{\delta x} + v \frac{\delta C_i}{\delta y} \right) = w_i^* - \frac{\delta}{\delta y} J_i^y \quad (3-4)$$

$i=1,2,3,\dots,j-1,j+1, \dots N$

Energy equation

$$\rho c_{pf} (u \frac{\delta T}{\delta x} + v \frac{\delta T}{\delta y}) = \sum_i h_i \frac{\delta}{\delta y} J_i^y - \sum_i h_i w_i^* + u \frac{\delta p}{\delta x} + \mu \left( \frac{\delta u}{\delta y} \right)^2 - \frac{\delta}{\delta y} (q^y + q_R^y) \quad (3-5)$$

equation of state

$$p = \rho \sum_i C_i R_i T \quad (3-6)$$

where the total enthalpy is given

$$h = \sum_i C_i h_i \quad (3-7)$$

and

the enthalpy for the  $i$ -th gas component

$$h_i = \int_0^T c_{pi} dT + h_i^0 \quad (3-8)$$

with

$$J_i^y = \left\{ \frac{p}{kT} \sum_j m_i D_{ij} C_j \left( \frac{\delta}{\delta y} \ln \rho + \frac{\delta}{\delta y} \ln T + \frac{\delta}{\delta y} \ln C_j \right) \right\} - D_i^T \frac{\delta}{\delta y} \ln T \quad (3-9)$$

$$\begin{aligned} q^y = & -\lambda \frac{\delta}{\delta y} T + \sum_i h_i J_i^y - kT \sum_i \frac{D_i^T}{m_i} \left( \frac{\delta}{\delta y} \ln \rho + \frac{\delta}{\delta y} \ln T + \frac{\delta}{\delta y} \ln C_i \right) + \\ & + \frac{k^2 T^2}{p} \left( \frac{\delta}{\delta y} \ln T \right) \sum_{i,j} \frac{C_j D_i^T}{m_i m_j D_{ij}} \left( \frac{D_j^T}{C_j} - \frac{D_i^T}{C_i} \right) \end{aligned} \quad (3-10)$$

and

$$q_R^y = \frac{4c\sigma\lambda_0 T^3}{3} \frac{\delta}{\delta y} T \quad (3-11)$$

#### 4. Boundary conditions

The integration of the boundary layer differential equation needs the fixing of the boundary conditions. These boundary conditions can be divided in two parts.

- **At the catalytic surface  $y=0$**

- **Velocity boundary conditions**

At catalytic wall surface the tangential and normal velocity are zero.

$$u(x,0)=0 \quad (4-1)$$

$$v(x,0)=0 \quad (4-2)$$

### - Temperature boundary condition

An adiabatic wall boundary condition can be assumed for a plate with catalytic active coating on both sides due to the symmetrical recombination process of the plate. Thus, it should be

$$q^y(x,0) + q_R^y(x,0) = 0 \quad (4-3)$$

which states, the released recombination energy will be conducted and absorbed by the flow due to conduction and radiation respectively.

### - Concentration boundary conditions

The concentration of the gas components at the surface of the plate will be controlled by mass and thermal diffusions taking into account, that only heterogeneous catalytic chemical reaction on the plate surface can take place without significant homogenous chemical reaction of the mixture in the boundary layer.

$$J_i^y(x,0) = \begin{cases} 0 & \text{for gas component without involving in the catalytic surface action} \\ J_i^w(x,0) & \text{for gas component which are involved in the catalytic surface action} \end{cases} \quad (4-4)$$

### At free stream outside the boundary layer $y \rightarrow \infty$

It will be assumed that the flow parameters vary only linearly with the  $x$  coordinate at the free stream. Thus the boundary conditions in the free stream are :

### - Velocity boundary conditions

$$u(x, \infty) = u_\infty(x) \quad (4-5)$$

### - Temperature boundary condition

$$T(x, \infty) = T_\infty(x) \quad (4-6)$$

### - Concentration boundary conditions

$$C_i(x, \infty) = C_{i\infty}(x) \quad (4-7)$$

### - Pressure boundary condition

$$p(x, \infty) = p_\infty(x) \quad (4-8)$$

## 5. Transformed boundary layer equations in ordinary differential equations

The partial differential boundary layer equations can be formed to the ordinary differential equations applying the Illingworth-Levy transformation technique /4,5/:

$$\eta = \frac{\rho_\delta(x)U(x)}{\sqrt{2s}} \int_0^y \frac{\rho(x,y)}{\rho_\delta(x)} dy \quad (5-1)$$

where

$$s = \int_0^x \mu_\delta(x)\rho_\delta(x)U(x)dx \quad (5-2)$$

and using the similar solutions for

**- Tangential Velocity**

$$u = U(x)f'(\eta) \quad (5-3)$$

**- Mass concentrations**

$$C_i = C_{i\delta}\alpha_i(\eta) \quad (5-4)$$

**- Volume concentrations**

$$\omega_i = \omega_{i\delta}\beta_i(\eta) \quad (5-5)$$

**- Gas temperature**

$$T = T_\delta\theta(\eta) \quad (5-6)$$

The conservation equations in ordinary differential equations become for :

**- Momentum equation**

$$(Cf'')' + ff'' + \frac{2s}{U} \frac{dU(x)}{ds} \left[ \frac{\rho_\delta}{\rho} - (f')^2 \right] - \frac{2sg}{U^2} \left[ 1 - \frac{\rho_\delta}{\rho} \right] \frac{dx}{ds} = 0 \quad (5-7)$$

**- Species equations**

$$\left\{ \frac{C}{\text{Pr}} \left( \left( \sum_k \frac{C_{k\delta}\alpha_k}{m_k} \right)^2 \sum_j m_i m_j L_{ij} \omega_{j\delta} \beta_j - L_i^T \frac{\theta'}{\theta} \right) \right\}' - C_{i\delta} f \alpha_i' + 2s \frac{dC_{i\delta}}{ds} f' \alpha_i = \frac{2sw_i^*}{\rho U^2 \mu_\delta \rho_\delta} \quad (5-8)$$

**- Energy equation**

$$\begin{aligned} \frac{1}{c_{pf} T_\delta \mu_\delta \rho_\delta} [\rho (q^\eta + q_R^\eta)]' - f \theta' &= \frac{1}{c_{pf} T_\delta \mu_\delta \rho_\delta} \sum_i h_i (\rho J_i^\eta)' - \frac{2s}{\rho c_{pf} T_\delta U^2 \mu_\delta \rho_\delta} \sum_i h_i w_i^* + \\ & \left( \frac{\rho_\delta}{\rho} f' - f' \theta \right) \frac{2s}{T_\delta} \frac{\delta T_\delta}{\delta s} + EcC(f'')^2 \end{aligned} \quad (5-9)$$

with

$$J_i^\eta = J_i^y \frac{\sqrt{2s}}{\rho U} \quad (5-10)$$

and

$$q^\eta = q^y \frac{\sqrt{2s}}{\rho U} \quad (5-11)$$

and

$$q_R^\eta = q_R^y \frac{\sqrt{2s}}{\rho U} \quad (5-12)$$

with the dimension-less transport parameters

**- Chapman-Rubesin's number**

$$C = \frac{\mu \rho}{\mu_\delta \rho_\delta} \quad (5-13)$$

**- Prandtl's number**

$$\text{Pr} = \frac{c_{pf} \mu}{\lambda} \quad (5-14)$$

**- Eckert's number**

$$Ec = \frac{U^2}{c_{pf} T_\delta} \quad (5-15)$$

**- Lewis's number based on multi-component diffusion coefficient**

$$Le_{ij} = \frac{\rho c_{pf} D_{ij}}{\lambda} \quad (5-16)$$

**- Lewis's number based on multi-component thermal diffusion coefficient**

$$Le_i^T = \frac{c_{pf} D_i^T}{\lambda} \quad (5-17)$$

## 6. Boundary conditions for the ordinary differential equations

Boundary conditions of the ordinary boundary layer differential equation are :

**At the catalytic surface**  $y = 0, \quad \eta = 0$

**- Velocity boundary conditions**

Two of the three necessary boundary conditions for the integration of the third order ordinary differential of momentum equation give the velocity conditions namely:

- At catalytic wall surface is the tangential velocity zero.

$$f'(0) = 0 \quad (6-1)$$

- normal velocity is also zero since the catalytic plate is not porous.

$$f(0) = 0 \quad (6-2)$$

#### - Temperature boundary condition

Adiabatic wall gives one of the two necessary boundary conditions for the integration of the second order ordinary differential equation for the energy conservation thus, it should be

$$q''(0) + q_R''(0) = 0 \quad (6-3)$$

#### - Concentration boundary conditions

The heterogeneous catalytic chemical reaction on the plate surface gives one of two necessary boundary conditions for the integration of the each second order ordinary differential equation for the species conservation equations

$$J_i''(0) = \begin{cases} 0 & \text{for gas component without involving in the catalytic surface action} \\ J_i^{\eta w}(0) & \text{for gas component which are involved in the catalytic surface action} \end{cases} \quad (6-4)$$

**At free stream outside the boundary layer**  $y \rightarrow \infty, \eta \rightarrow \infty$

The reminded necessary boundary conditions deliver the flow conditions in the free stream. The boundary conditions in the free steam are :

#### - Velocity boundary conditions

$$f'(\infty) = 1 \quad (6-5)$$

#### - Temperature boundary condition

$$\theta(\infty) = 1 \quad (6-6)$$

#### - Concentration boundary conditions

$$\alpha_i(\infty) = 1 \quad (6-7)$$

Integration of the above higher order ordinary boundary layer differential equations gives us the recombiner capacity and all other global and local key parameters.

## References

- /1/ J. O. Hirschfelder, C. F. Curtiss, R. B. Bird  
Molecular theory of gas and liquids  
John Wiley & sons, Inc.
- /2/ S. Chapman, T. G. Cowling  
The mathematical theory of non-uniform gases  
Cambridge university press
- /3/ W. G. Vincenti, C. H. Kruger  
Introduction to Physical Gas Dynamics  
John Wiley & Sons
- /4/ C. R. Illingworth  
Proc. Roy. Soc. London vol. 199, 1949
- /5/ S. Levy  
J. aeronaut. Sci. Vol. 21, no. 7, 1949

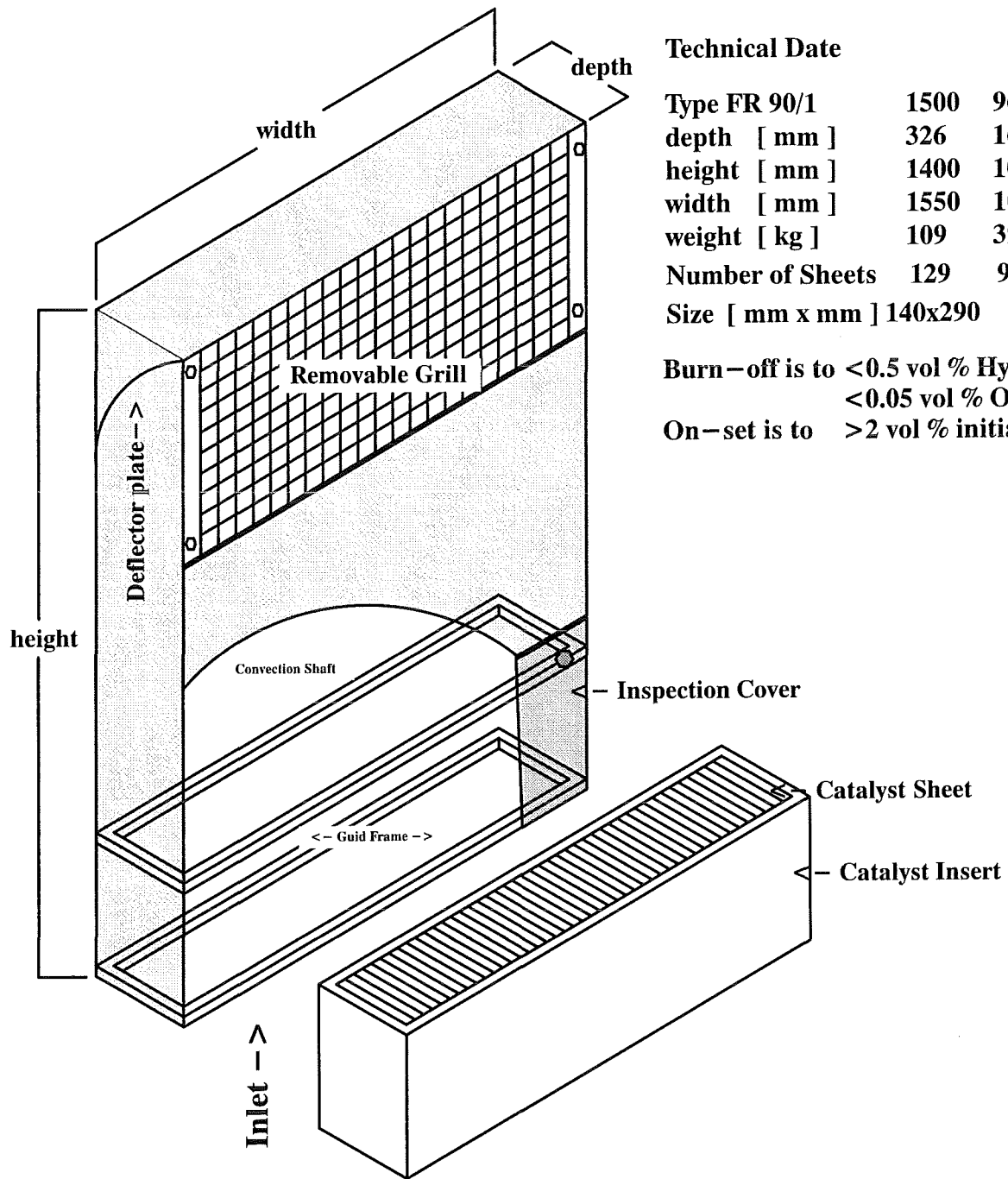
## Symbols and Notation

$c$	velocity of light
$c_{pf}$	frozen specific heat at constant pressure
$C$	Chapman-Rubesin's number
$C_i$	mass fraction of the $i$ -th gas component
$D$	distance of two parallel plate
$D_{ij}$	multi-component mass diffusion coefficient
$\overline{D}_{ij}$	binary mass diffusion coefficient
$D_i^T$	multi-component thermal diffusion coefficient
$e$	specific internal energy
$Ec$	Eckert's number
$f$	reduced tangential velocity
$g$	gravity
$h$	specific enthalpy
$h_i$	specific enthalpy of $i$ -th gas component
$\vec{J}_i$	mass flux vector of the $i$ -th gas component
$J_i^y$	mass flux of the $i$ -th gas component in $y$ -direction
$k$	Boltzmann constant
$k_{cr}$	equilibrium constant of the $r$ -th reaction
$k_{fr}$	reaction rates constant of the reactants
$L_{ij}$	Lewis's number based on multi-component diffusion coefficient
$L_i^T$	Lewis's number based on multi-component thermal diffusion coefficient
$m_i$	mass of the $i$ -th particle
$M_i$	molecular weight of the $i$ -th component

$R$	total number of reactions
$R_i$	gas constant of the $i$ -th component
$N$	number of gas components in the mixture
$p$	pressure
$P$	pressure tensor
$Pr$	Prandtl's number
$\vec{q}$	heat flux vector
$q^y$	heat flux in $y$ -direction
$\vec{q}_R$	heat flux vector of radiation
$q_R^y$	heat flux of radiation in $y$ -direction
$s$	transformed coordinate system
$t$	time
$T$	temperature
$u$	flow velocity in $x$ -direction
$U$	tangential flow velocity in free stream
$v$	flow velocity in $y$ -direction
$\bar{V}$	mass average velocity
$w_i^{\circ}$	net mass rate of production of particles of kind $i$ due to chemical reaction
$x$	coordinate
$\vec{X}_i$	external force acting on the molecules $i$
$y$	coordinate
$\alpha_i$	reduced mass fraction
$\beta_i$	reduced volume fraction
$\eta$	transformed coordinate system
$\lambda$	coefficient of thermal conductivity
$\lambda_R$	average length of mean free path corresponding to photon traveling with the velocity of light
$\mu$	coefficient of shear viscosity
$\rho$	density
$\rho_i$	partial density of $i$ -th gas component
$\theta$	reduced temperature
$\sigma$	Stefan-Boltzmann constant
$V_{ir}^r$	stoichiometric coefficients of reactants of the $i$ -th component in the $r$ -th reaction
$V_{ir}^p$	stoichiometric coefficients of products of the $i$ -th component in the $r$ -th reaction
$\omega_i$	volume fraction of the $i$ -th gas component

## Subscripts

$w$	at the wall surface
$\delta$	free stream
$\infty$	free stream



#### Technical Date

Type FR 90/1	1500	960	320	150
depth [ mm ]	326	166	166	166
height [ mm ]	1400	1000	1000	1000
width [ mm ]	1550	1010	370	200
weight [ kg ]	109	39	24	16
Number of Sheets	129	96	32	15
Size [ mm x mm ]	140x290	130	0 x 140	

Burn-off is to <0.5 vol % Hydrogen and/or  
<0.05 vol % Oxygen

On-set is to >2 vol % initial Hydrogen

Fig. 1 : Siemens Catalytic Recombiners

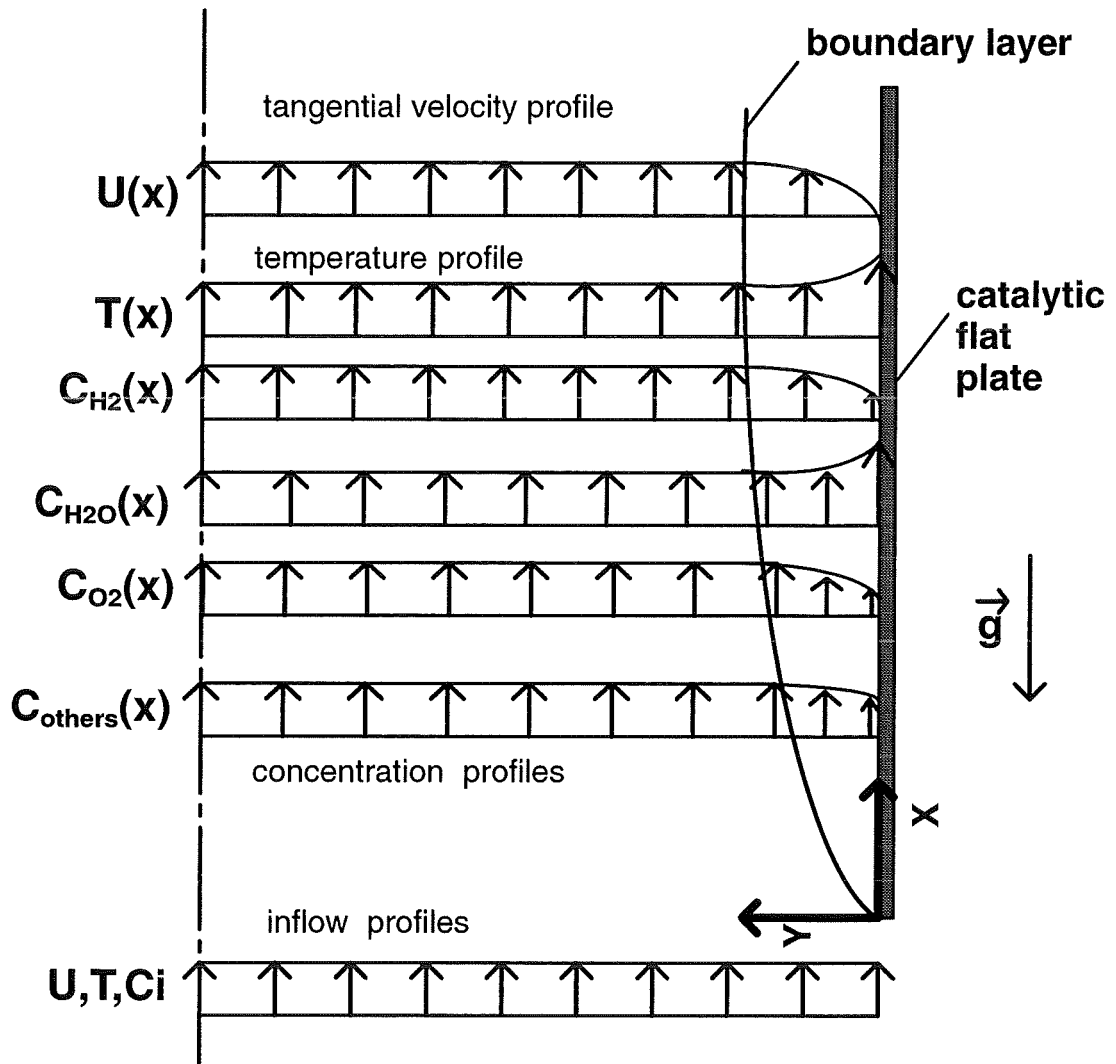


Fig. 2 : Boundary layer on a catalytic flat plate